

PROGRESS IN BIOMEDICAL OPTICS

Proceedings of

Ophthalmic Technologies VIII

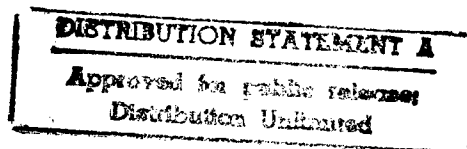
Pascal O. Rol
Karen M. Joos, M.D.
Fabrice Manns
Chairs/Editors

Abraham Katzir
Biomedical Optics Series Editor

24–25 January 1998
San Jose, California

Sponsored by
AFOSR—Air Force Office of Scientific Research
IBOS—International Biomedical Optics Society
SPIE—The International Society for Optical Engineering

19980828 038



DTIC QUALITY INSPECTED 1

Volume 3246

REPORT DOCUMENTATION PAGE

AFRL-SR-BL-TR-98-

Public reporting burden for this collection of information is estimated to average 1 hour per response, including the gathering and maintaining the data needed, and completing and reviewing the collection of information. Send comments regarding this burden estimate or any other aspect of this collection of information, including suggestions for reducing this burden, to Washington Headquarters Services, Directorate for Information Operations and Reports, 1215 Jefferson Davis Highway, Suite 1204, Arlington, VA 22202-4302, and to the Office of Management and Budget, Paperwork Reduction Project (0704-0188), Washington, DC 20503.

0592

1. AGENCY USE ONLY (Leave blank)		2. REPORT DATE		3. REPORT TYPE AND DATES COVERED FINAL 01 Feb 98 To 30 Nov 98	
4. TITLE AND SUBTITLE SPIE'S 1998 INTERNATIONAL SYMPOSIUM ON BIOS '98 <i>Proceedings of Ophthalmic Technologies VIII</i>				5. FUNDING NUMBERS F49620-98-1-0231 61102F 2312/DS	
6. AUTHOR(S) Dr J. Terrence Montonye					
7. PERFORMING ORGANIZATION NAME(S) AND ADDRESS(ES) SPIE - International Soc for Optical Enging P.O. Box 10, 1000 20th Street Bellingham WA 98227-1010				8. PERFORMING ORGANIZATION REPORT NUMBER	
9. SPONSORING / MONITORING AGENCY NAME(S) AND ADDRESS(ES) AFOSR/NL 110 Duncan Avenue Room B115 Bolling AFB DC 20332-8050 Maj William P. Roach				10. SPONSORING / MONITORING AGENCY REPORT NUMBER	
11. SUPPLEMENTARY NOTES					
12a. DISTRIBUTION / AVAILABILITY STATEMENT Approved for public release; distribution unlimited.				12b. DISTRIBUTION CODE	
13. ABSTRACT (Maximum 200 words) The 38 papers contained in this volume are part of the 46 scientific and clinical presentations given at the eighth conference on Ophthalmic Technologies, held 24-25 January, 1998, in San Jose, California. Clinicians, scientists, and engineers came from all regions of the world to attend this meeting, and to present the latest technical advances and clinical results in the field of ophthalmic techniques. This proceedings is divided into five main oral sections: ophthalmic diagnostics, laser interaction with ocular tissues, ocular surgery, ocular implants, and eye modeling, followed by a section containing poster presentations.					
14. SUBJECT TERMS				15. NUMBER OF PAGES	
				16. PRICE CODE	
17. SECURITY CLASSIFICATION OF REPORT (U)	18. SECURITY CLASSIFICATION OF THIS PAGE (U)	19. SECURITY CLASSIFICATION OF ABSTRACT (U)	20. LIMITATION OF ABSTRACT (UL)		

PROGRESS IN BIOMEDICAL OPTICS

Proceedings of

Ophthalmic Technologies VIII

Pascal O. Rol
Karen M. Joos, M.D.
Fabrice Manns
Chairs/Editors

24–25 January 1998
San Jose, California

Sponsored by
AFOSR—Air Force Office of Scientific Research
IBOS—International Biomedical Optics Society
SPIE—The International Society for Optical Engineering

Published by
SPIE—The International Society for Optical Engineering



Volume 3246

SPIE is an international technical society dedicated to advancing engineering and scientific applications of optical, photonic, imaging, electronic, and optoelectronic technologies.



The papers appearing in this book comprise the proceedings of the meeting mentioned on the cover and title page. They reflect the authors' opinions and are published as presented and without change, in the interests of timely dissemination. Their inclusion in this publication does not necessarily constitute endorsement by the editors or by SPIE.

Please use the following format to cite material from this book:

Author(s), "Title of paper," in *Ophthalmic Technologies VIII*, Pascal O. Rol, Karen M. Joos, M.D., Fabrice Manns, Editors, Proceedings of SPIE Vol. 3246, page numbers (1998)

ISSN 0277-786X
ISBN 0-8194-2685-7

Published by
SPIE—The International Society for Optical Engineering
P.O. Box 10, Bellingham, Washington 98227-0010 USA
Telephone 360/676-3290 (Pacific Time) • Fax 360/647-1445

Copyright ©1998, The Society of Photo Optical Instrumentation Engineers

Copying of material in this book for internal or personal use, or for the internal or personal use of specific clients, beyond the fair use provisions granted by the U.S. Copyright Law is authorized by SPIE subject to payment of copying fees. The Transactional Reporting Service base fee for this volume is \$10.00 per article (or portion thereof), which should be paid directly to the Copyright Clearance Center (CCC), 222 Rosewood Drive, Danvers, MA 01923. Payment may also be made electronically through CCC Online at <http://www.directory.net/copyright/>. Other copying for republication, resale, advertising or promotion, or any form of systematic or multiple reproduction of any material in this book is prohibited except with permission in writing from the publisher. The CCC fee code is 0277-786X/98/\$10.00.

Printed in the United States of America

Contents

vii	<i>Conference Committee</i>
ix	<i>Introduction</i>

SESSION 1 OPTHALMIC DIAGNOSTICS

- 2 **Dual-purpose laser irradiation and perfusion testing system for in-vitro experiments using cultured trabecular meshwork endothelial cells [3246-01]**
B. K. Rivera, C. J. Roberts, P. A. Weber, The Ohio State Univ.

- 14 **Corneal group refractive index measurement using low-coherence interferometry [3246-02]**
S. R. Uhlhorn, F. Manns, Univ. of Miami and Bascom Palmer Eye Institute/Univ. of Miami School of Medicine; H. Tahi, Bascom Palmer Eye Institute/Univ. of Miami School of Medicine; P. O. Rol, Univ. of Miami, Bascom Palmer Eye Institute/Univ. of Miami School of Medicine, and Univ. of Zurich (Switzerland); J.-M. A. Parel, Univ. of Miami and Bascom Palmer Eye Institute/Univ. of Miami School of Medicine

- 22 **Corneal autofluorescence in presence of diabetic retinopathy [3246-04]**
L. Rovati, F. Docchio, Univ. degli Studi di Brescia (Italy); C. Azzolini, San Raffaele Hospital/Univ. of Milan (Italy); J. A. Van Best, Leiden Univ. Hospital (Netherlands)

- 28 **Design and performance of a new fluorometer for corneal autofluorescence measurement [3246-05]**
F. Docchio, Univ. degli Studi di Brescia (Italy); J. A. Van Best, Leiden Univ. Hospital (Netherlands); L. Rovati, Univ. degli Studi di Brescia (Italy); H. J. van Schaik, Leiden Univ. Hospital (Netherlands)

- 35 **Measuring lens opacity: combining quasi-elastic light scattering with Scheimpflug imaging system [3246-35]**
R. R. Ansari, NASA Lewis Research Ctr.; M. B. Datiles III, National Institutes of Health; J. F. King, NASA Lewis Research Ctr.; D. Leftwood, National Institutes of Health

- 43 **New method for measurement of in-vivo penetration of UVR into the crystalline lens [3246-36]**
P. G. Söderberg, St. Erik's Eye Hospital/Karolinska Institute (Sweden), Karolinska Institute (Sweden), and Univ. of Miami; S. Löfgren, R. Michael, St. Erik's Eye Hospital/Karolinska Institute (Sweden), X. Gonzales-Cirre, Karolinska Institute (Sweden)

- 48 **Quantitative spatio-temporal image analysis of fluorescein angiography in age-related macular degeneration [3246-37]**
J. W. Berger, Scheie Eye Institute/Univ. of Pennsylvania and Univ. of Pennsylvania

- 54 **Optical coherence tomography using an interferometer with temporal output [3246-38]**
M. Balarin, Univ. of Northern California; S. Jutamulia, In-Harmony Technology Corp.

- 61 **Modification of the Heidelberg retinal laser tomograph and flowmeter to allow measurements in supine patients [3246-39]**
K. M. Joos, C. Singleton, J. H. Shen, W. Sun, D. M. O'Day, Vanderbilt Univ.

- 65 **Methodology and apparatus for using the human iris as a robust biometric** [3246-56]
M. A. Della Vecchia, Wills Eye Hospital; T. Chmielewski, T. A. Camus, M. Salganicoff,
M. Negin, Sensar, Inc.

SESSION 2 LASER INTERACTIONS WITH OCULAR TISSUES

- 76 **Erbium:YAG laser-tissue interactions** [3246-54]
R. W. Snyder, Univ. of Arizona; M. G. Jani, M. Yarborough, G. R. Marcellino, Coherent Lasers
Inc.; R. J. Noecker, T. R. Kramer, Univ. of Arizona; J. Vidaurri, Technological Institute of
Advanced Studies (Mexico)
- 89 **Spot diameters for scanning photorefractive keratectomy: a comparative study** [3246-15]
F. Manns, J.-M. A. Parel, Univ. of Miami and Bascom Palmer Eye Institute/Univ. of Miami
School of Medicine
- 97 **Evaluation of corneal ablation by an optical parametric oscillator (OPO) at 2.94 μm and an
Er:YAG laser and comparison to ablation by a 193-nm excimer laser** [3246-16]
W. B. Telfair, H. J. Hoffman, IR Vision, Inc.; R. E. Nordquist, Wound Healing of Oklahoma;
R. A. Eiferman, Veterans Administration Medical Ctr. Research Service
- 109 **Corneal haze induced by excimer laser photoablation in rabbits is reduced by preserved
human amniotic membrane graft** [3246-18]
M. X. Wang, Vanderbilt Univ. School of Medicine; T. Gray, P. Prabhasawat, X. Ma,
W. Culbertson, R. Forster, K. Hanna, S. C. Tseng, Bascom Palmer Eye Institute/Univ. of Miami
School of Medicine and Univ. of Miami School of Medicine
- 120 **Influence of optical aberrations on laser-induced plasma formation in water and their
consequences for intraocular photodisruption** [3246-19]
A. Vogel, K. Nahen, D. Theisen, R. Birngruber, Medizinisches Laserzentrum Lübeck (FRG);
R. J. Thomas, B. A. Rockwell, Air Force Research Lab.
- 132 **Human cornea wound healing in organ culture after Er:YAG laser ablation** [3246-21]
J. H. Shen, K. M. Joos, R. D. Robinson, D. J. Shetlar, D. M. O'Day, Vanderbilt Univ.
- 136 **Scleral indentation height after laser scleral buckling** [3246-22]
S. W. Kang, Bascom Palmer Eye Institute/Univ. of Miami School of Medicine and College of
Medicine/Chungbuk National Univ. (Korea); J.-M. A. Parel, Bascom Palmer Eye Institute/Univ.
of Miami School of Medicine, Univ. of Miami, Hôtel-Dieu Hospital/Univ. of Paris (France),
and Ctr. Hospitalier Sart-Tilman/Univ. de Liège (Belgium); F. Manns, Bascom Palmer Eye
Institute/Univ. of Miami School of Medicine and Univ. of Miami; J. Lee, College of Medicine/
Seoul National Univ. (Korea); W. E. Smiddy, Bascom Palmer Eye Institute/Univ. of Miami
School of Medicine

SESSION 3 OCULAR SURGERY

- 144 **Development and clinical application of excimer laser corneal shaping** [3246-08]
P. Homolka, R. Biowski, Univ. of Vienna (Austria); W. Husinsky, Ch. Blaas, Vienna Univ. of
Technology (Austria); C. Simader, I. Baumgartner, St. Kaminski, Univ. of Vienna (Austria);
G. Grabner, St. Johanns Hospital (Austria)

- 152 **Preliminary results of hyperopic photorefractive keratectomy (HPRK) at Cedars-Sinai Medical Center** [3246-09]
E. I. Maguen, A. B. Nesburn, Cedars-Sinai Medical Ctr. and Jules Stein Eye Institute/UCLA School of Medicine; J. J. Salz, Cedars-Sinai Medical Ctr. and Doheny Eye Institute/Univ. of Southern California School of Medicine
- 160 **Hyperopic photorefractive keratectomy and central islands** [3246-10]
P. G. Gobbi, F. Carones, A. Morico, L. Vigo, R. Brancato, San Raffael Hospital/Univ. of Milan (Italy)
- 172 **Erbium:YAG laser for cataract extraction** [3246-55]
R. W. Snyder, Univ. of Arizona; M. G. Jani, M. Yarborough, G. R. Marcellino, Coherent Lasers Inc.; R. J. Noecker, T. R. Kramer, Univ. of Arizona; J. Vidaaurri, Technological Institute of Advanced Studies (Mexico)
- 185 **Hybrid retinal tracking and coagulation system** [3246-30]
C. H. G. Wright, E. D. Oberg, S. F. Barrett, U.S. Air Force Academy
- 192 **Vitreoretinal surgery and mid-infrared cutting lasers** [3246-31]
C. Azzolini, P. G. Gobbi, R. Brancato, San Raffaele Hospital/Univ. of Milan (Italy)
- 196 **Anterior capsulotomy using the CO₂ laser** [3246-32]
A. Barak, T. Ma-Naim, M. Rosner, O. Eyal, M. Belkin, Goldschleger Eye Research Institute/Tel Aviv Univ. (Israel) and Tel Aviv Univ. (Israel)
- 199 **Er:YAG laser ablation of epiretinal membranes in perfluorocarbon fluid-filled eyeballs: a preliminary report** [3246-28]
M. Frenz, M. Ith, H. P. Weber, Univ. of Bern (Switzerland); Th. Wesendahl, P. Janknecht, Univ. of Freiburg (FRG)

SESSION 4 OCULAR IMPLANTS

- 210 **Deep sclerectomy with and without implant: an in-vivo comparative study** [3246-11]
M. Yamamichi, Bascom Palmer Eye Institute/Univ. of Miami School of Medicine and Fukuoka Univ. (Japan); P. Sourdille, Clinique Sourdille (France); H. Tahi, Bascom Palmer Eye Institute/Univ. of Miami School of Medicine and Ctr. Hospitalier Sart-Tilman/Univ. de Liège (Belgium); V. Jallet, Corneal Industrie SA (France); F. L. Villain, Corneal Industrie SA (France) and Univ. of Miami; F. Fantes, Bascom Palmer Eye Institute/Univ. of Miami School of Medicine; J.-M. A. Parel, Bascom Palmer Eye Institute/Univ. of Miami School of Medicine, Univ. of Miami, Hôtel-Dieu Hospital/Univ. of Paris (France), and INSERM (France)
- 216 **Gel injection adjustable keratoplasty (GIAK): keratometric evaluation on eye-bank eyes** [3246-13]
H. Tahi, Bascom Palmer Eye Institute/Univ. of Miami School of Medicine and Ctr. Hospitalier Sart-Tilman/Univ. de Liège (Belgium); H. Kondo, Bascom Palmer Eye Institute/Univ. of Miami School of Medicine and Fukuoka Univ. (Japan); B. Duchesne, Bascom Palmer Eye Institute/Univ. of Miami School of Medicine and Ctr. Hospitalier Sart-Tilman/Univ. de Liège (Belgium); W. E. Lee, W. Feuer, Bascom Palmer Eye Institute/Univ. of Miami School of Medicine; J.-M. A. Parel, Bascom Palmer Eye Institute/Univ. of Miami School of Medicine, Ctr. Hospitalier Sart-Tilman/Univ. de Liège (Belgium), Univ. of Miami, and Hôtel-Dieu Hospital/Univ. of Paris (France)

SESSION 5 EYE MODELING

- 228 **Eye aberration analysis with Zernike polynomials [3246-23]**
V. V. Molebny, I. H. Chyzh; V. M. Sokurenko, Institute of Biomedical Engineering (Ukraine);
I. G. Pallikaris, L. P. Naoumidis, Vardinoyannion Eye Institute of Crete/Univ. of Crete Medical
School (Greece)
- 238 **Aberration mapping for sight correction [3246-24]**
V. V. Molebny, V. N. Kurashov, D. V. Podanchuk, A. V. Kovalenko, Institute of Biomedical
Engineering (Ukraine); I. G. Pallikaris, L. P. Naoumidis, Vardinoyannion Eye Institute of
Crete/Univ. of Crete Medical School (Greece)
- 249 **Scleral tissue light scattering and matter diffusion [3246-51]**
V. V. Tuchin, Saratov State Univ. (Russia); I. L. Maksimova, Institute of Radio Engineering and
Electronics (Russia); A. A. Mishin, Institute of Precision Mechanics and Control (Russia);
A. Kh. Mavlutov, Saratov State Univ. (Russia)

SESSION 6 POSTER SESSION

- 262 **Automatic system for corneal ulcer diagnostics: II [3246-41]**
L. Ventura, C. Chiaradia, S. J. F. Sousa, Univ. de São Paulo (Brazil)
- 267 **Low-cost endothelium cell counter for slit lamp [3246-42]**
L. Ventura, S. J. F. Sousa, P. E. Ribeiro, Jr., C. A. C. Caetano, Univ. de São Paulo (Brazil)
- 272 **Weak laser radiation mechanism for ciliochoroidal detachment [3246-43]**
T. N. Semyonova, I. S. Maximova, S. N. Tatarintsev, Saratov Medical Univ. (Russia)
- 276 **Molecular mechanism of light damage to the eye [3246-45]**
V. A. Lapina, Institute of Physics (Belarus); G. V. Lyakhnovich, T. A. Gapeeva, Institute of
Photobiology (Belarus)
- 283 **Physical and optical limitations using ArF-excimer and Er:YAG lasers for PRK [3246-46]**
V. A. Semchishen, Laser Research Ctr. (Russia); M. Mrochen, T. Seiler, Univ. of Dresden (FRG)
- 290 **CWhatUC: a visual acuity simulator [3246-47]**
D. D. Garcia, Univ. of California/Berkeley; B. A. Barsky, Univ. of California/Berkeley and
School of Optometry/Univ. of California/Berkeley; S. A. Klein, School of Optometry/Univ. of
California/Berkeley
- 299 **Modeling of the light-scattering spectra by the human eye lens [3246-49]**
D. M. Zhestkov, Saratov State Univ. (Russia); I. L. Maksimova, Institute of Radio Engineering
and Electronics (Russia); V. V. Tuchin, Saratov State Univ. (Russia)
- 307 **Changes of superoxiddismutase and catalase activity in the aqueous humor in hyphema after
magnet-laser stimulation [3246-50]**
I. S. Maksimova, A. V. Borisov, V. Yu. Maximov, Saratov Medical Univ. (Russia)
- 311 *Addendum*
- 313 *Author Index*

Conference Committee

Conference Chairs

Pascal O. Rol, University of Miami, Bascom Palmer Eye Institute/University of Miami School of Medicine, and University of Zurich (Switzerland)
Karen M. Joos, M.D., Vanderbilt University
Fabrice Manns, University of Miami and Bascom Palmer Eye Institute/University of Miami School of Medicine

Program Committee

Michael Belkin, M.D., Goldschleger Eye Research Institute/Tel Aviv University (Israel) and Tel Aviv University (Israel)
Franco Docchio, Università degli Studi di Brescia (Italy)
Bernard Duchesne, M.D., Centre Hospitalier Sart-Tilman/Université de Liège (Belgium)
Pier Giorgio Gobbi, San Raffaele Hospital/University of Milan (Italy)
Benedikt J. Jean, M.D., Eberhard-Karls-Universität Tübingen (FRG)
Ezra I. Maguen, M.D., Cedars-Sinai Medical Center and Jules Stein Eye Institute/UCLA School of Medicine
Peter J. Milne, University of Miami
Jean-Marie A. Parel, Bascom Palmer Eye Institute/University of Miami School of Medicine, University of Miami, Hôtel-Dieu Hospital/University of Paris (France), and Centre Hospitalier Sart-Tilman/Université de Liège (Belgium)
Jerry Sebag, M.D., Doheny Eye Institute/University of Southern California School of Medicine
Jin Hui Shen, Vanderbilt University
Per G. Söderberg, M.D., St. Erik's Eye Hospital/Karolinska Institute (Sweden)
William B. Telfair, IR Vision, Inc.
Valery V. Tuchin, Saratov State University (Russia)
Franck Villain, Corneal Industrie SA (France)
John M. Williams, M.D., Marshfield Clinic

Session Chairs

- 1 Ophthalmic Diagnostics
 Ezra I. Maguen, M.D., Cedars-Sinai Medical Center and Jules Stein Eye Institute/UCLA School of Medicine
 Valery V. Tuchin, Saratov State University (Russia)
 Jerry Sebag, M.D., Doheny Eye Institute/University of Southern California School of Medicine
 Pier Giorgio Gobbi, San Raffaele Hospital/University of Milan (Italy)
- 2 Laser Interactions with Ocular Tissues
 Per G. Söderberg, M.D., St. Erik's Eye Hospital/Karolinska Institute (Sweden)
 Franco Docchio, Università degli Studi di Brescia (Italy)

- 3 Ocular Surgery
 Karen M. Joos, M.D., Vanderbilt University
 William B. Telfair, IR Vision, Inc.
 Benedikt J. Jean, M.D., Eberhard-Karls-Universität Tübingen (FRG)
 Pascal O. Rol, University of Miami, Bascom Palmer Eye Institute/University
 of Miami School of Medicine, and University of Zurich (Switzerland)
- 4 Ocular Implants
 Karen Margaret Joos, M.D., Vanderbilt University
 Pascal O. Rol, University of Miami, Bascom Palmer Eye Institute/University
 of Miami School of Medicine, and University of Zurich (Switzerland)
- 5 Eye Modeling
 Per G. Söderberg, M.D., St. Erik's Eye Hospital/Karolinska Institute (Sweden)
 Fabrice Manns, University of Miami and Bascom Palmer Eye Institute/University
 of Miami School of Medicine
- 6 Poster Session
 Jin Hui Shen, Vanderbilt University
 Pascal O. Rol, University of Miami, Bascom Palmer Eye Institute/University
 of Miami School of Medicine, and University of Zurich (Switzerland)

Introduction

The 38 papers contained in this volume are part of the 46 scientific and clinical presentations given at the eighth conference on Ophthalmic Technologies, held 24–25 January, 1998, in San Jose, California. Clinicians, scientists, and engineers came from all regions of the world to attend this meeting, and to present the latest technical advances and clinical results in the field of ophthalmic techniques.

This proceedings is divided into five main oral sections: ophthalmic diagnostics, laser interaction with ocular tissues, ocular surgery, ocular implants, and eye modeling, followed by a section containing poster presentations.

In the ophthalmic diagnostic sessions, speakers presented updates on recently developed measurement techniques (autofluorescence, Scheimpflug, dynamic light scattering), as well as new evaluation methods.

During the session on laser interactions with ocular tissues, the dynamics of photoablation with the free-electron laser, the Er:YAG laser, and the new OPO system at $2.94\ \mu\text{m}$ were discussed and compared to those obtained with the ArF laser. Also presented was a promising IR laser technique for retinal surgery, based on the use of a filling material transparent at $2.94\ \mu\text{m}$. The influence of different optical parameters, such as spot size and optical aberrations in the laser beam, were discussed.

In the ocular surgery sessions, the latest clinical results in laser surgery were shown: corneal photoablation with various ArF excimer and infrared lasers, and the cutting of different intraocular structures. An exciting advancement in tracked laser surgery was also described.

The session on intraocular implants was limited this year. However, the latest techniques on modeling the optical properties of the eye, and in particular the cornea, were presented. The poster session was truly an international event that included participants from South America, North America, and Europe.

The chairs would like to thank all the program committee members, session chairs, speakers, and participants, as well as the SPIE staff for making this conference a success.

We hope that Ophthalmic Technologies IX, to be held in San Jose, 23–24 January, 1999, will continue to offer a unique opportunity for clinicians, physicists, and engineers to discuss the latest advances in ophthalmic techniques.

Pascal O. Rol
Karen M. Joos, M.D.
Fabrice Manns

SESSION 1

Ophthalmic Diagnostics

Dual-purpose laser irradiation and perfusion testing system for *in-vitro* experiments using cultured trabecular meshwork endothelial cells

Brian K. Rivera¹, Cynthia J. Roberts^{1,2}, Paul A. Weber²

The Ohio State University

¹Biomedical Engineering Center, 270 Bevis Hall, 1080 Carmack Road, Columbus, OH 43210

²Department of Ophthalmology, UHC 5A, 456 W. 10th Avenue, Columbus, OH 43210

ABSTRACT

The means by which Argon laser trabeculoplasty (ALT) lowers intraocular pressure (IOP) is a matter of debate. Mechanical and biological laser-tissue interaction theories have been proposed. To investigate the effect laser irradiation has upon the aqueous outflow facility of trabecular meshwork (TM) cells, a suitable *in-vitro* model is required. Therefore the purpose of this study was to design, construct, and validate a laser irradiation and perfusion testing apparatus. The system was designed to utilize cultured TM cells seeded onto filter supports. Outflow facility will be quantified by calculating the hydraulic conductivity of the monolayer. An appropriate filter support was located, and its perfusion characteristics determined using water. Afterwards, the steady state perfusion flow rate of the filter was ascertained to be 0.096 ± 0.008 ml/min when culture medium is used. Following these tests, a single, baseline perfusion experiment was conducted using a TM cell monolayer. Analysis of the data produced a baseline hydraulic conductivity of 0.673 ± 0.076 $\mu\text{l}/\text{min}/\text{mm Hg}/\text{cm}^2$, well within the range found in previous reports. A dual purpose, *in-vitro* cellular perfusion and laser irradiation testing apparatus has been developed, tested, and validated using known baseline cellular perfusion values. Future experiments will be conducted to verify these initial findings, and further experiments will be conducted using Argon laser irradiation. The response of the TM cell monolayer will then be compared to the baseline figures.

Keywords: argon laser trabeculoplasty, trabecular meshwork, hydraulic conductivity, outflow facility, perfusion

1. INTRODUCTION

In 1979, Wise and Witter reported that Argon laser treatment of the trabecular meshwork (TM) found in the anterior chamber angle of the eye caused a reduction of intraocular pressure (IOP).¹ This finding caused some controversy in the world of ophthalmology, since only five years earlier, Gaasterland and Kupfer reported that the application of Argon laser energy in a similar manner could be used to induce glaucoma in Rhesus monkeys.² The treatment techniques differed, however, in the time of exposure and the number of burn spots applied to the TM. In the earlier study (Gaasterland and Kupfer), the total energy delivered by the laser was significantly higher. During the next several years following the report by Wise and Witter, data acquired from several limited clinical trials confirmed that Argon laser irradiation of the TM using a shorter exposure time and a restricted number of burn spots did serve to lower IOP.^{3,4,5,6,7}

Today, the procedure is now known as Argon laser trabeculoplasty (ALT), and it is commonly used clinically as a means of treatment in pharmacologically unresponsive cases of primary open angle glaucoma (POAG). Yet, the mechanism by which ALT produces this reduced IOP remains unknown. The currently accepted theory of action, initially proposed by Van Buskirk,⁸ is that Argon laser irradiation increases the metabolic function of the TM cells adjacent to the target site, causing an increase in the facility of outflow.

In order to study the interaction of laser irradiation with the cells of the TM, it is appropriate to develop a suitable *in-vitro* model, which pays particular attention to outflow facility. It would be impossible to perform such experiments on living human volunteers, or animals. The development of such an experimental system presents several unique complications. First, the model must suitably simulate the physiological conditions found *in-vivo* for the results to be credible. Second, the testing system must be able to quantify the behavior of the TM cellular material under investigation. Finally, the system must permit relatively simple and direct access to the cellular material being tested, for the purpose of evaluation both during and immediately following laser irradiation.

2. PURPOSE

The primary purpose of this project was to develop an *in-vitro* perfusion testing apparatus using cultured TM endothelial cell monolayers that would permit the application of laser irradiation to the cells, and quantify the cellular response to this stimulus with respect to outflow facility. The motivation for such a project is the need to optimize the treatment parameters of ALT. The current procedure is destructive in nature, and thus limits the number of treatments that may be applied. It is hoped that the future experiments for which this system is intended will lead to a less destructive procedure that could be repeated, if necessary. The purpose of the preliminary experiments detailed in this report was to determine if the proposed model is a viable means by which these more detailed experiments can be carried out. This will be accomplished by comparing the results obtained from the data analysis to those found in previous reports.

3. BACKGROUND / LITERATURE REVIEW

3.1 Mechanical Theories of Laser-TM Tissue Interaction

Wise believed that open angle glaucoma was caused by an age-related stretching of the collagen-elastin lamellae of the TM ring.^{1,9} Due to this stretching, the diameter of the TM ring would increase, pressing the TM tissue against the more rigid sclera of the eye. The rings would then collapse upon themselves, pressing the lamellae together, and closing the intertrabecular spaces. According to Wise's theory, it is this collapse of the lamellae and closure of the intertrabecular spaces that causes the decrease in the facility of aqueous outflow.

Wise proposed that ALT reduces the circumference of the TM ring by heat-induced shrinkage of the collagen fibers of the lamellae when laser burns are applied over 360° of the trabecular area, along the inner surface of the ring. The scar tissue that was produced at the burn sites would contract inward, pulling the trabecular ring back toward the center of the anterior chamber thereby decreasing the diameter of the ring, and elevating the lamellae. This action, in turn, would cause an increase in the width of the interlamellar spaces in regions that were not subjected to laser irradiation.⁹

A similar mechanism of action was hypothesized by Van der Zypen and Fankhauser.^{10,11} In this proposal, the widening of the intertrabecular spaces adjacent to the spot of the burn was due to disruption of the collagen fibrils of the TM, rather than heat-induced shrinking. The studies by Van der Zypen and Fankhauser were conducted using live monkeys, rather than human subjects or a similar *in-vitro* model. Despite the use of monkeys in the study, the authors noted that, "the decrease in IOP obtained after trabeculoplasty in glaucomatous human eyes coincides in time with that at which widening of the intertrabecular spaces by degeneration of cells and degradation of intercellular material was seen."¹¹

3.2 Biological Theories of Laser-TM Tissue Interaction

In 1983, Van Buskirk, et al, proposed a different mechanism of action for ALT following *in-vitro* experiments on pairs of donor globes and anterior chamber eye segments supported in organ culture. In each experimental set, one eye or anterior segment was treated with 80 burn spots over 360° using the same laser treatment parameters as Wise and Witter, while the other was used as a control. The studies confirmed that trabecular ring displacement did occur, but that this phenomenon was most noticeable at "high levels of intraocular pressure" (≥ 40 mm Hg).⁸

It was also noted that the density of trabecular cells at a location midway between adjacent burn spots in eyes treated with ALT was reduced by 39%. There was an increased rate of radioactive sulfate (³⁵S) uptake by the cells, suggesting that laser irradiation induced a marked increase in the production of the extracellular matrix and glycosaminoglycans (GAGs). From these results, it was hypothesized that ALT stimulates cellular division and migration, and increases the rate of extracellular matrix synthesis in the TM cells that remain following the procedure.⁸

This hypothesis was supported in 1988 and 1989 following studies by Bylsma, et al,¹² and Acott, et al,¹³ respectively. In the former study, corneoscleral organ cultures obtained from human donor globes were treated using ALT over 180° of the TM ring, after which they were returned to organ culture with radioactive, tritiated (³H) thymidine added to the culture medium as a DNA marker.¹² It was found that TM cells in the ALT treated chamber segments had a 180% increased rate of DNA replication over the basal level in the two days immediately following treatment. More importantly, this increase in DNA replication was observed throughout the entire 360° of the TM ring, in both the 180° treated area, and the 180° untreated area. From these observations, it was postulated that ALT, presumably by increasing the basal level of TM cellular division, provides a means by which the most robust TM cells are selected. These cells replicate in response to ALT stimulation, causing an increase in extracellular matrix (ECM) production and facility of aqueous outflow.¹²

The second study, conducted by Acott, et al, was likewise performed on corneoscleral organ cultures obtained from human donor globes using the same laser parameters as Bylsma, et al. Unlike traditional ALT treatments, the laser spots were applied just anterior to the center portion of the TM area. Tritiated thymidine, or radioactive carbon (¹⁴C) thymidine was used as a DNA marker. It was found that the majority of the labeled TM cell nuclei were localized within the anterior

portion of the TM within this same time period. By 7 to 14 days post-op, the number of radiolabeled nuclei had dropped to within normal levels consistent with controls. Concurrent with this decrease, there was an observed increase in the number of radiolabeled nuclei located within the posterior portion of AIT-treated TM. Following these results, it was hypothesized that the newly replicated TM cells originating within the anterior portion of the TM migrate to and repopulate the AIT burn sites.¹³

3.3 Previous *In-Vitro* Perfusion Studies

There are essentially three techniques whereby TM material has been maintained in *in-vitro* perfusion cell culture, ranging from simple to very complex. The most simple method was that used by Acott, Bylsma, Van Buskirk, and associates¹⁴, based upon a technique initially used by Funderburgh.¹⁵ In this procedure, the entire corneoscleral region was excised from a donor globe using a circular incision approximately 2.0 mm posterior to the limbus. Upon separation, the iris and ciliary body were carefully teased away. Under microscopic evaluation, any remaining iris root was carefully removed using tweezers so as not to dissociate the TM from the scleral spur.¹⁵ The entire corneoscleral explant was then rinsed and placed into whole organ culture, concave side down. Media was exchanged every 2 or 3 days, and the cultures were allowed to stabilize for a period of one week prior to experimental use.

The most complex TM culture method previously reported was that initially used by Johnson and Tschumper¹⁶, and later duplicated by Erickson-Lamy and associates.¹⁷ Both investigations used bisected anterior eye chambers supported in whole organ culture with the lens and vitreous removed. These anterior segments were placed in specially modified culture containers that, *in-vitro*, replicated a closed globe. Perfusion medium was forced through the aqueous outflow pathway under simulated physiological pressures through special access ports that were incorporated into the design of the culture containers. Pressure within the perfused segment was monitored throughout the experimental process using a pressure transducer introduced through a second access cannula.^{16,17} Perfusion took place either at a constant flow rate¹⁶, or at constant pressure¹⁷, and the perfused material was removed from the culture chambers daily.

In contrast to these two previous techniques, the final perfusion method did not require whole organ culture of the anterior chamber, but instead used single endothelial cell monolayers.^{18,19,20} In these studies, conducted by Perkins and associates,^{18,19} and Alvarado,²⁰ the cells were seeded and grown on filter membrane supports, which were then placed in a specialized perfusion testing apparatus. In the initial report by Perkins, et al, the purpose of the cellular perfusion system was "...to assess the physiological resistance to flow and the effects of pharmacological agents."¹⁸

In a more detailed article published by Perkins the following year, the results of flow studies carried out solely upon TM cell monolayers was reported.¹⁹ The response of the TM cells to pharmaceutical stimulation was quantified using a measure of the cellular hydraulic conductivity. This value can be thought of as the facility of fluid flow or the fluid permeability across the cell monolayer. Hydraulic conductivity (expressed in terms of $\mu\text{l} / \text{min} / \text{mm Hg} / \text{cm}^2$) was calculated using the formula $L_p = Q / PA$, where L_p represents the hydraulic conductivity, Q is defined as the flow rate of the perfusion medium, P is the perfusion pressure, and A is the surface area of the TM cell monolayer.¹⁹

A specialized TM-filter perfusion apparatus was designed and used in these studies.¹⁹ The perfusion medium passed under pressure from a reservoir bottle through a calibrated flowmeter. Flow rate measurements (Q) were taken at one minute intervals. Downstream from the flowmeter, a pressure tap was used to monitor the perfusion pressure (P). The perfusion medium then passed through the chamber housing the filter support and cell monolayer. According to Perkins, et al, "Perfusion of the cell monolayers was conducted using a pressure of 5 mm Hg, while the pressure at the back of the filter remained at zero (room air)."¹⁹ The perfusion medium consisted of the same growth mixture used to culture the cells, and the entire experimental apparatus (with the exception of the oscilloscope used to monitor the transducer output) was enclosed in a humidified incubator.

4. MATERIALS AND METHODS

In the proposed perfusion testing system, as in that employed by Perkins and Alvarado, the hydraulic conductivity (L_p) was used to quantify the outflow facility of the cell monolayer. As noted previously, two unknowns in the calculation of this figure were of particular importance – the perfusion flow rate (Q), and the perfusion pressure (P). It has been assumed that the area (A) covered by the cell monolayers would be a consistent and known value for the experiments reported herein, and in all future. This area was assumed to be equivalent to the surface area of the filter support.

4.1 Design of the Laser Irradiation and Perfusion Testing Apparatus

In light of the concerns outlined in the previous section, a new perfusion chamber has been designed such that the filter and monolayer are oriented vertically. Perfusion medium flows into the chamber through a side port, and the laser port is located at the top of the chamber, centered with respect to the location of the filter and the cell monolayer. The upper part of

the chamber serves two purposes: to establish a standing reservoir of perfusate, and to permit movement of the laser fiber tube in order to permit variation of the diameter of the output laser irradiation cone.

The standing reservoir of fluid would minimize the effect of any fluid phenomena that might endanger the health of the delicate cell monolayer, and would simulate the effect of aqueous fluid contained within the anterior chamber of the human eye. Movement of the laser fiber in the vertical direction would be required to vary the diameter of the output cone incident upon the cell monolayer. The output cone will vary according to the numerical aperture of the fiber used. Thus, in order to ensure that the energy cone will irradiate the entire cell monolayer equally, it must be adjustable.

The design of the perfusion chamber is shown in greater detail in Figures 1 and 2, as assembled and exploded views, respectively. The majority of the chamber was manufactured from a clear plastic that could be repeatedly gas sterilized or autoclaved. The clear plastic would permit observation of the cell monolayers during perfusion experimentation and allow visual inspection and adjustments to be made in the laser output cone when the laser irradiation experiments are to be conducted.

In order to obtain flow rate data, a variable-area, mechanical flowmeter was selected. Ideally, an electronic flowmeter would be used to reduce the chance of human error due to the observer, and to permit real-time tracking of the flow rate. Unfortunately, such devices are still under development, and those currently in existence would be unable to withstand repeated sterilization procedures. Mechanical flowmeters are very common, and several companies have produced models reportedly capable of detecting and measuring flow rates to as low as 0.2 $\mu\text{l}/\text{minute}$ within $\pm 2\%$ when used with water. However, it should also be noted that as the flow rate drops into this very low regime, so too does the accuracy of both the device and the human observer.

These flowmeters are all based upon the same principle. A small glass or stainless steel spherical float is constrained within a flowtube of variable area. The diameter of the flowtube is slightly larger than the diameter of the float at the input end of the tube, and increases progressively toward the output end. As a flowing fluid passes through the device, the float trapped inside is forced to move up the length of the flowtube in a known relation to the rate of flow. The flow rate is then determined by visually correlating the center of the spherical float with a calibrated scale that has been fused to the outside of the flow tube.

The flowtubes and floats of these devices are usually constructed of glass, which can be repeatedly sterilized without any threat of damage or loss of accuracy. The devices finally selected for use in the perfusion system are shielded, compact flowmeters, produced by Gilmont® Instruments. The size 10 flowmeter is capable of water flow rate measurements from 0.002 to 1.1 ml/minute, while the size 11 flowmeter is capable of measurements from 0.01 to 4.0 ml/minute.

TM cells are attachment-dependent, meaning that they must have a surface to adhere to in order to grow. Perkins^{18,19} and Alvarado²⁰ utilized a filter upon which to grown the cells for use in their perfusion experiments. This same, unique requirement was also carefully addressed in the design of the new perfusion and laser irradiation system. It was decided that the growth substrate should allow complete coverage of the membrane surface by the cells, while at the same time permitting perfusion medium to pass without a significant amount of hindrance to the fluid conduction activity of the monolayer.

One of the other motivating factors for the re-design of the perfusion testing chamber was the need to accommodate larger diameter filters, which were considered for use in the system. It was noted during an examination of the background literature that the flow rates would be extremely low, on the order 0.2 ml/minute. The larger filters were incorporated into the system design in the hopes of increasing the perfusion flow rate. Recall that in the hydraulic conductivity equation, the flow rate is divided by the product of the cellular/filter surface area and the perfusion pressure. In order to maintain a given hydraulic conductivity with this increase in perfused surface area, the flow rate would have to increase as well. It was believed that this would thereby increase the accuracy of the flow rate measurements.

In order to detect and track the perfusion pressure, a new approach was devised for the apparatus using an in-line pressure transducer produced by Abbott Critical Care Systems® which is normally used for blood pressure monitoring.

Figure 1 - Assembled Chamber View
(Part dimensions given in millimeters)

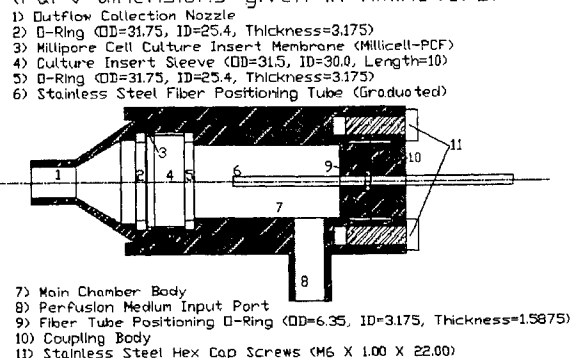
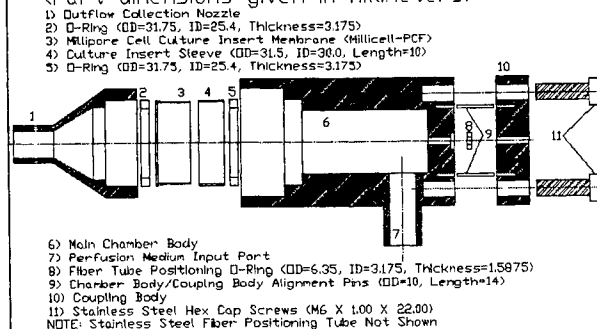


Figure 2 - Exploded Chamber View
(Part dimensions given in millimeters)



Because the new perfusion chamber has been designed to be oriented vertically, the pressure transducer should likewise be mounted in a vertical position against the side of the perfusion apparatus. These devices have the advantage of being relatively inexpensive, and have a known linear response at a given excitation voltage. The only difficulty in using this device with the proposed perfusion system was the need to develop a data acquisition system that could accurately detect and process transducer response voltages on the order of 150 μ V (6.0 V excitation \times 5.0 μ V/V/mm Hg transducer sensitivity \times 5 mm Hg approximate perfusion pressure).

Accurate measurements were necessary to ensure that the sensory element of the pressure transducer was placed as close to the position of the cellular monolayer and filter support as possible. This arrangement allows a more accurate dynamic response to changes in pressure by the transducer, as the pressure measurements taken at this location relative to the column height of the perfusion medium would be equivalent to the fluid pressure exerted upon the cellular monolayer. Additionally, the pressure drop that would normally be encountered due to the tubing used to conduct the fluid medium would be negligible, since the apparatus had been designed such that a standing column of liquid would be contained within the perfusion chamber itself. In the perfusion apparatus used by Perkins and Alvarado, the pressure tap located downstream from the flowmeter would not produce as accurate a measurement because there is a pressure between the pressure tap and the perfusion chamber housing the cell monolayer. This pressure drop is caused by friction between the flowing perfusate and the wall of the tubing conducting the medium.

To resolve the problem of providing support for the cell monolayer, specialized cell culture plate inserts, which resemble small petri dishes were used. While the primary structure of each culture plate insert is composed of an inert plastic material, the base of each insert is actually a filter membrane. According to the manufacturer, the applications for which these specialized inserts were intended include "transport across cell monolayers" and "permeability of cell monolayers".

These filter membranes are produced from a variety of different materials including PTFE, mixed cellular esters (MCE), and polycarbonate (PCF). For these perfusion experiments, a tissue culture treated polycarbonate membrane filter was selected. This differs from the previous experiments by Perkins and Alvarado, in which HATF filter membranes, composed of MCE, were used.^{19,20} The PCF filter type was selected because they have been specially produced to support and encourage cellular adhesion and growth, which in theory should reduce the number of cells required to ensure complete coverage of the filter support. In Perkins' report, it is noted that TM cells had to be seeded onto the HATF filter supports at a density of 10^5 cells/ml to achieve this.¹⁹

These PCF filter membranes were available in three different pore sizes, 0.4 μ m, 3.0 μ m, and 12.0 μ m, and diameters of 12.0 and 30.0 mm. The latter diameter was selected for use in these studies because, as mentioned previously, the flow rate range of the perfusing medium would be limited, and more difficult to measure accurately with the smaller diameter filter size. It was hoped that the larger diameter filter would increase the dynamic range of the perfusion flow rate, which in turn would permit more accurate detection and measurement. The primary drawback to the use of this larger filter, was that the cells would require a longer period of time to cover the entire surface of the filter with a confluent monolayer.

Only the 0.4 and 3.0 μ m pore size filter membranes were considered for use in these perfusion experiments. The smallest pore size is very close to that used by Perkins¹⁹ and Alvarado²⁰ in their experiments, however, it may also serve to impede the fluid conduction activity of the cell monolayer. Hypothetically, the larger pore size would permit a more accurate simulation of the true *in-vivo* condition, as well as an easier and more direct assessment of the cellular monolayer permeability. A preliminary series of tests was run using only the filter supports in order to determine which filter pore size was better suited for actual experimental perfusion studies.

A Pentium[®] based computer with a 120 MHz processing speed served as the base of the data acquisition system. To this, a number of components purchased from National Instruments[®] were added, as well as LabVIEW[™] software for analysis and processing of the data. This software package is the heart of the system for detecting and processing the pressure information. Using LabVIEW[®], block diagram programs with heads-up graphic interfaces and controls are assembled into virtual instruments (VIs) that are run from the computer. The VI's, in turn, read and process the data in real time from the computer acquisition board.

Because the data signals expected from the transducer would be on the order of 150 μ V (0.15 mV), an external amplifier was required. This unique device was one of the extra components that was purchased from National Instruments[®], and was specifically designed for easy calibration and processing of voltage data obtained from strain gauge-type transducers. Calibration and "zeroing" of the transducer signals prior to experimentation was accomplished using on-board potentiometers that were readily accessible to the user.

After the voltage output from the transducer was read and saved by the pressure monitoring VI, it needed to be converted to pressure readings. This was accomplished using the known sensitivity of the pressure transducer and the input voltage from the regulated power supply. Multiplying the transducer sensitivity by the excitation voltage produced the following conversion factor:

$$(6.011 \text{ V, excitation voltage}) \times (5.00 \text{ } \mu\text{V/V/mm Hg, transducer sensitivity}) = 30.055 \text{ } \mu\text{V/mm Hg}$$

The averaged transducer output data, given in terms of μV , was read by the data acquisition system and loaded into a buffer. To convert this output to pressure in terms of mm Hg, this voltage data was then divided by the calculated conversion factor:

$$\text{Transducer Response Voltage} \div 3.055 \times 10^{-5} \text{ V} = \text{Perfusion Pressure (mm Hg)}$$

Because of this conversion, it is easy to see why it is imperative that the transducer be calibrated and zeroed properly prior to experimentation, because even small deviations could have a significant impact upon the calculated average perfusion pressure. After this conversion had been completed, the calculated pressure values were plotted in real time, and the data was written to disk in a text format that could be imported into common spreadsheet programs.

The entire experimental apparatus, with computer and data acquisition components is shown in Figure 3. During experimentation, the entire apparatus with the exception of the computer components and the strain gauge signal-conditioning accessory, was contained within a humidified incubator. The pressure transducer was connected to the strain gauge accessory using 24-gauge telephone wire run through a rear access port of the incubator.

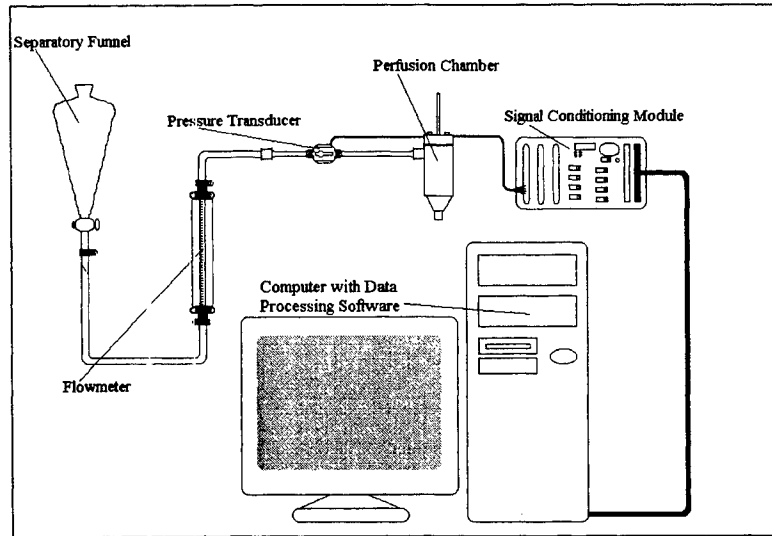


Figure 3 – *In-vitro* laser irradiation and perfusion testing apparatus.

4.2 Data Processing Methodology

A vital piece of information that was not included in previous reports was a detailed description of the numerical method employed to determine the hydraulic conductivity of the cell monolayer. Perkins' report simply states, "The contribution of the filter to the conductivity of the cell layers was subtracted by treating the filter as a resistance in series with the resistance of the monolayer."¹⁹ Using Perkins' statement and Ohm's law as applied to electrical circuit theory ($V=IR$) as a starting point, electrical analogues to the flow rate and perfusion pressure conductivity needed to be found.

Current (I) is defined as "the time rate of change of electrical charge", and is usually expressed in terms of coulombs/second. This would be analogous to the flow rate, which can be thought of as the time rate of change of a quantity of (flowing) fluid. Likewise, voltage (V) is defined as "the difference in energy level of a unit positive charge between two points." It is also commonly referred to as the electromotive force. This would be analogous to the perfusion pressure, which can be thought of as the difference in energy contained within a column of fluid between two different heights. Finally, the resistance (R) in an electrical circuit would be equivalent to the resistance to flow, which would be proportional to $1/A$.

When the perfusion apparatus has been constructed and tests are to begin, there will exist two separate situations with known quantities: perfusion of the filter using culture medium without the cells, and perfusion of the cells and the filter. Using the Ohm's law analogy as applied to the filter only perfusion situation:

$$P_{\text{transducer}} - P_{\text{out}} = Q_{\text{filter}} R_{\text{filter}}$$

That is, the pressure indicated by the transducer minus the pressure at the end of the perfusion system is equivalent to the filter perfusate flow rate multiplied by the resistance of the filter alone. Since the system is open to the outside environment at the end, P_{out} is equal to zero. Rearranging this equation, then, produces:

$$R_{\text{filter}} = P_{\text{transducer}} / Q_{\text{filter}} \quad (1)$$

Now applying Ohm's law to the second situation involving both the cells and the filter, and treating the cellular resistance and filter resistance as series resistors:

$$P_{\text{transducer}} - P_{\text{out}} = Q_{\text{cells+filter}} (R_{\text{cells}} + R_{\text{filter}}) \quad (2)$$

This equation states that the pressure measured by the transducer minus the pressure at the end of the perfusion system is equivalent to the flow rate across both the cell monolayer and the filter multiplied by the sum of the cellular and filter resistances. Substituting equation (1) and the known value for P_{out} into equation (2):

$$P_{\text{transducer}} = Q_{\text{cells+filter}} [R_{\text{cells}} + (P_{\text{transducer}} / Q_{\text{filter}})] \quad (3)$$

Using electrical node theory, the pressure drop across the cells alone (ΔP_{cells}) can be determined:

$$\Delta P_{\text{cells}} = Q_{\text{cells+filter}} R_{\text{cells}}$$

Rearranging this equation produces:

$$R_{\text{cells}} = \Delta P_{\text{cells}} / Q_{\text{cells+filter}} \quad (4)$$

Substituting equation ④ into equation ③:

$$P_{\text{transducer}} = Q_{\text{cells} \cdot \text{filter}} [(\Delta P_{\text{cells}} / Q_{\text{cell} \cdot \text{filter}}) + (P_{\text{transducer}} / Q_{\text{filter}})] \quad ⑤$$

Solve equation ⑤ for the quantity ΔP_{cells} :

$$\begin{aligned} (P_{\text{transducer}} / Q_{\text{cells} \cdot \text{filter}}) &= (\Delta P_{\text{cells}} / Q_{\text{cell} \cdot \text{filter}}) + (P_{\text{transducer}} / Q_{\text{filter}}) \\ (P_{\text{transducer}} / Q_{\text{cells} \cdot \text{filter}}) - (P_{\text{transducer}} / Q_{\text{filter}}) &= (\Delta P_{\text{cells}} / Q_{\text{cell} \cdot \text{filter}}) \end{aligned}$$

Multiplying through by $Q_{\text{cells} \cdot \text{filter}}$ produces:

$$\Delta P_{\text{cells}} = [(Q_{\text{cells} \cdot \text{filter}} P_{\text{transducer}}) / Q_{\text{cell} \cdot \text{filter}}] - [(Q_{\text{cells} \cdot \text{filter}} P_{\text{transducer}}) / Q_{\text{filter}}]$$

Simplifying the fractional values:

$$\Delta P_{\text{cells}} = P_{\text{transducer}} [1 - (Q_{\text{cells} \cdot \text{filter}} / Q_{\text{filter}})] \quad ⑥$$

Now, considering the hydraulic conductivity equation for the cell monolayer alone:

$$Lp_{\text{cells}} = Q_{\text{cells} \cdot \text{filter}} / (A_{\text{cells}} \Delta P_{\text{cells}}) \quad ⑦$$

Substituting equation ⑥ into equation ⑦:

$$Lp_{\text{cells}} = [Q_{\text{cells} \cdot \text{filter}} / (A_{\text{cells}} P_{\text{transducer}})] [1 - Q_{\text{cells} \cdot \text{filter}} / Q_{\text{filter}}]^{-1}$$

This is the key equation for calculating the hydraulic conductivity of the cell monolayer alone. As shown, it is dependent upon the average perfusion flow rate across the cells and the filter, the surface area covered by the cells (also assumed to be the surface area of the filter support), the pressure indicated by the pressure transducer, and the average flow rate across the filters alone.

4.3 0.4 μm and 3.0 μm Pore Size Filter Water Perfusion Experimental Protocol

The first two series of experiments conducted using the proposed apparatus were designed to determine which pore size filter would function best in the perfusion system. Repeating what was said earlier, the perfusion characteristics of the filters that were to provide support for the TM cell monolayer would have to be determined. As demonstrated in the cellular hydraulic conductivity equation, the flow rate across the filter should be a known quantity. Since this figure was to be an average over several tests, it was decided that the filter perfusion flow rate would have to be relatively consistent from test to test. A high degree of variability simply could not be acceptable, since this would present a significant impact upon the later hydraulic conductivities of the TM cell monolayers.

For these preliminary tests, filtered and distilled water was used as the perfusion medium. The bare filter supports were tested alone, no cells had been seeded and grown upon them. Seven filters of each pore size (0.4 and 3.0 μm) were tested. Before the tests began, the pressure transducer was calibrated and zeroed, and then the entire apparatus was assembled. The pressure monitoring virtual instrument was run, and the pressure was set as close to 5.0 mm Hg as possible. The data obtained during this setup period was discarded, and the test was then begun. Flow rate measurements were taken every 30 seconds for the duration of the experiment. The 3.0 μm pore size filters were perfused for a total of 25 minutes, while the 0.4 μm pore size filters were perfused over a period of 15 minutes.

4.4 0.4 μm Pore Size Filter Cell Culture Medium Perfusion Experimental Protocol

The next step was to determine the average hydraulic conductivity and flow rate when cell culture medium was used as the perfusate. It would have been a serious mistake to assume that the culture medium would have the same perfusion characteristics as water. Cell culture medium is actually a complex mixture of a number of biologically active materials, including a basal culture medium (DMEM) with pH indicator, serum, antibiotics, and antifungal additives.

The most significant impact to the perfusion characteristics would be due to the fetal bovine serum (FBS) that must be added to the culture medium. This material has a number of protein compounds that maintains the health of the cells, as other investigators have reported.^{19,21} Unfortunately, these compounds also have a tendency to bind to any surface that they come into contact with. Proteins coating the filter surface would lower the average hydraulic conductivity of the filters, as the flow rate would be hindered by an accumulation of a protein residue around and within the filter pores.

When the filters are used for cellular perfusion studies, they will have been sitting in culture media for some time, in an incubator. This would provide ample time for any protein coating to take place. Similarly, the filters used in these tests likewise were incubated in culture medium for at least three days prior to use in order to more accurately replicate this phenomenon, as was done in Perkins^{20,21} and Alvarado's²² test procedures. If this step was omitted and fresh filters had been used, the flow rate data obtained would have been significantly higher, and completely inaccurate. This would result in a higher average hydraulic conductivity for the filters, since any protein coating would not have had time to form completely.

Six of the 0.4 μm pore size PCF filter membrane supports were used in these procedures. Perfusion pressure was again kept as close to 5.0 mm Hg as possible, following calibration of the transducer and setup. Flow rate measurements were taken every 30 seconds. The filter supports were perfused for a total of 20 minutes. During the perfusion tests, the entire experimental apparatus, with the exception of the data acquisition boards, was housed in a humidified incubator set at 37° C.

4.5 TM Cell Monolayer Perfusion Experimental Protocol

The final, and most important experiment was conducted using a single TM cell monolayer grown *in-vitro* in the laboratory. This test, and others that will be performed in the future, was designed to provide baseline perfusion data for the cell monolayers. The results of these procedures will be used as a basis for comparison against the cell monolayers that will be tested in the future using laser irradiation or pharmacological stimuli. Three months prior to this experiment actually taking place, the cells were seeded onto the filter support.

Perfusion of the TM cell monolayer took place following virtually the same protocol as before with the filter supports alone, with one minor change. Perfusion pressure was again set as close to 5.0 mm Hg as possible after transducer calibration, and TM cell culture media was used as the perfusion medium. The only difference was the duration of the test. The TM cell monolayer was perfused for a total of 45 minutes, during which flow rate readings were taken at 30 second intervals. This was done to examine the long-term stability of the perfusion testing system, as well as the perfusion characteristics of the cell monolayer. As with the 0.4 μm filter perfusion tests, the entire experimental apparatus with the exception of the data acquisition boards, was contained in a humidified incubator set at 37° C.

5. RESULTS AND ANALYSIS

5.1 0.4 μm and 3.0 μm Pore Size Filter Water Perfusion Experiments

Before processing of any experimental data could occur, the point in time at which the system reached steady state perfusion was required. This steady state perfusion condition was defined as the period of time during which there is a relatively constant perfusion pressure, and the standard deviation of the flow rate is constrained to within $\pm 10\%$ of the average flow rate value. These specifications were selected solely by the authors of this report, as previous accounts have provided no clear definition of "steady state perfusion".^{18,19,20} The flow rate data and perfusion pressure plots were both carefully analyzed to determine a consistent point at which steady state perfusion was reached for both pore size filter types.

Following this first stage analysis of the data, it was determined that the 0.4 μm pore-size filters reached steady state perfusion within a general time period of 5 minutes, whereas the 3.0 μm filters took approximately 15 minutes to reach steady state. To illustrate this, a typical pressure plot from the respective experimental series conducted using the different pore size filters is shown in Figures 4 and 5. After this "general" time period had been determined, the standard deviation of the flow rate was then divided by the average flow rate value. This examination was performed in two steps, first over the full duration of the experiment, and then using only the estimated steady state perfusion time period that was determined using the pressure plots. These figures are included in Table 1, on the following page.

The flow rate data obtained from the 3.0 μm pore size filter perfusion experiments was highly variable, from a minimum of 6.086 ml per minute to a maximum of 11.276 ml per minute. These calculations are for the time period after steady-state perfusion is reached. The degree of variability is extremely high, despite the fact that the pressure was maintained within $\pm 2\%$. To illustrate this more clearly, the steady state perfusion flow rate and pressure data for all of the 3.0 μm pore size filter water perfusion experiments is plotted as bar graphs in Figures 6 and 7, on the following page. In contrast to these results, the flow rate across the 0.4 μm filters membranes remained relatively constant, from a minimum of 0.548 ml per minute to a maximum of 0.672 ml per minute. The flow rate information and pressure data for all 0.4 μm pore size filter water perfusion experiments during steady state perfusion is illustrated in Figures 8 and 9, also on the following page.

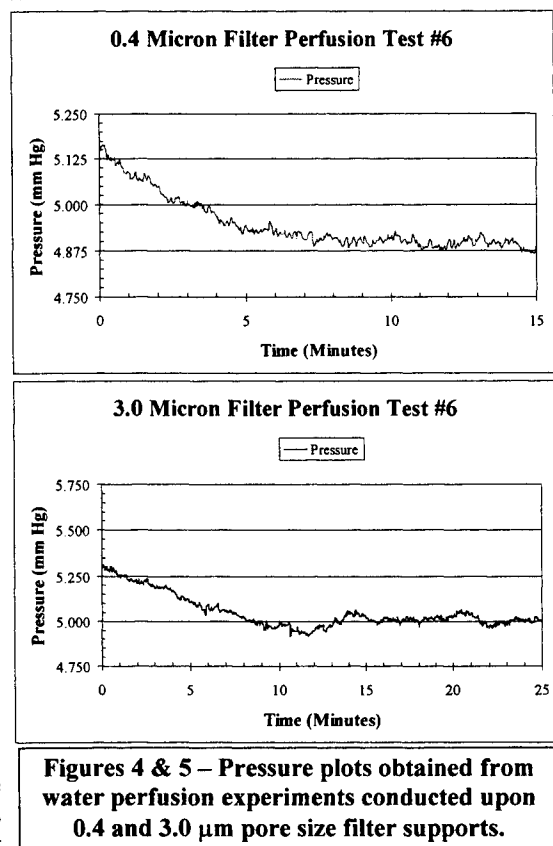
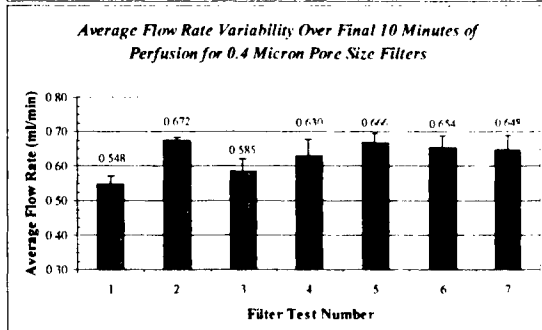
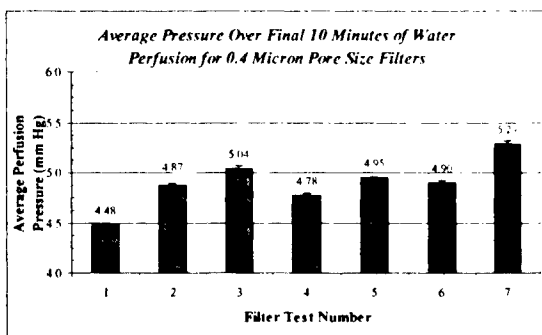
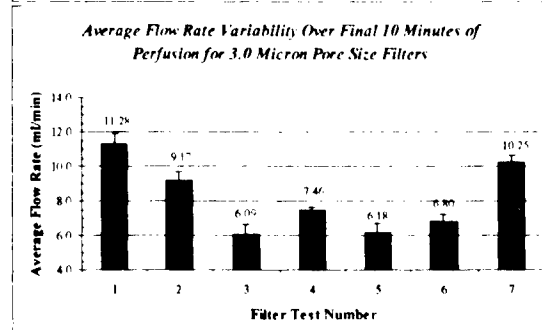
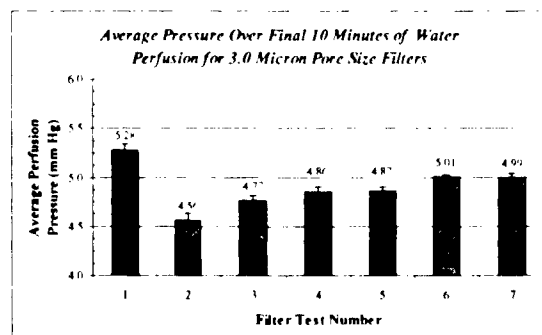


Table 1 – Overall and steady state water perfusion flow rate data for 0.4 and 3.0 μ m pore size filter supports.

Test Number	Average Flow Rate Over Full 15 Min (ml / min)	Std. Deviation of Flow Rate Over Full 15 Minutes (ml / min)	Std. Deviation Divided by Average Flow Rate (%)	Average Flow Rate Over Final 10 Min (ml/min)	Std. Deviation of Flow Rate Over Final 10 Minutes (ml/min)	Std. Deviation Divided by Average Flow Rate (%)
0.4 micron						
1	0.56677	0.03458	0.061	0.54762	0.02348	0.043
2	0.68548	0.03817	0.056	0.67238	0.01065	0.016
3	0.62581	0.06695	0.107	0.58524	0.03445	0.059
4	0.69161	0.10626	0.154	0.63000	0.04781	0.076
5	0.73290	0.10795	0.147	0.66619	0.02903	0.044
6	0.66710	0.03304	0.050	0.65429	0.03289	0.050
7	0.69258	0.07792	0.113	0.64762	0.03987	0.062
	Average Flow Rate Over Full 25 Min (ml / min)	Std. Deviation of Flow Rate Over Full 25 Minutes (ml / min)	Std. Deviation Divided by Average Flow Rate	Average Flow Rate Over Final 10 Min (ml / min)	Std. Deviation of Flow Rate Over Final 10 Minutes (ml/min)	Std. Deviation Divided by Average Flow Rate
3.0 micron						
1	13.82157	2.81030	0.203	11.27619	0.61482	0.055
2	11.79020	3.03575	0.257	9.17143	0.52567	0.057
3	8.10980	2.23837	0.276	6.08571	0.56677	0.093
4	11.84314	5.56890	0.470	7.46190	0.16176	0.022
5	8.83922	3.59275	0.406	6.18095	0.50579	0.082
6	10.03529	4.28151	0.427	6.80000	0.43861	0.065
7	12.79608	2.89949	0.227	10.25238	0.38498	0.038



Figures 6 and 7 – Steady state perfusion average pressure and flow rate graphs for 0.4 μ m membrane filter supports.



Figures 8 and 9 – Steady state perfusion average pressure and flow rate graphs for 3.0 μ m membrane filter supports.

5.2 0.4 μm Pore Size Filter Cell Culture Medium Perfusion Experiments

As was stated previously, the most important information that was required from this series of experiments was a mean value for the flow rate of perfusing TM cell culture medium across the filter, which is used in the calculation of the hydraulic conductivity of the cell monolayers (Q_{filter}). This mean flow rate was determined to be 0.096 ± 0.008 ml/minute. Average values for the steady state flow rates ranged from a high of 0.122 ± 0.007 ml/minute, to a low of 0.072 ± 0.009 ml/minute. Detailed flow rate results from all of these filter perfusion tests are shown in Table 2, below. Note that this table includes the average flow rates and standard deviations during both the entire 20 minute test period, as well as these same values once the system reached steady state perfusion. Graphical representations of the mean perfusion flow rates and pressures are shown in Figures 10 and 11.

In the article by Perkins, the average hydraulic conductivity of the 0.45 μm pore size HATF filter membranes alone was reported to be 50.5 ± 3.7 $\mu\text{l}/\text{min}/\text{mm Hg}/\text{cm}^2$.¹⁹ This number is more than ten times greater than the average hydraulic conductivity of the 0.4 μm pore size PCF filters tested here, at 4.457 ± 0.375 $\mu\text{l}/\text{min}/\text{mm Hg}/\text{cm}^2$. The difference in the pore sizes, 0.45 μm for the HATF filters and 0.4 μm for the PCF filters could not account for such a significant discrepancy, so focus shifted to the composition of the filters themselves. It was finally determined that the

Table 2 – Flow rate data from cell culture medium perfusion testing of 0.4 μm filter supports.

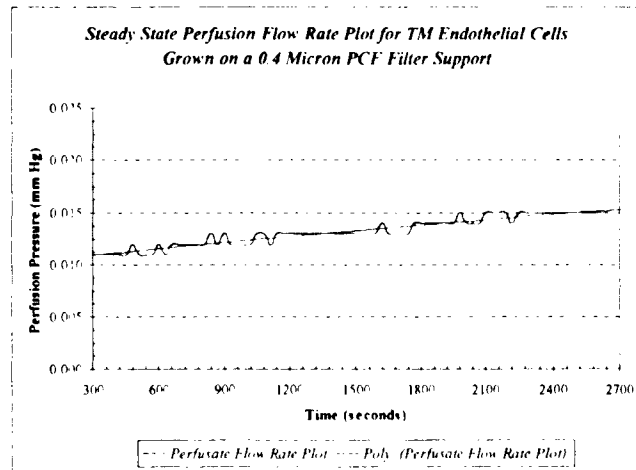
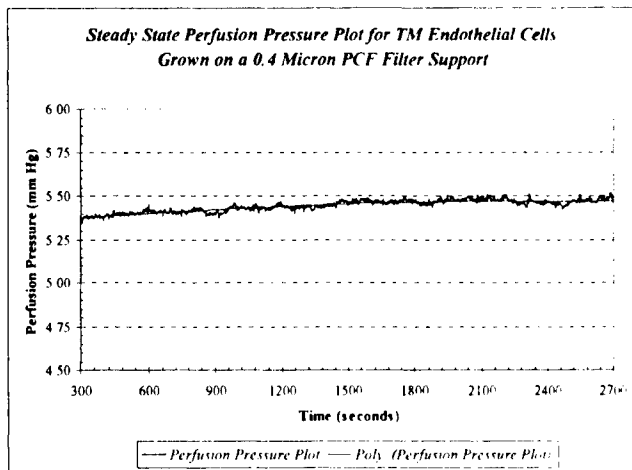
Perfusion Test Number (0.4 μm pore size PCF filters)	Average Flow Rate Over Full 20 Minutes of Perfusion (ml/min)	Std. Deviation of Flow Rate Over Full 20 Minutes of Perfusion (ml/min)	Average Flow Rate During Steady State Perfusion (ml/min)	Std. Deviation of Flow Rate During Steady State Perfusion (ml/min)
1	0.110915	0.015297	0.102586	0.008543
2	0.084329	0.021265	0.072328	0.008887
3	0.096625	0.018858	0.086786	0.009643
4	0.128750	0.013325	0.121786	0.006521
5	0.114854	0.014252	0.107500	0.009186
6	0.093476	0.013771	0.085948	0.005362
	Mean of Average Flow Rate Over Full 20 Minutes of Perfusion (ml/min)	Mean Std. Dev. of Flow Rate Over Full 20 Minutes of Perfusion (ml/min)	Mean of Average Flow Rate During Steady State Perfusion (ml/min)	Mean Std. Dev. of Flow Rate During Steady State Perfusion (ml/min)
	0.104825	0.016128	0.096156	0.008024

difference in the porosity of the two filter types was the cause. In a personal communication with a Millipore technical representative, it was found that the mixed cellular ester-based HATF filters used by Perkins and Alvarado had a porosity of roughly 80%, whereas the PCF filters used here had a porosity range from 10 to 20%. Nevertheless, testing continued using the PCF filters, because a mean perfusate flow rate using culture medium had been determined, which is all that was called for to perform cell monolayer hydraulic conductivity calculations.

5.3 TM Cell Monolayer Perfusion Experiment

Referring to the previous account by Perkins¹⁹ the average hydraulic conductivity of 15 TM cell monolayers was determined to be 1.1 ± 0.1 $\mu\text{l}/\text{min}/\text{mm Hg}/\text{cm}^2$ during steady state perfusion. Alvarado later reported that intact monolayers have hydraulic conductivity values between 0.3 and 2.0 $\mu\text{l}/\text{min}/\text{mm Hg}/\text{cm}^2$.²⁰ The result obtained using the current perfusion system compares well with these values with a steady state average hydraulic conductivity of 0.673 ± 0.076 $\mu\text{l}/\text{min}/\text{mm Hg}/\text{cm}^2$. The average perfusate flow rate during this time was determined to be 0.013 ± 0.001 ml/min, while the average perfusion pressure was 5.444 ± 0.033 mm Hg. The graphs for the steady state perfusion pressure, flow rate, and hydraulic conductivity are shown in Figures 10 – 12 on the following page.

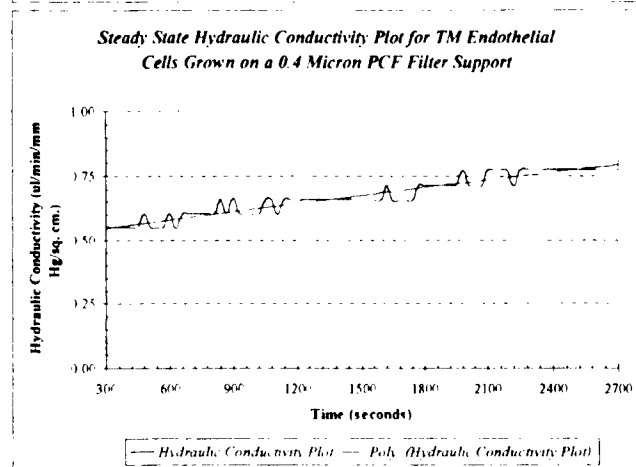
Two observations can be noted from simple examination of the graphs. First, the pressure plot during perfusion testing displays an overall increasing trend. At present, this phenomenon cannot be accounted for. Further perfusion tests should determine whether this is simply an anomalous occurrence or not. Secondly, the trend for the flow rate of perfusing medium across the TM cell monolayer, and therefore the hydraulic conductivity of the monolayer is increasing throughout the 45 minute duration of the experiment. As with the pressure plot, later baseline perfusion experiments will determine whether or not this is a consistent trend. Also of interest, note how the flow rate and hydraulic conductivity plots follow the same, exact pattern. This is due to the equation used to calculate the hydraulic conductivity (L_p), in which L_p is directly related to the perfusate flow rate (Q).



6. CONCLUSIONS

From the results of the preliminary TM monolayer baseline perfusion experiment, it has been ascertained that the proposed *in-vitro* perfusion testing system is a viable method by which to evaluate TM cellular hydraulic conductivity. The value for the steady state hydraulic conductivity of the cell monolayer tested, at 0.673 ± 0.076 $\mu\text{l}/\text{min}/\text{mm Hg}/\text{cm}^2$, falls well within the expected range that was reported previously by other investigators.^{18,19,20}

Additionally, as was shown in the results, it is believed that this conclusion will hold true regardless of the type of filter membrane used to support the cells, provided that the steady state perfusion flow rate through the filter is known or can be determined through perfusion testing. Despite the fact that there is a tenfold difference in the calculated hydraulic conductivities between the PCF filter supports used in the current model and the HATF filter supports used previously, the outcome for the hydraulic conductivity of the cells grown upon them is virtually the same. It has yet to be determined if the cells that were used in the preliminary test were in the ideal stage of growth and development for perfusion studies. Further growth and perfusion experiments, followed by further microscopic evaluations are required to determine what period of time following cell passage will be necessary to form a complete, healthy monolayer.



Figures 10-12 – Steady state pressure, flow rate, and hydraulic conductivity graphs with trendlines for TM cell monolayer perfusion experiment

7. FUTURE WORK

There is still much testing and some further validation that must be done before laser irradiation of the TM cells during perfusion can be attempted. First and foremost, several new cell monolayers must be grown to confluence upon the 0.4 μm pore size PCF filter membranes and evaluated to obtain additional baseline cellular hydraulic conductivity measurements. A new series of trials will also be conducted using cells at 1.5, 2.0, 2.5, and 3.0 months following passage to determine at what “age” the cells are best suited for perfusion testing. It is our intention to test TM cell monolayers within 1 week after the cells have completely covered the filter support with a confluent monolayer. Morphologic evaluations will be performed using conventional phase contrast light microscopy, but it is hoped that evaluation using both a scanning electron microscope (SEM) and a transmission electron microscope (TEM) will be possible as well. There is also a recognized need to conduct spectrophotometric evaluations of the TM cell culture medium to determine what effect, if any, the proteins will have upon laser energy absorption while perfusion is underway.

After these tests are complete, TM cell monolayers will be exposed to some of the same pharmaceuticals that were used by both Perkins²¹ and Alvarado²² in their studies. The response of the cells to these stimuli have been reported, and will therefore be used as additional validation of the applicability of the proposed perfusion system for laser-TM tissue interaction.

studies. Some of these drugs include: cytochalasin B, epinephrine, isoproterenol, cyclic AMP, and timolol. Additional compounds found in common anti-glaucoma medications may also be attempted, to determine what effect, if any, they have upon the TM cells.

Once these experiments have been completed, the experiments for which the perfusion testing apparatus was originally intended can be conducted. TM cells will once again be harvested and grown *in-vitro*, passaged onto filter supports, and allowed to grow to confluence. The monolayers will be placed in the apparatus, and perfused for approximately 30 minutes to obtain baseline measurements. After this time has passed, the entire cellular monolayer will be irradiated using either an Argon or a diode laser. The time of exposure and power will be the variable parameters in this series of trials, as the ideal laser energy dose required to optimize cellular hydraulic conductivity at clinically used laser wavelengths will be sought.

The authors thank the members of the Ohio Lions Eye Research Foundation for their sponsorship of this project.

- ¹ Wise, J.B. and Witter, S.L. "Argon laser therapy for open angle glaucoma: A pilot study." *Archives of Ophthalmology*. 97(2): 319-322, 1979.
- ² Gaasterland, D., and Kupfer, C. "Experimental glaucoma in the Rhesus monkey." *Investigational Ophthalmology and Visual Science*. 13(6): 455-457, 1974.
- ³ Wise, J.B. "Long-term control of adult open-angle glaucoma by Argon laser treatment." *Ophthalmology*. 88(3): 197-202, 1981.
- ⁴ Schwartz, A.L., et al. "Argon laser trabecular surgery in uncontrolled phakic open-angle glaucoma." *Ophthalmology*. 88(3): 203-212, 1981.
- ⁵ Wilensky, J.T., and Jampol, L.M. "Laser therapy for open-angle glaucoma." *Ophthalmology*. 88(3): 213-217, 1981.
- ⁶ Thomas, J.V., Simmons, R.J., and Belcher, C.D. "Argon laser trabeculoplasty in the presurgical glaucoma patient." *Ophthalmology*. 89(3): 187-197, 1982.
- ⁷ Pollack, I.P., Robin, A.L., Sax, H. "The effect of Argon laser trabeculoplasty on the medical control of primary open-angle glaucoma." *Ophthalmology*. 90(7): 785-789, 1983.
- ⁸ Van Buskirk, E.M., et al. "Argon laser trabeculoplasty: Studies of mechanism of action." *Ophthalmology*. 91(9): 1005-1010, 1984.
- ⁹ Wise, J.B. "Glaucoma treatment by trabecular tightening with the Argon laser." *International Ophthalmology Clinics*. 21(1): 69-78, 1981.
- ¹⁰ Van der Zypen, E., and Fankhauser, F. "Ultrastructural changes of the trabecular meshwork of the monkey (*Macaca speciosa*) following irradiation with Argon laser light." *Graefe's Archive for Clinical and Experimental Ophthalmology*. 221(6): 249-261, 1984.
- ¹¹ Van der Zypen, E., et al. "Morphology of the trabecular meshwork within monkey (*Macaca speciosa*) eyes after irradiation with the free-running Nd:YAG laser." *Ophthalmology*. 94(2): 171-179, 1987.
- ¹² Bylsma, S.S., et al. "Trabecular cell division after Argon laser trabeculoplasty." *Archives of Ophthalmology*. 106(4): 544-547, 1988.
- ¹³ Acott, T.S., et al. "Trabecular repopulation by anterior trabecular meshwork cells after laser trabeculoplasty." *American Journal of Ophthalmology*. 107(1): 1-6, 1989.
- ¹⁴ Acott, T.S., et al. "Human trabecular meshwork organ culture: Morphology and glycosaminoglycan synthesis." *Investigative Ophthalmology and Visual Science*. 29(1): 90-100, 1988.
- ¹⁵ Funderburgh, J.L., et al. "Corneal glycosaminoglycan synthesis in long-term organ culture." *Investigative Ophthalmology and Visual Science*. 24(2): 208-213, 1983.
- ¹⁶ Johnson, D.H., and Tschumper, R.C. "Human trabecular meshwork organ culture: A new method." *Investigative Ophthalmology and Visual Science*. 28(6): 945-953, 1987.
- ¹⁷ Erickson-Lamy, K., Rohen, J.W., and Grant, W.M. "Outflow facility studies in the perfused human ocular anterior segment." *Experimental Eye Research*. 52(6): 723-731, 1991.
- ¹⁸ Perkins, T.W., et al. "Flow resistance measurements in cultured cells using a filter supported system." *ARVO Abstracts. Investigative Ophthalmology and Visual Science*. 28(Supp.): 132, 1987.
- ¹⁹ Perkins, T.W., et al. "Trabecular meshwork cells grown on filters: Conductivity and cytochalasin effects." *Investigative Ophthalmology and Visual Science*. 29(12): 1836-1846, 1988.
- ²⁰ Alvarado, J.A. "Epinephrine effects on major cell types of the aqueous outflow pathway: *In-vitro* studies/clinical implications." *Transactions of the American Ophthalmological Society*. 88: 267-282, discussion 283-288, 1990.
- ²¹ Polansky, J.R., et al. "Human trabecular cells I: Establishment in tissue culture and growth characteristics." *Investigative Ophthalmology and Visual Science*. 18(10): 1043-1049, 1979.

Corneal group refractive index measurement using low-coherence interferometry

Stephen R. Uhlhorn^{1,2}, Fabrice Manns^{1,2}, Hassan Tahi², Pascal Rol^{1,2,3}, Jean-Marie Parel^{1,2}

¹ Department of Biomedical Engineering, University of Miami, Coral Gables, FL 33146

² Ophthalmic Biophysics Center, Bascom Palmer Eye Institute, University of Miami School of Medicine, Miami, FL 33136

³ Department of Ophthalmology, University of Zurich, Switzerland

ABSTRACT

Purpose. The goal of the study is to measure the group refractive index of the human cornea *in vitro* to improve the accuracy of corneal thickness measurements. **Methods.** Corneal buttons were trephined from 23 human cadaver eyes and the group refractive index of the cornea was measured at $\lambda = 840$ nm using a low-coherence Michelson interferometer and the technique proposed by Sorin and Gray (*Phot. Tech. Lett.* 4:105-107, 1992). The effect of dehydration on the measurement was studied by measuring the corneal optical thickness as a function of time. **Results.** Preliminary measurements of the group refractive index at 840 nm gave $n_g = 1.450 \pm 0.024$ for the human cornea, which is much higher than a calculated group refractive index of $n_g = 1.387$. Because of dehydration, the optical thickness of the cornea decreased at a rate of $5.5 \mu\text{m}/\text{min}$ which led to an artificially high value for the group refractive index. **Conclusion.** The calculated group refractive index of $n_g = 1.387$ appears to be an accurate value for the purpose of corneal thickness measurements using low-coherence interferometry, and corneal group refractive index measurements can be performed *in vitro* if the measurements are performed rapidly to avoid the effect of dehydration.

Keywords: cornea, refractive index, low-coherence interferometry

1. INTRODUCTION

1.1 Corneal thickness measurements

Exact measurement of corneal thickness is needed in many clinical situations, including the diagnosis of several disorders, such as corneal degenerations, endothelial dysfunction, and stromal dystrophy, as well as for the assessment of corneal refractive surgery. Since the cornea produces 70% of the refractive power of the eye, small changes to corneal shape can have a large effect on the focal length of the eye. In radial keratotomy, incisions are made in the stroma to within $10 \mu\text{m}$ of Descemet's membrane, so a precision of better than $10 \mu\text{m}$ is needed. In photorefractive keratectomy, the cornea is reshaped by ablation with a laser. For correcting 10 D of myopia, $90 \mu\text{m}$ of stromal tissue must be removed from the center of the cornea in a $5 \mu\text{m}$ diameter treatment zone¹. To investigate the effect that new contact lenses have on patients, the swelling of the cornea resulting from edema must be measured.

Currently, measurements of corneal thickness are performed with the optical slit-lamp pachometer or with ultrasound pachometers. Optical slit-lamp pachometers measure the central corneal thickness with a precision of about $13 \mu\text{m}$, but there is large interobserver and interinstrument variability². Ultrasound pachometers have been reported to have a precision of $5 \mu\text{m}$ ³, but interobserver variability is poor and the devices require mechanical contact with the cornea, resulting in discomfort, and possibly infection for the patient. Since ultrasound pachometers measure the time it takes for an acoustic pulse to return to a detector, a somewhat arbitrary value for the velocity of sound in corneal tissue ($v = 1640$ m/s) is used to calculate the thickness. This value depends on the relative concentrations of water and collagen, and as the level of hydration in the cornea changes, the actual velocity changes as well, inducing an error in the thickness measurement.

Recently, a new optical technique based on low-coherence interferometry has been developed for the measurement of corneal thickness⁴. Low-coherence interferometry has been used to measure the axial eye length^{7, 8} and corneal thickness⁶. It has also been developed into a new imaging technique called optical coherence tomography (OCT)⁹. OCT uses a low-coherence interferometer with a lateral scanning system so that cross-sectional images of structures can be obtained.

Low-coherence interferometry is advantageous for corneal pachometry because it offers excellent accuracy, it is a noncontact technique, and it allows for fast, repeatable measurements. However, this new technique suffers a drawback similar to ultrasound. Interferometry measures the optical thickness of the sample, which is the product of the physical thickness and the group refractive index of the sample. A value for the group refractive index of the cornea has not been published in the literature, so an approximate value has been used.

1.2 Group refractive index

The velocity of light, v , in an optical material is wavelength dependent. This phenomenon is known as dispersion, and because of it, the refractive index ($n = c/v$, where c is the speed of light in vacuum) of a material depends on the wavelength as well. When a source with a broadband spectrum (low-coherence source) is used to make optical measurements, each spectral component travels at a different velocity, and therefore, sees a different refractive index. The velocity of propagation for a group of lightwaves of different wavelengths over a narrow band is called the group velocity, v_g , and is defined as⁵

$$v_g = \frac{d\omega}{dk}, \quad (1)$$

where ω is the angular velocity of the corresponding propagation constant, k .

One can show that the group velocity corresponds to an equivalent refractive index, called the group refractive index, n_g , which is related to the refractive index, n , and the mean wavelength, λ_0 , by

$$n_g(\lambda_0) = \frac{c}{v_g} = \frac{n(\lambda_0)}{1 + \frac{\lambda_0}{n(\lambda_0)} \frac{dn}{d\lambda}(\lambda_0)}. \quad (2)$$

In low-coherence interferometry, the optical thickness measured is actually the product of the group refractive index and the geometrical thickness. In previous studies^{3, 4, 6}, the group refractive index of the cornea was calculated using the known refractive index of the cornea at $\lambda = 550$ nm ($n = 1.376$), and the dispersion curve for water, since it is the primary component of the cornea, giving $n_g = 1.385$ at $\lambda_0 = 855$ nm.

1.3 Application to corneal pachometry

Low-coherence interferometry can be used for making thickness measurements of the cornea if one of the mirrors in the interferometer is replaced with the cornea. Because of the difference between the refractive index of air, or the aqueous humor, and the cornea reflections are seen at both the front and back surfaces of the cornea. As the arm length difference of the interferometer changes by translating a reference mirror in the other arm, interference intensity peaks are seen when the optical path length difference between the reference mirror and the corresponding surface of the sample is less than the coherence length of the source (Figure 1). The distance that the reference mirror was translated between the detected interference peaks, is the optical thickness of the sample. The geometrical thickness is determined by dividing the optical thickness by the group refractive index.

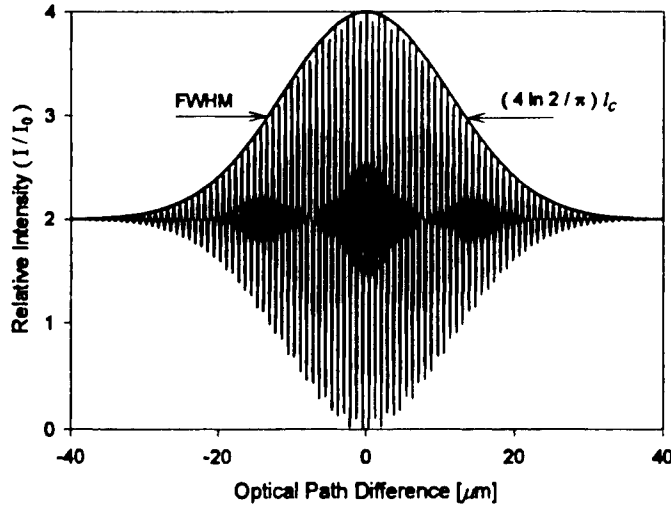


Figure 1: The interference signal seen with a low-coherence interferometer and its visibility curve .

1.4 Objective

Thickness measurements using low-coherence interferometry depend on accurate knowledge of the group refractive index at the measurement wavelength, much as ultrasound measurements depend on the velocity of sound in the medium of interest. The group refractive index for the cornea has not been previously measured, but a somewhat arbitrary value based on the refractive index at $\lambda = 550$ nm, and the dispersion curve of water has been calculated and used to determine the geometrical thickness.

As the measurement of corneal thickness by low-coherence interferometry is dependent upon the group refractive index of the cornea and the spectral characteristics of the light source used, the primary goal of this study is to measure the group refractive index of the cornea. With this information, more accurate measurements of corneal thickness will be possible.

2. MATERIALS AND METHODS

2.1 Light source

The short coherence length (broadband) source used for the low-coherence interferometer was a semiconductor emitter called a superluminescent diode. An SLD has characteristics which combine the advantages of a laser diode and a light-emitting diode; a high radiant output and low coherency. The SLD used in the interferometer (L-3302, Hamamatsu Corp., Bridgewater, NJ) had a maximum output power of $P_0 = 3.0$ mW with a forward current of 100 mA, a mean wavelength of $\lambda_0 = 840$ nm, and a specified typical coherence length of $l_c = 50$ μ m.

2.2 Michelson interferometer

The experimental setup (Figure 2) for performing the optical measurements was a Michelson interferometer. Two light sources were used to illuminate the interferometer, a superluminescent diode (SLD) to perform the measurements, and a red laser diode ($\lambda = 635$ nm, $P_0 = 5$ mW) for alignment since the SLD emits in the near-infrared. These two sources were coupled into an optical fiber for delivery to the interferometer. The output of the optical fiber was collimated, and then split by the beam splitter. After reflection at the two mirrors of the interferometer, the two beams were recombined at the beam splitter, focused onto a detector, and the interference signal was viewed with an oscilloscope. The reference mirror, M_2 , was

mounted on a piezo-electric transducer to increase the sensitivity of the instrument, and was translated with a precision micrometer.

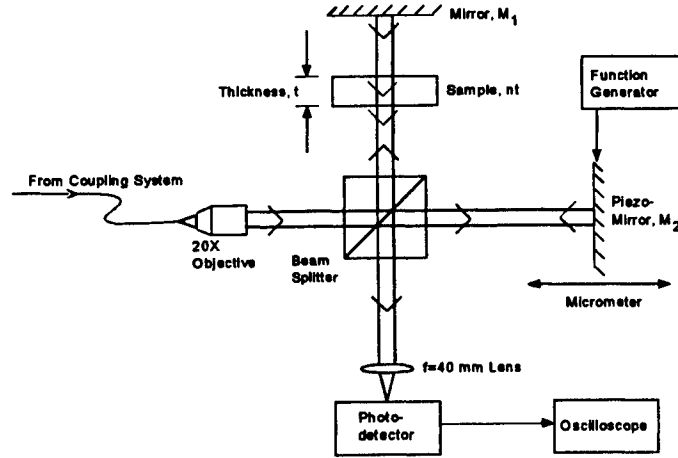


Figure 2: Low-coherence Michelson interferometer setup for measuring group refractive index.

2.3 Measurement of thickness and group refractive index

The thickness and group refractive index of a transparent sample can be determined by measuring two different properties of the sample, the optical thickness and the optical shift. The optical thickness of a transparent sample can be measured by placing the sample in the measurement arm of the interferometer (Figure 2). Fresnel reflection occurs at both the front and back surfaces of the sample. As the light waves associated with each of the reflections combine with the light wave from the reference arm (mirror M_2), an interference signal is seen (Figure 1) when the optical path difference is less than the coherence length of the source. The interference signals corresponding to each surface of the sample are detected by translating the reference mirror along the axis to the points where a maximum interference intensity is seen. For the case of a single transparent sample, two interference peaks are seen, with the distance traveled by the reference mirror between the peaks corresponding to the optical thickness of the sample. With the low-coherence interferometer, the measured optical thickness ($n_g t$) is the product of the group refractive index and the geometrical thickness of the sample.

The optical shift is the difference between the optical thickness and the geometrical thickness of the sample, and is given by

$$l = (n_g t) - t. \quad (3)$$

It is measured by replacing the sample with a mirror, and translating the reference mirror so that interference occurs between the two waves associated with the reflections at the two mirrors. This is the point of zero path length difference, and here the interferometer is said to be balanced. If the same transparent sample, whose optical thickness is known, is placed in the beam of the measurement arm (Figure 2), the interference signal from the reflection at mirror M_1 is shifted backward a distance corresponding to the difference between the optical thickness and the geometrical thickness of the sample, which is the optical shift.

With Eq. (3), and the optical thickness of the sample ($n_g t$), the geometrical thickness (t), and the group refractive index (n_g) can be determined using

$$t = (n_g t) - l, \quad (4)$$

$$n_g = \frac{(n_g t)}{t} \quad (5)$$

In order to decrease the time it took to measure both the thickness and group refractive index, the two measurements required for determining the thickness and group refractive index were made simultaneously¹⁰. Like for the separate measurements, the interferometer is first balanced (zero-path length difference between the arms). The sample is placed in the measurement arm of the interferometer, the reference mirror is translated backward, and the optical shift ($n_g t$) is measured as before. If the sample is placed close enough to mirror M_1 (Figure 2), the optical thickness ($n_g t$) can be measured by translating the mirror forward to detect the reflections at the front and back surfaces of the sample, and interference peaks like the ones in Figure 3 are seen.

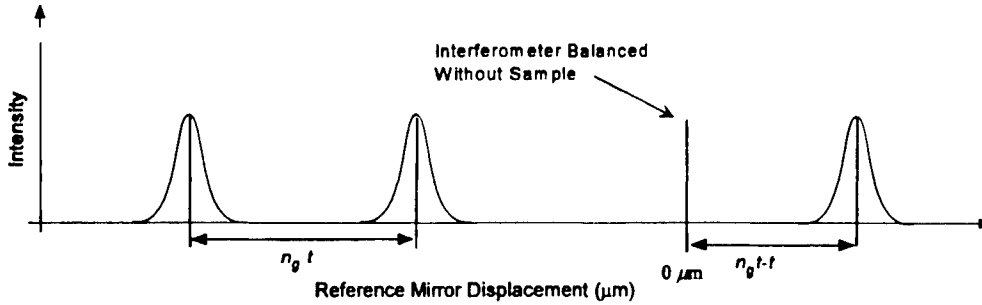


Figure 3: Interference peaks detected during simultaneous measurement of optical thickness and optical shift. The left peak is due to the reflection at the front surface of the sample, the middle peak is due to the back surface of the sample, and the right peak is due to the reflection at the reference mirror behind the sample.

3. RESULTS

3.1 Transparent window thickness and group refractive index measurement

Measurements were made with the interferometer on transparent calcium fluoride (CaF_2) windows to test the accuracy and repeatability of the interferometer. In addition, a precision micrometer was used to make thickness measurements and dispersion curves available in the literature were used to calculate the group refractive index of the materials. The calculating values served as a reference for comparison with the interferometer measurements. The group refractive index was calculated from Eq. (2). At $\lambda = 840 \text{ nm}$, the calculated phase refractive index of CaF_2 , is $n = 1.430$, while its group refractive index is $n_g = 1.438$. The geometrical thickness of the window was measured with a micrometer to be $t = 1218 \pm 5 \mu\text{m}$.

The measurements performed with the low-coherence interferometer gave a thickness of $t = 1214 \pm 8 \mu\text{m}$ and a group refractive index of $n_g = 1.440 \pm 0.004$, which are close to the expected values.

3.2 Corneal thickness and group refractive index measurement

The corneas were prepared from fresh donor eyes provided by the Florida Lions Eye Bank by injecting the posterior chamber with a 15 % Dextran solution using a 27 gauge needle. The epithelium was gently scraped off with a blade, and the eye was dehydrated by immersing it in a 15% Dextran solution for 1 hour. After the cornea was dehydrated, it was trephined with a custom built 16 mm trephine and fixed in a holder for measurement. The trephine removed the entire cornea with an intact 1 mm rim of sclera, and the holder was designed to maintain the natural shape of the cornea.

The thickness and group refractive index of the cornea were measured on six cadaver eyes. The interferometer was first balanced (zero path length difference between the arms) without any sample. Then, the corneal sample was placed in the interferometer, and the optical shift was measured by translating the reference mirror backward to detect the reflection from the mirror placed behind the cornea. Because the corneal mount maintained the curvature of the cornea, the

collimated beam that was used to measure the optical shift had to be focused onto the cornea, otherwise, it would be divergent after reflection at the curved surface. So, after the optical shift was measured, a positive lens ($f = 20$ mm) was placed in measurement arm to focus the beam on the anterior surface of the cornea, with a depth of focus of about 20 μm . Then, the reflected beam was aligned with the beam from the reference mirror, and the optical thickness was measured by translating the reference mirror in the opposite direction to detect the reflections from the posterior and anterior surface of the cornea.

Six cadaver corneas were measured. The average group refractive index measured was 1.450 ± 0.024 with a range from 1.415 to 1.475. These values are significantly larger than the calculated value of 1.385 used by previous researchers³.

3.3 Variation of corneal measurements with time

Because of the large variability in the preliminary measurements, the effect of corneal dehydration on the measurement was studied. The corneal optical thickness ($n_g t$) and the optical shift ($n_g t - t$) as a function of time was measured for 17 eyes. The measurements were performed separately to see how each measurement varied with time. 9 eyes were measured for the optical shift and 8 eyes were measured for the optical thickness. Measurements were made each minute for 15 minutes. A linear regression was performed on each eye to determine the rate at which the corneal measurement changed. The optical shift decreased at a rate of 1.60 ± 0.56 $\mu\text{m}/\text{min}$, and the optical thickness decreased at a rate of 5.53 ± 1.21 $\mu\text{m}/\text{min}$.

3.4 Discussion

Since the group refractive index of the cornea had not been measured, Drexler, et. al.³, calculated a value based on the dispersion curve of water ($n_g = 1.385$ at $\lambda = 855$ nm). This value was confirmed by plotting corneal refractive index data available in the literature and fitting it with the dispersion curve of water. We were able to find only one paper that contained data for the corneal refractive index at several wavelengths, and it was for the rabbit cornea¹¹. Assuming that the relative concentrations of water and collagen in the rabbit cornea are within the natural variability of the human cornea, the rabbit cornea refractive index data from Tagawa¹¹ were used to establish an approximate dispersion curve for the cornea. Using this curve, the group refractive index was calculated at our SLD's mean wavelength ($\lambda = 840$ nm) to be $n_g = 1.387$.

The measurements of the cornea as a function of time revealed that the changes that are occurring in the cornea are nearly linearly dependent on time (Figures 5 and 6). If the change in corneal thickness with time is indeed linear, and the rate of this change is consistent between eyes, then the average slope of the lines can be used to correct for errors that are introduced into the measurement by performing it over a long range of time. On the assumption that the rates of change for the two measurements (the optical shift and optical thickness) are proportional, the time period of concern is the time in between measuring the optical shift and measuring the optical thickness. If the two measurements were performed at exactly the same time, they should return an accurate reading of the thickness and group refractive index at that time. But, as the time between the two measurements increases, the error does as well.

To demonstrate this, consider a hypothetical cornea of thickness $t = 500$ μm , and group refractive index $n_g = 1.385$. The corresponding optical thickness is $n_g t = 693$ μm , and optical shift is $n_g t - t = 193$ μm . Since, the first measurement performed is the optical shift, and it is made immediately after the cornea had been mounted, the optical shift is at its initial value of $n_g t - t = 193$ μm . The optical thickness would be decreasing at a rate of approximately 5.5 $\mu\text{m}/\text{min}$, so if the measurement takes 5 minutes to perform, the optical thickness would be measured as $n_g t = 665$ μm . Using Eqs. (4-5) to calculate the thickness and group refractive index as before, the results give $t = 472$ μm and $n_g = 1.408$. After 10 minutes, the measured thickness and group refractive index is $t = 445$ μm and $n_g = 1.434$.

It appears that this is the dominant factor in the measurement error for the thickness and group refractive index. The measurements can be corrected to a certain extent, but the only way to measure the group refractive index accurately is to perform the measurement very rapidly, using a computer controlled system to axially scan the reference mirror.

4. CONCLUSIONS

A low-coherence interferometer was constructed to measure corneal thickness and refractive index and was tested for accuracy and repeatability using transparent windows. As the thickness that is measured using low-coherence interferometry depends on the group refractive index, the measurement of it was the primary goal of the study. To the best of our knowledge, these were the first measurements of corneal group refractive index.

The group refractive index was measured on 6 corneas and resulted in a value of $n_g = 1.450 \pm 0.024$. This is much higher than the expected value, $n_g = 1.387$ at $\lambda = 840$ nm, based on the phase refractive index of the cornea, $n = 1.376$ at $\lambda = 550$ nm, and the dispersion curve of water, since this is the primary component of the cornea. It was suspected that the large value measured for the group refractive index was due to changes in the thickness of the cornea because of dehydration during the measurement. The optical shift and optical thickness—the two measurements necessary to determine the thickness and group refractive index—were measured as a function of time, revealing a linear dependence. The average rate of change for the corneal measurements was used to consider the effect of dehydration on the measurements, which appeared to be the dominant factor in the error.

Based on the results of the experiments, several conclusions can be drawn from this study. It appears that the value for the corneal group refractive index ($n_g = 1.385$) used by previous researchers³ is a good approximation. This is also confirmed by the measurements by others on rabbit corneal refractive index *in vitro*¹¹. Also, low-coherence interferometry as a technique, is good for performing *in vitro* group refractive index and thickness measurements on the cornea, if they are performed rapidly.

5. ACKNOWLEDGEMENTS

This work was supported in part by Fight for Sight, the research division of Prevent Blindness America, in memory of Lee S. Hochwald, the Florida Lions Eye Bank, Research to Prevent Blindness, New York, NY, and Dr. David Robinson.

6. REFERENCES

1. C. R. Munnerlyn, S. J. Koons, and J. Marshall, "Photorefractive keratectomy: a technique for laser refractive surgery", *Journal of Cataract And Refractive Surgery* **14**, pp. 46-52, 1988.
2. N. Ehlers and F. K. Hansen, "On the optical measurement of corneal thickness," *Acta Ophthalmologica* **49**, pp. 65-81, 1971.
3. W. Drexler, A. Baumgartner, O. Findl, C. K. Hitzenberger, H. Sattman, and A. F. Fercher, "Submicrometer precision biometry of the anterior segment of the human eye," *Investigative Ophthalmology and Visual Science* **38**, pp. 1304-1313, 1997.
4. C. K. Hitzenberger, "Measurement of corneal thickness by low-coherence interferometry," *Applied Optics* **31**, pp. 6637-6642, 1992.
5. M. Born and E. Wolf, *Principles of Optics*, 4th ed., Pergammon Press, New York, 1970.
6. C. K. Hitzenberger, A. Baumgartner, W. Drexler, and A. F. Fercher, "Interferometric measurement of corneal thickness with micrometer precision," *American Journal of Ophthalmology* **118**, pp. 468-476, 1994.
7. C. K. Hitzenberger, "Optical measurement of the axial eye length by laser Doppler interferometry," *Investigative Ophthalmology and Visual Science* **32**, pp. 616-624, 1991.
8. A. F. Fercher, C. Hitzenberger, and M. Juchem, "Measurement of intraocular optical distances using partially coherent laser light," *Journal of Modern Optics* **38**, pp. 1327-1333, 1991.

9. D. Huang *et al.*, "Optical coherence Tomography," *Science* **254**, pp.1178-1181, 1991.
10. Sorin and Gray, "Simultaneous thickness and group refractive index measurement using optical coherence reflectometry," *IEEE Photonics Technology Letters* **4**, pp. 105-107, 1993.
11. S. Tagawa, "Über die dispersion der brechenden medien des auges," *Archive fur Augenheilkunde* **99**, pp. 576-610, 1928.

Corneal autofluorescence in presence of Diabetic Retinopathy

L. Rovati^a, F. Docchio^a, C. Azzolini^b and J.A. Van Best^c

^aDipartimento di Elettronica per l'Automazione, Università degli Studi di Brescia, Brescia (Italy)

^bDipartimento di Oftalmologia e Scienze della Visione, Ospedale S. Raffaele, Milano (Italy)

^cDepartment of Ophthalmology, Leiden Hospital, Leiden (The Netherlands)

ABSTRACT

Recently corneal autofluorescence has been proposed as an ocular diagnostic tool for diabetic retinopathy. The method is based on the sensible increase of the natural fluorescence of corneal tissue within specific wavelength in presence of early stage of diabetic retinopathy. The main advantages of this method are that the corneal autofluorescence has been demonstrated to be not age-related and that the cornea is readily accessible to be investigated. In this study 47 insulin-dependent diabetes mellitus and 51 non-insulin-dependent diabetes mellitus patients aged 20-90 years have been considered. Patients were selected from the Eye Clinic of S. Raffaele Hospital. The modified Airlie House classification was used to grade the diabetic retinopathy. Corneal autofluorescence has been measured by using both a specifically designed instrument and the Fluorotron Master. Corneal autofluorescence mean value for each diabetic retinopathy measured by using both the instruments correlated with the retinopathy grade.

Keywords: Corneal autofluorescence, diabetic retinopathy, ophthalmic instrument

1. INTRODUCTION

Several diagnostic techniques, based on direct evaluation of the natural fluorescence of ocular tissues, have been proposed for diagnosis of ocular pathologies. In particular, retinopathy diagnosis through corneal autofluorescence (AF) measurements has been recently proposed as innovative diagnostic tool^{1,2}.

Corneal tissue contains pyridine nucleotides ($\lambda_{ex}=366$ nm, $\lambda_{em}=450$ nm) and flavoproteins ($\lambda_{ex}=450$ nm, $\lambda_{em}=550$ nm) distributed uniformly across the corneal tissues. These fluorophores supposedly determine AF characteristics of the corneal tissue. In general, no marked change in AF intensity with age in healthy subjects are observed. In contrast modification in intensity and possibly spectral characteristics have been observed with some types of pathologies. Such is, in particular, the case of diabetic retinopathy (DR)¹. Corneal AF can be also combine with other innovative diagnostic techniques such as dynamic light scattering of the vitreous to improve the quality of the DR diagnosis³.

Presently, diagnosis of ocular diseases through corneal AF is mainly performed by using fluorophotometers, suitably modified with anterior chamber adapters. The peak fluorescence of the cornea, or the area subtended by the corneal area, is taken as the quantity of interest to be correlated to the degree of DR. From clinical studies performed on populations of diabetic patients of different degrees of DR, it has been demonstrated that corneal AF is indeed a reliable marker for this kind of disease^{1,2}.

A collaboration between our group, the Ophthalmic clinic of S. Raffaele hospital and the Ophthalmic clinic of Leiden University led to develop and test a simple corneal fluorometer (CF) for DR screening based on corneal AF⁴. In the present study, corneal AF has been measured using this CF and a commercial scanning fluorometer (FM, Fluorotron Master, Coherent Radiation, Palo Alto, CA). Forty-seven insulin-dependent diabetes mellitus (IDDM) and fifty-one non-insulin-dependent diabetes mellitus (NIDDM) patients aged 20-90 years have been considered. Patients were selected from the Eye Clinic of S. Raffaele Hospital. The modified Airlie House classification has been used to grade the DR. Corneal AF of this patient group has been measured by using both CF and FM, and the obtained results have been compared.

2. MATERIAL AND METHODS

2.1 Corneal autofluorescence

The corneal epithelium and the endothelium contain pyridine nucleotide and flavoproteins. The pyridine nucleotide shows fluorescence in the reduced state whereas flavoproteins fluorescence in the oxidated form. The accumulation of these fluorophores in diabetic cornea related to the duration of diabetes cannot adequately explain the increased AF in patients with DR⁵. Two speculative explanations are so far been reported, (i) the vascular component of DM causing specific microangiopathy and consequently progressive retinopathy may induce a metabolic disorder resulting in an increase of the corneal AF or (ii) neovascularisation mediating substances produced in the retina with retinopathy and inducing neovascularisation of the iris may reach the cornea as well and consequently induce changes in the corneal metabolism resulting in increased value of AF¹. Nevertheless experimental investigations report a modification in AF intensity with DR and ocular surgery such as penetrating keratoplasty (PKP)^{1,2}.

Corneal AF can be measured by a simple noninvasive technique, without discomfort to the patient and, using the dedicated CF, it can be measured by non-specialized personnel in few seconds.

2.2 Subject selection

Forty-seven IDDM and fifty-one NIDDM patients aged 20-90 years have been considered. Patients were selected from the Eye Clinic of S. Raffaele Hospital. Great care was taken to select patients with normal aspect of all cornea layers assessed by slit lamp examination. Individuals with contact lenses were excluded.

Patient age distribution is uniform as shown in figure 1a.

The modified Airlie House classification was used to grade the DR according the following four grades:

Grade 1. No or negligible retinopathy; at most two microaneurysms per field.

Grade 2. Minimal background retinopathy; three or more microaneurysms per field only.

Grade 3. Background proliferative retinopathy; microaneurysms and one or more of the following items: retinal haemorrhages, hard or soft exudated and/or interretinal microvascular abnormalities (IRMA), venous beading.

Grade 4. (Pre-) proliferative retinopathy; haemorrhages and microaneurysms, and the following features present in more than 2 field: soft exudates, IRMA, venous beading, and/or new vessel and fibrous proliferations, and/or vitreous haemorrhages.

After visual inspection by slit lamp, the patients have been graded according figure 1b.

2.3 Instrumentation and measurements

Corneal AF has so far been measured by using commercial scanning fluophotometers such is the FM. However these instruments are expensive, not specifically design to detect corneal AF and not easy to use. To overcome all these problems we designed a simple, compact and inexpensive CF to measure corneal AF.

In the present study corneal AF has been measured by using both the CF and the FM. FM was suitably modified with anterior chamber adapters in order to scan only cornea and lens. The peak intensity of the corneal scan was taken as the quantity of interest to be correlated to the degree of DR. Three corneal AF measurements by using the CF were performed from each eye just after FM examinations. The average value of the results were calculated. An extensive description of the CF is presented in the paper 3246-05 of the present conference proceeding, nevertheless the working principle of the instrument can be briefly explained by referring to figure 2. The excitation light from two Blue LEDs passes trough a suitable set of barrier filters and impinges tangentially the patient cornea. The excitation light so obtained has a spectrum included between 450 and 500 nm. The fluorescence light from the cornea is collected axially using a camera objective. A suitable set of emission filters select the wavelengths of interest. The fluorescence light is then converted to an electric signal by a photomultiplier tube (PMT). The current signal at the output of the photomultiplier tube is processed using a custom front-end electronics and an appropriate data analysis. The tangential excitation minimizes both the excitation light that reaches directly the photomultiplier tube and the amount of excitation light that reaches the patient lens; this feature ensures that the contribution of the lens AF is minimized. The AF data was recorded in sixteen measurement cycles of 200 ms during a period of 10 seconds, and then the average value has been considered.

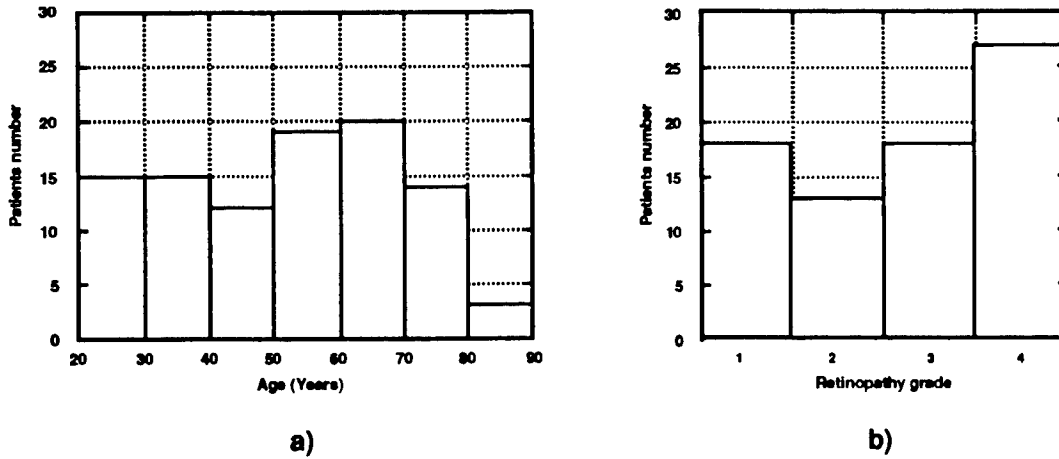


Figure 1. Distribution of the patients number as a function of a) the patients age and b) the retinopathy grade. Both distributions are almost uniform.

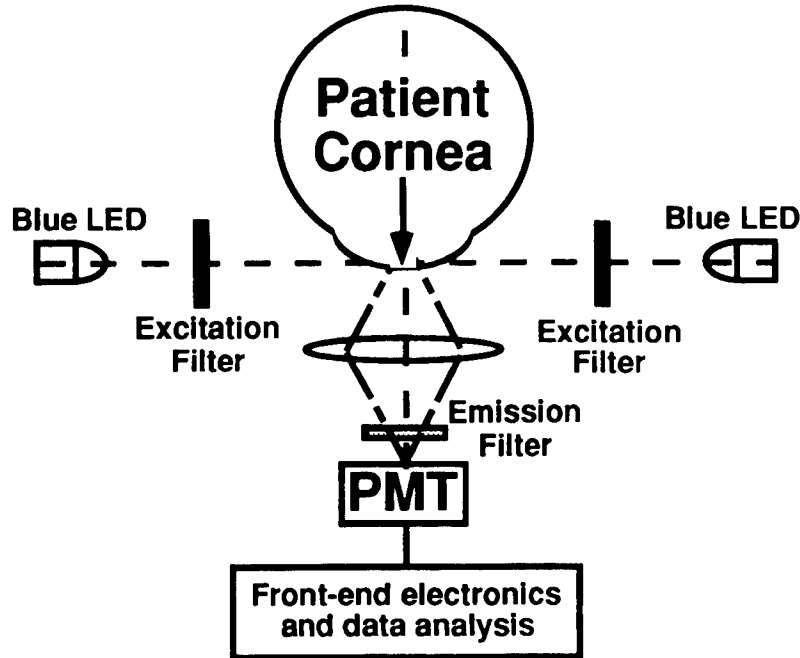


Figure 2. Principle scheme of the corneal fluorometer.

3. RESULTS AND DISCUSSION

Table I and figure 3 summarize the mean and standard error (SE) of the corneal AF in each retinopathy grade. An average increase of about 50.7% of the corneal AF between patients with negligible DR grade 1 and with proliferative DR grade 4 was observed using the CF and of about 28.8% using the FM. Mean values of AF detected by the FM increase monotonically with the grade of DR whereas using the CF DR grade 3 exhibits a mean value of AF lower than DR grade 2. Despite the CF measurements exhibit higher standard errors than the FM measurements, the ratio between mean SE and average increase of the corneal AF between grade 4 and grade 1 is similar for both the instruments.

Table II and figure 4 summarize the mean and standard error (SE) of the corneal AF in each retinopathy grade obtained considering exclusively IDDM patients. An average increase of about 95.8% of the corneal AF between DR grade 1 and DR grade 4 was observed using the CF and of about 86.4% using the FM. Mean values of AF detected by the CF increase monotonically with the grade of DR whereas using the FM DR grade 4 exhibits a mean value of AF lower than DR grade 3.

Comparing the results reported in Table I and Table II, it can be noted that IDDM patients with DR grade 1 exhibit a lower corneal AF than the average of the whole considered population. This effect, observed by using both the instruments, allows a better discrimination between patients with no or negligible DR and other grades of DR.

Confirming results reported in literature¹⁻³ no significant dependence of corneal AF from patients age and diabetes duration has been observed, the correlation coefficients between corneal AF, patients age and diabetes duration were 0.17 and 0.093 respectively. Corneal AF values of right and left eyes were found to be correlated in each retinopathy grade.

As shown in figure 5, excellent correlation between CF and FM measurements has been observed, that confirming the efficiency of our simple CF.

4. CONCLUSIONS

The present study demonstrates that corneal AF could be efficiently used for an early diagnosis of DR. High sensitivity and specificity could be obtained from corneal AF by fixing a proper threshold to discriminate negligible (grade 1) to pathological DR (grade 2-4). The diagnostic method is more efficient on IDDM patients, whereas no significant dependence of corneal AF from patients age and diabetes duration has been observed. The high correlation between corneal AF measurement obtained from CF and FM proves the good performance of our dedicated CF. Such a system would have a large impact in the prevention of blindness as a result of DR.

ACKNOWLEDGMENTS

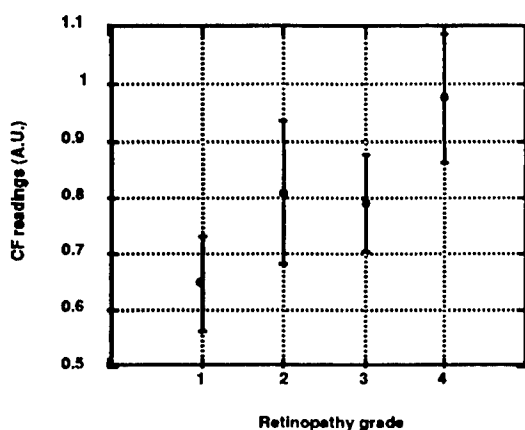
The authors wish to thank Dr. L. Guarisco, Dr. F. Patelli, Ing. F. Gori and Ing. E. Nocera for their valuable contributions during the experimental activities.

Table I: Mean and standard error of the corneal AF for each retinopathy grade measured on the whole patient group.

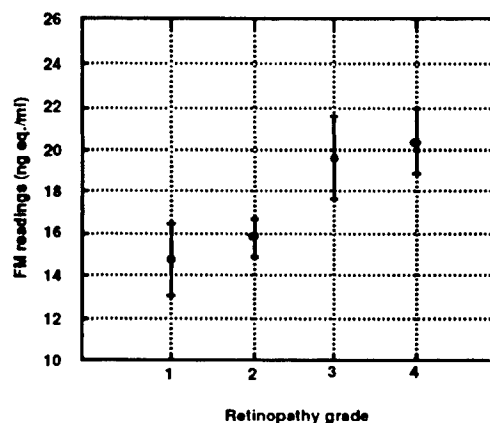
Retinopathy Grade	Corneal fluorometer		Fluorotron Master	
	Mean value (A.U.)	Relative Standard Error %	Mean value (ng.eq./ml)	Relative Standard Error %
1	0.647	12.3	15.760	7.7
2	0.808	14.8	15.840	5.5
3	0.790	10.1	19.610	9.8
4	0.975	10.2	20.300	6.0

Table II: Mean and standard error of the corneal AF for each retinopathy grade measured on IDDM patients.

Retinopathy Grade	Corneal fluorometer		Fluorotron master	
	Mean value (A.U.)	Relative Standard Error %	Mean value (ng.eq./ml)	Relative Standard Error %
1	0.478	20.9	11.327	22.6
2	0.782	17.9	16.237	5.7
3	0.845	20.1	22.062	14.2
4	0.936	13.8	21.105	9.1

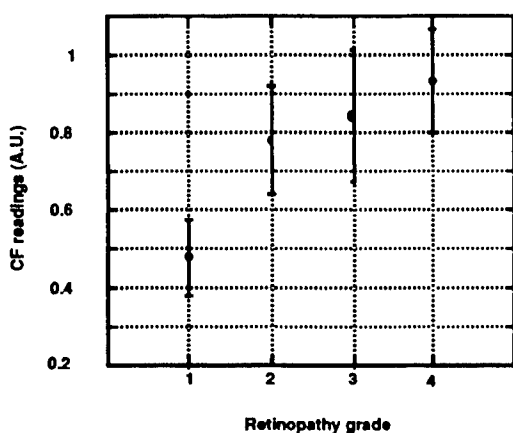


a)

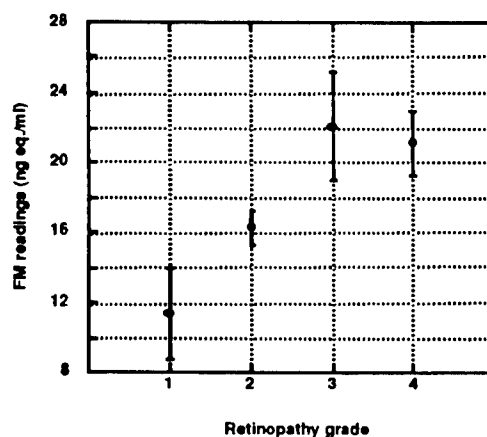


b)

Figure 3. a) Corneal fluorometer (CF) and b) Fluorotron Master (FM) readings as a function of the retinopathy grade for the whole patient group.

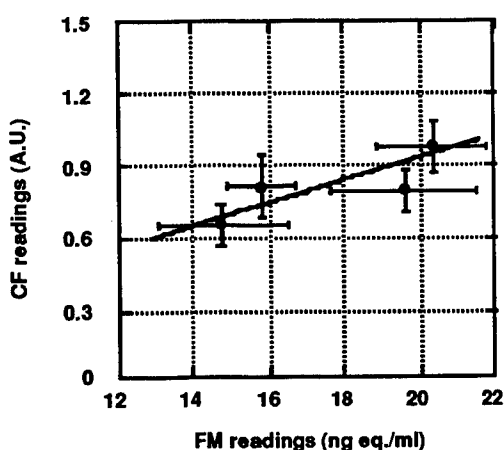


a)

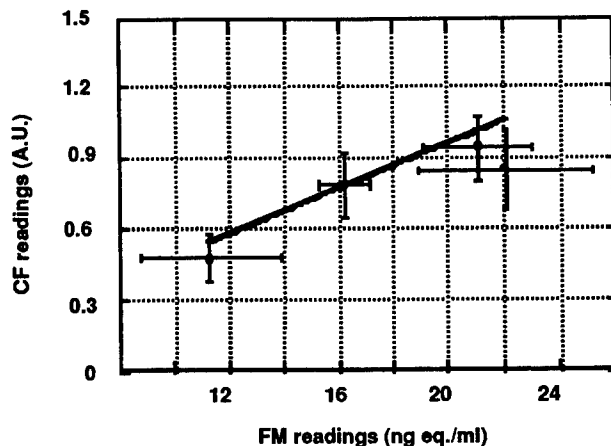


b)

Figure 4. a) Corneal fluorometer (CF) and b) Fluorotron Master (FM) readings as a function of the retinopathy grade for IDDM patients.



a)



b)

Figure 5. Corneal fluorometer (CF) readings as a function of the Fluorotron Master (FM) for a) the whole patient group and b) IDDM patients.

REFERENCES

1. T. R. Stolwijk, J. A. Van Best, J. A. Oosterhuis JA, and W. Swart, "Corneal autofluorescence: An indicator of diabetic retinopathy," *Invest. Ophthalmol. Vis. Sci.* **33**, pp. 92-97, 1992.
2. T. R. Stolwijk, J. A. Van Best, J. P. Boot, and J. A. Oosterhuis, "Corneal autofluorescence in diabetic and penetrating keratoplasty patients as measured by fluorophotometry," *Exp. Eye Res.* **51**, pp. 403-409, 1990.
3. L. Rovati, F. Fankhauser, F. Docchio and J.A. Van Best, "Diabetic retinopathy accessed by dynamic light scattering and corneal autofluorescence," in press on *Journal of Biomedical Optics*, 1998.
4. J.A. Van Best and F. Docchio "A simple, low cost, portable corneal fluorometer for the early detection of diabetic retinopathy," submitted to *Appl. Opt.*, 1998.
5. F. Docchio (Ed.), *Introduction to Ocular Fluorometry*, Gráfica de Coimbra, Coimbra, 1997.

Design and performance of a new fluorometer for corneal autofluorescence measurements

F. Docchio^a, J.A. Van Best^b, L. Rovati^a, H.J. van Schaik^b

^aDipartimento di Elettronica per l'Automazione, Università degli Studi di Brescia, Brescia, Italy

^bDepartment of Ophthalmology, Leiden University Hospital, Leiden, the Netherlands

ABSTRACT

An optical instrument for *in-vivo* corneal autofluorescence measurements in the human eye is described. This instrument measures corneal autofluorescence without burden to the patient. The corneal tissues are excited tangentially by wavelengths in the spectral region of 450-500 nm and the fluorescence emitted by the corneal tissue passing through a suitable set of barrier filters is collected by a miniature photomultiplier. Autofluorescence data are recorded in sixteen measurement cycles during a period of 10 seconds and the average value has been considered. The instrument demonstrates good safety characteristics.

Keywords: Corneal autofluorescence, diabetic retinopathy, ophthalmic instrument, cornea.

1. INTRODUCTION

Early detection of the onset of diabetic retinopathy (DR) in diabetic patients is of crucial interest in health care, as this type of ocular disease is one of the main causes of blindness in the western world.¹⁻³ Detecting DR in time, in most cases, postpones or even prevents the onset of blindness through a timely start of laser therapy.⁴ Recently, it has been shown that the autofluorescence of the corneal tissue within specific wavelength regions is sensibly increased in the presence of diabetic retinopathy.⁵ This is of particular relevance since (i) the cornea is readily accessible to investigation, and (ii) corneal autofluorescence, in contrast to the lens autofluorescence,⁶ is not age-related in non-diabetic subjects.⁷

Although the nature and the exact excitation/emission wavelength ranges of the fluorophore(s) of interest are still subject of investigation, the use of corneal autofluorescence as an indicator of DR in early stages is promising.^{5,7-10} Following the initial investigations, it was thought that a very simple, compact and low-cost instrument designed to measure changes in corneal autofluorescence could be of great interest for the public health care. Such a system would have a large impact in the prevention of blindness as a result of diabetic retinopathy, since its low cost and simplicity of use would allow its diffusion among ophthalmologists and even general practitioners.

We present a novel measuring apparatus developed in our laboratories, for the measurement of corneal autofluorescence. The system performs the measurement of the autofluorescence of the cornea over a suitable excitation and emission range. The prototype is based onto a photographic camera equipped with a fluorescence excitation adapter for the tangential illumination of the corneal tissue, with appropriate excitation and barrier filters, and with a photomultiplier in the image plane of the camera for the detection of the emitted fluorescence. To minimize the contribution of the much higher fluorescence of the underlying crystalline lens, special geometry and measurement procedures have been expressly designed. This paper describes in detail the instrument developed, and reports on its characterization, and on a preliminary session of tests on volunteers to assess its potential.

2. DESCRIPTION OF THE SYSTEM

The portable corneal fluorometer is described with reference to the block diagram of Fig. 1.a. The instrument is basically composed of (i) a modified photographic camera (Pentax Reflex camera K1000, lens 50mm f/2) equipped with a flexible bellows. A special adapter is mounted onto the camera lens to include all light sources for the excitation of the fluorescence, plus additional light sources.

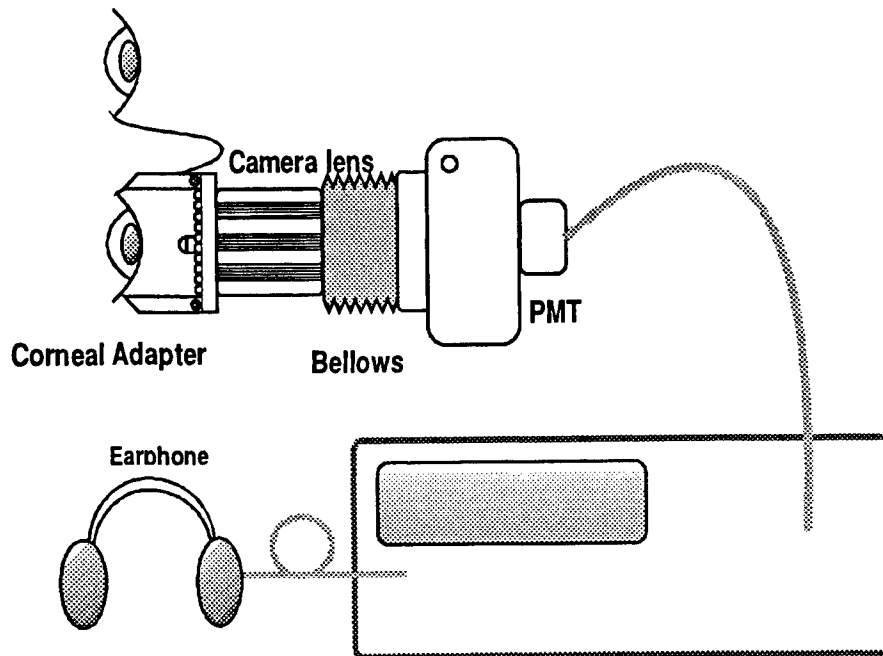


Fig. 1.a: General layout of the portable fluorometer.

The optical head of the portable corneal fluorometer is described with reference to Fig. 1.b. The excitation light sources consist of six blue LEDs (470 nm, 7-14 mcd). The outgoing LED light emitted parallel to the optical axis of the camera, passes through a set of wide-band interference filters that select only the wavelength region of interest for

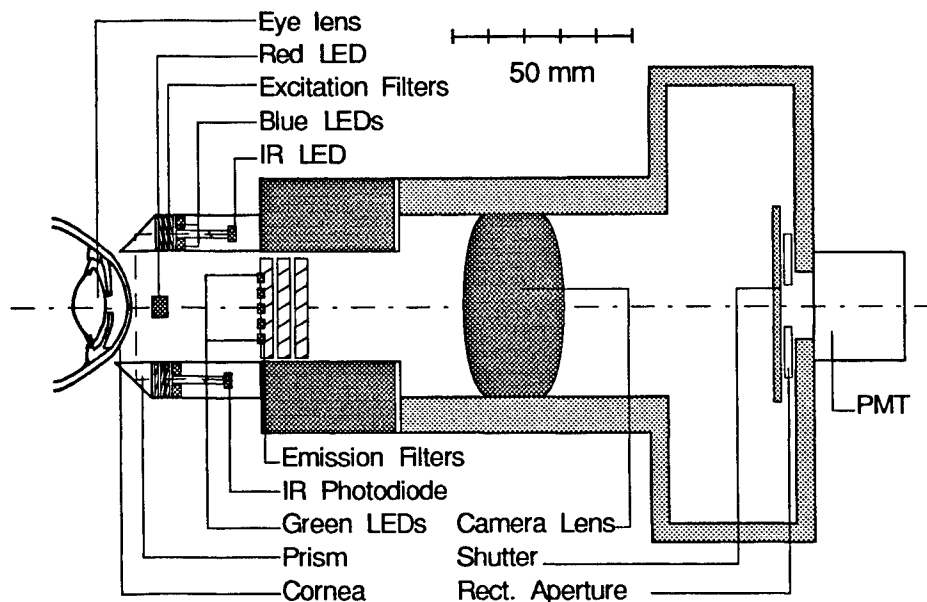


Fig. 1.b: Detailed view of the optical head (on scale).

corneal excitation. It is then deflected by a total internal reflection prism and is used to illuminate the cornea tangentially at the left and right side of the eye. Exciting the cornea tangentially is necessary for the following reason. The fluorescence emitted by the cornea is very weak, when compared to the much higher fluorescent emission of the underlying crystalline lens, with largely overlapping excitation and emission spectra. Therefore the tangential excitation has the purpose of minimizing the amount of excitation light that reaches the lens (Fig. 1.b).

The fluorescence emission passes through a suitable set of barrier filters and is imaged by the camera lens ($f/2$) onto the photosensitive area of a miniature photomultiplier (Hamamatsu Mod. HC120), fixed at the back of the camera. In addition to the blue light sources, 16 green LEDs are mounted on a ring onto the illumination adapter (Fig. 1.b). They help the operator to correctly position the eye within the field of view of the Reflex camera objective. An additional purpose is to force the closure of the iris of the target eye, to further reduce excitation of fluorescence of the ocular lens. The green LEDs are turned off immediately before the measurement of the green fluorescence is started. As a third light source there is a single, high efficiency, red LED mounted at the center of the adapter, on the optical axis of the system. Firstly, it is used as a fixation aid for the patient. Secondly, it maintains the pupil constricted and reduces the interference by the crystalline lens fluorescence. Thirdly, it prevents central fluorescent emission, originating from the crystalline lens, from reaching the photodetector in a direct way.

Fig. 2.a shows the transmission curves of the excitation (left) and the barrier filters D, the LED spectral emission (A), the excitation filter transmission curve (B) and the resulting spectrum of the excitation light (C) that reaches the cornea. Minimum overlapping between excitation and emission spectral regions has been achieved, to be less than one part over 10^{10} with a sequence of three excitation filters, and of three emission filters.

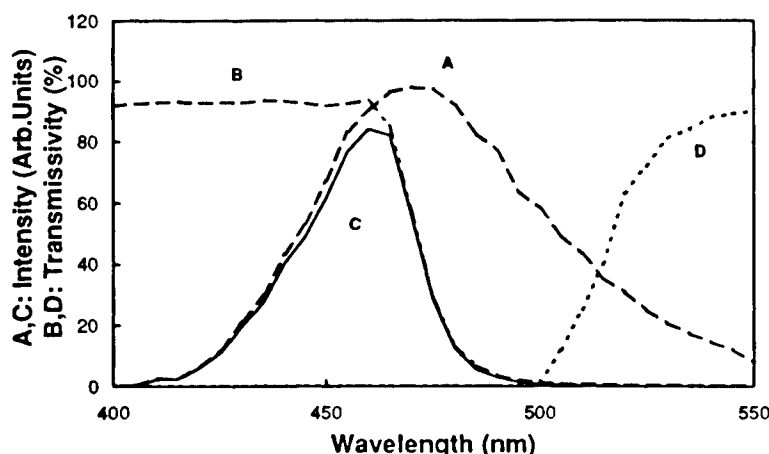


Fig. 2: Spectral emissivity of the blue LED (A), Spectral transmissivity of the excitation filter (B). Spectral emissivity of the filtered blue filter (C). Spectral transmissivity of the emission filter (D).

Finally, the optical head is equipped with an IR transmitter-receiver combination. The transmitter is located inside one of the two illuminators, whereas the receiver is housed in the other. The transmitter is square-wave modulated; the receiver signal, suitably shaped, drives an earphone set (alternatively, it operates a bar-display) which the operator wears during the measurement. When the cornea is in place at the right distance from the camera lens, the transmitter-receiver path is on the border of being interrupted and the earphone signal becomes inaudible, thus indicating that the system is ready for operation.

The signal from the photomultiplier is sent to a compact electronic unit for elaboration and display. The unit is based on a single-chip microcontroller (Motorola 68HC11) and on a specifically designed elaboration board. The latter one performs single channel gated integration of the PMT signal within a programmable time interval, using a very low-noise operational amplifier.

The measurement steps for the acquisition of the corneal fluorescence have been designed to optimize the signal-to-noise ratio of the measurement. Initially, the operator can position the optical head at the right place with respect to the target eye by looking at the viewer of the camera and by moving the camera until the cornea is properly positioned. By pressing the camera shutter the green LEDs and the red LED are turned off. After a convenient delay, the blue LEDs are turned on for a pre-set time interval, and the elaboration board integrates the fluorescence signal over this interval. Then the output of the gated integrator is transferred to a sample and hold circuit and converted by the A/D converter. The gated integrator is then zeroed by a controllable FET switch. Following this procedure, the blue LEDs are turned off, and the acquisition of the background signal is performed in exactly the same way. The background signal is then subtracted from the fluorescence signal. When the S/B subtraction is finished, the RED diode is turned on at full current, in order to prevent the pupil from dilating. After the turn off of the red LED, the sequence starts again. The S/B acquisition is repeated for a suitable number of times and the result is averaged. These repetitive sequences are required since the pupil starts to re-open at about 200 ms after the front illumination has been turned off. In the virtual instrument, turn-on duration, delay, and number of measurements are selectable. In the stand alone system a pre-optimized set of parameters is available.

3. SYSTEM CHARACTERIZATION

The axial sensitivity of the IR transmitter-receiver combination has been tested to check the accuracy in the positioning. A standard 1-cm glass cuvette has been mounted onto a translation unit, positioned between both prisms, the output of the IR amplifier has been connected to an oscilloscope and the output voltage has been monitored varying the position of the cuvette relative to the optical head. As shown in Fig. 3. The 10-90% range is no larger than 0.4

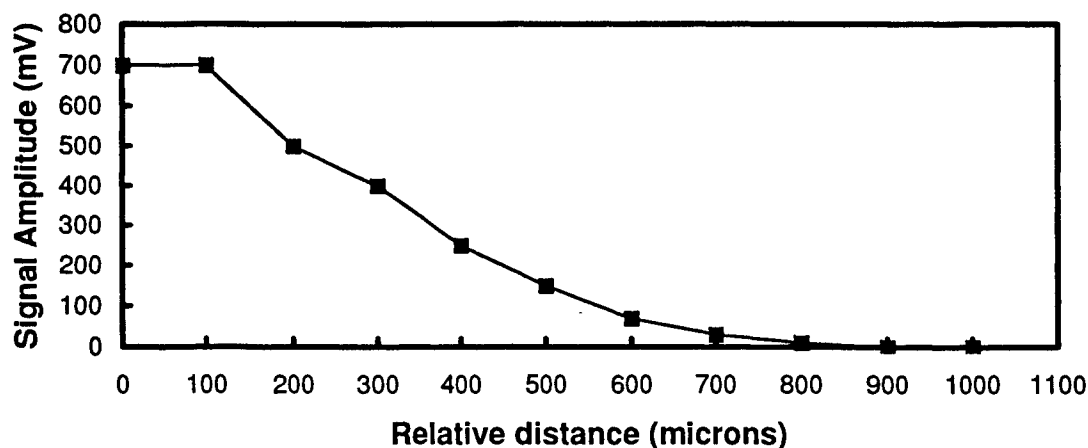


Fig. 3: Plot of the IR receiver output as a function of the position of a glass cuvette with respect to the optical head. The center of the beam is at 330 μ m, and corresponds to the front surface of prisms.

mm, and it is very easy for the operator to distinguish the position where the acoustic signal is 10% of the maximum, and choose that as the optimum value.

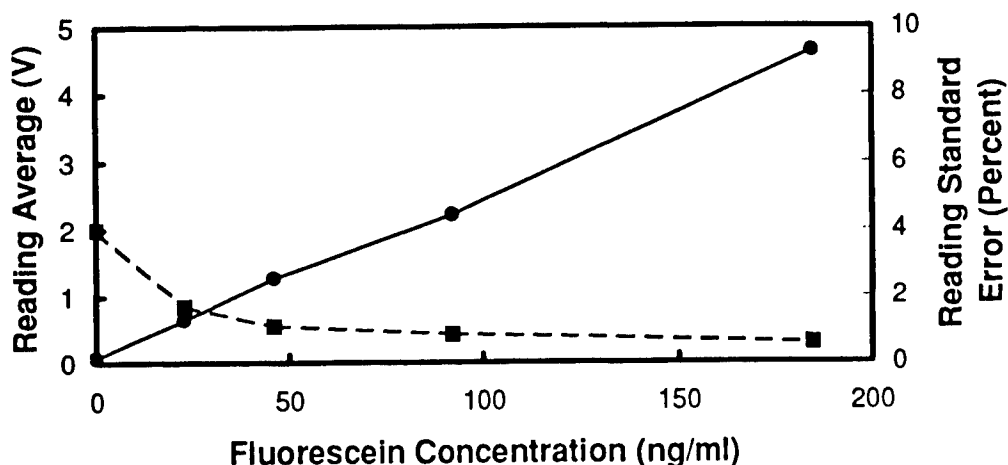


Fig. 4: Plots of average fluorescence values (solid line, left scale) and standard deviation (dashed line, right scale) as a function of the concentration of NaFl in a cuvette

The linearity and sensitivity of the corneal fluorometer have been measured by means of a set of square quartz cuvettes of 10mm width filled with solutions of Di-sodium Fluorescein ($\lambda_{exc}=490\text{nm}$, $\lambda_{em}=520\text{nm}$) in buffer medium at pH 4.2, with concentrations C ranging from 0 to $200\mu\text{g/l}$, as measured using a spectrophotometer. Fig. 4 shows a plot of average values (solid, left scale) and standard error (dashed, right scale) for all the concentrations tested. The standard error can be seen to be less than 1% in the range of concentrations mentioned.

4. EXPERIMENTAL RESULTS

Fig. 5 shows the overview of the data on healthy subjects as a function of age. For each subject, 5 measurements were performed on the left eye, and 5 on the right eye. The age independence of the signal collected seems to rule out any contribution of crystallin lens. The instrument was then tested for repeatability. One of the cuvettes of NaFl was used for the test. The cuvette was positioned at the optimum position as detected with the earphone, and a series of subsequent measurements was performed over a time interval of 2h. The standard error of the readout values was about 1% of the average value.

A preliminary evaluation of healthy vs diabetic volunteers has been carried out. Other sets of clinical evaluation have been successively performed in various centers. Healthy volunteers were obtained among the coworkers of the

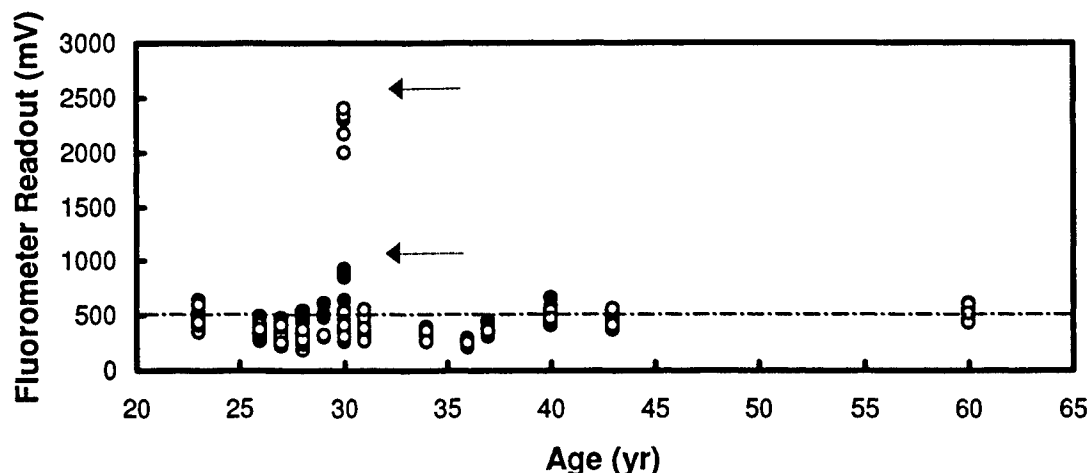


Fig. 5: Plot of the fluorometer readings as a function of age, for a sample of twenty-one subjects at the University of Brescia, including one severely diabetic patient (right and left eye marked with arrows). Broken line: average value for normal subjects. Solid marks: readings of left eye (aphakic). Open marks: readings of right eye (phakic).

Leiden University Medical Center and their relatives. The patients were obtained from the Ophthalmology Outpatient Department. Patients had Type-II diabetes mellitus with background or pre-proliferative retinopathy.

The values of corneal fluorescence of healthy volunteers and diabetic patients obtained with the fluorometer were compared to those obtained with a scanning commercial fluorophotometer ($\lambda_{exc}=490$ nm, $\lambda_{em}=520$ nm, Fluorotron Master, OcuMetrics, Mountain View, CA, USA). The latter instrument scans stepwise the fluorescence along the optical axis of the eye. The autofluorescence at the position of the cornea is usually increased by the amount of residual autofluorescence of the lens as the result of the limited spatial resolution of the scanning fluorophotometer (about 0.5 mm). A correction for this lens tailing was performed by subtracting the residual lens curve from the corneal scan. The residual lens curve was obtained by exponential interpolation of the lens curve at the position of the cornea¹¹.

5. CONCLUSIONS

A prototype of a new ocular fluorometer is presented. The apparatus has proven to be very easy to use, automatic, flexible, sensitive, linear and repeatable. Clinical tests presently underway will decide upon the effectiveness of the system as a low-cost, compact and inexpensive system, with a valid diagnostic potential for populations at risk for diabetic retinopathy.

6. REFERENCES

1. F. A. L'Esperance Jr., and W. A. James Jr., "The problem of diabetic retinopathy," in Diabetic Retinopathy, H. L. Little, R. L. Jack, A. Patz and P. H. Forham, eds (New York, Thieme-Stratton Inc., 1983), pp 11-20.
2. T. J. Merimee, "Diabetic retinopathy: a synthesis of perspectives," N. Engl. J. Med. 322, pp. 978-983, 1990.
3. J. C. Will, L. S. Geiss, and S. F. Wetterhall, "Diabetic retinopathy," N. Engl. J. Med. 323, pp. 613-623, 1990.
4. G. M. Haik Jr., W. L. Terrel, and G. M. Haik Sr., "Diabetic retinopathy: a leading cause of new blindness," South. Med. J. 82, pp. 575-579, 1989.
5. T. R. Stolwijk, J. A. Van Best, J. A. Oosterhuis JA, and W. Swart, "Corneal autofluorescence: An indicator of diabetic retinopathy," Invest. Ophthalmol. Vis. Sci. 33, pp. 92-97, 1992.

6. J. C. Bleeker, J. A. Van Best, L. Vrij, E. A. Van der Velde, and J. A. Oosterhuis, "Autofluorescence of the lens in diabetic and healthy subjects by fluorophotometry," *Invest. Ophthalmol. Vis. Sci.* 27, pp. 791-794, 1986.
8. T. R. Stolwijk, J. A. Van Best, J. P. Boot, and J. A. Oosterhuis, "Corneal autofluorescence in diabetic and penetrating keratoplasty patients as measured by fluorophotometry," *Exp. Eye Res.* 51, pp. 403-409, 1990.
8. S. Janiec, M. Rzendkowski, and S. Bolek, "The relation between corneal autofluorescence, endothelial cell count and severity of diabetic retinopathy," *Int. Ophthalmol.* 18, pp. 205-209, 1994.
9. S. Fantaguzzi, F. Docchio, L. Guarisco, and R. Brancato, "Corneal autofluorescence in diabetic and normal eyes," *Int. Ophthalmol.* 18, pp. 211-214, 1994.
10. M. Ishida, N. Yokoi, J. Okuzawa, K. Maeda, and S. Kinoshita, "Corneal autofluorescence in patients with diabetic retinopathy (in japanese)," *Nippon Ganka Gakkai Zasshi* 99, pp. 308-311, 1995.
11. E. P. M. Boets in "Fluorophotometry of the anterior segment of the eye with special attention to contact lenses", Ph.D. Thesis, Leiden State University, Leiden, The Netherlands, March 1995, Ch. 5, "Accuracy of the Fluorophotometer," pp. 48-68.

Measuring lens opacity: combining quasi-elastic light scattering with Scheimpflug imaging system

Rafat R. Ansari¹, Manuel B. Datiles III², James F. King¹, and Doretha Leftwood²

¹NASA Lewis Research Center
National Center for Microgravity Research in Fluids and Combustion Science
21000 Brookpark Road, Mail Stop 333-1, Cleveland, Ohio 44135, USA
Tel: (216) 433-5008, Fax: (216) 977-7138, E-mail: rafat.r.ansari@lerc.nasa.gov

²National Institutes of Health
National Eye Institute
Building 10, Room 10N226
Bethesda, MD 20892, USA
Tel: (301) 496-3577, Fax: (301) 402-1214, E-mail: mannyd3@box-m.nih.gov

ABSTRACT

Two powerful techniques: quasi-elastic light scattering (QELS) and Scheimpflug imaging (SI), are combined to provide simultaneous (within a few seconds) and objective measurements of lens opacity. The sensitivity and performance of the two techniques is evaluated by inducing cold cataract in the lens of a calf eye. The QELS detects the onset of cataractogenesis much earlier while the Scheimpflug imaging system detects it much later.

1. INTRODUCTION

Earliest, quantitative, and non-invasive detection of lens opacity has remained a desired goal of ophthalmologists. Such ability would help achieve uniform standards for objective analysis normally required in a longitudinal study in which the natural history of the disease process is followed. It would also be helpful in the screening of potential candidates/patient population for clinical trials of possible drugs in the treatment of cataracts. Measurements of early lens opacities have been carried out by several investigators using the techniques of quasi-elastic or dynamic light scattering (QELS or DLS) and Scheimpflug imaging (SI). Most recent clinical studies using these methods include studies by Thurston et al.¹, Rovati et al.², and Datiles et al.³, and the references contained in their publications. However, these two techniques, to best of our knowledge, have never been combined to gather data on lens opacity and having the results compared against each other. Recent technology developments for space (microgravity fluids) experiments⁴ at NASA have provided extremely compact, robust, non-invasive, and highly sensitive fiber optic DLS probes which can catch cataracts at the macromolecular level. These probes have shown their utility in accomplishing ocular tomography⁵ in animal models for studies of cataractogenesis, easy adaptation to clinical instruments used routinely in an ophthalmologists office, and in accessing several types of turbid media.⁶ The SI technique provides a semi-quantitative measure of turbidity of the lens tissue by converting Scheimpflug images into a parameter called optical density units (O.D.U.).⁷ A O.D.U. value of 0.01 represents transparency of an ultra clean sample of water. Clinically, the range of values, <0.1 O.D.U., are assigned to a normal (non-cataractous) lens while 0.1 to 1.0 > O.D.U. < 1.0 is considered to having a nuclear cataract from early to moderate stage. Fundamental details of the SI⁸ and DLS⁹ techniques have been covered elsewhere.

The laser light transmitted by a compact DLS fiber optic probe to the eye, monitor Brownian motion of the protein crystallins inside the lens. The particles scatter light and the intensity of this scattered light fluctuates in time due to the Brownian or thermal motion of the dispersed particles in the suspending medium. In a dynamic medium such as eye, when illuminated by laser light, a rapidly changing interference pattern due to the differences in the optical density of the scattering medium can be coherently detected by a DLS spectrometer. The rapidly fluctuating interference pattern at a photodetector contains information about the dynamics of the scattering medium and can be extracted by constructing a correlation function. A time correlation function (TCF) is constructed after detecting the scattered light by a photodetector and appropriate electronic processing via a amplifier-discriminator stage (built into the APD module) and a digital correlator. In the simplest case of dilute dispersions of spherical particles the slope of the correlation function provides quick and accurate determination of the particle's translation diffusion

coefficient. The diffusion coefficient data can easily be transformed into average particle size, using Stokes-Einstein equation, provided the viscosity of the suspending medium, its temperature, and refractive index are known. For particle size determination, the time correlation functions were analyzed using standard data inversion techniques of cumulant analysis and exponential (histogram) sampling. These were supplied with the BI9000 correlator system. Details can be found in references by Chu,⁹⁻¹⁰ Provencher,¹¹ and Stock and Ray.¹² In the experiments reported here viscosity of water at the respective lens temperature was used in the recovery of average crystallin size.

2. EXPERIMENTAL SET UP

The laboratory bench-top experimental set up is shown in Fig. 1. It consists of a Marcher Oxford Scheimpflug imaging system, a laser-detector box, a compact DLS fiber optic probe mounted on a custom designed swing-arm, a eye holder, custom built sample assembly for inducing cold cataract in the lens, temperature monitoring equipment, water circulation unit, and a lap-top computer containing a digital correlator card. In later experiments, performed at NEI and reported in this paper, the Marcher SI system was replaced by a Zeiss SI system which yields better images in combination of the NEI's Scheimpflug Image Analysis System.

Figures 2 and 3 offer a detailed and close-up view of some components. The DLS probe has been described elsewhere⁴⁻⁵ and therefore it will not be repeated. The probe used in this study has a diameter of 10.2 mm and a scattering angle of 170°. Laser light ($\lambda = \sim 670$ nm) was launched into the DLS probe through FC/PC connectors available on a custom built laser-detector box. The DLS probe was mounted on a custom designed three axis optical stage attached to the Scheimpflug imaging system currently used for human eye examinations. An arm, securing the probe head, has been designed to allow simultaneous DLS-SI measurements to be taken for comparison purposes. This arm easily swings out of the way when it is not needed.

The laser box consists of the Following components: Melles Griot (57-STL-102 57-FSN-602/FC/0.5 4 mw 671.3 nm) diode laser with a thermoelectric cooler (TEC), fiber coupled output power (output at fiber $\cong 1$ mW). Laser Driver: Thorlabs ANDL-TEC, controlling the TEC. We built our own laser power controllers. Photo Detector: EG & G Model SPCM-AQ, Active Quench. Power

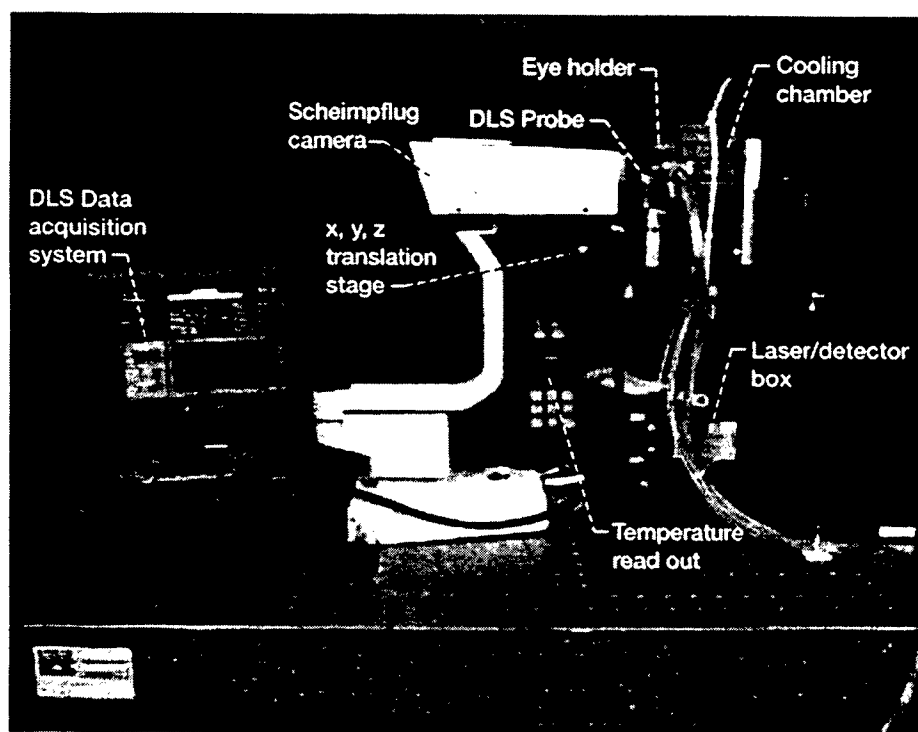


Figure 1.—DLS-SI benchtop experimental setup for simultaneous (within a few seconds) measurements of lens opacity.

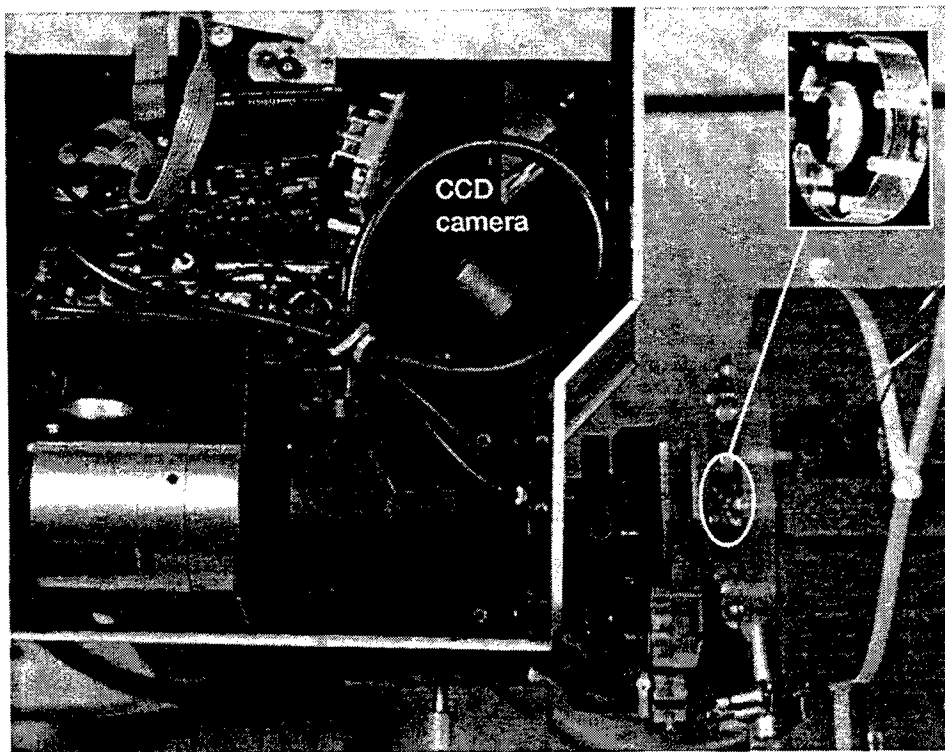


Figure 2.—Top view of the SI camera and the eye holder.

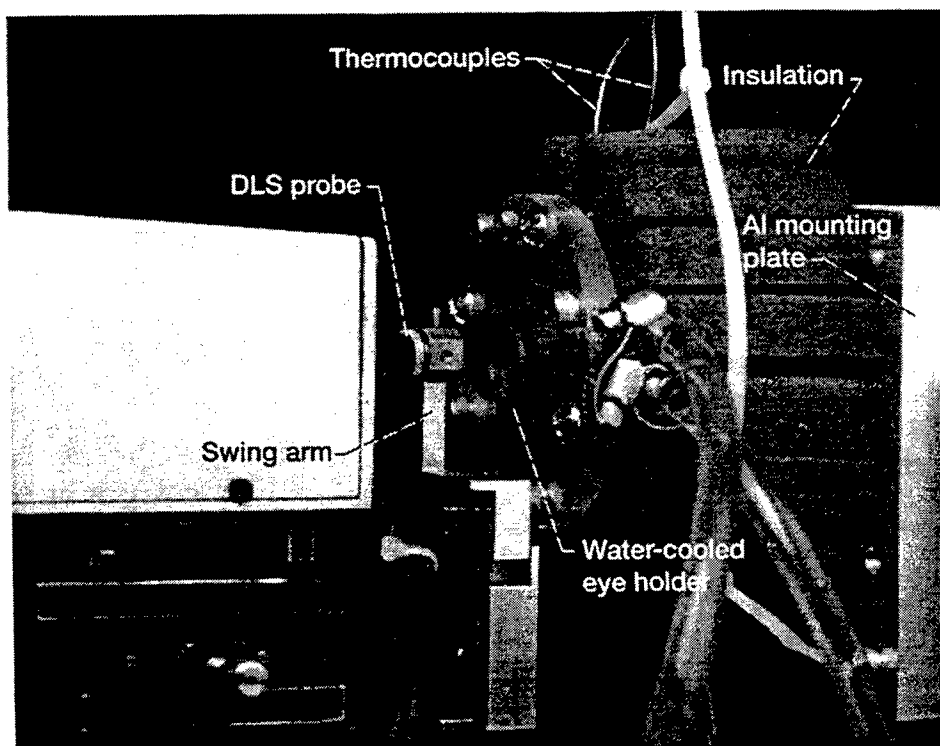


Figure 3.—Eye holder assembly for inducing cold cataracts.

Supply: Power One Model MAP 40-3000 +5v, +/- 12 v, 40 W. A BI-9000 digital correlator card housed in a lap-top IBM computer connected to the APD output in the laser-detector box. The DLS data was analyzed using the commercial software provided by the Brookhaven Instruments Company of New York. DLS measurements were made at a laser power of 50 μ W for a 5 to 10 second duration. The output power is controlled by a calibrated potentiometer ranging from 0 to 580 μ W located on the front panel of the laser box.

The eye holder cavity was machined in a block of plexi-glass material measuring 83.3 mm in diameter X 38.1 mm in thickness. A cooling jacket has been machined around the base of the housing to provide adequate cooling necessary to refrigerate the eye from the base. This plexi-glass eye holder is mounted on an aluminum manifold measuring 83.3 mm in diameter X 25.4 mm in thickness. This aluminum manifold provides access from the bottom to the plexi-glass cooling jacket. A top cover has been machined to an optically smooth finish which snugly fits the bottom cavity covering the entire eye. The top cover is then surrounded by an upper cooling jacket, exposing 15.2 mm in diameter of the eye. This cover also keeps the cornea moist throughout the measurements. These cooling jackets allow the eye to quickly achieve equilibrium as the temperature is slowly dropped. Using an Endocal refrigerated circulating bath model RTD-5DD, cooling water with a flow rate of 0.5 gallons/minute is connected in series using tygon tubing. The water is circulated through both the upper and the lower cooling jackets of the eye holder, controlling the eye temperature (or lens temperature). Through access holes, the temperature is continuously monitored and recorded at the back of the eye (T_b) as well as the front (T_f) using two 0.5 mm diameter stainless steel sheath closed end, grounded, type "K" thermocouples. A 57.2 mm I.D. X 76.2 mm O.D. X 6.4 mm thick ring, fabricated from Sali-1200 insulating material, thermally isolates the assembly from an aluminum mounting plate. This assembly is mounted to a Newport M-410 vertical slide. DLS and SI measurements were made at every 1° C interval. When $T_f = T_b$, 10 minutes are given for temperature equilibration before the DLS/SI measurements are made on the eye lens. Fresh calf eyes from animals ranging in age 14-16 weeks were obtained from slaughter houses (Tucker Packaging, Orville, Ohio) and (Ruppersberger & Sons Baltimore, Maryland) for experiments conducted at NASA LeRC in Cleveland and NEI in Bethesda respectively. The experiments were concluded within 24 hours after collecting the eyes. The intact eyes were used as received with the exception of trimming excess tissue from the back of the eye so that it can fit the plexiglass cavity in the sample holder described above. No dissections or pupil dilations were carried out. The calf eye was then positioned in front of the SI camera and the DLS probe in a manner similar to positioning a human subject. The DLS probe was then positioned to focus the scattering volume (or volume under test $\sim 20 \mu$ m) in the nuclear region of the lens and this set up remain unchanged for the entire duration of the experiment.

3. RESULTS

Before making actual measurements on the eye, we ensured that DLS measurements be free of all artifacts due to temperature cycling. This was accomplished by testing and calibrating the instrumentation using solutions of polystyrene latex standards. The 85nm latex solution was filled into the cavity of the eye holder in which a whole eye fits snugly. Figure 4 represents typical DLS data at three temperature settings. From these correlation functions, size distribution can be extracted at each temperature setting. This is shown in Fig. 5. These results indicate that our instrumentation give consistent values for the standard solutions from 20° C to 5° C. These results verify that falling temperature does not affect the reasonable and accurate determination of particle sizes. After this verification, a calf eye was housed in the holder and static. DLS, and SI measurements were made.

Figure 6 shows the static lightscattering data as a function of temperature in which scattered photons were collected from the nuclear region of the lens of a calf eye. The total scattered intensity slowly increases as temperature decreases in the beginning stages and then sharply increases after reaching the 14° C mark. The onset of cataractogenesis can be contemplated around 17° C. As temperature continues to drop, the intensity increases sharply and consistently, showing the progression of cataract.

The DLS data is presented in terms of time autocorrelation function (TCF) profiles as a function of temperature and is presented in Figs. 7 and 8. The slope of each individual TCF curve yields a translational diffusion coefficient which can be converted into average protein crystalline size. A change in the amplitude or spatial coherence factor (β) and slope is evident as soon as the temperature is reduced to 19° C. Among the family of TCF curves between 19° C and 17° C, the β values drop slightly but the slopes do not change appreciably.

For the family of curves shown in Fig. 8, both the β values and slope change consistently and appreciably indicating a gradual progression of cataract. This indicates the onset of cataractogenesis occurring around 17° C. Around 14° C and below severe lens opacity can be produced. This can be seen by converting the DLS data into particle size distributions.

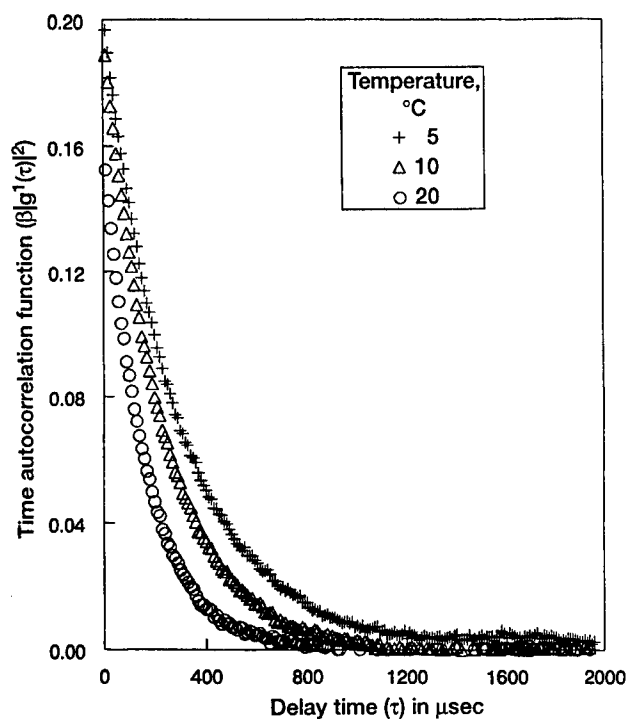


Figure 4.—Auto correlation functions for 85nm polystyrene standards, at three different temperatures.

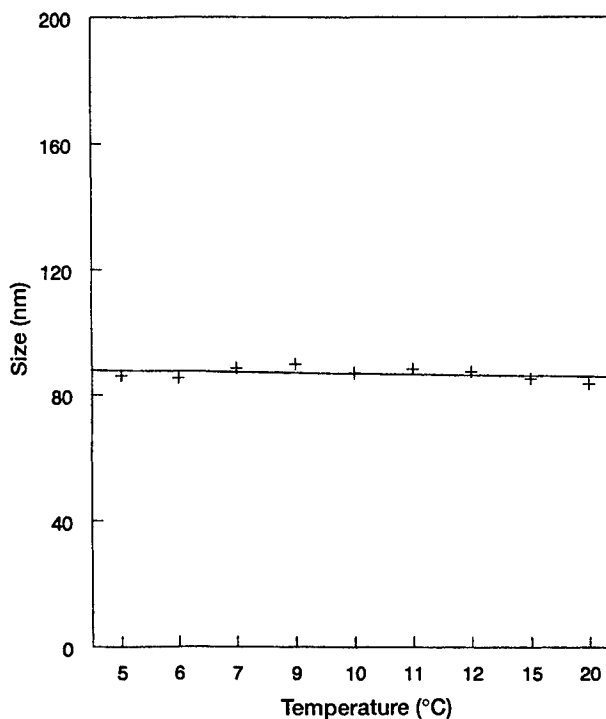


Figure 5.—Average particle size of 85nm polystyrene standards using 2nd cumulant analysis.

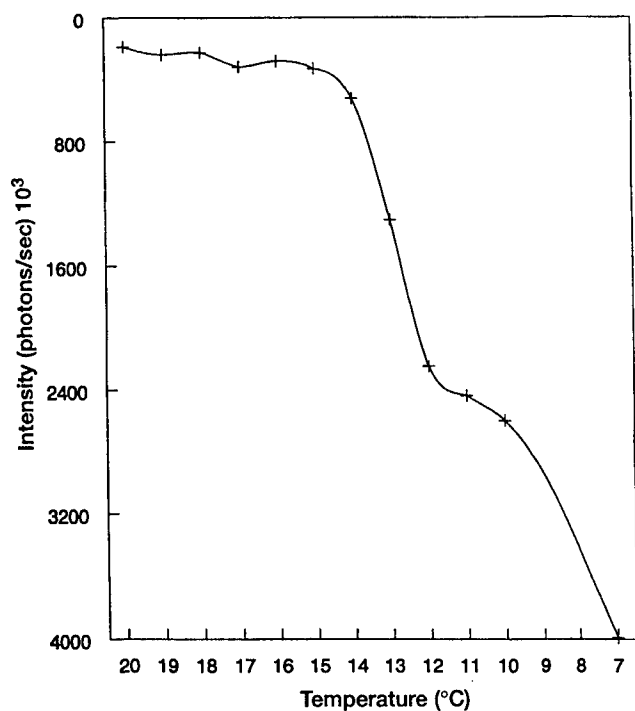


Figure 6.—Static light scattering data showing onset of cataractogenesis around 17 °C

Temperature, °C	Optical Density (O.D.U.)
19	0.01
18	0.01
17	0.01
16	0.01
15	0.01
14	0.01
13	0.01
12	0.01
11	0.01
10	0.02
9	0.03
8	0.04
7	0.05

Table 1.—Scheimpflug evaluation of cold-induced cataract in a calf eye lens.

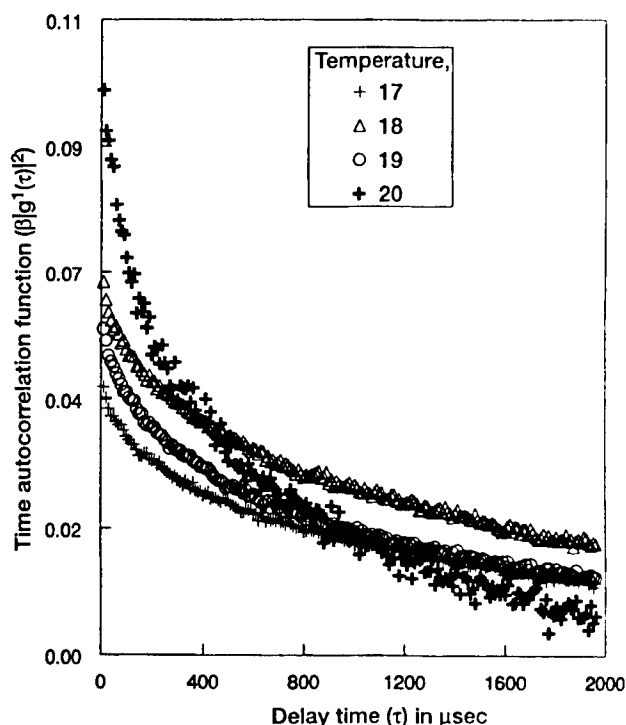


Figure 7.—Autocorrelation function profiles for the calf lens.

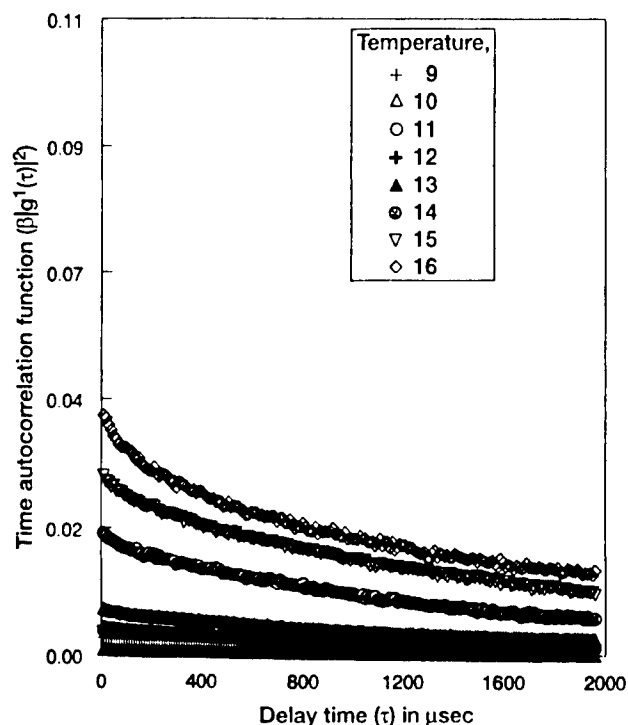


Figure 8.—Autocorrelation function profiles for the calf lens.

In Fig. 9, we present size distributions, obtained by inverting DLS data using the exponential sampling algorithm, for some representative samples or curves from Figs. 7 and 8. For a one to one equivalence, Scheimpflug images are compared in Fig. 9 against the DLS data. The size distributions are quite broad but they shift to the right consistently as expected in a growing cataract by forming bigger aggregates or protein complexes. Experimental evidence for this has been given by Spector,¹³ Jedziniak et al.¹⁴⁻¹⁵, and Tanaka and Benedek,¹⁶ amongst several others. Scheimpflug images, however, do not show any change up until 10° C when the optical density changed from 0.01 to 0.02 O.D.U. Based on these observations, we conclude that DLS has the ability to show the onset of cataractogenesis much earlier (~17° C), while the Scheimpflug imaging system detects it at a much later stage (~10° C).

4. DISCUSSION

The total intensity and DLS measurements show the onset of cataractogenesis much earlier (~17° C) While the SI measurements show a change at a much later stage (~ 10° C). O.D.U. values are reported in Table 1. However, DLS data (see Fig. 9) show a considerable change in the particle size distribution. Based on our results, it seems that SI evaluation underestimates a growing lens opacity or cataract, therefore, limiting its usefulness in the longitudinal studies of patients or in drug screening. On the other hand, DLS measurements show a very high sensitivity. In future clinical trials of anti-cataract drugs, it is important to give the drug to the patient at a stage when the cataract is still reversible. If the cataract is advanced and non-reversible, the drug would be ineffective. Hence, if the DLS can detect the earliest cataract change, it will be very useful in determining the patient eligibility for the clinical trial of an anti-cataract drug.

The DLS data, when converted into particle size distributions, show quite nicely how a cataract is progressing. However, we do not wish to emphasize the exact number for the particle size in a dynamic system such as a cataractous eye because of unknown factors such as the changing viscosity or the effects due to multiple light scattering occurring in a turbid media. We do, however, point out the good dynamic range of the DLS probe to follow a systematic trend as a marker for the cataract progression. Further, we have shown elsewhere that our DLS probe can be used effectively in the determination of accurate particle size from transparent to extremely turbid (~7 orders of magnitude higher than the turbidity of water) samples ranging in size from few nanometers to almost a micron.⁶

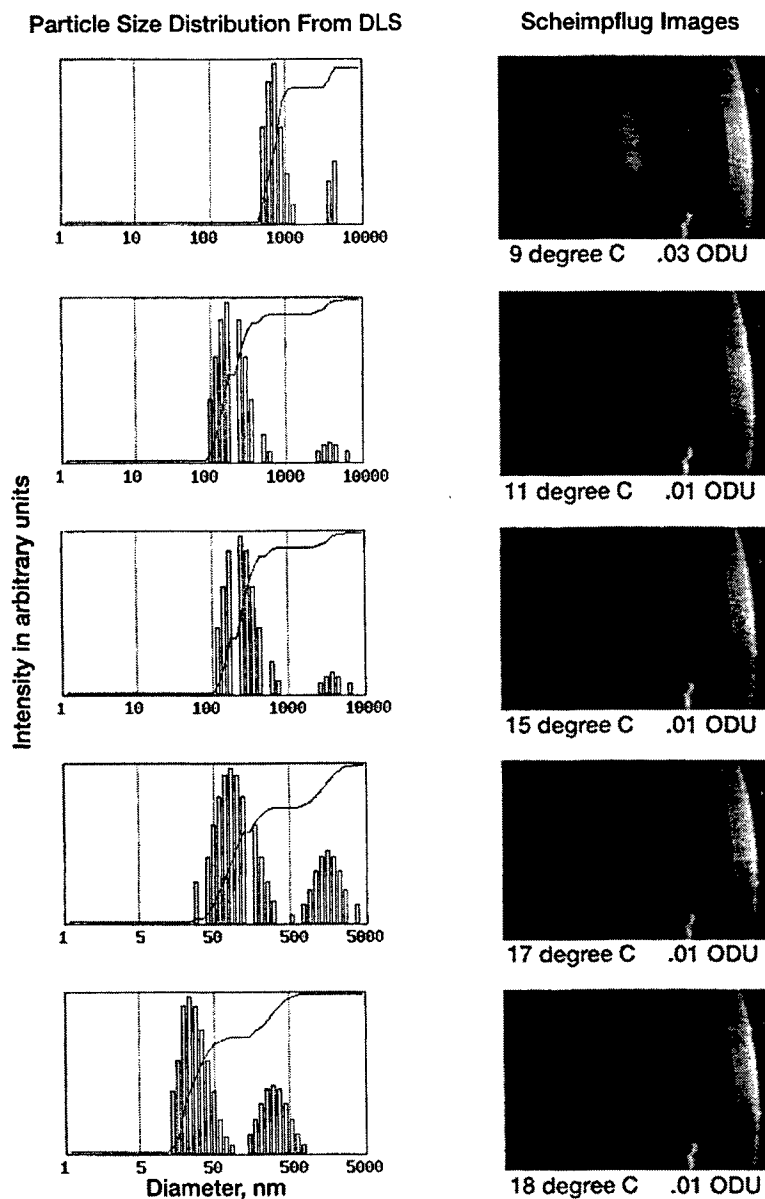


Figure 9.—Comparison of particle size distributions and Scheimpflug images.

5. CONCLUSION

We have combined two powerful techniques (QELS and SI) by implementing a compact DLS fiber optic probe on the NEI's SI system for the objective study of lens opacity. We find DLS or QELS to be far more superior in sensitivity over the SI technique in the evaluation of cataractogenesis.

6. ACKNOWLEDGMENTS

The authors are grateful to NASA's office of Life and Microgravity Sciences and Applications for supporting this work under a NASA-NIH interagency agreement on the use of novel fiber optic probes for the early detection of eye diseases. Cindy Doss (JK's sister) is acknowledged for her help in providing calf eyes for the experiments reported in this paper. Help provided by Art Birchenough and Mike Hahn in building the custom designed laser-detector box is gratefully acknowledged.

7. REFERENCES

1. Thurston, G.M., Hayden, D.L., Burrows, P., Clark, J.I., Taret, V.G., Kandel, J., Courogen, M., Peetermans, J.A., Bowen, M.S., Miller, D., Sullivan, K.M., Storb, R., Stern, H., and Benedek, G.B., Light Scattering from the Aging Human Lens In Vivo, *Current Eye Research*, 197–207, 1996.
2. Rovati, L., Frankhauser II, F., and Ricka, J., *Rev. Sci. Instrum.* 67(7), 2615–2619, (1996).
3. Datiles, M., "Clinical Evaluation of Cataracts, in: Tasman, W. and Jaeger, E. Duane's Clinical Ophthalmology. Philadelphia, PA, Lippincott Co., Inc., 73B: 1–15, 1992.
4. Ansari, R.R., Suh, K.I., Arabshahi, A., Wilson, W.W., Bray, T.L., and DeLucas, L.J., A Fiber Optic Probe for Monitoring Protein Aggregation, Nucleation, and Crystallization, *J. Crystal Growth*, 168 (1996), 216–226.
5. Ansari, R.R., Suh, K.I., Tumminia, S.J., Russell, P., and Zigler, Jr., J.S., In-vivo "Cataractograms" Using a Compact Backscatter Dynamic Light-Scattering (DLS) Probe, *SPIE Vol. 3192*, pp. 202–210, 1997.
6. Ansari, R.R., and Suh, K.I., Dynamic Light Scattering Particle Size Measurements in Turbid Media, Invited paper, *SPIE Vol. 3251*, to be published.
7. Vivino, M., Chintalagiri, S., Trus, B., and Datiles, M., "Development of a Scheimpflug Slit Lamp Camera System for Quantitative Densitometric Analysis. Eye, 7:791–798, 1993.
8. Datiles, M., Magno, B., Friedlin, V.: Nuclear Cataract Progression Study Using the NEI Scheimpflug Imaging System. Brit. J. Ophthalmol., 79:527–534, 1995.
9. Chu, B., *Laser Light Scattering: Basic Principles and Practice*, Academic Press, New York, 1991.
Chu, B., and Gulari, E., "Photon Correlation Measurements of Colloidal Size Distributions. II. Details of Histogram Approach and Comparison of Methods of Data Analysis," *Phys. Scripta* 19, 476–485, 1979.
10. Chu, B., and Gulari, E., "Photon Correlation Measurements of Colloidal Size Distributions. II. Details of Histogram Approach and Comparison of Methods of Data Analysis," *Phys. Scripta* 19, 476–485, 1979.
11. Provencher, "Inverse Problems in Polymer Characterization: Direct Analysis of Polydispersity with Photon Correlation Spectroscopy," *Makromol Chem.*, 180, 201–209, 1979.
12. Stock, R.S. and Ray, W.H., "Interpretation of Photon Correlation Data: A Comparison of Analysis Methods", *J. Polym. Sci.: Polymer Physics Edition*, 23, 1393–1447, 1985.
13. Spector, S. Li and J. Sigelman, "Age-Dependent Changes in the Molecular Size of Human Lens Proteins and Their Relationship to Light Scatter," *Investigative Ophthalmology*, 13(10), 795–798 (1974).
14. Jedziniak, A., Kinoshita, J.H., Yates, E.M., Hocker, L.O. and Benedek, G.B. "On the Presence and Mechanism of Formation of Heavy Molecular Weight Aggregates in Human Normal and Cataractous Lenses." *Exp. Eye. Res.*, 15, 185–189 (1973).
15. Jedziniak, A., Nicoli, D.F., Baram, H. and Benedek, G.B., "Quantitative Verification of the Existence of High Molecular Weight Protein Aggregates in the Intact Normal Human Lens by Light Scattering Spectroscopy," *Investigative Ophthalmology*, 17(1), 51–57 (1978).
16. Tanaka, T. and Benedek, G.B., "Observation of Protein Diffusivity in Intact Human and Bovine Lenses with Application to Cataract," *Investigative Ophthalmology*, 14(6), 449–456 (1976).

New method for Measurement of *in vivo* penetration of UVR into the crystalline lens

Per G. Söderberg^{a,b,c}, Stefan Löfgren^a, Ralph Michael^a, Xochitl Gonzalez-Cirre^b

^aSt. Erik's Eye Hospital, Karolinska Institutet, S-104-01 Stockholm, Sweden

^bOptometry Education, Karolinska Institutet, S-104 01 Stockholm, Sweden

^cDept. Of Biomedical Engineering, University of Miami, FL 331 36

ABSTRACT

The penetration of 300 nm ultraviolet radiation (UVR) in the anterior cortex of the crystalline lens was 0.45 mm, penetration being expressed as the distance attenuating the transmittance to $1/e^2$. The estimation is based on measurement of *in vivo* inactivation of lactate dehydrogenase (LDH) due to *in vivo* exposure to UVR 300 nm. The inactivation of LDH was independent of the latency interval after the exposure within 0-6 h. There was a 30-40 % inactivation of LDH in the cornea that dropped to 0 % in the inner anterior cortex. The currently described method allows spatially resolved measurement of the *in vivo* dose of UVR 300 nm within the cornea and the crystalline lens.

Keywords: ultraviolet, radiation, 300 nm, rat, crystalline, lens, penetration, absorption coefficient

1. INTRODUCTION

The eye is during day time continuously exposed to ultraviolet radiation (UVR). The UVR has known toxic effects to the cornea and the lens¹⁻³. When UVR hits eye tissues, it may be transmitted, absorbed or scattered. The transmittance of the eye tissues is classically measured on isolated tissues in a spectrophotometer⁴⁻⁷. For the lens, Maher⁵ found with such measurements a linear absorption coefficient (α) of 2.18 mm^{-1} corresponding to a penetration ($2/\alpha$) of 0.92 mm, the transmittance being $1/e^2$ at the depth of penetration. The transmittance *in vivo* may be measured by introduction of an optical fiber into the eye⁸. This requires however a surgical intervention which may disturb the measurement.

Lactate dehydrogenase (LDH) is an enzyme that is photochemically inhibited by UVR *in vitro*⁹. It has been shown that the glycolysis is inhibited in the lens *in vivo*¹⁰. It is possible to histochemically determine the regional distribution of lactate dehydrogenase activity in a lens¹¹.

In a lens exposed *in vivo* to UVR, the LDH activity should decrease. The decrease due to the UVR exposure can be estimated by comparison with the contralateral not exposed lens. Thus, LDH can be used as a chromophore that can spatially resolve UVR exposure within the lens.

The purpose of the present paper was to estimate the penetration of UVR in the lens using LDH as a biological chromophore.

2. METHODS AND MATERIALS

Sprague-Dawley rats were exposed unilaterally *in vivo* to UVR. The distribution of LDH activity in the lens was estimated histochemically. The penetration of UVR in the lens was finally modeled.

2.1 EXPOSURE TO ULTRAVIOLET RADIATION

UVR was generated with a high pressure mercury lamp filtered with a water filter and an interference filter centered at 300 nm with a half band width of 10 nm. The rat was anesthetized with xylazine (11 mg/kg) and ketamin (80 mg/kg) intraperitoneally. Both eyes were dilated with tropicamide (5 mg/ml). Then, one eye was exposed to 90 kJ/m^2 (19 min.) while the other eye was kept as a control.

2.2 HISTOCHEMISTRY

After sacrificing the rat, the eye was enucleated, embedded in methyl-cellulose and frozen in iso-pentane to -150 C° in liquid nitrogen.

The eye was freeze-sectioned close to parallel to the optical axis, the section thickness being 10 µm. For each eye, three sections were collected to both a test slide and a control slide.

The test medium consisted of 4 mM NAD, 2 mM nitroblue tetrazolium (NBT) 0.25 mM phenazine methosulfate, 5 mM sodium azide, 150 mM lactate and 10 mM ethylmalcimine in 50 mM glycyl-glycine buffer, the pH being adjusted to 8 with NaOH. The control medium was similar apart from an additional 20 mM pyruvate and lack of lactate.

Sections on test and control slides were covered with 0.2 ml test and control medium respectively. The enzyme reaction was run at 24 C° and was stopped by rinsing 45 s in rotating hot water. Finally, the sections were mounted with Kaiser's glycerol-gelatine.

2.3 DENSITOMETRY

The sections were measured with a Leitz microscope based densitometer with a measuring spot of 9 µm in diameter. The densitometric measurements were done at 585 nm.

2.4 ESTIMATION OF LDH ACTIVITY

Transmittance through the histological section was calculated as the ratio between tissue reading and blank reading (just outside the section) and transformed to absorbance. Absorbance for test slide was then reduced with absorbance for control slide to get relative enzyme activity for the region for the lens.

2.5 EXPERIMENTAL DESIGN

In total, 30 rats were distributed on 3 latency groups with 10 rats each. The groups were sacrificed immediately and 2 and 6 h after exposure to UVR. From each lens, slide pairs (test and control) were obtained. Each slide pair contained three independent section pairs (test and control) of which two were selected for measurement. In each section pair, the basal corneal epithelium and outer anterior lens cortex, inner anterior lens cortex, nucleus and posterior cortex were measured along the visual axis 210, 630, 1460 and 2500 µm from the outer capsular edge, respectively. For each region and each section, three readings were obtained and averaged.

2.6 MODEL

The inactivation of LDH (%), Ω , is in the present paper used as a measure of the intensity of UVR in the tissue during exposure. Inactivation was calculated as one minus the relative activity in the exposed lens (Absorbance units), A_e , related to the relative activity in the contralateral lens (Absorbance units), A_c (Eq. 1).

$$\Omega = 1 - \frac{A_e}{A_c} \quad (1)$$

According to the second law of photochemistry and the law of reciprocity, the inactivation of LDH (%), Ω , is at each point in the lens directly proportional to the dose of UVR (J/m^2), H_e (Eq. 2).

$$H_e = k \Omega \quad (2)$$

Here, k is a proportionality constant.

According to the Lambert-Beer law the linear absorption coefficient, α , can be estimated if the intensity of the radiation is known at two points along the path of the radiation according to (Eq. 3), the distance between the points being l_2-l_1 .

$$\alpha = \frac{\ln\left(\frac{H_{e:1}}{H_{e:2}}\right)}{l_2 - l_1} \quad (3)$$

Substituting H_e in Eq 3 according to Eq. 2, it is seen that the linear absorption coefficient, α , can be calculated from the inactivation of LDH (%) at the two points along the path of the radiation (Eq. 4).

$$\alpha = \frac{\ln\left(\frac{\Omega_1}{\Omega_2}\right)}{l_2 - l_1} \quad (4)$$

In the current paper the definition of penetration depth, $2/\alpha$, is used, corresponding to a transmittance of $1/e^2$ at the penetration depth.

3. RESULTS

3.1 INACTIVATION OF LACTATE DEHYDROGENASE

It was found that the inactivation varied from 30-40% in the cornea to none in the inner anterior cortex (Fig. 1). The inactivation was approximately the same within a tissue depth for all latencies studied. In the nucleus, there was a considerable variation.

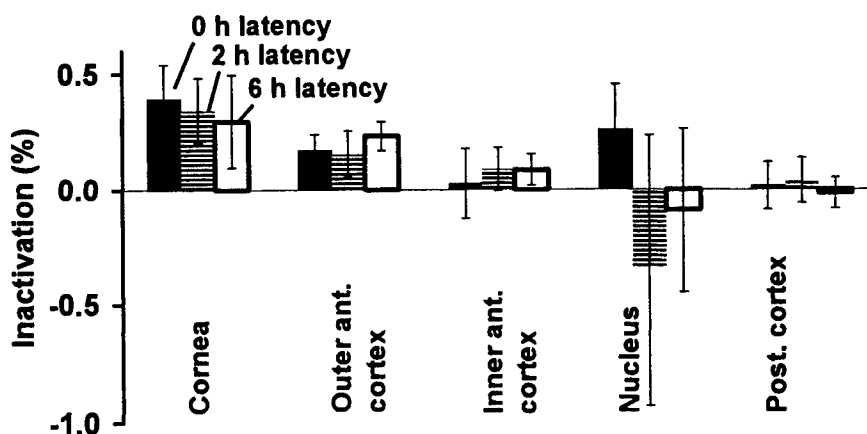


Fig. 1 *In vivo* inactivation of lactate dehydrogenase in the crystalline lens with 300 nm ultraviolet radiation.

3.2 *IN VIVO* PENETRATION DEPTH FOR UVR 300 NM IN THE ANTERIOR LENS CORTEX

In Fig 2, the penetration depth of UVR 300 nm *in vivo*, in the anterior cortex, of the crystalline lens has been estimated from the inactivation of LDH at 0 h latency after the exposure to UVR 300 nm according to Eq. 4. The penetration depth was estimated to 0.45 mm.

In the figure is also plotted the attenuation of UVR 300 nm as expected from *in vitro* measurements of the linear absorption coefficient in monkey lenses⁵. It is seen that Maher's data suggest a slightly deeper penetration than the current data. However, it should be kept in mind that Maher's data are based on whole lens measurements on monkey lenses.

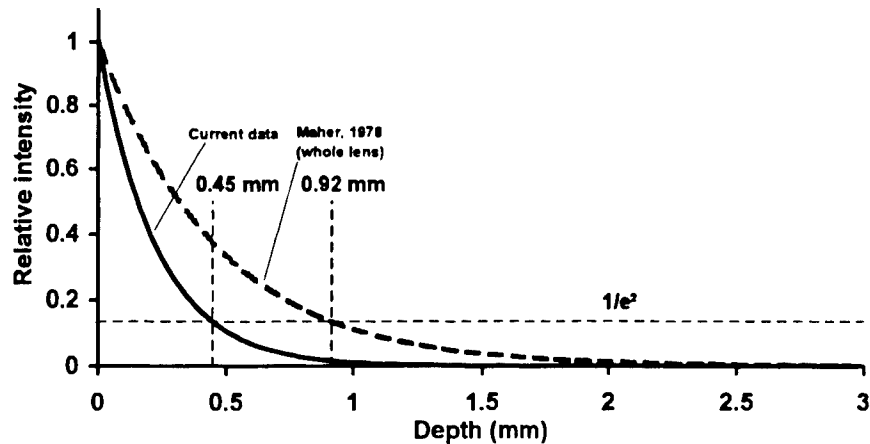


Fig. 2 Penetration depth of 300 nm ultraviolet radiation in the anterior cortex of the living crystalline lens.

4. DISCUSSION

The present investigation aimed at establishing a method for estimation of *in vivo* penetration of 300 nm UVR in the crystalline lens.

Current knowledge on the penetration of optical radiation in eye tissues is based on spectrophotometric measurements of isolated eye tissues⁴⁻⁷ or *in vivo* measurements of the attenuation of optical radiation introduced fiberoptically into the living eye⁸. The primary drawback of these methods is that the measurement is done *in vitro* or with a surgical intervention. Both of these factors induce errors in the estimation.

Data on transmittance of optical radiation into tissue are often used to estimate the exposure at various depths in the tissue. It is however known that scattering may induce higher exposure than that expected from the transmittance measurement. Further, a classical transmittance measurement is limited to measurements of anatomical units such as the complete crystalline lens. This renders the transmittance integrated over the complete anatomical unit although for e.g. the transmittance of the lens is expected to vary considerably spatially.

The currently introduced method spatially resolves the actual dose of UVR 300 nm, under *in vivo* conditions reflected as LDH inhibition. Thus, also scattered radiation is considered. Further, the method provides information on spatial variation of penetration.

The method requires that LDH is a quantitatively insignificant chromophore for UVR 300 nm. Since the major chromophore for UVR 300 nm in the lens is structural proteins that are abundant, there are good reasons to believe that that is the case.

Further, the method requires that inactivation of LDH is not modulated by any intrinsic factor. Since the inactivation of LDH is an immediate photochemical response to the exposure to UVR 300 nm⁹, it is preferable to measure as soon as possible after the exposure. For this reason, the 0 h latency data were used to estimate penetration in Fig. 2.

The fact that multiple scattering occurs in tissue makes the estimation of the penetration depth based on the Lambert-Beer relationship (Fig. 2) questionable. The current estimation of penetration depth should therefore be considered cautiously

and not used to mathematically derive spatially resolved flux. For this, it is better to use the primary data on LDH inactivation. However in the lack of data on real penetration, the model has the advantage to allow comparison of the current data with classical transmittance measurements. It is seen in Fig. 2 that the penetration depth currently estimated (0.45 mm) is less than that obtained by Maher (0.92 mm)⁵.

The recording of *in vivo* inactivation of LDH provides a tool to spatially resolve dose distribution within the crystalline lens at *in vivo* exposure to UVR 300 nm.

5. ACKNOWLEDGMENTS

The current work was supported by Karolinska Institutets forskningsfonder, S:t Eriks Ögonforskningsstiftelse, Loo och Hans Ostermans stiftelse för medicinsk forskning, KI resebidragsfond med Hirschs studieresefond för kirurger, Gun och Bertil Stohnes Stiftelse, Rasmussens Stiftelse, Carmen och Bertil Regners Stiftelse, Anders Otto Svärds Stiftelse and Svenska Sällskapet för Medicinsk Forskning.

6. REFERENCES

1. P. G. Söderberg, Acute cataract in the rat after exposure to radiation in the 300 nm wavelength region. A study of the macro-, micro- and ultrastructure. *Acta Ophthalmol (Copenh)* 66, 141-152, 1988.
2. J. P. G. Bergmanson and P. G. Söderberg, The significance of ultraviolet radiation for eye diseases. A review with comments on the efficacy of UV-blocking lenses. *Ophthalmic Physiol Opt* 15, 83-91, 1995.
3. R. Michael *Threshold dose estimation for ultraviolet radiation induced cataract. Thesis.* Karolinska Institutet, Stockholm, 1997.
4. E. A. Boettner and J. R. Wolter, Transmission of ocular media. *Invest Ophthalmol* 1, 776-783, 1962.
5. E. F. Maher *Report SAM-TR-78-32 USAF School of Aerospace medicine, Aerospace Medical Div.* USAF SCHOOL OF AEROSPACE MEDICIN, Aerospace Medical Division, AFSC, 1978.
6. F. M. Barker *The transmittance of the electromagnetic spectrum from 200 nm to 2500 nm through the optical tissues of the eye of the pigmented rabbit. Thesis.* University of Houston, Houston, 1979.
7. P. G. Söderberg, P. Rol, D. B. Denham and J. -M. Parel, Transmittance of the lens capsule. *Proc of Ophthalmic Technologies VI, SPIE* 2173, 21-24, 1996.
8. P. G. Söderberg, P. Torstensson, C. Beckman, J. Ren, P. Algvere and B. Tengroth, Fiber optic point-source for *in vivo* measurement of light transmission and scattering in the eye. *Proc of Ophthalmic Technologies IV, SPIE* 2126, 324-330, 1994.
9. E. Chen, P. G. Söderberg, A. D. MacKerell, B. Lindström and B. Tengroth, Inactivation of lactate dehydrogenase by UV radiation in the 300 nm wavelength region. *Radiat Environ Biophys* 28, 185-191, 1989.
10. S. Löfgren and P. G. Söderberg, Rat lens glycolysis after *in vivo* exposure to narrow band UV or blue light radiation. *J Photochem Photobiol B* 30, 145-151, 1995.
11. S. Löfgren and P. G. Söderberg, Histochemical determination of lactate dehydrogenase activity in rat lens; influence of different parameters. Submitted, 1997.

Quantitative, spatio-temporal image analysis of fluorescein angiography in age-related macular degeneration

Jeffrey W. Berger

Scheie Eye Institute and School of Engineering and Applied Science,
University of Pennsylvania, Philadelphia, PA 19104

ABSTRACT

Interpretation and analysis of retinal angiographic studies has been largely qualitative. Quantitative analysis of pathologic fundus features will facilitate interpretation and potentiate clinical studies where precise image metrology is vital. Fluorescein angiography studies of patients with age-related macular degeneration were digitized. Sequential temporal images were spatially-registered with polynomial warping algorithms, allowing for the construction of a three-dimensional (two spatial and one temporal) angiogram vector. Temporal profiles through spatially-registered, temporally-sequential pixels were computed. Characteristic temporal profiles for fundus background, retinal vasculature, retinal pigment epithelial atrophy, and choroidal neovascular (CNV) membranes were observed, allowing for pixel assignment and fundus feature quantitation. Segmentation and quantitation of fundus features including geographic atrophy and CNV is facilitated by spatio-temporal image analysis.

Keywords: age-related macular degeneration, choroidal neovascularization, fluorescein, image processing, retina

1. INTRODUCTION

Retinal angiographic studies augment information derived from direct ophthalmoscopic inspection of the eye fundus facilitating diagnosis and treatment of retinal disease. Fluorescein angiography, and more recently, indocyanine green angiography studies allow for detailed investigation of the retina and choroid yielding diagnostic information in diseases such as age-related macular degeneration and diabetic retinopathy---the major causes of blindness in developed countries. Information derived from these studies guide treatment and contribute towards the prevention of severe visual morbidity including blindness.

Heretofore, interpretation of retinal angiographic studies has been largely qualitative. Analysis and interpretation of fundus angiography relies on a skilled observer to discern normal and pathologic features on single angiographic images, and to synthesize information derived from multiple images acquired during dye transit. The angiography reader superimposes sequential frames of the angiogram in his or her "mind's eye", and determines the temporal characteristics of dye fluorescence as a function of space (across the fundus image) and time (for spatially corresponding regions through phases of the angiogram). Considerable experience has been obtained and features of interest including leaking microaneurysms, choroidal neovascular membranes (CNV), retinal pigment epithelial atrophy, cystoid macular edema, and pigment epithelial detachment are readily identified by the experienced reader¹. However, quantitation of the "known" fluorescein fluorescence behavior for common normal and pathologic fundus features has not been previously reported.

Age-related macular degeneration (AMD) is the most common cause of blindness in the United States. At present, laser therapy as guided by the Macular Photocoagulation Studies² is the only proven form of treatment. However, only a small fraction of eyes affected by AMD are eligible for laser treatment, and in many cases, the benefits of laser when compared with natural history are quite modest. Accordingly, alternative therapies including

photodynamic therapy, radiation therapy, pharmacologic agents, nutritional agents, and surgical approaches are being developed and evaluated for treatment and prophylaxis of the vision-limiting sequelae of AMD.

While quality of life and visual acuity are the primary outcomes in clinical studies evaluating efficacy for these approaches, fundus feature quantitation including the areas corresponding to choroidal neovascularization (CNV), retinal pigment epithelial atrophy, and drusen serve as important secondary outcomes. However, current methods for fundus feature quantitation are subjective, laborious, prone to error, and are poorly suited to highly accurate image comparison.

Advances in digital image processing methodologies allow for sophisticated manipulation of fundus images. Image registration---the spatial alignment of similar images---allows for precise quantitation of the temporal properties of fluorescein fluorescence attributable to spatially-corresponding regions (pixels). Quantitative, spatio-temporal image analysis of fundus fluorescein angiography was performed in order to investigate the veracity of qualitatively-derived principles of angiography interpretation. Moreover, the temporal properties associated with fluorescein fluorescence of normal and pathologic fundus features in age-related macular degeneration were quantified to potentiate pixel assignment and fundus feature quantitation for clinical studies where precise image metrology and image comparison are vital.

2. METHODS

Fundus fluorescein angiography studies were acquired using standard photographic techniques. Thirty-five millimeter, black and white slides were then digitized at 675 pixels per inch using a Polaroid SprintScan slide scanner.

Temporally-sequential images were spatially-registered on a personal computer with custom-developed, polynomial warping algorithms. A three-dimensional (two spatial and one temporal) angiogram vector was constructed containing the complete spatial and temporal data set.

Temporal profiles through spatially-registered, temporally-sequential pixels were computed. Pixels readily identified as background, venule, arteriole, retinal pigment epithelial atrophy, drusen, and classic and occult choroidal neovascularization were selected and analyzed, allowing for determination of characteristic temporal fluorescence behavior. The temporal properties of known normal and pathologic fundus features allowed for pixel assignment; the temporal behavior of each pixel in the fundus image was computed, and compared with the behavior of known fundus features. The results are corroborated with standard qualitative methods of fluorescein angiography interpretation.

3. RESULTS

Figure 1 depicts the venous laminar and arteriovenous phases of a fluorescein angiogram in a patient with age-related macular degeneration. A well-defined area of classic CNV is noted just nasal to the fovea, and an area of poorly-demarcated, occult CNV is seen in the temporal aspect of the macula. Several, punctate areas of hyperfluorescence correspond to drusen seen on color fundus photographs.

Temporal fluorescein fluorescence profiles are depicted for pixels readily identified as corresponding to both the classic and occult CNV, drusen, a retinal venule, and fundus background (Figure 2). The hyperfluorescence of pixels corresponding to the classic CNV, the occult CNV, and the drusen peaks at approximately 30-40 seconds. The drusen pixel intensity falls to half its peak value in approximately 200 seconds, while the pixels associated with the classic CNV remain bright with only a very modest decrease in pixel intensity. There is a mild increase in the fluorescence intensity of the pixels corresponding to the occult CNV from 80 to 600 seconds post-injection.

Determination of characteristic temporal profiles allows for pixel assignment. Pixels with temporal fluorescence behavior consistent with CNV were identified (Figure 3). There is good correlation with qualitatively derived determination of CNV extent.

Figure 4 depicts one frame of the fluorescein angiogram in a patient with a subfoveal choroidal neovascular membrane. The pixels corresponding to the CNV are readily identified

4. DISCUSSION

Several groups have explored the application of advanced image processing methodologies to fundus image analysis and interpretation (for example Goldbaum et al.³). Most effort has concentrated on analysis of color fundus photographs for detection of fundus pathology in diabetic retinopathy, and to a lesser extent, age-related macular degeneration. Due to technical and algorithmic limitations, few studies have attempted to derive useful information from an angiographic image sequence

Nagin et al.⁴, using crude registration algorithms, measured the fluorescein fluorescence intensity as a function of time for the major retinal vessels, the choroid, and the optic nerve head. However, the coarse spatial digitization (128 x 128), did not permit highly accurate spatial characterization of the temporal fluorescence behavior. Phillips et al.⁵ considered pixel by pixel analysis of fluorescein angiography for leakage quantitation in diabetic retinopathy. However, they relied on manual image registration during acquisition, and limited their analysis to two images of the fluorescein angiography sequence. Considerable temporal information is lost; discrimination among hyperfluorescent lesions such as CNV, RPE atrophy, and drusen requires more than two points. Saito et al.⁶ attempted to apply image analysis techniques to fluorescein angiography interpretation. They applied registration methods correcting only for image translation, which did not permit pixel-accuracy calculations. Only larger areas of interest were evaluated. No attempt was made to quantify or recognize fundus features.

Digitization and highly accurate registration of fundus fluorescein angiography image sequences allowed for quantitative spatio-temporal image processing. The temporal properties associated with fluorescein fluorescence of normal and pathologic fundus features are quantified; temporal fluorescence properties are consistent with qualitative principles of angiography interpretation. Moreover, characteristic temporal profiles for fundus background, retinal vasculature, retinal pigment epithelial atrophy, and choroidal neovascular (CNV) membranes were observed, allowing for pixel assignment. Fundus feature segmentation based on spatio-temporal fluorescence properties facilitated fundus feature quantitation and will enable highly accurate image comparison. Importantly, there is excellent correlation between clinical judgement and computer-assisted fundus feature segmentation.

Currently, a database of fluorescein angiography studies of patients with age-related macular degeneration is being compiled. Accumulation of these studies will allow for learning and algorithmic development and refinement to potentiate robust image segmentation. These refined algorithms will be applied to fundus images enabling highly accurate image quantitation and image comparison, facilitating the design and implementation of clinical trials relevant to treatment and prophylaxis for the vision-limiting sequelae of age-related macular degeneration.

5. ACKNOWLEDGEMENTS

Supported by the National Eye Institute, NIH K-08 EY00374, and a Career Development Award from Research to Prevent Blindness.

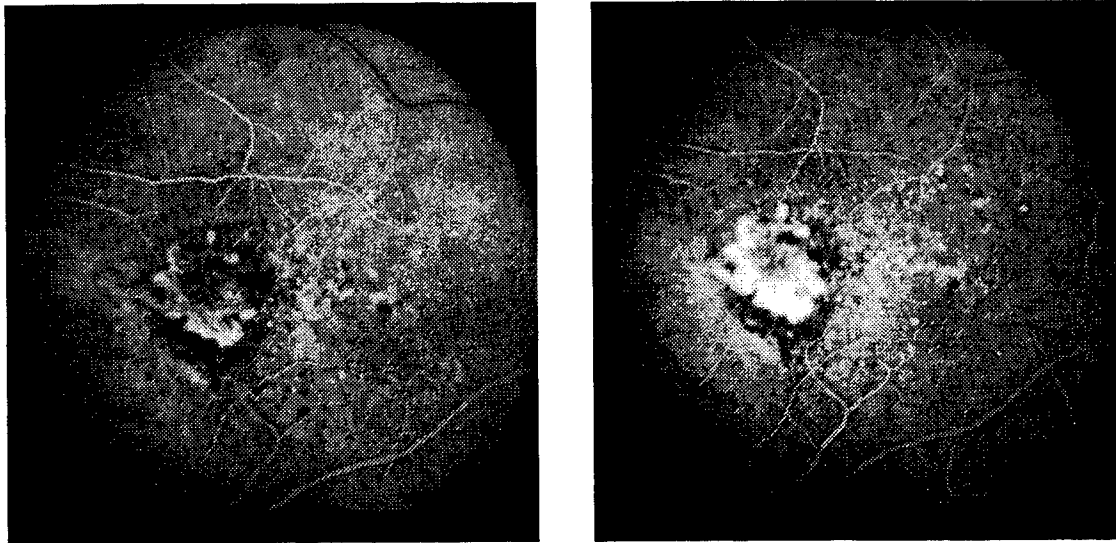


Figure 1. Venous laminar and arteriovenous phases of a fluorescein angiogram in an eye of a patient with age-related macular degeneration. An area of classic CNV is noted just nasal to the fovea, and a larger area of poorly-demarcated occult CNV is noted in the temporal aspect of the macula .

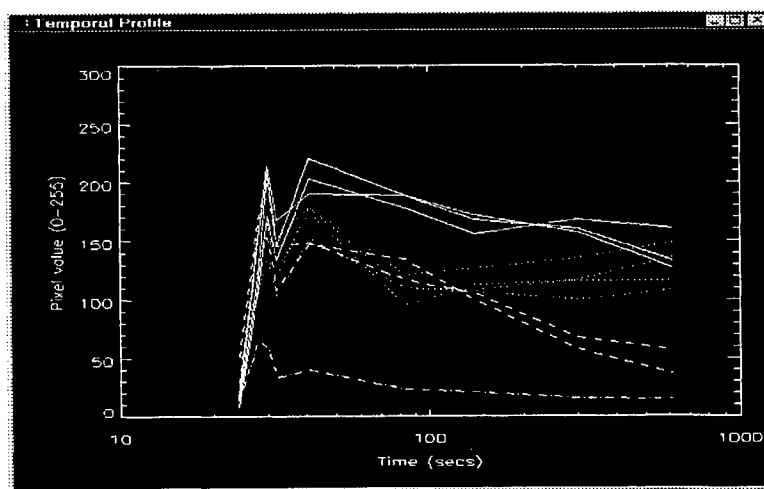


Figure 2. Fluorescence intensity as a of time following intravenous fluorescein injection. Temporal profiles for representative pixels of the classic CNV (solid line), occult CNV (dotted line), drusen (dashed line), and background (dot-dashed line) are shown.

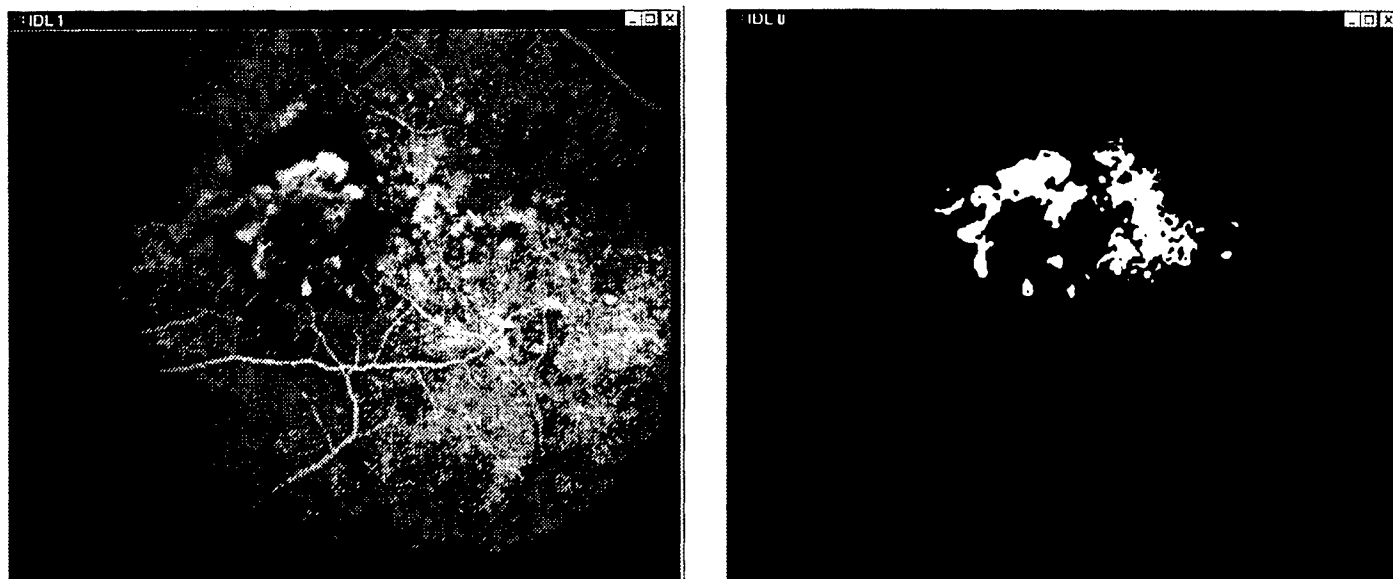


Figure 3. Left, arteriovenous phase of the fluorescein angiogram depicted in Figure 1. Right, pixels identified as CNV based on the temporal profiles determined on a pixel by pixel basis.

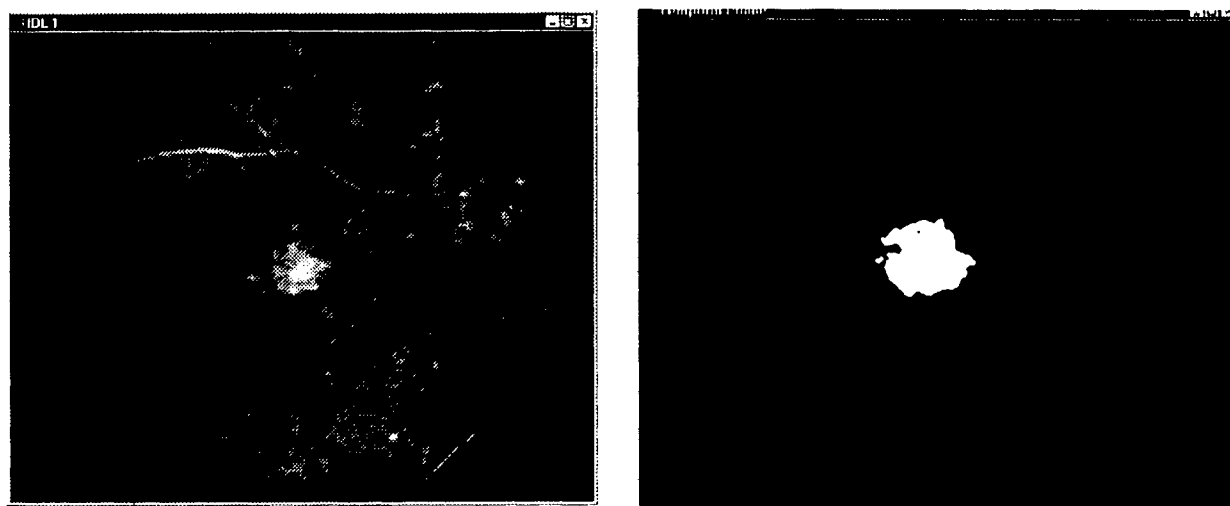


Figure 4. Left, Venous laminar phase of a fluorescein angiogram depicting a subfoveal choroidal neovascular membrane (CNV). Right, pixels identified as corresponding to the CNV are shown.

6. REFERENCES

1. JDM Gass. *Stereoscopic Atlas of Macular Diseases*, Mosby Year-Book, Inc, 1997.
2. JW Berger, MG Maguire , SL Fine. The Macular Photocoagulation Studies, in *Clinical Trials in Ophthalmology*, M. Conway, P. Kertes, eds. Williams and Wilkins, in press.
3. MH Goldbaum, V Kouznetsova , BL Cote , WE Hart, M Nelson. "Automated registration of digital ocular fundus images for comparison of lesions." *Proc SPIE* 1877: 94-99, 1993.
4. P Nagin, B Schwartz, G Reynolds. "Measurement of fluorescein angiograms of the optic disc and retina using computerized image analysis." *Ophthalmology* 92:547-552, 1985.
5. RP Phillips, PG Ross, M Tyska, PF Sharp, JV Forrester. "Detection and quantification of hyperfluorescent leakage by computer analysis of fundus fluorescein angiograms." *Graefes Arch Klin Exp Ophthalmol* 229: 329-335, 1991.
6. J Saito J, STD Roxburgh, D Sutton, A Ellingford. "A new method of image analysis of fluorescein angiography applied to age-related macular degeneration." *Eye* 9: 70-76, 1995.

Optical coherence tomography using an interferometer with temporal output

Maja Balarin^a, Suganda Jutamulia^b

^aDepartment of Biomedical Engineering, University of Northern California,
Petaluma, CA

^bIn-Harmony Technology Corporation, Petaluma, CA

ABSTRACT

We are proposing a topographic measurement technique using a motion-less interferometer with temporal output. We suggest that its use can be extended to tomographic measurements. Thus, it can eventually replace the mechanically scanning Michelson interferometer in optical coherence tomography.

Keywords: topography, optical coherence tomography, Michelson interferometer, low-coherence interferometry.

1. INTRODUCTION

Optical coherence tomography, or OCT, is a non-contact, noninvasive imaging technique used to obtain high resolution cross-sectional images in biological systems.¹ The heart of the system is the fiber optic Michelson interferometer,² which is illuminated by low-coherence light from a superluminescent diode. The sample is placed in one interferometer arm, and its reflections are combined with the reflection from the reference mirror. The amplitudes and delays of tissue reflections are measured by scanning the reference mirror and simultaneously recording the amplitude of the interferometric signal.

The interferometer with temporal output, proposed by Jutamulia and Asakura,³ is similar to the Michelson interferometer, but instead of scanning a reference mirror it applies an optical loop in which interfering light partially leaves the loop at every pass. The resulting interfering effect includes the interference with multiple delays, and no reference mirror scanning is needed. Here, we study measurement of dimensions using this interferometer with temporal output, which is the first step in replacing the Michelson interferometer.

2. THE INTERFEROMETER WITH TEMPORAL OUTPUT

Jutamulia and Asakura³ proposed an interferometer with temporal output shown in Figure 1. It consists of a light source, a beamsplitter, and several mirrors arranged to make an optical loop. The energy of the incoming light beam is divided equally by the beamsplitter (BS) into beam A (reflected) and beam B (transmitted). Assuming that the incoming light intensity is 1, then the amplitudes of beams A and B are $1/\sqrt{2}$, which will be denoted as a .

After transmission through the beamsplitter BS, beam B is returned by the set of mirrors. The returned beam B is now reflected by the beamsplitter BS and will interfere with the incoming beam, to form a new beam B. The length of the loop can be adjusted to obtain constructive interference in beam B; therefore, according to the law of the conservation of the energy, destructive interference will occur in beam A concurrently.

While beam B is in the first pass around the loop, both amplitudes of beam A and B equal a . When beam B is in the second pass, its amplitude is $(a + a^2)$, and at the same time the amplitude of beam A is $(a - a^2)$. When beam B is in the third pass, its amplitude is $(a + a^2 + a^3)$, and the amplitude of beam A is $(a - a^2 - a^3)$, and so forth.

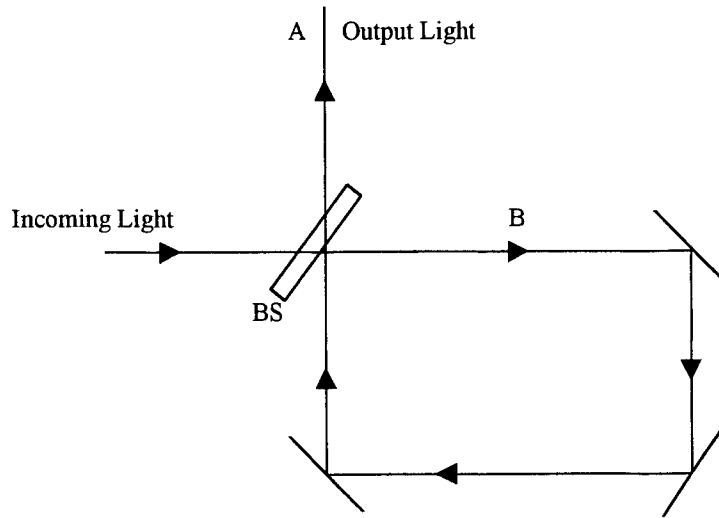


Figure 1.

For the N-th pass of beam B through the loop, the amplitude is:

$$A_B = a + a^2 + a^3 + \dots + a^N, \quad (1)$$

and consequently the amplitude of beam A is:

$$A_A = a - a^2 - a^3 - \dots - a^N. \quad (2)$$

Simple calculation shows that as N approaches infinity, the energy of beam A approaches 1, so it is equal to incoming energy, but the phase is changed by 180° .

Jutamulia and Asakura³ proposed to utilize this temporal output by combining the basic interferometer with a Mach-Zehnder⁴ interferometer. The resulting arrangement is shown in Figure 2. They assumed that the intensity of the incoming light is 2; thus its amplitude is $\sqrt{2}$. The first beamsplitter BS1 divides incoming light equally into beams C and D, both having an amplitude of 1. The second beamsplitter BS2 again divides the amplitude equally so that the amplitude in A can still be expressed with Eq. (2). The last beamsplitter BS3 combines beams C and A into beams E and F. The optical path of the Mach-Zehnder interferometer can be adjusted to obtain constructive interference in beam F, and consequently, destructive interference in beam E. Since the Mach-Zehnder interferometer is symmetric, beams C and D will always interfere regardless of the coherence length of the incoming light.

If the coherence length of the incoming light is infinity, the intensity of beam E is:

$$I(\infty) = |a + a(a - a^2 - a^3 - \dots - a^N)|^2 \quad (3)$$

and as $N \rightarrow \infty$, it would be zero. If the coherence length of the incoming light is finite, the detected intensity of beam E should be larger than zero, so it is related to the incoming coherence length.

Using coherence lengths, that were in different relation to the size of the optical loop, Jutamulia and Asakura calculated intensities of the output light as the function of the coherence length of the source.³ Thus, the coherence length can be directly measured from the detected intensity at one point. Since this interferometer contains no moving parts it makes a very simple and quick (e.g. 10 ns) device for measurement of the coherence length of the light source.

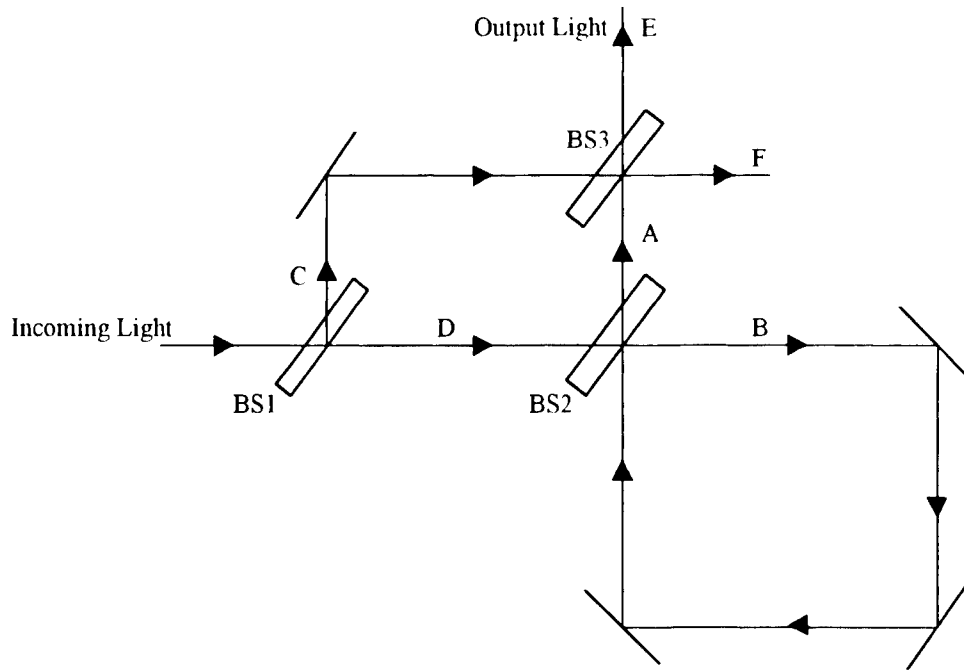


Figure 2.

3. LENGTH MEASUREMENT

In the previous section we have shown that the interferometer with temporal output can be used to relate the unknown coherence length of incoming light (ℓ_c) and the known length of the loop (L) with the measured intensity of the output light. Here we propose a similar approach to measure the unknown length using the known coherence length and the measured output light intensity.

We modify the previous interferometer arrangement by replacing the mirror in the Mach-Zehnder part of the interferometer in Figure 2 with the additional beamsplitter BS4. It is used to direct one beam to the sample. This arrangement is shown in Figure 3.

Beamsplitter BS1 divides the incoming light equally into beams C and D. Beamsplitter BS3 sends one beam to the sample. The reflected beam from the sample is again reflected by beamsplitter BS3 becoming beam G. To achieve the best measurement contrast, we would like the intensities of beams D and G to be equal. Therefore, we attenuate the amplitude of beam D by $\frac{1}{2}$ to account for losses in beamsplitter BS3. It is convenient to assume that the intensity of the incoming light is 8, so that the intensities of beams D and G are 1. Since beamsplitter BS2 again divides the beam equally, the amplitude of beam A can still be expressed by Eq. (2). In real measurements we have to normalize the detected light intensity using the measured intensities of beam D or beam G. Beamsplitter BS4 recombines beam G with beam A into beams E and F, one with destructive and the other with constructive interference.

If the coherence length of the incoming light is infinitely long, the output detected at E will have the minimum value,

$$I(\infty) = |a + a(a - a^2 - a^3 - \dots a^N)|^2 \quad \text{for } N \rightarrow \infty \Rightarrow I(\infty) = 0, \quad (4)$$

and at the same time, the detected intensity at F will have the maximum value

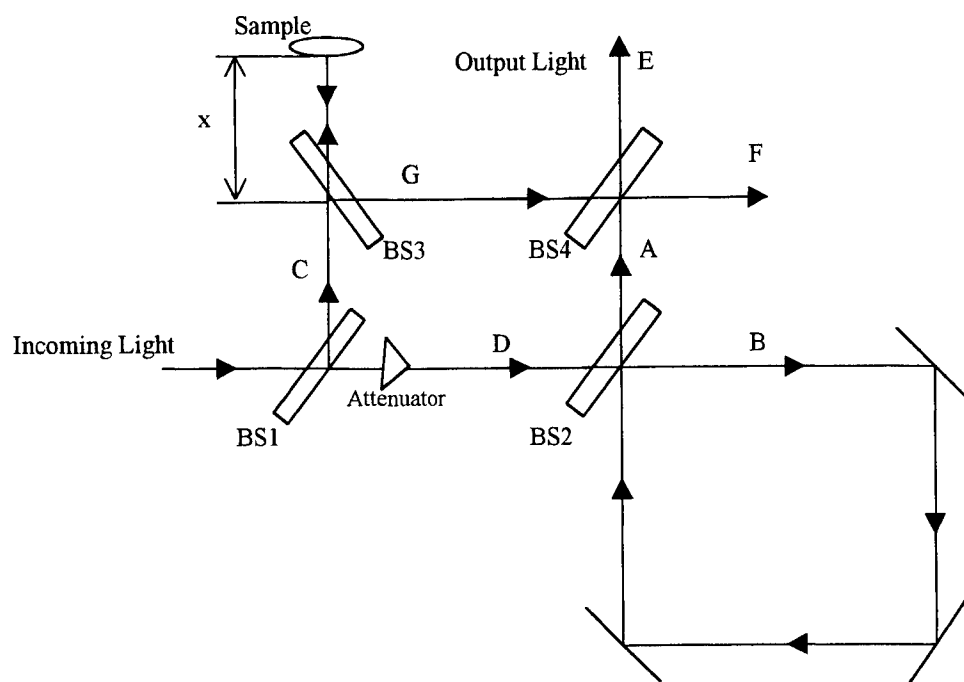


Figure 3.

Assuming that the coherence length (ℓ_c) of the incoming light is smaller than the length of loop B (L), we can calculate the change of the intensity in beam E with the change of the length designated as x . If the optical path length $2x$ is equal to L , then beam G interferes with the component of beam A that has passed through the optical loop exactly once. Therefore the intensity will be:

$$I(L) = |a^2|^2 + |a - a^3|^2 + |a^4|^2 + \dots + |a^{N+1}|^2. \quad (5)$$

Similarly, if $2x$ is equal to $2L$:

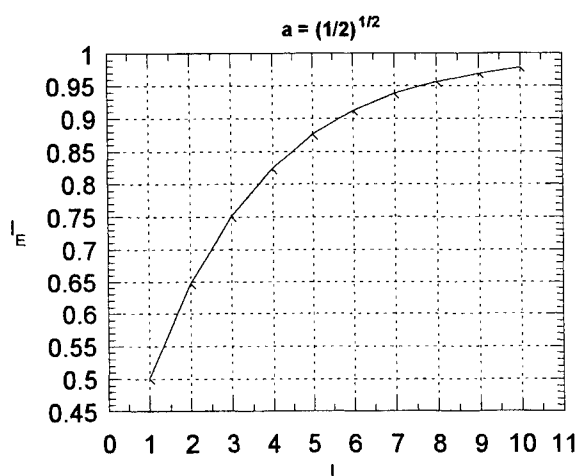
$$I(2L) = |a^2|^2 + |a^3|^2 + |a - a^4|^2 + \dots + |a^{N+1}|^2, \quad (6)$$

because beam G now interferes with the component of beam A that has passed through the loop twice, and so forth for different values of the optical path lengths $2x$. The intensity values for different path lengths are shown in Table 1 and Graph 1.

Table 1. ($\ell_c < L$)

$2x$	I_F
L	0.49985
$2L$	0.64629
$3L$	0.74985
$4L$	0.82307
$5L$	0.87485
$6L$	0.91146
$7L$	0.93735
$8L$	0.95568
$9L$	0.96859
$10L$	0.97775

Graph 1.



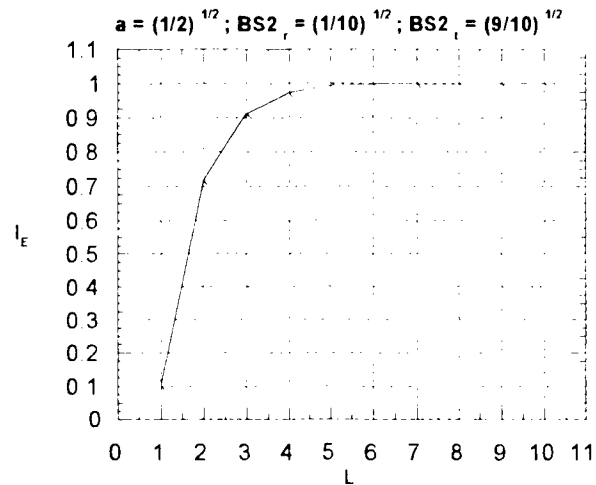
The range of measurement is determined by the smallest change in intensities that can be distinguished accurately. From Table 1 it can be seen that if that change is 1%, then the range is 10L. From the measured intensity of beam E we can determine the optical path length (2x) with the precision of L, i.e. the resolution of x is L/2

Let us now consider the influence of different beamsplitters on the output intensity, sensitivity and measurement range. We focus our analysis on beamsplitters BS2 and BS4, because it can be shown that both sensitivity and range are optimized when beamsplitters BS1 and BS3 divide beams equally. We first check the influence of beamsplitter BS2. We examine the case of a beamsplitter that reflects 1/10, and transmits 9/10 of the intensity. The results are presented in Table 2 and Graph 2.

Table 2. ($\ell_c < L$)

2x	I_F
L	0.09999
2L	0.71539
3L	0.90999
4L	0.97154
5L	0.99099
6L	0.99715
7L	0.99909
8L	0.99972
9L	0.99991
10L	0.99997

Graph 2.

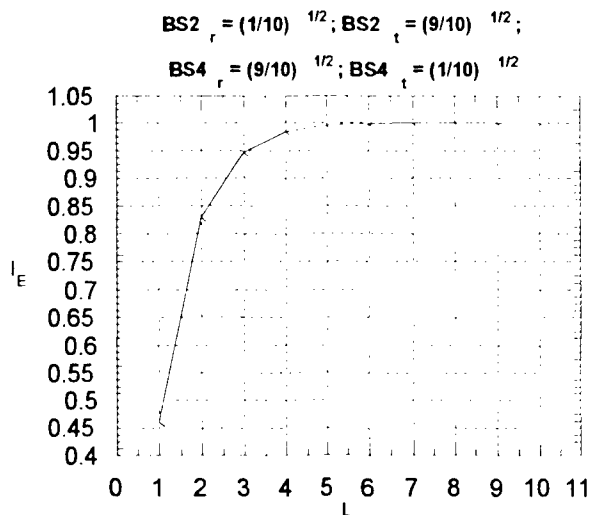


It is apparent from Table 2 and Graph 2 that the sensitivity (the rate of change in intensity with a change in length) of the measurements is improved but the range is shortened. If the change in intensity that can still be resolved accurately is 1%, then the range is 5L. Next we check the influence of beamsplitter BS4. We keep the same arrangement as in the previous calculations, but use beamsplitter BS4 which transmits 1/10, and reflects 9/10 of the intensity. The results are shown in Table 3 and Graph 3.

Table 3. ($\ell_c < L$)

2x	I_F
L	0.45999
2L	0.82924
3L	0.94599
4L	0.98292
5L	0.99459
6L	0.99829
7L	0.99946
8L	0.99983
9L	0.99995
10L	0.99998

Graph 3.



This change returns no improvement in the sensitivity, nor in the range, therefore it is not useful. We decided not to analyze the case when beamsplitter BS4 transmits 9/10, and reflects 1/10 of intensity, because such a beamsplitter would lower the influence of the light that carries information about the sample.

We turn our attention to the influence of the coherence length of the incoming light. We check the case when the incoming coherence length is between L and $2L$. We assume (as did also Jutamulia and Asakura in their original work³) the beam to be perfectly coherent along the whole optical path of the coherence length ℓ_c , and completely incoherent in between. For $2x$ equal to L we have:

$$I(L) = |a + a^2 - a^3|^2 + |a^4 + a^5|^2 + |a^6 + a^7|^2 + \dots + |a^N + a^{N+1}|^2, \quad (7)$$

and for $2x$ equal to $2L$ or $3L$ we have:

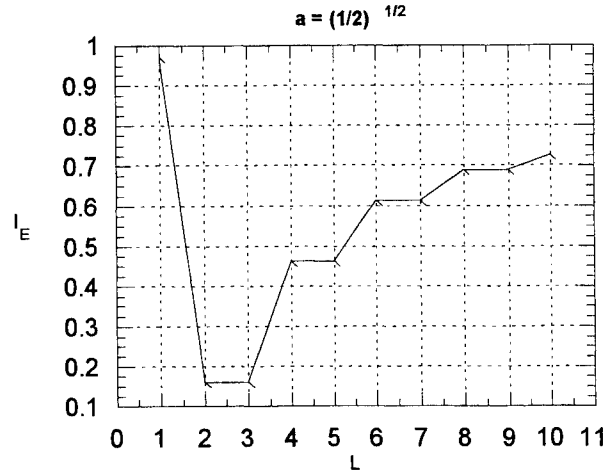
$$I(2L, 3L) = |a^2 - a^3|^2 + |a - a^4 - a^5|^2 + |a^6 + a^7|^2 + \dots + |a^N + a^{N+1}|^2, \quad (8)$$

and so on, as shown in Table 4 and Graph 4.

Table 4. ($L < \ell_c < 2L$)

$2x$	I_F
L	0.97116
$2L$	0.16050
$3L$	0.16050
$4L$	0.46227
$5L$	0.46227
$6L$	0.61317
$7L$	0.61317
$8L$	0.68862
$9L$	0.68862
$10L$	0.72634

Graph 4.



Obviously, this arrangement is not good since the graph is not monotonic, therefore making it hard to determine the length from the measured intensity. Also, the resolution of length x is now only L , as opposed to $L/2$ in the previous cases.

In summary, the resolution of the length measurement with the interferometer with temporal output is determined by $L/2$, half of the length of optical loop B, provided that the coherence length of the source (ℓ_c) is smaller than the length of the optical loop (L). Thus, the improvement in the resolution can be obtained by lowering the coherence length and the length of the optical loop together. Sensitivity of the measurement can be improved by changing the rate in which beamsplitter BS2 transmits and reflects light, but the tradeoff is that the range is shortened.

4. CONCLUSIONS

We have demonstrated that the interferometer with temporal output can be used for length measurements, and we have analyzed the tradeoffs in sensitivity and range measurements. We can easily imagine making topographic measurements by setting the same interferometer in the setup that will enable longitudinal scanning.⁵ However, to obtain proper measurement we need to have a system with no absorption or scattering as well as perfectly matching recombining wavefronts. Since this is a multiple beam system, small levels of mismatch can be catastrophic, so the interferometer with temporal output should be constructed using integrated optics.³

For topographic measurements, we have just one unknown in the transversal direction, and thus we need just one measurement. For tomographic measurements, we will need as many measurements as there are points of interest in the transversal direction. If we want n points in the transversal direction, we may use n measurements with n different coherence lengths to obtain a system of n equations with n unknown lengths. It is important to note that the transversal resolution will still be determined by the coherence length of the incoming light. We expect that by eliminating the use of the scanning reference mirror, image acquisition will be much faster.

5. ACKNOWLEDGMENTS

The first author sincerely thanks Felice Balarin for his unlimited support, valuable ideas and discussions, and his fruitful comments on this paper.

6. REFERENCES

1. D. Huang, E. A. Swanson, et al., "Optical Coherence Tomography", *Science*, **254**, pp. 1178 - 1181, 1991.
2. G. R. Fowles, *Introduction to Modern Optics*, pp.63, Dover Publications, New York, 1975.
3. S. Jutamulia, T. Asakura, "Interferometer with Temporal Output", *Opt. Mem. Neu. Netw.*, **6**, pp. 83 - 89, 1997.
4. S. G. Lipson, H. Lipson, D. S. Tannhauser, *Optical Physics*, pp. 233, Cambridge University Press, Cambridge, 1995.
5. A. F. Fercher, W. Drexler, C. K. Hitzenberger, "Ocular Partial Coherence Tomography", *SPIE*, **2732**, pp. 229-241, 1996.

Further author information -

^aMaja Balarin (correspondence): Email: MajaBalarin@msn.com

^bSuganda Jutamulia: Email: suganda@netcom.com

Modification of the Heidelberg retinal laser tomograph and flowmeter to allow measurements in supine patients

Karen M. Joos, Chasidy Singleton, Jin H. Shen, Wensi Sun, Denis O'Day

Vanderbilt University, Department of Ophthalmology and Visual Sciences,
Nashville, TN 37232-8808.

ABSTRACT

Purpose: To determine if the Heidelberg Retinal Laser Tomograph (HRT) and Flowmeter (HRF) can be modified to obtain images in supine patients. **Methods:** A mount was customized to securely attach the Heidelberg scanning head to an operating microscope stand. This mount was designed to allow rotation for viewing of the macula or optic nerve head region in either eye. The HRT was used to acquire 3 consecutive images of the optic nerve head in supine subjects to obtain a mean topographic image. The HRF was then used to obtain capillary flow measurements in supine subjects. **Results:** The optic nerve area in either the right or left eye can be safely and easily visualized with the modified Heidelberg system in supine patients for evaluation of optic nerve head topography or capillary flow. However, the configuration of the Heidelberg scanning head requires the images to be taken 180 degrees from the normal orientation of the scanning head to the patient's body. Therefore, the images are rotated 180 degrees from those taken in upright subjects. This must be considered when analyzing the data. **Conclusion:** The Heidelberg Retinal Tomograph and Flowmeter are capable of acquiring images in supine subjects. However, these images are rotated 180 degrees.

Keywords: retinal tomograph, retinal flowmeter, optic nerve, blood flow

1. INTRODUCTION

Retinal arteriole narrowing near the optic nerve head may be present in glaucoma and throughout the retina in diseases including diabetes mellitus and hypertension. A generalized reduction of retinal arteriole diameters also may have a role in the progression of glaucoma.^{1,2} Decreased blood flow to the optic nerve head with nocturnal systemic arterial hypotension has been hypothesized as a mechanism for glaucomatous progression.³ Optic nerve head blood flow is calculated as:⁴

$$\text{Flow} = \frac{\text{Perfusion pressure}}{\text{Resistance to flow}}$$

Perfusion pressure is dependent on mean arterial blood pressure minus intraocular pressure. Because most humans are supine during nocturnal sleep, this study sought to determine if adequate images with the Heidelberg retinal tomograph and flowmeter could be obtained in supine subjects. Images normally are collected with subjects in the sitting position.

2. MATERIALS AND METHODS

The Heidelberg retinal tomograph is a confocal scanning laser ophthalmoscope that allows topographic recording of the optic nerve head and retina.⁵ The retinal flowmeter is a scanning laser Doppler that measures the flow in retinal and optic nerve head capillaries.⁶ Both use a 670 nm diode laser which is aimed through the pupils of subjects. A mount was customized to securely attach the Heidelberg scanning head to an operating microscope stand (Figure 1). This mount was designed to allow rotation for viewing of the macula or optic nerve head region in either eye. The HRT was used to acquire 3 consecutive images of the optic nerve head in supine subjects to obtain a mean topographic image. The HRF was then used to obtain capillary flow measurements in supine subjects.

3. RESULTS

The optic nerve area in either the right or left eye can be safely and easily visualized with the modified Heidelberg system in supine patients for evaluation of optic nerve head topography or capillary flow. A secure mounting on an operating microscope stand allows adjustment in the x, y, and z-axis as well as providing safety for the subjects. Clear topographical and flow images are possible in supine subjects with fixation directed at a point projected onto the ceiling by a laser pointer.

However, the configuration of the Heidelberg scanning head requires the images to be taken 180 degrees from the normal orientation of the scanning head to the patient's body. Therefore, the images for both the topography and flow acquisitions are rotated 180 degrees from those taken in upright subjects. This must be considered when selecting areas for imaging as well as when analyzing the data. Also, another operator is required to align the scanner when it is mounted on the microscope stand.

4. DISCUSSION

The Heidelberg Retinal Tomograph and Flowmeter are capable of acquiring adequate images in supine subjects. An additional operator is required to manipulate the scanner and maintain alignment in supine subjects. The images obtained are clear. However, these images are rotated 180 degrees. This must be carefully considered if comparison to images acquired in the standard manner is desired.

5. ACKNOWLEDGEMENTS

Supported by an unrestricted grant from Research to Prevent Blindness, Inc, NY, by National Medical Fellowships, Inc. and a donation from James Rice.

6. REFERENCES

1. S. Wolf, O. Arend, W.E. Sponsel, K. Schulte, L.B. Cantor, and M. Reim, "Retinal hemodynamics using scanning laser ophthalmoscopy and hemorrheology in chronic open-angle glaucoma." *Ophthalmology*. 100:1561-66, 1993.
2. D. Shin, C.S. Tsai, K.A. Parrow, C. Kim, J.Y. Wan, and D.X. Shi, "Intraocular pressure-dependent change in adult chronic open-angle glaucoma patients." *Ophthalmology*. 98:1087-92, 1991.
3. S.S. Hayreh, M.B. Zimmerman, P. Podhajsky, and W.L.M. Alward, "Nocturnal arterial hypotension and its role in optic nerve and ocular ischemic diseases." *American Journal of Ophthalmology*. 117:603-24, 1994.
4. S.S. Hayreh, "Factors influencing blood flow in the optic nerve head." *Journal of Glaucoma*. 6:412-25, 1997.
5. M. Luskey, M.E. Bosem, and R.N. Weinreb, "Reproducibility of optic nerve head topography measurements in eyes with undilated pupils." *Journal of Glaucoma*. 2:104-9, 1993.
6. G. Michelson, and B. Schmauss, "Two-dimensional mapping of the perfusion of the retina and optic nerve." *British Journal of Ophthalmology*. 79:1126-32, 1995.

7. FIGURES

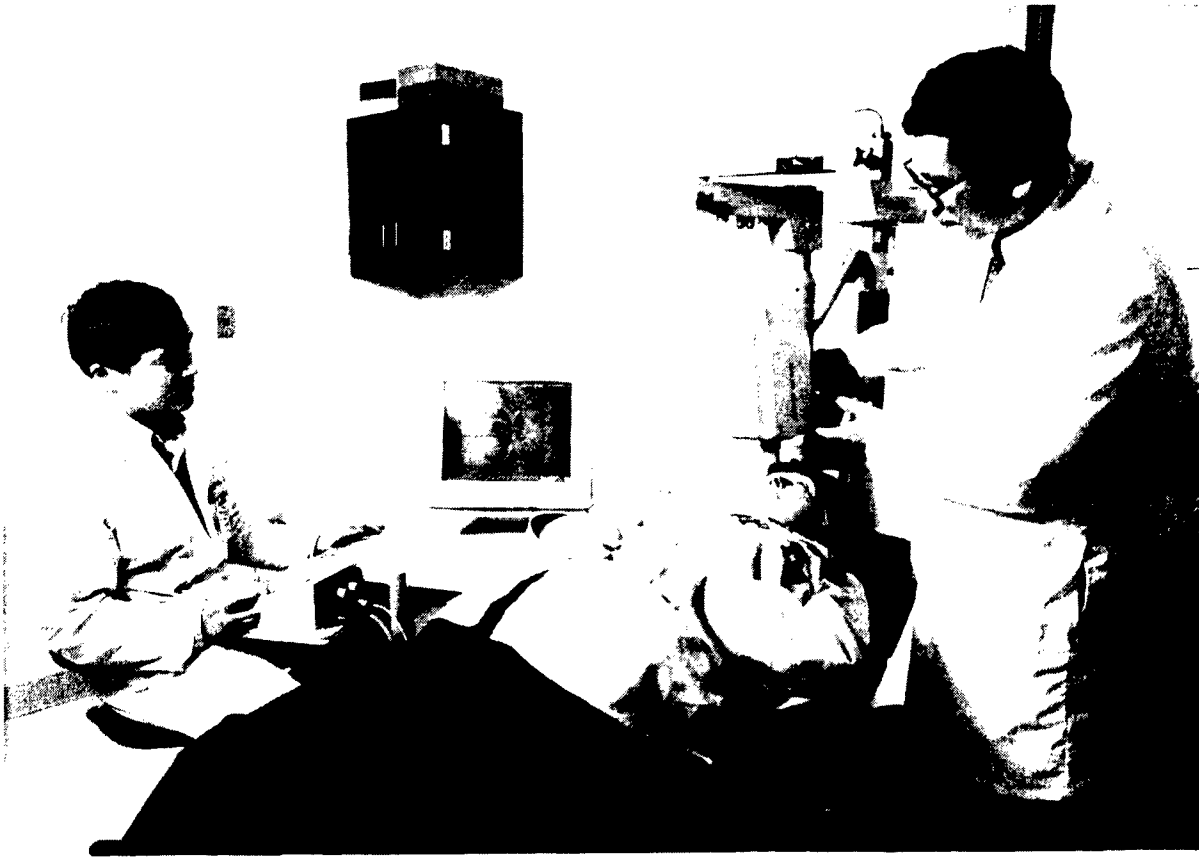


Figure 1: A mount was customized to securely attach the Heidelberg scanning head to an operating microscope stand.

Methodology and apparatus for using the human iris as a robust biometric

Michael DellaVecchia, Wills Eye Hospital, Philadelphia, PA. and
Thomas Chmielewski, Ted Camus, Marcos Salganicoff,
Michael Negin all of Sensor, Inc., Moorestown, NJ

Abstract

The human iris possesses characteristics that make it significantly more robust for use as a biometric identifier when compared with conventional techniques such as fingerprints, face recognition or retinal scan.

The iris is an overt body, thereby allowing a remote acquisition system to capture the image. Visual patterns in individual irises are highly distinctive and clearly apparent thereby minimizing the likelihood of false positives and false negatives enrollments. Such visual iris patterns are stable over time thereby requiring a single enrollment that can last over the user's lifetime. Furthermore, the digital information of the iris can be coded very effectively, requiring a modest amount of computer storage and processing.

This paper describes an automated system which allows non-intrusive acquisition of quality iris images for the purposes of enrollment, verification or identification. In essence, user locale within a prescribed volume and unobtrusive gaze toward the image acquisition devices are the only engineering hardware criteria for enrollment and verification.

The device operates with non-visible near infrared illumination. The initial image acquisition uses a stereo camera pair (3D vision) system to locate the subject within a relatively large operational volume. The resulting coordinates of the user's right or left eye are used to position a pan/tilt mirror and focus mechanism associated with a higher magnification camera. This camera, called the narrow field of view (NFOV) camera, is then used to acquire a high contrast fine resolution iris image which is presented to a proprietary algorithm for the generation of an "iris code". Finally the computed iris code is compared to a previously stored enrollment code associated with the user for verification.

Keywords: biometrics, iris biometric, iris, iris code, stereo, remote imaging of eye, unobtrusive imaging, personal identification

1. Introduction

This paper describes an automated system for the non-intrusive acquisition of iris images for the purpose of enrollment or identity verification. The system utilizes stereo vision to find the right or left eye of a user positioned in a designated acquisition volume. Eye coordinate information is then used to direct the positions of a pan/tilt mirror and focus mechanism connected to a narrow field of view camera. The narrow field of view camera obtains an in-focus centered image of the user's eye. By utilizing various vision processing techniques, the process described does not require the user to make any physical contact with the system, nor does the user have to position himself in any special way, other than the natural pose of using a device such as an Automated Teller Machine (ATM).

Once a quality iris image has been obtained, it is used to compute an iris code. The iris code is a unique 256 byte code computed by using a proprietary algorithm developed by John Daugman. The iris code is designed to be extremely easy to compare to previously stored iris codes, thereby providing a fast method of comparing the acquired iris code of an individual to his enrolled code and verifying his identity or potentially comparing the acquired individual's iris code to a set of irises and thereby identifying the person. The entire verification process takes less than 5 seconds, that is from the time that the system begins to find the eye to the time that iris codes are compared.

2. The Iris as a Biometric

The iris is an integral part of the eye and one of the most unique structures of the entire human body. Its presence extends beyond anatomy and physiology and into sociology. Physiological states such as emotion, excitement or stimulation are shown by the iris. Indeed, it is the gaze at this structure referred to in "eye to eye contact". Even more importantly, a person's identity may be assigned by their iris' appearance, "person with sparkling eyes", the girl with the "Betty Davis' eyes". Thus even when no specific biometric perimeter is measured, there is a tendency to identify a person by their eyes or more specifically their iris.

The iris is well suited as a biometric identifier. The eyes are used for tracking manual actions. Thus the iris presents instinctively to the field of attention and gaze that tend to attract a person such as lights and displays or monitors. When such a manual action is performed by an individual, it is possible to determine the angle of vision and the presenting direction of the face. This natural human response essentially aligns an individual for detection, either intentionally or covertly through their natural gaze response.

The most distinctive property of the iris which makes it a truly unique biometric identifier is its integral and individual anatomy. The iris is a readily visible yet totally internal and extremely delicate structure of the human body. Its surface topography is highly detailed; composed of multiple crypts and furrows unique to each individual. By childhood, the iris has grown to its full size. The surface topography, except for rare anomalous conditions and trauma, remains constant. The iris is the pupillary diaphragm positioned behind the cornea; that clear anterior 1/6 surface of the eye which allows visualization of the internal structures. A distinctive light reflection is associated with the corneal surface. The peripheral border of the iris is readily seen in distinct contrast with its outlining white sclera. These definitive borders permit location for imaging analysis.

The iris surface and structure itself is composed of many contours, depressions and substructures which in effect allow it to be used as an excellent biometric or "optical fingerprint" for personal identification³. The uses of this anatomical structure was in fact suggested several years ago by ophthalmologists and even as early as over a hundred years ago by the forefathers of criminology. As noted in Figure 1, the enclosed sectional diagram of the human eye, the iris is an extremely delicate structure and located reasonably interior. Modification of the iris by any reasonable means would mean extremely intricate microsurgery. Fraudulent manipulation could result in drastic visual jeopardy to the individual and an obvious enough variation of topography and morphology to be easily detectable by visual means including image analysis. Furthermore, the individual's iris would not have a normal reactive or possibly symmetric reflex to light and because of possible alterations in the flow of the anterior chamber aqueous fluid there could also be risk to the eye from glaucoma.

The formation of the iris is a genetic expression that determines form, physiology, color and general appearance. This detailed and intricate embryogenesis depends only on the initial conditions of the three present embryonic layers. Thus identical twins having the same genotype will express uncorrelated minutia in their irises with a uniqueness in each individual. This is not only seen in the fact the identical twins have un-identical irises, but also within the same individual where the right iris differs from the left iris, while both irises have totally identical genetic makeup. In this respect, the iris parallels that uniqueness and individuality that is inherent to every fingerprint, but incorporates a much greater amount of topographic knowledge.

Thus the iris inherently excels as a human biometric. It is a natural structure for light- tissue interaction and therefore image analysis. The iris is unique to each individual and the result of an extremely intricate and highly random embryonic process.

This results in a tissue topography which is replete with information and which remains relatively static after birth. The iris is a totally internal, very delicate dynamic structure which cannot be altered without great physical risk and detection. Even though it is internal, the iris is accessible and measurable by visible and invisible light allowing cooperative and covert enrollment. The advent of future technological advances in solid state light sources, image analysis and computers will further strength the iris as a premier human biometric.

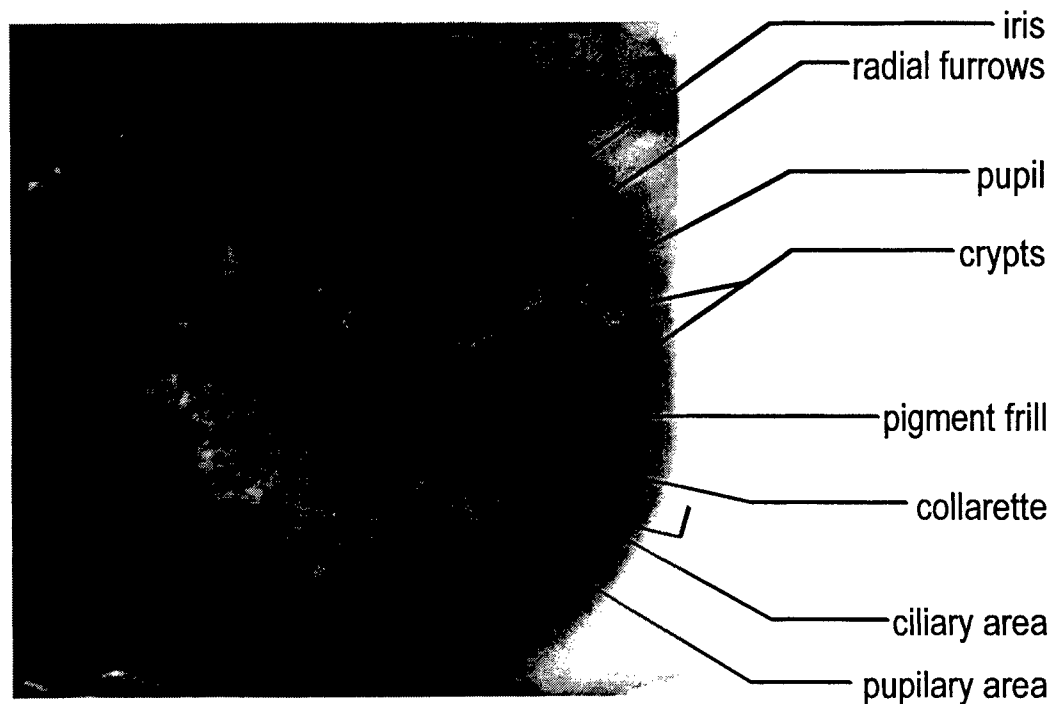


Figure 1: The Iris

2.1 Iris codes

The process of extracting the subject's "iris code", developed by John Daugman² and licensed through IriScan^{3,4}, requires beginning with a quality iris image. A quality iris image is one in which the subject's iris is in focus, and essentially centered in the image, additionally, any rotation of the image, due to beam steering via a pan/tilt mirror needs to be minimized. Once a proper image has been obtained, the subject's iris boundaries are defined by finding the maximum of a partial derivative of contour integrals of various positions and radii. The actual construction of the "iris code" consists of the concatenation of the numeric signs of 2048 two-dimensional Gabor wavelet filter coefficients of differing positions and sizes. These Gabor filters are mapped onto the iris using a deformable rubber-sheet model which automatically adjusts for variable iris and pupil sizes.

Figure 2 shows eight circular bands of the rubber-sheet model (demarcated zones of analysis) which have been adjusted to fit into the iris of the image. Four of the outer bands do not cover the entire iris so as to accommodate variations in eyelid opening. The two gray boxes slightly below the horizontal center of the iris represent regions which should not be included in the iris code computation. These boxes can be positioned in a region where a specular reflection occurs. The top left of Figure 2 shows a graphic representation of a binary iris code.



Figure 2: Iris Code and Demarcated Zones of Analysis.

3. Non-obtrusive Remote Imaging of the Iris

A key element of the adaptation of iris technology in the mass-market place is the requirement for unobtrusive acquisition of the subject's iris¹. To be unobtrusive, requires that the users of the system do not have to do anything special or out of the ordinary when using the system coupled to a specific application, such as an ATM. Additionally, the users should not be made to feel uncomfortable during the use of the system such as having bright lights shine on them when the image acquisition and verification process is initiated. Furthermore, the user should not need any special training to use the system.

The apparatus described in this paper, called the IrisIdent™ System, makes this process nearly transparent to the subject by employing several real-time computer vision technologies as well as non-visible near infrared illumination techniques. The user merely needs to be positioned in the acquisition volume which is defined by a vertical angle of 60 degrees, a horizontal angle of 46 degrees and a distance between 15 to 30 inches, all measured from the center of the face of the optical platform. A single constraint is placed on the user, namely that the person look towards a blinking light called the gaze director. Looking at the gaze director forces the user's eye to be nearly perpendicular to the field of view of the cameras. In a commercial application, the gaze director's function would be replaced by the display screen of an ATM.

4. Hardware Description

Figure 3 shows the functional block diagram of the IrisIdent™ System. The system consists of two major components: the IrisIdent™ Processing Platform (IPP) and the IrisIdent™ Optical Platform (IOP). The IrisIdent™ System can be interfaced to various applications through a well defined Application Program Interface (API). The API provides the appropriate calls to control various functions of the IrisIdent™ System as well as a data interface for iris codes.

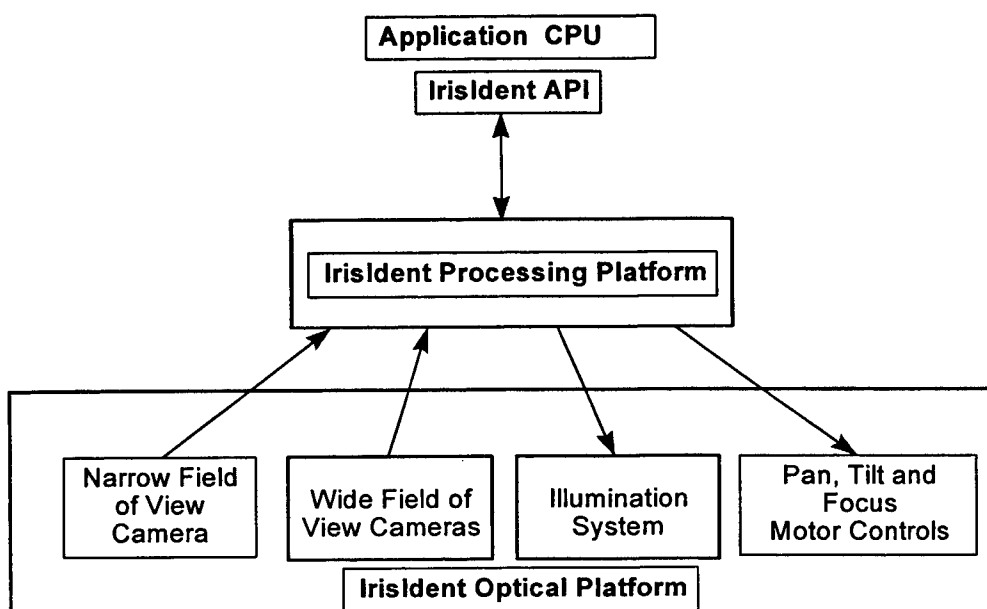


Figure 3: Functional Block Diagram of the IrisIdent™ System

The IOP contains all the hardware components which are associated with the acquisition of images prior to digitization. In this context, the optical platform includes three cameras (two WFOV, one NFOV), illuminators, optical components (lenses and mirrors), mechanical stages, motors, electronic control circuitry and a microcontroller. It provides analog video from the WFOV stereo cameras and the NFOV camera and receives commands from the IPP to direct the NFOV camera's field of view and control the illumination or change camera parameters.

The IPP contains the electronic hardware to digitize the analog video signals as well as to perform computations required for stereo processing, NFOV processing and computation and comparison of iris codes. The IPP contains a specialized image processing card called the Vision Accelerator Board (VAB) which digitizes and processes the WFOV stereo video. It also contains a commercial off the shelf (COTS) Intel Pentium™ and digitizer which is used for NFOV image processing and iris code generation and comparison. The IPP also contains additional communications hardware to interface to both the IOP and an external CPU.

4.1 WFOV and NFOV subsystems

Figure 4 shows a distributed process model for the IrisIdent™ System. The system is partitioned into the wide field of view (WFOV) and narrow field of view (NFOV) processing subsystems.

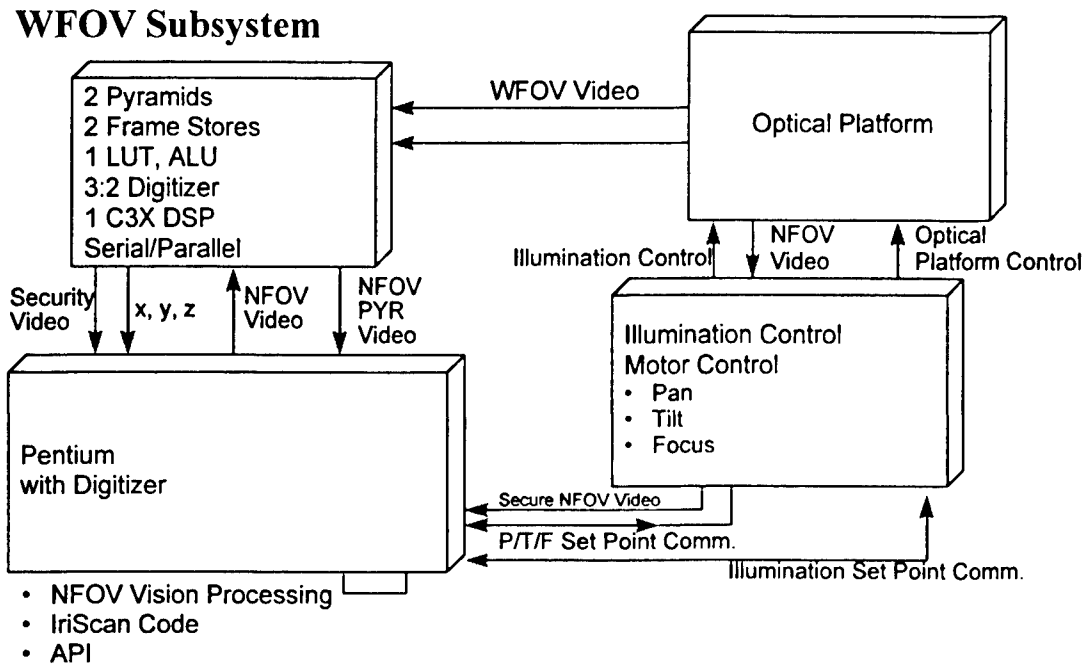


Figure 4: Distributed Processing Architecture

The WFOV optical system consists of an aligned stereo camera pair with standard monochrome video outputs (RS-170). The WFOV image processing is performed on a specialized image processing platform known as the Vision Accelerator Board (VAB). This board is derived from the Sensor Pyramid Vision I™ real-time vision front end especially designed for the real-time generation and correlation of multi-resolution images. The code running in the VAB allows the system to continuously provide (X,Y,Z) coordinates corresponding to a user's eye position to the pan/tilt mirror and focus control axis with an overall cycle time of ½ second.

The NFOV optical system consists of a pan/tilt mirror assembly, a fixed focal length lens with computer controlled focus axis, and a camera with standard monochrome video output (RS-170). The NFOV image processing is performed on a common-off-the-shelf Pentium™ Intel motherboard running at 166 MHz without any special acceleration. After the initial eye position estimate is communicated to the NFOV, the WFOV is able to run in parallel with the NFOV, providing eye estimates asynchronously via a serial interface. Each eye position estimate is translated to a pan, tilt, and focus triple via a LUT generated from a one-time manual calibration procedure. The total time taken for a single cycle of the NFOV is data-dependent.

5. Algorithms/Software

5.1 Face and eye finding via stereo processing

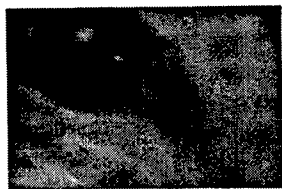
The first step in the automatic acquisition of the subject's eye is finding their eye in 3-dimensional space (the WFOV). Correlation-based stereo is used to determine depth and provide segmentation of the field of view. A template based

algorithm is then used to detect facial features confirming the presence of a face. The results of this processing are shown in Figure 5.

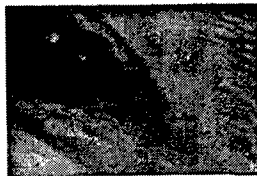


Figure 5: Results of Face and Eye Find

The results of the stereo processing, (X,Y,Z) coordinates of the subject's eye are transmitted to the NFOV processing module. After an initial motorized pan/tilt servo and focus adjustment the NFOV attempts to confirm the presence and location of an eye. If necessary, additional refinement to center the eye is performed. Finally, the image is passed through a rotational transform to compensate for rotational error introduced by the pan/tilt beam steering mirror. Figure 6 shows a sequence of initial acquisition, focus refinement , and the results of secondary centering and compensation for rotation.



1. Adjust focus



2. Rotate and center



Figure 6: NFOV Image Processing

5.2 Iris code generation and processing

Once the iris image is found, the processed image (centered and rotationally corrected) is used to compute the subject's "iris code". This code can then be XOR'ed with an previously enrolled image from a database to determine the number of mismatched bits i.e. the Hamming Distance, (HD). Subjects whose HD is below a certain threshold are confirmed as authentic; those above the threshold are rejected as impostors. Figure 7 depicts the process described.

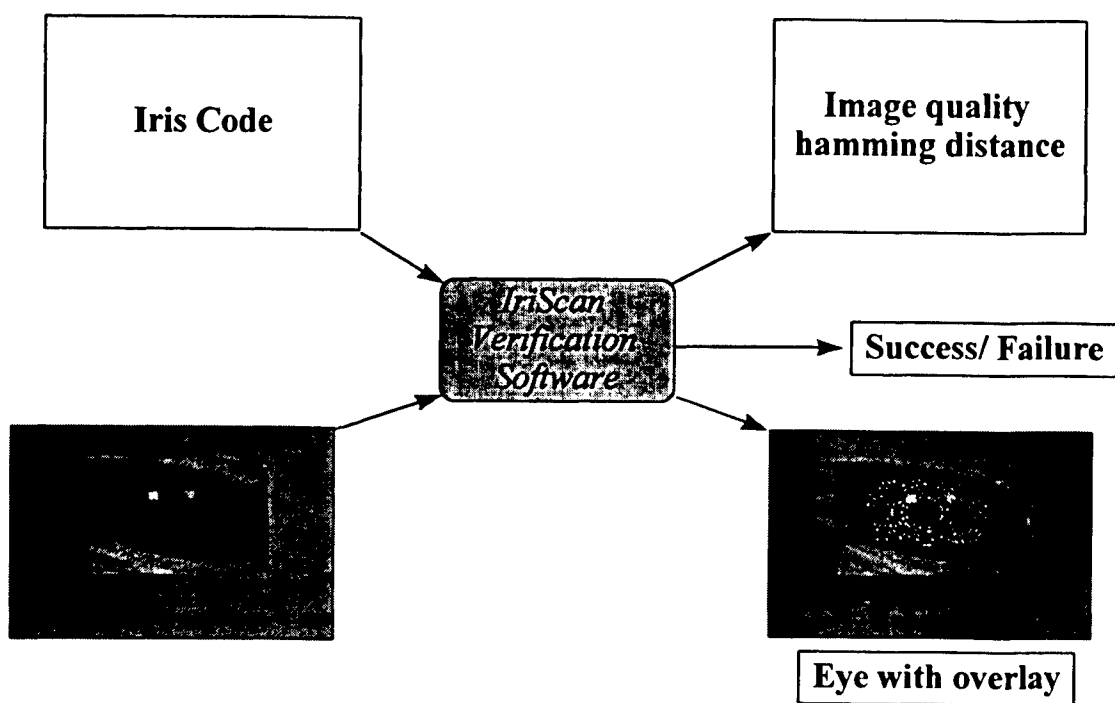


Figure 7: Verification Process

The threshold currently in use between authentic and impostor corresponds to a HD of 0.32 (68% of the bits of the two iris codes matching). The probability of an impostor being accepted at this threshold is about 1 in 10^6 . As the number of matching bits increase the probability of an impostor being accepted decreases. For a HD of 0.1 (90% match) the probability of an impostor is 1 in 10^{28} . Figure 8 shows the probability of error for a single identity verification event.

6. Performance Statistics

A recent test of the system consisted of 450 tries total, 225 each of the subject wearing glasses and not wearing glasses. All subjects passed when not wearing glasses with an average Hamming Distance of 0.15 and an average time of 3.38 sec with a standard deviation of 1.36 seconds. When the subjects were wearing glasses, 9 of the tries resulted in an inability to find the subject's eye, for a failure to acquire (FTA) rate of 4.0%. All other subjects wearing glasses passed with an average Hamming Distance of 0.19 and with an average time of 4.81 sec with a standard deviation of 3.77 seconds.

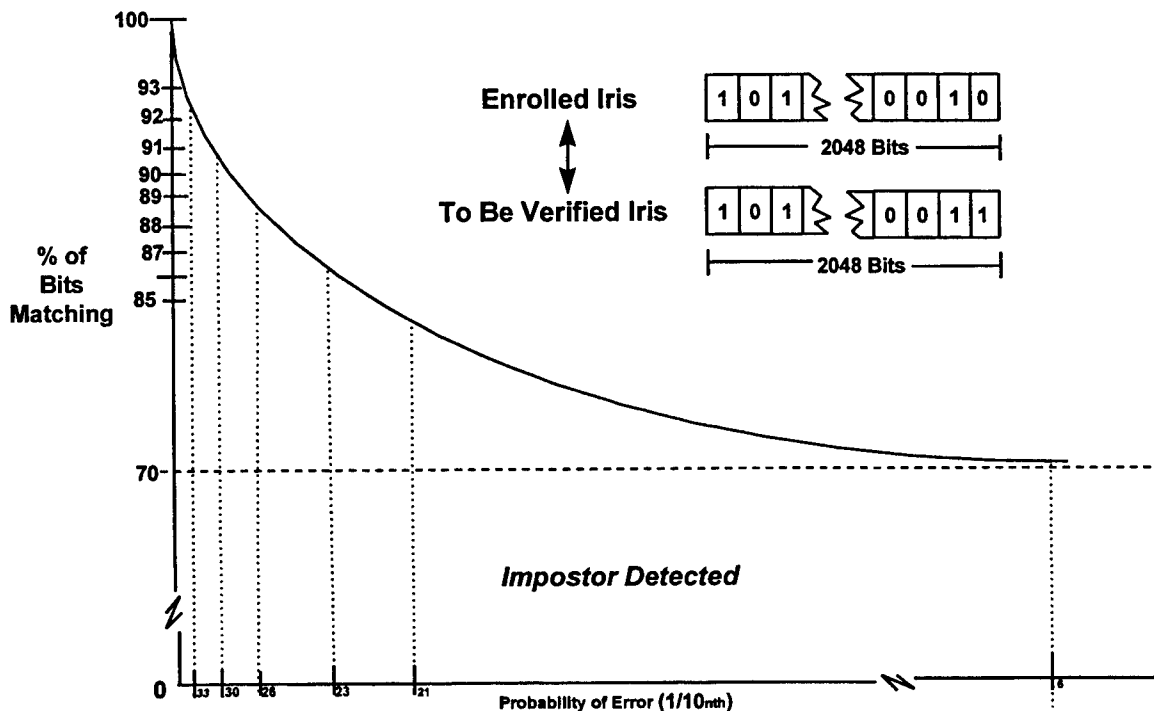


Figure 8: Probability of Error for a Single Identity Verification Event

7. Conclusions

The iris is well suited as a biometric identifier and well developed mathematical techniques for generating and comparing iris codes exist. Since eyes naturally track manual actions, the iris aligns instinctively to the field of attention and gaze that tend to attract a person such as lights or displays. By first utilizing stereo vision to find a user's face and eyes in a designated work volume and then using the results of the stereo processing, (X, Y, Z), to command both pan/tilt and focus mechanisms, a quality image of a user's eye can be obtained in an unobtrusive and non-cooperative manner. The system described in this paper perform the remote acquisition of an iris and then utilizes licensed technology to compute an iris code and compare it to a previously generated iris code. The performance of the system shows that for the minimum threshold the probability of an impostor about 1 in 10⁶ as the threshold is decreased, the probability of an impostor decreases significantly.

8. Acknowledgments

IriScan, Inc., of Mount Laurel, New Jersey, USA, holds the exclusive world-wide patents on the iris recognition software and process technology invented by Dr. John Daugman, Cambridge University, England. Sensor, Inc. uses the iris recognition software and process technology in its IrisIdent™ product line to identify an individual. Sensor uses this iris recognition technology under license from IriScan, Inc., the owner and licensor. IRISCAN is a trademark of IriScan, Inc. of Mount Laurel, New Jersey, and is used by Sensor, Inc. under license from IriScan, Inc.

9. References

1. Hanna, K., Mandelbaum, R., Mishra, D., Paragano, V., Wixson, L., "A System for Non-intrusive Human Iris Acquisition and Identification", *Proceedings of Machine Vision Applications 96*, Tokyo, Japan, November 1996
2. Daugman, J., D., "High-confidence Visual Recognition of Persons by a Test of Statistical Independence", in *IEEE PAMI*, 15(11):1148-1160, 1993
3. Flom, L., and Safir, A., Iris Recognition System, US Patent: 4,641,349, 3 February 1987
4. Daugman, J., Biometric Personal Identification System based on Iris Analysis. US Patent: 5,291,560, 1 March 1994.

SESSION 2

Laser Interactions with Ocular Tissues

Erbium:YAG laser tissue interactions

Robert W. Snyder^a, Mahendra Jani^b, Mike Yarborough^b, George Marcellino^b, Robert Noecker^a,
Theresa Kramer^a, Jesus Vidaurri^c

^aDepartment of Ophthalmology, University of Arizona, 1801 N. Campbell, Tucson, AZ 85719

^bCoherent Lasers, 4605 S. Palo Verde, Suite 607, Tucson, AZ 85714

^cTechnologic Institute of Advanced Studies, Mexico

ABSTRACT

In this paper, we present our findings of the effect of the Erbium:YAG laser on cornea, trabecular meshwork, and retinal tissue. We believe the laser is a safe and effective cutting tool with tremendous potential for surgical application.

Keywords: Erbium:YAG, laser, tissue interactions, cornea, trabecular meshwork, retina

1. TISSUE INTERACTIONS

Erbium:YAG lasers emit energy at $2.94\mu\text{m}$. This wavelength is at the peak of absorption for water. (Fig. 1) Thus, biological tissues which contain water are nearly opaque to this laser. When the Erbium:YAG energy strikes tissue, it is absorbed and heats the water forming a gas bubble which expands and contracts faster than the elasticity of the tissue can comply. This results in tissue disruption. Since the absorption coefficient is 10^{-13}cm this disruption can occur in a very confined space with minimal damage to surrounding tissue. The Erbium:YAG has potential to be a very precise cutting instrument and may be well suited for work on or within the eye where precise cutting with minimal collateral damage is very important.

The Erbium:YAG is also advantageous to other lasers such as the Excimer at 193 nm because it is solid state and potentially more economical and reliable. The laser can be delivered via fiber optics and permits instrument designs that are similar to current hand held cutting tools.

The areas of potential use for the Erbium:YAG are substantial. We have investigated some of these potential areas over the last few years. These include cornea, lens, trabecular meshwork, sclera, vitreous, and retina. In this paper, we report, in detail, our findings of the Erbium:YAG laser tissue interactions with cornea. We review our findings with trabecular meshwork¹ and retina². The lens work will be described in detail in a succeeding talk in Session 6 and published in this volume.

1.1 Cornea

In early studies,³ we compared the histology of corneal ablations created on the surface of cadaver eyes. We compared Erbium:YAG - $2.94\mu\text{m}$, 5 Hz, 2-20mJ per pulse through a $200\mu\text{m}$ sapphire fiber to Erbium YSGG - $2.79\mu\text{m}$, 5Hz, 2-20mJ pulse via a $200\mu\text{m}$ sapphire probe

and Holmium - $2.13\text{ }\mu\text{m}$, 5Hz , 5-50mJ via a $400\text{ }\mu\text{m}$ quartz probe. We found that the Erbium:YAG produced the most efficient cut, i.e., with the least surrounding thermal damage. We then went on to evaluate Erbium:YAG surface ablation, with human eye bank corneas and live rabbit corneas.

The morphology of the central cornea after Erbium:YAG (Er:YAG) laser ablations was analyzed with routine light microscopy (LM), scanning electron microscopy (SEM) and transmission electron microscopy (TEM). Several methods of ablation were utilized: (1) 1 mm, circular spots at energy levels of 16.5 mJ and 31.5 mJ per pulse and a constant number of pulses (2) 1 mm, circular spots delivered at a constant energy level with a variable number of pulses (5 to 20) and (3) a computer controlled, concentric, circular, raster pattern of single pulse, 1 mm circles with 50% overlap delivered at an energy level of 30 mJ per pulse. Although some coagulative damage and scrolling of collagen could be seen, (Fig. 2) we concluded that the Er:YAG and Er:YSGG lasers may be utilized to perform central corneal ablation and warranted further investigation.

We then evaluated the short and long term effects of Erbium:YAG laser ablation on rabbit corneas. New Zealand white rabbits were anesthetized and Erbium:YAG ablations were created with a circular raster pattern created with 1mm circles with 50% overlay or single pulses (the laser energy was $30\text{mJ}/\text{cm}^2$ with a 500 ns pulse duration). Prior to ablation, the epithelium was removed with a "69 blade" and the surface of the cornea was wetted with Cellufresh (Allergan, Irvine, CA). A HeNe aiming beam was used to center the optical zone on the central rabbit cornea.

Four rabbits were sacrificed immediately, four sacrificed at ten days, and four were followed clinically for three months. Clinical examinations were performed daily until epithelial healing was complete. Rabbits were sacrificed at ten days and three months following ablation.

Specimens were submitted and evaluated by light microscopy (LM), scanning electron microscopy (SEM), and transmission electron microscopy (TEM). All animals were treated in accordance with the ARVO Statement for the Use of Animals in Ophthalmic and Vision research.

Slit lamp examination of acute corneal ablations revealed mild anterior stromal haze localized to the ablation area. There was minimal edema in the surrounding stroma, but the deeper corneal stroma was completely clear in the acute ablations. At seven days, slit lamp evaluation revealed 1+ subepithelial haze. Over the next seven days, epithelial healing occurred. Over the next month, the amount of subepithelial haze in the corneas of all rabbits decreased and at one month, slit lamp evaluation revealed trace to 0.5 haze for the Er:YAG laser ablation areas.

Evaluation of the acute corneal ablation areas by light microscopy with toluidine blue stained sections revealed increased basophilia of the anterior stroma, indicative of coagulative change in the base of the Er:YAG laser ablation. Undulations of the anterior stromal collagen could be seen at very high levels of magnification. The deep corneal stroma appeared unaffected.

The endothelium appeared normal in some areas and markedly vacuolated in other areas beneath the laser ablations.

Evaluation of laser ablation craters by SEM revealed that the surface roughness was similar in morphologic quality to that seen in our other excimer laser studies.³ Scanning electron microscopy of the base of the Er:YAG laser ablation was irregular and individual collagen fibrils appeared to be fused together. Whitening /collagen shrinkage and bleb formation was also present at the base of the Er:YAG ablation crater but absent from the excimer laser craters as seen in other studies.

Transmission electron microscopy of acute ablation craters for Erbium:YAG laser ablations revealed that in many areas there were regular and fairly evenly spaced surface undulations of the anterior stromal collagen. Some coagulative damage was noted in areas with repeated ablation. Microfibrillary membranes were not found in Erbium:YAG ablations. Polymorphonuclear leucocytes were found in the adjacent corneal stroma after Er:YAG laser ablation.

Evaluation of the epithelium in the area of the ablation crater for the erbium:YAG lasers revealed that there was evidence of epithelial hyperplasia within the ablation crater at one and four weeks. At six weeks after ablation, the epithelial junction appeared smooth. (Fig. 3) There was normal basal to apical maturation sequence and most of the hyperplasia was a result of the morphologic change of the basal cells.

Our current study showed that the Er:YAG laser with mechanical, optical, and microprocessing control of a central raster pattern appears to be effective in ablating tissue in the cornea. Clinically and histopathologically it produces results that are similar to those with the excimer laser. Initially, the ablation results in an irregular surface with mild haze in the ablated region. The ablation appears to be localized without involvement of deeper stromal or surrounding tissues, however, there is evidence of laser induced vacuolation of the endothelium after ablation with the Erbium:YAG. This is also seen in other studies with the excimer laser.³ Epithelial healing appears to occur within several days in an orderly fashion and late healing results in minimal residual surface and anterior stromal structural changes. Histopathologic and ultrastructural evaluation of acute ablative lesions and the long term healing in rabbits revealed that changes are comparable morphologically to laser ablations with the excimer laser.⁴ We are not presently working in any clinical trials with the Erbium:YAG laser for keratectomy but we believe that this laser may be useful for corneal work.

1.2 Trabecular Ablation

The trabecular meshwork is the structure in the anterior portion of the eye which permits the flow of fluid out of the eye. When glaucoma occurs, it may be the result of "plugging" of the trabecular meshwork outflow channels with debris. We believe this could be treated by ablation of the diseased tissue to open an unobstructed channel for fluid to flow from one side of the trabecular meshwork to another. This has been proposed by a variety of researchers.^{5,6,7,8} To evaluate this further, we performed trabecular ablation on autopsied human eyes. The posterior

poles were removed from the globe and the iris, lens and ciliary body dissected free. The remaining corneoscleral rim was utilized for all experiments. A prototype of a pulsed Erbium:YAG laser (wavelength $2.94\ \mu\text{m}$), equipped with a fiberoptic was coupled to a sapphire tip measuring $400\ \mu\text{m}$ in diameter. The sapphire tip was threaded through a 16 gauge irrigation/aspiration cannula and balanced salt solution (Alcon, Ft Worth, Tx) was utilized as a constant irrigation fluid. Thus, the laser tip and the tissue was always kept moist to prevent charring. The frequency of the laser pulse was 10 Hz and the pulse duration 300 microseconds. Energy levels of 5, 10, 15, 20 and 40 mJ per pulse were used and the laser output energy measured with a Joule-meter. The corresponding fluence values were 4.0, 8.0, 11.9, 15.9, $31.8\ \text{J}/\text{cm}^2$, respectively. The corneoscleral rim was viewed through an operating microscope and the probe placed directly onto the trabecular meshwork. Focal ablation was performed with single pulses by moving the probe briskly along the circumferential extent of the trabecular meshwork. Immediately following ablation, specimens were placed in fixative.

Histologic examination of the laser treated trabecular meshwork specimens demonstrated a graded response that correlated with the laser energy used. The more pronounced changes accompanied the higher energy pulses. (Table 1) Both the ablation area and the surrounding coagulative damage increased with increasing energy levels. Minimal ablation accompanied the 5 mJ laser pulses resulting in disruption of a few of the trabecular beams immediately adjacent to the anterior chamber angle. (Fig. 4) There was no visible coagulative damage to the surrounding tissue at this energy level. At 10 mJ the ablation area extended almost completely through the trabecular meshwork to Schlemm's canal. (Fig. 5) The surrounding coagulative damage was minimal. The histopathologic study of the laser treated trabecular meshwork specimens revealed that an energy level of 15 mJ was optimal for ablating through the trabecular meshwork to Schlemm's canal with a minimal amount of coagulative damage to the surrounding tissue. The mean width of ablated tissue at the 15 mJ energy level was $150\ \mu\text{m} \pm 29\ \mu\text{m}$ ($n=18$) and the mean depth of ablation was $133 \pm 48\ \mu\text{m}$ ($n=18$). The mean width of coagulative damage to the adjacent tissue at the 15 mJ energy level was $16 \pm 8\ \mu\text{m}$ ($n=18$). Figure 6 shows an example of the histopathology of ablation at 15 mJ. The ablation extends into Schlemm's canal which is filled with erythrocytes.

We believe the Erbium:YAG laser equipped with a contact probe effectively ablates trabecular meshwork with little surrounding coagulative damage. This feature may minimize scarring and result in a high long-term patency rate for outflow channels created by laser trabecular ablation. Further studies are needed to determine safety and long-term efficacy under in vivo conditions.

1.3 Retinal Surgery

Margolis and colleagues used an Erbium:YAG laser to successfully cut experimentally induced vitreous membranes in rabbits by using an intraocular fiberoptic delivery system. They concluded that a pulsed Erbium:YAG laser can perform tractionless cutting of vitreous membranes in many cases without evidence of retinal injury.⁹

We used an Erbium:YAG laser to create retinotomy sites in the retina of human eye bank

eyes and examined the effectiveness of retinal ablation and the extent of surrounding coagulative damage using routine light and scanning electron microscopy.

Human autopsy eyes were obtained and all experiments were conducted within 24 hours of death to minimize autolytic changes. The eyes were maintained in a moist chamber at 4- C prior to the experiments. The posterior poles were separated from the anterior segment with an incision at the pars plana. The specimens were then warmed to room temperature prior to laser treatment. The vitreous was left intact when possible.

A pulsed Erbium:YAG laser (wavelength 2.94 μm) equipped with an infrared transmitting glass fiber was coupled to a 400 μm sapphire tip. The sapphire tip was threaded through a 16 gauge two-way irrigation/aspiration cannula. A balance salt solution was used as a constant irrigation fluid.

Laser was applied directly to the retinal surface in single and multiple pulses at energy levels ranging from 4.0 to 16 mJ/pulse (fluence ranging from 2.79 to 12.74 J/cm²). The frequency of the laser pulse was 10 Hz and the pulse duration 300 microseconds. Laser was applied to the macula and peripheral retina surrounding the vascular arcades by a hand-held fiberoptic delivery system positioned approximately 0.5 mm from the retinal surface. Immediately following ablation, specimens were processed for light microscopy.

Single pulse treatments at low energy levels resulted in partial thickness ablation with minimal damage to surrounding layers of the retina. (Fig 7) Light microscopy demonstrated that an energy level of 4mJ was optimal for ablating superficial layers of the retina. The mean width of ablated tissue at the 4 mJ energy level was $141 \pm 27 \mu\text{m}$ (n=23) and the mean depth of ablation was $65 \pm 17 \mu\text{m}$ (n=21). At all energy levels, the mean width of coagulative damage to adjacent tissue was less than 20 μm .

The Erbium:YAG laser equipped with a contact probe appeared to be an effective means of creating retinotomies in human autopsy eyes when used in the single pulse mode at higher energy levels. When used in the single pulse mode at lower energy levels, the laser may be capable of removing superficial retinal layers or preretinal membranes without damaging deeper structures.

Human studies are currently underway and headed by Dr. D'Amico. A 200Hz Erbium:YAG laser is currently being employed. Results for retinotomy and a variety of procedures look very promising.^{10,11}

2. ACKNOWLEDGEMENTS

This work was supported by Coherent Lasers and Sensory Research Foundation of Arizona.

3. REFERENCES

1. T. R. Kramer, R. J. Noecker, L. G. Ellsworth, J. M. Yarborough, R. W. Snyder, "Laser trabecular ablation of human autopsy eyes with Erbium:YAG laser: A histopathologic study," *SPIE's International Symposium on Biomedical Optics*, January 1994.
2. L. G. Ellsworth, T. R. Kramer, R. J. Noecker, J. M. Yarborough, R. W. Snyder, "Retinotomy using Erbium:YAG laser on human autopsy eyes," *SPIE's International Symposium on Biomedical Optics*, January 1994.
3. L. L. Kirshner, T. R. Kramer, R. W. Snyder, M. Yarborough, H. Jones, "Histopathology and electron microscopy of the morphology of corneal ablation with the Erbium:YAG and Erbium:YSGG lasers." *Association for Research in Vision and Ophthalmology* (IOVS, Vol. 36, No. 4), 1995.
4. R. W. Snyder, T. R. Kramer, M. Yarborough, G. Marcellino, "Histopathological and electron microscopic evaluation of the early effects of the Erbium:YAG (2.94uFm), neodymium:YAG (213NM) and the Excimer laser (193NM) ablation of the cornea." *Association for Research in Vision and Ophthalmology* (IOVS, Vol. 37, No. 3), 1996.
5. M. M. Krasnov, "Laserpuncture of anterior chamber angle in glaucoma," *American Journal of Ophthalmology*, Vol. 75, pp. 674-678, 1973.
6. M. M. Krasnov, "Q-switched laser goniopuncture," *Archives of Ophthalmology*, Vol. 92, pp. 37-41, 1974.
7. S. Melamed, M. A. Latina, and D. L. Epstein, "Neodymium:YAG laser trabeculopuncture in juvenile open-angle glaucoma," *Ophthalmology*, Vol. 94, pp. 163-170, 1987.
8. S. Melamed, I. Ashkenazi, I. Gutman, and M. Blumenthal, "Nd:YAG laser trabeculopuncture in angle-recession glaucoma," *Ophthalmic Surgery*, Vol 23, pp. 31-35, 1992.
9. T.I. Margolis, D.A. Farnith, M. Destro, and C.A. Puliafito, "Erbium:YAG laser surgery on experimental vitreous membranes," *Archives of Ophthalmology*, Vol. 107, p. 424, 1989.
10. D. J. D'Amico, D. J. Brazitikos, G. Marcellino, S. M. Finn, J. L. Hobart, "Initial clinical experience with an Erbium:YAG laser for vitreal retinal surgery." *American Journal of Ophthalmology*, 121, pp. 414-425, 1996.
11. P. D. Brazitikos, D. J. D'Amico, M. T. Bernal, A. W. Walsh, "Erbium:YAG laser surgery of the vitreous and retina," *Ophthalmology*, 102, pp. 278-290, 1995.

TABLE 1

HISTOPATHOLOGY OF LASER ABLATION

Energy Level (mJ)	Fluence (J/cm ²)	Ablation Width (μm)	Ablation Depth (μm)	Coagulation (μm)
5 (4)	4.0	-	-	-
10 (10)	8.0	142±40	74±22	4±2
15 (18)	11.9	150±29	133±48	16±8
20 (21)	15.9	174±24	102±19	29±9
40 (15)	31.8	146±52	237±106	50±20

All energy levels are expressed in millijoules with the number of results in parentheses. Fluences were calculated from the measured energy level and the tip diameter and are expressed in Joules per square centimeter. Ablation measurements represent linear measurements made with a calibrated micrometer. Results are expressed as the arithmetic means ± standard deviation of the mean. Minimal ablation accompanied the 5 mJ laser pulses resulting in disruption of a few of the trabecular beams immediately adjacent to the anterior chamber angle. There was no visible coagulative damage to the surrounding tissue at this energy level.

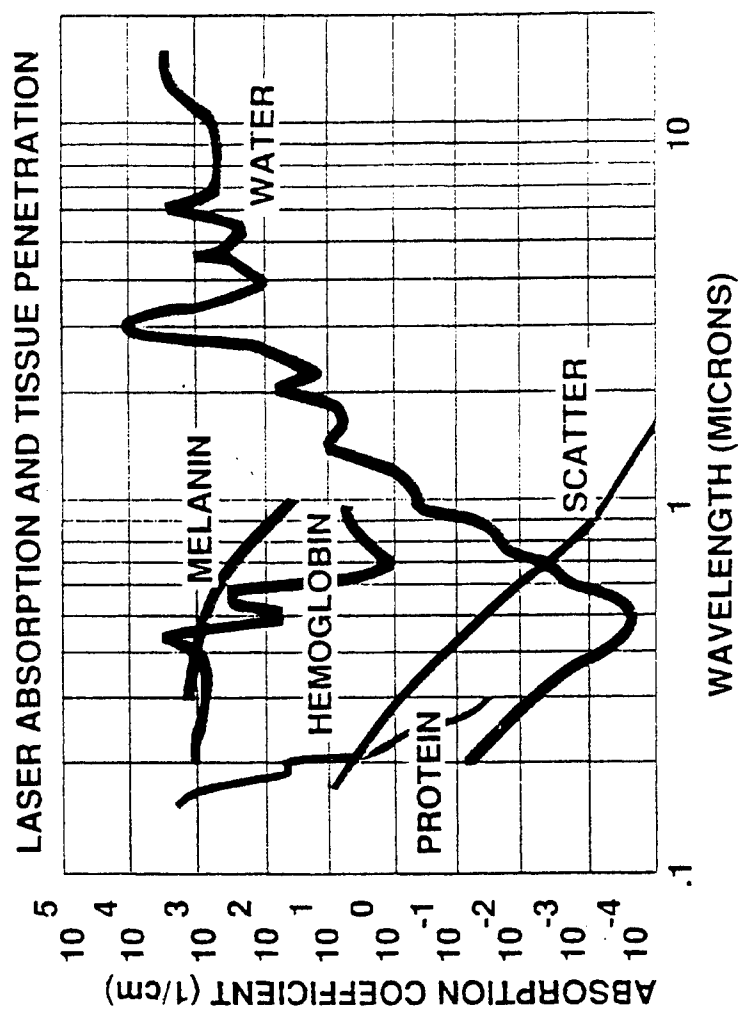


Fig 1. Laser absorption and tissue penetration (Courtesy of Coherent Medical and Coherent Lasers, Palo Alto, CA)

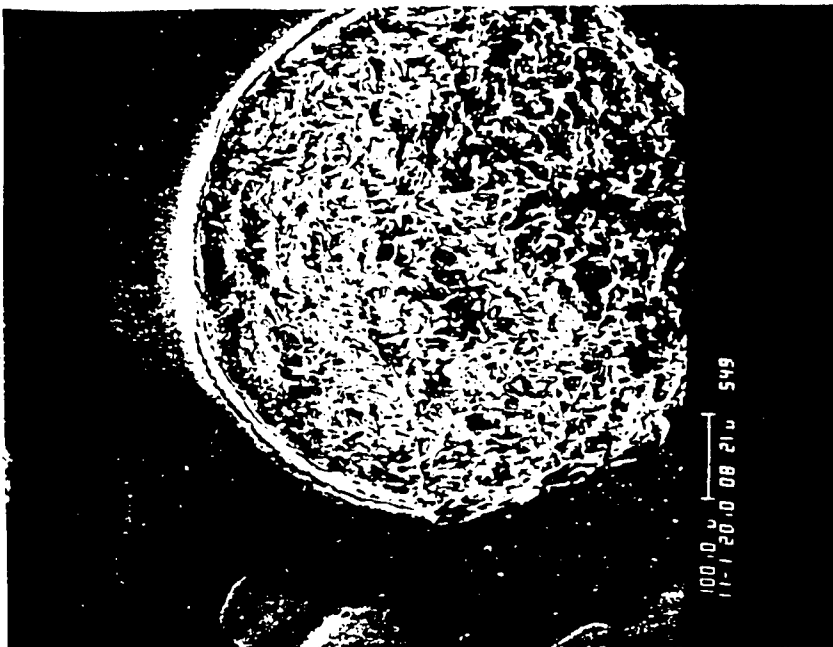


Figure 2: Scanning electron micrograph of an Er:YAG laser ablation of the human cornea. Scrolling and whitening of collagen is indicative of coagulative damage of the surface collagen.



Figure 3: Transmission electron micrograph of the base of the Er:YAG laser ablation of a rabbit cornea 6 weeks after ablation. The epithelial junction is smooth, but, increased numbers of keratocytes are present in the anterior stromal lamellae. Increased profiles of rough endoplasmic reticulum are indicative of active collagen synthesis.

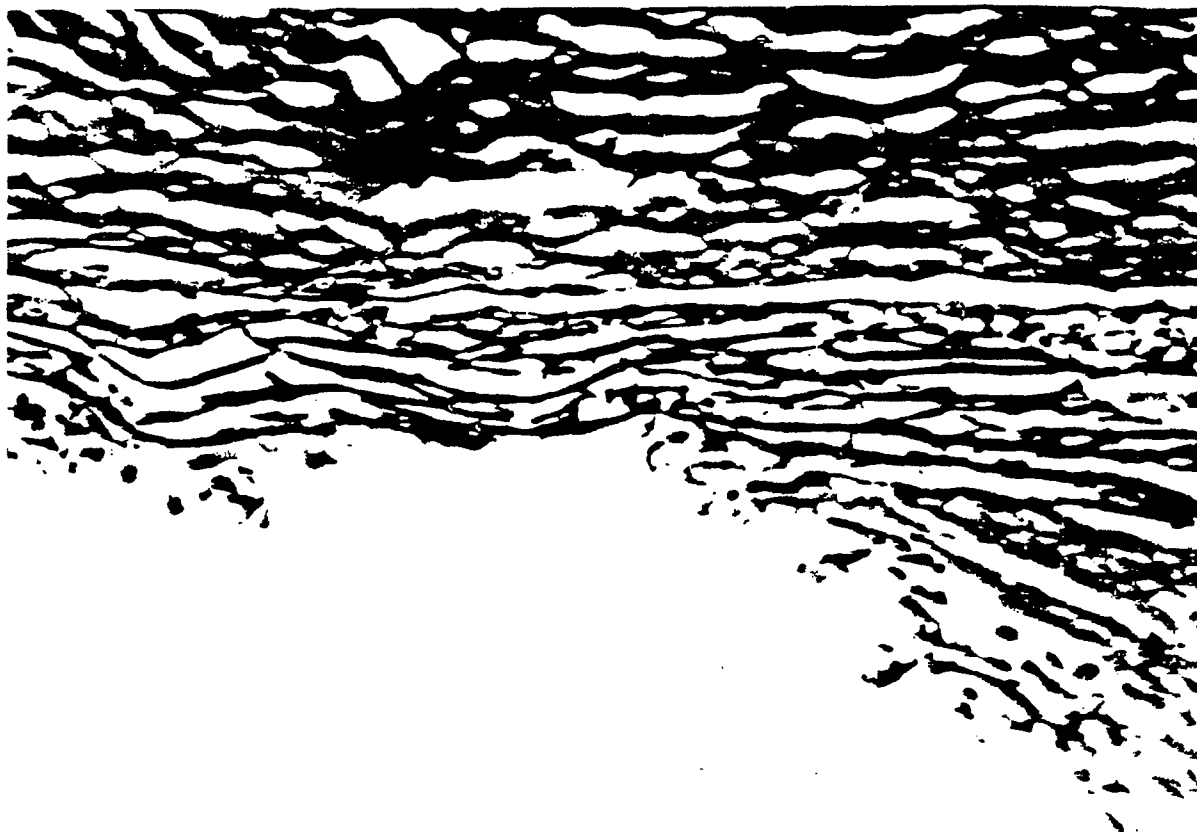


Fig. 4. Light micrograph demonstrating laser trabecular ablation at 5 mJ. Minimal ablation of the outermost trabecular beams adjacent to the anterior chamber angle. There is no evidence of coagulative damage to the structures (Hematoxylin and Eosin), MAG. = 125 X

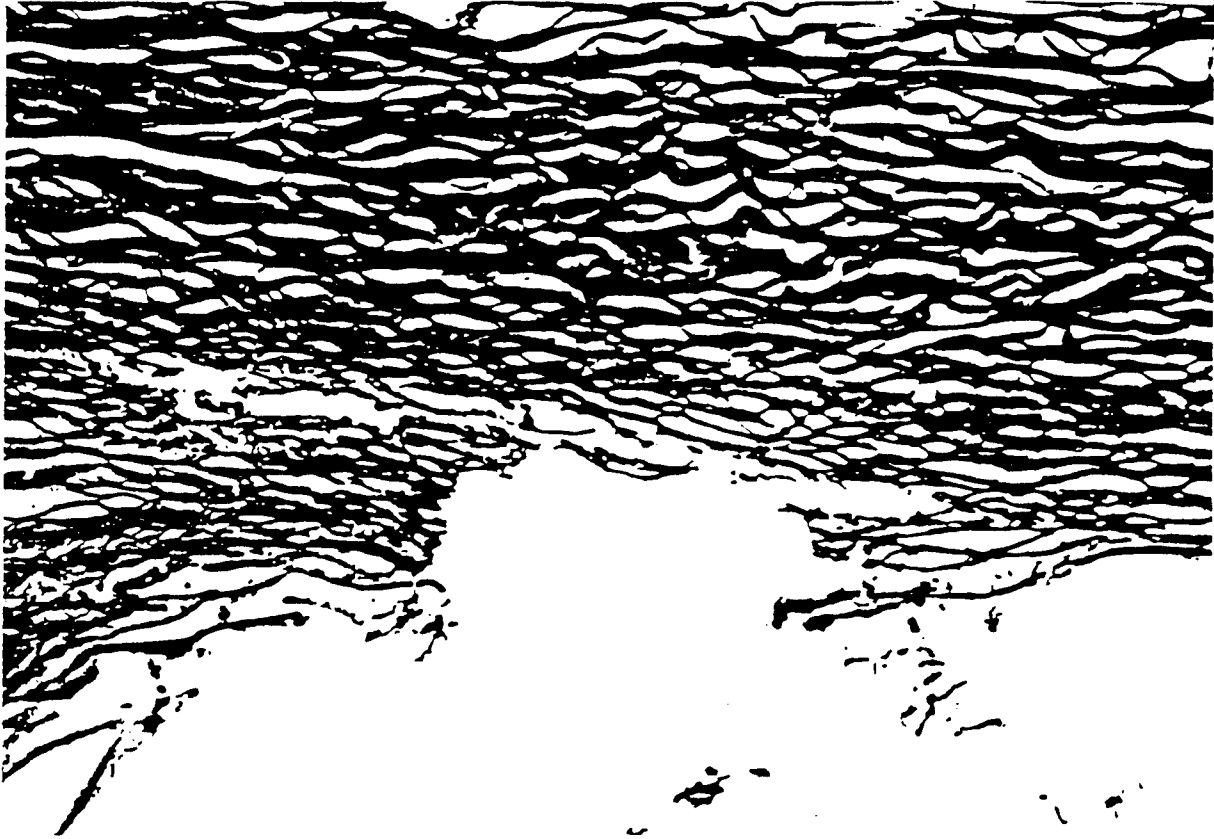


Fig. 5. Light micrograph demonstrating laser trabecular ablation at 10 mJ through to the juxtacanalicular trabecular meshwork. The surrounding coagulative damage is highlighted by the deeper eosinophilic staining (Hematoxylin and Eosin), MAG. = 80 X

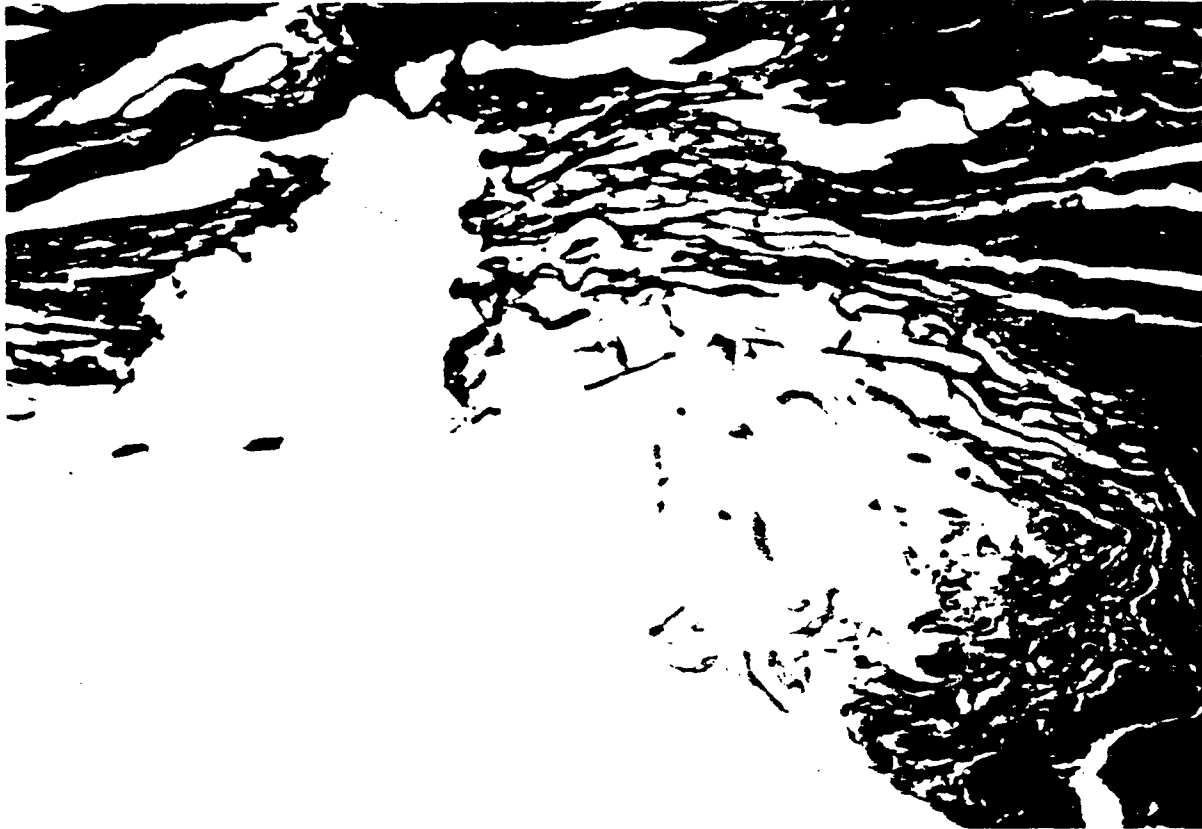


Fig. 6. Light micrograph demonstrating laser trabecular ablation at 15 mJ through to Schlemm's Canal. The surrounding coagulative damage is highlighted by the deeper eosinophilic staining (Hematoxylin and Eosin), MAG. = 125 X



Fig. 7. A single pulse partial ablation (40 X) at 7 mJ) demonstrates coagulative damage to superficial layers of the retina.

Spot Diameters for Scanning Photo-Refractive Keratectomy: A Comparative Study

Fabrice Manns, Jean-Marie Parel

Department of Biomedical Engineering
University of Miami College of Engineering, Coral Gables, FL 33124
Ophthalmic Biophysics Center, Bascom Palmer Eye Institute
University of Miami School of Medicine, Miami FL 33136

ABSTRACT

Purpose: The purpose of this study was to compare with computer simulations the duration, smoothness and accuracy of scanning photo-refractive keratectomy with spot diameters ranging from 0.2 to 1 mm. **Methods:** We calculated the number of pulses per diopter of flattening for spot sizes varying from 0.2 to 1 mm. We also computed the corneal shape after the correction of 4 diopters of myopia and 4 diopters of astigmatism with a 6 mm ablation zone and a spot size of 0.4 mm with 600 mJ/cm² peak radiant exposure and 0.8 mm with 300 mJ/cm² peak radiant exposure. The accuracy and smoothness of the ablations were compared. **Results:** The repetition rate required to produce corrections of myopia with a 6 mm ablation zone in a duration of 5s per diopter is on the order of 1 kHz for spot sizes smaller than 0.5 mm, and of 100 Hz for spot sizes larger than 0.5 mm. The accuracy and smoothness after the correction of myopia and astigmatism with small and large spot sizes were not significantly different. **Conclusions:** This study seems to indicate that there is no theoretical advantage for using either smaller spots with higher radiant exposures or larger spots with lower radiant exposures. However, at fixed radiant exposure, treatments with smaller spots require a larger duration of surgery but provide a better accuracy for the correction of astigmatism.

Keywords: photorefractive keratectomy, scanning, model, laser, refractive surgery, cornea, ablation

1. INTRODUCTION

In scanning photorefractive keratectomy (SPRK), the cornea is photo-ablated with a scanning laser beam for the correction of myopia or astigmatism. Several delivery systems and scanning algorithms are currently being investigated or developed for SPRK, as well as for Laser-Assisted In-Situ Keratomileusis (LASIK)¹⁻⁸. These systems use different spot sizes, energies per pulse, repetition rates, and wavelengths. Typically, the spot size ranges from 0.2 to 1 mm, the energy per pulse ranges from 0.2 to 1.0 mJ, and the repetition rate ranges from 50 Hz to 1 kHz. The laser sources currently investigated for SPRK include miniature Argon-Fluoride excimer lasers (193 nm), frequency-quintupled solid-state lasers (213 nm), and mid-infrared lasers emitting at wavelengths close to 3 μ m.

The purpose of this study was to determine whether using smaller spot diameters (0.2 to 0.5 mm) is more advantageous in theory for SPRK than using larger spot diameters (0.5 to 1 mm). We calculated the duration of surgery for spot sizes ranging from 0.2 to 1 mm and computed the corneal shape after SPRK for the correction of myopia and astigmatism to compare the accuracy of the corrections and the smoothness of the calculated postoperative corneal surface.

2. MODEL AND ALGORITHM

2.1. Laser and beam characteristics

We simulated SPRK with a frequency-quintupled Nd:YAG laser emitting at a wavelength of 213 nm. The intensity distribution on the cornea was assumed to be Gaussian, with $1/e^2$ beam diameter b , and peak radiant exposure I_0 (figure 1):

$$I(r) = I_0 e^{-8 \frac{r^2}{b^2}} \quad \text{Eq. (1)}$$

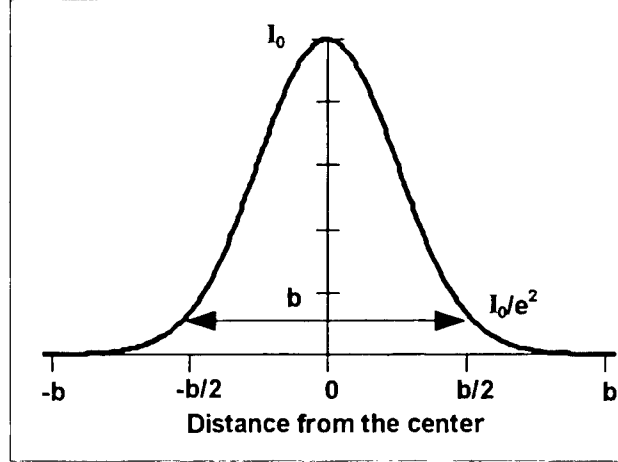


Figure 1: Cross-section of the intensity distribution of the Gaussian spot with spot size b .

In the following, the $1/e^2$ beam diameter will be called the *spot diameter*. The total energy per pulse, E , is proportional to the square of the spot diameter, b , and to the peak radiant exposure, I_0 :

$$E = I_0 \frac{\pi b^2}{8} \quad \text{Eq. (2)}$$

2.2. Ablation rate and ablation per pulse

The variations of the corneal ablation rate with radiant exposure measured at 213 nm⁹ were fitted with a linear curve (figure 2). The curve fit yielded a threshold radiant exposure for ablation, I_{th} , equal to 80 mJ/cm², and a slope, α , equal to 0.003 $\mu\text{m}/(\text{mJ}/\text{cm}^2)$. The ablation depth per pulse as a function of the distance from the center of the spot, $z(r)$ was calculated by combining the corneal ablation rate and the Gaussian beam intensity distribution:

$$z(r) = \alpha \left(I_0 e^{-8 \frac{r^2}{b^2}} - I_{th} \right) \quad \text{if } r < r_{th} \quad \text{Eq. (3)}$$

$$z(r) = 0 \quad \text{if } r > r_{th}$$

where r_{th} is given by:

$$r_{th} = b \sqrt{\frac{1}{8} \ln \frac{I_0}{I_{th}}} \quad \text{Eq. (4)}$$

In the following, $b_{eff} = 2 r_{th}$ will be called the effective spot diameter. The effective spot diameter delimits the parts of the Gaussian spot that are below and above the ablation threshold, and thus corresponds to the diameter of the crater created on the corneal surface by the Gaussian laser spot.

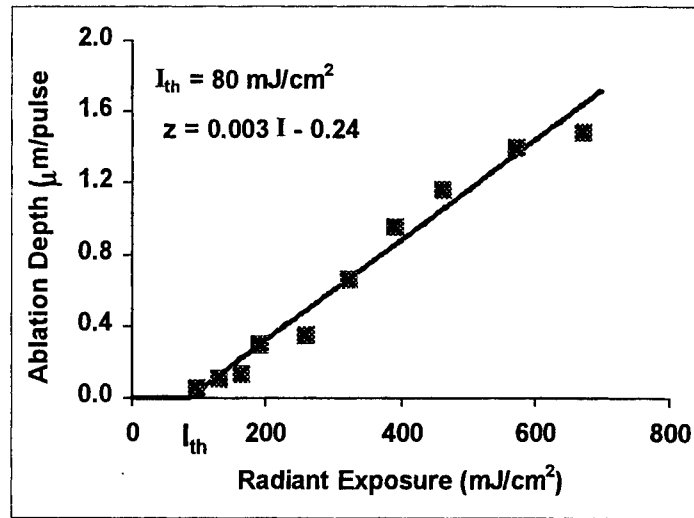


Figure 2: Corneal ablation rate at 213 nm.

For the linear approximation of the corneal ablation rate (figure 2), the ratio of the effective spot diameter, b_{eff} , to the actual spot diameter, b , is given by:

$$\frac{b_{\text{eff}}}{b} = \sqrt{\frac{1}{8} \ln \frac{I_0}{80}} \quad \text{Eq. (4)}$$

2.3. Scanning algorithm

In our scanning system, laser pulses are applied at fixed positions in the ablation zone. The spot positions are separated by a constant distance, h , which is related to the spot overlap, w , and to the spot diameter, b , by the equation:

$$w = 1 - \frac{h}{b} \quad \text{Eq. (5)}$$

The number of pulses to be applied at each position for a given ablation was calculated with the mathematical method that we described previously^{8,10,11}.

3. NUMBER OF PULSES

The duration of surgery is equal to the total number of pulses applied divided by the repetition rate of the laser. We have shown previously⁸ that the number of pulses for a correction of myopia is proportional to the amount of correction in diopters, proportional to the fourth power of the diameter of the ablation zone, and inversely proportional to the square of the spot size. If we assume that the number of pulses per diopter of correction, N , is equal to the volume of tissue to be ablated divided by the volume of tissue removed by each pulse, then, with the ablation rate of figure 2, we have:

$$N = \frac{110 \times d^4}{b^2 \times \left\{ I_0 - 80 \times \left(1 + \ln \frac{I_0}{80} \right) \right\}} \quad \text{Eq. (6)}$$

where d (in mm) is the diameter of the ablation zone, b is the spot diameter in units of mm, and I_0 is the peak radiant exposure in units of mJ/cm^2 .

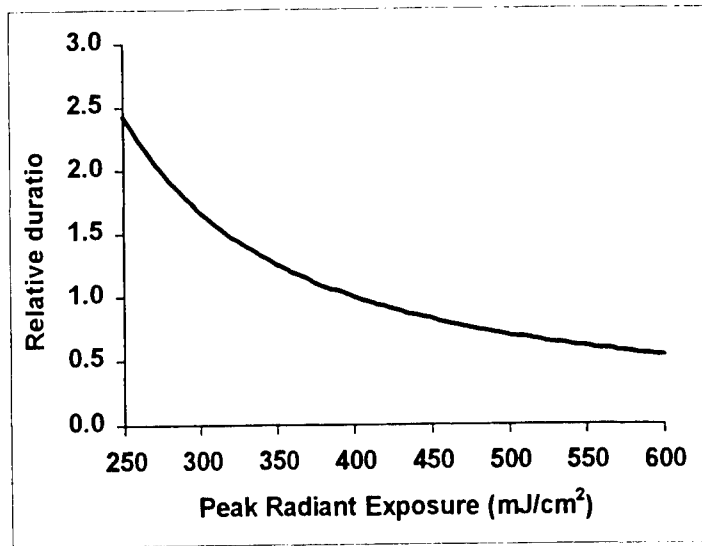


Figure 3: Relative duration of surgery versus peak radiant exposure (the duration is 1.0 at 400 mJ/cm²).

According to figures 2 and 3, the peak radiant exposure, I_0 , should be selected between 300 and 600 mJ/cm² in order to minimize the duration of surgery, while limiting the ablation depth per pulse. With these values of the peak radiant exposure, the peak ablation depth per pulse is between 0.66 and 1.56 μ m.

To evaluate the effect of spot size on the duration of surgery, the total number of pulses per diopter of correction for a correction of myopia with a 6 mm ablation zone was calculated with Eq. (6) for spot diameters ranging from 0.2 to 1 mm, and a peak radiant exposure of 300 and 600 mJ/cm² (Table 1). In addition, we also calculated the repetition rate required in order to produce a correction of myopia with a 6 mm ablation zone with a speed of 5 seconds per diopter, as a function of the spot size (Table 2).

Spot \varnothing (mm)	300 mJ/cm ²		600 mJ/cm ²	
	Energy (mJ)	Pulses per diopter	Energy (mJ)	Pulses per diopter
0.2	0.05	31192	0.09	9933
0.4	0.2	7798	0.4	2483
0.6	0.4	3466	0.8	1104
0.8	0.8	1950	1.5	621
1.0	1.2	1248	2.4	397

Table 1: Energy per pulse and number of pulses per diopters for a correction of myopia with a 6 mm ablation zone versus spot size and peak radiant exposure. The peak ablation is 0.7 μ m at 300 mJ/cm² and 1.6 μ m at 600mJ/cm².

Spot \varnothing (mm)	Repetition rate (Hz)	
	$I_0 = 300 \text{ mJ/cm}^2$	$I_0 = 600 \text{ mJ/cm}^2$
0.2	6200	2000
0.4	1550	500
0.6	700	220
0.8	400	120
1.0	250	80

Table 2: Repetition rate required to produce corrections of myopia with a 6 mm ablation zone at a speed of 5 seconds per diopter.

Since the duration of surgery is inversely proportional to the square of the spot diameter, using a larger spot size for SPRK seems to be more advantageous, as shown in Table 1. On the other hand, a smaller energy per pulse is required to produce the same peak ablation depth when a smaller spot size is used (Table 1). In practice, the repetition rate of the laser can generally be increased if less energy is required on the cornea. The higher repetition rate may compensate for the increase in time when a smaller spot size is used. According to Tables 1 and 2, a speed of 5 seconds per diopter of flattening can be achieved with a 6 mm ablation zone by using either a spot diameter smaller than 0.5 mm with a repetition rate between 1 and 5kHz and an energy per pulse of less than 0.2 mJ, or a spot diameter larger than 0.5 mm with a repetition rate between 100 and 500 Hz and an energy per pulse of approximately 1 mJ.

4. CORRECTION OF MYOPIA

In order to evaluate the effect of the spot size on the smoothness and accuracy of SPRK for the correction of myopia, we calculated the corneal shape after a correction of 4 diopters of myopia. All calculations were performed for a 6 mm ablation zone and a small spot ($b=0.4$ mm) and large spot ($b=0.8$ mm).

4.1. Selection of the peak radiant exposure and spot overlap

Peak radiant exposure: The peak radiant exposure was selected so that the duration of surgery was approximately the same with both spot sizes. Based on the results of section 3, we selected a peak radiant exposure of 600 mJ/cm^2 for the 0.4 mm spot (2480 pulses per diopter) and 300 mJ/cm^2 for the 0.8 mm spot (1950 pulses per diopter), respectively. We could also have simulated SPRK with the same peak radiant exposure for both spot sizes. However, previous simulations^{8,11} with a fixed peak radiant exposure of 400 mJ/cm^2 showed that there is no significant difference in the accuracy and smoothness of the ablation for the correction of myopia when the spot size is varied from 0.5 to 1 mm.

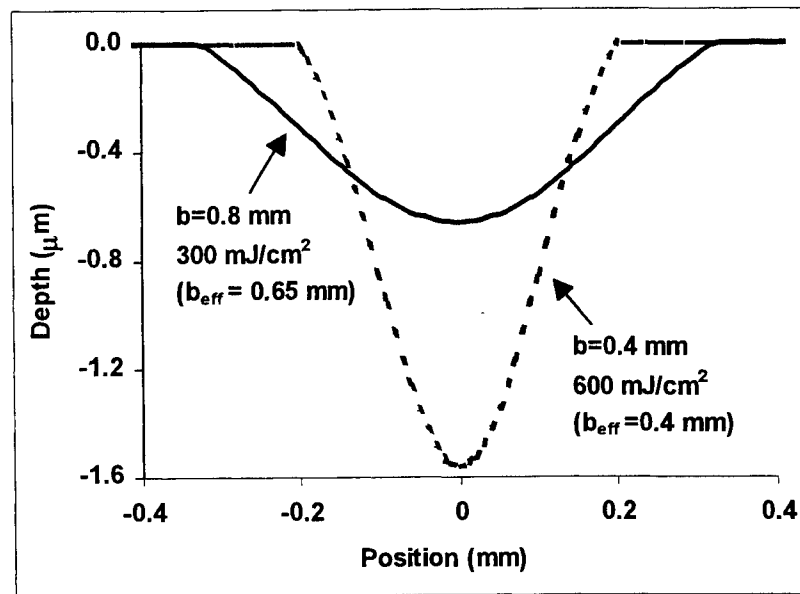


Figure 4: Cross-section of the ablation per pulse for the selected parameters.

Spot Overlap: Based on previous simulations^{8,11}, we selected an overlap of 80% for the simulations with the 0.8 mm spot, which yields an effective overlap ($1-h/b_{\text{eff}}$) of 75% when the peak radiant exposure is 300 mJ/cm^2 , according to Eq. (4). We selected an overlap of 60 % for the simulations with the 0.4 mm spot, which corresponds to an effective overlap of 60% when the peak radiant exposure is 600 mJ/cm^2 . This value of the overlap was selected so that the depth of the ablation crater created when one pulse is applied at each spot position was approximately the same as with the 0.8 mm spot used with 80% overlap (figure 5). The flat ablation crater of figure 5 is equivalent in principle to the ablation crater created by each pulse during broad-beam PRK. With the selected parameters, the ablation depth of the flat crater was $3.4 \mu\text{m}$ for the large spot and $4.7 \mu\text{m}$ for the small spot. With 80% overlap and a peak radiant exposure 600 mJ/cm^2 the depth of the flat crater would have been $12 \mu\text{m}$ for the 0.4 mm spot.

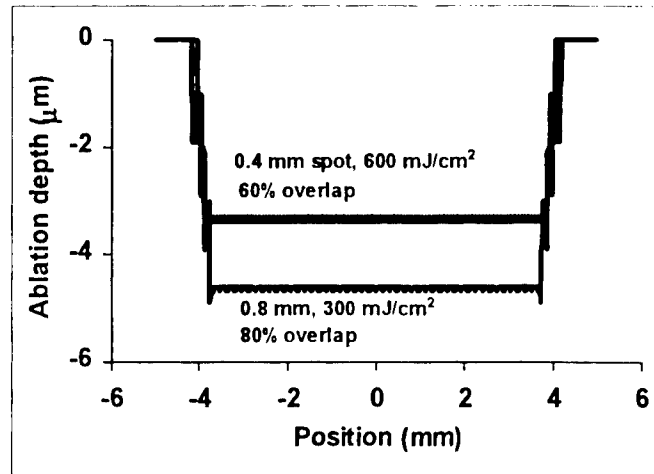


Figure 5: Cross-section of the simulated ablation crater created with the selected parameters when one pulse is applied at each spot position.

4.2. Accuracy and smoothness

The accuracy was calculated for both spot sizes by fitting 180 meridians of the calculated postoperative corneal shape with elliptic functions and calculating the average curvature of the fits. The roughness was expressed as the root mean square error between the elliptical fits and the calculated corneal shape. The accuracy was 0.15 D with the 0.4 mm spot and 0.19 D with the 0.8 mm spot. The roughness was 1.3 μm with the 0.4 mm spot and 0.7 μm with the 0.8 mm spot. These results seem to indicate that varying the spot size does not significantly affect the accuracy or smoothness of ablations for the correction of myopia. The surface produced with the smaller beam was slightly rougher, most probably because the spot overlap was smaller. However, the calculated difference in roughness (0.6 μm) may not be clinically relevant firstly because it may not be sufficient to affect re-epithelialization, and secondly because factors such as optomechanical stability, corneal inhomogeneities, and pulse to pulse energy variations will also affect surface roughness after corneal ablation.

Small surface irregularities were observed in cross-sections of the simulated ablation craters (figure 6 and figure 7). These irregularities were also observed by profilometry of ablated PMMA surfaces¹² and by light microscopy after ablation of rabbit corneas¹³. The presence of these irregularities in simulations seems to indicate that they are intrinsic to the ablation algorithm rather than caused by vibrations in the scanning system or by inhomogeneities in the ablated material. If necessary, it might be possible to reduce or remove these irregularities by adding a random factor of appropriate range in the positioning of the beam.

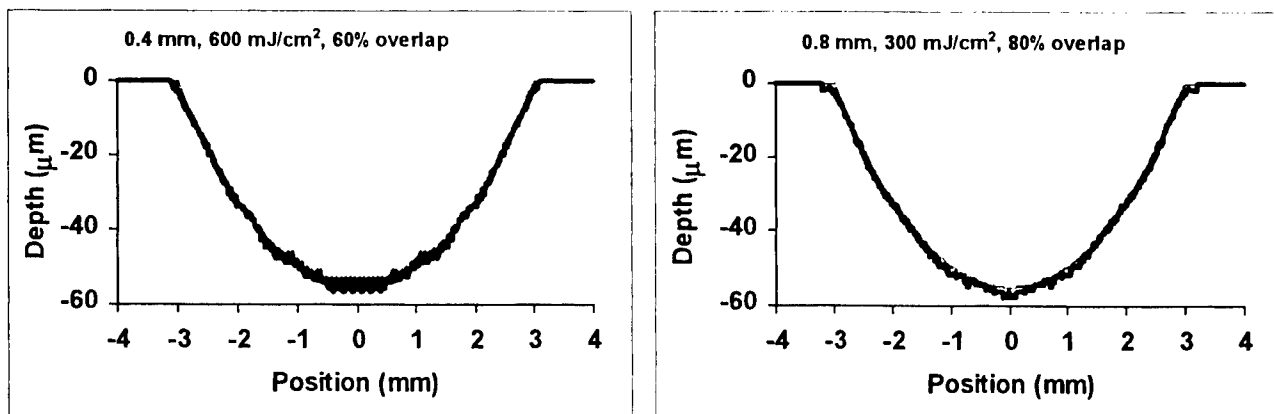


Figure 6: Cross-sections of the simulated ablation craters for 4 diopters of flattening with a 6 mm ablation zone.

5. CORRECTION OF ASTIGMATISM

To determine whether small spots are advantageous for the correction of asymmetric refractive errors, we calculated the dioptric maps of the cornea before (figure 7) and after (figure 8) ablations for the correction of 4 diopters of astigmatism, with the same parameters as in the previous section. Some astigmatism remains in both cases (small spot and large spot). There are no significant differences between the dioptric maps after ablation with the 0.4 and 0.8 mm spots. However, previous simulations¹¹ showed that astigmatism could totally be corrected by using a small spot (0.5 mm) with a lower radiant exposure (400 mJ/cm²). However, using these parameters also significantly increases the duration of surgery. In summary, using a smaller spot with a higher peak radiant exposure or a larger spot with a lower peak radiant exposure is equivalent for the correction of astigmatism. However, at fixed peak radiant exposure, smaller spots require a larger number of pulses but provide a better accuracy for the correction of astigmatism.

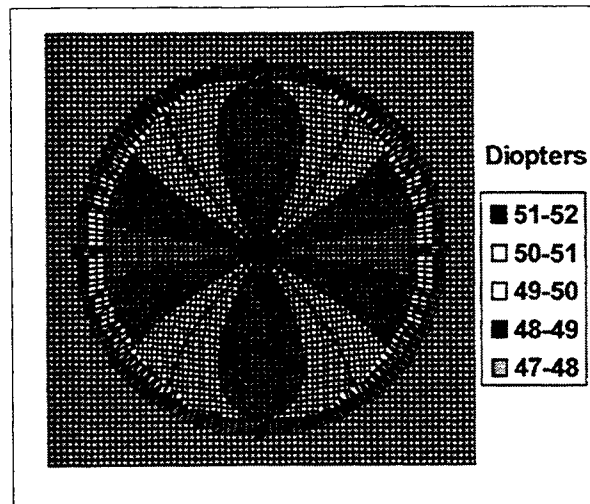


Figure 7: Dioptric map of the cornea with 4 diopters of astigmatism.

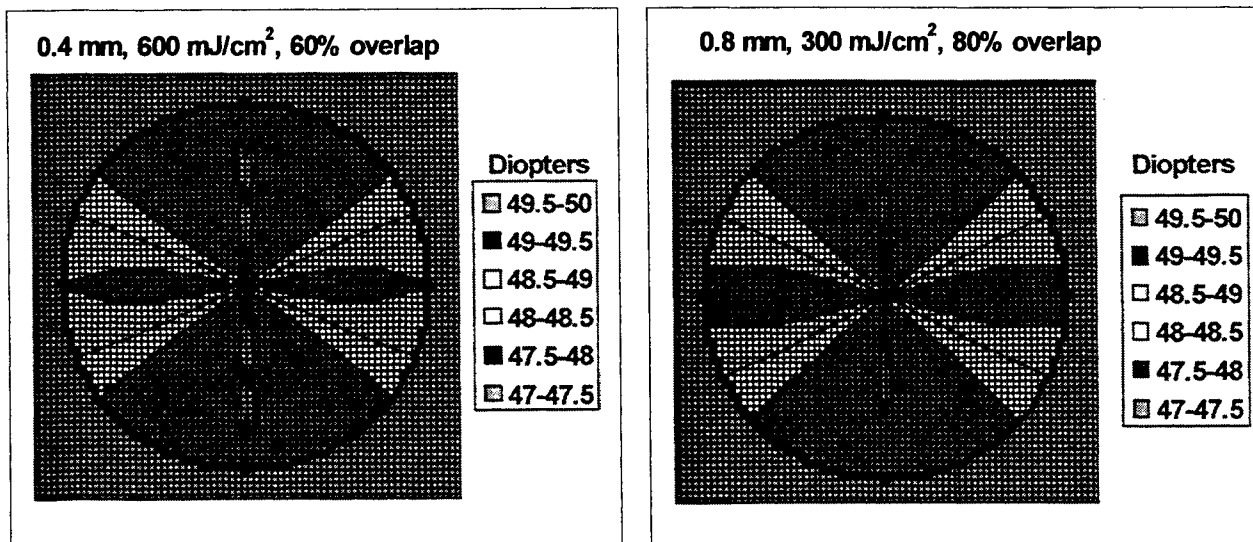


Figure 8: Postoperative dioptric maps after the correction of 4 diopters of astigmatism.

6. CONCLUSION

This study indicates that there is no theoretical advantage for using either smaller spots with higher radiant exposures or larger spots with lower radiant exposures, for spot diameters varying from 0.2 to 1mm. At fixed radiant exposure, treatments with smaller spots require a larger duration of surgery but provide a better accuracy for the correction of astigmatism.

However, large spots and small spots with different radiant exposures may produce significantly different physical effects, for instance because of differences in the amplitude of the pressure wave or thermal effect generated during the ablation. In addition, the absolute positioning accuracy is more critical when small spots are used, and ablations with larger spot may not be affected as much by local corneal inhomogeneities.

7. ACKNOWLEDGMENTS

This work was supported in part by BioVision International and Quantel, SA; The Florida Lions Eye Bank; Fight For Sight, The Research Division of Prevent Blindness America, in memory of Lee S Hochwald; Research to Prevent Blindness, New York, NY; The Henri and Flore Lesieur Foundation.

8. REFERENCES

1. J Pallikaris, MB McDonald, D Siganos, G Klonos, S Detokaris, R Frey, R Downes, CA Gauthier, "Tracker-assisted photorefractive keratectomy for myopia of -1 to -6 diopters", *Journal of Refractive Surgery* 12:240-247, 1996.
2. WB Telfair, RE Nordquist, RA Eiferman, C Bekker, PR Yoder, HH Zenzie, "Acute damage evaluation of corneal ablation by two mid-infrared sources and comparison to excimer results", *Arvo Abstract, Investigative Ophthalmology and Visual Sciences* 38:S540, 1997.
3. ST Lai, CA Swinger, E Williams, E Kornmehl, R Davis, J Sutphin, M Kraff, W Zheng, M Lai, "Surface photorefractive keratectomy for myopia using the Novatec laser - 6 month results of the Phase IIa US FDA study", *Arvo Abstract, Investigative Ophthalmology and Visual Sciences* 37:S53, 1996.
4. T Salah, GO Waring, A el Maghraby, K Moadel, SB Grimm, "Excimer laser in situ keratomileusis under a corneal flap for myopia of 2 to 20 diopters", *American Journal of Ophthalmology* 121:143-155, 1996.
5. Q Ren, G Simon, J-M Parel, "UV solid state laser (213 nm) photo-refractive keratectomy: in vitro study", *Ophthalmology* 100:1828-1834, 1993.
6. Q Ren, G Simon, J-M Legeais, J-M Parel, W Culbertson, J H Shen, Y Takesue, M Savoldelli, "UV solid state laser (213 nm) photo-refractive keratectomy: in vivo study", *Ophthalmology* 101:883-889, 1994.
7. PG Söderberg, T Matsui, F Manns, JH Shen, JM Parel, JM Legeais, M Savoldelli, I Drubaix, M Menashe, G Renard, Y Pouliquen, "Three-month follow up of changes in the rabbit cornea after photoablation with a pulsed scanning beam at 213 nm", *Proceedings SPIE* 2393:55-60, 1995.
8. F Manns, J-H Shen, P Söderberg, T Matsui, J-M Parel, "Development of an algorithm for corneal reshaping with a scanning beam", *Applied Optics* 34:4600-4608, 1995.
9. J Shen, K Joos, F Manns, D Denham, Q Ren, F Fankhauser, P Soderberg, JM Parel, "Ablation rate of cornea and PMMA with a frequency-quintupled Nd:YAG laser", *Lasers in Surgery and Medicine* 21:179-185, 1997.
10. F Manns, JH Shen, PG Söderberg, T Matsui, JM Parel, "Calculation of laser pulse distribution maps for corneal reshaping with a scanning beam", *Proceedings SPIE* 2393:48-54, 1995.
11. F Manns, JH Shen, PG Soderberg, T Matsui, JM Parel, "Scanning Photorefractive keratectomy: mathematical method", *Investigative Ophthalmology and Visual Science* 36:S704, 1995.
12. F Manns, P Rol, J Shen, P Soderberg, T Matsui, J-M Parel, "Optical profilometry of poly(methylmethacrylate) (PMMA) surfaces after reshaping with a scanning photorefractive keratectomy (SPRK) system", *Applied Optics* 35:3338-3346, 1996.

Evaluation of corneal ablation by an optical parametric oscillator (OPO) at 2.94 microns and an Er:Yag laser; and comparison to ablation by a 193 nm excimer laser.

William B. Telfair^a, Hanna J. Hoffman^a, Robert E. Nordquist^b, and Richard A. Eiferman, MD^c

^a IRVision, Inc., San Jose, CA, 95124.

^b Wound Healing of Oklahoma, Oklahoma City, OK., 73105.

^c VA Medical Center Research Service, Louisville, KY, 40205.

ABSTRACT

Purpose: This study first evaluated the corneal ablation characteristics of 1) an Nd:YAG pumped OPO (Optical Parametric Oscillator) at 2.94 microns and 2) a short pulse Er:YAG laser. Secondly, it compared the histopathology and surface quality of these ablations with 3) a 193 nm excimer laser. Finally, the healing characteristics over 4 months of cat eyes treated with the OPO were evaluated.

Methods: Custom designed Nd:YAG/OPO and Er:YAG lasers were integrated with a new scanning delivery system to perform PRK myopic correction procedures. After initial ablation studies to determine ablation thresholds and rates, human cadaver eyes and in-vivo cat eyes were treated with 1) a 6.0 mm Dia, 30 micron deep PTK ablation and 2) a 6.0 mm Dia, -5.0 Diopter PRK ablation. Cadaver eyes were also treated with a 5.0 mm Dia, -5.0 Diopter LASIK ablation. Finally, cats were treated with the OPO in a 4 month healing study.

Results: Ablation thresholds below 100 mJ/cm² and ablation rates comparable to the excimer were demonstrated for both infrared systems. Light Microscopy (LM) showed no thermal damage for low fluence treatments, but noticeable thermal damage at higher fluences. SEM and TEM revealed morphologically similar surfaces for low fluence OPO and excimer samples with a smooth base and no evidence of collagen shrinkage. The Er:YAG and higher fluence OPO treated samples revealed more damage along with visible collagen coagulation and shrinkage in some cases. Healing was remarkably unremarkable. All eyes had a mild healing response with no stromal haze and showed topographic flattening. LM demonstrated nothing except a moderate increase in keratocyte activity in the upper third of the stroma. TEM confirmed this along with irregular basement membranes.

Conclusions: A non-thermal ablation process called photospallation is demonstrated for the first time using short pulse infrared lasers yielding damage zones comparable to the excimer and healing which is also comparable to the excimer. Such Infrared sources are, therefore, potentially attractive competitors to the excimer to perform PRK and LASIK.

Key Words: PRK, LASIK, Mid-infrared, laser surgery, histology, cornea, ablation, spallation

1. INTRODUCTION

During the last 12 years excimer laser systems have been patented, developed, and approved to perform laser surgical techniques for modifying the corneal surface of the eye¹⁻⁵. These refractive surgical procedures, known as photorefractive keratectomy or PRK and laser-assisted in-situ keratomileusis or LASIK, directly reshape the cornea by means of selective volumetric removal of corneal tissue.

These systems utilize ultraviolet (UV) radiation with a wavelength which is around 200 nanometers. Many of these devices utilize an Argon Fluoride excimer laser operating at 193 nm. Generally, radiation at such short ultraviolet wavelengths is characterized by high photon energy, namely, greater than 6 eV, which, upon impact with tissue, causes molecular decomposition, i.e., the direct breaking of intramolecular bonds. Such an ablation technique is a photochemical process. It has the advantage of producing minimal collateral thermal damage in cells adjacent to the surgical site, since the broken

molecules generally leave behind only small volatile fragments which evaporate without heating the underlying substrate. Furthermore, the depth of decomposition for each laser pulse is typically very small, i.e., less than 1 micron, thus achieving accurate tissue removal with minimal risk of damage to the underlying structures from UV radiation.

In view of this small depth of penetration, coupled with the need to remove sufficient depth of tissue while minimizing the overall time for the surgical procedure, the early corneal sculpting systems utilizing the excimer laser employ "wide area ablation". Generally, wide area ablation uses a laser beam with a relatively large spot size to successively remove thin layers of corneal tissue. The spot size is of a sufficient size to cover the entire optical zone of the cornea, namely, a region of 5 to 7 millimeters in diameter. Consequently, to assure required flux densities on the cornea, relatively high energy output UV lasers are typically required. Since the delivery systems of these systems usually transmit only 15 to 30 % of the laser output energy to the eye, the energy required from the laser to deliver around 150 mJ/cm² to an area of 5 to 7 mm is 100 to 200 mJ per pulse. Such lasers tend to be prohibitively large and expensive systems.

Furthermore, efficacious wide area ablation requires that the projected beam be spatially homogenous and uniform to achieve the desired smooth corneal profiles. Accordingly, additional beam shaping devices, such as rotating prisms, mirrors, or spatial integrators, must be employed within the excimer beam delivery systems. Of course, such a multiplicity of optical elements contributes to overall transmission loss, while adding substantial optical complexity, cost, and maintenance requirements to the system.

Alternative techniques⁶⁻⁷ based on utilization of a scanning UV laser beam have been developed to achieve controlled and localized ablation of selected corneal regions of the cornea. In the scanning approach, a relatively small laser spot is scanned rapidly across the cornea in a predefined pattern to accumulatively shape the surface into the desired geometry. A scanning approach may offer a number of advantages, including lower power and energy requirements, added flexibility for refractive corrections and smooth ablation profiles, without the need for spatially uniform output beam profiles. For example, a laser scanning technique allows a tapered optical treatment zone to be achieved, which may have advantages for the correction of high myopia, for performing therapeutic tissue removal and for treating areas up to 9 millimeters in diameter which may be required for the correction of hyperopia.

While laser surgical techniques based on the excimer laser have proved beneficial for many applications, such techniques suffer from a number of limitations, which, if overcome, could significantly advance the utility of optical laser surgery. For example, techniques based on excimer lasers utilize toxic gases as the laser medium, suffer from persistent reliability problems, require lossy optics in the delivery systems, and suffer from the possibility that the UV radiation is potentially mutagenic through secondary fluorescence, which may cause undesirable long term side effects to the unexposed tissues of the eye.

Accordingly, alternatives⁸ to the excimer laser have been suggested in recent years which involve frequency-shifted radiation from a solid state laser. Current limitations of nonlinear elements used as frequency-shifting devices, however, place a lower limit of approximately 205 nm on the available wavelengths of such lasers, which may be too close to the mutagenic range, which exhibits a broad peak at 250 nm. In addition, multiply-shifted laser devices also face certain difficulties in providing the requisite energy outputs and are fairly complex and cumbersome, leading again to potential laser reliability problems, as well as added cost and maintenance.

With early feasibility studies⁹⁻²², another alternative has been suggested, involving mid-infrared wavelengths and, in particular, radiation around 3 microns corresponding to the absorption peak of water, the main constituent of the cornea. One solid state laser in particular, the Erbium:YAG laser (Er:YAG), emits radiation at a wavelength of 2.94 microns, corresponding to an absorption coefficient of over 13,000 cm⁻¹ in water. This high absorption results in a small region of impact with potentially less than two micron penetration depths.

Contrary to the photoablation mechanism associated with the excimer laser, i.e., photochemical decomposition, which is due to energy absorption in molecular bonds, ablation with prior art mid-IR lasers, e.g. the Er:YAG laser, is attributed to photovaporization, or photothermal evaporation, of water molecules. The laser's thermal heat induces a phase change (i.e. boils the water), and thus a sudden expansion of the tissue material, thereby ablating the corneal surface tissue. This boiling water causes high temperatures in the adjacent tissue. This thermally damaged tissue induces healing responses which are generally associated with regression and the formation of haze.

In later studies^{16,21,23,24}, it has been recognized that mid-infrared lasers emitting shorter pulses (Q-switched lasers) cause less thermal damage than lasers with longer pulsewidths. However, even with pulses on the order of hundreds of nanoseconds, as compared to hundreds of microseconds for previous studies, the collateral damage zone still extends up to 21 μm . While this amount of thermal damage is less than that caused by free running lasers, which produced up to 50 microns of damage, such an extent of damage is still considered too much for PRK or LASIK. This is because such extensive thermal damage zones are typically accompanied by haze, regression of the refractive correction, loss of visual acuity, and other deleterious healing side-effects. This puts prior art mid-infrared lasers at a disadvantage when compared with excimer lasers for corneal ablation.

Two other prior studies^{9,11} used mid-infrared lasers with even shorter pulsewidths, but still achieve ablation using a photothermal evaporation technique. More specifically, Seiler et. al. reported use of the HF laser operating near 3 microns with pulsewidths of 50 nanoseconds and damage layers of 5 to 20 microns. However, it is likely that the multi-wavelength character of the HF laser affected these results with increased thermal damage by effectively lowering the average absorption coefficient of the tissue. In the second study, Stern et. al. reported use of a Raman-shifted Nd:YAG at 2.92 microns with a pulsewidth of 8 nanoseconds. They found the ablation threshold to be about 250 mJ/cm^2 with collateral thermal damage layers between 2 and 4 microns wide on the average.

Thus, while the prior literature refers to the use of shorter pulses in the mid-infrared region, each involves ablation using a photothermal technique. Such photothermal techniques cause damage zones greater than 2 microns, which result in tissue effects that do not approach those achieved with the excimer laser. Moreover, typically, the only criteria cited to lessen thermal damage is that the pulse duration be shorter than the characteristic thermal relaxation time, which is about 2 microseconds in corneal tissue. The underlying assumption is that at pulse durations well below this limit, the thermal damage is less extensive because the tissue evaporation process is faster and less explosive. Such lasers are in no case shown to approach the submicron effects routinely obtained with excimer lasers.

We report results from a new mid-infrared (MIR) corneal ablation process called photospallation^{25,26}. Photospallation is a photomechanical ablation process which removes a thin layer of tissue from the front surface by creating a bi-polar stress wave with both compressive and tensile components. The stretching forces of the tensile component pull the tissue apart, thus ejecting a thin surface layer without heating the tissue to the boiling point. Therefore it has much less thermal damage associated with it compared to the photothermal ablation normally used by infrared lasers. Besides the short pulsewidth, low ablation thresholds and low fluences are also necessary to achieve the photospallation mechanism of ablation with its attendant very low damage.

TABLE 1: HISTOLOGY STUDY LASER TREATMENT PARAMETERS

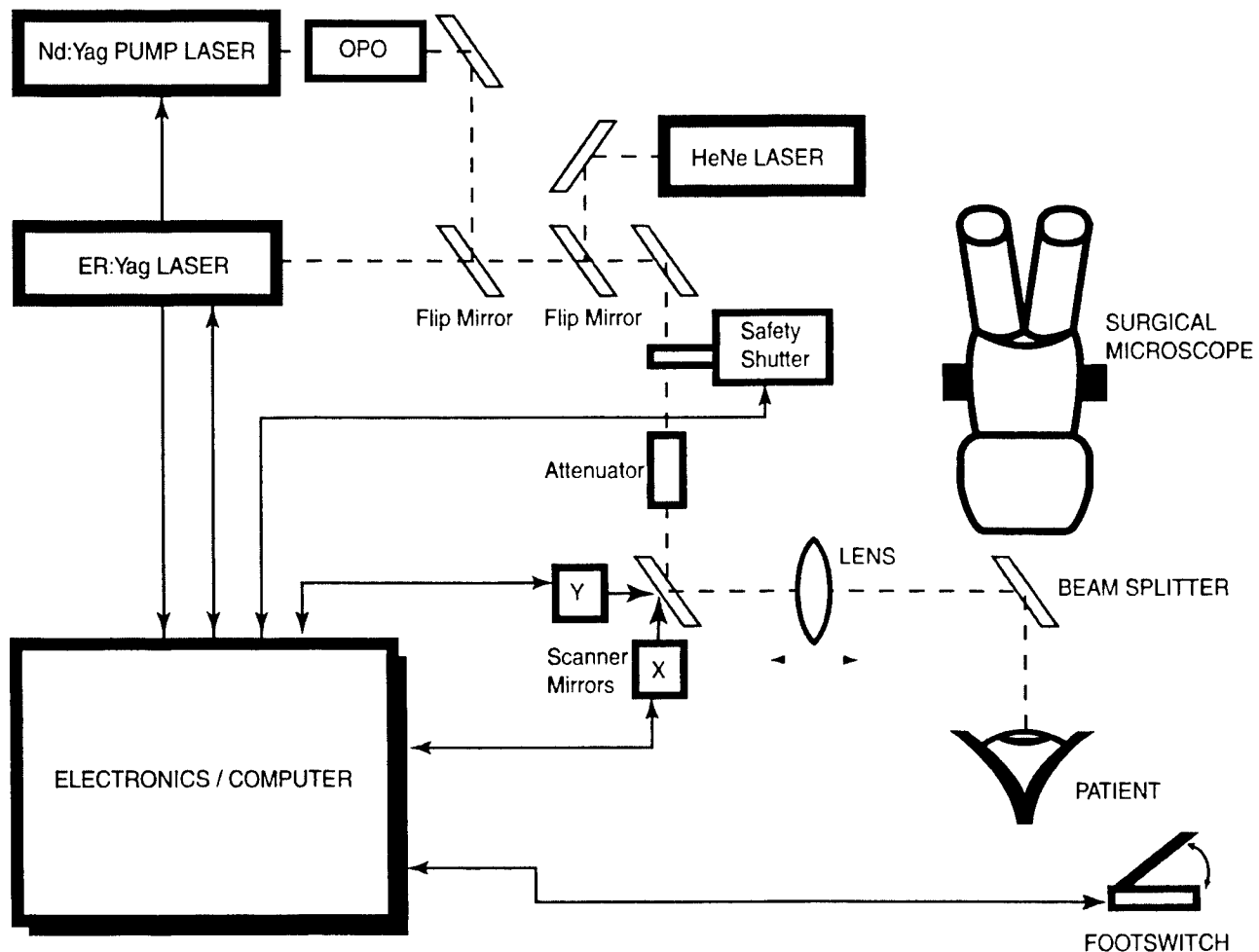
Treatment Parameters	OPO Laser	Q-Switched Er:YAG Laser	Free Running Er:YAG Laser	Visx STAR Excimer Laser
Wavelength	2.94 microns	2.94 microns	2.94 microns	0.193 microns (193 nm)
Pulsewidth	7 nanoseconds	70 nanoseconds	50 microsecond burst of pulses lasting 1 to 2 microseconds	18 nanoseconds
Total pulses (typical)	1000 - 3000	1000 - 3000	1000 - 3000	125 - 307
Repetition Rate	10 Hz	7 Hz	7 Hz	6 Hz
Fluence	100 to 500 mJ/cm^2	100 to 600 mJ/cm^2	500 to 800 mJ/cm^2	160 mJ/cm^2
Ablation technique	1 - 2.0 mm diameter spot scanned by software algorithm	1 - 1.5 mm diameter spot scanned by software algorithm	1 - 1.5 mm diameter spot scanned by software algorithm	5 or 6 mm area ablation with an increasing aperture

2. MATERIALS and METHODS

We first used a novel Optical Parametric Oscillator (OPO) as well as a new shorter pulselength Q-switched Er:YAG laser on Eye Bank and in-vivo cat eyes. Both lasers generate a wavelength of 2.94 microns with nanometer pulsewidths. The histopathology of the OPO treated tissue is comparable to the commercially available Visx excimer laser. We then used the OPO laser to treat adult cats and follow their healing for 4 months.

A MIR laser surgical system was designed with two proprietary short pulse lasers (a Q-switched Er:YAG and an OPO) at 2.94 microns wavelength with custom designs to meet the laser treatment parameters shown in Table 1. Note that the pulsewidths of the two lasers - 70 nsec and 7 nsec, respectively - are both shorter than any previous studies at 2.94 microns. The Seiler and Stern studies were at other wavelengths.

FIGURE 1. LASER SURGICAL SYSTEM SCHEMATIC



A schematic of this new delivery system with these two lasers is shown in Figure 1. The two MIR lasers are co-aligned with the HeNe laser using flip mirrors. The same X-Y scanning delivery system is used with both lasers, but with different calibrations and focusing of the lens for each laser and for different ablation spot sizes. The plate glass attenuator is used to get the energy within 10% of the desired value. The high voltage on the laser flash lamp is used as the final adjustment of the energy, which was measured by a Molectron J25LP-2 Joulemeter at the surgical site. This maintains a relatively constant

laser energy output resulting in a relatively constant beam profile over the whole range of energies and spot sizes delivered to the eye surface. The laser, spot size, and fluence can be selected and calibrated in a few minutes, thus allowing a rapid succession of test conditions without long delays between each ablation.

Adult cats were anesthetized with intramuscular Ketamine/Rompum. A lid speculum was inserted and the epithelium removed by a blunt spatula after soaking with a 8 mm circular filter paper saturated with 10% alcohol. In-vivo cat eyes received the following treatments by each of the MIR-lasers with a variety of fluence, spot overlap, and spot size conditions: 1) a 4 mm diameter, 30 micron deep PTK ablation and 2) a 6 mm diameter, -5.0 Diopter PRK ablation.

After optimum conditions were chosen from the first two set of tests of the MIR lasers on cat eyes, one last set of cats eyes along with some human donor eyes were treated with the MIR lasers and an excimer laser for analysis and comparison. The excimer laser was a Visx STAR system and followed the standard calibration and treatment procedures outlined in the documentation of this FDA approved system.

The in-vivo cat eyes received the following treatments by each of the lasers: 1) a 6 mm diameter, 30 micron deep PTK ablation and 2) a 6 mm diameter, -5.0 Diopter PRK ablation. Lasik was not attempted on the cat eyes.

Human donor eyes unsuitable for transplantation were placed in a suction holder. The epithelium was removed by a blunt spatula after soaking with an 8 mm circular filter paper saturated with 10% alcohol. Using each of the lasers, a set of eyes were treated with 1) a 6 mm diameter, 30 micron deep PTK ablation, 2) a 6 mm diameter, -5.0 Diopter PRK ablation, and 3) a 5 mm diameter, -5.0 Diopter LASIK ablation. In addition, one had a LASIK flap with no ablation as a control. For the LASIK treatments, a Chiron microkeratome created a 9 mm, 160 micron thick flap. The laser treatment was performed on the bed.

After the results of these histology studies were examined, the optimum set of parameters were chosen to treat 6 adult cats for a healing study. This choice was the OPO laser with the following parameters: a 1 mm spot and a fluence of 150 mJ/cm². The cats were housed and fed for two weeks prior to the ablations to assure healthy animals and to allow pre-operative examination of the eyes. The 6 adult (more than 11 months old) cats were all prepped and treated in a single day.

The cats were anesthetized with intramuscular Ketamine/Rompum. A lid speculum was inserted and the epithelium removed by a blunt spatula after soaking with a 8 mm circular filter paper saturated with 10% alcohol. Three (3) cats received a 6 mm diameter, -3.0 Diopter PRK ablation and three (3) cats received a 6 mm diameter, -6.0 Diopter PRK ablation.

TABLE 2. FOLLOW-UP EXAMINATION CHART

PROCEDURE	PRE-OP	DAY 0	Day 1, 2, 3, etc.	Week 1, 2, 4, & 6, Month 2, 3 & 4
	Pre-op Day	Treatment Day	Interim exams	Post-op exams
General Ocular Exam	X	X	X	X
Slit Lamp Biomicroscopy	X		X	X
Corneal Topography	X			X
Pachymetry	X			X
Treatment Surgery		X		
Ocular/Systemic Adverse Reactions	X	X	X	X

The cats were followed out to 4 months as shown in the examination schedule in Table 2. At the end of the follow-up period the eyes were harvested for examination. Tissue fixation and examination proceeded at its required pace.

3. RESULTS

For fluences of 300 mJ/cm² or higher there was significant thermal damage from all the lasers, which was visible to the naked eye and under the microscope. For fluences under 200 mJ/cm² there was no visible damage. In fact, we were unsure we had any ablation at all until we got the Light Microscopy (LM) slides. Half-ablated keratocytes and other evidence of ablation were found at the top surface of the specimens treated with the short pulse MIR lasers, showing very clean ablation with no damage below. The long pulse laser showed no ablation below about 500 mJ/cm².

We chose as the set of parameters to use in the final set of histological treatments, a 1 mm spot and fluences of 150 mJ/cm² for the OPO, 200 mJ/cm² for the Q-switched Er:YAG, and 500 mJ/cm² for the free-running Er:YAG. The following results are from this last set of specimens.

LM of cat and human eyes demonstrated a thin (1 to 4 microns) "pseudo-membrane" at the surface of all ablations. This was thinner (1 to 2 microns) for the OPO and excimer than for the Er:YAG (2 to 4 microns). The center surface was fairly smooth on all LM's, but the excimer was rougher (3 to 5 microns) than the scanning treatments (1 to 3 microns). The LM in Figure 2 was the edge of an ablation on cat 13 OD by the OPO. Note the ablation (to the left) has a slightly darker surface layer than the unablated surface to the right of the ablation knee.

Scanning Electron Microscopy (SEM) of cat and human eyes showed smooth surfaces for all ablations. The long pulse Er:YAG seemed to be the smoothest with a glassy appearance due to the coagulated surface. The short pulse Er:YAG and OPO were the next smoothest. The excimer was the roughest, but the surface variations extended only 1-5 microns. LASIK ablations by the OPO and excimer were smoother than the microkeratome cut on both the flap and on the unablated bed surface.

TABLE 3: SURFACE LAYER THICKNESS IN MICRONS FOR THE LAST SET OF CAT EYES.

Layer Type	Free Running Er:YAG	Q-Switched Er:YAG	OPO	Excimer (Visx STAR)
Surface Debris	0 to 0.2	0 to 1.0	0 to 0.4	0 to 0.3
Damage Layer	3 to 6	0.5 to 2	0.1 to 0.2	0.1 to 0.2
Underlying Zone	5 to 12 with large vacuoles	2 to 6 with medium vacuoles	0.3 to 2.0 with small vacuoles	0.2 to 2.0 with no vacuoles
Base	Normal stroma & Endothelium	Normal stroma & Endothelium	Normal stroma & Endothelium	Normal stroma & Endothelium

Transmission Electron Microscopy (TEM) of cat and human eyes demonstrated the following surface layers after ablation: 1) residual surface debris, 2) a sub-ablation damage layer, 3) an underlying collagen layer with increased fibril spacing - sometimes with vacuoles, and then 4) a base of normal unaffected tissue. The example shown in Figure 3 was a PTK ablation on cat 21 OD by the OPO. Average thicknesses for these layers are shown in Table 3. The human tissue showed results similar to the cat tissue but was less consistent, due to the variable age of the Eye Bank tissue.

For the healing study, we chose the OPO with 1.0 mm spot size and 150 mJ/cm². The following are this study's results.

The epithelial defect of all eyes healed within the first week. This showed a steady healing rate which was perhaps slightly slower than humans. During the first week while the epithelium was healing, three of seven eyes showed more than one day of haze. These haze readings were mild and ranged from 0 to 1.0 on a scale of 0 to 4.0. After the first week there was no haze in any eye. The eyes teared more than normal during the first two weeks. The epithelium was irregular during the second week. After the second week, it was difficult to discover by slit lamp examination which eye had been treated.

Since the cats were given an intra-muscular anesthetic and then topical anesthetic on the eye surface, some of the tear film was washed away and the eyes dried out during the data collection period. They were moistened periodically during the data

collection, which led to variable hydration of the eye. This variable state of the eyes' hydration caused large variations in the Pachymetry and topography data. Since topography was taken first during all exams, the Pachymetry data was quite variable. The left eye was measured first in all cases and, since the right eye was treated in all cases, this could adversely affect the difference data. The Pachymeter was broken at the Pre-op exams and was not repaired until the one week exams; hence there is no Pre-op data for Pachymetry. The difference between the treated eye and the untreated eye at the same exam was used as the primary data for changes in thickness.

The average pachymetry data showed a decrease in thickness in the first two weeks and then an increase in thickness. This is consistent with the epithelium being very thin as it covers the wound and then thickening as the healing progresses. At 4 months the treated eyes appear to be thicker than the untreated eyes.

Topography showed flattening in most post-op images as expected. Figure 4 is an example of a "OD/OS Comparison" for cat 30 for the follow-up exam at 6 weeks. OD was treated and is flattened compared to OS, which was the control.

The difference of the post-op topography minus the pre-op topography was measured and recorded for each exam at up to 8 rings, starting in the center. The differences of the first 5 rings for the three cat eyes treated with -3.0 diopters were averaged at each post-op time. These showed flattening for all times post-op - ranging from 0.4 to 1.6 diopters. Similarly, the differences of the first 5 rings for the three cat eyes treated with -6.0 diopters were averaged at each post-op time. These also showed flattening for all times post-op. Not including the one week data, which often was very difficult to measure and was unreliable due to variable epithelial healing, these ranged from 0.8 to 1.6 diopters. Similar differences and averages for the six untreated eyes showed a tendency toward flattening although the average was less than 0.4 diopters. This flattening of the untreated eyes could be due to natural flattening of the eyes as the cats age. This is much less than the flattening of the treated eyes, however.

The short term correction (2 & 4 weeks averaged) was very similar to the long term correction (12 & 16 weeks averaged). For the -3.0 treatments, the results showed a slight change from 0.95 diopters to 0.90 diopters. For the -6.0 treatments, this change is also small - from 1.10 diopters to 1.20 diopters. This shows excellent stability with very little regression.

Histological examination (LM) was performed on 11 of the 12 corneas harvested. The 12th was a control eye, which was lost. LM studies of the treated eyes after 16 weeks showed smooth surfaces and a normal epithelial thickness as shown in Figure 5. The stroma in the ablation zone was populated by higher numbers of keratocytes than normal - averaging 77% higher. The epithelial stromal junction was slightly wavy but had no abnormalities such as cysts, inflammatory cells, etc. When compared to the control eye, the only significant difference in the ablated eye was the increased keratocyte number and a slight disruption of the collagen lamellae in the upper 20% of the cornea.

Transmission electron microscopy (TEM) of the samples revealed discontinuities in the basement membrane with fewer hemidesmosomes and junction complexes than controls as shown in Figure 6. However, there was no evidence of epithelial loss and replacement which is normally characterized by multiple stacks of basement membrane. There was a moderate amount of electron opaque wound debris and some disruption in the lamellar pattern in the upper stroma.

4. DISCUSSION

The high fluence required to get above the ablation threshold combined with the long pulsewidth cause the long pulse Er:YAG to generate 3 to 6 microns of thermal collateral damage to the tissue left behind after the ablation. This agrees with previous studies^{10,12-14} and is unacceptable for PRK or LASIK.

The lower fluence and shorter pulsewidth of the short pulse Er:YAG cause less thermal collateral damage to the residual tissue, but it is still 0.5 to 2 microns. Presumably, this will induce a greater healing response with more haze and more regression than the excimer. If the pulsewidth could be shortened to 50 (or better 30) nanoseconds, the Er:YAG could possibly become competitive with the excimer.

All prior studies⁹⁻²⁴ of infrared laser PRK treatment of the cornea showed a damage layer of 2 microns or more after the ablation. This is generally thought to be too much for an efficacious healing process. The OPO is an infrared laser source

which is new to Ophthalmology. Our histological results using the OPO are strikingly similar to the excimer^{27,28}. The lower fluence and shorter pulsewidth of this OPO source achieve much less collateral damage - 0.1 to 0.2 microns - comparable to the excimer.

Slit lamp exams showed a remarkably clear healing process with no outwardly visible healing responses to the surgery beyond the epithelial defect healing. There was no stromal haze at all; only epithelial haze during the first week. This is dramatically less haze than with the excimer on rabbits, less than with the excimer on humans, and less than the cat study by ISL using the intrastromal technique²⁹. Pachymetry showed a thinning of the cornea right after the procedure with a later thickening. This is inconsistent with the normal thickness epithelial findings from LM and the ablation and central flattening of the stroma. Perhaps the total thickness of the cornea increases with aging.

Topography showed a decrease in refractive power, which was quite stable over the term of this study. However, topography on animals is very difficult in general. One should read this data only as an indication that the eyes were flattened with the procedure. Also diopters of topographic change do not correspond very well with dioptric changes in visual acuity - for animals or for humans. Hence, the change of only 0.4 to 1.6 diopters for treatments which were supposed to be 3 and 6 diopters is a positive result. Additional studies on eyes where good refractive data can be obtained is the next logical step to further the progress of this system.

LM at 16 weeks postop showed increased keratocyte activity in the upper third of the cornea in all treated corneas compared to the controls. There was no apparent damage for any of these ablations. The epithelium/stroma interface was fairly smooth on all LM's with good strong adherence by the epithelium.

TEM at 16 weeks postop confirmed increased keratocyte numbers and showed disruption of the lamellar structure in the anterior stroma and discontinuities in the basement membrane. There was virtually no inflammatory reaction to the ablation. At four months all eyes appeared quiet and unremarkable.

The development of the OPO at 2.94 microns, with its very short pulsewidth which allows the use of very low fluences, introduces, for the first time, an infrared laser which has the ability to ablate corneal tissue in a delicate, smooth and controllable fashion with the same low damage as the excimer - less than a micron. The healing response of these treated corneas was remarkably mild - less haze than with the excimer on humans. The treatment appeared to be less than planned. If true, this might explain part of the reason for the mild response. Clearly from this study, the IR-PRK procedure appears to be as safe or more so than the excimer-PRK procedure. More studies on humans are needed to fine tune the ablation rate and correction algorithm as well as study the healing response to determine the safety and efficacy of this new laser surgical system.

5. ACKNOWLEDGMENTS

This research was partially supported by NIH under contract SBIR # 5-R44-EY09154-03. The authors would like to thank Scottye Davis, Carsten Bekker, Paul Yoder, and Henry Zenzie for their assistance.

6. REFERENCES

1. Trokel, S.L.; "Excimer Laser Surgery of the Cornea"; Amer. J. Ophthal., Vol 96, pp 710-715, 1983.
2. L'Esperance, F.A.; U.S. patents #4,665,913 and #4,732,148.
3. Munnerlynn, C.R.; Koons, S.J.; & Marshall, J.; "PhotoRefractive keratectomy: a technique for laser refractive surgery"; J. Cataract Refract. Surg., Vol 14, pp 46-52, 1988.
4. Telfair, W.B.; U.S. patent #4,911,711.
5. Warner, J.W.; U.S. patent #4,903,695.
6. Manns, F.; Shen, J-H.; Soderberg, P., Matsui, T. & Parel, J-M.; "Scanning Photo Refractive Keratectomy: Mathematical Method"; Invest. Ophthal & Vis Sci, Vol. 36, No. 4; 1995. (Abstract)
7. Lin, J.T.; "Critical review of refractive surgical lasers"; Optical Engineering, Vol. 34, No. 3, pp 668-675; March 1995.

8. Gailitis, R.P.; Waring, G.O.; & Thompson, K.P.; "Solid State Ultraviolet Laser (213 nm) Ablation of the Cornea and Synthetic Collagen Lenticules"; *Lasers in Surgery and Medicine*, Vol. 11, pp 556-562; 1991.
9. Seiler, T.; Marshall, J.; Rothery, S.; & Wollensak, J.; "The Potential of an infrared hydrogen fluoride (HF) laser (3.0µm) for corneal surgery"; *Lasers in Ophthalmology*, Vol. 1, No. 1, pp 49-60; 1986.
10. Peyman, G. A. & Katoh, N.; "Effect of erbium:Yag Laser on ocular structures"; *International Ophthalmology*, Vol. 10, pp 245-253; 1987.
11. Stern, D. ; Puliafito, C. A.; Dobi, E. T.; et. al.; "Infrared laser surgery of the cornea: studies with a Raman-shifted neodymium:YAG laser at 2.80 and 2.92 microns"; *Ophthalmology*, Vol. 95, pp 1434-1441; 1988.
12. Bende, T.; Kriegerowski, M.; & Seiler, T.; "Photoablation in different ocular tissues performed with an Erbium YAG laser"; *Lasers and Light in Ophthalmology*, Vol. 2, No. 4, pp 263-269; 1989.
13. Walsh, J.T.; Flotte, T.J.; & Deutsch, T. F.; "Er:YAG laser ablation of tissue: effect of pulse duration and tissue type on thermal damage"; *Lasers in Surgery & Medicine*, Vol. 9, No. 3, pp 314-326; 1989.
14. Peyman, G. A.; Badaro, R. M.; & Khoobehi, B.; "Corneal Ablation in Rabbits Using an Infrared (2.9-µm) Erbium:Yag Laser"; *Ophthalmology*, Vol. 96, No. 8, pp 1160-1170; 1989.
15. Peyman, G. A.; Beyer, C.; Kuszak, J.; Khoobehi, B.; Mohsen, S.; & Badaro, R.; "Long-term effect of erbium-Yag Laser (2.9 µm) on the primate cornea"; *International Ophthalmology*, Vol. 15, No. 3, pp 249-258; 1991.
16. Ren, Q.; Venugopalan, V.; Schomacker, K.; Deutsch, T. F.; Flotte, T. J.; Puliafito, C. A.; & Birngruber, R.; "Mid-Infrared Laser Ablation of the Cornea"; *Lasers in Surgery and Medicine*, Vol. 12, pp 274-281; 1992.
17. Seiler, T. & Wollensak, J.; "Fundamental mode photoablation of the cornea for myopic correction: 1. theoretical background"; *Lasers and Light in Ophthalmology*, Vol. 5, No. 4, pp 199-203; 1993.
18. Wang, Kang-sun; Li, Qi; & Lan, Zhi-lin; "Comparison of Er:Yag and Excimer laser corneal ablation in rabbits"; *Lasers and Light in Ophthalmology*, Vol. 6, No. 2, pp 69-75; 1994.
19. Jean, B.; Kriegerowski, M.; Matallana, M.; & Bende, T.; "Correction of Myopia with Er:Yag laser Fundamental Mode PhotoRefractive Keratectomy"; *J. Refract. Surgery*, Vol. 11, pp 392-396; 1995.
20. Ren, Q.; Keates, R. H.; Hill, R. A.; & Berns, M. W.; "Laser Refractive Surgery: a review and current status"; *Optical Engineering*, Vol. 34, No. 3, pp 642-660; 1995.
21. Lian, Jing-cai & Wang, Kang-sun; "Effects of Er:YAG laser of different pulse widths on rabbit corneas"; *SPIE Vol. 2393*, pp 160-166; 1995.
22. Seiler, T.; Schmidt-Petersen, H.; Leiacker, R.; Steiner, R.; & Wollensak, J.; "Erbium:YAG laser Photoablation of Human Cornea"; *American Journal of Ophthalmology*, Vol. 120, No. 5, pp 668-669; 1995.
23. Kirshner, L.L.; Kramer, T.R.; Snyder, R.W., Yarborough, M., & Jones, H.; "Histopathology and Electron Microscopy of the morphology of corneal ablation with the Er:YAG and Er:YSGG lasers"; *Invest. Ophthal & Vis Sci*, Vol. 36, No. 4; 1995. (Abstract)
24. Snyder, R.W.; Kramer, T.R.; Yarborough, M., Marcellino, G. & Rottler, T.L.; "Histopathological and Electron Microscopic Evaluation of the early effects of the Er:YAG (2.94 µm), Nd:YAG (213 nm) and Excimer laser (193 nm) ablation of the cornea"; *Invest. Ophthal & Vis Sci*, Vol. 37, No. 3; 1996. (Abstract)
25. Jacques, S.L.; "Laser-Tissue Interactions: photochemical, photothermal, and photomechanical"; *Lasers in General Surgery*, Vol. 72, No. 3, pp 531-558, 1992.
26. Dingus, R.S. & Scammon, R.J.; "Gruneisen-stress induced ablation of biological tissue"; *SPIE*, Vol. 1427, pp 45-54; 1991.
27. Binder, P.; Anderson, J.A.; Rock, M.E.; Vraker, M.P.; "Human Excimer Laser Keratectomy. Clinical & Histopathologic Correlations"; *Ophthalmology*, Vol. 101, pp 979-989, 1994.
28. L'Esperance, F.A.; Taylor, D.M.; & Warner, J.W.; "Human excimer laser keratectomy: short-term histopathology"; *J. Refract. Surg.*, Vol 4, pp 118-124, 1988.
29. Juhasz, T.; Speaker, M.G.; Habib, M.S., & Kaiser, R.; "Refractive Effects of Myopic IntraStromal Ablation of the Cat Cornea with the Nd:YLF Picosecond laser"; *Invest. Ophthal & Vis Sci*, Vol. 35, No. 4; 1994.

Figure 2. LM at 100X of the edge of an ablation on cat 13 OD by the OPO.

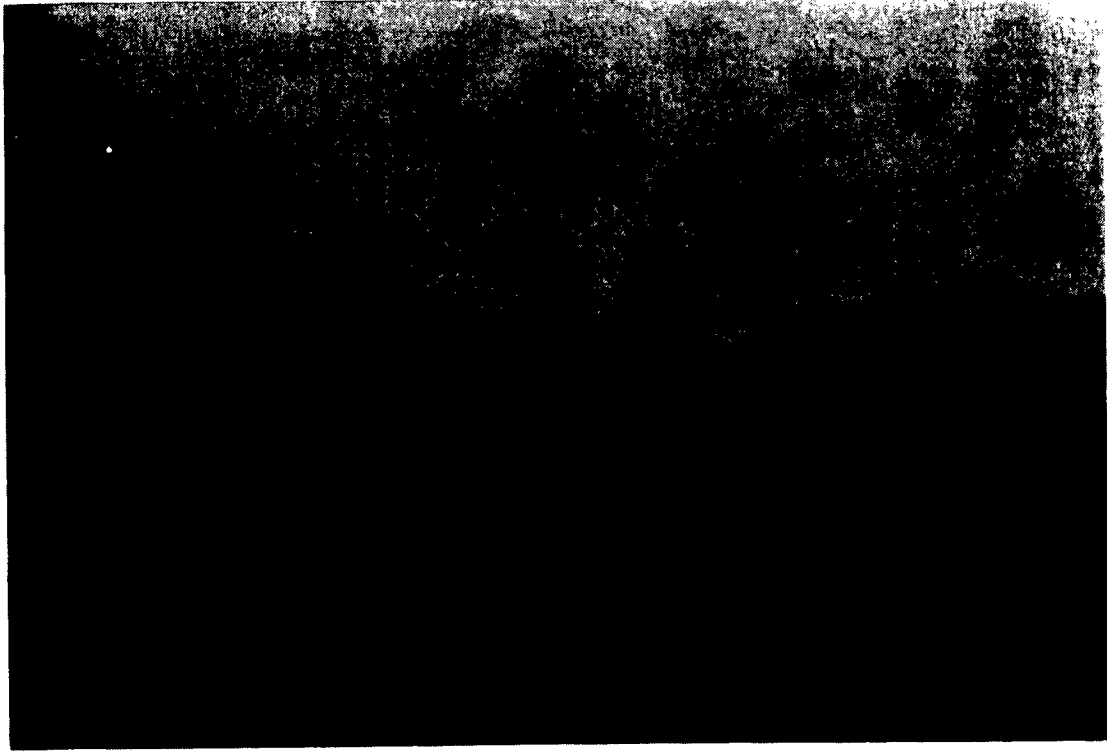


Figure 3. TEM at 3150X of a PTK ablation on cat 21 OD by the OPO.



Figure 4. Topography - Cat 30 OD (Right eye) Comparison to 30 OS (Left eye) at 6 weeks.

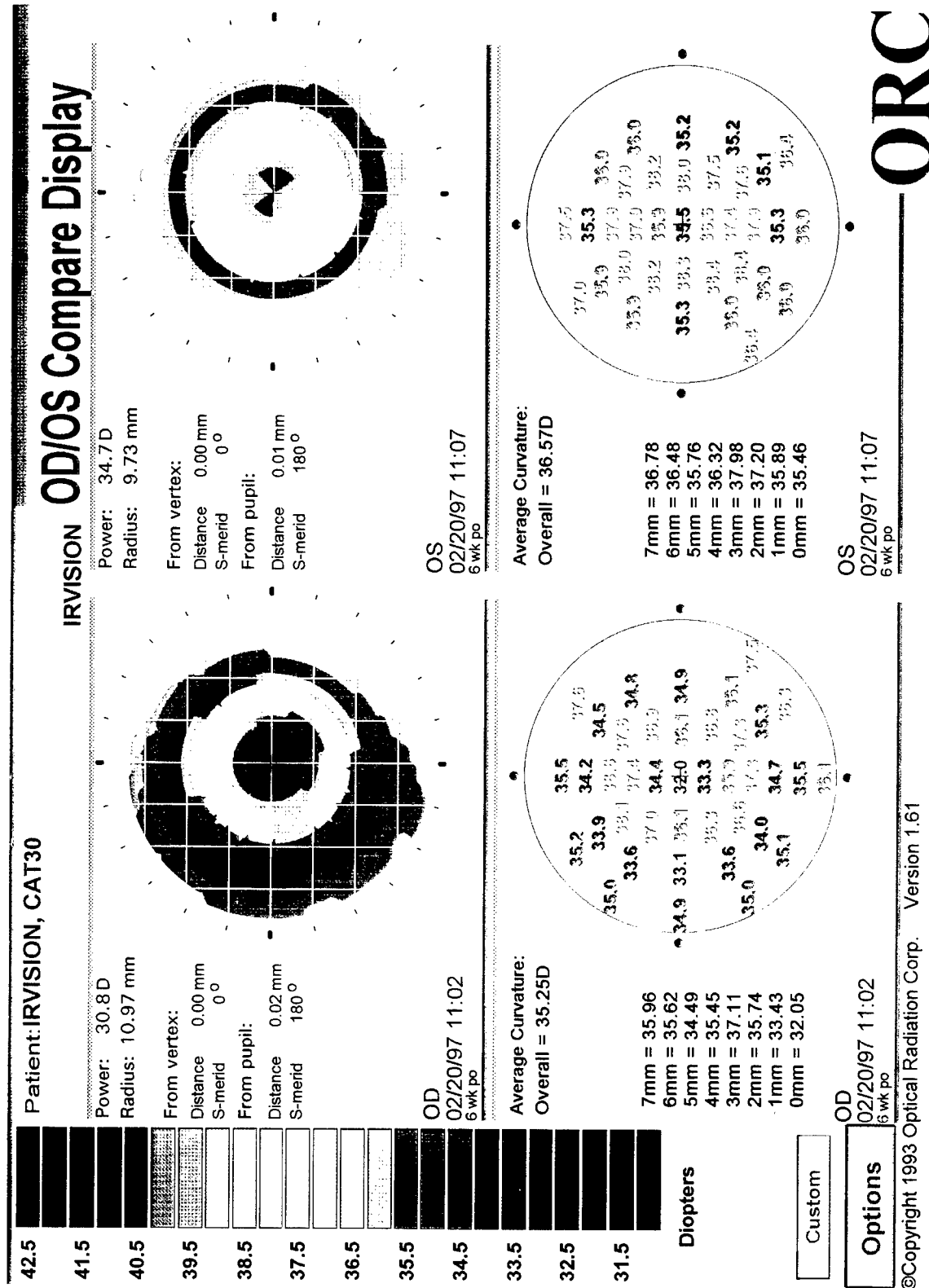


Figure 5. LM at 100X of cat 28 OD at 4 months



Figure 6. TEM at 2500X of cat 27 OD at 4 months



Corneal haze induced by excimer laser photoablation in rabbit is reduced by preserved human amniotic membrane graft

Ming X. Wang^a, Trevor Gray^b, Pinnita Prabhasawat^b, Xiong Ma^b, William Culbertson^b, Richard Forster^b, Khalil Hanna^b, Scheffer Tseng^b.

^aLaser Vision Center, Department of Ophthalmology and Visual Sciences, Vanderbilt University School of Medicine, 8030 MCE, Nashville, TN 37232-8808

^bOcular Surface and Tear Center, Cornea Service, Bascom Palmer Eye Institute, and Department of Cell Biology & Anatomy, University of Miami School of Medicine, P.O. Box 016880, Miami, FL 33101

ABSTRACT

We conducted a study to determine if preserved human amniotic membrane can reduce corneal haze induced by excimer laser photoablation. Excimer photoablation was performed bilaterally on 40 New Zealand white rabbits with a 6 mm ablation zone and 120 μ m depth (PTK) using the VISX Star. One eye was randomly covered with a preserved human amniotic membrane and secured using four interrupted 10-0 nylon sutures; the other eye served as control. The amniotic membranes were removed at one week, and the corneal haze was graded with a slit-lamp biomicroscopy by three masked corneal specialists (WC, KH and RF) biweekly for the ensuing 12 weeks. Histology and in situ TUNEL staining (for fragmented DNA as an index for apoptosis) was performed at days 1, 3 and 7 and at 12 weeks. One week after excimer photoablation, the amniotic membrane-covered corneas showed more anterior stromal edema, which resolved at the second week. A consistent grading of organized reticular corneal haze was noted among the three masked observers. Such corneal haze peaked at the seventh week in both groups. The amniotic membrane-covered group showed statistically significant less corneal haze (0.50 ± 0.15) than the control groups (1.25 ± 0.35) ($p < 0.001$). The amniotic membrane-covered corneas had less inflammatory response at days 1 and 3, showing nearly nil DNA fragmentation on keratocytes on the ablated anterior stromal and less stromal fibroblast activation. There is less altered epithelial cell morphology and less epithelial hyperplasia at 1 week in these amniotic membrane-treated eyes. We concluded from this study that amniotic membrane matrix is effective in reducing corneal haze induced by excimer photoablation in rabbits and may have clinical applications.

Keywords: excimer laser, photorefractive keratectomy, phototherapeutic keratectomy, corneal haze, rabbit, amniotic membrane transplantation, apoptosis, corneal wound healing, extracellular matrix.

Further author information -

Ming X. Wang: Email: ming.wang@mcmail.vanderbilt.edu; Telephone: 615-936-1464; Fax: 615-936-3949.

1. INTRODUCTION

Corneal haze occurs in a majority of patients following excimer photorefractive keratectomy (PRK) for correction of myopia¹. Such haze typically peaks at two to four months and is noted to increase with an increasing degree of myopia corrected (e.g., 2+ stable haze occurs in 11% of patients with corrections greater than eight diopters¹). The corneal stromal remodeling influencing the formation of haze after PRK is thought to be responsible for reduced best corrected visual acuity, regression of refractive correction and limited predictability of the attempted correction.

The formation of the corneal haze after PRK is a result of laser corneal ablation and stromal wound healing. In recent years, despite significant advances made in the understanding of the physics aspect of PRK technology (i. e., laser-tissue interaction, optical profile of the laser beam, multi-zone multi-pass approaches and edge-smoothing techniques), the characterization of the biology aspect of the PRK procedure, namely the wound healing, appears to be the limiting factor of the PRK technology today²⁻⁷. Various methodologies have been used in an attempt to reduce the corneal haze after PRK without significant effect⁸⁻¹⁶.

In order to search for an effective method to reduce or eliminate corneal haze after PRK, we sought to approach the problem by examining the unique scarless wound healing process in fetus and seeking for ways to recreate a fetal wound-healing environment in adult cornea after PRK. There are many important differences in wound healing between adult and fetus^{17,25}. In the acute phase of adult wound healing, significant inflammation occurs, presumably as a protective mechanism to combat infection. In contrast, in a fetus the sterile intrauterine environment does not provide antigenic stimulations for inflammatory reaction^{17,25}. Epithelialization is rapid in fetus with an epidermis that is similar in structure and thickness compared with uninjured skin²⁵. Neovascularization and excessive collagen deposition, typically present in adult wound healing, is absent in fetus^{17,25,26}. It is believed that one of the major components in the fetal extracellular matrix responsible for the above mentioned biological activities is hyaluronic acid, a polyanionic glycosaminoglycan capable of sequestering many scar-inducing cytokines such as TGF-beta and platelet derived growth factor (PDGF). In fetal wound healing, these inflammatory cytokines are significantly attenuated. A primary wound scaffolding is rapidly established^{17,25,26} and the subsequent orderly cellular migration, proliferation and matrix synthesis lead to a scarless mesenchymal regeneration (rather than scarring).

Amniotic membrane has been used with remarkable success to reduce inflammation, fibrovascular ingrowth, and to facilitate epithelialization in animal models and more recently human eyes^{34,41}. Amnion is a biological membrane, which lines the inner surface of the amniotic cavity and consists of a simple cuboidal epithelium, a thick basement membrane and an avascular mesenchymal layer containing hyaluronic acid. Amniotic membrane is believed to play an important role in the scarless wound healing process in a fetus. The mechanism by which the amniotic membrane modulates adult wound healing is not well understood. It may exert its effect through the basement membrane which facilitates epithelialization^{22,23}, or through biochemical effect of hyaluronic acid contained in the mesenchymal layer^{22,23}. It is not clear whether the amniotic membrane reduces inflammation and fibrovascular ingrowth by affecting fundamental molecular and cellular processes in wound healing such as cellular activation and apoptosis observed in animal corneas after superficial injuries^{32,33,44}.

In this report, we describe a new approach to achieve consistent and successful reduction of corneal haze after PRK by employing human amniotic membrane transplantation in the acute phase of wound healing.

2. MATERIALS AND METHODS

All experiments were conducted according to the ARVO Resolution on the Use of Animals in Research.

1. Preparation of preserved human amniotic membrane

Preparation of preserved human amniotic membrane is as follows³⁴. Human placentas which passed the routine screening for infections were obtained immediately after elective cesarean sections with normal gestations. The amniotic membrane was obtained from the placenta through blunt dissection and phosphate buffered saline (PBS) containing penicillin (1,000U/ml), streptomycin (20 mg/ml) and amphotericin B (2.5 ug/ml) was used multiple times to clean the amniotic membranes which were then layered on to a nitrocellulose membrane in such a way that the mesenchymal side of the amniotic membrane was facing the filter. Additional washes of the membrane-filter blot were performed using the same PBS solution, and the membrane were trephined into 9 mm diameter circles and stored at 4 C in 100% glycerine.

2. Excimer ablation of rabbit corneas and amniotic membrane transplantation

40 New Zealand albino male rabbits were used in this experiment. The rabbits weighing 2-3 kg were anesthetized with intramuscular injection of xylazine hydrochloride (50 mg) and ketamine hydrochloride (50 mg). Each rabbit received

transepithelial bilateral excimer laser ablation using the VISX Star. The ablation diameter was 6 mm with a uniform depth of 120 μ m in a PTK mode without using any edge smoothing computer software.

The rabbits were divided into 2 groups. The first group consisted of 28 rabbits. One eye of each rabbit was randomly covered with a 9 mm disc of preserved human amniotic membrane, and the other eye served as control. The amniotic membrane was secured with four interrupted 10-0 nylon sutures in such a way that the sutures were placed well outside of the ablation zone. The orientation of the amniotic membrane was such that the mesenchymal side of the amniotic membrane faced the rabbit cornea. A drop of ocuflox and voltaren was given for each eye immediately after the excimer procedure.

3. Labelling of existing and newly synthesized corneal stroma using DTAF.

One additional rabbit received a bilateral treatment of dichlorotriazinyl aminofluorescein (DTAF) (Molecular Probes, Inc., Junction City, OR). Five drops of 0.5% solution of DTAF dissolved in 0.2 M sodium bicarbonate was instilled in each eye and after 30 seconds normal saline was used to copiously rinse the eye to remove the residual dye.

4. Removal of amniotic membrane at one week and prospective evaluation of corneal haze.

The 28 rabbits received daily ocuflox treatment for 3 days and were examined daily for intactness of the amniotic membrane and the epithelium. At one week, all amniotic membranes were removed and the corneal haze graded at the slit lamp following a standard grading system² in a masked fashion and independently by three corneal specialists (WC, RF and KH). The procedure was then repeated biweekly for the ensuing 12 weeks after PTK. All rabbits were sacrificed at 12th week postoperatively.

5. Histologic examination of the rabbit corneas.

All corneas were trephined and bisected into two halves. One half was imbedded in O.C.T. compound (Miles Laboratories, Elkhart, IN) and frozen in liquid nitrogen. Five micron thick sections that extended transversely across the central corneas were cut and placed on slides. The other half of the cornea was fixed in 2.5% buffered glutaraldehyde and processed for hematoxylin and eosin stain. One rabbit died inadvertently at one week post PTK which was attributed to anesthetic overdose and the cornea was processed as described above.

6. Study of acute changes in rabbit PTK corneas and the effect of sutures and exposure.

The second group consisted of 12 rabbits that were subdivided into four groups. The first group had one eye randomly covered with amniotic membrane, and the other eye served as the control; The second group had four cardinal sham sutures placed at corneal periphery, and the other eye served as the control; The third group had one eye receive a total tarsorrhaphy using 2 interrupted 6-0 sutures, and the other eye served as the control; The fourth group had one eye tarsorrhaphied, and the other eye covered with amniotic membrane. All rabbits received the standard postoperative antibiotic treatment. One rabbit from each group was sacrificed at 24 hours, 3 days, and at 7 days. All corneas were bisected into two halves, one for Hematoxylin and eosin staining, and the other for frozen section as a preparation of the apoptosis assay described below.

7. Fluorescence microscopic examination of newly synthesized corneal stroma with DTAF dye.

Eyes that were treated with DTAF dye were imbedded in O.C.T. compound (Miles Laboratories, Elkhart, IN) and frozen in liquid nitrogen. Five micron thick sections that extended transversely across the central corneas were cut and placed on slides. Fluorescence microscopy was used to evaluate the pre-existing corneal stroma (stained with DTAF) and the newly synthesized (unstained with DTAF).

8. Assay for cellular apoptosis and DNA nucleosome-size fragmentation.

In order to determine the degree of apoptosis, the peroxidase-based TUNEL assay was performed for each cornea. The assay measures the amount of nucleosome size DNA fragments which are hallmarks of apoptosis. The technique uses non-isotopic DNA end-extension in situ, and subsequent immunohistochemical staining of the extended DNA. Terminal deoxynucleotidyl transferase (TdT) was used to add residues of digoxigenin-nucleotide to the DNA. TdT catalyzed a template independent addition of deoxyribonucleotide triphosphate to the 3'-OH ends of double- or single- stranded DNA. The incorporated nucleotides form a random heteropolymer of digoxigenin-11-dUTP and dATP for optimal anti-digoxigenin antibody binding. The antibody was conjugated to a fluorescein molecule and, when excited by light of 494 nm wavelength, generates a

secondary fluorescence at 523 nm. The Oncor ApopTag in situ Apoptosis Detection Kit was used (Oncor, Gaithersburg, MD). The technique allows specific staining of the very high concentrations of 3'-OH ends that are characteristically localized to apoptotic bodies. In comparison to the traditional avidin binding apoptosis assay, the digoxigenin-based TUNEL assay has lower background staining due to the normal absence of digitalis in animal tissues.

For the labeling of nucleosome size DNA fragments, the corneal frozen sections were incubated with TdT for one hour at 37 C. After rinsing twice with PBS, the tissue was incubated with fluorescein-tagged anti-digoxigenin antibody for 30 minutes at room temperature. As a positive control, randomly selected sections were incubated with DNase I (Sigma, St. Louis, MO) 1 ug/ml in PBS, PH 7.4 for 10 minutes at 37 C. The rest of the procedure remained the same. For a negative control, TdT was replaced by distilled water. Counterstain using Oncor Preputium Iodine/Antifade was performed. Standard excitation and emission filters were used to view the PI stain (for cell nuclei) and fluorescein stain (for apoptotic DNA fragments) using epifluorescent microscopy.

3. RESULTS

1. Corneal haze is reduced with amniotic membrane transplantation.

Fig. 1a shows a rabbit cornea after excimer ablation and the contralateral eye (**Fig. 1b**) with an amniotic membrane secured with four cardinal sutures (10-0 nylon) placed well outside of the ablation zone. 28 rabbits were included in this protocol.

The amniotic membranes were removed at one week and the corneal haze graded at the slit lamp. There appeared to be more corneal cloudiness at one week in the amniotic membrane-covered eye (**Fig. 2b**) which was due to edema or residual adherent membrane matrix. This largely resolved at the second week after PTK (**Fig. 2d**). A more organized and reticular type of corneal haze (**Fig. 2c**) began to emerge at week 2 and peaked at 7-8 weeks for both the amniotic transplanted and the control groups. During these weeks the amniotic membrane group demonstrated a statistically significant less amount of haze than the control (**Figs. 2d vs. 2c, and 2f vs. 2e**).

The temporal profile of the corneal haze is shown in **Fig. 3**. The consistency of grading of the haze among the three masked evaluators was excellent (80 to 90%). It can be seen that at 12th week, the average degree of haze in the amniotic membrane group is 0.50 ± 0.15 , compared with 1.25 ± 0.35 in the control group. The difference is statistically significant ($p < 0.001$). It should be noted however that the difference is small in its absolute magnitude (0.5 vs 1.25) though the relative difference is appreciably much larger. It thus appears that amniotic membrane transplantation after excimer ablation of rabbit corneas is effective in reducing corneal haze.

2. Amniotic membrane inhibits inflammation and keratocyte activation in the acute phase of wound healing.

Among the 12 rabbits included in the study of the acute changes and the effect of sutures and exposure 1,3 and 7 days after PTK, significant amount of inflammatory reaction and fibroblast activation was observed in the control corneas without amniotic membrane coverage one day post PTK (**Fig. 4a**). In contrast, the amniotic membrane treated eyes showed significantly less inflammation and cellularity (**Fig. 4b**). At day 3 and day 7 after PTK, the control corneas showed epithelial hyperplasia with abnormal morphology (loss of basoloid phenotype and orderly architecture of the cell layers in the epithelium), while the amniotic membrane covered eye demonstrated an orderly healed epithelium with normal phenotypes (data not shown). The sham suture control and tarsorrhaphy specimen appeared to be not significantly different from control corneas (PTK ablation alone). Taken together, it appears that within the first week after PTK, the amniotic membrane appears to inhibit anterior stromal inflammation and keratocyte activation. These corneas showed a normal phenotypical epithelial healing with less hyperplasia.

3. Amniotic membrane reduced collagen synthesis in one rabbit at 12th week after PTK using DTAF analysis.

The amount of newly synthesized collagen matrix is less in the amniotic membrane treated eye in one rabbit, compared with the contralateral eye. The new collagen was distinguished from the previously existing collagen by DTAF stain.

4. Inhibition of keratocyte apoptosis in the PTK wound healing by the amniotic membrane transplantation.

Fig. 5a shows a control cornea (PTK alone) using the TUNEL assay at 1 week post PTK. Remarkably, a significant apoptotic signal can be seen in the anterior stroma throughout the ablation zone. As a nuclei control, **Fig. 5b** shows a PI stain

of the same cornea demonstrating the location of cell nuclei throughout the corneal stroma as expected. In contrast to the control cornea, the amniotic membrane-treated contralateral eye showed remarkably no apoptotic signal (Fig. 5c, with Fig. 5d serving as the nuclei control with the PI stain). The difference was also observed at day 1 and day 3). In addition, we examined the sham suture control and tarsorrhaphy specimen and it appears that these corneas demonstrated findings similar to that of the control (excimer ablation alone) and did not show any decrease in apoptotic signal. Taken together, it appears that the amniotic membrane significantly down-regulates keratocyte apoptosis in the acute phase of the post PTK wound healing process in this rabbit model.

4. DISCUSSIONS

The present work represents a novel approach in the reduction of corneal haze after excimer laser ablation. The result indicates that the preserved human amniotic membrane is efficacious in reducing the corneal haze after PTK for up to 12 weeks in this rabbit model. Furthermore, histologic examination and DNA apoptosis studies in the acute phase of the wound healing process show that the amniotic membrane reduces inflammation and keratocyte activation. The epithelium heals with a normal phenotype and less hyperplasia in the amniotic membrane-treated eyes. Remarkably, amniotic membrane appears to inhibit keratocyte apoptosis, a programmed cell-death process believed to play an important role in disorganized and scarred adult wound healing processes. Such an antiapoptotic effect may provide clues to the underlying mechanism by which the amniotic membrane exerts its modulatory effect in wound healing. In one rabbit, the amniotic membrane appears to inhibit excessive collagen matrix synthesis.

Various methods have been attempted to reduce corneal haze after excimer laser ablation. For example, the use of topical steroid has been tried and found to be ineffective. In a prospective, randomized, double-masked study, O'Brart et al⁸ and Gartry et al⁹ reported no statistically significant effect on anterior stromal haze by the administration of topical steroid. With regard to refractive outcome, although corticosteroids can maintain a hyperopic shift during their administration, the effect is reversed on cessation of treatment. There appears to be no justification for subjecting patients routinely to long-term treatment of steroids with their associated side effects. Other pharmacological interventions have been tried to decrease the post PRK haze without significant effect. Those include the use of, fibroblast inhibitors¹⁰, mitomycin C¹¹, fibroblast growth factor¹², interferon-alpha 2b¹³, cyclosporin A¹⁴, active form of vitamin D¹⁵, as well as cooling of the corneal surface¹⁶.

In our effort to search for a rational design for means to reduce or eliminate corneal haze after PRK, we sought to approach the problem by examining the molecular and cellular mechanisms of haze formation in the context of corneal wound healing, a complex biological process involving cellular migration, activation and proliferation, and matrix synthesis and remodeling influenced by a host of cytokines and growth factors. We have noted several important observations.

- 1) An intact basement membrane appears to be important in corneal wound healing as superficial corneal abrasion without violating basement membrane typically heals without scarring. Procedures such as LASIK result in minimal haze presumably due to the preservation of the Bowmans and basement membranes.
- 2) Changes in the acute phase of wound healing such as inflammation and cellular activation and migration may be critical. Absence of inflammation in the acute phase of wound healing appears to be correlated with a decreased scarring¹⁹.
- 3) Epithelia-mesenchymal interaction appears to be important for the activation of corneal stromal cells to repair fibroblast phenotype^{22,23}. There is evidence that extracellular matrix and basement membrane down-regulate the expression of transforming growth factor-beta₁ (TGF-beta₁)²². This is a remarkable finding since TGF-beta₁ modulates hyaluronan synthesis for the control of cell migration and activation²³, and neutralization of TGF-beta₁ reduces scarring in cutaneous rat wounds²⁴.

These observations have led us to consider approaches to modify PRK wound healing in the acute phase using a biological basement membrane matrix which inhibits inflammatory response by blocking inflammatory cytokines such as TGF-beta₁ and PDGF. Such a matrix should contain extracellular macromolecules such as hyaluronic acid believed to have an effect in down-regulating the expression of inflammatory cytokines such as TGF-beta₁. This may result in the modification of epithelial-mesenchymal interaction and reduction of scarring through a more orderly wound healing process such as that found in a fetus. To this end, human amniotic membrane transplantation in the acute phase of wound healing after PRK appears to be the logical option.

In the present study, a rabbit model was chosen because rabbits have been shown to demonstrate similar fibrotic reaction after excimer laser ablation as in humans^{3,4}. With respect to the design of the laser ablation profile in this work (6 mm diameter, 120 μ m depth with no edge smoothing ablation), these parameters were chosen so the amount of haze post PTK was maximized in order to observe the difference, if any, of haze between the amniotic membrane-treated and the control eyes. With respect to the corneal edema within one week after PTK, the etiology is not clear although it can be speculated. It has been described that within a week after excimer laser ablation, there is an increase in the number of keratocytes beneath epithelium with a characteristic surrounding hydrated region, which is matrix-free^{27,28}. Proteoglycan filaments of abnormally large sizes are produced. However, these hydrated regions are believed to be in fact beneficial to wound healing^{27,28}. Overhydration of tissue may facilitate deposition of collagen bundles, assist passage of cells through tissue and expedite the removal of breakdown product^{27,28}. In the present study, we did note more corneal edema in the amniotic membrane-treated eyes at one week post PTK. The edema did however resolve and these amniotic membrane-treated corneas developed less reticular and organized haze than the controls for the remaining duration of the study.

As a part of the study, we have included groups with sham suture controls and tarsorrhaphy. It appears that these corneas behave similarly to the control cornea (PTK alone) with respect to our histologic examination and apoptosis study. With respect to the possible effect of physical barrier provided by the amniotic membrane in terms of, for example, reducing exposure, the observation that tarsorrhaphy appears to exert no beneficial effect indicates that the biologically active components in the amniotic membrane (rather than just being a physical barrier to prevent exposure) are probably responsible for the haze-reducing effect observed.

It is interesting to note that in addition to the reduction of the haze by the amniotic membrane, there is evidence in the present study that amniotic membrane may inhibit excessive collagen formation as suggested by the DTAF stains in one rabbit. Further studies using larger sample sizes are certainly needed to ascertain the reproducibility of this effect. If true, amniotic membrane transplantation may have the additional benefit of preventing the regression of refractive correction.

The anti-apoptotic effect exerted by amniotic membrane observed in the present study is remarkable and warrants intensive further experimental investigation. Apoptosis is a process of programmed cell death which differs fundamentally from necrosis. Apoptosis is characterized by many unique features such as deletion of single cells, cell shrinkage and membrane blebbing^{29,33}. At a molecular level, apoptosis is controlled by *de novo* gene transcription and is characterized by nonrandom oligonucleosomal length fragmentation of DNA, a process based on which the TUNEL assay in the present study was developed. Apoptosis has been observed in the cornea after epithelial injuries^{32,33}, the present study, however, represents a first line of evidence that the apoptotic process during the corneal wound healing process can be modulated using biologically active matrix elements such as human amniotic membrane. It appears that the apoptosis occurs mainly in the anterior stroma of the cornea after excimer ablation and persists throughout the first week. The anti-apoptotic effect observed in the present study may provide clues for the mechanisms underlying the clinically identified beneficial effect with the amniotic membrane transplantation with regard to wound healing^{35,41}. If keratocyte apoptosis does indeed represent a stress response of the cornea to injuries which subsequently causes a cascade of activation of inflammatory cytokines, then inhibition of apoptosis would be beneficial in down-regulating the excessive wound healing response which leads to scar formation.

Further investigations at the molecular levels may provide clues for the anti-apoptotic and scar-reducing effect of the biologically active components within the amniotic membrane. There are several alternative approaches. The biologically active component in the amniotic membrane, such as hyaluronic acid, has been shown to down-regulate inflammatory cytokines such as TGF- β ₁²³. These cytokines are known to induce cellular differentiation, and eventually programmed death. Hence it is possible the anti-apoptotic effect by the amniotic membrane is exerted through the hyaluronic acid embedded in the matrix. In order to test this theory, one may want to examine the biological activity of the TGF- β using activity assays such as the determination of the secondary expression of connective tissue growth factor (CTGF) believed to be induced by TGF- β ⁴². Alternatively, neutralization of TGF- β using antibodies against various isoforms of TGF- β ²⁴ can certainly be used to ascertain whether TGF- β plays any role in the amniotic membrane mediation of corneal wound healing. Furthermore one may examine the TGF- β ₁-responsive elements such as the plasminogen activator

inhibitor gene to determine if amniotic membrane induces any changes in the activity of these TGF-beta-responsive genes. Such studies may shed new light into the mechanism of TGF-beta action and wound healing in general.

Clinically the present study may prove to be useful in improving the PRK technology. Although procedures such as LASIK are rapidly becoming popular in recent years, the inherent potential of significant surgical complication of LASIK still exists and PRK may still remain a viable and safer option for refractive surgical correction. With respect to the clinical application of the amniotic membrane technology to PRK, the reduction of haze may be significant in reducing the potential of loss of best corrected visual acuity. It may be particularly significant in correction of higher degrees of myopia for which a moderate amount of haze has been frequently noted¹. In addition to the reduction of haze, the present study suggests that amniotic membrane may also inhibit excessive collagen synthesis. If true, the observation may find a wide range of clinical application, particularly in higher myopic correction and in hyperopic treatment in which regression of refractive correction occurs frequently and is believed to be due to excessive collagen synthesis and epithelial hyperplasia. In terms of adapting the amniotic membrane transplantation technology to clinical use, an effective and non-invasive delivery system certainly needs to be established. Extraction of the biologically active component in the amniotic membrane can be considered for topical treatment. The use of amniotic fluid has been reported after PRK to facilitate the recovery of corneal sensitivity and nerve regeneration, as well as reduction of haze⁴³. Incorporation of the biologically active component of the amniotic membrane or amniotic fluid into contact lenses may be viable options as patients routinely use contact lens after PRK.

5. ACKNOWLEDGEMENTS

The work is supported in part by the National Institute of Health (EY 10900), Joe C. Davis Foundation, Research to Prevent Blindness, Burroughs Wellcome Fund, University Research Council of Vanderbilt University and the Skin Disease Research Center.

6. REFERENCES

1. C. Lohmann, D. Gartry, M. Kerr Muir, Et al. "Haze" in photorefractive keratectomy: its origins and consequences. *Lasers and Light in Ophthal.* 4:15-34, 1991.
2. F. E. Fante, K. D. Hanna, G. O. Waring, et al. Wound healing after excimer laser keratomileusis (photorefractive keratectomy) in monkeys. *Arch Ophthal.* 108:665-675, 1990.
3. K. D. Hanna, Y. Pouliquen, G. O. Waring, et al. Corneal stromal wound healing in rabbits after 193-nm excimer laser surface ablation. *Arch Ophthal.* 107:895-901, 1989.
4. R. J. Holm, B. D. Fouraker, D. J. Schanzlin. A comparison of an face and tangential wide-area excimer surface ablation in the rabbits. *Arch Ophthal.* 108:876-881, 1990.
5. D. M. Taylor, F. A. L'Esperence, R. A. Del Pero, et al. Human excimer laser lamellar keratectomy. A clinical study. *Ophthal.* 96:654-664, 1989.
6. J. Marshal, S. Trokel, and S. Rothery, et al. Photoablative reprofiling of the cornea using an excimer laser: photorefractive keratectomy. *Lasers in Ophthal.* 1:21-48, 1986.
7. S. Tuft, J. Marshall, S. Rothery. Stromal remodeling following photorefractive keratectomy. *Lasers Ophthal.* 1:177-183, 1987.
8. D. O'Brart, C. P. Lohmann, G. Klonos, M. C. Corbett, W. Pollock, M. G. Ker-Muir and J. Marshall. The effects of topical corticosteroids and plasmin inhibitors on refractive outcome, haze, and visual performance after photorefractive keratectomy. *Ophthal.* 101:1565-1574, 1994.

9. D. S. Gartry, M. G. Kerr Muir, and J. Marshall. The effect of topical corticosteroids on refraction and corneal haze following excimer laser treatment of myopia: An updated. A prospective, randomized double-masked study. *Eye*, 7:584-590, 1993.
10. R. H. Bergman, A. V. Spidelman. The role of fibroblast inhibitors on corneal healing following photorefractive keratectomy with 193-nm excimer laser in rabbits. *Ophthalm Surg*. 25(3): 170-174, 1994.
11. J. H. Talamo, S. Gallamudi, W. R. Green, Z. De La Cruz, V. Filatov, W. J. Stark. Modulation of corneal wound healing after excimer laser keratomileusis using topical mitomycin C and steroids. *Arch Ophthalmol*. 109(8): 1141-1146, 1991.
12. P. Rieck, T. David, C. Hartman, G. Renard, Y. Courtois and Y. Pouliquen. Basic fibroblast growth factor modulates corneal wound healing after excimer laser keratomileusis in rabbits. *German J. Ophthalmol*. 3:105-111, 1994.
13. N. Morlet, M. C. Gillies, R. Grouch, A. Mallof. Effect of topical interferon-alpha 2b on corneal haze after excimer laser photorefractive keratectomy in rabbits. *Refract Corneal Surg*. 9(6):443-451, 1993.
14. M. Filipec, T. Mai Phan, T. Z. Zhao, B. A. Rice, A. Merchant, and C. Foster. Topical cyclosporine A and corneal wound healing. *Cornea*, 11(6): 546-552, 1992.
15. M. Mastubara, A. Sasaki, S. Ito. The effect of active vitamin D to the wound healing after excimer laser phototherapeutic keratectomy (PTK). *ARVO*, 37(3):S198, 1996.
16. T. Niizuma, S. Ito, Hayashi M Futemma M, Utsumi T, Ohashi K. Cooling the cornea to prevent side effects of photorefractive keratectomy. *Suppl to J Refract & Corneal Surg*. 10:S262-S266, 1994.
17. N. S. Adzick and P. Lorenz. Cells, Matrix, Growth factors, and the Surgeon. The biology of scarless fetal wound repair. *Annals of Surgery*, 220:10-18, 1994.
18. K. J. Strissel, W. B. Rinehart and M. E. Fini. A corneal epithelia inhibitor of stromal cell collagenase synthesis identified as TGF-beta2. *Invest. Ophthalmol. & Vis Sci*. 36:151-162, 1995.
19. V. Weimer. Healing processes in the cornea: In: Duke-Elder S, Perkins ES, eds. *The transparency of the cornea*. Oxford: Blackwell Scientific, 111-124, 1960.
20. G. K. Smelser. Role of epithelium in incorporation of sulfate in the corneal connective tissue. In: Duke-Elder S, Perkins, ES, eds. *The transparency of the cornea*. Oxford: Blackwell Scientific, 125, 1960.
21. J. H. Dunnington. Tissue responses in ocular wounds. *Am J Ophthalmol*. 43:667, 1957.
22. C. H. Streuli, C. Schmidhauser, M. Kobrin, M. J. Bissell and R. Derynck. Extracellular matrix regulates expression of the TGF-beta₁ gene. *J. Cell Biology*, 120:253-260, 1993.
23. I. Ellis and S. L. Schor. The interdependent modulation of hyaluronan synthesis by TGF- beta₁ and extracellular matrix: consequences for the control of cell migration. *Growth factors*, 12:211-222, 1995.
24. M. Shah, D. M. Foreman, M. W. J. Ferguson. Neutralization of TGF-beta₁ and TGF-beta₂ or exogenous addition of TGF-beta₃ to cutaneous rat wounds reduces scarring. *J of Cell Science*, 108:985-1002, 1995.
25. A. N. Goss. Intra-uterine healing of fetal rat oral mucosal, skin and cartilage wounds. *J. Oral Pathol*, 6:35-43, 1977.
26. B. A. Mast, R. F. Diegelmann, T. M. Krummel and I. K. Cohen. Scarless wound healing in the mammalian fetus. *Surgery, Gynecology & Obstetrics*, 174:441-451, 1992.

27. I. M. Rawe, R. W. Zabel, S. J. Tuft, V. Chen and K. M. Meek. A morphological study of rabbit corneas after laser keratectomy. *Eye*, 6:637-642, 1992.
28. W. C. S. Wu, W. J. Stark and W. R. Green. Corneal wound healing after 192-nm excimer laser keratectomy. *Arch Ophthalmol*. 109:1426-1432, 1991.
29. I. D. Bowen and S. M. Bowen eds. Programmed cell death in tumors and tissue. Chapman and Hall, New York, 1990.
30. L. D. Tomei and F. O. Cope, eds. Apoptosis: the molecular basis of programmed cell death in current Communications in Cell and Molecular Biology 3, Cold Spring Harbor Laboratory press, 1991.
31. J. M. Sarmus, et al. Dicing with death: dissecting the components of the apoptosis machinery in *TIBS*, 19:26-30, 1994.
32. H. Ren and G. Wilson. Apoptosis in the corneal epithelium. *Invest. Ophthalmol & Vis Sci*. 37:1017-1025, 1996.
33. S. E. Wilson, Y. G. He, J. W. Gian, Q. Li, A. McDowell, M. Vital and E. L. Chwang. Epithelial injury induces keratocyte apoptosis: hypothesized role for the interleukin-1 system in the modulation of corneal tissue organization and wound healing. *Exp. Eye Res*, 62:325-337, 1996.
34. J. C. Kim, S. C. G. Tseng. Transplantation of preserved human amniotic membrane for surface reconstruction in severely damaged rabbit corneas. *Cornea*, 14:473-84, 1995.
35. K. Tsubota, Y. Satake, M. Ohyama, et al. Surgical reconstruction of the ocular surface in advanced ocular cicatricial pemphigoid and Stevens-Johnson syndrome. *Am J Ophthalmol*. 122:38-52, 1996.
36. S. Lee, S. C. G. Tseng. Amniotic membrane transplantation for persistent epithelial defects with ulceration. *Am J Ophthalmol*. 123:303-312, 1997.
37. P. Prabhasawat, K. Barton, G. Burkett, S. C. G. Tseng. Comparison of conjunctival autografts, amniotic membrane grafts and primary closure for pterygium excision. *Ophthalmology*. In press, 1997.
38. S. C. G. Tseng, P. Prabhasawat, S. Lee. Amniotic membrane transplantation for conjunctival surface reconstruction. *Am J Ophthalmol*. In press, 1997.
39. P. Prabhasawat, S. C. G. Tseng. Impression cytology study of epithelial phenotype of ocular surface reconstructed by preserved human amniotic membrane. *Arch Ophthalmol*. In press, 1997.
40. K. Barton, D. L. Budenz, P. T. Khaw, S. C. G. Tseng. Amniotic membrane transplantation in glaucoma surgery. *Invest Ophthalmol Vis Sci*. 38:S473, 1997.
41. T. B. Gray, P. Prabhasawat, S. C. G. Tseng. Amniotic membrane transplantation before limbal transplantation before limbal stem cell allografts for ocular surface reconstruction in patients with limbal stem cell deficiency. *Invest Ophthalmol Vis Sci*. 38:S511, 1997.
42. G. R. Grotendorst, H. Okochi, and N. Hayashi. A novel transforming growth factor beta responsive element controls the expression of the connective tissue growth factor gene, *Cell Growth and Differ*. 7:469-480, 1996.
43. H. S. Lee and J. C. Kim. Effect of amniotic fluid in corneal sensitivity and nerve regeneration after excimer laser ablation. *Cornea*, 15(5): 517-524, 1996.
44. Gau et al. Apoptosis in the rabbit cornea after photorefractive keratectomy. *Cornea*, 16:200-208, 1997.

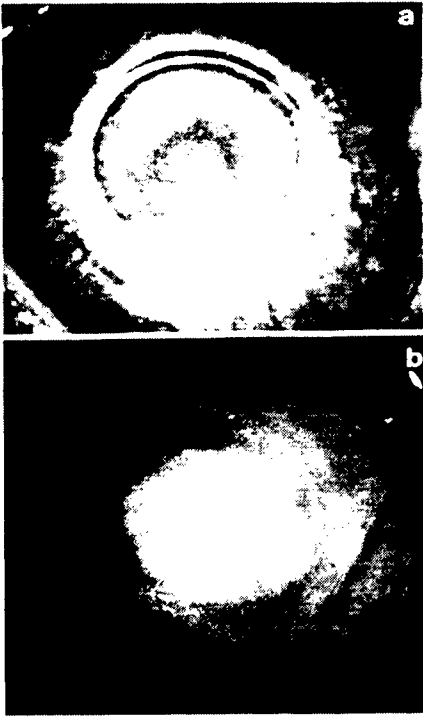


Fig.1: External appearance of a representative pair of rabbit eyes immediately after PTK (6 mm diameter and 120 μ m uniform depth) showing (a) the control cornea and (b) the experimental cornea, receiving additional amniotic membrane graft secured with 4 cardinal 10-0 nylon sutures placed well outside of the ablation zone.

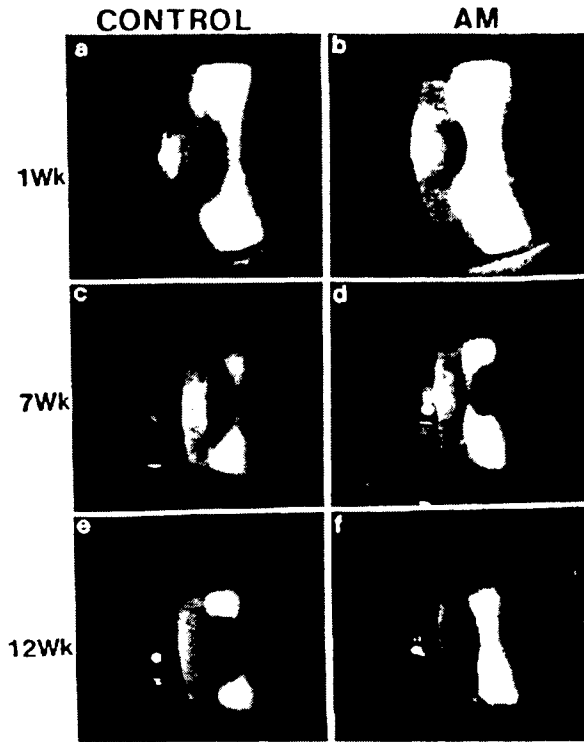


Fig.2: Composite photos showing the corneal haze at 1 (a, b), 7 (c, d) and 12 (e, f) weeks after PTK in the control (a, c, e) and the experimental (b, d, f) eye of a representative rabbit. At 1 week after PTK, the surface of the amniotic membrane covered cornea appeared to be more irregular. An organized and reticular haze appeared thereafter and is more notable in the control eye at 7 and 12 weeks.

Temporal Profile of Haze

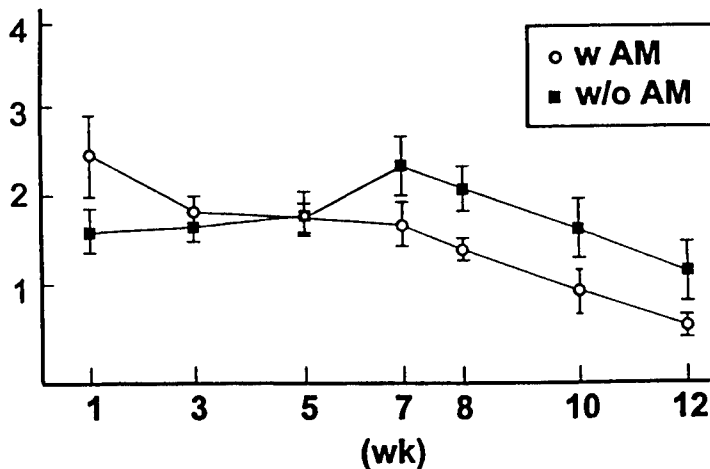


Fig.3: Comparison of scores of corneal haze between the experimental group receiving amniotic membrane (w AM, ○) and the control group without amniotic membrane (w/o AM, ■). At one week, there was more surface irregularity in the amniotic membrane-treated eyes. However, this appearance resolved at 2 weeks and an organized reticular haze ensued thereafter which peaked at 7 weeks in both groups. The differences noted from 7 to 12 weeks are statistically significant (each with $p < 0.001$), supporting that corneal haze was more in the control eyes than the experimental eyes.

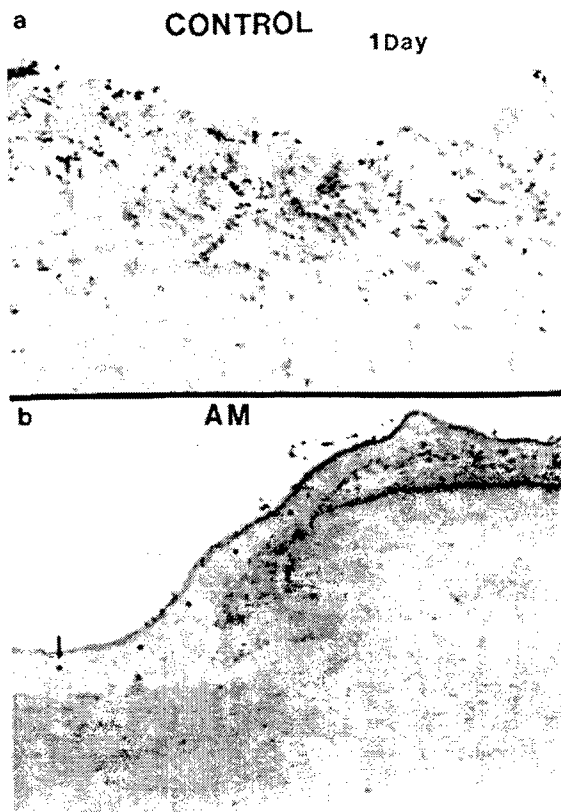
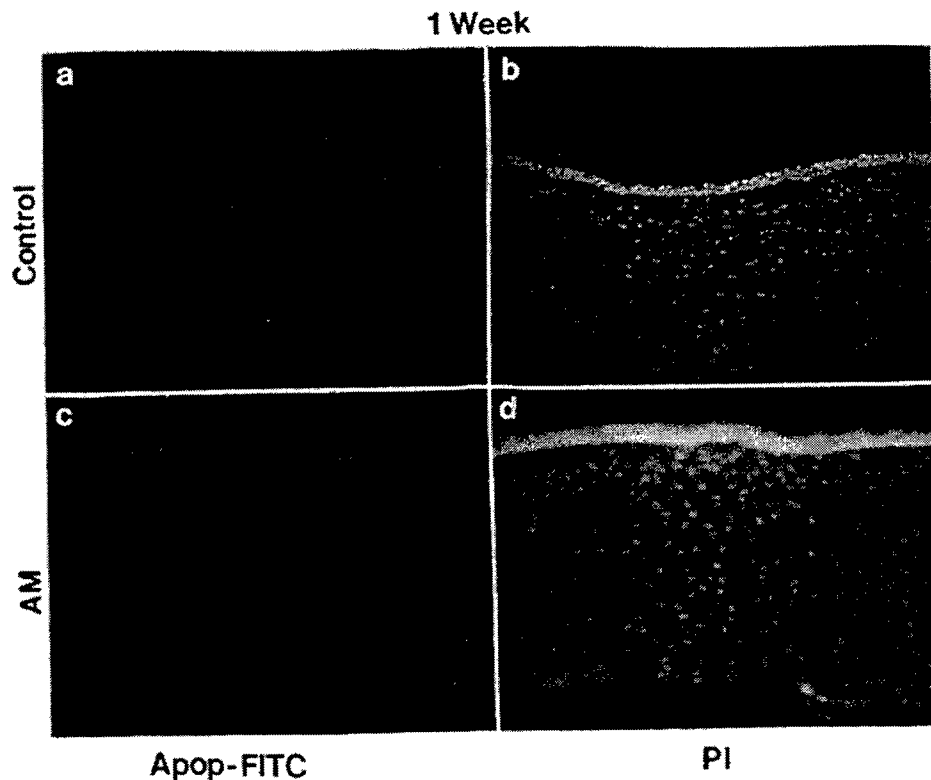


Fig.4 (Left upper and lower panels): Histologic appearance of the control (upper panel) and the amniotic membrane (AM)-treated experimental cornea (lower panel) of a representative rabbit euthanized at one day. Acute inflammatory cell infiltrate was noted in the anterior denuded stroma of the control (a), but was absent in the amniotic membrane- (indicated by* with an arrow) covered experimental (b) cornea.

Fig.5 (Below): Comparison of apoptosis, measured by an *in situ* TUNEL assay, between the control (upper panels) and the amniotic membrane (AM)-treated experimental cornea (lower panels) of a representative rabbit at 1 week after PTK. As compared to the red fluorescence which reveals all nuclei by propidium iodide (right panels), the apoptotic nuclei detected by Apop-FITC stain (green fluorescence, left panels) are found only in the control cornea (a), but not in the experimental cornea (c).



Influence of optical aberrations on laser-induced plasma formation in water, and their consequences for intraocular photodisruption

Alfred Vogel¹, Kester Nahen¹, Dirk Theisen¹, Reginald Birngruber¹,
Robert J. Thomas², and Benjamin A. Rockwell²

1) Medizinisches Laserzentrum Lübeck, D-23562 Lübeck, Germany

2) Optical Radiation Division, Armstrong Laboratory, Brooks AFB, TX 78235

ABSTRACT

The influence of spherical aberrations on laser-induced plasma formation in water by 6-ns Nd:YAG laser pulses of 1064 nm wavelength was investigated. Experiments and numerical calculations were carried out for focusing angles similar to those used for intraocular microsurgery. Wave form distortions of 5.5λ and 18.5λ between the optical axis and the $1/e^2$ irradiance values of the laser beam were introduced by replacing laser achromats in the delivery system by plano-convex lenses. Aberrations of 18.5λ led to an increase of the energy threshold by a factor of 8.5. The threshold irradiance calculated using the diffraction limited spot size was 10 times increased as compared to the case of minimized aberrations and 48 times larger than the actual threshold. The threshold calculated with the measured focus diameter was, on the other hand, reduced by a factor of 35. This reduction is due to the presence of hot spots in the focal region of the aberrated laser beam. In these hot spots, the threshold irradiance is probably unchanged, but the threshold value is reduced when averaged over the whole measured diameter of the beam waist. The determination of breakdown threshold in the presence of aberrations leads, hence, to strongly erroneous results. In the presence of aberrations, the plasmas are up to 3 times longer and the transmitted energy is 17-20 times larger than without aberrations. Aberrations can thus strongly compromise the precision and safety of intraocular microsurgery where they may arise through the use of inappropriate contact lenses, tilting of the lens, and oblique light passage through the ocular media. They can further account for a major part of the differences in breakdown threshold and plasma transmission values reported in previous investigations.

Keywords: laser-induced breakdown, plasma formation, aberrations, intraocular microsurgery, laser safety

1. INTRODUCTION

Laser-induced plasma formation (optical breakdown) in water or aqueous fluids is used in various medical laser applications^{1,2}, such as laser lithotripsy², laser angioplasty³, and intraocular microsurgery⁴⁻⁶. Additionally, laser induced breakdown is of great importance in the field of laser safety, as it is a possible mechanism for ocular damage by short and ultrashort laser pulses⁷.

Correspondence: Alfred Vogel, PhD, Medical Laser Center Lübeck, Peter-Monnik-Weg 4, D-23562 Lübeck, Germany.
FAX: xx49-451-505 486; e-mail: vogel@mll.mu-luebeck.de

Theoretical investigations of laser-induced plasma formation are usually based on the assumption of diffraction limited focusing. In previous experimental investigations of optical breakdown phenomena we have also attempted to realize such conditions in order to guarantee reproducibility and facilitate comparison with theory⁸⁻¹⁰. In many practical laser applications, however, the laser focus is deteriorated by aberrations. This is the case, for example, in intraocular microsurgery, especially when the application site is located in the ocular periphery where an oblique passage of the laser beam through the ocular media and the crystalline lens is unavoidable⁴. Similar considerations apply for laser-induced retinal damage, since the retinal image is influenced by the aberrations of the eye¹¹⁻¹³. Aberrations will change the irradiance distribution in the region of the laser focus and thus alter the breakdown threshold, the plasma shape and the plasma length. This may lead to changes of the plasma transmission and to differences in the conversion from light energy to the mechanical energy of the shock wave and cavitation bubble created by the expanding plasma. These phenomena have an influence on the precision of intraocular photodisruption^{6,10} and may also affect the characteristics and severity of ocular damage occurring in a laser accident. They are investigated in this study to complete earlier investigations performed with minimized aberrations^{9,10}.

Besides having practical importance for intraocular photodisruption and laser safety, a study of the effects of aberrations on optical breakdown may also explain some of the discrepancies between previous studies on optical breakdown thresholds and plasma shielding in aqueous media^{8-10,14-24}. The assumption of diffraction limited focusing conditions in the presence of optical aberrations leads to wrong conclusions about the physics of optical breakdown. The breakdown irradiance threshold I_{th} is overestimated, and, since the aberrations tend to be more pronounced at large focusing angles (small spot sizes), an apparent dependence of the breakdown threshold on spot size will be created^{9,25,26}. Even if the aberrations of the delivery system are minimized in air, the liquid cell introduces additional aberrations, if simple cuvettes with plane walls are used²⁷. A way out is to build suitable lenses into the cuvette wall, for example aplanatic meniscus lenses^{8,9,14}. In this case, however, great care has to be taken that the focus is located in the aplanatic point of the lens. If the focus is located behind the aplanatic point, strong spherical aberrations are created²⁸. Few researchers have taken all these precautions in their investigations of optical breakdown in liquids. The measurement results were, hence, often influenced by aberrations, but since the experimental conditions were frequently not well documented, it is difficult to assess by which degree. The present investigations show the wide range in which optical breakdown phenomena vary when the quality of the laser focus is changed by aberrations.

The parameter range investigated covers the parameters used for intraocular microsurgery. The delivery system for the laser pulses was first optimized to achieve minimal aberrations, and known spherical aberrations were then introduced by replacing achromatic laser doublets by simple plano-convex lenses. The breakdown phenomena investigated include the optical breakdown threshold, the plasma shape and length, the plasma transmission, and the conversion of light energy into the mechanical energy of the shock wave and cavitation bubble.

2. METHODS

The experimental arrangement for the investigation of the influence of aberrations on plasma formation is shown in Figure 1. The optical system for plasma generation is described in detail in Ref. [9]. All experiments were performed with Nd:YAG laser pulses having a duration of 6 ns and a nearly Gaussian intensity profile. When minimal aberrations were desired, the laser beam was expanded by a biconcave lens ($f = -40$ mm), collimated by a Nd:YAG laser achromat L_1 ($f = 200$ mm), and focused into a cuvette filled with distilled, filtered water using a second laser achromat L_2 ($f = 120$ mm). An ophthalmic contact lens (Rodenstock RYM) was built into the cuvette wall, and the laser focus coincided with the aplanatic point of the contact lens. The focusing angle was 22° , and the focus diameter measured with a knife edge technique⁹ was $7.6 \mu\text{m}$ (diffraction limited spot diameter: $3.5 \mu\text{m}$).

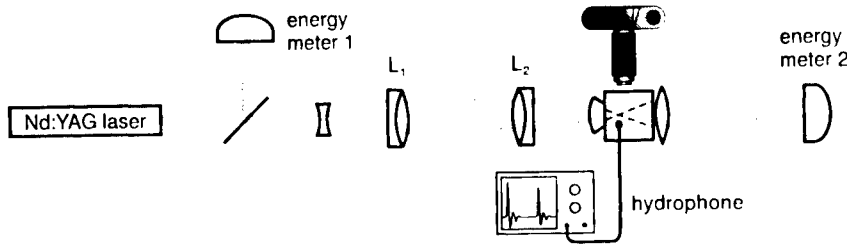


Figure 1: Experimental arrangement for the investigation of plasma formation. The achromats L_1 and L_2 were replaced by plano-convex lenses to introduce spherical aberrations of different degrees.

To introduce known aberrations, the achromats L_1 and L_2 were replaced by plano-convex lenses (achromatic doublets minimize not only chromatic, but also spherical aberrations), and a stronger beam expansion ($f_1 = -30$ mm) was used. The degree of the aberrations can be described in terms of an aberration function Φ defined as the displacement between the perfectly spherical wavefront and the distorted wavefront. For a plano-convex lens of focal length f , radius r_0 , and refractive index n , the aberration function is given by²⁹

$$\Phi(\rho) = -\frac{(r_0 \rho)^4}{32 f^3} \left[\frac{n^2}{(n-1)^2} - \frac{n}{n+2} + \frac{(2n^2 - n - 4)^2}{n(n+2)(n-2)^2} \right]. \quad (1)$$

where $\rho = r/r_0$, and where r represents distances measured orthogonal to the optical axis. The maximum value Φ_{\max} of Φ occurs at the beam edge defined by the lens aperture. For a Gaussian intensity distribution, the quality of the focus does not only depend on Φ_{\max} , but also on the location r_G of the $1/e^2$ irradiance values relative to the lens aperture. We therefore use $\Phi(r_G)$ to characterize the aberrations of the optical system. When the achromat L_1 was replaced by a plano-convex lens with 200 mm focal length, this led to $\Phi(r_G) = 5.5 \lambda$. Stronger aberrations of $\Phi(r_G) = 18.5 \lambda$ were created by additionally replacing the achromat L_2 by a plano-convex lens with 150 mm focal length. The corresponding focusing angles were 28° for $\Phi(r_G) = 5.5 \lambda$, and 24° for $\Phi(r_G) = 18.5 \lambda$. The measured spot diameters were $96 \mu\text{m}$, and $130 \mu\text{m}$, respectively. The aberrations investigated in this paper are fairly strong in order to clearly demonstrate the effects of focal

distortions. Aberrations of that degree sometimes occurred in investigations of the physics of photodisruption^{25,29}, and they may arise (mainly in the form of astigmatisms and coma) during laser treatment in the ocular periphery, or in laser accidents where the beam is incident from an oblique angle.

The energy thresholds E_{th} for optical breakdown (50% breakdown probability) were determined by visual detection of the plasma spark as described in Ref. [9]. We also determined the sharpness $S = E_{th}/\Delta E$ of the threshold which is given by the ratio of E_{th} and the energy difference ΔE between 10% and 90% breakdown probability⁹. The plasma shape and length were analyzed with a spatial resolution of about 4 μm by open shutter photography in a darkened room⁹. The plasma transmission was measured using calibrated energy detectors in front and behind the water-filled cuvette (Fig. 1), as described in Ref. [10].

Mechanical effects arising during the optical breakdown process are cavitation and shock wave emission³⁰. The bubble energy E_B can be easily determined in an indirect way through a hydrophone measurement of the bubble oscillation period which is marked by the shock waves emitted during optical breakdown and bubble collapse³¹. The oscillation period T_B is related to the maximum bubble radius R_{max} by³²

$$R_{max} = \frac{T_B}{2 \times 0.915 \sqrt{\frac{\rho_0}{p_\infty - p_v}}}, \quad (2)$$

whereby ρ_0 is the density of the liquid, p_∞ the hydrostatic pressure, and p_v the vapour pressure inside the bubble (2330 Pa at 20° C). The maximal bubble radius, in turn, yields the bubble energy

$$E_B = (4\pi/3)(p_\infty - p_v)R_{max}^3. \quad (3)$$

The shock wave energy E_S cannot be easily determined; since it depends on the shock wave amplitude and profile near the laser plasma which are difficult to measure³⁰. Previous investigations have shown, however, that the ratio between bubble energy and shock wave energy is similar for 1 mJ and 10 mJ pulses of 6 ns duration³⁰ ($E_B/E_S \approx 0.65$). We assume that this is also true in a wider parameter range and consider the transformation of light energy into bubble energy E_B to be indicative for the conversion of light energy into mechanical energy ($E_B + E_S$).

To support the interpretation of the experimental results, we calculated the light intensity distribution in the focal region of the laser beam by evaluating the diffraction integral²⁵

$$I(r, z) = \left(\frac{2\pi A_0 r_0^2}{\lambda f^2} \right)^2 \left| \int_0^1 \exp(0.5\rho^2) \exp\left\{i\left[k\Phi(\rho) - 0.5u\rho^2\right]\right\} J_0(v\rho) \rho d\rho \right|^2, \quad (4)$$

where $\Phi(\rho)$ is the aberration function given by Eq. (1), $k = 2\pi/\lambda$, A_0 is the incident beam amplitude, J_0 is the Bessel function of order zero, z defines the direction of the optical axis, and u and v are the so-called optical coordinates

$$u = \frac{2\pi}{\lambda} \left(\frac{r_0}{f} \right)^2 z, \quad \text{and} \quad v = \frac{2\pi}{\lambda} \left(\frac{r_0}{f} \right) r. \quad (5)$$

3. RESULTS AND DISCUSSION

3.1 Breakdown thresholds

The breakdown parameters for various degrees of spherical aberrations are summarized in Table 1. With the strongest aberrations investigated ($\Phi(r_G) = 18.5 \lambda$), the energy threshold is 8.5 times as large as with minimized aberrations. The sharpness of the threshold decreases with increasing degree of aberrations. When the *diffraction limited spot size* is used for the calculation of the threshold irradiance I_{th} , the value obtained for $\Phi(r_G) = 18.5 \lambda$ is 48 times larger than the actual I_{th} - value (based on the measured spot size) and 10 times larger than for the case of minimized aberrations. Even in the case of the optimized delivery system the actual irradiance threshold is lower than the threshold obtained using the diffraction limited spot, because at large focusing angles residual aberrations are hard to avoid. When the *measured spot size* is used for the threshold calculations, the I_{th} - values in the presence of aberrations are considerably lower (by a factor of 35 in the case of $\Phi(r_G) = 18.5 \lambda$) than the value obtained with the optimized system. It will be shown in the next section that this reduction is due to the presence of hot spots in the focal region of the aberrated laser beam where plasma formation starts. In these hot spots, the threshold irradiance is probably unchanged, but calculations using the whole measured diameter of the beam waist yield a reduced threshold value, because they average over the hot spots and the low-intensity regions (all threshold calculations assume a constant intensity across the laser beam). We can conclude that the presence of aberrations leads to erroneous values of the optical breakdown threshold even when the measured spot size is used for its determination.

	Spherical aberrations		
	minimized	$\Phi(r_G) = 5.5 \lambda$	$\Phi(r_G) = 18.5 \lambda$
Focusing angle θ	22°	28°	24°
Spot diameter (μm) diffraction limited	3.5	2.7	3.2
Spot diameter (μm) measured	7.6 ± 0.6	96.6 ± 3.6	130.2 ± 5.9
E_{th} (μJ)	141 ± 1.3	371 ± 3	1202 ± 9
I_{th} ($10^{11} \text{ W cm}^{-2}$) diffraction limited	2.44	10.8	24.9
I_{th} ($10^{11} \text{ W cm}^{-2}$) measured	0.52	0.0084	0.015
Sharpness S of threshold	2.05	1.88	1.48

Table 1: Breakdown parameters for various degrees of optical aberrations

3.2 Plasma Shape

Figure 2 shows the plasma form as a function of laser pulse energy for various degrees of spherical aberrations. The plasmas produced with minimal aberrations are compact and fill the whole cone angle of the laser beam. Spherical aberrations lead to plasmas which are longer, less compact and often consist of several individual parts. Furthermore, they feature a sharp tip in the cone angle beyond the laser focus.

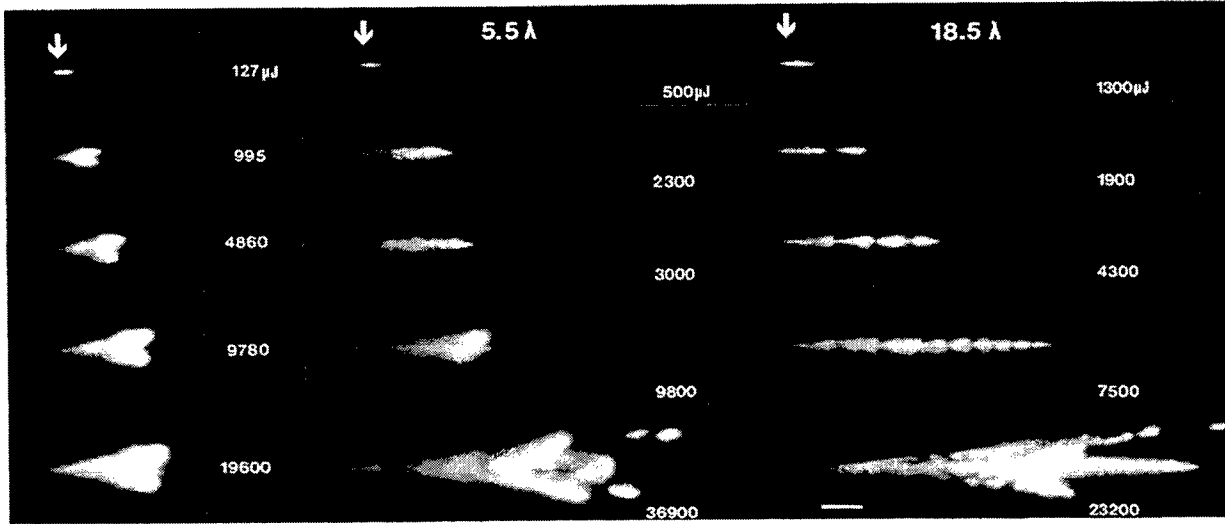


Figure 2: Plasma form as a function of laser pulse energy for various degrees of aberrations. Left: minimized aberrations, middle: $\Phi(r_G) = 5.5 \lambda$, right: $\Phi(r_G) = 18.5 \lambda$. The arrows indicate the location of the beam waist. The bar represents a length of 100 μm . The pulse energies are given in μJ .

According to the "Moving Breakdown Model"³⁴, the plasma shape follows iso-intensity lines in the cone angle proximal to the laser. Figure 3 shows the intensity distribution in the focal region of the laser beam calculated by evaluation of the diffraction integral in Eq. (4). The spherical aberrations lead to the formation of "hot spots" which are arranged in a line of irradiance maxima along the optical axis, and to various conical zones of high irradiance in the periphery of the incoming laser beam. The tip of the conical zones located "downstream" the beam waist result from the fact that the central part of the beam is focused farther away from the lens than the peripheral part. The region of peak irradiance is very small compared to the total size of the beam waist. This explains the strong reduction of the threshold value when I_{th} is calculated assuming a homogeneous intensity distribution across the whole measured beam diameter. The calculated irradiance distribution closely resembles the plasma shapes in Figure 2. At small normalized pulse energies $\beta = E / E_{th}$, plasma is formed only in the intensity maxima along the optical axis (for example in the case of $\Phi(r_G) = 18.5 \lambda$ and $E = 4300 \mu\text{J}$, corresponding to $\beta = 3.6$). At larger pulse energies, the individual breakdown sites grow together and plasma is also produced in the high-intensity "wings" in the beam periphery. Besides the tip of the conical high-

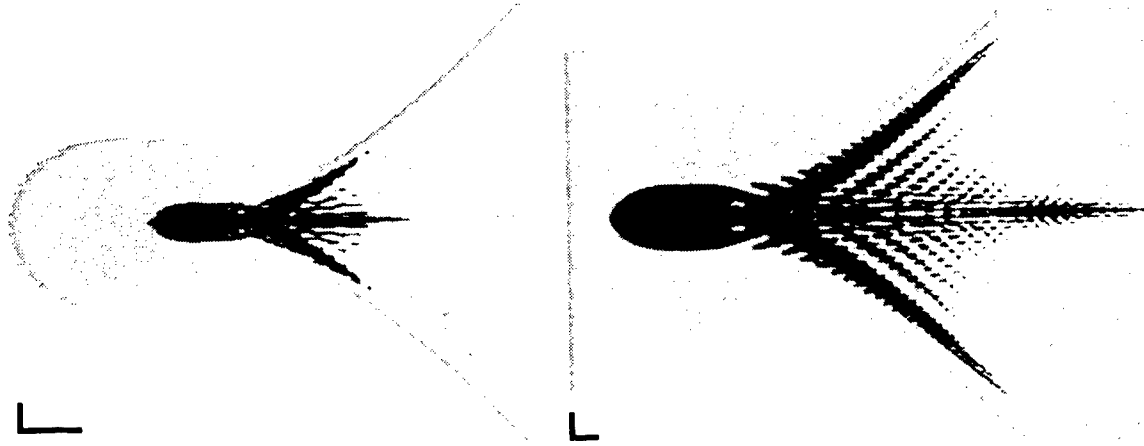


Figure 3: Calculated intensity distribution in the focal region a) for $\Phi(r_G) = 5.5 \lambda$, b) for $\Phi(r_G) = 18.5 \lambda$. The laser light is incident from the right. The vertical and horizontal bars represent a length of $10 \mu\text{m}$ and $100 \mu\text{m}$, respectively.

intensity region, very little plasma is actually produced beyond the beam waist, because most of the laser light is absorbed by the plasma proximal to the laser ("plasma shielding")¹⁰. The plasma shielding was, however, not considered in the calculations for Fig. 3.

3.3 Plasma length

At energies well above the breakdown threshold the plasmas are up to 3 times longer in the presence of aberrations (Fig. 4), and even at threshold the plasma length increases slightly with increasing aberrations. The larger length is due to distortions of the plasma form and to individual plasma spots outside the main body of the plasma (Figs. 2 and 3).

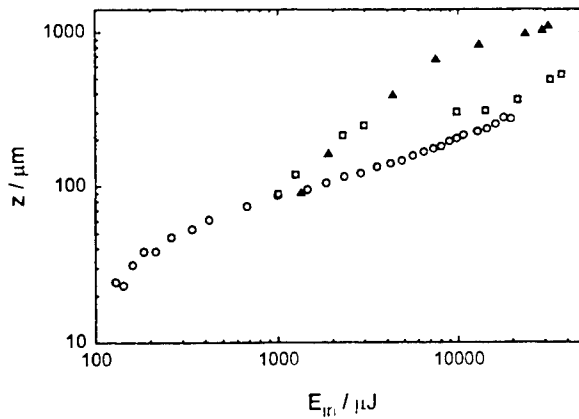


Figure 4: Plasma length as a function of laser pulse energy for minimized aberrations (o), $\Phi(r_G) = 5.5 \lambda$ (□), and $\Phi(r_G) = 18.5 \lambda$ (Δ).

3.4 Plasma Transmission

In Figure 5, the energy E_{out} transmitted through the plasma is plotted as a function of the incident energy E_{in} for the extreme cases of minimal aberrations and strong aberrations ($\Phi(r_G) = 18.5 \lambda$). E_{out} is 17 - 20 times larger with aberrations than without over the whole energy range investigated.

In Figure 6 the plasma transmission T is plotted as a function of the normalized laser pulse energy β . It is also considerably higher in the presence of aberrations. The increase of energy transmission through the plasma in the presence of aberrations is partly due to the higher breakdown threshold resulting from the increased spot size, and partly a consequence of the irregular irradiance distribution in the focal region. The incident light is absorbed only in the

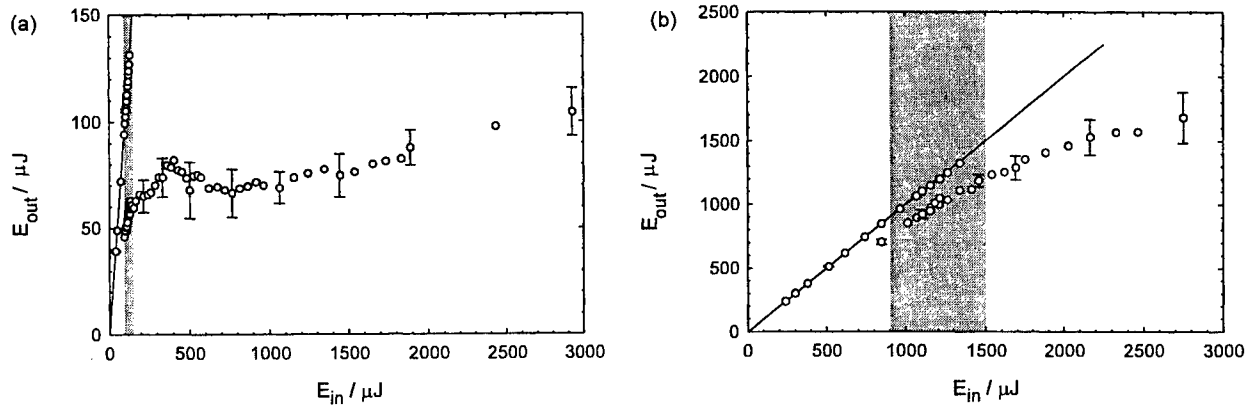


Figure 5: Transmitted energy as a function of incident laser energy a) for minimized aberrations, b) for $\Phi(r_G) = 18.5 \lambda$. The shaded areas indicate the threshold region between 10% and 90 % breakdown probability. E_{th} (50% breakdown probability) lies in the center of the shaded area.

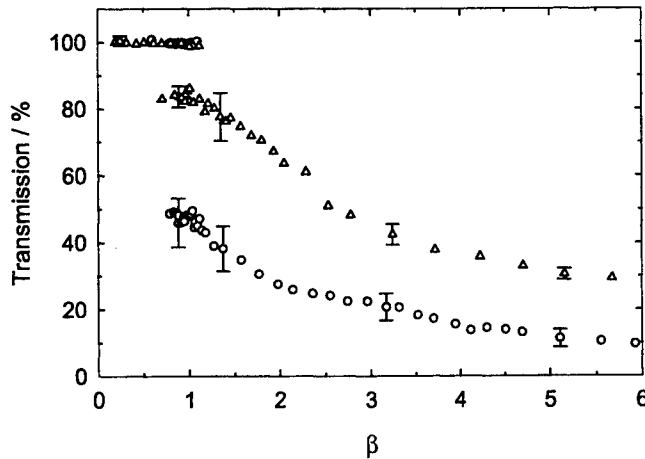


Figure 6: Transmission as a function of the normalized laser energy $\beta = E/E_{th}$ for minimized aberrations (o) and $\Phi(r_G) = 18.5 \lambda$ (Δ).

irradiance maxima where plasma is formed, but partially transmitted between the maxima. In the periphery of the focal region, the irradiance will stay below the threshold for plasma formation even within the maxima. Although the irradiance in this region is low, the energy passing through the peripheral maxima can be fairly large due to their large cross section. Therefore, a large percentage of the laser light is transmitted

Various other authors have previously performed measurements of the transmission of plasmas created in water and saline by nanosecond Nd:YAG laser pulses^{14-16,18-21,24} and reported a large variety of results. These results cannot in detail be compared with the data of the present study, because the medium of plasma formation, the laser beam profile, the focusing angle and the interface between liquid cell and air (plane wall or lens built into the cell) differ from case to case and are sometimes not even reported. However, all transmission values are, at equal β , larger than the values obtained by us with minimized aberrations, and most values are smaller than our values for $\Phi(r_G) = 18.5 \lambda$. This suggests that optical aberrations in the delivery system of the laser pulses can account for a major part of the differences in transmission values reported by different authors.

3.5 Conversion of Light Energy into Cavitation Bubble Energy

Figure 7 shows that the conversion rate of laser light energy E_L into cavitation bubble energy E_B decreases as the aberrations of the optical system increase. This is partly, but not completely, explainable by the higher light transmission through the plasma in the case of aberrations (Fig. 6). The conversion into bubble energy is higher for focusing with minimized aberrations also when the bubble energy is related to the *absorbed* laser energy. The absorbed energy can be approximated by $E_{abs} = E_{in}(1 - T)$, because light scattering and reflection by the plasma are negligibly small¹⁰. In the case of strong aberrations ($\Phi(r_G) = 18.5 \lambda$), we thus obtain for $E_{in} = 1$ mJ that $E_B/E_{abs} = 10$ %, as compared to 21 % for focusing with minimized aberrations. The respective values for $E_{in} = 8$ mJ (highest energy value for which T was measured) are 13 % and 22%. The conversion of absorbed laser energy into cavitation bubble energy is thus approximately twice as effective with minimized aberrations as in the case of $\Phi(r_G) = 18.5 \lambda$, regardless of laser pulse energy.

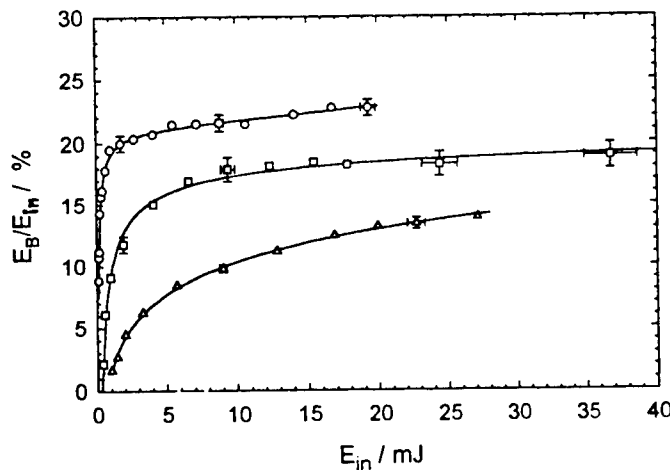


Figure 7: Conversion rate E_B/E_{in} of incident light energy E_{in} into cavitation bubble energy E_B for minimized aberrations (o), $\Phi(r_G) = 5.5 \lambda$ (□), and $\Phi(r_G) = 18.5 \lambda$ (Δ).

The reason is probably that the average energy density in the plasma is smaller in the presence of aberrations due to the irregular irradiance distribution in the focal region and the larger plasma length (Fig.4). This means that the plasma volume corresponding to a certain amount of absorbed laser energy is larger, and, hence, that a larger percentage of the absorbed laser energy is required to evaporate the liquid within the plasma volume. Therefore, less energy is available for mechanical effects like shock wave and bubble generation.

The present investigations explain some discrepancies in previous work on the mechanical effects of optical breakdown in water. In an early paper from our group³⁵, where optical breakdown was generated without paying special attention on the minimization of aberrations, the conversion rate of light energy into cavitation bubble energy was found to be not larger than 8%, but in later studies, where aberrations were minimized, we observed a conversion rate of up to 25 %^{8,30}, although the laser pulse duration and focusing angle were similar.

3.6 Consequences for Intraocular Photodisruption

The increase of the breakdown threshold due to spherical aberrations demands that larger pulse energies are used for intraocular microsurgery. At the same time, aberrations go along with an increase of transmission, and thus with a reduction of the efficacy of intraocular laser surgery. At equal incident energy, the transmitted energy increases by a factor of about 20 for $\Phi(r_G) = 18.5\lambda$ (Fig. 5). The increased transmission leads to a higher risk of retinal damage. For all these reasons it is essential that aberrations are minimized for clinical laser applications. A key element is the appropriate choice and use of the contact lens used for laser treatment (A contact lens is placed on the corneal surface to immobilize the eye, prevent blinking, adjust the focusing angle, and to improve the optical surface determining the beam quality within the eye^{4,5}). Rol et al.²⁸ showed that focusing behind the aplanatic point of a contact lens introduces severe spherical aberrations. It is therefore very important to use different contact lenses for surgical application in the different segments of the eye²⁸. In particular, it should be avoided to use contact lenses designed for the anterior segment (i.e. for iridotomies and capsulotomies) to do surgery behind the posterior lens capsule. In clinical practice, aberrations may also arise from a tilting of the contact lens, and from oblique light passage through the optical media^{4,36} which occurs during treatment in the retinal periphery. Coma and astigmatism have not been investigated in this study, but will probably have similarly deleterious effects as spherical aberrations. They can be minimized by avoiding oblique incidence of the laser beam onto the contact lens and oblique light passage through the ocular media.

4. ACKNOWLEDGEMENTS

The authors thank Stefan Rein for his contribution in the early phase of the project, and appreciate helpful discussions with Daniel X. Hammer and Joachim Noack. The research was supported by the Deutsche Forschungsgemeinschaft (Grant Bi-321/2-3).

5. REFERENCES

1. S. J. Gitomer and R. D. Jones. "Laser-produced plasmas in medicine." *IEEE Trans. Plasma Sci.* **19**, pp. 1209-1219, 1991.
2. A. Vogel, "Non-linear absorption: Intraocular microsurgery and laser lithotripsy," *Phys. Med. Biol.* **42**, pp. 895-912, 1997.
3. M. R. Prince, G.M. LaMuraglia, P. Teng, T. F. Deutsch, and R. R. Anderson, "Preferential ablation of calcified arterial plaque with laser-induced plasmas." *IEEE J. Quantum Electron.* **QE-23**, pp. 1783-1786, 1987.
4. R. F. Steinert and C. A. Puliafito. *The Nd:YAG Laser in Ophthalmology*, Saunders, Philadelphia, 1985.
5. F. Fankhauser and S. Kwasniewska. "Neodymium:yttrium-aluminium-garnet laser," in *Ophthalmic Lasers*, Third Edition, F. A. L'Esperance, Ed., Mosby, St. Louis, MO, 1989, pp. 781-886.
6. A. Vogel, P. Schweiger, A. Frieser, M. Asiyu, and R. Birngruber, "Intraocular Nd:YAG laser surgery: Light-tissue interaction, damage range, and reduction of collateral effects," *IEEE J. Quantum Electr.* **QE-26**, pp. 2240-2260, 1990.
7. C. P. Cain, C. D. DiCarlo, B. A. Rockwell, P. K. Kennedy, G. N. Noojin, D. J. Stolarski, D. X. Hammer, C. A. Toth, W. P. Roach, "Retinal damage and laser-induced breakdown produced by ultrashort-pulse lasers," *Graefe's Arch. Clin. Exp. Ophthalmol.* **234**, suppl. 1, pp. S28-S37, 1996.
8. A. Vogel, S. Busch, K. Jungnickel, and R. Birngruber, "Mechanisms of intraocular photo-disruption with picosecond and nanosecond laser pulses," *Lasers Surg. Med.* **15**, pp. 32-43, 1994.
9. A. Vogel, Kester Nahen, and Dirk Theisen, "Plasma formation in water by picosecond and nanosecond Nd:YAG laser pulses - Part I: Optical breakdown at threshold and superthreshold irradiance," *IEEE J. Sel. Top. Quantum Electron.* **2**, pp. 847-860, 1997.
10. K. Nahen and A. Vogel, "Plasma formation in water by picosecond and nanosecond Nd:YAG laser pulses - Part II: Plasma transmission, scattering and reflection," *IEEE J. Sel. Top. Quantum Electron.* **2**, pp. 861-871, 1997.
11. F. W. Campbell, R. W. Gubish, "Optical quality of the human eye," *J. Physiol. (London)* **186**, pp. 558-578, 1966.
12. W. M. Rosenblum, J. L. Christensen, "Objective and subjective spherical aberration measurement of the human eye," *Progress in Optics* **13**, pp. 69-91, 1976.
13. J. Liang, B. Grimm, S. Goelz, and J. Bille, "Objective measurement of wave aberrations of the human eye with the use of a Hartmann-Shack wave-front sensor," *J. Opt. Soc. Am. A* **11**, pp. 1949-1957, 1994.
14. H. P. Loertscher, "Laser-induced breakdown for ophthalmic applications," in *YAG Laser Ophthalmic Microsurgery*, S. C. Trokel, Ed., Appleton-Century-Crofts, Norwalk/Conn., 1983, pp. 39-66.
15. R. F. Steinert and C. A. Puliafito, "Plasma formation and shielding by three ophthalmic neodymium-YAG lasers," *Am. J. Ophthalmol.* **96**, pp. 427-434, 1983.
16. R. F. Steinert, C. A. Puliafito, and C. Kittrell, "Plasma shielding by Q-switched and mode-locked Nd:YAG lasers," *Ophthalmology* **90**, pp. 1003-1006, 1983.
17. F. Docchio, C. A. Sacchi, and J. Marshall, "Experimental investigation of optical breakdown thresholds in ocular media under single pulse irradiation with different pulse durations," *Lasers Ophthalmol.* **1**, pp. 83-93, 1986.
18. M. R. C. Capon, F. Docchio, and J. Mellerio, "Nd:YAG laser photodisruption: an experimental investigation on shielding and multiple plasma formation," *Graefe's Arch. Clin. Exp. Ophthalmol.* **226**, pp. 362-366, 1988.
19. F. Docchio and C. A. Sacchi, "Shielding properties of laser-induced plasmas in ocular media irradiated by single Nd:YAG pulses of different durations," *Invest. Ophthalmol. Vis. Sci.* **29**, pp. 437-443, 1988.
20. F. Docchio, "Spatial and temporal dynamics of light attenuation and transmission by plasmas induced in liquids by nanosecond Nd:YAG laser pulses," *Nuovo Cimento* **13**, pp. 87-98, 1991.
21. S. A. Boppart, C. A. Toth, W. P. Roach, and B. A. Rockwell, "Shielding effectiveness of femtosecond laser-induced plasmas in ultrapure water," *SPIE Proc.* **1882**, pp. 347-354, 1993.
22. D. X. Hammer, R. J. Thomas, G. D. Noojin, B. A. Rockwell, and A. Vogel, "Ultrashort pulse laser induced bubble creation thresholds in ocular media," *SPIE Proc.* **2391**, pp. 30-40, 1995.
23. P. K. Kennedy, S.A. Boppart, D. X. Hammer, B. A. Rockwell, G. D. Noojin, and W. P. Roach, "A first-order model for computation of laser-induced breakdown thresholds in ocular and aqueous media: Part II - Comparison to experiment," *IEEE J. Quantum Electron.* **QE-31**, pp. 2250-2257, 1995.
24. D. X. Hammer, R. J. Thomas, B. A. Rockwell, E. D. Jansen, A. J. Welch, G. D. Noojin, M. Frenz, J. Noack, and Alfred Vogel, "Shielding properties of laser-induced breakdown in water for pulse durations from 5 ns to 125 fs," *Appl. Opt.* **36**, pp. 5630-5640, 1997.
25. L. R. Evans and C. Grey Morgan, "Lens aberration effects in optical-frequency breakdown of gases," *Phys. Rev. Lett.* **22**, pp. 1099-1102, 1969.

26. C. Grey Morgan, "Laser-induced breakdown in gases," *Rep. Prog. Phys.* **38**, pp. 621-665, 1975.
27. W. L. Smith, J. H. Bechtel, and N. Bloembergen, "Dielectric-breakdown threshold and nonlinear-refractive-index measurements with picosecond laser pulses," *Phys. Rev. B* **12**, pp. 706-714, 1975.
28. P. Rol, F. Fankhauser, and S. Kwasniewska, "Evaluation of contact lenses for laser therapy, Part I," *Lasers Ophthalmol.* **1**, pp. 1-20, 1986.
29. J. M. Aaron, C. L. M. Ireland, and C. Grey Morgan, "Aberration effects in the interaction of focused laser beams with matter," *J. Phys. D: Appl. Phys.* **7**, pp. 1907-1917, 1974.
30. A. Vogel, S. Busch, and U. Parlitz, "Shock wave emission and cavitation bubble generation by picosecond and nanosecond optical breakdown in water," *J. Acoust. Soc. Am.* **100**, pp. 148-165, 1996.
31. A. Vogel, W. Hentschel, J. Holzfuss, and W. Lauterborn, "Cavitation bubble dynamics and acoustic transient generation in ocular surgery with pulsed Neodymium:YAG lasers," *Ophthalmology* **93**, pp. 1259-1269, 1986.
32. J. W. Rayleigh, "On the pressure developed in a liquid during the collapse of a spherical cavity," *Phil. Mag.* **34**, pp. 94-98, 1917.
33. B. Zysset, J. G. Fujimoto, and T. F. Deutsch, "Time-resolved measurements of picosecond optical breakdown," *Appl. Phys. B* **48**, pp. 139-147, 1989.
34. F. Docchio, P. Regondi, M. R. C. Capone, and J. Mellerio, "Study of the temporal and spatial dynamics of plasmas induced in liquids by nanosecond Nd:YAG laser pulses. 1: Analysis of the plasma starting times," *Appl. Opt.* **27**, pp. 3661-3668, 1988.
35. A. Vogel and W. Lauterborn, "Acoustic transient generation by laser-produced cavitation bubbles near solid boundaries," *J. Acoust. Soc. Am.* **84**, pp. 719-731, 1988.
36. F. Fankhauser, U. Dür, H. Giger, P. Rol, S. Kwasniewska, "Lasers, optical systems and safety in ophthalmology: a review," *Graefe's Arch. Clin. Exp. Ophthalmol.* **234**, pp. 473-487, 1996.

Human cornea wound healing in organ culture after Er:YAG laser ablation

Jin H. Shen, Karen M. Joos, Richard D. Robinson, Debra J. Shetlar, Denis M. O'Day

Department of Ophthalmology and Visual Sciences, Vanderbilt University, Nashville, TN.

ABSTRACT

Purpose. To study the healing process in cultured human corneas after Er:YAG laser ablation. **Methods.** Human cadaver corneas within 24 hours post mortem were ablated with a Q-switched Er:YAG laser at 2.94 μm wavelength. The radiant exposure was 500 mJ/cm^2 . The cornea was cultured on a tissue supporting frame immediately after the ablation. Culture media consisted of 92% minimum essential media, 8% fetal bovine serum, 0.125% HEPES buffer solution, 0.125% gentamicin, and 0.05% fungizone. The entire tissue frame and media container were kept in an incubator at 37°C and 5% CO_2 . Serial macroscopic photographs of the cultured corneas were taken during the healing process. Histology was performed after 30 days of culture. **Results.** A clear ablated crater into the stroma was observed immediately after the ablation. The thickness of thermal damage ranges between 1 and 25 μm . Haze development within the crater varies from the 3rd day to the 14th day according to the depth and the roughness of the crater. Histologic sections of the cultured cornea showed complete re-epithelization of the lased area. Loose fibrous tissue is observed filling the ablated space beneath the epithelium. The endothelium appeared unaffected. **Conclusions.** The intensity and time of haze development appears dependent upon the depth of the ablation. Cultured human corneas may provide useful information regarding the healing process following laser ablation.

Keywords: organ culture, Er:YAG laser, cornea, wound healing, epithelium, histology, haze, human

1. INTRODUCTION

A model using organ-cultured human corneas has offered a useful alternative to the use of animals in experimental studies. Richard, et al. have shown that this model was able to maintain normal corneal morphology for up to 21 days.¹ Cultured cornea after a knife incision showed complete epithelium coverage of the wound, and close approximation of the cut edges of the stromal tissue.² Thermally injured human corneas also showed re-growth of epithelium over the surface of the lesion after 7 days of culture.³

Lasers have been used successfully in corneal surgeries such as phototherapeutic keratectomy and photorefractive keratectomy using an excimer laser at 193 nm.^{4,5} Other laser surgical procedures such as laser trephination using HF laser at 2.7 μm ,⁶ laser photothermal keratoplasty using Ho:YAG laser at 2.1 μm ,⁷ and erbium:YAG laser keratectomy⁸ are under investigation.

We investigated the usefulness of this model to assess corneal healing following infrared ablation by the Er:YAG laser.

2. MATERIAL AND METHODS

Er:YAG Laser: The laser used was a Q-Switched Er:YAG laser. The parameters of the laser were as follows:

Wavelength: 2.94 μm
Pulse duration: 100 ns
Repetition rate: 1 Hz
Energy per pulse: 22 mJ
Fluence: 800 mJ/cm^2

Cornea: Human cadaver eyes were obtained from the Middle Tennessee Lions Eye Bank 48 hours post mortem. The entire cornea, with a scleral rim, was dissected and placed in culture media. The epithelium was not removed.

Ablation of the cornea: Three parallel lines across the cornea were lased. The central line was ablated with an average two pulse per spot, while the outer two lines were ablated with an average of one pulse per spot.

Cornea culture: Immediately after the ablation procedure, the corneas were placed on sterilized tissue supporting frames with the epithelial side exposed to the air and the endothelium totally immersed in the culture medium. Culture media consisted of 92% minimum essential media, 8% fetal bovine serum, 0.125% HEPES buffer solution, 0.125% gentamicin, and 0.05% Fungizone. The entire media container was kept in an incubator at 37°C and 5% CO₂. Culture media was changed every three to four days.

Processing: Serial macroscopic photographs of the cultured corneas were taken during the healing process. After 30 days of culture, the corneas were formalin-fixed and processed for routine histology.

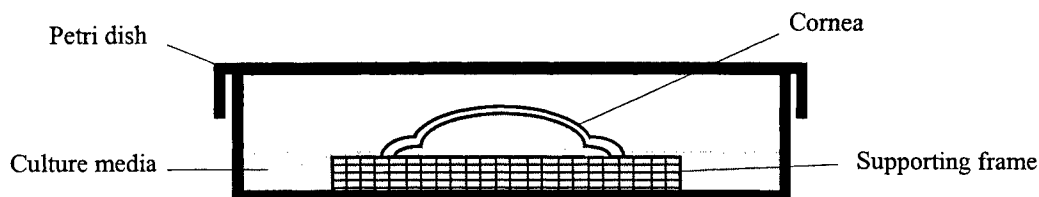


Figure 1. Each cornea was cultured on a sterilized supporting frame with the epithelial side exposed to the air and the endothelium totally immersed in the culture medium. The petri dish was kept in an incubator at 37°C and 5% CO₂.

3. RESULTS

Figure 2. (on the next page), showed the macroscopic photographs taken during the corneal culture. Figure 3 and Figure 4. showed the histological information of the Er:YAG laser ablated cornea before and after the culture.

Figure 2. (next page) Serial macroscopic photographs during the corneal culture period showed the following:

- A,B) Day 2:** Three ablated lines can be seen. Haze has started to develop in some part of the lines.
- C,D) Day 5:** Haze, which can be seen in all of the lines of ablation, appears more prominent in the central line (2 pulses per spot).
- E,F) Day 9:** Haze has started to fade from the less ablated portion of the lines. In the more deeply ablated spots, haze persists.
- G,H) Day 12:** Haze has disappeared from all the lines. The ablated areas were barely discernable.



Figure 3. Histological section of a control cornea, ablated with Er:YAG laser at 2.94 μm wavelength, 5 Hz, 25 mJ per pulse. The thickness of thermal damage ranged between 5 to 15 μm .

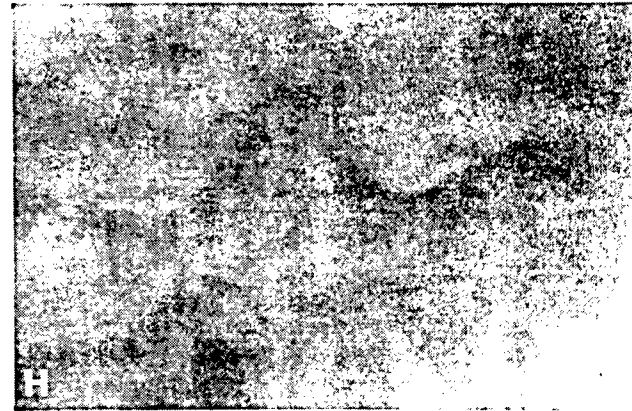
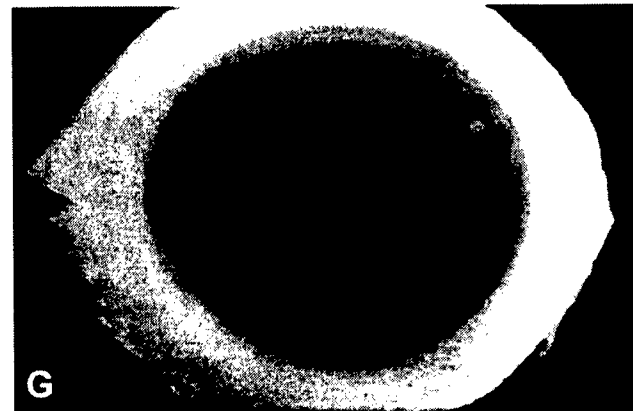




Figure 4. Histologic section of a 30 day cultured cornea that was ablated using the Er:YAG laser at 2.94 μm wavelength, 5 Hz, 22 mJ per pulse. **Top:** All lased areas showed complete re-epithelialization. The thickness of thermal damage was from 1 to 25 μm . Subepithelial fibroblasts were observed within the ablated regions.

4. CONCLUSIONS

1. The intensity and time of haze development appears dependent upon the depth of the ablation.
2. Cultured human corneas may provide useful information regarding the healing process following laser ablation without the use of live animals.

5. ACKNOWLEDGMENTS

The authors are grateful for the assistance of Susan Bigham, Min Chang, Rong Yang, and the support from the Middle Tennessee Lion's Eye Bank, and unrestricted grant from Research to Prevent Blindness, Inc.

6. REFERENCES

1. Richard NR, Anderson JA, Weiss, JL, and Binder PS. Air/liquid corneal organ culture: a light microscopic study. *Curr. Eye Res.* 10:739-49, 1991.
2. Medin W, Davanger. Wound healing of rabbit cornea in organ culture. *Acta Ophthalmologica.* 65:257-262, 1987.
3. Collin HB, Anderson JA, Richard NR, Binder PS. In vitro model for corneal wound healing; organ-cultured human corneas. *Current Eye Research.* 14:331-339, 1995.
4. Trokel S, Srinivasan R, and Braren B. Excimer laser surgery of the cornea. *Am J Ophthalmol.* 96:710-715, 1983.
5. Trokel S. Evolution of excimer laser corneal surgery. *J Cataract Refract Surg.* 15:373-383, 1989.
6. Loertscher H, Mandelbaum S, Parel JM, Parrish RK. Noncontact trephination of the cornea using a pulsed hydrogen fluoride laser. *Am J Ophthalmol.* 104:471-5, 1987.
7. Parel JM; Ren Q; Simon G. Noncontact laser photothermal keratoplasty. I, II, III. *J Refractive & Corneal Surgery.* 10:511-518; 519-528; 529-539, 1994.
8. Ren Q, Venugopalan V, Schomacker K, Deutsch TF, Flotte TJ, Puliafito CA, Brimgruber R. Mid-infrared laser ablation of the cornea: a comparative study. *Lasers in Surgery & Medicine.* 12:274-81, 1992.

Further author information -

J.H.S. (correspondence): Email: shenjh@ctrvax.vanderbilt.edu; Telephone: 615-936-1564; Fax: 615-936-3466
 K.M.J.: Email: karen.joos@mcm.vanderbilt.edu
 R.D.R.: Email: Richard.Robinson@mcm.vanderbilt.edu
 D.J.S.: Email: debra.shetlar@mcm.vanderbilt.edu
 D.M.O.: Email: denis.m.oday@mcm.vanderbilt.edu

Scleral Indentation Height after Laser Scleral Buckling

Se Woong Kang^{1,2}, Jean-Marie Parel^{1,3,5,6}, Fabrice Manns^{1,3},
Jaeheung Lee⁴, William E. Smiddy¹

¹Ophthalmic Biophysics Center, Bascom Palmer Eye Institute, University of Miami School of Medicine, Miami, FL 33101; ²Department of Ophthalmology, College of Medicine, Chungbuk National University, Cheongju, Korea; ³Biomedical Engineering Department, University of Miami College of Engineering, Coral Gables, FL 33146; ⁴Department of Ophthalmology, College of Medicine, Seoul National University, Seoul, Korea; ⁵University of Paris Hôtel-Dieu Hospital, Paris, France; ⁶Department of Ophthalmology, A. Galand, Faculté de Médecine, Université de Liège, Belgium

ABSTRACT

Laser scleral buckling (LSB) and scleral buckling are methods of inducing scleral indentation, a necessary objective in standard retinal reattachment surgery. The purpose of this study was to compare the height of scleral indentation produced by both modalities. Twenty (4 columns, 5 rows) overlapping spots of pulsed Holmium:YAG or Thulium:YAG laser were applied at the equatorial sclera in 20 human cadaver eyes (LSB group). The diameter of each laser spot was set to 2.5mm using a custom-made laser probe. Total energy of Holmium:YAG and Thulium:YAG applied to each laser spot were 1285mJ and 815mJ, respectively. Scleral shrinkage and change in scleral thickness were measured. A radially oriented 5mm silicone band was placed at the equator in 10 human cadaver eyes (explant group). The intraocular pressure (IOP) was adjusted to 4mmHg preoperatively, and to 16mmHg postoperatively in all eyes and monitored during the procedure. Scleral indentation height, assessed in frozen sections made along the eyeball equator, produced by Holmium:YAG (1.07mm) and Thulium:YAG (1.30mm) was less than that of explant group (3.12mm)($p < 0.05$). Each application of a laser spot elevated the IOP by 4.9mmHg and the IOP decreased into a quarter of its elevation after 3.64 seconds. LSB with Thulium:YAG laser is potentially useful in retinal detachments when combined with vitrectomy for creating a shallow and broad buckling effect (i. e. in proliferative vitreoretinopathy cases).

Keywords: laser scleral buckling, indentation height, IOP, retinal detachment, Holmium YAG, Thulium YAG, fiber optics

Further author information -

S.W.K. (correspondence): E-mail: swkang@med.chungbuk.ac.kr; Telephone 305-326-6174; Fax: 305-326-6139

J.M.P.: E-mail: jparel@mednet.med.miami.edu; Telephone 305-326-6069; Fax: 305-326-6139

F.M.: E-mail: fmanns@obc.med.miami.edu; Telephone 305-326-6137; Fax: 305-326-6139

W.E.S.: E-mail: wsmiddy@bpei.med.miami.edu; Telephone 305-326-6172; Fax: 305-326-6417

1. INTRODUCTION

Scleral buckling is the most common technique for retinal detachment repair. Although the surgical success rate is high, complications such as ocular motility abnormalities¹, induced refractive errors², perforation of globe during suturing and explant infection may follow scleral buckling with episcleral explant. Laser scleral buckling (LSB) has been introduced to induce scleral indentation by causing scleral shrinkage using a mid-infrared laser. In a feasibility study, scleral indentation was produced without apparent chorioretinal damage by LSB³. Several parameters which affect scleral shrinkage rate during the LSB procedure have been identified experimentally⁴. Efficient shrinkage is mainly dependent upon the hypotony of globe, total fluence and the laser penetration depth.

Although scleral indentation height is supposed to correlate with scleral shrinkage, such factors as ocular dimension may also influence the indentation height. Optimal indentation height and width are necessary to reapproximate the retinal break onto the retinal pigment epithelium for retinal detachment repair. Therefore, it is imperative to assess absolute scleral indentation produced by LSB or explant. We also evaluated the effect of LSB on the IOP as, considering the importance of IOP on scleral shrinkage, there were insufficient data available.

2. MATERIAL AND METHODS

2.1. Buckling Procedures

Fresh human cadaver eyes, provided by the Florida Lions Eye Bank, less than 48 hours after death were used for this *in vitro* study. The cadaver eyes were divided into a LSB group and a conventional scleral buckling group (explant group). For the LSB group, either a pulsed Holmium:YAG laser emitting radiation at a wavelength of $2.10\mu\text{m}$ (Sunrise Technologies Inc., Fremont, CA) or a pulsed Thulium:YAG laser of $2.01\mu\text{m}$ (New Star lasers Inc., Auburn, CA) was used. The pulse duration and pulse repetition rate of both lasers were $250\mu\text{s}$ and 5Hz, respectively. The laser energy was transmitted via a low-OH silica fiber and a custom-made laser probe which, being in contact with sclera, ensures scleral laser irradiation with a constant spot diameter of 2.5mm.

The scleral surface was exposed by conjunctival and episcleral dissection in all experimental eyes. A pair of 7.6mm spaced scleral points at the equator of superior temporal quadrant was marked with ink or 10-0 nylon suture material. The anterior chamber was tapped in the explant group and cannulated in the LSB group with a 30 gauge needle. In the 10 eyes of the explant group, a radial scleral buckle was placed at the marked area using a 5mm silicone band (MIRA[®] #32). The buckling material was secured by 7.6mm spaced mattress suture. Among the 20 eyes of the LSB group, 10 eyes received Holmium:YAG and 10 received Thulium:YAG irradiation. Twenty (4 columns, 5 rows) overlapping laser spots were applied between the two marking sutures. The laser energy was measured with a calibrated energy meter (JD-500, Molelectron Inc., Campbell, CA) before and after each case of LSB. The mean total fluence of Holmium:YAG and Thulium:YAG applied to each laser spot was $25.7 (2.6\text{J}/\text{cm}^2 \text{ per pulse})$ and $16.3\text{J}/\text{cm}^2 (2.7\text{J}/\text{cm}^2 \text{ per pulse})$, respectively. The postoperative IOP was restored to 16mmHg in all experimental eyes. In the LSB group, the scleral shrinkage rate after LSB was evaluated with an electronic digital caliper with a precision of $\pm 0.01\text{mm}$ (Mitsutoyo Inc., Japan). An ultrasonic pachymeter (Pachette, DGH Inc., Frazier, PA) was used to evaluate scleral thickness change at the irradiated site. Five measurements were averaged.

2.2. Indentation Height Evaluation

Scleral indentation height induced by LSB or by the explant was measured using frozen section techniques. The globe, fixed with anchoring sutures at the anterior and posterior pole, was transferred into a custom-made eye container. The globe in its container was immersed in embedding medium (Tissue-Tek[®], Sakura Finetek U.S.A., Inc., USA) and frozen overnight at -70°C . The eye container was designed to verify the orientation and to prevent lateral expansion of eyeball during freezing. Frozen

sections were made along the equator. Assuming a circular cross section along the equator of a normal eyeball, we calculated the scleral indentation height by comparing the diameter in the buckled meridian with the diameter perpendicular to it (radius method). The diameter, which was the distance from the choroid of one side to the choroid of the opposite side, was measured with a millimetric grid. The indentation height was also evaluated by measuring the distance from base to the apex of the indentation (direct method).

2.3. IOP Assessment

We monitored the IOP during LSB performed with the Thulium:YAG laser in 10 eyes to evaluate the effect of this procedure on IOP. With baseline IOP of 5 to 75 mmHg in 5 mmHg steps, one laser spot (total energy per spot: 815 mJ in five pulses) was applied to the eye while measuring IOP with a calibrated 20 gauge pressure sensor (Dräger Medical Electronics, Best, Netherlands) cannulated through corneal limbus. Varying baseline IOP, we evaluated the maximum IOP elevation (P_{max}) after one laser spot application and the time required for the pressure elevation to decrease to half ($T_{1/2max}$) and a quarter ($T_{1/4max}$) of P_{max} .

3. RESULTS

3.1 Indentation Height

Since the distances between equatorial marking sutures before freezing (mean: 6.17 mm) and after frozen section (6.16 mm) were the same, lateral expansion of the eyeball after freezing did not occur within the eye container. The frozen section along the equator of the eyeball could be obtained in the majority of cases (24/30 eyes). When sections oblique to the equator were encountered, the equation described below was applied to avoid overestimation of indentation height.

$$\text{Height of Indentation} = \frac{(T-P)*S}{T}$$

[P = distance from center to the apex of indentation, T = radius to the opposite side of indentation, S = the shortest radius]

The average (\pm standard deviation) scleral indentation height produced by the Holmium:YAG LSB, Thulium:YAG LSB and explant were 1.07 ± 0.31 mm, 1.30 ± 0.55 mm and 3.12 ± 0.47 mm, respectively (Fig. 1). The differences were statistically significant between both LSB subgroups and explant group ($p < 0.05$), but not between the Holmium:YAG LSB and Thulium:YAG LSB subgroups. When measured by the direct method, the indentation height of the explant group (2.10 ± 0.37 mm) was also higher than that of Holmium:YAG LSB (0.87 ± 0.24 mm) and Thulium:YAG LSB (0.70 ± 0.24 mm).

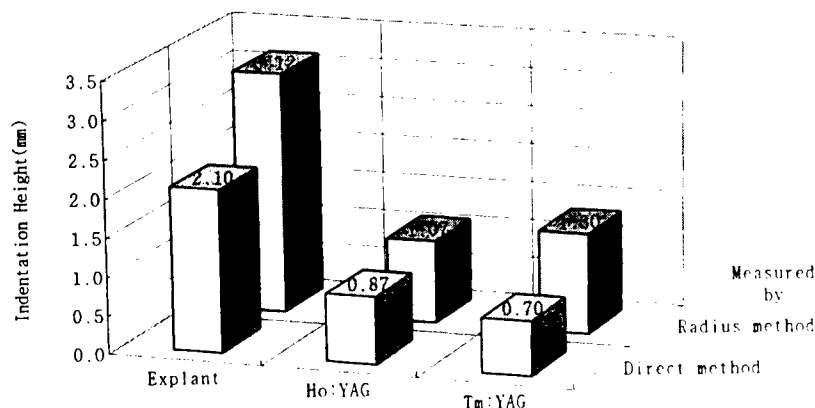


Fig. 1. The scleral indentation height after explant is constantly higher than that produced by LSB. Comparing with the radius method, the direct method underestimates the indentation height.

We analysed the indentation heights according to two measurement methods - the radius method and the direct method - by paired t-test. The indentation height measured by the radius method was significantly larger than that measured by the direct method ($p < 0.05$) in all groups.

The mean degrees of scleral shrinkage and thickness increase after Holmium:YAG LSB were 20.5% and 37.2%; 16.9% and 31.1% after Thulium:YAG LSB.

3.2. IOP

Mean P_{\max} , regardless of baseline IOP, was $4.9 \pm 0.88 \text{ mmHg}$. And mean $T_{1/2}$ and $T_{1/4}$ were 0.76 ± 0.18 and 3.64 ± 0.94 seconds, respectively. There was a tendency that P_{\max} decreased and $T_{1/4}$ shortened as the baseline IOP elevated (Fig. 2).

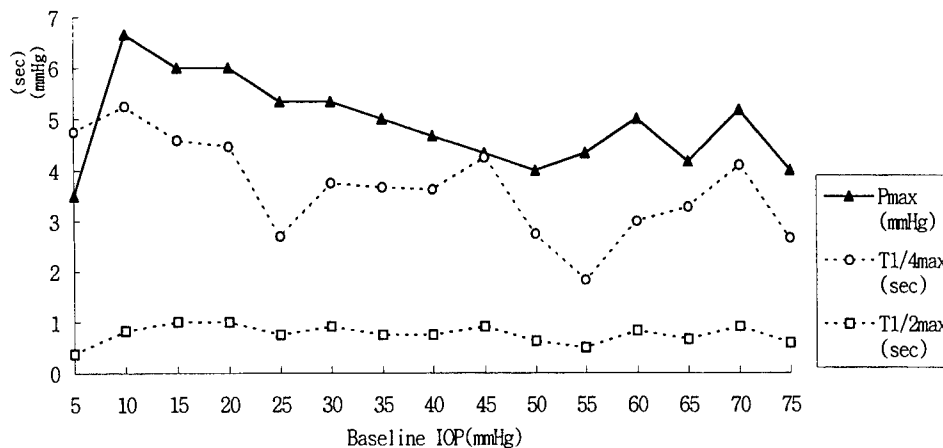


Fig. 2. The effect of LSB on IOP is assessed. The mean IOP elevation from each baseline IOP after one laser spot application is 4.9 mmHg . The IOP decreases into the one fourth of its elevation after 3.64 seconds.

[P_{\max} : maximum IOP elevation after one laser spot application;
 $T_{1/2\max}$, $T_{1/4\max}$: time required for the peak IOP elevation to decrease into half and a quarter of its value, respectively]

These data imply that the final IOP would be approximately 25 mmHg , if sixteen laser spots were made consecutively with 4 seconds interval [$24.6 = 16 \times 4.9 \times 1/4 + 5$ (baseline IOP)]. The final IOP of the actual experiment ($27, 24 \text{ mmHg}$) nearly coincided with the predicted value (Fig. 3).

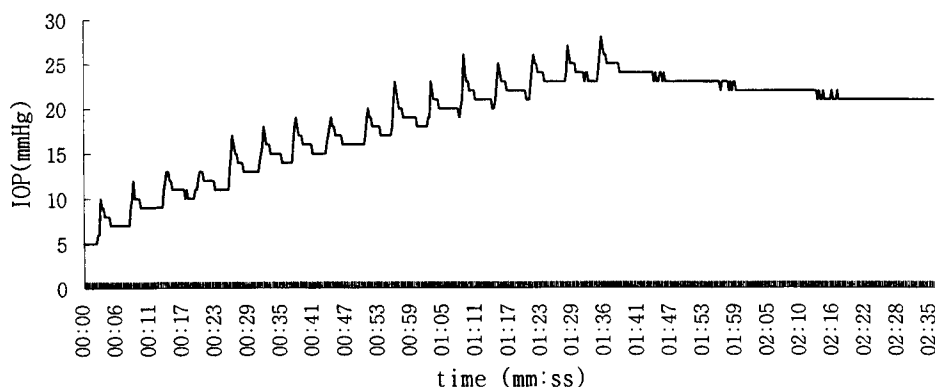


Fig. 3. The IOP change is monitored during the formation of 16 Thulium:YAG laser spots with 4 second interval. The final IOP of 27 mmHg in this example nearly coincides with the predicted final IOP.

4. DISCUSSION

This is the first study to evaluate the height of scleral indentation after scleral buckling procedure, not with indirect method like ultrasonography, but with cross sections of the eyeball. Scleral indentation height of fresh explant measured by ultrasonography is reported as 4mm ^{5, 6}. Compared with the indentation height of the explant group in this study, the previously reported buckle height was significantly larger. The apparent overestimation of buckle height in previous studies may be caused by a posterior image magnification associated with ultrasonography.

Although the indentation height of 1.30mm produced by Thulium:YAG LSB was less than that of the explant, it could still be adequate for use in retinal detachment since the recommended equatorial circumference shortening for encircling procedure is of 10 to 20%^{7, 8}, which corresponds to a 1.2 to 2.4mm scleral indentation height.

The reason for inconsistency in indentation height according to the different measurement methods is described in Fig. 4. Because the external circumference of the eyeball is apparently shortened by LSB or by explant, the radius of eyeball in the treated meridian decreases, which augments the indentation height produced mainly by local buckling effect. In contrast to the radius method, the direct method does not reflect the radius decrease in the buckled meridian.

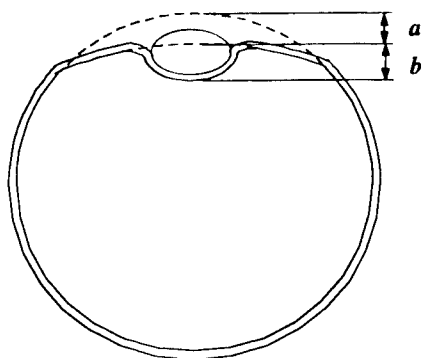


Fig. 4. Factors associated with scleral indentation height: Factor b is directly related to the local buckling effect, whereas factor a is dependent on decrease in eyeball circumference. In contrast to the direct method, measurement by the radius method takes account of both factors a and b.

The total energy delivered to each treatment spot was 1285 and 815mJ with the Holmium:YAG and the Thulium:YAG, respectively. These were equivalent to total fluence of 25.7 and 16.3J/cm² with which Sasoh et al. produced about 20% of scleral shrinkage without significant tissue damage⁴. Although the amount of scleral shrinkage by LSB is known to decrease exponentially as IOP increases⁴, there are few data about the influence of LSB on IOP. The degree of scleral shrinkage in the baseline IOP of 20mmHg was known to be 80% of that in the baseline IOP of 5mmHg⁴. Our study results suggest that at least 4 seconds be allowed between each laser spot application for efficient LSB.

In consideration of the interaction with IOP, LSB may be most useful when combined with vitrectomy, since hypotony is easily produced and maintained during vitrectomy. Cases (i. e. selected cases of proliferative vitreoretinopathy) which require broad and shallow scleral indentation in combination with vitrectomy are well suited for LSB to simplify the operation by avoiding complications associated with scleral explant.

5. ACKNOWLEDGEMENTS

This study was supported in part by the Florida Lions Eye Bank, Research to Prevent Blindness, the Henri and Flore Lesieur Foundation, New Star Lasers and Fight for Sight, in memory of Lee S Hochwald. We wish to thank David Denham MS for fabrication of the eye-container, and William Lee for fabrication of the laser probe.

6. REFERENCES

1. W. E. Smiddy, D. N. Loupe, R. G. Michels, C. Enger, B. M. Glaser, and S. deBustros, "Refractive changes after scleral buckling surgery", *Arch. Ophthalmol* 107, pp. 1469-1471, 1989.
2. W. E. Smiddy, D. N. Loupe, R. G. Michels, C. Enger, B. M. Glaser, and S. deBustros, "Extraocular muscle imbalance after scleral buckling surgery", *Ophthalmology* 96, pp. 1485-1489, 1989.
3. Q. Ren, G. Simon, J. M. Parel, and W. E. Smiddy, "Laser scleral buckling for retinal reattachment", *Am. J. Ophthalmol* 115, pp. 758-762, 1993.
4. M. Sasoh, J. M. Parel, F. Manns, I. Nose, J. Commander, and W. E. Smiddy, "Quantification of Holmium:YAG and Thulium:YAG laser induced scleral shrinkage for buckling procedures", *Ophthalmic Surg Lasers* (in press; April-May issue) 1998.
5. A. R. Irvine, and R. D. Stone, "An ultrasonographic study of early buckle height after sponge explants", *Am. J. Ophthalmol* 92, pp. 403-406, 1981.
6. R. D. Stone, A. R. Irvine, E. Santos, "An ultrasonographic study of the persistence of buckle height three years after segmental sponge explant", *Am. J. Ophthalmol* 84, pp. 508-513, 1977.
7. H. Lincoff, I. Kreissig, and L. Parver, "Limit of constriction in the treatment of retinal detachment", *Arch. Ophthalmol* 94, pp. 1473-1477, 1976.
8. A. M. Hamilton, and W. Taylor, "Controlled encircling procedure for retinal detachment", *Br. J. Ophthalmol* 56, pp. 695-699, 1972.

SESSION 3

Ocular Surgery

Development and clinical application of Excimer Laser Corneal Shaping

P. Homolka^a, R. Biowski^b, W. Husinsky^c, C. Blaas^c, Ch. Simader^b, I. Baumgartner^b, St. Kaminski^b, and G. Grabner^d

^aDepartment of Biomedical Engineering and Physics, University of Vienna, Austria

^bDepartment of Ophthalmology, University of Vienna, Vienna, Austria

^cInstitut für Allgemeine Physik, University of Technology Vienna, Wiedner Hauptstrasse 8-10, A-1040 Vienna, Austria

^dDepartment of Ophthalmology, St. Johanns Hospital, Salzburg, Austria

ABSTRACT

Excimer Laser Corneal Shaping using an 193 nm Excimer Laser (ArF) provides a possibility for the fabrication of corneal transplants of various forms for various clinical applications such as (epi-)keratoplasty. Another area of application envisioned is the production of „living contact lenses“ for epikeratophakia. A device for lathing and perforating corneal donor tissue with a scanning laser beam is presented. A new ablation algorithm (Optimized Scanning Laser Ablation) was recently developed and increased the quality of lenticules and donor buttons considerably.

Keywords: Corneal transplants, Keratoplasty, Epikeratophakia, Laser-Tissue Interaction, Excimer Laser, Non Thermal Ablation, Photoablative Decomposition

1. INTRODUCTION

Corneal grafts are needed in ophthalmology for curative surgery on a regular basis. Thus transplants are often used in congenital abnormalities like a dermoid, to replace scarred tissue or in healing dystrophical defects like pemphigoid. There are several possibilities for their production, the most common being mechanical shaping and cutting of donor tissue.

„Contact lenses“ made of corneal tissue can be produced using a cryolathe. This procedure is hampered with the disadvantage, that freezing and lyophilisation alters the stromal matrix and the viability of the keratocytes.

Not only does laser lathing and perforation avoid these problems, but they also allow a much higher degree of flexibility, in particular, in the overall shape and wing zone geometry, which can be chosen to meet the surgeons' preferences.

2. THE ELCS METHOD

The Excimer Laser Corneal Shaping (ELCS) System - a schematic view is shown in **Fig. 1** and a detailed view of the beam delivery system in **Fig. 2** - was developed in close cooperation of the Institut für Allgemeine Physik, Technische Universität Wien, and the Department of Ophthalmology, University of Vienna¹⁻³. The prototype has been built at the University of Technology Vienna, Institut für Allgemeine Physik and first clinical applications have been reported⁴. The system is now commercially available from Schwind, Kleinostheim, Germany, as an add-on device for the Keratom, an in-vivo Corneal Shaping system. The ELCS System uses a 193 nm (ArF) excimer laser beam to lathe and perforate corneal donor tissue in vitro. Ablation is performed in a scanning mode where a laser spot of about 1 mm diameter scans the corneal surface in concentric rings to lathe the tissue to the thickness required before it is perforated using a semi-circular laser spot to cut the form of the transplant of choice. If refractive lenticules for epikeratophakia or grafts to be used for epikeratoplasty are produced, i. e. grafts where it is necessary to lathe the corneal tissue to a thickness smaller than the original, the donor cornea rests in a molded metal holder while the laser beam treats the tissue from the endothelial side. If donor buttons for penetrating keratoplasty are produced, the cornea rests on a viscous gel facing the laser beam (only used for trephination) on the epithelial side.

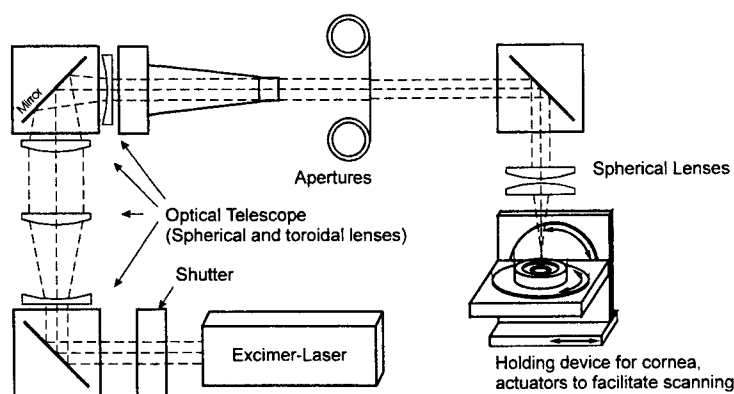


Fig. 1: Schematic drawing and partial view of the ELCS System (Schwind Keratom).

Since in the case of the ELCS the laser-tissue interaction takes place *in vitro*, several differences and advantages as compared to *in vivo* applications are evident. The hazard of dangerous secondary radiation, particularly about 300 nm⁵, is avoided. Laser fluence is also not severely restricted to low values since no negative side effects on other tissues have to be considered. Thus the plateau in the ablation rate vs. fluence dependence^{2, 5-9} at approx. 500 to >1000 mJ/cm² can be utilized reducing effects of an inhomogeneous laser spot and pulse-to-pulse fluctuations in the laser's energy output (see also Fig. 3).

The ELCS System at the eyebank of the Department of Ophthalmology, University of Vienna, is equipped with a Lambda Excimer Laser (193 nm) with a pulse energy of 400 mJ and a pulse widths of 23 ns. During preparation of a graft repetition frequencies ranging from 0.5 to 40 Hz (in 1/100 Hz steps) can be used. The beam is shaped by changeable apertures; semi-circular and circular spots ranging from 0.1 to 2 mm diameter in the working plane can be selected. By regulating the high voltage in the laser generator an output fluence of approx. 0.8 J/cm² on the cornea is selected.

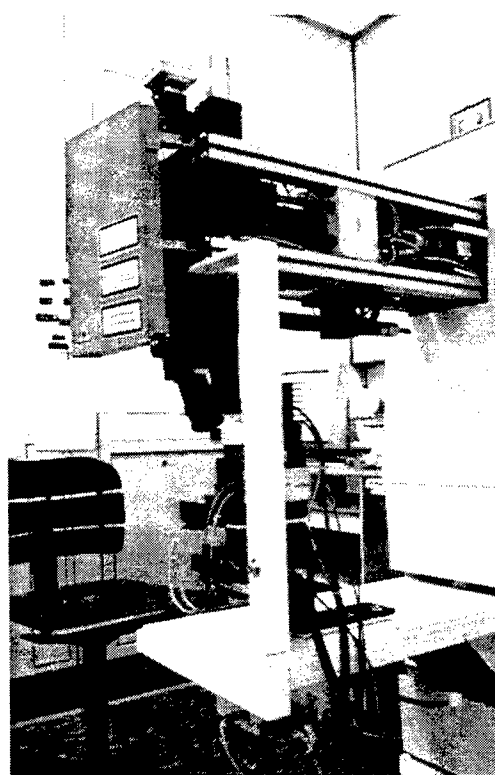


Fig. 2: Vie of the beam delivery system of the Schwind ELCS System

3. MODELS OF LASER - TISSUE INTERACTION

Studies on model systems as well as measurements of tissue ablation have established three different mechanisms for how the energy deposited by the laser photons into electronic transitions of the tissue molecules can be converted into kinetic energy of the desorbing molecules. The specific characteristics of these mechanisms then critically determine the damage induced in the tissue surrounding the interaction zone of the laserlight with the tissue.

"Thermal" ablation is observed whenever the photon flux is sufficiently high to heat the tissue by conversion of electronic excitations into vibrational energy. An explicit threshold flux for ablation and strong damage induced in the surrounding tissue is characteristic for this process. For practical use, situations in which thermal ablation occurs should be avoided in applications like corneal shaping. "Photochemical (non-thermal) ablation", also called photochemical or photoablative decomposition¹⁰, on the other hand, shows extremely low damage, due to the strong localization of the energy. The direct conversion of electronic energy into fragmentation happens on a time scale short enough to avoid thermalisation and does not create vibrating ("heated") molecules. This process in its pure form should not exhibit a flux-threshold for ablation. However, it is not quite understood whether the fragmentation can happen only at the topmost layer or whether bond-breaking in several layers of the tissue can take place accompanied by immediate ejection of the molecules. In all cases rather low ablation rates are expected. This seems to be confirmed by experimental data, if one compares the ablation rates with those achieved by other mechanisms. However, typical ablation rates of a few $\mu\text{m}/\text{pulse}$ demand the bond-breaking to evolve in a corresponding large volume of the tissue.

A third mechanism has also been experimentally identified⁶, which is basically of thermal nature, but differs from the conventional thermal ablation in that it requires extremely high heating (energy deposition), resulting in "explosive ablation" of the irradiated material. The main difference of this mechanism as compared to the thermal situation is the fast time scale in which the energy is transformed to kinetic energy, not allowing the unwanted thermal energy transfer to non-irradiated tissue. This makes this mechanism interesting for practical applications. E.g., the interaction of infrared laser light around 3 μm with water in corneal or dental tissue is believed to fall into this category of ablation mechanism.

4. LASER ABLATION OF CORNEAL TISSUE

Laser Ablation of Corneal Tissue has been studied to greater extent over the last couple of years than any other biological tissue. In spite of many attempts to use different laser wavelengths and laser pulse times, ablation with 193 nm laser light, as produced by an ArF excimer laser, still represents the case with the least damage and overall best quality. Other wavelengths, believed to couple via water or specific absorbers and resulting in "explosive ablation", can basically be used and the damage is relatively small, but the quality of 193 nm ablation cannot be achieved. In this case a substantial part of the ablation is generally assumed to be of non-thermal, photochemical (photoablative) nature.

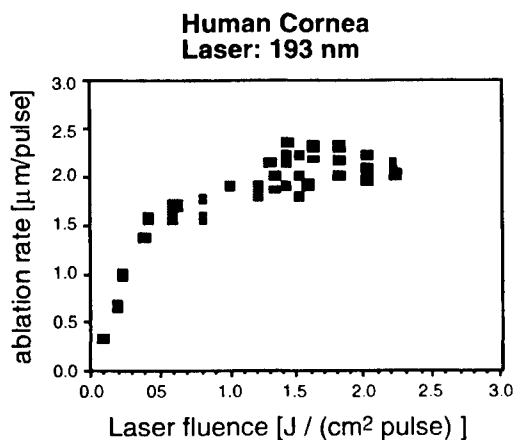


Fig. 3: Ablation rate vs. laser Fluence: A plateau in the ablation rate starting at approximately 0.5 J/cm² can be observed.

patient's eye.

The three different types of grafts are:

1. Donor buttons for penetrating keratoplasty. In this case, the graft extends over the full thickness of the cornea, from the epithelium (a very regenerative layer separating the eye against the air), Bowman's layer, the stroma, Descemet's layer to the endothelium, a very sensitive cell layer separating the cornea against the aqueous humor. Great care is necessary to ensure viability of the endothelium.
2. Transplants for epikeratoplasty. In this case, the transplant consists only of the upper layers of the donor cornea. To achieve this, the donor tissue is lathed to the desired thickness before trephination. Typically, a wing zone (thinner than the rest of the graft) is made in the peripheral part of a circular transplant. If the graft is used to fit into an arbitrarily formed excision wound (as after excision of a dermoid as shown in this work) no wing zone is desired.
3. Lenticules for correction of the eye's refractive power: In epikeratophakia, „living contact lenses“, i. e. lenticules with defined refractive power, are used. For this type of grafts, highest precision is necessary. In contrast to the other types,

* The data for this plot was measured using donor corneas not suitable for transplantation purposes. These corneas, since stored in a medium were swollen, thus differences in the ablation rate to native corneas in the literature are to be expected

A typical curve showing the ablation rate vs. laser fluence is shown in Fig. 3. The absolute values will vary slightly, depending on the specific parameters of the cornea, but the general features have been well established. For in vitro applications, where the limitations on the laser fluence used are not as strict as for in vivo applications, the regime between 0.5 and 1.3 J/cm² is of particular interest. In this case the ablation rate is practically independent of the laser fluence. Therefore, the influence of intensity fluctuations of the lasers can be minimized, as already outlined above.

5. DIFFERENT TYPES OF CORNEAL GRAFTS

With the ELCS (or other methods) different types of corneal grafts can be produced. In the ELCS, combinations are also possible, e. g. a refractive lenticule with an arbitrary (non-circular) shape. The possibility to produce grafts with arbitrary shape is one of the major advantages of the ELCS as compared to other systems. In many cases, as in the one shown in this publication, it is highly desirable to produce a graft of a predefined shape given by the expected form of the tissue excision necessary in the

refractive lenticles are - until now - produced on an experimental basis and are not yet available for transplantation purposes.

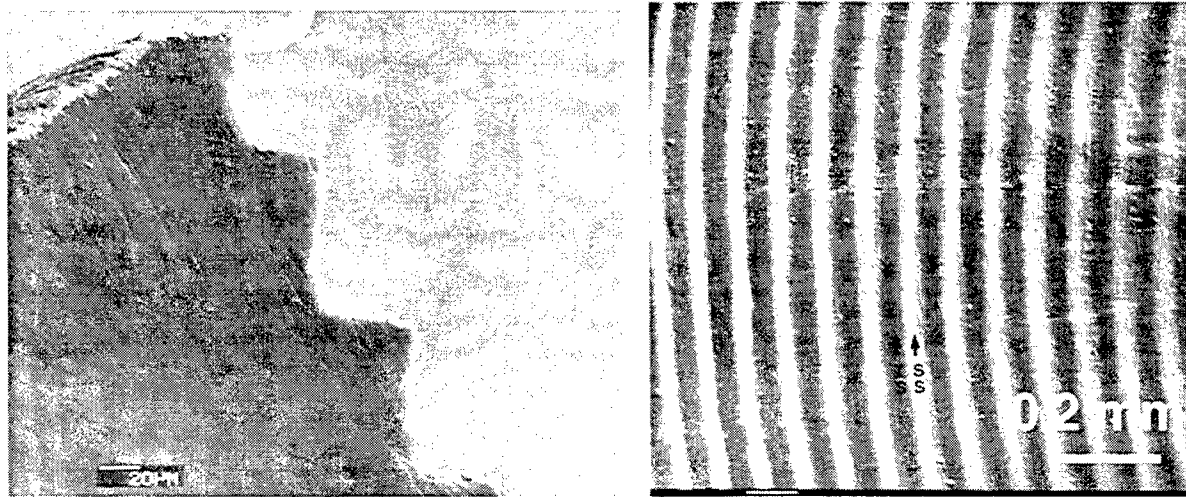


Fig. 4: Surface structure of treated donor Cornea using equidistant ablation radii.

6. OPTIMIZED SCANNING LASER ABLATION

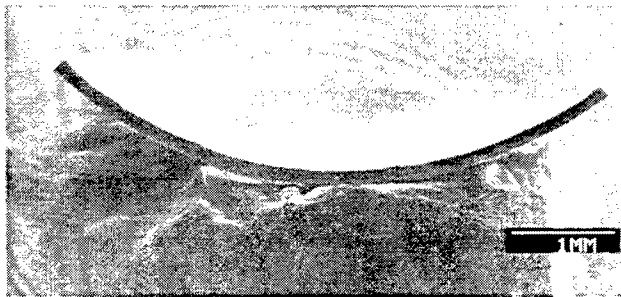


Fig. 5: Lamellar graft prepared using OSLA.

only used for trephination, i. e. cutting the shape of the desired corneal button. Depending on form and size, typical preparation times are about 10 minutes. If the donor tissue has to be lathed, the situation is different. The longest preparation times are caused by the combination of both, i. e. lathing followed by trephination of a complicated, large form.

Scanning with equidistant ablation radii manifests itself as waves with a period of the radial stepping distance, which usually was 100 µm. Optimized Scanning Laser Ablation eliminates this problem by optimizing the ablation radii in a manner to achieve a smoother surface with optimal quality in the central area. This is of crucial importance to assure best vision for the patient receiving the transplant. Still, a careful consideration of surface smoothness versus preparation time has to be done, since on the one hand the longer the preparation time the better the theoretically achievable quality of the lathed surface. On the other hand, the maximum preparation time is limited by desiccation related shrinking of the donor corneal tissue. Using Optimized Scanning Laser Ablation the technician can influence these two parameters interactively. In most cases surface smoothness at larger radii, like in the wing zone, is not as critical. This allows a reduction in preparation time.

In *Fig. 4* and *Fig. 5* a comparison of the new method in respect to the former (equidistant scanning radii) is given. While in *Fig. 4* the wavelike structure is evident, it does not appear in *Fig. 5* due to the optimization of the ablation radii.

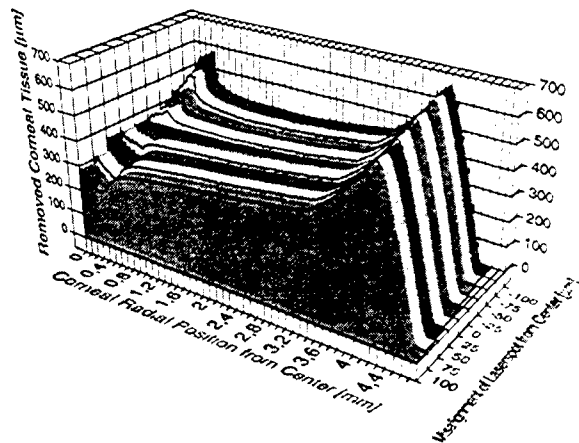


Fig. 6: Influence of laser spot misalignment from ideal central position.

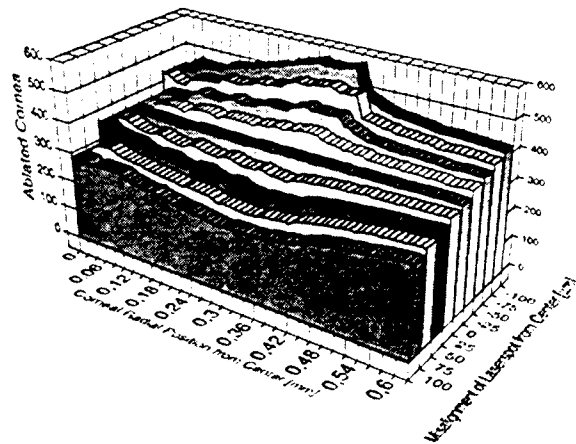


Fig. 7: Influence of laser spot misalignment from ideal central position; detail from Fig. 6.

In Optimized Scanning Laser Ablation (OSLA) several hardware related specifications are also taken into account. Since toroidal lenses and tilted mirrors are used, it is hardly possible to form an ideally circular laser spot. Indeed, the spot exhibits the shape of an ellipse, with differences of the radii in the per cent region. Not only is this exact form taken into account, but also the divergence angle of the laser radiation. This is of importance, because tilting the cornea under the laser beam slightly alters the distance to the optical system.

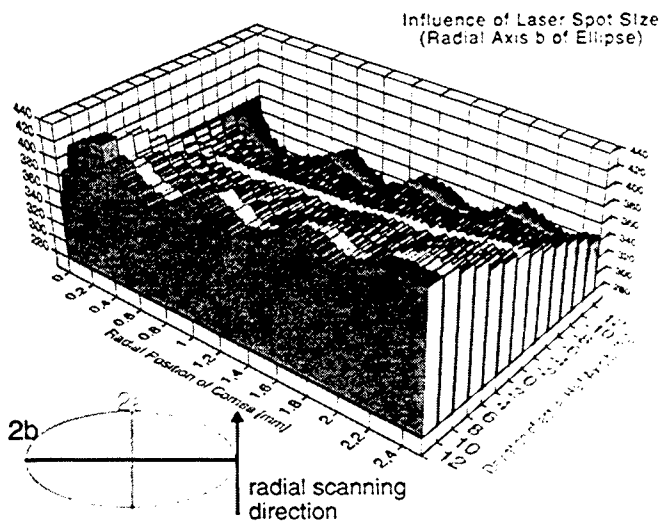


Fig. 8: Influence of errors of laser spot size (axis b) on the quality of ablation. Compare the wavelike structure for errors in the b -axis larger than a few % with Fig. 4. The curve for error zero is shown in the middle of the y -axis (white curve).

evident, that a great deal of care has to be taken to assure perfectly aligned beam incidence to get good results. Thus, the alignment is checked and corrected before each treatment.

Another very sensitive parameter is the actual spot size (and form) as illustrated in Fig. 8. The elliptically shaped beam is measured in the working plane after the alignment procedure prior to calculating the ablation profile since the actual values are used as input parameter for the calculation of the ablation.

Central ablation is of particular concern, since in most cases it is this part of the graft being transplanted into the optical center of the patient's eye. In order to form very fine structures, two approaches were used: The original ELCS applied smaller laser spots, typically three different sizes to form the center. In principle a feasible attempt this is hampered with the problem, that changing the apertures to form different spot sizes may (and does) change the actual point of incidence of the beam on the corneal tissue. Although only a tiny effect, it is a major problem since lathing is very sensitive to errors of this kind. In OSLA only one size of spots, namely 1 mm nominal diameter, is used. To form structures with arbitrary radial resolution, the central spots are set eccentrically, i. e. in a manner where the center of rotation of the cornea does not coincide with the center of the laser spot. Enabling one to gain much better results in the center, this necessitates an extremely well adjusted beam, being very sensitive to spot misalignment from central position as demonstrated by Fig. 6 and Fig. 7. They show calculations of ablation profiles (ablation depth vs. radius) for an optimally aligned and a misaligned beam, respectively. It becomes

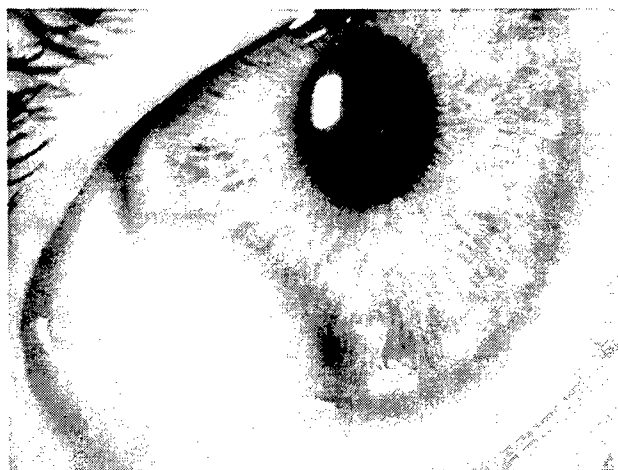


Fig. 9: Connatale dermoid of the conjunctiva, preoperative. Using digital image processing, the form of the desired graft was determined from this photograph.



Fig. 10: Postoperative photograph of the patient's eye. A 350 µm thick lamellar graft prepared with the ELCS covers the defect after excision of the dermoid.

7. CLINICAL APPLICATIONS: AN EXAMPLE

In the case of a five year old patient a lamellar keratoplasty was used to treat a connatal dermoid, a benign proliferation of the conjunctiva spreading into the cornea. Operation indication is justified by the growing tendency of the dermoid which leads to irregular astigmatism adversely affecting vision. In the area of the dermoid metabolism deficits may also occur in the cornea.

In the operation (Prof. Skorpik, Department of Ophthalmology, University of Vienna) (*Fig. 9, Fig. 10*) the dermoid was lamellarely excised. Its largest dimension was 6.3 mm. The incurred tissue defect was replaced with a lamellar graft of 350 µm thickness prepared with the ELCS. The form of the transplant was determined using digital image processing and a preoperative photograph of the patient's eye. To allow more flexibility for the surgeon three different transplants were prepared, having the same form but different thickness. During the operation, the graft with 350 µm was chosen. It fit perfectly into the excision defect where it was fixated. The transplant remained clear and showed good healing tendencies.

8. CONCLUSIONS AND OUTLOOK

Since the donor cornea is a biological tissue, there is a variation in thickness and radius of curvature that has to be taken into account. For that reason, every individual donor cornea has to be measured. Especially central and peripheral thickness at a radius of 3 to 4 mm are very crucial input parameters for the ablation algorithm.

Currently ultrasound pachymetry is used, although a more convenient and precise method would be preferable. Current work is focused on applying a Laser Scanning Microscope to measure the topography of the donor cornea. This method will also be used to evaluate the produced graft before transplantation.

In the ELCS photo ablation is achieved with the method considered most accurate and least damaging to adjacent tissue, namely photoablative decomposition¹⁰⁻¹² of the bio-molecular structure using 193 nm wavelength. Using this wavelength (produced with an ArF excimer laser) corneal tissue can be cut with a damage zone < 0.3 µm^{1, 2, 6, 7, 13-15} assuring the

viability of the keratocytes in the area adjacent to trephination. Another advantage when producing donor buttons for penetrating keratoplasty is that a smaller damage zone of the endothelium is expected for laser trephination than for mechanical cutting^{16, 17}.

The use of small laser spots in a scanning mode, what is specific to the ELCS, allows the design of nearly arbitrarily shaped transplants with almost any surface topography. With the introduction of Optimized Scanning Laser Ablation surface smoothness and quality could be drastically improved. This newly developed algorithm optimizes ablation radii (in contrast to equidistant radii used by the commercially available ELCS System) and applies a more sophisticated mathematical model, taking the actual spot form and size into account. These parameters (radial axes lengths of the elliptical spot) are measured before every treatment. Prior to measuring, the ELCS is adjusted to assure optimal alignment of laser spot - center of cornea. As shown in this article, alignment is extremely critical since a misalignment of the laser spot from center will result in severe inaccuracies in the lathed transplant.

Several patients have received lamellar keratoplasty grafts produced with this system.

Employing the methods discussed we believe this procedure to be an optimal preparation for corneal grafts.

9. ACKNOWLEDGMENTS

We want to thank A. Lametschwandtnr and W. Muss (Department of Zoology, University of Innsbruck, Austria) for making the SEM images.

10. LITERATURE

1. J. Altmann, G. Grabner, W. Husinsky, S. Mitterer, I. Baumgartner, F. Skorpik and T. Asenbauer, "Corneal Lathing Using the Excimer Laser and a Computer-Controlled Positioning System: Part I-Lathing of Epikeratoplasty Lenticules", *Journal of Refr. and Corneal Surgery*, **7**, pp. 377-384, 1991
2. W. Husinsky, S. Mitterer, J. Altmann, G. Grabner, I. Baumgartner, F. Skorpik and T. Asenbauer, "Corneal Lathing Using the Excimer Laser and a Computer-Controlled Positioning System: Part II-Variable Trephination of Corneal Buttons", *Refractive & Corneal Surgery*, **7**, pp. 385-389, 1991
3. R. Biowski, I. Baumgartner, T. Barisani, S. Kaminski, P. Homolka, W. Husinsky, A. Lametschwandtnr and G. Grabner, "Zum Einsatz eines spezialisierten Excimer-Laser-Systems (ELCS-System) in der Hornhautbank", *Spektrum Augenheilkd.*, **11**, 2 pp. 51-63, 1997
4. D. Gruber, W. Husinsky, G. Grabner, I. Baumgartner, J. Scholman, J. Krüger and W. Kautek "Nano- and Femtosecond - Laser Processing of Human Donor Corneal Transplants and Lenticules for Corneal Surgery" *LaserMed* 95, München, Germany, 1995.
5. G. Petit, M. Ediger and Weiblinger, "Excimer laser ablation of the cornea", *Opt. eng.*, **34**, 3 pp. 661, 1995
6. W. Husinsky, S. Mitterer, G. Grabner and I. Baumgartner, "Photoablation by UV and Visible Laser Radiation of Native and Doped Biological Tissue", *Applied Physics B - Photophysics and Laser Chemistry*, **49**, pp. 463-467, 1989
7. W. Husinsky, G. Grabner, I. Baumgartner, F. Skorpik, S. Mitterer and T. Temmel "Mechanisms of Laser-Ablation of Biological Tissue" Desorption Induced by Electronic Transitions. DIET IV, Kranichberg, Austria, 1990.
8. W. Kautek, S. Mitterer, J. Kruger, W. Husinsky and G. Grabner, "Femtosecond-Pulse Laser Ablation of Human Corneas", *Applied Physics A - Solids and Surfaces*, **58**, 5 pp. 513-518, 1994
9. M. Campos, X.W. Wang, L. Hertzog, M. Lee, T. Clapham, S.L. Trokel and P.J. McDonnell, "Ablation Rate and Surface Ultrastructure of 193 nm Excimer Laser Keratotomy", *Invest Ophthalmol Vis Sci*, **34**, 8 pp. 2493-2500, 1993
10. G.H. Petit and R. Sauerbrey, "Pulsed Ultraviolet Laser Ablation", *Applied Physics A*, **56**, pp. 51-63, 1993
11. R. Srinivasan, J.J. Wynne and S.E. Blum, "Far-UV photoetching of organic material", *Laser Focus*, **19**, pp. 62, 1983
12. R. Srinivasan and B. Braren, "Ultraviolet laser ablation and etching of polymethyl methacrylate sensitized with an organic dopant.", *Appl. Phys. A*, **45**, pp. 289, 1988
13. J. Marshall, S. , S. Trokel, S. Rothery and H. Schubert, "An ultrastructural study of corneal incisions induced by an excimer laser at 193 nm.", *Ophthalmology*, **92**, pp. 740, 1985

14. R.R. Krueger, S.L. Trokel and H.D. Schubert, "Interaction of ultraviolet laser light with the cornea.", *Invest. Ophthalmol. Vis. Sci.*, **26**, pp. 1455, 1985
15. J. Marshall, S. Trokel, S. Rothery and R.R. Krueger, "A comparative study of corneal incisions induced by diamond and steel knives and two ultraviolet radiations from an excimer laser.", *Br. J. Ophthalmol.*, **70**, pp. 482, 1986
16. T.E. Clinch, K.L. Fung and P.L. Laibson, "Corneal Endothelial Cell Loss Following Trephination", *Ophthalmic Surg.*, **19**, 10 pp. 703-705, 1988
17. H. Bull, S. Deutschmann and H.W. Scholte, "Doppelt geführtes Vakuumtrepansystem „Asmotom“, *Fortschr. Ophthalmol.*, **88**, 5 pp. 574-576, 1991

Preliminary results of hyperopic photorefractive keratectomy (HPRK) at Cedars-Sinai Medical Center

Ezra Maguen^(1,2), Anthony B. Nesburn^(1,2), James J. Salz^(1,3)

⁽¹⁾Ophthalmology Research Laboratories, Cedars-Sinai Medical Center, ⁽²⁾The Jules Stein Eye Institute, UCLA School of Medicine and the ⁽³⁾Doheny Eye Institute, USC School of Medicine, Los Angeles, CA, USA.

ABSTRACT

The preliminary results of hyperopic photorefractive keratectomy (HPRK) performed with the VISX-Star excimer laser on 25 eyes of 25 patients are presented. 13 of 25 eyes had vision of $\geq 20/40$ at 1 month and 17 of 19 eyes saw $\geq 20/40$ 3 months postoperatively. 15 of 25 patients were over corrected $\geq 1.00D$ at one month and 2 patients were overcorrected with the same amount at three months postop. At three months, no undercorrections of $\geq 1.00D$ were observed. At three months postop, all eyes saw for near J5 or better. Complications included one case of induced astigmatism and one case of a loss of two lines of best corrected vision - from 20/16 to 20/25. HPRK appears to be safe and effective in correcting hyperopia of up to 4.00D in the short term.

1. INTRODUCTION

Vision correction with the excimer laser has been practiced clinically for the past eight years. Initially, myopia and myopic astigmatism could be corrected. Following lengthy FDA guided studies, two systems from VISX and Summit Technologies were approved by this agency in the US for the correction of myopia of up to 7.00D. VISX subsequently obtained FDA approval for the correction of myopic astigmatism of up to 4.00D and recently obtained approval for the correction of higher myopias of up to 12.00D. The correction of Hyperopia (far sightedness) with the excimer laser was studied by VISX investigators since 1993. In early 1997, a phase III FDA guided protocol was undertaken at Cedars-Sinai Medical Center using the VISX Star excimer laser for the correction of hyperopia of up to 4.00D with 1.00D or less of astigmatism. The ability to correct hyperopia was made possible by adding a proprietary module into the laser delivery system which is capable of diverting the beam to the periphery of the cornea. With deeper ablation in the corneal periphery than in its center, a steeper profile of the surface of the cornea can be created thereby allowing the correction of hyperopia.

2. PATIENTS AND METHODS

2.1 Inclusion criteria

The patient minimum allowable age was set at 21 years. Refraction needs to be stable within $\pm 0.50D$ within the last year. Pathology of the anterior segment of the eye and some systemic diseases such as autoimmune disease, pregnancy and breast feeding were grounds for exclusion. Because of the higher mean age of the hyperopic population, recruitment of the patient population was more difficult.

2.2 Patient demographics

Twenty five patients participated in the study and 25 eyes were evaluated. Males and females participated. The mean age was 55 years (range: 32-72 years).

2.3 Preoperative data:

In addition to a complete eye examination including cycloplegic refraction and corneal topography, the following testing was undertaken:

2.3.1 Contrast sensitivity with a Vector Vision CSV-1000E test face at 3,6,12,18 cycles per degree intensity, in dim (mesopic) conditions ($<3\text{cd/m}^2$) with and without a glare source and bright (photopic light (average 85cd/m^2) without glare.

2.3.2 Schirmer II test to document adequate tearing

2.3.3 Evaluation of the anterior chamber angle by Gonioscopy.

2.3.4 Central and Peripheral (nasal) endothelial cell count and cell analysis with a Konan Noncontact Robo[™] SP100fa[™].

The mean (\pm SD) preoperative spherical equivalent was $2.69\pm 0.8\text{D}$ with a range of 1.00 to 4.00 D. The mean best corrected visual acuity was 20/19.1 with a standard deviation of 4.59 and a range between 20/32 to 20/12.5 on the ETDRS scale.

2.4 Surgical procedure and postoperative management

Topical anesthesia was given preoperatively using a total of 4 doses of Proparacaine in the operated eye. With the patient in the supine position and lid speculum in place, the epithelium of the cornea is removed within a optical zone of 9mm centered on the pupil entrance. After ensuring proper centration, the laser is activated. At the close of the procedure, topical antibiotics ,NSAID's, and steroids are applied along with a therapeutic contact lens. The contact lens was worn on an extended wear basis for a minimum of 4 days or until complete healing of the corneal epithelium. NSAID's were discontinued within 24 hours and topical antibiotics were used for as long as the lens remained in place. Fluorometholone 0.1% (topical steroid was used in a tapering mode for 4 months then discontinued. Postoperative evaluations were carried out daily until lens removal and at 1,3,4,5,6, 9,12,24 months thereafter.

3. RESULTS

Postoperative results are reported for 1 and 3 months postoperatively and for the last evaluation which occurred between 4 and 6 months postoperatively.

3.1 Uncorrected visual acuity (UCVA):

The distribution of UCVA is detailed for the postoperative periods of one month (Fig.1), 3 months (Fig.2) and last evaluation (Fig.3).

Figure 1
DISTRIBUTION OF UCVA 1 MONTH
POSTOPERATIVELY
N = 25

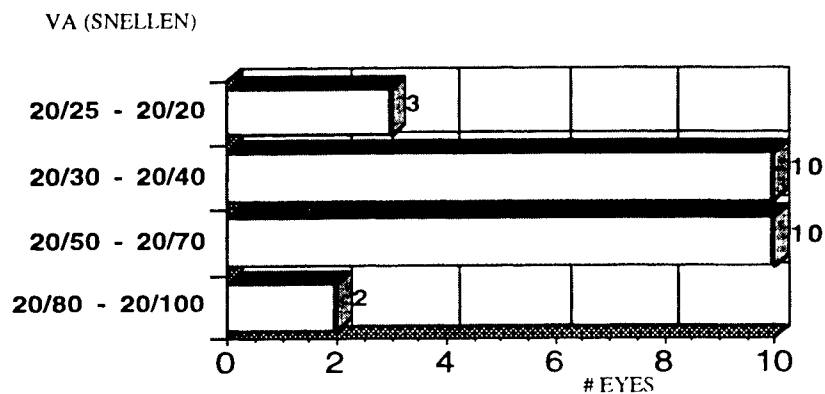


Figure 2
DISTRIBUTION OF UCVA 3 MONTHS
POSTOPERATIVELY N = 19

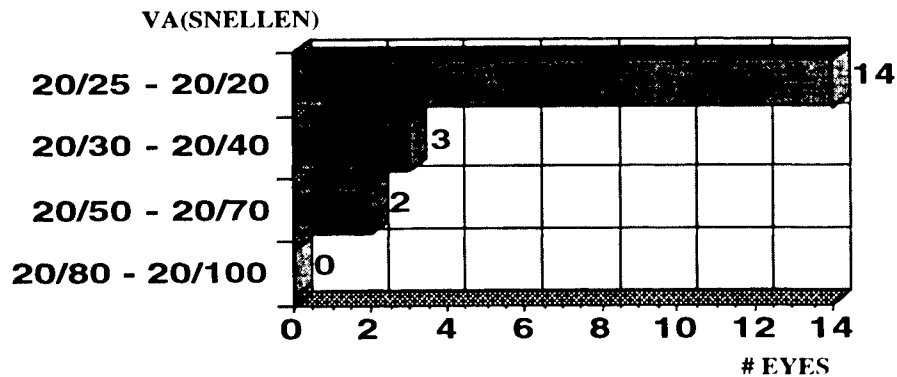
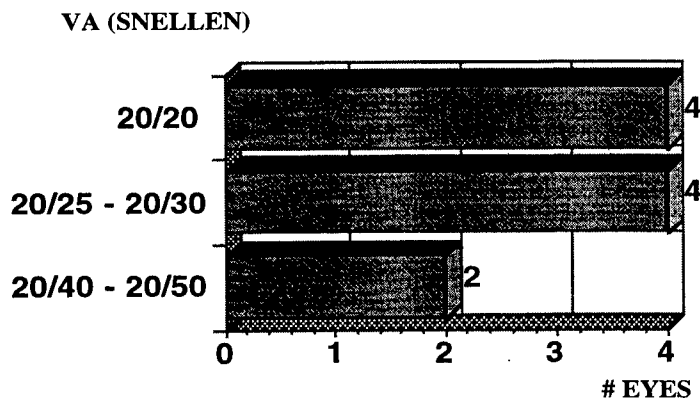
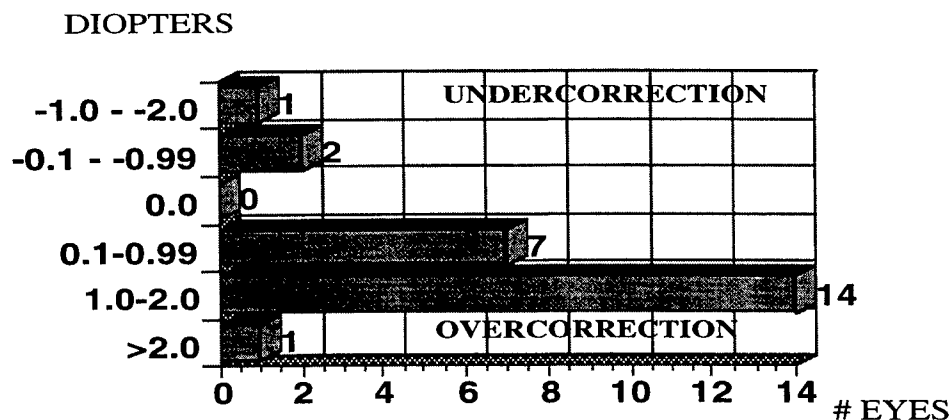


Figure 3
DISTRIBUTION OF UCVA - LAST EXAM
N = 10



3.2 Refractive outcome:

Figure 4
OVER / UNDERCORRECTION 1 MONTH
POSTOPERATIVELY N = 25



The progression of refraction over the postoperative period is somewhat different than that seen following myopic corrections with the excimer laser. Basically, an overcorrection is expected at the first month postoperatively followed by emmetropia at about three months postoperatively. Nearsightedness is therefore initially induced and decreases over time. The distribution of refractive outcomes will be therefore presented in terms of under and overcorrection relative to the intended correction in figures 4-6 for 1 and 3 months postop. And the last evaluation (4-6 months postop).

Figure 5

OVER / UNDERCORRECTION 3 MONTHS POSTOPERATIVELY N = 19

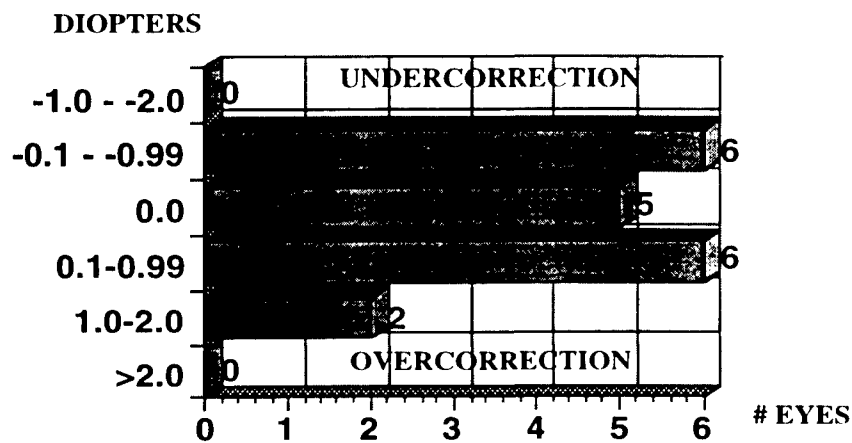
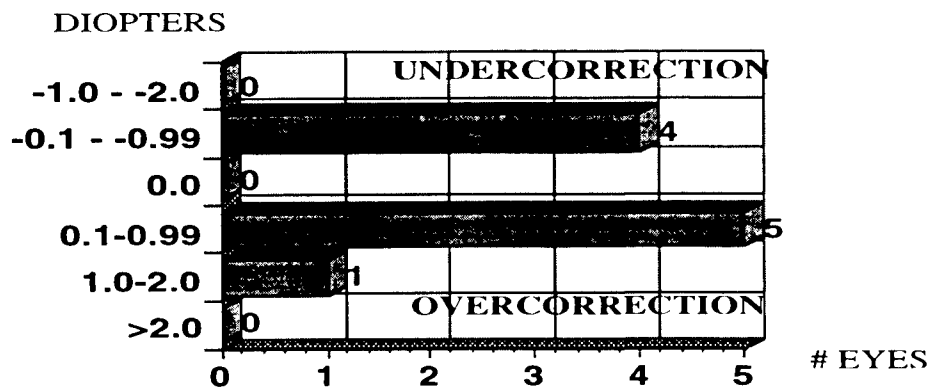


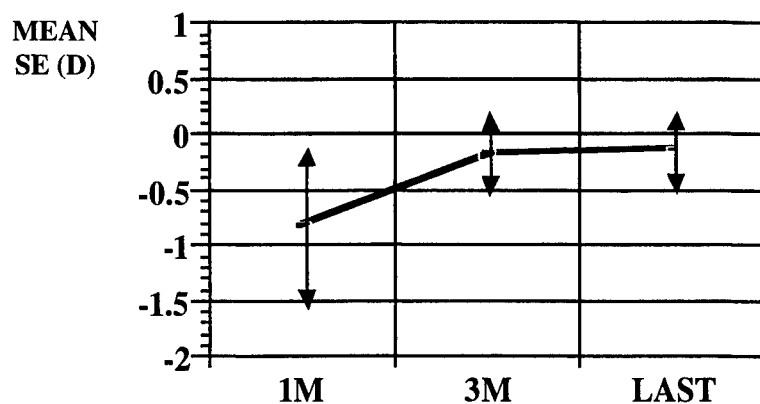
Figure 6

OVER / UNDERCORRECTION LAST EXAM N = 10



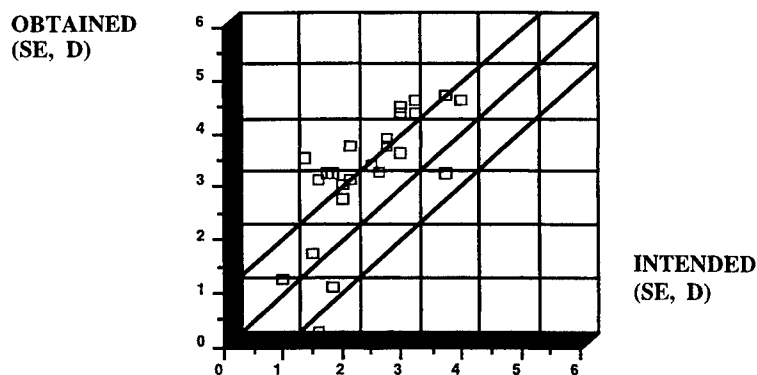
The mean correction over time is illustrated in Fig. 7. It shows indeed an initial over correction which recedes by the third month postoperatively.

Figure 7
MEAN CORRECTION OVER TIME



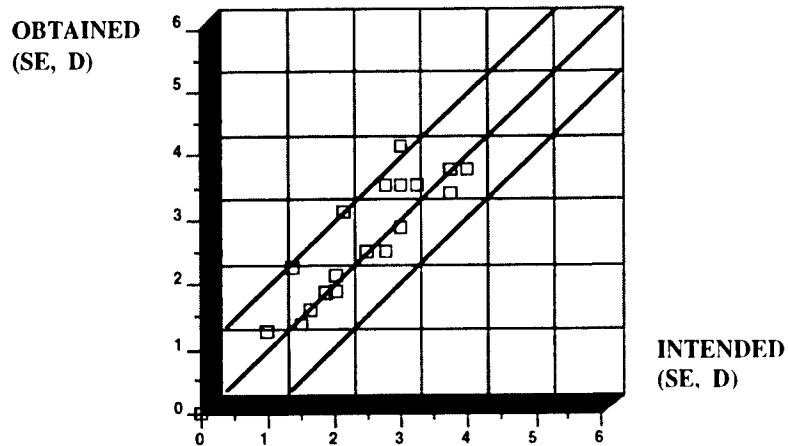
3.3 Comparison of intended vs. Obtained correction

Figure 8
REFRACTIVE OUTCOME ONE MONTH POSTOPERATIVELY



Scattergrams 8-10 provide a comparison between intended and obtained correction for each eye at 1, 3, months postoperatively

Figure 9
REFRACTIVE OUTCOME 3 MONTHS
POSTOPERATIVELY



3.4 Near visual acuity

Hyperopes become aware of decreased visual acuity for near earlier and are more severely handicapped than myopes in this fashion as presbyopia takes hold from age 40. Because HPRK is performed in the midperipheral and peripheral cornea, the newly induced profile steepening the center of this organ has in all probability the added effect of favorably affecting near vision. Figures 10-11 show the distribution of uncorrected near vision at 1, 3, and between 4-6 months postoperatively.

Figure 10
DISTRIBUTION OF NEAR UCVA 1
MONTH POSTOPERATIVELY N = 25

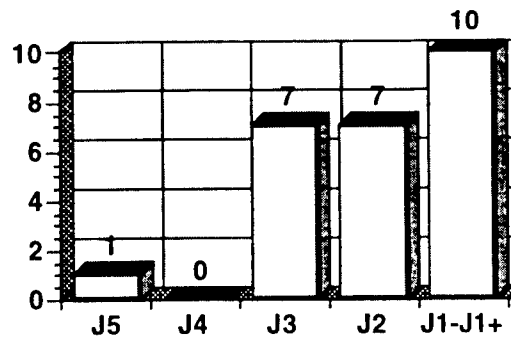
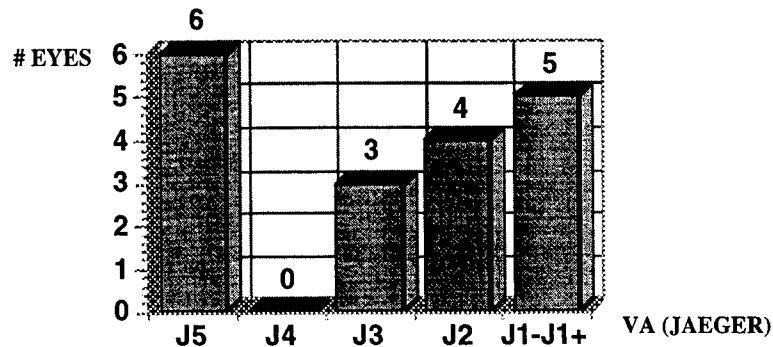


Figure 11
**DISTRIBUTION OF NEAR UCVA 3
 MONTHS POSTOPERATIVELY N = 18**



3.5 complications

3.5.1 Induced astigmatism: one of 25 eyes had induced astigmatism of 1.25D both at one and three months postoperatively

3.5.2 Reduction of two or more lines of best corrected visual acuity: At one month postoperatively, 7 eyes had a decrease of 2 lines in BCVA. All eyes had BCVA of 20/30 or better. At three months one eye lost 2 lines of BCVA from 20/16 to 20/25.

4. DISCUSSION

Overall, the preliminary results of HPRK were quite encouraging with high degrees of satisfaction expressed by patients who underwent the procedure. These results also correlated well with a similar series of patients operated by Bruce Jackson in Ottawa, Canada. Complications were minimal and not sight threatening. An apparent added effect of the surgery seems to be an improvement of near vision. This is most probably due to the creation of an aspheric profile in the midperiphery of the cornea by the performance of HPRK and is not exclusively due to an initial overcorrection. Further study and follow up need to be undertaken in order to ascertain the efficacy over the long run of HPRK.

Hyperopic photo-refractive keratectomy and central islands

Pier Giorgio Gobbi¹, Francesco Carones², Alessandro Morico², Luca Vigo², Rosario Brancato^{1,2}

¹ Laser Medicine Research, H S. Raffaele, Milan, Italy

² Department of Ophthalmology and Visual Sciences, H S. Raffaele, University of Milan, Italy

ABSTRACT

We have evaluated the refractive evolution in patients treated with hyperopic PRK to assess the extent of the initial overcorrection and the time constant of regression. To this end, the time history of the refractive error (i.e. the difference between achieved and intended refractive correction) has been fitted by means of an exponential statistical model, giving information characterizing the surgical procedure with a direct clinical meaning. Both hyperopic and myopic PRK procedures have been analysed by this method.

The analysis of the fitting model parameters shows that hyperopic PRK patients exhibit a definitely higher initial overcorrection than myopic ones, and a regression time constant which is much longer. A common mechanism is proposed to be responsible for the refractive outcomes in hyperopic treatments and in myopic patients exhibiting significant central islands. The interpretation is in terms of superhydration of the central cornea, and is based on a simple physical model evaluating the amount of centripetal compression in the apical cornea.

Keywords: photorefractive surgery, hyperopic PRK, central islands, corneal hydration, photoablation, photoacoustic effects

1. INTRODUCTION

Excimer laser correction of hyperopic refractive errors involves reshaping the anterior corneal surface so as to steepen its curvature, above the pupillary entrance, through the removal of a negative meniscus of stromal tissue, thicker at the periphery than at its center. To avoid abrupt steps on the corneal surface, a convenient transition must then be provided to connect the central refractive zone to the unaffected outer cornea. Hyperopic Photo-Refractive Keratectomy (HyPRK) thus represented both a technical and clinical challenge, and it developed much later than the corresponding technique to treat myopic errors.

The first human trials demonstrated the safety of the treatment and its effectiveness in reducing hyperopia, but issues like long-term predictability and short-term visual acuity still require consideration¹⁻⁵. In particular, a large myopic overshoot is constantly observed immediately after surgery, often affecting the patient's uncorrected visual acuity. The overcorrection steadily decreases with time, but it takes a very long time to achieve refractive stabilization and recovery of visual acuity, in comparison with myopic treatments.

In this paper we analyze the refractive behaviour in a group of patients treated for HyPRK with a maximum follow-up of 2.5 years, with particular emphasis on the refractive regression from the initial myopic overshoot.

2. METHODS

2.1 - SURGICAL PROCEDURE

Thirtyseven eyes of 28 patients have been treated at the S. Raffaele Hospital for Hyperopic Photo-Refractive Keratectomy (HyPRK), using an ArF excimer laser system (SVS Apex Plus, Summit Technology Inc., Waltham, MA). With this laser station, the desired corneal ablation for hyperopia is achieved by means of an "erodible disc", that is a polymethylmethacrylate disc deposited on a transparent quartz substrate, which is interposed on the laser beam path and which is given a predetermined thickness profile. During laser exposure the plate starts being ablated, and when it is completely eroded in its thinnest portion, it acts on the beam as a diaphragm with a time-varying shape, thus modulating the actual ablation of the cornea. For HyPRK, the plastic disc is in the form of a plano-convex plate. Discs are available for corrections from +1 to +4 D, in 0.5 D steps.

The diameter of the hyperopic ablation is 6.5 mm, and the ablation maximum depth occurs at the circular edge. Immediately after the HyPRK ablation, a suitable transition zone is created in order to linearly taper the ablation edge to zero outside of the optical zone. This is achieved by firing again the laser with a properly shaped axicon on the beam path, thus providing an annular transition zone up to 9.4 mm in diameter.

All patients had several control examinations (from 2 to 10) distributed in a follow up time ranging from 3 to 31 months. At each check up, anterior biomicroscopy, full refraction measurement, videokeratography, tonometry and haze grading were performed. The postoperative therapy was based on antibiotic drops and non-steroidal anti-inflammatory drops four times per day in the first week, and corticosteroid drops for three months tapered from 4 instillations per day in the first month down to one per day in the last two weeks.

2.2 - STATISTICAL ANALYSIS

The refractive data of the majority of patients show a common feature, namely a time evolution characterized by an initial overcorrection followed by a slow regression toward a stabilized outcome. This behaviour has been fitted with a non-linear statistical model, given by the exponential formula: $\varepsilon(t) = \varepsilon_{\infty} + \varepsilon_0 \exp[-\ln(2) \cdot t/T_{1/2}]$, where $\varepsilon(t)$ represents the refractive error as a function of time. In contrast to other regression curves,⁶ the parameters in the above formula have a direct clinical meaning, which can be easily derived with the help of Fig. 1, showing a typical plot of $\varepsilon(t)$. Thus ε_{∞} is the long term error at stabilization ($t \gg T_{1/2}$); ε_0 represents the amount of overcorrection, being the difference of refractive errors immediately after surgery ($\varepsilon(t=0) = \varepsilon_{\infty} + \varepsilon_0$) and at stabilization ($\varepsilon(t \rightarrow \infty) = \varepsilon_{\infty}$); the time constant $T_{1/2}$ gives the temporal scalelength by which the error halves (overcorrection half life). Note that after 4 time constants, the transient phase can be considered completed from a practical point of view, the difference from the steady state level being only 6% of ε_0 .

In the above model, the dependence from the parameter $T_{1/2}$ is non-linear and a specific statistical software was developed for the purpose of achieving the best fit values of the three parameters ε_{∞} ; ε_0 ; $T_{1/2}$, in the least squares sense. The program was written in MATLABTM environment and was based on the Levenberg-Marquardt algorithm^{7,8}.

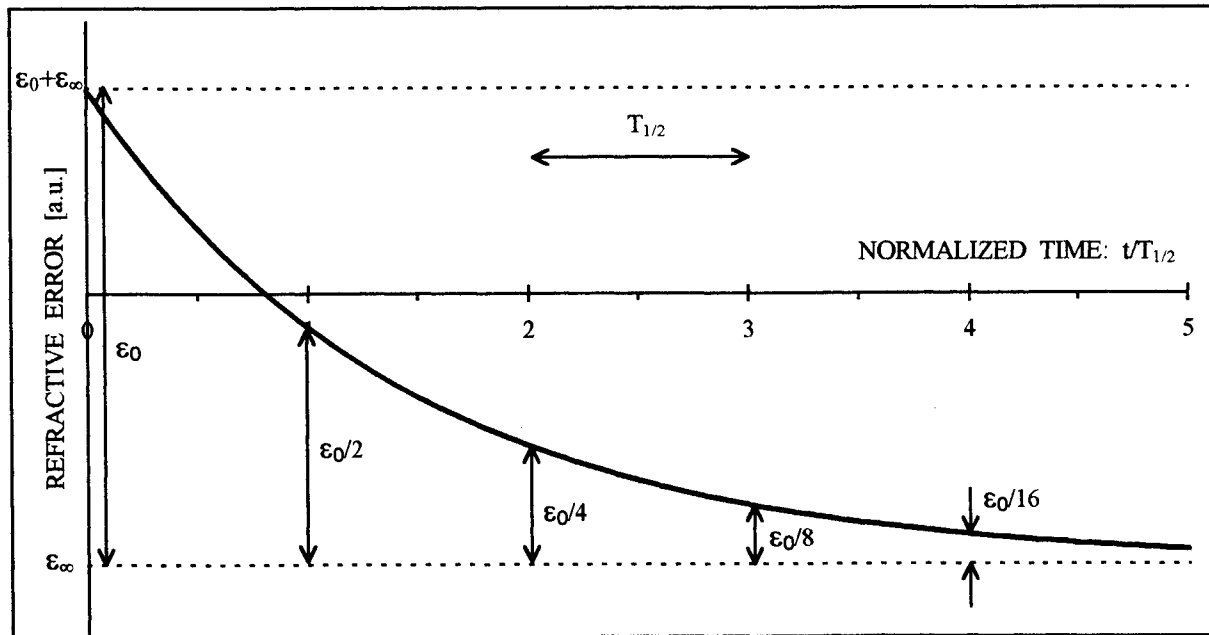


Fig. 1. Plot of the fitting function $\varepsilon(t)$ as a function of $t/T_{1/2}$.

3. RESULTS

The mean attempted correction of the 37 eyes was +3.31 D, with a distribution illustrated in table I.

Of the many data available from each control examination, we focus here our attention on the spherical-equivalent refractive error, that is the difference between achieved and intended refractive corrections, both evaluated as spherical equivalent values. With such a choice, a negative (positive) error value corresponds to a myopic (hyperopic) shift relative to the intended refraction.

In Fig. 2 we report the evolution of the refractive error as a function of the time elapsed after surgery, for three patients, all treated for +4 D ablation. The symbols (triangles, squares, circles) represent the actually measured values, while the broken lines describe the exponential fits obtained for each data series. The values of the fitting parameters for the 3 cases are reported in Table II. It is apparent that the chosen exponential function fits reasonably well the general behaviour of the refractive error (consider the correlation coefficients R) for all the three patients considered. The same applies as well to all patients with a suitably long follow up and at least five observations available. The treatments of Fig. 2 were chosen to show the large variability of the individual refractive response to HyPRK treatments, in terms of overcorrection amount, refractive goal error and recovery time.

CORRECTION [D]	TREATED EYES
1	1
1.5	2
2	7
3	3
3.5	1
4	23

Table I

PATIENT	ϵ_r [D]	ϵ_0 [D]	$T_{1/2}$ [mo]	R
F.P.	+ 0.1	- 5.1	1.8	0.99
A.L.D.	+ 2.6	-5.8	21.6	0.96
C.S.	+ 0.6	-9.1	3.3	0.91

Table II

By combining the data from all the 37 patients, for a total of 179 observations, and averaging the refractive error values at homogeneous time delays from surgery, the plot of Fig. 3 is obtained. Here squares represent the mean values of the experimental data, and both horizontal and vertical error bars refer to standard deviation values. The number of samples is reported close to each data point. The solid line describes the least squares best fit, where the parameters assume the following values: $\epsilon_\infty = -0.19 \pm 0.32$ D; $\epsilon_0 = -3.38 \pm 0.37$ D; $T_{1/2} = 3.60 \pm 1.1$ mo. The uncertainties in the parameters refer to the 95% confidence interval for their estimates. The fit still appears to describe well the mean data behaviour, even if the scattering of data due to individual variability results in a reduction of the correlation coefficient down to $R = 0.56$.

DISCUSSION

The quantitative data description obtained with the above approach highlights two essential features of the HyPRK treatment performed with the erodible disc: the algorithm appears to be reasonably well conformed as to the final refractive outcome, while the transient phase is characterized by a very large myopic shift and a prolonged time duration. In fact, if the long term achievement of -0.19 ± 0.32 diopters displacement from the intended goal is to be considered a satisfactory result, it must be remarked that such a result is reached after a sudden reversal of the pre-op refraction (passing in average from +3.3 to -3.4 D immediately after surgery) and through a year long ($4 \cdot T_{1/2} = 14$ months) regression across nearsightedness toward emmetropia and stability.

These numbers substantially differ from those we obtained by an analogous analysis performed on myopic PRK treatments. In fact, we examined the refractive data of 216 eyes from 169 patients treated for myopia in the range -1 to -12.7 D, with a mean correction of -5.6 ± 2.5 D, and a maximum follow up time of 27 months. The myopic procedures were performed under the same conditions of the hyperopic cases: the geometry of course was different, being a 3-zone ablation with diameters of 5, 6 and 6.5 mm, respectively. Also the therapeutic protocol was identical. The same exponential statistical model described above was applied to the myopic population (reported in Fig. 4), and the following results were obtained: $\epsilon_\infty = -0.54 \pm 0.04$ D; $\epsilon_0 = +1.39 \pm 0.32$ D; $T_{1/2} = 0.80 \pm 0.19$ mo.

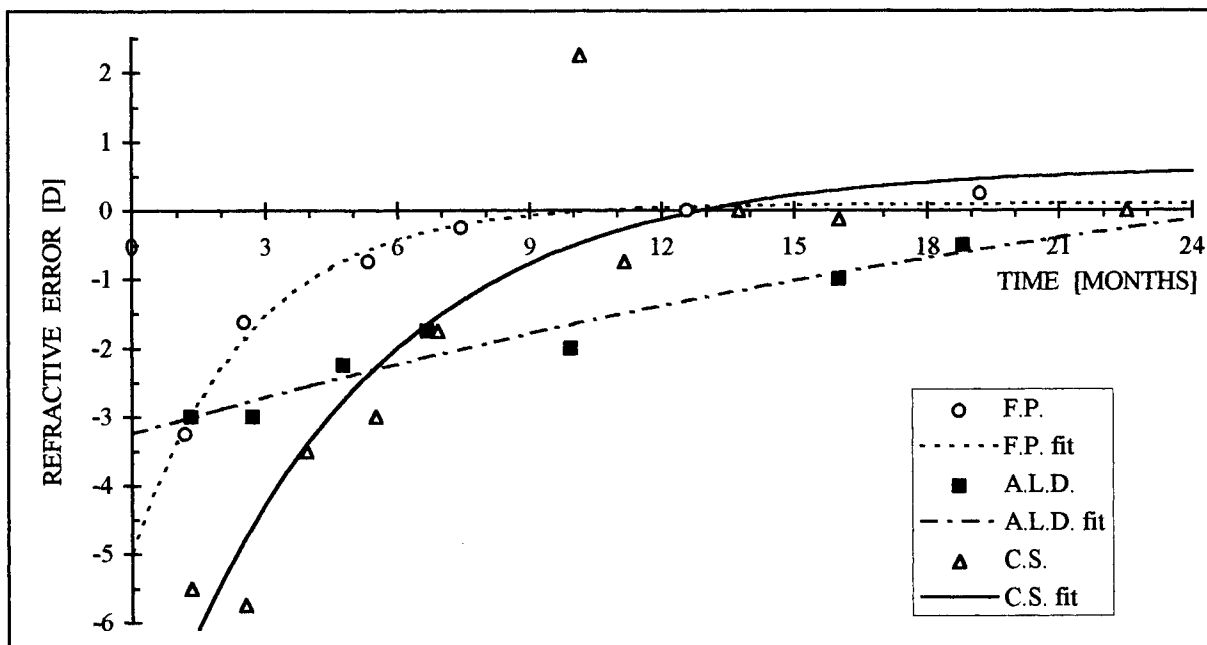


Fig. 2. Plot of the refractive error as a function of time for three patients treated for +4 D HyPRK. Lines represent the least squares exponential fits to each data set. The values of fit parameters are given in Table II.

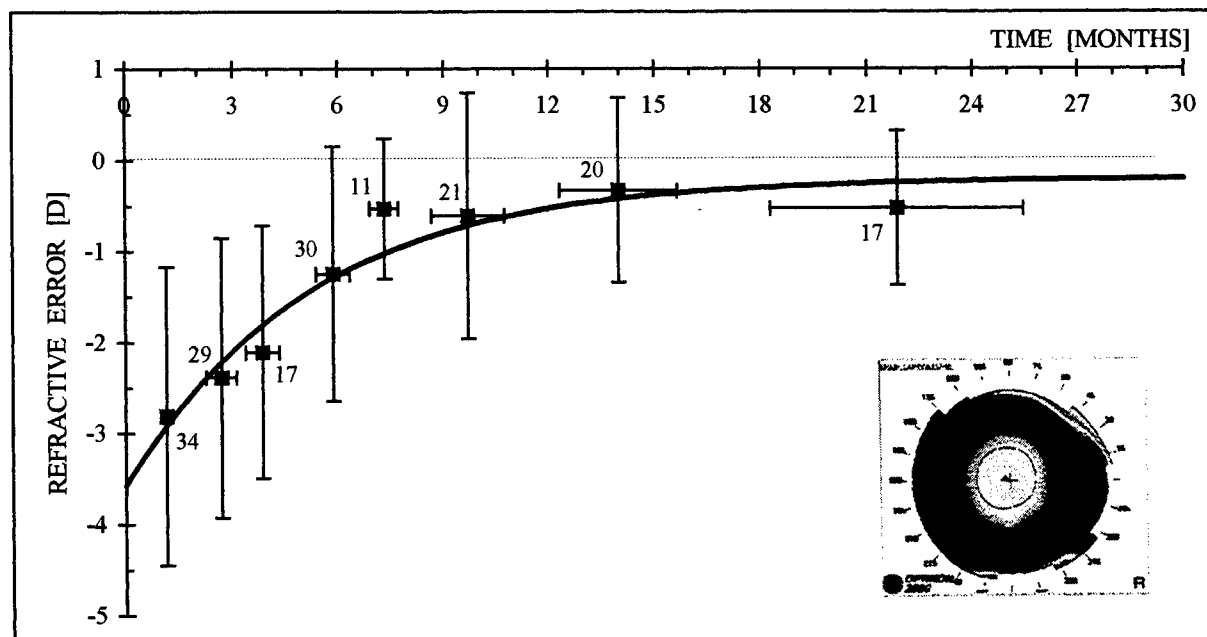


Fig. 3. Plot of the mean refractive error for the whole hyperopic group. Horizontal and vertical bars refer to one standard deviation. Labels give the number of observations. The inset shows a typical topographic map one month after surgery, for a +2 D correction.

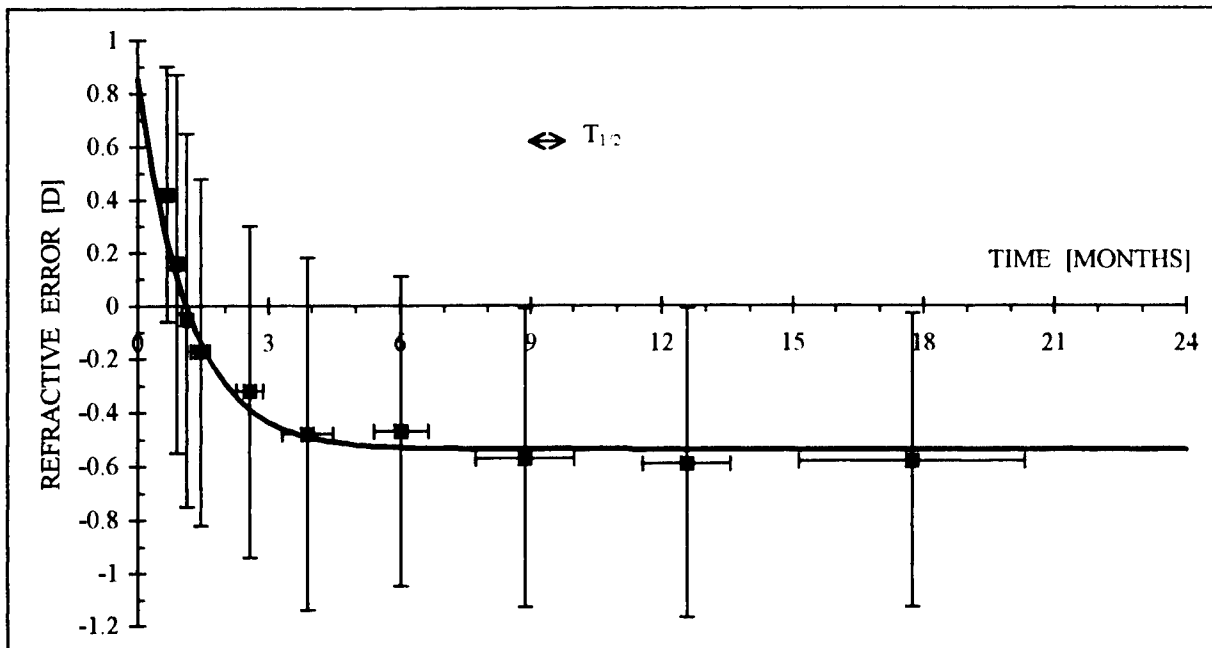


Fig. 4. Plot of the mean refractive error for the myopic group (216 eyes).

Apart from the obvious sign change in ϵ_0 , the most striking differences lie in the marked reduction of both the regression amount relative to the preop refraction (in absolute values, it amounts to 102% for HyPRK and 25% for MyPRK), and the regression time constant $T_{1/2}$. Note that for the low myopia population (-1 to -6 D correction, 139 eyes), this time constant further reduces to 0.43 ± 0.09 mo.

Any tentative interpretation of such a different behaviour must first tackle the problem of addressing the mechanisms underlying the genesis of overcorrection and of the subsequent regression. In case of myopic treatment, an overcorrected refractive outcome corresponds to an exceeding flattening of the cornea relative to the geometrical goal, while on the contrary for hyperopic ablations it means a curvature steepening beyond what is required.

Overcorrection can be observed very early after surgery, as soon as the epithelial regrowth is complete and allows the patient a clear vision⁹⁻¹¹. In this respect, the causes of overcorrection can be essentially attributed to the ablation algorithm implemented in the laser and to epithelial hyperplasia. Regression on the contrary, which we have seen to take place in the time range from one month to one year, and which is susceptible of modulation by pharmacological therapy, can be ascribed to epithelium rearrangement and stromal reaction.

As far as the ablation algorithms are concerned, it must be noted that the multi-zone algorithm used in our myopic treatments reported above actually adopted an undercorrection of 20 % below the purely geometrical indications given by Munnerlyn's formula¹². This choice was suggested by the analysis of the ablation performances observed on PMMA discs used as a reference test for the corneal ablation. The clinical refractive data however did not fully support this choice, showing a net resulting undercorrection equivalent to 10 % ($\epsilon_r/\epsilon_{pre} = 0.54/5.6$). Following these results, in fact, the myopic algorithm was changed to include a smaller undercorrection of only 10 %.

As to the hyperopic algorithm, on the contrary, the erodible HyPRK masks were lathed so as to incorporate an overcorrection of 60 %, because of the expected regression due to wound healing. On one side this could explain at least part of the observed overcorrection of Fig. 3, but on the opposite side the excellent long term results obtained ($\epsilon_r \approx 0$) appear to exclude that an actual over-ablation does take place onto the cornea.

Another difficulty arises when considering the mechanism generally invoked to explain the onset of overcorrection in myopic treatments¹³⁻¹⁵, namely the temporary epithelium thickening at the edge of the ablation zone, that is in the region where the curvature rate of change is maximum. In fact the same mechanism applied to HyPRK would yield a partial filling by

new epithelium of the circular well surrounding the central optical zone (where the curvature changes sign), and as a consequence a global flattening of curvature would be obtained rather than the observed extra steepening. A different effect must be at the origin of hyperopic overcorrection.

5. SUPERHYDRATION MODEL

The interpretation that we support here is based on the progressive superhydration of the central portion of the cornea during the course of ablation. The picture can be naively sketched as follows. As a consequence of the recoil momentum of the ablated volume, a force component is applied to each ablation point, lying in a plane perpendicular to the corneal axis and directed toward the center of the ablation. Due to the circular symmetry, the resulting compression tends to squeeze the corneal tissue centripetally. While the stromal collagen fibres respond elastically to the acoustic transient, the stress gradient can space water molecules apart from the glycosaminoglycans (GAGs) gel to which they are bond. Subsequent pulses superimpose their effect and tend to push water molecules toward the center of the ablated area, thus leading to a central region with higher water content than in the periphery. This "apical" superhydration can result both in reduced central ablation and in central swelling of the cornea. The former effect leads to permanent consequences to the ablated surface, the latter produces transient bulging which can take long time to dissolve spontaneously.

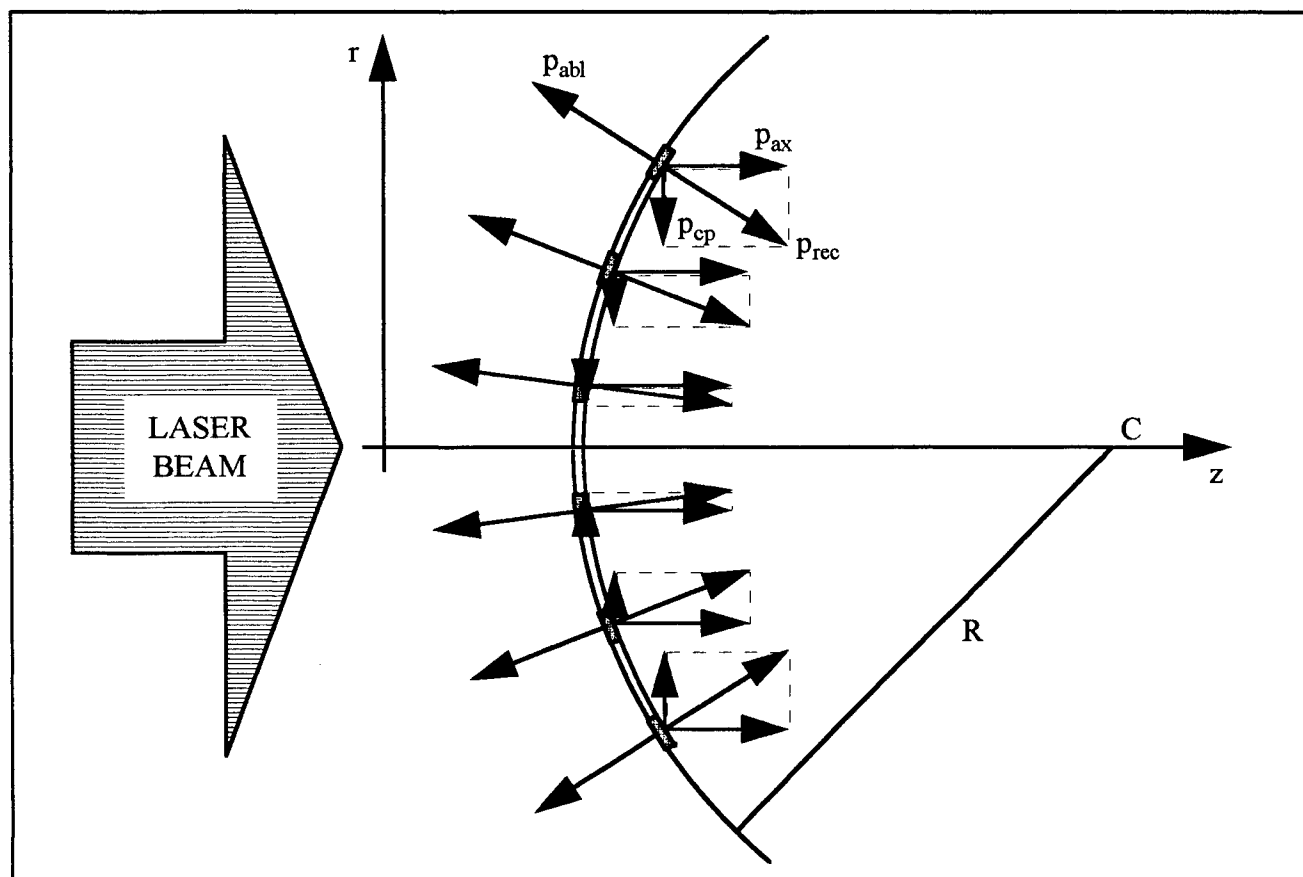


Fig. 5. Schematic of the photoacoustic interaction following a broad-beam laser pulse ablating the cornea. R , C : radius and center of curvature of the anterior corneal surface. P_{abl} : momentum of the ablated material; P_{rec} : recoil momentum; P_{ax} , P_{cp} : axial and centripetal components of the recoil momentum.

Phenomenologically, a first support to this picture comes from the visual experience of progressive wetting of the ablated corneal surface in the course of ablation, well known to all photorefractive surgeons, and which is common both to myopic and hyperopic treatments. However big differences are to be expected in the two opposite cases, since myopic corrections imply deeper ablation in the center of the cornea and the recoil momentum is mostly longitudinal. In hyperopic corrections, on the contrary, the centripetal momentum (that is, the component normal to the corneal axis) is greatly increased because: i) the ablated mass is prevalently distributed in the periphery; ii) the ablation extends much farther to provide the transition zone.

The simple geometrical model of Fig. 5 is helpful to derive a quantitative scaling law for the extent of compression to the apical cornea in different ablation geometries. Consider a pulsed laser beam with diameter σ impinges onto a spherical cornea of radius R , centered on the corneal axis. The fast thermal explosion induced by the ablating laser beam removes a uniform corneal layer of thickness τ , provided the beam fluence is constant across its section. Each point Q of the ablated interface experiences a momentum recoil proportional to the mass of the elementary volume dV centered in Q : $dp \propto dm \propto dV$. For the symmetry of the corneal cap, the momentum is directed toward the center of the corneal surface. The recoil momentum can be decomposed into an axial component directed along the corneal axis, and a centripetal component lying in a transverse plane perpendicular to the corneal axis. The latter component has magnitude given by $dp_{cp} = dp \sin(r/R)$, r being the distance of point Q from the corneal axis. The superposition of all the transverse components from the whole spherical surface gives rise

to a radially symmetrical compression wave with magnitude proportional to: $dF(\sigma) = 2\pi \cdot dt \int_0^{\sigma/2} \sin\left(\frac{r}{R}\right) \cdot r \cdot dr$.

By superimposing the contributions of all the laser pulses required to achieve the desired correction, one gets

$$F = \int_0^{s/2} dF(\sigma) = 2\pi \int_0^{s/2} t(r) \cdot \sin\left(\frac{r}{R}\right) \cdot r \cdot dr \quad (1)$$

In the formula, $t(r)$ represents the radial thickness profile of the desired ablation and s is the maximum ablation diameter. A purely spherical geometry (without astigmatism) has been assumed for simplicity. The quantity F , that we call the apical compression factor, is a measure of the cumulative stress experienced by the axial portion of the cornea. Dimensionally, F is a volume and represents the part of the ablated volume that gives a contribution to the centripetal compression.

Fig. 6 shows the scaling behaviour of factor F as a function of the applied correction (expressed as absolute value) for different geometries and ablation algorithms. The optical and geometrical parameters required to evaluate F are taken from the standard Gullstrand's eye model and from Munnerlyin's formula. In Fig. 6 squares and triangles refer to single-zone, myopic corrections with 5 and 6.5 mm diameter, respectively. Diamonds refer to the 3-zone myopic algorithm with 5; 6; 6.5 mm diameters and 100 %; 70 %; 30 % corrections. Finally circles describe the hyperopic correction with 6.5 mm optical zone and tapering up to 9.4 mm.

The behaviour of F vs correction can be fairly well linearized for all geometries and algorithms, and the slopes directly compared (slope units are: $10^{-2} \text{ mm}^3/\text{D}$). For single-zone myopic ablations, the slope increases from 1.54 at 5 mm diameter to 6.1 at 6.5 mm, showing a quadratic dependence with the size of the optical zone. The 3-zone myopic algorithm is effective in reducing both the ablated volume and F , resulting in a slope of 3.9. As expected, the HyPRK algorithm gives the highest slope: 22.8.

Experimental measurements performed in vitro and in animal eye models have shown that the recoil momentum generates compressional acoustic pulses lasting ≈ 50 ns with magnitudes of the order of 100 bar at the posterior corneal surface¹⁶⁻¹⁹. Other measurements evidenced the "focusing" effect caused by the convex shape of the acoustical source, and the contrasting action of diffraction at small beam sizes²⁰. The axial component of the recoil imparts the cornea a sequence of longitudinal compression pulses which propagate down the eye bulb. Their main effect is likely to trigger microscopic oscillations and distortions of the corneal cap.

On the contrary, the transverse component of the recoil momentum gives rise to concentric compression pulses which propagate within the stromal thickness and collapse at the corneal vertex. The evaluation of the compression pulse amplitude reaching the center depends on many concomitant mechanisms like attenuation, geometrical magnification, diffraction, and reflection from the corneal surfaces. The pulse temporal envelope is grossly given by the convolution of the recoil pulse shape with a flat pulse having a duration equivalent to the acoustic transit time across the radial size of the source. Diffraction effects can further significantly distort the resulting time shape. Complete description of the physical model turns out to be cumbersome and beyond our present purposes, and we limit here to rely on F to compare different ablation geometries.

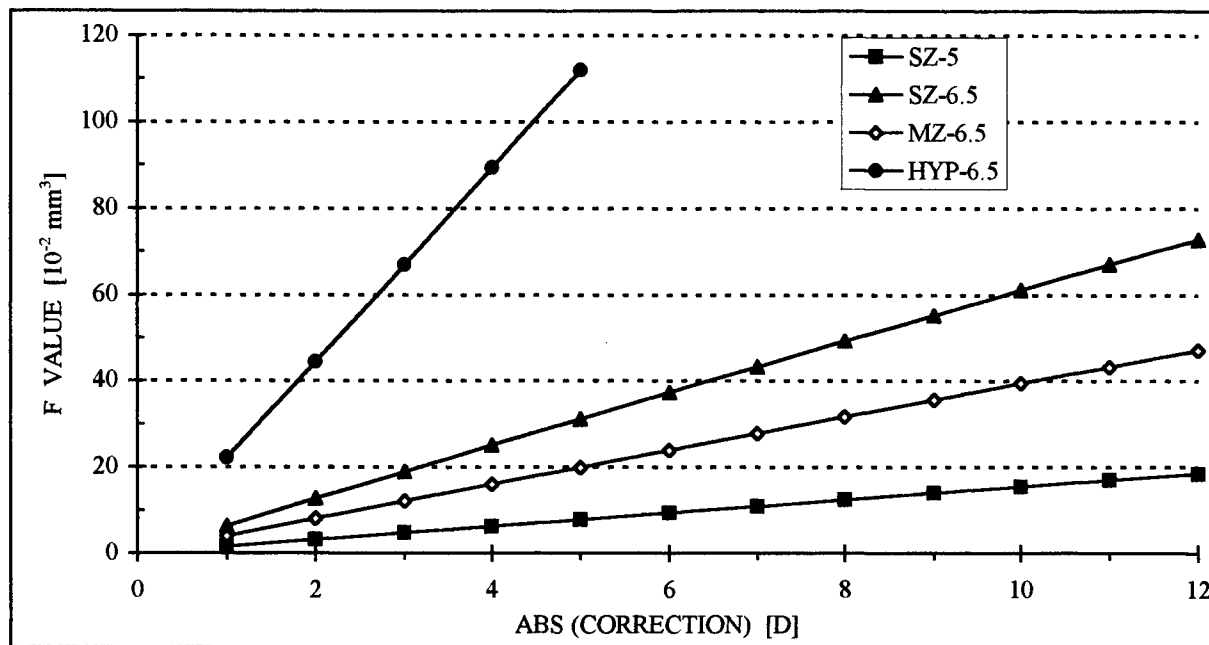


Fig. 6. Plot of F as a function of the dioptric correction (absolute value), for different ablation geometries.

Physically, what is required to displace water inside the tissue is a pressure gradient (in time or equivalently in space) large enough to overcome the ionic coupling between water molecules and the GAGs gel which is responsible for the high water content in the cornea. Once that water molecules get free, they can move forward within the same compression pulse. Iteration of the interaction process for hundreds of time may eventually result in a radial gradient of stromal hydration oriented to the corneal axis. By the same mechanism a longitudinal hydration gradient must be expected to develop across the corneal thickness.

The radial gradient can have two refractive consequences: it can locally reduced the ablation rate, as often experimentally observed^{16,21-23}, thus leaving a permanent zone of defective ablation at the center of the ablation, smoothly tapering toward the periphery. Secondly, an increased water content is always accompanied by an increase in stromal volume with a linear relationship: this gives a central bulge of swelling tissue. The reverse process of water uniform redistribution has been shown to be a very slow one, due to the strong resistance opposed by the tissue to water flow²⁴.

According to the previous analysis, HyPRK treatments can induce water accumulation in the central cornea more likely than myopic ones, due to the higher F factor. In our opinion this mechanism is responsible for most of the overcorrection and regression we observed in our patients. Given that the final refractive outcome is close to emmetropia, we are lead to conclude that the effective stromal ablation obtained in our conditions seems to be less than expected, when considering that the erodible discs are 60 % overdimensioned compared to the theoretical predictions. The full amount of overcorrection and consequent regression should thus be ascribed to the stromal edema following the ablation. Because topographic maps clearly show that the effectively steepened zone is limited to a circle with diameter in the range 3.5 to 4.5 mm (see inset of Fig. 4), this should roughly be the area involved by corneal superhydration. Under this hypothesis, the bulge height required to account for a -4 D overcorrection ranges from 17 to 28 μ m.

6. CENTRAL ISLANDS

The long time constant driving recovery in HyPRK patients leads us to associate this type of broad-beam treatment with those myopic PRK procedures resulting in the development of topographic central islands (CI), which typically take long time to vanish. In our opinion, the same superhydration effect is related with CI formation.

A unique definition of CI does not exist, but there is general agreement to consider CI any spot region of elevated curvature which can be topographically observed near the center of the ablation zone. CIs can occur after MyPRK of medium-high correction, performed with broad-beam laser systems, particularly with large ablation diameters²⁵⁻²⁸. Not always the presence of CI adversely affects the visual performance, depending on the magnitude and extent of the CI, and also on its position relative to the line of sight. They usually regress with time, often almost completely.

Fig. 7 depicts the time evolution of two important central islands, that we observed on both eyes of a single patient. In this picture, squares refer to data for the right eye, which was treated for a -8 D myopic correction in a single zone ablation geometry of 6 mm diameter; circles are relative to the left eye, which underwent a myopic correction of -8.5 D but with an ablation segmented into three zones with diameters of 4.5, 5.5 and 6.5 mm, respectively. The magnitude of the CI is expressed in diopters, and each point value is calculated as follows: on the topographic map (evaluating the instantaneous radius of curvature), the dioptric power in the CI center is recorded together with the power values of 4 points lying on a circle of 3 mm diameter concentric with the CI, at the intersection with two orthogonal diameters; the power difference between the center and the mean of the 4 points outside the island is assumed as the dioptric magnitude of the CI itself. The same procedure is performed on the pre-operative topographic map, in the position where the CI will develop, in order to provide the baseline value and to account for initial irregularities of the anterior surface. For both cases in Fig. 7, the baseline values are very close to zero. The error bars represent the power SD of the 4 points external to the CI.

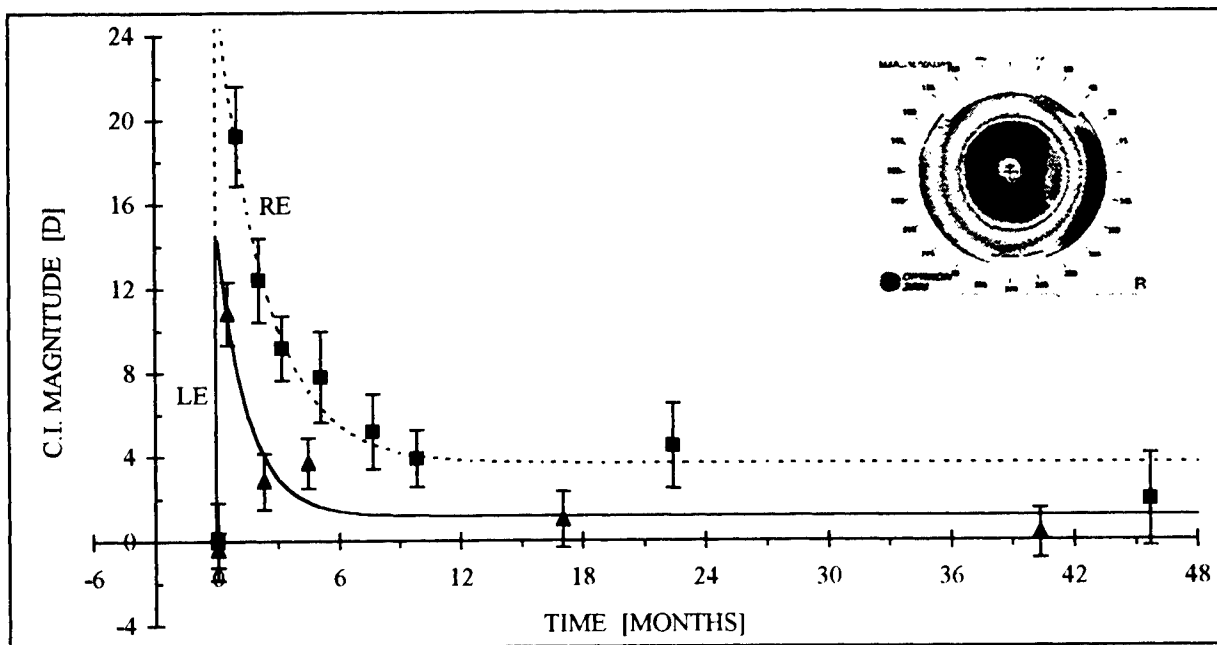


Fig. 7. Temporal evolution of the central island magnitude topographically measured on a single patient's eyes, after myopic PRK of -8 D in the right eye (RE) and -8.5 D in the left one (LE). The inset shows the RE topographic map (instantaneous radius of curvature) one month after PRK.

The representation obtained in this way turns out to be very meaningful, showing a regular regression of the CI magnitudes from extremely high values immediately after surgery (19 D for the right eye and 11 D for the left one, as measured after 4 and 2 weeks, respectively) down to very low values after one year or more. The solid and broken lines in Fig. 7 again represent the behaviour of the exponential fits drawn through the data, with the following values of parameters:

RE: $\epsilon_{\infty} = 3.7$ D; $\epsilon_0 = 22.2$ D; $T_{1/2} = 1.7$ mo; LE: $\epsilon_{\infty} = 1.6$ D; $\epsilon_0 = 13.1$ D; $T_{1/2} = 1.0$ mo.

The regression span, as given by the ϵ_0 values, is extremely high for both eyes, and the long-term residuals (ϵ_{∞} values) appear negligible as compared to the magnitudes at the onset. The footprint of the CIs is very regular and slightly elliptical in

shape, with maximum areas of 1.6 and 0.7 mm² for right and left eye, respectively. The areas appear to decrease regularly with time, by a factor 2 to 3. Given these sizes, and the extrapolated magnitudes at time 0, the observed CIs can be represented as spherical caps superimposed onto the cornea with estimated maximum elevations of 15 and 4 μ m, approximately (Munnerlyn's formula). For comparison, the calculated apical compression factor F amounts to $35.3 \cdot 10^{-2}$ and $27 \cdot 10^{-2}$ mm³ for the right and left eye, respectively.

Concurrently, the spherical-equivalent refractive error of the two eyes showed the usual overshoot-regression behaviour, with the following values of the fit parameters:

RE: $\epsilon_{\infty} = -0.39$ D; $\epsilon_0 = 2.88$ D; $T_{1/2} = 4.9$ mo; LE: $\epsilon_{\infty} = -0.36$ D; $\epsilon_0 = 3.06$ D; $T_{1/2} = 1.3$ mo.

Surprisingly, the right eye refractive error is much slower to recover than the corresponding CI magnitude. In both eyes the presence of CI only moderately affected the best corrected visual acuity, which showed a loss of 2 and 1 lines for the right and left eye, respectively, one month after surgery, and fully recovered at three months.

The regression of the CI magnitude with time down to very low levels has been observed in all the relevant cases of CI we have analysed by this videokeratographic technique, with an extent of CI residual at stabilization never exceeding 20% of the exordium magnitude. This has an important consequence in the interpretation of CI dynamics, because it turns out that the major part of the effect is of transient character, and only a minor fraction is structurally stable.

Such a finding is in contrast with any interpretation involving a defective ablation in the central portion of the laser beam, like defective optics, inhomogeneous beam, but also axial material deposition by the ablation plume²⁹. This theory moves from the well documented evidence that particles initially ejected in radial direction from the cornea rapidly bend their trajectory toward the center of the ablation, slowing down their motion and gathering into a narrow pedestal, which moves parallel to the corneal axis and finally evolves into a mushroom-like vortex³⁰. To account for CI formation, it is assumed that particles close to the ablation center, where their speed is lower, can be redeposited onto the stromal surface, thus reducing the effective ablative power of each laser pulse.

There are two main difficulties with this model. First, the plume deposition model would intrinsically produce stable, permanent CIs (apart from the effect of epithelial and stromal smoothing), while Fig. 7 demonstrates that they are slow, transient effects. Secondly, the claimed observation of CIs on irradiated PMMA plates^{30,31}, which clearly would be in contrast with the theory of superhydration, is not convincing. In fact the islands obtained on PMMA were always present for any ablation diameter from 1 to 7 mm, and covered 70 to 90 % of the crater size; such features are quite different from those observed on corneas, where CIs are much smaller, if any (see inset in Fig. 7). Furthermore PMMA islands were detected through surface profilometry on plane targets, and not by means of videokeratography, which is the only reference instrument for the comparative assessment of CIs. On the contrary, we have never been able to reproduce any topographic CIs on PMMA spheres with our excimer laser.

We finally comment that the strategy of CI prevention in high myopia PRKs through some sort of central pretreatment with small optical size (1.5 to 3 mm in diameter) does not appear to represent a proper solution to the CI problem, in view of the transient character of the CI itself. It is further to be expected that different ablation approaches, like the flying spot or the scanning slit delivery systems, will likely result in better refractive response in HyPRK treatments and a substantial reduction of CI occurrence.

7. CONCLUSIONS

We have demonstrated the long-term accuracy of the "erodible disc" algorithm in performing HyPRK up to +4 D, and we have quantified extent and duration of the overcorrection transient phase following photorefractive surgery. We propose an interpretation for overcorrection based on acute stromal hydration, as a consequence of photo-acoustic interaction leading to water accumulation in the central part of the cornea. A parameter has been derived to evaluate the amount of centripetal compression. We believe that the same mechanism is responsible for the formation of central islands in myopic PRK procedures, in contrast to the plume redeposition theory. The almost completely transient nature of the central island phenomenon has been demonstrated through topographic analysis. Adoption of scanning corneal ablation should provide reduced overcorrection in HyPRK treatments and disappearance of central islands in MyPRK.

8. REFERENCES

1. D. Dausch, R. Klein, and E. Schroder, "Excimer laser photorefractive keratectomy for hyperopia", *Refract. Corneal Surg.* **9**, pp. 20-28, 1993.
2. R. Brancato, F. Carones, A. Morico, E. Venturi, L. Vigo, A. Spinelli, and P.G. Gobbi, "Hyperopia correction using an erodible mask excimer laser delivery system coupled to an axicon: preliminary results", *Eur. J. Ophthalmol.* **7**, pp. 203-210, 1997.
3. D. Dausch, Z. Smecka, R. Klein, E. Schröder, and S. Kirchner, "Excimer laser photorefractive keratectomy for hyperopia", *J. Cataract Refract. Surg.* **23**, pp. 169-176, 1997.
4. J.P. Danjoux, R.S. Kalski, P. Cohen, M.A. Lawless, and C. Rogers, "Excimer Laser Photorefractive Keratectomy for Hyperopia", *J. Refract. Surg.* **13**, pp. 349-355, 1997.
5. B. Sener, A. Özdamar, C. Aras, and A. Yanyali, "Photorefractive Keratectomy for Hyperopia and Aphakia with a Scanning Spot Excimer Laser", *J. Refract. Surg.* **13**, pp. 620-623, 1997.
6. J.H. Kim, W.J. Sah, C.K. Park, T.W. Hahn, and M.S. Kim, "Myopic Regression After Photorefractive Keratectomy", *Ophthalmic Surg. Lasers* **27** (suppl.), pp. S435-S439, 1996.
7. P.R. Bevington, *Data reduction and error analysis for the physical sciences*, McGraw Hill Inc., New York, 1969.
8. W.H. Press, B.P. Flannery, S.A. Teukolsky, and W.T. Vetterling, *Numerical Recipes*, Cambridge University Press, Cambridge, 1986.
9. J. Marshall, S.L. Trokel, S. Rothery, and R.R. Krueger, "Long-term healing of the central cornea after photorefractive keratectomy using an excimer laser", *Ophthalmology* **95**, pp. 1411-1421, 1988.
10. F.E. Fantes, K.D. Hanna, G.O. Waring III, et al., "Wound healing after excimer laser keratomileusis (photorefractive keratectomy) in monkeys", *Arch. Ophthalmol.* **108**, pp. 665-675, 1990.
11. P. Fagerholm, H. Hamberg-Nystrom, and B. Tengroth, "Wound healing and myopic regression following photorefractive keratectomy", *Acta Ophthalmol.* **72**, pp. 229-234, 1994.
12. C.R. Munnerlyn, S.J. Koons, and J. Marshall, "Photorefractive keratectomy: a technique for laser refractive surgery", *J. Cataract Refract. Surg.* **14**, pp. 46-52, 1988.
13. S.E. Wilson, S.D. Klyce, M.B. McDonald, et al., "Changes in corneal topography after excimer laser photorefractive keratectomy for myopia", *Ophthalmology* **98**, pp. 1338-1347, 1991.
14. E. Shieh, H. Moreira, J. D'Arcy, et al., "Quantitative analysis of wound healing after cylindrical and spherical excimer laser ablations", *Ophthalmology* **99**, pp. 1050-1055, 1992.
15. S.J. Tuft, D.S. Gartry, I.M. Rowe, and K.M. Meerk, "Photorefractive keratectomy: implications of corneal wound healing", *Br. J. Ophthalmol.* **77**, pp. 243-247, 1993.
16. R. Srinivasan, P.E. Dyer, and B. Braren, "Far-ultraviolet laser ablation of the cornea: Photoacoustic studies", *Lasers Surg. Med.* **6**, pp. 514-519, 1987.
17. A. Oraevsky, R. Esenaliev, S. Jacques, and F. Tittel, "Mechanism of precise tissue ablation with minimal side effects (under confined stress conditions of irradiation)", *Laser Interaction with Hard and Soft Tissue II*, H.J. Albrecht et al. Eds., **SPIE 2323**, pp. 250-261, 1994.
18. P.G. Gobbi, F. Carones, R. Brancato, R. Pini, and S. Siano, "Acoustic transients following excimer laser ablation of the cornea", *Eur. J. Ophthalmol.* **5**, pp. 275-276, 1995.
19. S. Siano, R. Pini, P.G. Gobbi, R. Salimbeni, M. Vannini, F. Carones, G. Trabucchi, and R. Brancato, "Intraocular Measurements of Pressure Transients Induced by Excimer Laser Ablation of the Cornea", *Lasers Surg. Med.* **20**, pp. 416-425, 1997.
20. S. Siano, R. Pini, F. Rossi, R. Salimbeni, and P.G. Gobbi, "Acoustic focusing associated to laser ablation of biotissue", to be published in *Appl. Phys. Lett.*
21. C.A. Puliafito, K. Wong, R.F. Steinert, "Quantitative and ultrastructural studies of excimer laser ablation of the cornea at 193 and 248 nanometers", *Lasers Surg. Med.* **7**, pp. 155-159, 1987.
22. D.S. Aron-Rosa, J.L. Boulnoy, F. Carre, et al., "Excimer laser surgery of the cornea: Qualitative and quantitative aspects

- of photoablation according to the energy density", *J. Cataract Refract. Surg.* **12**, pp. 27-33, 1986.
23. M. Ediger, G. Petit, R. Weiblinger, and C. Chen, "Transmission of corneal collagen during ArF excimer laser ablation", *Lasers Surg. Med.* **13**, pp. 204-210, 1993.
 24. I. Fatt and B.A. Weissman, *Physiology of the Eye*, Chapter 6, Butterworth-Heinemann, Boston, 1992.
 25. D.T.C. Lin, H.F. Sutton, and M. Berman, "Corneal topography following excimer photorefractive keratectomy for myopia", *J. Cataract Refract. Surg.* **19** (suppl.), pp. 149-154, 1993.
 26. S. Levin, C.A. Carson, S.K. Garrett, and H.R. Taylor, "Prevalence of central islands after excimer laser refractive surgery", *J. Cataract Refract. Surg.* **21**, pp. 21-26, 1995.
 27. C.N.J. McGhee and I.G. Bryce, "Natural history of central topographic islands following excimer laser photorefractive keratectomy", *J. Cataract Refract. Surg.* **22**, pp. 1151-1158, 1996.
 28. A. Castillo, F. Romero, J.A. Martin-Valverde, D. Diaz-Valle, N. Toledano, and O. Sayagues, "Management and Treatment of Central Steep Islands after Excimer Laser Photorefractive Keratectomy", *J. Refract. Surg.* **12**, pp. 715-720, 1996.
 29. R.R. Krueger, "Steep Central Islands: Have We Finally Figured Them Out ?", *J. Refract. Surg.* **13**, pp. 215-218, 1997.
 30. J. Noack, R. Tönnies, K. Hohla, R. Birngruber, and A. Vogel, "Influence of Ablation Plume Dynamics on the Formation of Central Islands in Excimer Laser Photorefractive Keratectomy", *Ophthalmology* **104**, pp. 823-830, 1997.
 31. J.K. Shimmick, W.B. Telfair, C.R. Munnerlyn, J.D. Bartlett, and S.T. Trokel, "Corneal Ablation Profilometry and Steep Central Islands", *J. Refract. Surg.* **13**, pp. 235-245, 1997.

Erbium:YAG laser for cataract extraction

Robert W. Snyder^a, Mahendra Jani^b, Mike Yarborough^b, George Marcellino^b, Robert Noecker^a,
Theresa Kramer^a, Jesus Vidaurri^c

^aDepartment of Ophthalmology, University of Arizona, 1801 N. Campbell, Tucson, AZ 85719

^bCoherent Lasers, 4605 S. Palo Verde, Suite 607, Tucson, AZ 85714

^cTechnologic Institute of Advanced Studies, Mexico

ABSTRACT

The Erbium:YAG laser may be an effective laser for use in cataract surgery. At 2.94mm the energy is maximally absorbed by water thereby efficiently disrupting tissue with minimal surrounding thermal damage. The laser may be safer to use in the eye than conventional ultrasonic emulsifiers. Preliminary clinical studies of the safety and efficacy have begun.

Keywords: Erbium:YAG, cataract extraction, phacoemulsification

1. CATARACT EXTRACTION

In 1967, Kelman introduced ultrasonic phacoemulsification for cataract removal. The goal was to find a safer and more efficient way of removing the lens. There have been many significant improvements in both technology and technique and cataract extraction via phacoemulsification can be accomplished in less than 20 minutes under topical anesthesia, and through a 3 mm corneal incision. However, despite the high level of technological achievement, modern ultrasonic phacoemulsification is not a perfect procedure and has some recognized drawbacks.

Phacoemulsification is difficult to learn and can be associated with high complication rates among beginning surgeons.¹ Capsule rupture has been reported to occur in 5% to nearly 20% of the early cases with beginning surgeons. Fifty percent of the time that the capsule is ruptured, it occurs during nucleus removal with the ultrasonic probe. Capsule rupture reduces the likelihood of an excellent outcome and places the patient at greater risk for retinal detachment, postoperative inflammation and cystoid macular edema. The ergonomics of the ultrasonic handpiece are also not ideal. Compared to a common pencil or ink pen, the phacoemulsification handpiece is somewhat bulky and awkward to use, particularly when operating from a temporal approach where the surgeon's hand support is less than optimal. Furthermore, minimization of the size of the ultrasonic phaco handpiece is limited by the piezoelectric "motor," which pushes the tip at ultrasonic frequency.

1.1 Mid-infrared lasers-safety

Lasers that emit energy in the mid---infrared region, Holmium:YAG (2100 nm), Erbium:YSGG (2790 nm), and the Erbium:YAG (2940 nm), may be ideal for cataract surgery. These wavelengths operate near the absorption peak for water and are well-absorbed by the water contained in biological tissues. (Fig. 1) If the energy absorption is great enough, and if the pulse duration of the laser is shorter than the time it takes for the external energy to dissipate in the tissue (thermal relaxation time), the water in the tissue heats to boiling, causing a gas bubble, which expands and contracts in a very short period of time (microseconds). This expansion and contraction is faster than the elastic coefficient of the tissue, and as the gas bubble contracts, a vacuum or cavity is formed resulting in a cavitation effect and shock wave. The expanding gas bubble and cavitation effect crack and disrupt the tissue.² The efficiency of laser energy absorption and the photothermal ablation process is a function of the wavelength and pulse duration. Of the lasers, the erbium:YAG emits the wavelength that is most efficiently absorbed by water ($\alpha = 13,000 \text{ cm}^{-1}$). (Fig. 2) This produces the most efficient heating of water in the lens and results in tissue disruption with the least amount of surrounding thermal damage. The penetration is inversely proportional to the absorption coefficient. Thus for Er:YAG 2940 nm, $1/\alpha$ is less than 1 micron. The advantage of less thermal damage by the Er:YAG has been shown in studies that we have performed with human lens³ (Fig. 3) and sclera^{9, 14} and by others using the human lens.⁴ Theoretically, we can work closer to other important eye structures without damaging them.

Experiments have been designed to look at the safety of the Er:YAG laser with respect to lens capsule rupture.⁵ In these studies, an experimental system was designed so that the posterior lens capsule could be isolated from post-mortem eyes, fixed via glue to a small cylinder, the cylinder with capsule is immersed in water, and then the Er:YAG or ultrasonic phaco probe brought into close proximity to the capsule using a micrometer stand. The point at which the capsule ruptures could be directly visualized, and the distance recorded from a micrometer. The resultant torn capsule analyzed by scanning electron microscopy. When this was done, it was apparent there was a wide range of distances in which the ultrasonic phacoemulsification unit would rupture a capsule. (Fig. 4) It appeared that the Er:YAG laser, at energies commonly used for lens emulsification, could be brought in much closer proximity to the capsule. The nature of the lens tear also appeared to be different. With the ultrasonic phaco, the capsule tear appeared to be rough and irregular, extending to the periphery. (Fig. 5) With the Er:YAG laser, the tears appeared to be a central hole, which often remained intact without extending further. (Fig. 6)

The Er:YAG laser delivers less thermal energy to the eye when compared with current ultrasonic phaco emulsification. In studies with a 10 Hz laser, Talamo et al showed that the amount of total energy transmitted into the eye was approximately 1/15th that of an ultrasonic phaco running at 70% power.⁶ More recent studies in our lab have shown that the thermal rise with the Er:YAG laser running at 200 Hz is significantly less than an ultrasonic phaco unit at 70% power.⁷

Endothelial cell studies have also been done with the Er:YAG laser, and there appears to be significantly less damage to the endothelium with the Er:YAG compared to the ultrasonic phaco.⁸

1.2 Capsulotomy

We have found the Er:YAG to be useful for circular capsulotomy. We can use a side --- firing fiber with low energy and direct contact with the capsule to create smooth circular capsulotomies. This has been accomplished in our early clinical studies with humans. We have also performed inVtro studies of Er:YAG laser capsulotomy using cadaver eyes. Following capsulotomy with the laser we see a very smooth edge in scanning electron micrographs of Er:YAG capsulotomies.⁹ (Fig. 7) In addition, SEM studies have shown that the posterior lens capsule is unscathed following nucleus removal.

In human studies, the early capsulotomies appear to be able to withstand hydrodissection and hydrodelineation and should provide an additional benefit for laser cataract surgery.

1.3 Status of Er:YAG clinical trials

There are three companies currently in various phases of developing the Er:YAG for lensectomy. Premier has a prototype Er:YAG laser which is an FDA-approved "510K" protocol in the United States. Initial studies were done by Mike Colvard, M.D. and more recently, Garth Stevens, M.D. at the University of Virginia, and Dr. Lucio Barratto in Milan. These studies are in a development phase, in which the handpiece design continues to evolve. So far, approximately 50 or more patients have been treated and the results appear to be quite promising. (Garth Stevens, M.D., personal communication) The initial device was a single-function fiber optic that ablated the lens with a second irrigating/aspirating handpiece held in the non---dominant hand. The lens was ablated via direct contact with the Er:YAG laser and the particles removed with the irrigating/aspirating handpiece. This has since evolved to a "unimanual" handpiece, which has a central fiber optic to deliver the erbium laser, a central aspiration function, and a surrounding irrigation sleeve. The fiber optic position can be adjusted within this handpiece. (Fig. 8) The handpiece remains ergonomically satisfactory, both in weight and overall size, and can be placed through a 2 mm incision. Dr. Stevens has performed Er:YAG cataract extraction on at least 19 patients at the Medical College of Virginia, and believes the laser is safe and effective. Endothelial cell studies reported on those patients showed 10% or less loss of endothelial cells at three months. (Table 1) The Premier laser is capable of generating significant laser energies, with cases being performed with 45 mJ per pulse with a 600 micron silica tip, using 5--30 Hz rep rate. The laser system has advanced fluidics that are under continued evaluation and improvement. Strategies for Er:YAG lensectomy have included conventional divide-and-conquer, as well as phacochopping techniques.

Aesculap-Meditec (Jena, Germany) has also developed an Er:YAG irrigating/aspirating system with a multifunctional handpiece. This system uses a central fiber optic delivery of

erbium laser to the tip and center of an aspirating tube, and has irrigation surrounding the outside of the aspiration tube. Studies are underway in three sites in Europe, and to date at least 30 patients have been treated. Again, preliminary results show the laser is behaving safely and satisfactorily.

At the University of Arizona, we have used a system developed by Coherent Lasers (Palo Alto, California) and are just beginning human studies. Initial studies are being performed in collaboration with Dr. Jesus Vidaurri at the Technologic Institute of Advanced Studies in Monterrey, Mexico through a local institutional review board and via approval of the Mexican government. Prototype handpieces in this system also use a central laser fiber with surrounding aspiration sleeve. This laser operates at a higher repetition rate of 200 Hz and can efficiently ablate a lens of 2+ to 4+ nuclear sclerosis with relatively low pulse energies of 6--8 mJ/pulse with a 365 micron fiber. The irrigation is facilitated through a second Bluementhal anterior chamber maintainer. We have performed nucleus removal with phaco fracture techniques. However, strategies remain to be refined so that the lens can be removed with a proficiency that parallels ultrasonic phacoemulsification.

We believe there is definitely a role for lasers in small incision cataract surgery. These lasers have the potential to provide a safer and more reliable method for cataract removal.

2. ACKNOWLEDGEMENTS

This work was supported by Coherent Lasers and Sensory Research Foundation of Arizona.

3. REFERENCES

1. R. W. Snyder, R. A. Allinson, R. G. Fante, M. L. Stanko, D. C. Metrikin, "Learning phacoemulsification surgery." *American Academy of Ophthalmology*, May 1992.
2. W. Shi, H. Loertscher, W. Grundfest, "Tissue interaction with mid-infrared lasers in saline," *Bulletin of Am Phys Soc*, 36(7), p. 1978, 1991.
3. S. A. Limstrom, T. R. Kramer, R. W. Snyder, J. Talamo, H. Jones, J. M. Yarborough, G. Marcellino, R. J. Noecker, "Histopathology of erbium:YAG laser ablation of the cornea and the effect of variable hydration," *Investigative Ophthalmology & Visual Science* (Supp), 36, p. 4561, 1995.
4. R. Gailitis, S. Patterson, M. Samuels et al, "Comparison of laser phacovaporization using the Er:YAG and the Er:YSGG laser," *Archives of Ophthalmology*, Vol 111, p. 697, 1993.
5. R. W. Snyder, R. J. Noecker, H. Jones, "In vitro comparison of phacoemulsification and the Erbium:YAG laser in lens capsule rupture," *Investigative Ophthalmology & Visual Science*, 35(Supp), p. 3136, 1994.
6. J. W. Berger, J. H. Talamo, K. J. LaMarche, et al, "Temperature measurements during phacoemulsification and erbium:YAG laser phacoablation in model systems," *Journal of Cataract & Refractive Surgery*, 22, p. 372, 1996.
7. M. G. Jani, R. J. Noecker, R. W. Snyder, G. Marcellino, M. Yarborough, "Comparison of thermal effects of phacoemulsification and the 200 Hz erbium:YAG laser (2.94 μ m) in human cadaver eyes," *Investigative Ophthalmology & Visual Science*, (Supp), 38, p. 875, 1997.
8. G. Stevens, B. Long, J. Hamann, R. Allen, "Erbium-YAG laser assisted cataract surgery," *Investigative Ophthalmology & Visual Science*(Supp), 38, p. 872, 1997.
9. R. W. Snyder, R. J. Noecker, T. R. Kramer, et al, "Electron microscopic evaluation of the effects of the 200 Hz Erbium:YAG laser (2.94 μ m) on the lens capsule following nucleus removal and capsulorhexis," *Investigative Ophthalmology & Visual Science*, 38(Supp), p. 1621, 1997.

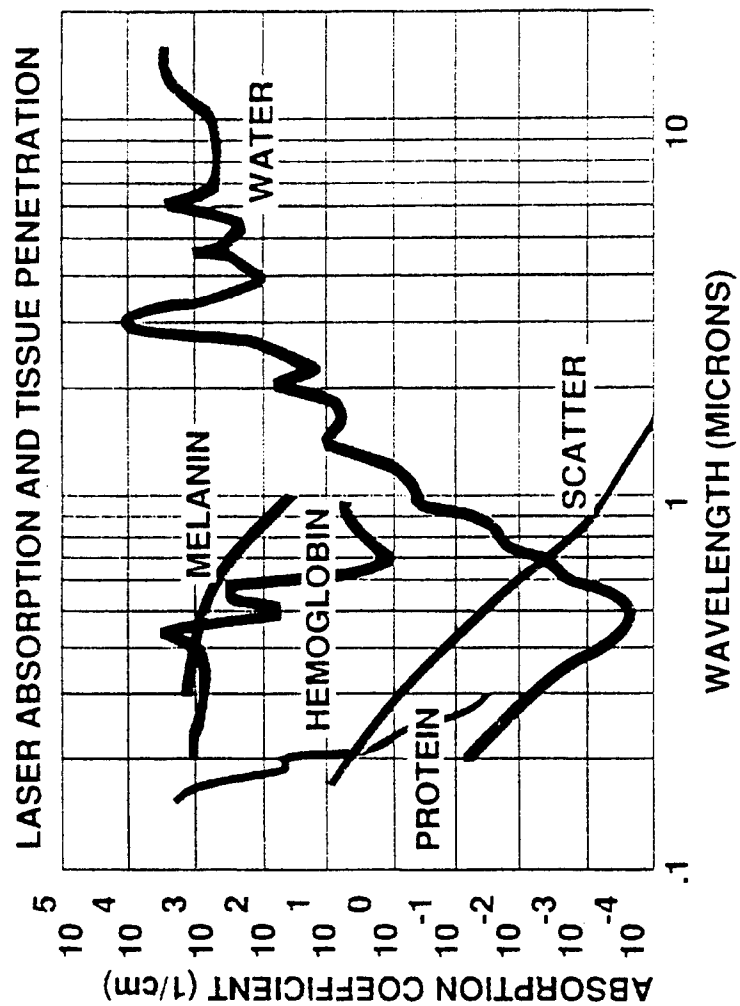


Fig 1. Laser absorption and tissue penetration (Courtesy of Coherent Medical and Coherent Lasers, Palo Alto, CA)

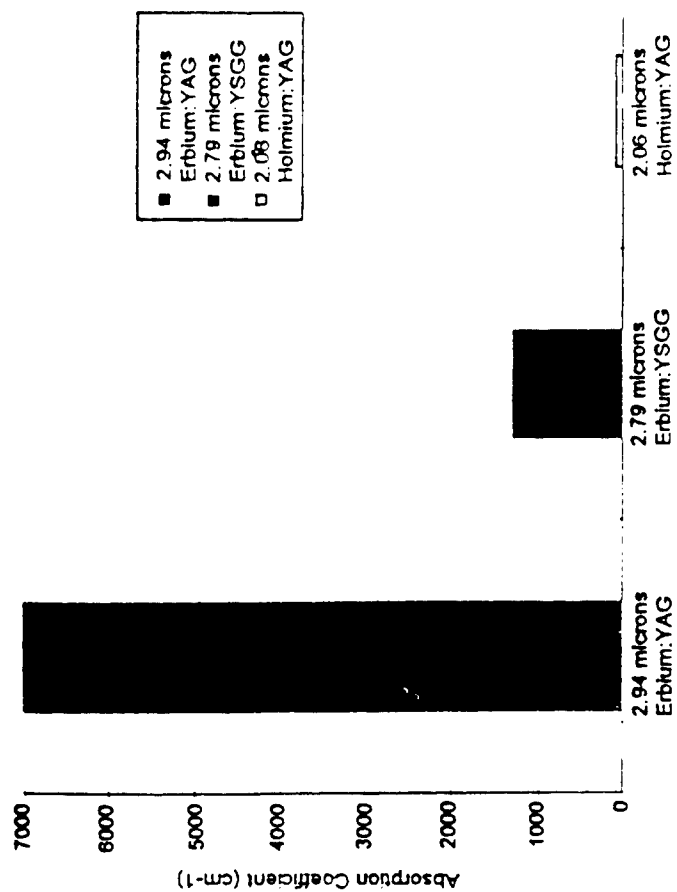


Fig 2. Absorption coefficient of infrared lasers.

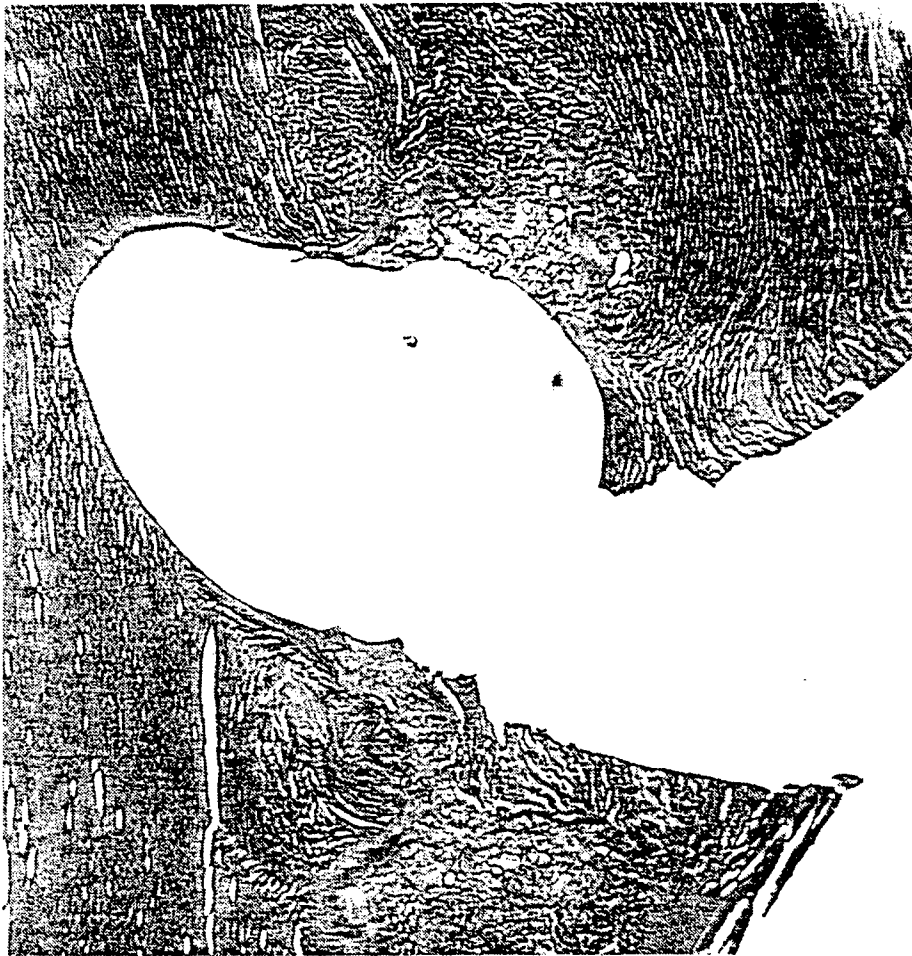


Fig 3. Histology of Er:YAG photothermal ablation craters in human cadaver eyes.

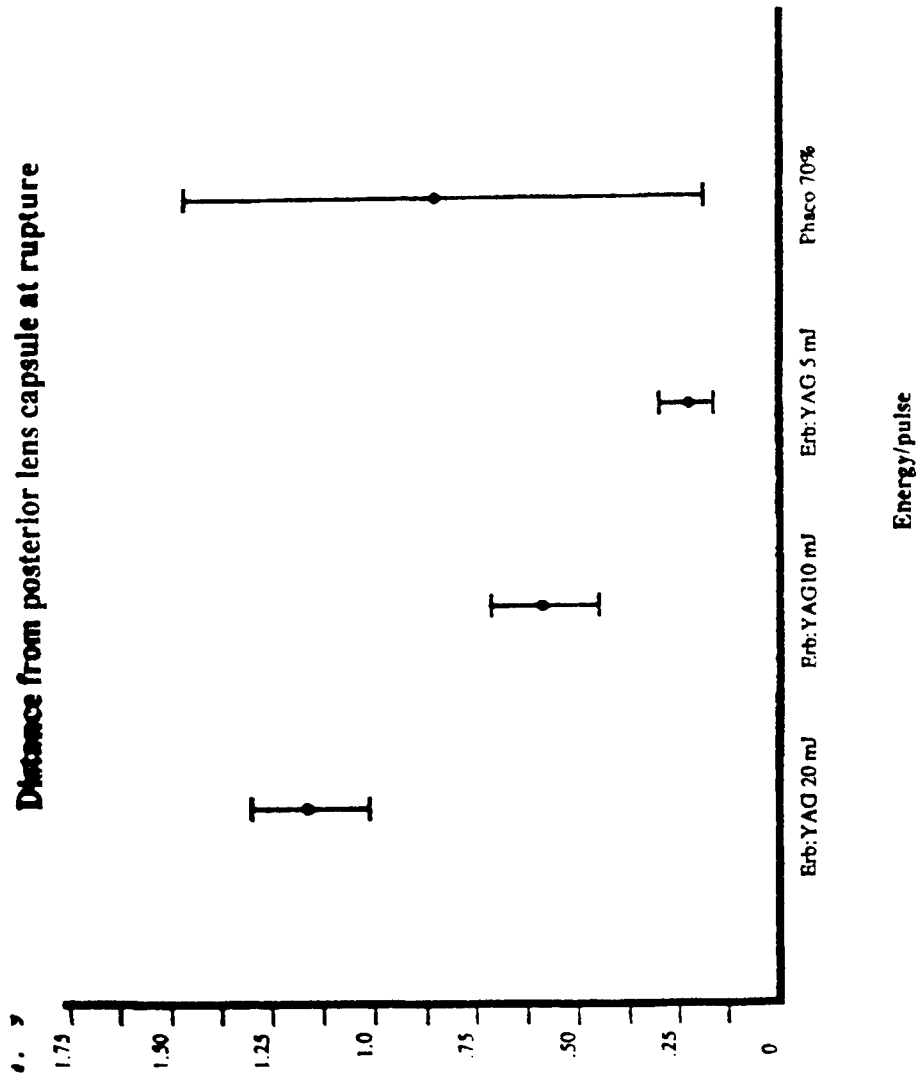


Fig 4. Distance in mm from ultrasound or Er:YAG laser probe where capsule rupture occurs (ARVO abstract-Snyder).



Fig 5. SEM of capsule rupture from ultrasonic phaco (ARVO abstract-Snyder/Noecker/Jones).



Fig 6. SEM of capsule rupture from Er:YAG (ARVO abstract-Snyder/Noecker/Jones).



Fig 7. SEM of human capsule following Er:YAG capsulotomy at $\sim 2\text{mJ/pulse}$ with a $365\text{ }\mu\text{m}$ quartz tip (ARVO abstract-Snyder/Noecker/Kramer et al.

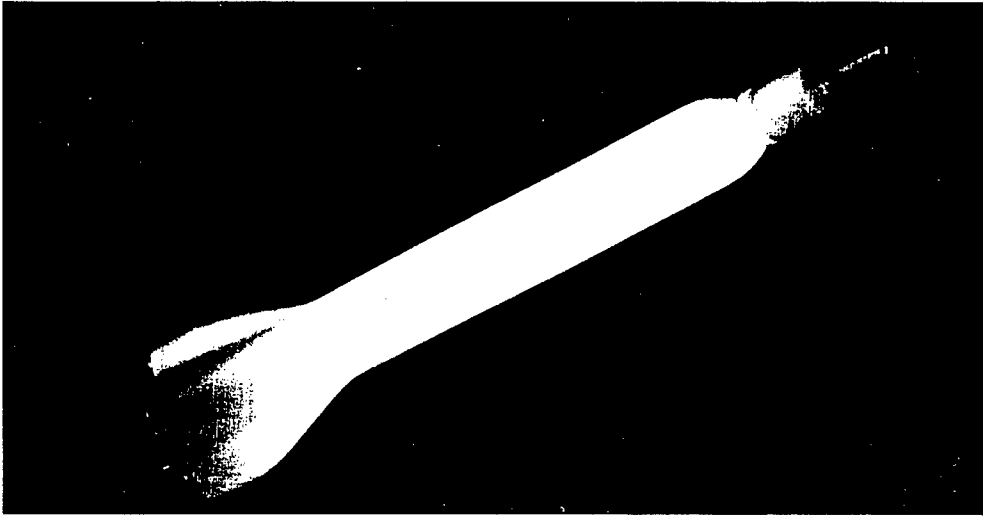


Fig 8. Premier "unimodal" Er:YAG handpiece with adjustable filter protrusion, central aspiration, outer irrigation (Courtesy of Premier Lasers).

Table 1

Best Corrected Endothelial Cell Counts
Visual Acuity(Cells/mm³)

Subject #	Pre-operative	Post-operative	Pre-operative	Post-operative
1	20/50	20/25+	1500	1500
2	20/50	20/25	2600	2300
3	CF 1'	20/30	800	750
4	20/80-	20/30	2000	2000
5	20/70	20/30	2200	2000
6	20/50	20/30	1700	2000
7	20/50-	20/20	1500	1800
8	20/50	20/20	2500	2600
9	20/50	20/25+	2200	Lost to follow-up
10	20/50	20/20+	2200	Lost to follow-up
11	20/80+	20/20-	2100	2000
12	30/60	20/20	1600	1600
13	20/50	20/20	2000	1900
14	20/60	Deceased	2200	Deceased
15	20/80	20/25	2300	2200
		Mean	1864 ± 490(SD)	1859 ± 453

Adapted from Stevens G, Invest Ophthal Vis Sci 38(suppl):872, 1997.

Hybrid retinal tracking and coagulation system

Cameron H.G. Wright, Erik D. Oberg, Steven F. Barrett

United States Air Force Academy, Department of Electrical Engineering, USAF Academy, CO 80840

ABSTRACT

Laser photocoagulation is used extensively by ophthalmologists to treat retinal disorders such as diabetic retinopathy and retinal breaks and tears. Currently, the procedure is performed manually and suffers from several drawbacks: it often requires many clinical visits, it is very tedious for both patient and physician, the laser pointing accuracy and safety margin are limited by a combination of the physician's manual dexterity and the patient's ability to hold their eye still, and there is a wide variability in retinal tissue absorption parameters.

A computer-assisted hybrid system is under development that will rapidly and safely place multiple therapeutic lesions at desired locations on the retina in a matter of seconds. In the past, one of the main obstacles to such a system has been the ability to track the retina and compensate for any movement with sufficient speed during photocoagulation. Two different tracking modalities (digital image-based tracking and analog confocal tracking) were designed and tested *in vivo* on pigmented rabbits. These two systems are being seamlessly combined into a hybrid system which provides real-time, motion stabilized lesion placement for typical irradiation times (100 ms). This paper will detail the operation of the hybrid system and efforts toward controlling the depth of coagulation on the retinal surface.

Keywords: retinal surgery, diabetic retinopathy, automated surgery, reflectance, argon laser, retinal tracking

1. INTRODUCTION

Researchers at the United States Air Force Academy and at the University of Texas at Austin have worked toward the development of an automated laser system to treat human retinal diseases. The goal is a clinical prototype system to place therapeutic laser lesions of desired parameters at desired retinal coordinates while compensating for retinal movement. The requirements for this system are summarized in Table 1 below:

Function	Performance	
Retinal Tracking	> 10 deg/sec	5 ms response time
Laser Pointing	100 μ m accuracy	5 ms response time
Lesion Control	uniform within 5%	5 ms response time

Table 1: Design specifications, suitable for treatment of diabetic retinopathy and retinal breaks. ¹⁻³

Two different tracking modalities (digital image-based tracking and analog confocal tracking) have been investigated and tested successfully *in vivo* on pigmented rabbits.¹⁻¹¹ Each system was found to have its own inherent strengths and weaknesses.

The digital image-based system is a *global* tracker using a "fingerprint" of six retinal blood vessel locations to update the position of the irradiating laser on the retinal surface. However, the digital system is hardware limited. Current technology does not provide the required resolution (512 x 512 pixels) and frame rate (200 frames per second) to achieve the requisite 5 ms system response time.⁴⁻¹¹

The analog confocal system is a fast, *local* tracker. This system steers a dithering beam on a retinal reference lesion and simultaneously measures the reflectance signal from the lesion. As the retina (and hence the reference lesion) moves the dithering beam's reflectance signal from the lesion varies. Correction signals are derived from the reflectance signal variations to maintain the irradiating laser on the desired therapeutic lesion location.^{2,3} However, if an abrupt retinal

movement occurs, the dithering beam can fall off the reference lesion and tracking lock is lost. There is no method for the confocal tracker to re-establish lock should loss of system lock occur.¹⁻³ Reference Figure 1.

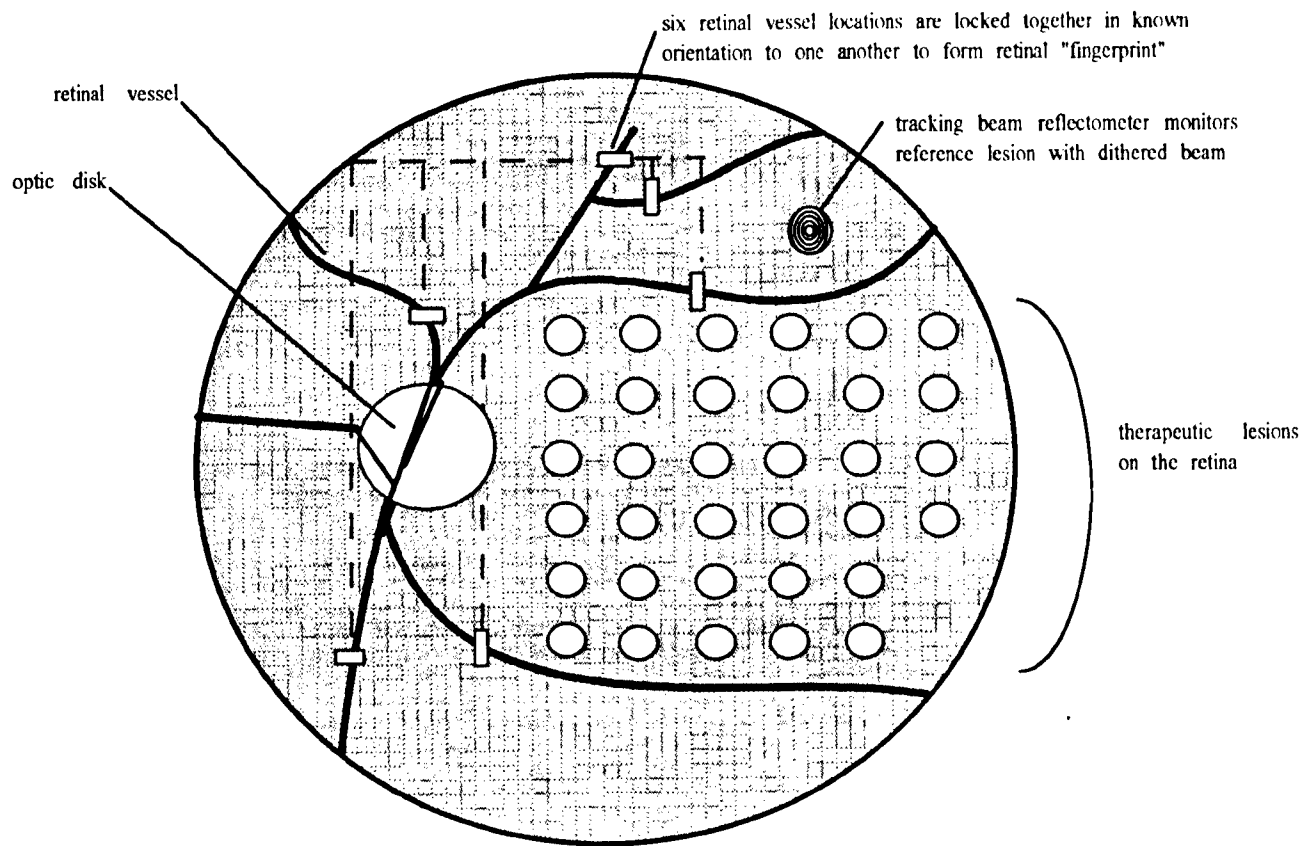


Figure 1: Simulated 50 degree retinal field of view as imaged through a fundus camera. The optic disk is the white orb where the retinal vessels converge. Two different tracking modalities are used to track and compensate for movements of the retina. The digital image-based system is a *global* tracker using a "fingerprint" of six retinal blood vessel locations to update the position of the irradiating laser on the retinal surface. The analog confocal system is a fast, *local* tracker. This system steers a dithering beam on a retinal reference lesion and simultaneously measures the reflectance signal from the lesion.

To compensate for the limitations and capitalize on the strengths of each system, a *hybrid* tracking system has been developed to achieve desired system performance specifications. Section two of this paper details the design of the hybrid system. Section three details the development of the subsystem to control lesion depth on the retinal surface in real-time and section four describes current work in progress.

2. THE HYBRID TRACKING SYSTEM

Figure 2 details the hybrid system. Note that the Digital Tracking Subsystem and the Analog Tracking Subsystem are shown as block diagrams. The details of these subsystems have been previously reported.¹⁻¹¹ This paper will provide a conceptual discussion of how these two subsystems work together with the Optical Subsystem to keep an irradiating laser stabilized on the retinal surface. We'll begin by tracing the path of the laser through the Optical Subsystem to the retina and the return path of the reflected signal to two different reflectometers. We will then discuss Hybrid Tracking System operation.

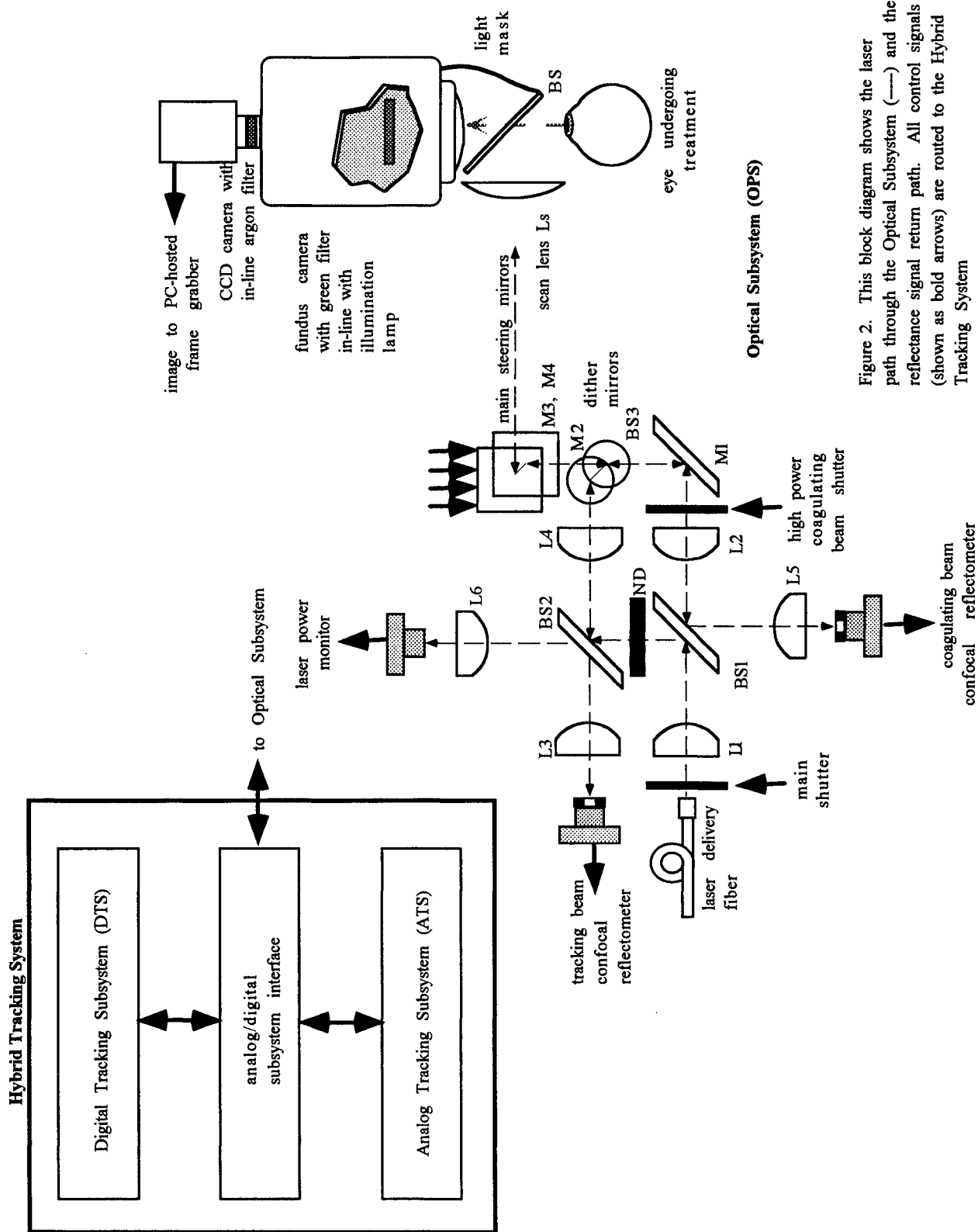


Figure 2. This block diagram shows the laser path through the Optical Subsystem (—) and the reflectance signal return path. All control signals (shown as bold arrows) are routed to the Hybrid Tracking System

The Optical Subsystem. An all lines argon laser is introduced to the system via a laser delivery fiber. The irradiating beam is routed to the retinal surface via mirror M1 and the main steering mirrors M3 and M4. From the main steering mirrors the beam is directed to beam splitter (BS) at the fundus camera through the patient's dilated pupil and onto the retina. On this path the beam passes through other optical components (lens L1, beam splitter BS1, lens L2, two shutters, and a dithering beam splitter BS3). These components are used to condition and control the beam and to tap off a portion of the main beam for use as the dither beam. A portion of the main beam is also reflected off of beam splitter BS1 to the laser power monitor which measures the instantaneous laser power.

As the retinal lesion begins to form, the retinal tissue coagulates, the scattering coefficient increases, and it reflects an increasing portion of the irradiating beam back along the same optical path put in the opposite direction. This signal is reflected off of BS1 to the coagulating beam confocal reflectometer as an indicator of lesion depth.

The dither beam is obtained by tapping off a portion of the main coagulating beam in the forward direction of the light path at beam splitter BS1. The dither beam is significantly attenuated by beamsplitters BS1 and BS2 (80/20) and the neutral density filter (ND). The dither beam is reflected off of beam splitter BS2 to the dither mirrors M2 and BS3. The dither mirrors are driven by quadrature related sinusoid signals such that the beam is driven in a circular dither pattern. The dither beam then passes through the main mirrors M3 and M4 and onto the retina. *It is important to note that the dithering beam and the coagulating beam are directed at two different locations on the retinal surface.* The low power dithering beam traces a circular pattern on the reference lesion (a previously formed lesion) while the high power coagulating beam forms the therapeutic lesions on the retinal surface. Correction signals are derived from the reflected dither signal's variation to maintain the irradiating laser on the desired therapeutic lesion location and the dither beam on the reference lesion.¹⁻³

The Hybrid Tracking System. The Hybrid Tracking System consists of the Digital Tracking Subsystem (DTS) and the Analog Tracking Subsystem (ATS). The Hybrid Tracking System processes the signals from the Optical Subsystem (OPS) and produces the control signals to the shutters, the dither mirrors, and the main steering mirrors to maintain the coagulating beam on the prescribed therapeutic lesion site on the retinal surface. This is accomplished in the following manner:

- The DTS obtains a digital map of the retina from a CCD (charge-coupled device) camera attached to the OPS's fundus camera. The video image is converted to digital image via the frame grabber within the system computer. A retinal "fingerprint" of six retinal blood vessel templates locked into known orientation to one another is then formed automatically. Also, desired therapeutic lesion sites are determined in reference to the retinal "fingerprint". The critical vision anatomy (fovea, optic disk, and retinal vessels) and the vessel template locations are then designated as laser "stay out" regions. At this point, the ATS is not engaged.
- Initial tracking lock is then accomplished by the DTS by correlating the retinal fingerprint with live video from the fundus camera. Correction signals are sent to the main steering mirrors to point the laser at the desired location of the reference lesion. The reference lesion has no therapeutic value. In fact, it is geographically separated from the desired therapeutic lesions' location. The laser shutter is then opened for a fixed irradiation time to form the reference lesion.
- Correction signals are then sent by the DTS to the dither mirrors to place the dither beam on the freshly formed reference lesion. Correction signals are also sent to the main steering mirrors to place the main coagulating beam on the first desired therapeutic lesion site.
- If the analog system achieves tracking lock, tracking control is transferred from the DTS to ATS. The shutter is then opened to irradiate the first therapeutic lesion site. The coagulating beam confocal reflectometer's signal indicates when the lesion has reached desired therapeutic parameters on the retina. When the lesion is complete, the laser shutter is closed and the DTS regains tracking control. Correction signals are then issued to the main mirrors to place the main coagulating beam on the next therapeutic lesion site. This process continues until all desired therapeutic lesion sites are irradiated.

- Should the ATS lose lock while it has tracking control, the laser shutter is closed within 5 ms and control is transferred back to the DTS to re-establish tracking lock with the retina. Should the DTS lose lock it attempts to re-establish lock. If lock is not re-established, the treatment session is aborted.

This is an abbreviated discussion of Hybrid Tracking System operation but it provides enough detail to illustrate the hand-shaking that takes place between the DTS and the ATS. A key component still under development is the Lesion Depth Control Subsystem. We do not anticipate that any additional hardware is required to implement this system.

3. THE LESION DEPTH CONTROL SUBSYSTEM

Considerable work has been completed over the past two decades to correlate visible lesion reflectance with immeasurable lesion parameters. This work has been accomplished by Birngruber et al.¹², Weinberg et al.¹³, Yang et al.¹⁴, Jerath et al.¹⁵⁻²⁰, Inderfuth et al.²¹, and Maharajh et al.²² Maharajh furthering the work of Inderfuth investigated the relationship between lesion depth and lesion parameters *in vitro* including central reflectance, lag time between laser onset and lesion formation, and the rate of reflectance intensity increase in a model medium. He gathered reflectance data using a confocal reflectometer similar to that developed by Ferguson (Inderfuth's co-author). Maharajh found no correlation (0.03) between lesion depth and lag time, some correlation (0.52) between lesion depth and the maximum slope of the reflectance curve, and a strong correlation (0.84) between lesion depth and initial reflectance slope.²² Further work in this area will yield a signal to indicate completion of a lesion.

To that end, we are currently re-investigating Maharajh's work. We are interested in deriving a signal to indicate when the lesion has achieved therapeutic value. The system used to obtain this data is shown in Figure 3. Note the similarity to the

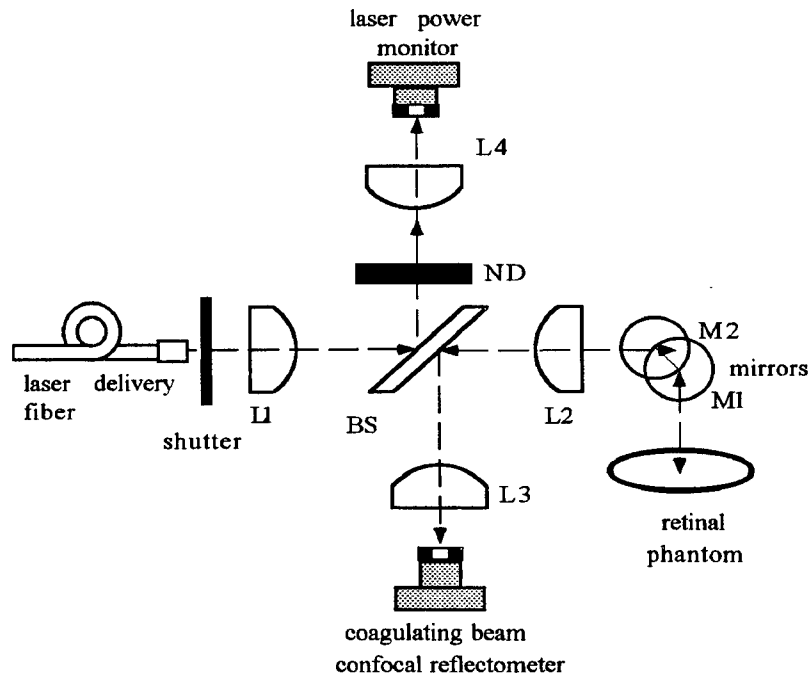


Figure 3. Experimental configuration used to measure confocal reflection. Note the similarity to the Optical Subsystem illustrated in Figure 2.

Optical Subsystem illustrated in Figure 2. An all lines laser is introduced to the system via a laser delivery fiber. The beam is passed through the shutter which controls irradiation time, lens L1, a beamsplitter BS, and lens L2. The beam is then

directed to a retinal phantom target via the galvanometer controlled mirrors M1 and M2. The retinal phantom consists of albumen (egg white) on a black high absorbing layer. As the egg white coagulates it turns white and provides a reflectance signal back up the optical path to the beam splitter BS where it is reflected to the coagulating beam reflectometer. A portion of the main beam is reflected by the beamsplitter through the neutral density filter to the laser power monitor reflectometer. This reflectometer provides an instantaneous measurement of laser power. The reflectometers contain a monolithic photodiode and transimpedance amplifier (Burr Brown OPT210) which converts the light intensity to a proportional voltage. The output voltage from both reflectometers, after passing through a low pass filter, is collected at a sample rate of 1000 Hz by a DT2801A (Data Translation) data acquisition and control board. The instantaneous laser power measurements are used to normalize the confocal reflectance measurements. The signals are inherently noisy. Currently, a new research team member is investigating methods to minimize the noise using real-time filtering techniques without compromising measured data. His results will be used to develop a control algorithm to indicate when the lesion has reached desired parameters. This work is in progress.

4. WORK IN PROGRESS

As previously discussed, we do not yet have an operational Lesion Depth Control Subsystem. Once this subsystem is functional we will integrate it with the rest of the Hybrid Tracking System. Our first prototype of the Hybrid Tracking System is currently under redesign for an effortless hand-off between the Digital and Analog Tracking Subsystems. Our goal is to have a fully operational prototype by July 1998 when *in vivo* testing on rhesus monkeys is scheduled to begin.

5. CONCLUDING REMARKS

In this paper, we have detailed the continuing development of a hybrid system capable of controlling lesion parameters and placement for the treatment of various retinal diseases. For brevity, we have not described individual subsystem operation in detail; this has been covered separately.¹⁻¹¹ During development other system applications have become evident:

- An earlier system prototype has already been used to place an array of ultrashort pulse lesions on primate retina for laser-tissue interaction studies. This capability is of great importance since in minimum visible lesion (MVL) studies, retinal damage is not visibly apparent. This system allows precise placement of lesions for further analysis by a microscopist.
- The system may also be used to stabilize a lower power laser on the retina for extended periods for Photo Dynamic Therapy (PDT) treatments.²³
- The system may also be adapted to for dermatology applications -- specifically, stabilizing a laser for Port Wine Stain treatment and tattoo removal.

In closing, although system development has been ongoing since 1984, we are on the verge of clinical practicality. We hope to have a clinically significant prototype in operation by July 1998

6. ACKNOWLEDGMENTS

This research has been supported in part by the Air Force Office of Scientific Research and the Optical Radiation Division (AL/OEOP) Brooks AFB, Texas. This research program was recognized in April 1997 with the Air Force Research and Development Award.

7. REFERENCES

1. C.H.G. Wright, "A Unified Design for the Image Processing, Tracking, and Control of a Real-time Robotic Laser System for Ophthalmic Surgery," PhD Dissertation, The University of Texas at Austin, August 1996.
2. C.H.G. Wright, R.D. Ferguson, H.G. Rylander III, A.J. Welch, S.F. Barrett, "A Hybrid Approach to Retinal Tracking and Laser Aiming for Photocoagulation," *Journal of Biomedical Optics*, in press.
3. C.H.G. Wright, R.D. Ferguson, S.F. Barrett, H.G. Rylander III, A.J. Welch, "Hybrid Retinal Photocoagulation System," *BiOS '97 International Biomedical Optics Symposium, Ophthalmic Technologies VII*, San Jose, CA, Feb 1997.
4. S.F. Barrett, M.R. Jerath, H.G. Rylander, and A.J. Welch, "Digital Tracking and Control of Retinal Images," *Optical Engineering*, Vol 31, Jan 94, 150-159.
5. S.F. Barrett, M.R. Jerath, H.G. Rylander, and A.J. Welch, "Automated Lesion Placement in the Rabbit Eye," *Lasers in Surgery and Medicine*, Volume 17, pp 172-177, 1995.
6. S.F. Barrett, M.R. Jerath, H.G. Rylander III, and A.J. Welch, "Instrumentation for Feedback Controlled Retinal Photocoagulation," *Proc. SPIE 1892*, pp. 76-85, 1993.
7. S.F. Barrett, "Digital Tracking and Control of Retinal Images," PhD Dissertation, The University of Texas at Austin, May 1993.
8. S.F. Barrett, M.R. Jerath, H.G. Rylander III, and A.J. Welch, "Digital Tracking and Control of Retinal Images," *Proc. SPIE 1877*, 272-283, 1993.
9. S.F. Barrett, C.H.G. Wright, M.R. Jerath, R.S. Lewis II, B.C. Dillard, H.G. Rylander III, and A.J. Welch, "Automated Placement of Retinal Laser Lesions In Vivo," *SPIE 2374, Photonics West*, Feb 1995.
10. S.F. Barrett, C.H.G. Wright, M.R. Jerath, R.S. Lewis II, B.C. Dillard, H.G. Rylander III, and A.J. Welch, "Automated Retinal Robotic Laser System Instrumentation," *SPIE 2396, Photonics West*, Feb 1995.
11. S.F. Barrett, C.H.G. Wright, M.R. Jerath, R. Stephen Lewis II, Bryan C. Dillard, H.G. Rylander, and A.J. Welch, "Computer Aided Retinal Photocoagulating System," *Journal of Biomedical Optics*, Volume 1, Number 1, 1996.
12. R. Birngruber, V.P. Gabel, and F. Hillenkamp, "Fundusreflectometry: A Step Towards Optimization of Retina Photocoagulation," *Modern Problems in Ophthalmology*, Volume 18, 1979, pp. 383-390.
13. W. Weinberg, R. Birngruber, and B. Lorenz, "The Change in Light Reflection of the Retina During Therapeutic Laser Photocoagulation," *IEEE Journal of Quantum Electronics*, QE-20, 1984, pp. 1481-1489.
14. Y. Yang, M.S. Markow, A.J. Welch, H.G. Rylander III, "Automatic Control of Lesion Size in a Simulated Model of the Eye," *IEEE Journal of Quantum Electronics*, QE-26, No. 12, 1990, pp. 2232-2239.
15. M.R. Jerath, C. Gardner, H.G. Rylander III, and A.J. Welch, "Dynamic Optical Property Changes: Implications for Reflectance Feedback Control of Photocoagulation," *J. Photochem. Photobio.*, Volume 16, 1992, pp. 113-126.
16. M.R. Jerath, "A Software Package for the Analysis of Laser Induced Retinal Lesions," Master's Thesis, The University of Texas at Austin, 1989.
17. M.R. Jerath, R. Chundru, S.F. Barrett, H.G. Rylander III, and A.J. Welch, "Reflectance Feedback Control of Photocoagulation In Vivo," *Proc. SPIE 1877*, pp. 254-261, 1993.
18. M.R. Jerath, R. Chundru, S.F. Barrett, H.G. Rylander III, and A.J. Welch, "Preliminary Results of Reflectance Feedback Control of Photocoagulation In Vivo," *IEEE Transactions on Biomedical Engineering*, Volume 41, Number 2, February 1994.
19. M.R. Jerath, R. Chundru, S.F. Barrett, H.G. Rylander III, and A.J. Welch, "Reflectance Feedback Control of Photocoagulation In Vivo," *Archives of Ophthalmology*, Volume 111, April 1993, pp. 531-534.
20. M.R. Jerath, "Real Time Control of Laser Induced Retinal Lesions" PhD Dissertation, The University of Texas at Austin, 1992.
21. J.H. Inderfurth, R.D. Ferguson, M.B. Frish, and R. Birngruber, "Dynamic Reflectometer for Control of Laser Photocoagulation on the Retina," *Lasers in Surgery and Medicine*, Volume 15, 1994, pp. 54-61.
22. N. Maharajh, "Use of Reflectance for the Real Time Feedback Control of Photocoagulation," Masters Thesis, The University of Texas at Austin, May 1996.
23. "Ciba and QLT Test Photodynamic Treatment for Macular Degeneration," *Biophotonic News*, July/August 1996, p. 25.

Vitreoretinal surgery and mid-infrared cutting lasers

Claudio Azzolini¹, Pier Giorgio Gobbi², Rosario Brancato^{1,2}

¹ Department of Ophthalmology and Visual Sciences, Scientific Institute H S. Raffaele,
University of Milan

² Laser Medicine Research, Scientific Institute H S. Raffaele, Milan

ABSTRACT

Mid infrared lasers are considered a potential interesting approach for safer and tractionless removal of pathological tissue in vitreoretinal surgery. They include the Erbium:YAG laser emitting at 2.94 μm and the semiconductor diode laser at 1.93 μm . Due to their capability of inducing photothermal incision and ablation effects, procedures like precise tissue cutting, tissue removal and coagulation can be achieved.

Examples of various steps of surgery performed with such laser sources are shown, including retinotomies, retinectomies, and removal of vitreous, epiretinal and subretinal membranes. Advantages and drawbacks of each wavelength are physically and clinically discussed in relation to the surgical procedure type (contact, noncontact), the target tissue and the absorbance of the vitreous substitute adopted (hydrated fluids, silicone oils, perfluorocarbons).

According to our three years experience with these cutting lasers, it can be said that: (i) they require special knowledge and the frequent presence of a technician, (ii) they surely represent a useful tool in vitreoretinal surgery, but not yet able to entirely replace conventional surgical instrumentation, (iii) even if some surgical steps are better performed with such lasers, cost and complexity of use limit their effective diffusion into the clinical practice.

Keywords: Infrared laser, Er:YAG laser, diode laser, laser surgery, vitreoretinal surgery, photoablation, vitreous substitutes.

1. INTRODUCTION

Instruments with high performance cutting capabilities are required in vitreoretinal surgery in order to achieve peeling, delamination and segmentation of different types of vitreoretinal membranes. Various kinds of mechanical scissors and picks are being used to remove such membranes, and moreover unwanted retinal damage can occur. The use of laser emissions with adequate cutting capabilities would allow the possibility of safer and extended tractionless removal of such membranes. In recent years experimental investigations have used different laser sources and wavelengths, as well as different interaction regimes. Among these, the most appealing candidates as cutting lasers for vitreoretinal surgery seem to be, for a number of reasons, those emitting in the mid-infrared spectral region. These include the Erbium:YAG laser emitting at 2.94 μm ¹⁻⁷ and the semiconductor diode laser at 1.93 μm ⁸⁻¹⁰.

2. MATERIALS AND METHODS

Laser instruments. The laser sources used for the present study were: (i) a continuous wave SDL-6432-P2 laser diode (SDL Inc., San Jose, CA), emitting up to 300 mW of optical power at 1.94 μm wavelength (the instrument was developed in our lab⁸). The device was based on heterojunctions of quaternary semiconductors: InGaAsP/InP; the laser radiation was delivered to the interaction site through a low-hydroxyl fused silica optical fiber (for minimum absorption at this wavelength) of 200 μm diameter and 0.22 NA (25 degrees full divergence); (ii) a fixed-Q pulsed Er:YAG laser (VersaPulse[®] Select[™] Erbium, Coherent Inc., Palo Alto, CA), emitting at 2.94 μm wavelength, with pulse energy in the range 0.2 to 10 mJ and repetition rate adjustable from 10 to 200 Hz. The system was equipped with special flexible fibers and endoprobes with tips ranging from 100 to 365 μm in diameter³⁻⁵ (Acculite[™] VitreoTome[®] delivery system).

Laser treatments. Laser cutting capabilities were tested on different vitreoretinal diseases under the operative microscope in many surgical steps: vitreous removal, epiretinal membranes removal, retinotomies and retinectomies, as well as in contact and no-contact procedures and through many types of vitreous substitutes. The semiconductor laser was also tested on experimental epiretinal membranes induced in rabbits⁸, before use on humans.

Transmittance measurements. Optical transmittance of vitreous substitutes commonly used during vitreoretinal surgery was measured with a double-beam spectrophotometer (Lambda 9 UV/VIS/NIR, Perkin Elmer Corp, Norwalk, Conn). Measurements were performed in a wide spectral range of infrared radiation, including the 1.93 μm and the 2.94 μm wavelengths^{11,12}. For each vitreous substitute, a spectrophotometric curve reporting the measured optical density as a function of wavelength was obtained.

3. RESULTS

Using the diode laser in a contact procedure, good retinotomies with a modest white surrounding halo were performed with an energy of around 120 mJ. The retinal hole diameter was slightly larger (about 300 μm) than the fiber core diameter. Retinal holes were more easily induced on detached retina. Under threshold, adhesion of the retina to the probe tip was sometimes observed, and extreme care was then necessary to avoid tractional retinal tears. We observed in these cases a reduced transmission of the probe, due to cellular debris deposited on the tip. Therefore, accurate cleaning of the probe tip was necessary to restore previous efficacy.

Using a non-contact procedure, with a probe tip-retina distance of less than 0.5 mm, retinal holes were obtained with the same energy of 120 mJ. The hole size was smaller, surrounded by a white halo with an extension of 100-200 μm across, due to photocoagulation of the tissue by the tails of the divergent laser beam. We did not observe any intrasurgery complications like choroidal haemorrhages.

Extended retinal incisions could be obtained with the continuous sliding of the probe onto the retina, working at the smallest tip-to-retina distance to avoid traction (quasi-contact mode).

When irradiating epiretinal membranes, e.g. in proliferative diabetic retinopathy, we observed ablation of the surface layers closer to the probe tip. The maximum ablative effect was obtained irradiating at full power (240 mW) with 0.5-0.6 sec. exposures, resulting in an estimated thickness of the removed tissue of 40-60 μm per stroke. At the same time, the deep membrane layers suffered mild shrinkage, which was secondary to thermal damage.

Complete transection of the robust membranes was difficult to achieve, because of the time length of the procedure (many tens of laser pulses) and due to the torsion and contraction movements of the fibrotic membrane, thus thwarting precise overlap of successive laser pulses onto the same target zone. Lengthening the laser pulse duration increased the thermal reaction of the tissue, without yielding an appreciable improvement in the ablation performance.

Using the Er:YAG laser, resection of epiretinal membranes could be easily obtained at pulse energies in the range 1.5-3.5 mJ with the 200 μm sapphire tip probe. Working at the maximum repetition rate of 200 Hz greatly improved the cutting speed. Retinotomies and retinectomies were easily performed both in attached and detached retina at about 2 mJ per pulse, using the smallest tip quartz endoprobe in contact procedure. In both procedures, coagulation of retina and fibrovascular membranes was achieved at the edges of the excised tissue, with an extension of about 50 μm , thus easing surgery.

The Erbium laser allowed the really complete removal of remnants of vitreous base attached to the retina, not always possible with the conventional vitrectomy probe. This was achieved fairly well at low pulse energy, but it turned out to be time-consuming.

The optical transmittance of vitreous substitutes greatly differs at the two laser wavelengths considered. In fact, the penetration depths at 1.93 μm and 2.94 μm are respectively: 80 μm and 1 μm in water-based vitreous substitutes like balanced salt solutions or hyaluronate sodium; 1500 mm and 13 mm in perfluorocarbon liquid; and 20 mm and 2.5 mm in silicone and fluorosilicone oils.

4. DISCUSSION

The surgical use of mid infrared lasers is essentially based upon the strong absorption exhibited by tissue water. At these wavelengths, in fact, there are no natural chromophores available for the optical interaction. Water has two main absorption peaks at 1.93 and 2.94 μm , where light can penetrate 80 and 1 μm in depth, respectively¹³⁻¹⁵. If an adequate amount of optical energy is delivered to such small layers of tissue penetrated by the infrared light, then vaporization of the water

content is obtained together with decomposition of tissue constituents. This is the basis for photothermal incision and ablation effects.

The Er:YAG laser emits at 2.94 μm , thus directly matching the main water absorption peak, and requires the minimum amount of energy to get water vaporization, while causing the minimum collateral tissue damage^{16,17}. Due to the shallow penetration of its wavelength, the volume of ablated tissue is also very small, thus requiring high repetition rates for an effective cutting action.

The Er:YAG laser demonstrated good effectiveness in obtaining transection of vitreous membranes as well as creation of retinotomies and retinectomies, and accurate removal of vitreous base. The tissue coagulation concomitant with the photoablating action is very useful for surgery.

To our experience, the main drawbacks of this laser source lie in the difficult handling of the endocular probe, due to the poor flexibility of the optical fiber, and in the very long learning curve required to the surgeon to become fully acquainted with this technique. Moreover, the costs of the instrument and of the disposable probes can represent a major concern for a wide diffusion of the Er:YAG laser endocutter.

The CW semiconductor laser at 1.94 μm , on the other hand, might be a lower cost alternative as endocutter laser source. It exhibits good electrical-to-optical conversion efficiency, small size, high reliability and long lifetime. Our prototype allowed good retinal incisions as well as vitreous base removal. Due to the low power available, transection of thick membranes is not practically feasible. At the same time, more severe thermal effects are produced on tissue, like shrinkage and extensive coagulation, as a consequence of the long interaction time adopted. A tenfold increase of the output irradiance is expected to promote this laser as an effective endocutter tool.

Using these cutting lasers, the surgeon has to take into account that mid-infrared optical radiation shows dramatic differences of penetration depth in different fluids used as vitreous substitutes. This inhomogeneous behaviour can strongly influence surgical procedures. High-absorbing liquids (all vitreous substitutes containing water) should be used mainly in contact procedures and could provide a shield for remote structures. Perfluorocarbon liquid shows the lowest absorption at all wavelengths, allowing use in contact and noncontact surgical procedures. Using silicone and fluorosilicone oils, different effects can take place depending on the exact probe tip-to-retina distance, as the penetration depth approaches the typical working distance in vitreoretinal surgery. The surgeon must be aware of the different wavelength transmittance of vitreous substitutes to better evaluate and optimize the efficacy and safety of these cutting laser sources.

After three years experience with vitreoretinal cutting lasers, we can conclude that they surely represent a useful tool in vitreoretinal surgery, but not yet able to entirely replace conventional surgical instrumentation. Moreover, their use requires special knowledge on the interaction process of specific laser wavelengths with tissues and vitreous substitutes. Assistance by a physicist or a laser technician can be very helpful to properly manage the laser endocutter and to reduce the learning time. Finally, even if some surgical steps are better performed with such lasers, the present cost and complexity of use can limit nowadays their effective diffusion into the clinical practice.

Further technological developments as well as clinical developments (like extension of use to other ophthalmic procedures) will definitely demonstrate the efficacy of these endocutting lasers compared to traditional surgical instruments.

5. REFERENCES

1. Margolis TI, Farnath DA, Destro M, Puliafito CA. "Erbium:YAG Laser Surgery on Experimental Vitreous Membranes", *Arch. Ophthalmol.* **107**, pp. 424-42, 1989.
2. D'Amico DJ, Moulton RS, Panagiotis G, Theodossiadis PG, Yarborough JM. "Erbium:YAG Laser Photothermal Retinal Ablation in Enucleated Rabbit Eyes", *Am. J. Ophthalmol.* **117**, pp. 783-790, 1994.
3. D'Amico DJ, Brazitikos PD, Marcellino GR, Finn SM, Hobart JL. "Initial clinical experience with an erbium:YAG laser for vitreoretinal surgery", *Am. J. Ophthalmol.* **121**, pp. 414-425, 1996.
4. Brazitikos PD, D'Amico D, Bernal MT, Walsh AW. "Erbium-YAG Laser Surgery of the Vitreous and Retina", *Ophthalmology*. **102**, pp. 278-290, 1995.
5. D'Amico DJ, Blumenkranz MS, Lavin MJ, Quiroz-Mercado H, Pallikaris IG, Marcellino GR, Brooks GE. "Multicenter Clinical Experience Using an Erbium:YAG Laser for Vitreoretinal Surgery", *Ophthalmology* **103**, pp. 1575-1585, 1996.
6. Peyman GA, Katoh N. "Effects of an erbium:YAG laser on ocular structures", *Int. Ophthalmol.* **10**, pp. 245-253, 1987.
7. Tsubota K. "Application of erbium:YAG laser in ocular ablation", *Ophthalmologica* **200**, pp. 117-122, 1990.

8. Azzolini C, Gobbi PG, Brancato R, Trabucchi G, Codenotti M, "New semiconductor laser for vitreoretinal surgery". *Laser. Surg. Med.* **19**, pp. 177-183, 1996.
9. Major JS Jr., Nam DW, Osinski JS, Welch DF, "High-Power 2.0 μm InGaAsP Laser Diodes", *IEEE Photon. Technol. Lett.* **5**, pp. 594-596, 1993.
10. Major JS Jr, Nam DW, Osinski JS, Welch DF, "High-Power Single-Mode 2.0 μm InGaAsP Laser Diodes", *IEEE Photon. Technol. Lett.* **5**, pp. 733-734, 1993.
11. Azzolini C, Gobbi PG, Brancato R, Bosi L, Galli D, Zelada M, Patelli F, "Vitreoretinal cutting lasers: absorption of different vitreous substitutes at 2 and 3 μm wavelengths", *Invest. Ophthalmol. Vis. Sci.* **37/3**, pp. 695, 1996.
12. Azzolini C, Gobbi PG, Brancato R, Bosi L, Gallo D, Zelada M, Patelli F, "Interaction between infrared radiation and vitreous substitutes", *Arch. Ophthalmol.* **115**, pp. 899-903, 1997.
13. Hale GM, Querry MR. "Optical Constants of Water in the 200-nm to 200- μm Wavelength Region", *Applied Optics*, **12**, pp. 555-563, 1973.
14. Zolotarev VM, Mikhailov BA, Alperovich LI, Popov SI, "Dispersion and absorption of liquid water in the infrared and radio regions of the spectrum", *Opt. Spectrosc.* **27**, pp. 430-432, 1969.
15. Muller G, Dorschel K, Kar H, "Biophysics of the Photoablation Process", *Lasers. Med. Sci.* **6**, pp. 241-254. 1991.
16. Walsh JT Jr, Flotte TJ, Deutsch TF. "Er:YAG Laser Ablation of Tissue: Effect of Pulse Duration and Tissue Type on Thermal Damage", *Laser. Surg. Med.* **9**, pp. 314-326, 1989.
17. Berger JW, Bochow TW, Kim RY, D'Amico DJ, "Biophysical Considerations for Optimizing Energy Delivery During Erbium:YAG Laser Vitreoretinal Surgery", *Proc. SPIE* 1996; 2673; pp. 146-156.

Anterior capsulotomy using the CO₂ laser

Adiel Barak, MD, Tova Ma -Naim, MD, Mordechai Rosner, MD, Ophir Eyal,
Micahel Belkin, MD

The Goldschleger Eye Research Institute, Sheba Medical Center, Israel,
The Department of applied Physics, Tel Aviv University.

Continuous circular capsulorhexis (CCC) is the preferred technique for removal of the anterior capsule during cataract surgery(1) due to this technique assuring accurate centration of the intraocular lens. During modern cataract surgery, especially with small or foldable intra ocular lenses, centration of the lens is obligatory(2). Radial tears at the margin of an anterior capsulotomy may be associated with the exit of at least one loop of an intraocular lens out of the capsular bag ("pea pod" effect) and its subsequent decentration. The anterior capsule is more likely to remain intact if the continuous circular capsulorhexis (CCC) technique is used (3).

Although manual capsulorhexis is an ideal anterior capsulectomy technique for adults, many ophthalmologists are still uncomfortable with it and find it difficult to perform, especially in complicated cases such as these done behind small pupil, cataract extraction in children and pseudoexfoliation syndrome. We have developed a technique using a CO₂ laser system for safe anterior capsulotomy and tested it in animal eyes.

Materials and methods

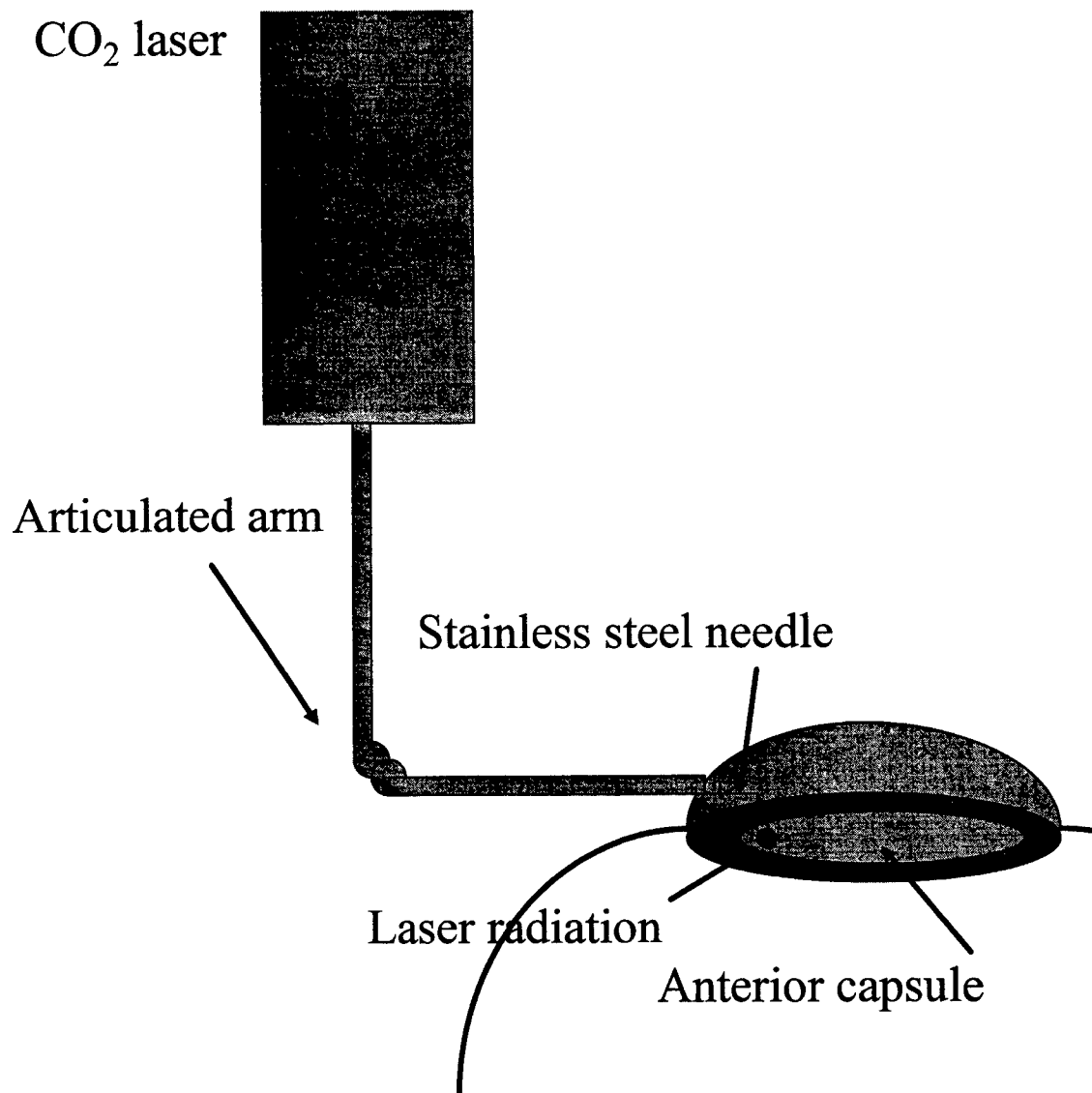
The laser used in these experiments was a DC excited CO₂ Laser.(Kaplan PenduLaser 115, OPTOMEDIC Ltd. Or-Yehuda ISRAEL). This laser has output power of 5W to 15W. It can be operated either in continuous (CW) mode or pulsed, 1 p.p.s. -10 p.p.s. mode. Pulse width is 50ms for all pulse rates. The output radiation (wavelength 10.55 μ m - 10.65 μ m) was delivered to the tissue by means of an articulated arm, (2 or 3 mirrors). A hand piece, with a $f = 125$ mm ZnSe lens, was attached to the articulated arm. A 17G (O.D. = 1.4mm) , 50mm long stainless steel needle with a 45 degrees mirror at the distal end was added to the hand-piece. Through the needle both laser radiation and continuous flow of air were delivered to the anterior chamber. The air

was injected through the needle to the anterior chamber by an air pump (DC powered, type 8009-25, ASF THOMAS. Maximum throughput at ambient atmospheric pressure: 4 Lit./min).

The surgical technique

All procedures were done on fresh enucleated bovine eyes. Determination of optimal laser parameters for the creation laser capsulotomy were performed on 60 fresh

CO₂ laser



enucleated bovine eye. The best laser parameters were determined as the minimal laser energy required to create laser burns on the anterior capsule which was easily pulled after the completion of the laser application.

The anterior chamber was gradually filled with air continuously flowing from the hollow needle laser probe. After the complete filling of air in the anterior chamber, laser radiation was applied to the anterior capsule, creating a coagulated circle 8 mm in diameter. The laser probe was withdrawn from the anterior chamber, and the chamber was filled with the BSS flowing through the anterior chamber maintainer. Using forceps, the central portion of the anterior capsule with coagulated edges was pulled from the remaining of the capsule and removed from the eye.

Results

laser capsulotomy of the anterior capsule was very easy, quick and simple to perform. The size and shape of the capsulotomy created was determined by the surgeon during the laser irradiation. After the laser coagulation of the lens capsule, the capsule was readily pulled from its site using a forceps, creating a round capsulotomy. The capsulotomy created was round with no radial tears or any other deformity on visual inspection. The average duration of the laser irradiation was 3 second (range 2-5 seconds).

Discussion

Laser capsulotomy of anterior lens capsule was shown to be safe, easy to perform and quick. The technique developed seems promising and with clinical potentials. Further evaluation is needed before it can be applied to clinical use.

Bibliography

1. Ohrloff C, Zubcov AA. Comparison of phacoemulsification and planned extracapsular extraction. [Review] [24 refs]. *Ophthalmologica*. 1997;211:8-12.
2. Tana P, Belmonte J. Experimental study of different intraocular lens designs implanted in the bag after capsulorhexis. *Journal of Cataract & Refractive Surgery*. 1996;22:1211-21.
3. Assia EI, Apple DJ, Barden A, Tsai JC, Castaneda VE, Hoggatt JS. An experimental study comparing various anterior capsulectomy techniques [see comments]. *Archives of Ophthalmology*. 1991;109:642-7.

Er:YAG laser ablation of epiretinal membranes in perfluorocarbon fluid filled eye-balls: a preliminary report

M. Frenz, M. Ith, H.P. Weber

Institute of Applied Physics, University of Bern, Sidlerstr. 5, CH-3012 Bern, Switzerland

Th. Wesendahl, P. Janknecht

From the Retina Service,
Department of Ophthalmology, University of Freiburg, Germany

ABSTRACT

Purpose: The Er:YAG laser emitting radiation at a wavelength of 2.94 μm has been shown to produce precise tissue ablation because of the high water absorption at this wavelength. These studies evaluated the effects of the Er:YAG laser on pig retina utilizing a perfluorocarbon/retina interphase with the goal to precisely ablate epiretinal membranes.

Method: Various laser pulse energies were applied to the surface of pig retinas in perfluorocarbon filled enucleated eyes using a specially designed rotating sample holder. Free running ($\tau = 250 \mu\text{s}$) Er:YAG laser pulses were transmitted through a zirconium fluoride (ZrF_4) fiber guarded by a low OH-quartz fiber at its distal tip. The tip diameters measured 400 μm and 1 mm. The fiber probe was elevated 1 mm above the retinal surface. The laser energy was applied in a systematic fashion while alternating energy settings and probe diameters. Radiant exposures were set to 1 J/cm^2 , 3 J/cm^2 , 5 J/cm^2 , and 10 J/cm^2 .

Results: Eight of ten eyes were treated with concentric circles of 3.5 mm, 6.5 mm, and 9.5 mm radius. The remaining two eyes were treated with a hand held probe. Tissue ablation increased with radiant exposure in a linear fashion. At a radiant exposure of 1 J/cm^2 , tissue ablation was minimal with a maximum tissue ablation depth of 10 μm and minimal thermal damage to adjacent tissue. A radiant exposure of 10 J/cm^2 produced an ablation depth of 30 - 50 μm . As the ablation was performed under perfluorocarbon fluid, used as transmitting medium, no laser-induced pressure transients have been measured.

Conclusion: The Er:YAG laser in combination with perfluorocarbon fluid produced precise and homogeneous tissue ablation of the pig retina. Such precise tissue ablation needs to be achieved in order to safely ablate epiretinal membranes in close proximity to the retina surface. Further in-vivo experiments will be done to examine the functionality of the retina after laser treatment.

Keywords: retina, laser-ablation, bubble formation, tissue damage pressure transients

1. INTRODUCTION

Membranes developing on the inner surface of the retina (epiretinal membranes) occur under a number of circumstances, including proliferative retinopathy, ocular inflammation, nonproliferative vascular disorders, after penetrating injury, associated with rhegmatogenous

retinal detachment and even after successful retinal reattachment [1]. Other circumstances include retinal photocoagulation, or cryotherapy and as an idiopathic condition in otherwise healthy eyes [1-3]. Epiretinal membranes in eyes with proliferative retinopathy are usually vascularized, whereas in other conditions membranes are usually avascular [3]. These membranes however often exert adhesive traction on the underlying retina causing visual impairment in the form of tractional detachment of the macula [4].

Currently, the basic principle of surgical treatment of retinal detachment complicated by proliferative vitreoretinopathy (PVR) is the same as that for retinal reattachment surgery in general [5-8]. That is the closure and sealing of retinal tears and the complete release of membrane traction on the retina. In moderate to severe cases of PVR, vitrectomy in conjunction with dissection and removal of epiretinal membranes is the basis for successful reattachment. The dissection of the epiretinal membranes releases the tractional forces on the retina which subsequently allows for retinal reattachment [5,6]. In some cases where extensive PVR is present retinotomy and retinectomy is applied to those areas where particularly strong membrane adhesion to the retina or residual retinal traction following membrane dissection takes place. Especially in the latter case, the retinal surgeon often faces a situation where it is almost impossible to mechanically dissect epiretinal membranes because of their transparency and strong adhesion to the retina. Often it is the last resort to perform retinectomy of that area in order to release tractional forces on the retina and allow for the adjacent retina to reattach. In doing so, one produces a retinal opening which exposes the vitreous cavity and the inner retinal surface to the risk of being invaded by pigment epithelial cells which in turn are a major cause of PVR [1,3,4]. It would be much more favorable to completely remove epiretinal membranes instead. The problem is that often size and visibility of the epiretinal membranes and physical limitations of the surgical instruments as well as manual expertise of the surgeon restrict the removal of such membranes.

The Er:YAG laser has been shown to produce precise tissue ablation because of the high water absorption of the 2.94- μm wavelength emitted by this laser [9-11]. Based on the precision of the Er:YAG laser tissue ablation in vitreoretinal surgery [12-14] and dissection of vitreous membranes, a potential benefit of this laser in the ablation of epiretinal membranes seemed possible [15-17]. As with conventional vitrectomy and mechanical removal of such membranes the proximity to the retinal surface exhibits a potential risk of damage to the underlying retina.

If the fiber tip is in the eye in the natural surrounding of the vitreous, the main risk of damage during Er:YAG laser ablation of the epiretinal membranes is the fast expansion and subsequent collapse of a water vapor bubble that is created at the distal fiber tip [18]. Both the formation and the collapse of the vapor bubble have been shown to be associated with the emission of a strong pressure transient [19]. This water vapor bubble however is essential for a successful ablation of tissue in an aqueous environment since it establishes a delivery path for the highly absorbed infrared radiation through the water as demonstrated in Fig. 1 [20]. To avoid any pressure-induced damage of the retina, the aqueous vitreous has been replaced by perfluorocarbon fluid that is highly transparent at 2.94 μm radiation.

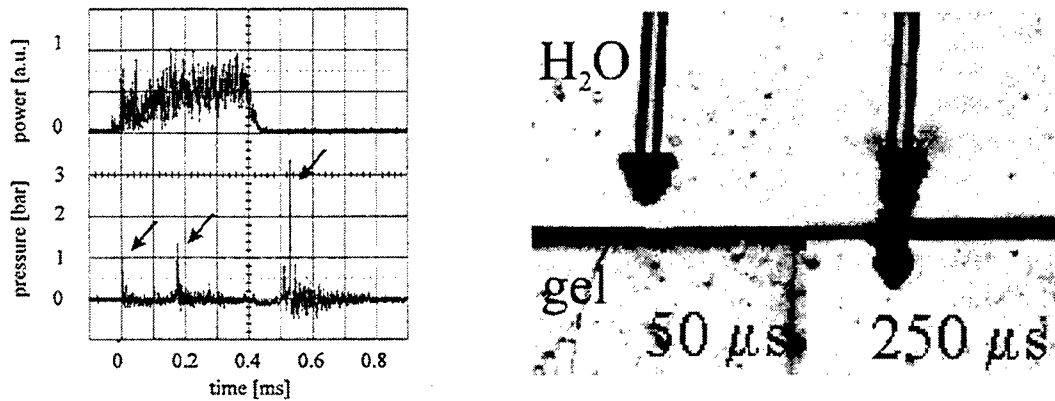


Fig. 1: Pressure transients and corresponding images of the bubble formation in water after Er:YAG laser impact. The pressure was measured at a distance of 3 mm to the fiber tip. The pressure signal reveals the explosive formation of the bubble, a closure during the laser pulse and the pressure transient generated during the bubble collapse (see arrows in the pressure signal). Er:YAG: $E = 200 \text{ mJ}$, $\tau = 400 \mu\text{s}$, fiber diameter = $400 \mu\text{m}$. The pictures show the formation of the water vapor bubble at the submerged fiber tip and the ablation of polyacrylamide gel used as a substitute for tissue [21].

The intention of the present study was to evaluate the effects of the Er:YAG laser on pig retina utilizing a perfluorocarbon / retina interphase with the goal to determine optimum laser parameters for the ablation of epiretinal membranes without altering the morphology and the functionality of the retina.

2. MATERIAL AND METHODS

2.1. Laser

A flashlamp pumped Er:YAG laser emitting at a wavelength of $2.94 \mu\text{m}$ was used in free running mode. The laser emitted bursts of spikes with a total pulse length of $250 \mu\text{s}$. A single spike duration last ≈ 0.5 to $1 \mu\text{s}$ and was separated from the following spike by $2 - 5 \mu\text{s}$. The repetition rate could be adjusted within a range from zero to 10 Hz . The laser could be tuned to emit variable pulse energies ranging from 1.25 mJ to 83.0 mJ resulting in a radiant exposure at the fiber tip of 0.995 J/cm^2 to 10.57 J/cm^2 . Laser energy was delivered onto the retinal surface via a flexible zirconium fluoride (ZrF_4) fiber with a core diameter of $350 \mu\text{m}$. A low-OH quartz fiber rod with a tip diameter of $400 \mu\text{m}$ and 1 mm were coaxially mounted at its distal fiber end in order to protect the brittle and hygroscopic ZrF_4 fiber from damage [22]. The whole system was incorporated into a sterilizable handpiece.

2.2. Target tissue

Freshly enucleated pig eyes available from the local slaughter-house were used in this study. Within a few hours after enucleation the eyes were sectioned at the equator and separated into an anterior and a posterior segment. The posterior segment containing the retina and the vitreous body was used for the laser experiment. The vitreous was removed from the retinal surface with a cotton swab. In addition air was injected into the vitreous with a miniature canula to produce a posterior vitreous detachment. In doing so, removal of the vitreous body was facilitated. The posterior cup was centered in a specially designed eye holder. A vacuum was applied to create a smooth bowl shaped retinal surface. This was done in order to maintain the physiological layering of the sensory retina, pigment epithelium, uvea, and sclera.

All experiments were performed with a fluid / retina interphase. Perfluorocarbon fluid was used to fill the eye cavity and the laser probe was immersed in the fluid. Perfluorocarbon fluids are characterized by a high transmission in the near infrared region with a broad but small absorption peak at 2800 nm [21]. The absorption coefficient for 2.94 μm was measured to be $\mu_a(2.94\mu\text{m}) = 0.5 \text{ cm}^{-1}$. Perfluorocarbon fluids are a group of $\text{CF}_3(\text{CF}_2)_x\text{CF}_3$ with x to be 7, 8 or 9. Perfluorooctane ($x = 8$), is already clinically used as a contrast agent for MR imaging of the abdomen and pelvis and in ophthalmology as intraoperative non-permanent vitreous substitute and as liquid for attaching the retina. These liquids are chemically characterized by a high affinity for oxygen and therefore have been also proposed as a blood substitute. They have a boiling point slightly above that of water ($104^\circ\text{C} - 140^\circ\text{C}$). The index of refraction was measured to be between $n = 1.27$ and 1.303 .

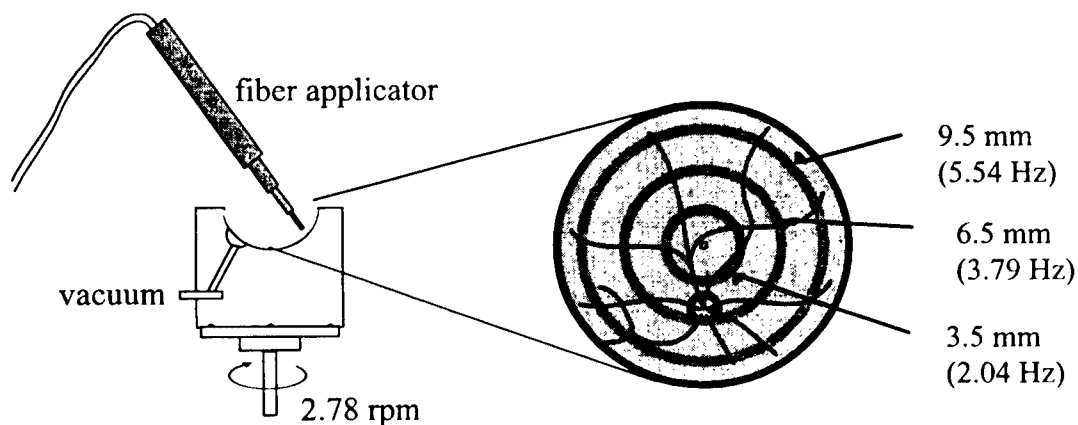


Fig. 2: Schematic of the experimental setup

2.3. Laser experiments

In order to create long laser incisions at a constant fiber - retina distance of $1\text{mm} \pm 0,1 \text{ mm}$ the holder of the posterior cup was placed on a rotating axis (2.78 rpm) as seen in Fig. 2. Depending on the radius of the laser incisions, the repetition rate of the laser was chosen such that a 50 %

overlap of the laser spot between two consecutive pulses was obtained. The radiant exposures used were 1, 3, 5 and 10 J/cm².

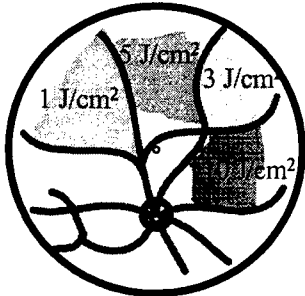


Fig. 3: Schematic of the hand held retina ablation.

In order to simulate the real life conditions as closely as possible, we additionally performed retina ablation with a hand held fiber. Again the four different radiant exposures were applied. The characteristic blood vessels of the retina served as natural lines of demarcation as schematically shown in Fig. 3. For these experiments the laser was running at 8 Hz.

The processes taking place at the fiber tip were monitored using a standard fast flash photography setup (shadow images) see Fig. 4. For illumination we used a white flash lamp emitting pulses of 20 ns (FWHM) duration which was synchronized with the Er:YAG laser via a variable delay and trigger unit. Pictures were taken at variable delay times of 0 - 2000 μ s after the start of the IR-laser pulse. The submerged fiber tip was placed at a distance of 1 mm above the target.

Synchronously, pressure transients induced in the liquid were recorded using a piezoelectric polyvinylidenefluoride (PVDF) needle hydrophone. The diameter of the active area was 0.5 mm and the rise time 30 ns. The sensitive area of the hydrophone was positioned at the same level as the fiber tip, and separated from it by 2 mm. The signal from the hydrophone was displayed on a 500 MHz digital storage oscilloscope. The hydrophone which was factory calibrated permitted measurements of pressure amplitudes in the range between 10 mbar and several kbar.

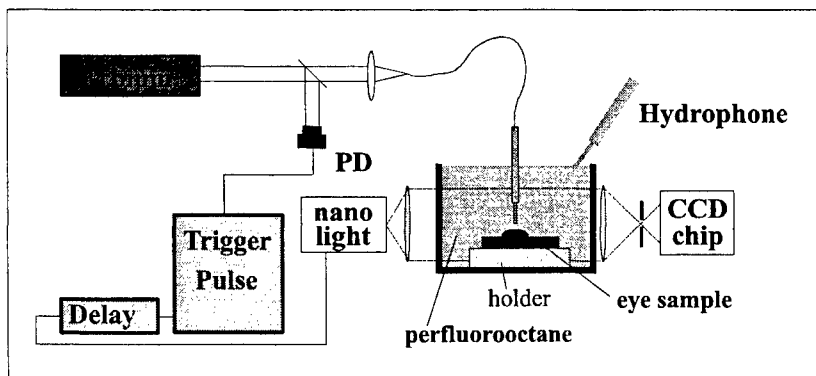


Fig. 4: Fast flash photography setup to study the dynamics of the ablation process

2.4. Sample preparation

After completion of the Er:YAG laser exposure, each posterior segment was prepared for routine histologic examination. First the perfluorocarbon was removed from the retinal surface and replaced by 4% buffered formaldehyde to achieve proper fixation of the retina. Simultaneously the outer surface was immersed in formaldehyde. Subsequently the entire

posterior cup was embedded in an agar gel using a 2.5% agar solution heated to approximately 40°C. The inside as well as the outside of the globe were covered with the agar gel. The gel needed a few minutes to cool off and to harden. After forming a gel, the agar provided a protective shell that held the retina in place and prevented artificial retinal detachment during the processing of the tissue. Agar gel provides some potential advantages in the processing of retinal tissue. Besides the fact, that it is readily available and inexpensive, agar gel behaves identical to real tissue during routine tissue processing but does not stain with most widely used staining techniques i.e. HE and PAS. It is therefore possible to process the entire tissue-agar sample in the same way one would process the tissue sample itself. The only restriction that needs to be made is the limited diffusion length of formaldehyde in agar of 5-6 mm. This means that the distance from the surface of the agar to the embedded tissue sample should not be thicker than 5-6 mm. Therefore, in practice some of the agar from the inside of the cup shaped sample needed to be carved out.

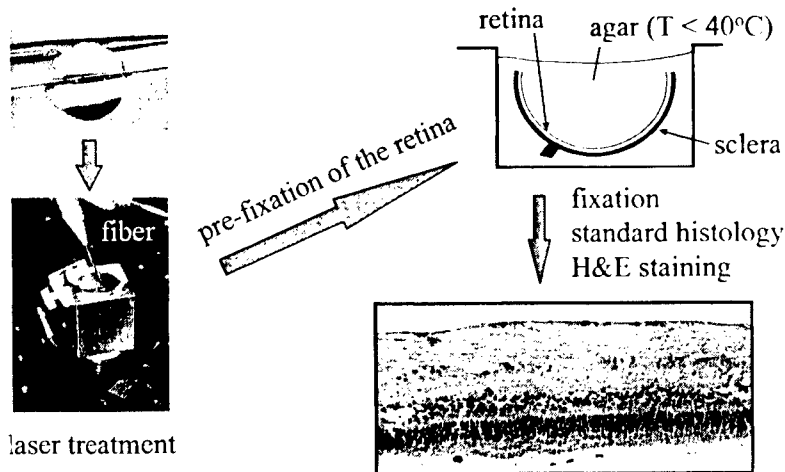


Fig. 5: Temporal development of the sample preparation for the laser experiments and the histological evaluations.

3. RESULTS

The fast flash photography images revealed the high transmission of perfluorocarbon liquid. In contrast to the ablation in the aqueous surrounding where a water vapor bubble is generated attached to the fiber tip (see Fig. 1), the ablation under perfluorocarbon fluid is characterized by a vapor bubble generated above the tissue surface as seen in Fig. 6. This perfluorocarbon vapor bubble is generated by ejected tissue particles and/or by heating of perfluorocarbon by the laser heated tissue surface. A series of pictures taken at different times after the start of the laser pulse have shown that a bubble was only formed at the end of the fiber as had been seen in the case of water (see Fig. 1) if tissue particles ejected by a previous laser pulse got attached to the distal fiber tip (Fig. 6b). The simultaneously recorded pressure signal showed no pronounced pressure transient amplitude, as found during the bubble formation in water. Therefore, a pressure induced damage of the retina seems to be very unlikely.

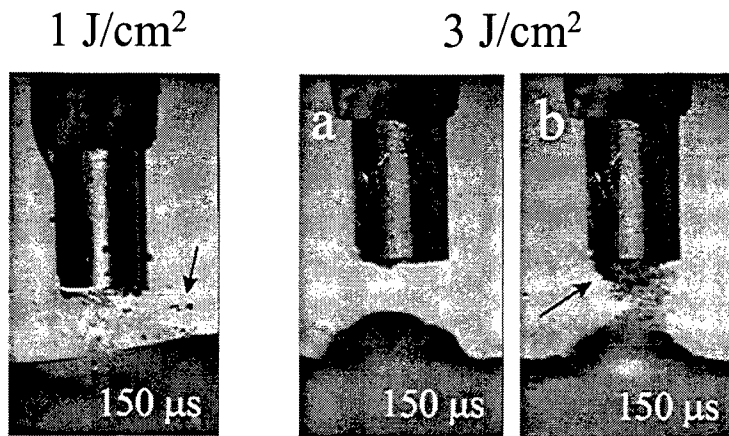
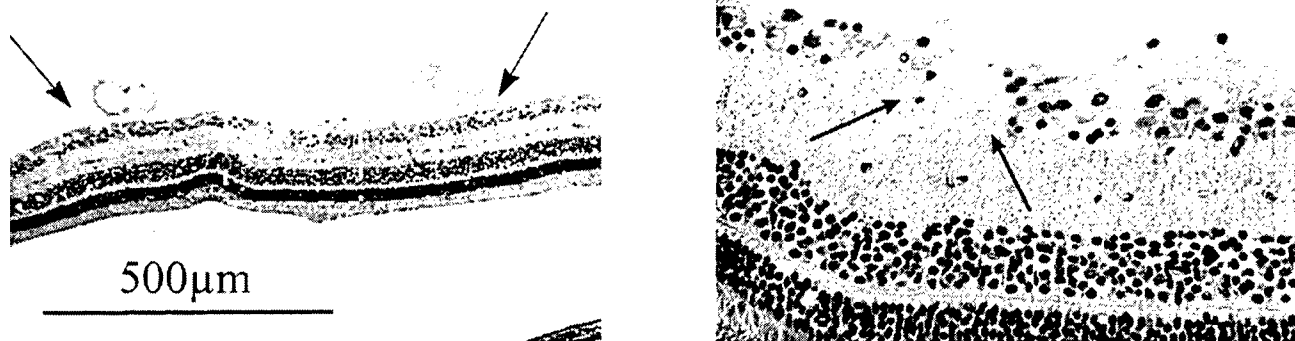


Fig. 6: Videographs of laser impacts on retina under perfluorocarbon liquid. The distance between the fiber and the tissue surface was 1 mm. Fiber diameter = 1 mm. At a radiant exposure of 1 J/cm^2 the ablation product are clearly visible (arrow). At 3 J/cm^2 a vapor bubble is formed on the tissue surface (a). If ejected tissue material got attached to the distal fiber tip, an additional small water vapor bubble (arrow (image b)) is formed at the fiber tip.

Figure 7 shows the light photomicrograph of an Er:YAG laser incision on pig retina under perfluorocarbon fluid with a radiant exposure of 3 J/cm^2 . At the low magnification a detachment of the superficial layer of the retina (indicated by arrows) is seen in the margin area of the laser spot. At higher magnification the zone of ablated and altered tissue can be seen. Micro-morphological evaluation of the sample revealed a zone of damaged tissue of $10 - 30 \mu\text{m}$.

A typical histological light photomicrograph after the hand held fiber experiment is shown in Fig. 8.

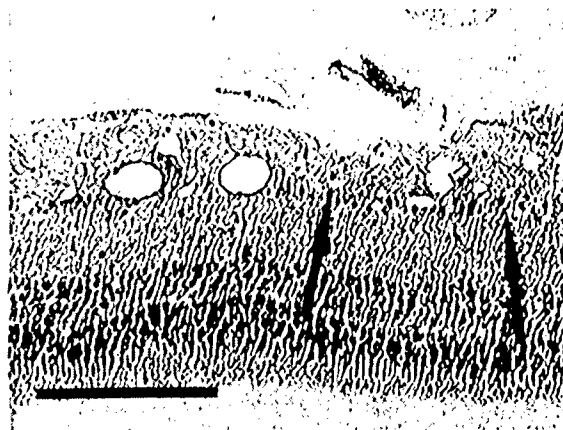


Er:YAG laser: $H = 3 \text{ J/cm}^2$

Fig. 7: Pig retina: Histologic section (Hematoxylin and Eosin staining) showing an ablation crater resulting from 50% overlapping laser pulses from an Er:YAG laser applied under perfluorocarbon liquid via a ZrF_4 fiber with an end-piece of 1 mm diameter. The arrows mark the detachment of the superficial membrane of the retina. The magnification shows the maximum damaged area of about $25 \mu\text{m}$.



1 J/cm²



10 J/cm²

Fig. 8: Histological microsections after Er:YAG laser ablation of the retina. The ablation was performed under perfluorocarbon liquid. The ablation depth marked by arrows was $5 \pm 2 \mu\text{m}$ in the case of 1 J/cm^2 and $40 \pm 10 \mu\text{m}$ for 10 J/cm^2 (bar = $100 \mu\text{m}$).

Table I summarizes the experimental results. These findings suggest that a radiant exposure between 1 J/cm^2 and 3 J/cm^2 seems to be optimum for precise ablation of epiretinal membranes with a thickness of $10 - 20 \mu\text{m}$.

radiant exposure	ablation depth
1 J/cm^2	$0 - 10 \mu\text{m}$
3 J/cm^2	$10 - 30 \mu\text{m}$
5 J/cm^2	$20 - 40 \mu\text{m}$
10 J/cm^2	$30 - 50 \mu\text{m}$

Table I: Histologically determined ablation depth for the various radiant exposures used in the experiments.

4.CONCLUSION

On the basis of our experimental data, highly precise ablation of epiretinal membranes under perfluorocarbon liquid seem to be possible. The high precision with minimal thermal damage to the adjacent tissue is a result of the strong absorption of $2.94 \mu\text{m}$ radiation in water. By using a perfluorocarbon liquid that exhibits a low absorption of IR-radiation, tissue ablation is possible without creating strong pressure transients as it is the case if ablation is performed in an aqueous environment such as saline or blood.

5. ACKNOWLEDGMENTS

This work was supported in part by the Swiss Commission of the Encouragement of Scientific Research.

6. REFERENCES

- 1 W. R. Green, in *Spencer: Ophthalmic Pathology: an Atlas and Textbook* (Saunders, W.B., 1996), p. 780-799.
- 2 M. Weller, P. Esser, K. Heimann, and P. Wiedemann, "Die idiopathische proliferative Vitreoretinopathie. Die Aktivierung von Mikrogliazellen als entscheidender Faktor", *Ophthalmologie* 89, 387-390 (1992).
- 3 T. Kono, T. Kohno, and Inomata, "Epiretinal membrane formation. Light and electron microscopic study in an experimental rabbit model", *Arch Ophthalmol* 113, 359-363 (1995).
- 4 H. P. Heidenkummer and A. Kampik, "Morphologische Analyse epiretinaler Membranen bei chirurgisch behandelten idiopathischen Makulaforamina: Licht und elektronenmikroskopische Ergebnisse", *Ophthalmologie* 93, 675-679 (1996).
- 5 M. S. Blumenkranz, S. P. Azen, T. Aaberg, D. C. Boone, H. Lewis, N. Radtke, and S. J. Ryan, "Relaxing retinotomy with silicone oil or long-acting gas in eyes with severe proliferative retinopathy", *Am J Ophthalmol* 116, 557-564 (1993).
- 6 E. H. Bovey, E. DeAncos, and M. Gonvers, "Retinotomies of 180 degrees or more", *Retina* 15, 394-398 (1995).
- 7 D. G. Charteris, "Proliferative vitreoretinopathy: pathobiology, surgical management, and adjunctive treatment", *Am J Ophthalmol* 79, 953-960 (1995).
- 8 A. Kampik, K. R. Kenyon, R. G. Michels, R. Green, and Z. C. de la Cruz, "Retinal and Vitreous membranes: Comparative study of 56 cases", *Arch Ophthalmol* 99, 1445-1454 (1981).
- 9 A. D. Zweig, B. Meierhofer, O. M. Muller, C. Mischler, V. Romano, M. Frenz, and H. P. Weber, "Lateral thermal damage along pulsed laser incisions", *Lasers Surg Med* 10, 262-274 (1990).
- 10 T. Bende, T. Seiler, and J. Wollensak, "Photoablation with the Er:YAG laser in ocular tissues", *Fortschr Ophthalmol* 88, 12-16 (1991).
- 11 V. M. Zolotarev, B. A. Mikhailov, L. I. Alperovich, and S. I. Popov, "Dispersion and absorption of liquid water in the infrared and radio regions of the spectrum", *Opt Spectrosc* 27, 430-432 (1969).
- 12 D. J. D'Amico, R. S. Moulton, P. G. Theodossiadis, and J. M. Yarborough, "Erbium:YAG Laser Photothermal Retinal Ablation in Enucleated Rabbit Eyes", *Am J Ophthalmol* 117, 783-790 (1994).

- 13 D. J. D'Amico, M. S. Blumenkranz, M. J. Lavin, H. Quiroz-Mercado, I. G. Pallikaris, G. R. Marcellino, and G. E. Brooks, "Multicenter Clinical Experience Using an Erbium:YAG Laser for Vitreoretinal Surgery", *Ophthalmology* 103, 1575-1585 (1996).
- 14 D. J. D'Amico, P. D. Brazitikos, G. R. Marcellino, S. M. Finn, and J. L. Hobart, "Initial Clinical Experience With an Erbium:YAG Laser for Vitreoretinal Surgery", *Am J Ophthalmology* 121, 414-425 (1996).
- 15 G. A. Peymann and N. Katoh, "Effects of Erbium:YAG Laser on Ocular Structures", *International Ophthalmology* 10, 245-253 (1987).
- 16 T. I. Margolis, D. A. Farnath, M. Destro, and C. A. Puliafito, "Erbium-YAG Laser Surgery on Experimental Vitreous Membranes", *Arch Ophthalmol* 107, 424-428 (1989).
- 17 K. Tsubota, "Application of Erbium:YAG Laser in Ocular Ablation", *Ophthalmologica* 200, 117-122 (1990).
- 18 M. Frenz, H. Pratisto, F. Könz, E. D. Jansen, A. J. Welch, and H. P. Weber, "Comparison of the effects of absorption coefficient and pulse duration of 2.12 μm and 2.79 μm radiation on laser ablation of tissue", *IEEE-JQE* 32, 2025-2036 (1996).
- 19 M. Frenz, H. Pratisto, M. Ith, K. Rink, G. Delacrétaz, V. Romano, R. P. Salathé, and H. P. Weber, "Transient Photoacoustic effects induced in liquids by pulsed Erbium laser", in *Laser-Tissue-Interaction V*, (1994) (SPIE, Bellingham, Vol 2134), p. 402-412.
- 20 H. Pratisto, M. Ith, M. Frenz, and H. P. Weber, "Infrared multiwavelength laser system for establishing a surgical delivery path through water", *Appl Phys Lett* 67, 1963-1965 (1995).
- 21 M. Frenz, H. Pratisto, C. Toth, E. D. Jansen, A. J. Welch, and H. P. Weber, "Perfluorocarbon compounds: transmitting liquids for infrared laser-tissue ablation", in *Biomedical Optics, Laser-Tissue-Interaction VII*, (1996) (SPIE, Bellingham, Vol 2681), p. 343-352.
- 22 D. Helfer, "Endoscopic beam delivery systems for erbium laser radiation", Diploma work Thesis, University of Berne, 1993.

SESSION 4

Ocular Implants

DEEP SCLERECTOMY WITH AND WITHOUT IMPLANT :AN IN-VIVO COMPARATIVE STUDY

Mitsumo Yamamichi, MD^{1,2}; Philippe Sourdille, MD³; Hassan Tahi MD^{1,4}; Valerie Jallet, Ph.D.⁵,
Franck L Villain Ph.D.^{5,6}, Francisco Fantes, MD¹, Jean-Marie Parel, Ph.D., Ing.ETS-G^{1,6,7}

From the (1) Ophthalmic Biophysics Center, Bascom Palmer Eye Institute, University of Miami School of Medicine, Miami, Florida; (2) Department of Ophthalmology, Fukuoka University, Fukuoka, Japan; (3) Clinique Sourdille, Nantes, France; (4) CHU, Dept. of Ophthalmology, Prof. A. Galand, Faculté de Médecine, Université de Liège, Belgique; (5) Corneal SA, Paris, France; (6) Biomedical Engineering Department, University of Miami College of Engineering, Coral Gables, Florida; (7) University of Paris Hôtel-Dieu Hospital and INSERM U86, Paris, France.

ABSTRACT

Purpose: Establish the effects of pre-Descemetic sclero-keratectomy, a new nonpenetrating Deep-Sclerectomy filtration procedure, with and without crosslinked sodium hyaluronic acid (SKgel) implant in the rabbit animal model.

Materials and Methods: Ten adult NZW rabbits had surgery only (group A) and 15 other had surgery and a crosslinked sodium hyaluronate implant inserted under the scleral flap (group B). Weekly intraocular pressure (IOP), outflow facility, and central and peripheral corneal thicknesses were measured in both the operated and the contralateral eye over a period of five months in Group A and six months in Group B.

Results: IOP was consistently lower until POD 21 for Group A and POD 161 for Group B, respectively ($P < 0.05$). Outflow facility was significantly higher than control eyes until POD 14 in Group A and until POD 84 in Group B. Peripheral corneal thickness returned to normal by POD 14 in Group A and POD 28 in Group B. By POD 35, there was no statistical significance between both groups in the mean of peripheral corneal thickness.

Conclusion: Pre-Descemetic Sclero-Keratectomy with crosslinked sodium hyaluronate implant is effective in reducing IOP and safe operation in rabbit eyes.

KEY WORDS: Nonpenetrating filtering surgery, Deep Sclerectomy, Glaucoma, Sodium Hyaluronate, Hyaluronic Acid (HA), implant, biodegradation.

1. INTRODUCTION

In 1984, Zimmerman et al^{1,2} and then Fyodorov³, described a then novel non-penetrating trabeculectomy procedure and reported their results in aphakic patients with glaucoma. The aim of these surgical methods are to excise a portion of the juxtacanalicular trabecular meshwork and to excise a portion of the canal of Schlemm, where the major resistance to aqueous outflow is believed to occurs.^{4,6} The technique was later modified and a biodegradable collagen implant was placed in the cavity formed by the deep sclerectomy procedure to act as a drain. In 1990, Fyodorov⁷ and Kozlov⁸ reported a success rate of 85 % with follow-up ranging from 6 months to 3 years, and in 1995, Demailly^{9,10} using a similar implant reported a success rate of 75.6 % at 16 months.

Concurrently, Robert Stegmann of Pretoria reported similar results in patient undergoing viscocanalostomy¹¹, a modified non-penetrating deep sclerectomy technique in which a high viscosity sodium hyaluronate viscoelastic material (Healon GV, Pharmacia-Upjohn, Sweden) is injected in Schlemm's canal to clear potential obstructions and under the scleral flap to delay the filling of the surgical cavity by fibrotic tissues.

It is unclear if the reported success of the above techniques is due to the surgical techniques or to the space filling effect initially generated by the collagen and viscoelastic biomaterials. No experimental proof were reported in the literature. However, collagen is known to favor fibrosis and hyaluronic acid solution are known to be rapidly evacuated by the body. We therefore selected the use of a crosslinked sodium hyaluronate implant to test the hypothesis. This paper describes the duration of the hypnotizing effect of a modified non-penetrating deep sclerectomy technique, Pre-Descemetic Sclero-Keratectomy (PDSK), in a rabbit model with and without implant.

2. MATERIAL AND METHODS

We performed deep sclerectomy on 25 six months old adult New Zealand white rabbits weighing 3.15 to 4.75 kg. The ARVO and USDA resolutions for animal use were followed. In each rabbits only the right eye had surgery. Anesthesia was achieved with intramuscular injections of ketamine hydrochloride (14 mg/kg of body weight) and Xylazine hydrochloride

(7 mg/kg of body weight). The rabbits were divided into 2 groups. 10 rabbits for Pre-Descemetic Sclero-Keratectomy alone (Group A), 15 rabbits for Pre-Descemetic Sclero-Keratectomy with SKgel implantation (Group B).

2.1 Surgical technique

After the superonasal conjunctiva and Tenon's capsule were dissected from the limbus, a scleral flap measuring 5 x 6 mm and of $\approx 50\%$ scleral thickness, was created using a diamond knife. The scleral flap was extended 1.0 mm further from the limbus into clear cornea. A second flap (3.5 x 3.5 mm) was then delaminated from the deeper layers of the sclera, leaving a thin scleral layer over the choroid and ciliary body, trabecular meshwork, Schwalbe's line, and Descemet's membrane (Figure 1). In Group B (15 rabbits), a SKgel implant was positioned in the pre-Descemetic space using a micro-sponge (Miniature surgical sponge, Alcon Inc, Ft. Worth, TX) and a custom-made 2 mm wide 100 μm thick stainless steel spatula. The scleral flap was then closed with a 10-0 nylon suture. Tenon's capsule and the conjunctiva were then closed with 6-0 polyglactin 910 sutures. To avoid artifacts, no pre-, intra- or postoperative medications were given to the animals.

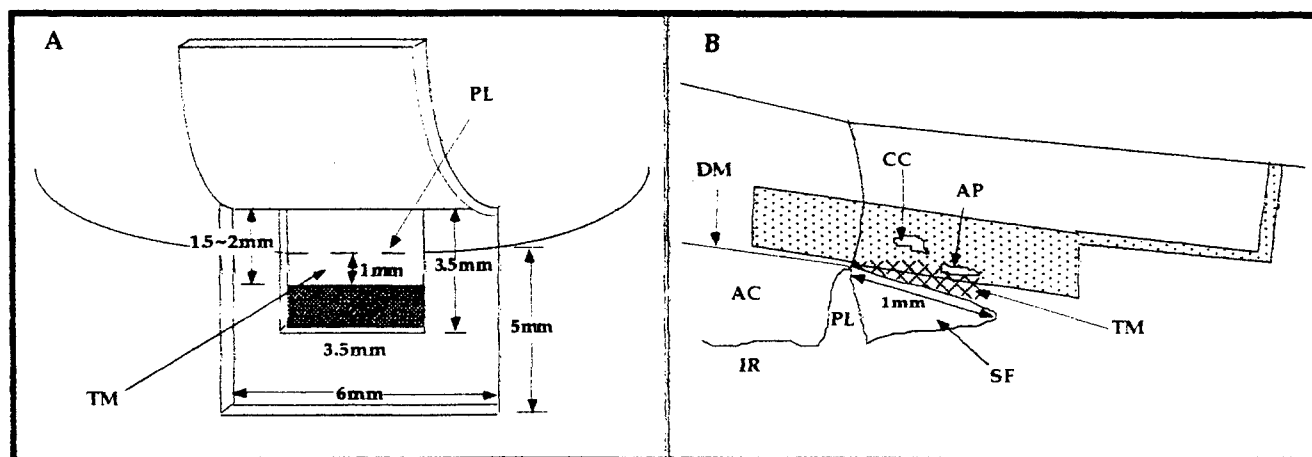


Figure 1. Deep Sclerectomy. (A: Front view, B: Side view). AC, Anterior chamber; AP, Aqueous plexus; CC, Collector channel; DM, Descemet's membrane; IR, Iris; TM, Trabecular meshwork; SF, Spaces of Fontana; PL, Pectinate ligament.

2.2 Implant

Sodium hyaluronate issued from bacterial fermentation was crosslinked with butanediol diglycidylether (BDDE) to obtain a solid hydrogel. The resulting gel was purified by deionized water extraction to remove any residual BDDE and by-products of the reaction. It contains more than 95% H_2O when hydrated in a phosphate buffer solution at pH 7.2. Square implants of 500 μm thickness and 3 mm on each sides were cut in the gel and stored in vials containing a 100 μl buffer solution. The vials were sealed and sterilized by autoclave. The implants were stored at 4 $^{\circ}\text{C}$ until the surgery. The total weight of the implant was 4.5 mg.

2.3 Postoperative measurements

The central and peripheral corneal thickness of the both eyes were measured five times, using a calibrated ultrasonic pachymeter ($\pm 5 \mu\text{m}$, 1640 m/s, Pachette, DGH Inc). After the tear film of both eyes were stained with sterile sodium fluorescein strip (1mg, Fluoret, Smith & Nephew, UK), the IOPs were measured (eye selected at random) using a Goldmann applanation tonometer (Haag-Streit type mounted on a Topcon SL6 slit-lamp) with a standard 7.0 mm diameter tip. To perform these measurements accurately, the rabbit was placed on the custom made cast to obtain an appropriate eye position. Because the tonometer tip size was not calibrated for rabbit eyes, the tonometric values were expressed with the reading scale. IOP measurements were performed at fixed intervals (15 min.) after induction (IM injection) of the general anesthesia. At the end of the examination, the outflow facility was measured (eye selected at random) with a calibrated Schiötz tonometer (5.5 gr). The Schiötz tonometer was placed on the cornea, a reading was taken, the tonometer was left vertically on the eye for two 2 minutes and a second reading of the scale was taken, and the original 4 minutes values were estimated by doubling the values.

2.4 Statistical analysis

Statistical significance of the data was determined with the paired Student t-test, and the Kaplan-Meyer method was used for survival analysis. A p value of <0.05 was considered to be significant. Data are expressed as the mean and standard deviation ($\bar{x} \pm \text{SD}$).

3. RESULTS

3.1 Clinical observations

Slit-lamp and microscope examinations showed, in both groups a minor conjunctival injection at POD 3 which resolved by POD 14. An edema of the corneal tissues adjacent to the surgical keratectomy site was observed in both groups. The edema extended to about 2 mm from the sides of the posterior keratectomy and subsisted to POD 7 and POD 14 in group A and POD 14 and POD 21 in Group B. A conjunctival elevation was observed at the slit-lamp until POD 14 in Group A and POD 35 in Group B.

3.2 Intraocular pressure

In Group A, the operated eyes IOP were significantly lower than in the control eyes, from POD 3 to POD 21 and again at POD 35 ($p < 0.05$). Thereafter, the IOP returned to control eye levels. In Group B, the IOP remained lower in the operated eye up to POD 140 ($p < 0.05$). Average IOP of Group B were significantly lower than Group A (Figure 2). The relative ratios of IOP in both Groups between operated and non-operated are shown Figure 3. The mean IOP ratio of the SKgel implanted eyes were significantly lower than non-implanted eyes from POD 21.

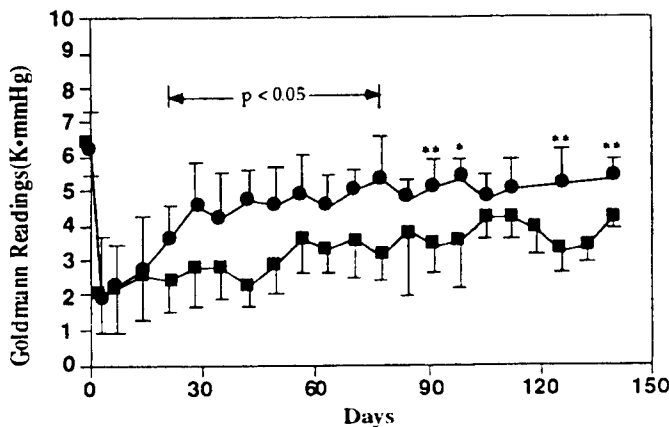


Figure 2. Average intraocular pressure (IOP) readings for without implant (●), and with implant (■) up to POD 140. (Paired Student-T Test; * : $p < 0.05$, ** : $p < 0.01$).

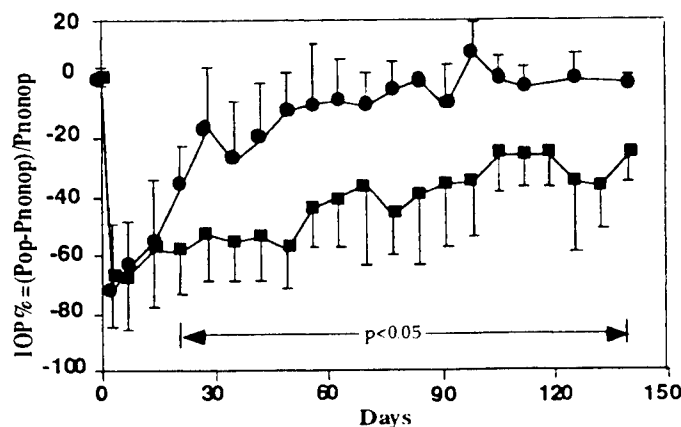


Figure 3. The relative ratio of IOP for without implant (●), and with implant (■) between the IOP of the operated eye (Pop) and the IOP of the nonoperated eye (Pnonop) up to POD 140.

Shown in Figure 4 are Kaplan-Meier survival curves calculated with failure defined as the ratio of IOP reduction between the operated and control eyes of ≤ 0.25 in 3 consecutive periods ($n = 6$) for both groups. Group B survival was significantly longer the Group A ($p < 0.001$).

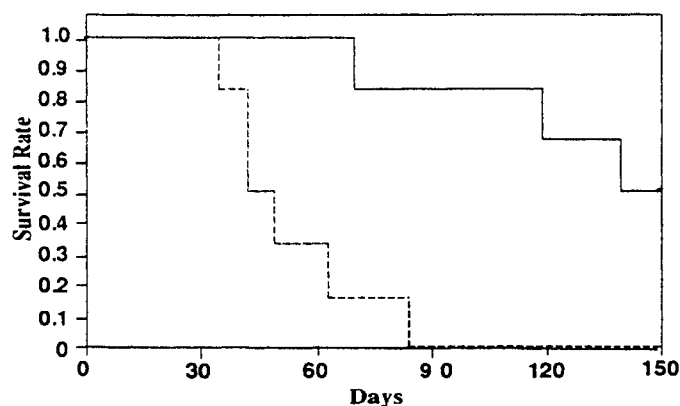


Figure 4. Kaplan Meier survival curves of eyes treated without implant (Dotted line) and with implant (solid line) with failure defined as the ratio of IOP reduction between the operated and nonoperated eyes of ≤ 0.25 in 3 consecutive periods. Survival distribution of Group A and Group B differed significantly ($p < 0.001$).

3.3 Outflow facility

The operated eyes had a higher outflow facility than the control eyes up to POD 14 in Group A and up to POD 56, and again at POD 77 and 84 in Group B. The SKgel implanted eyes had a higher outflow facility than the non-implanted eyes up to POD 84 (Figure 5).

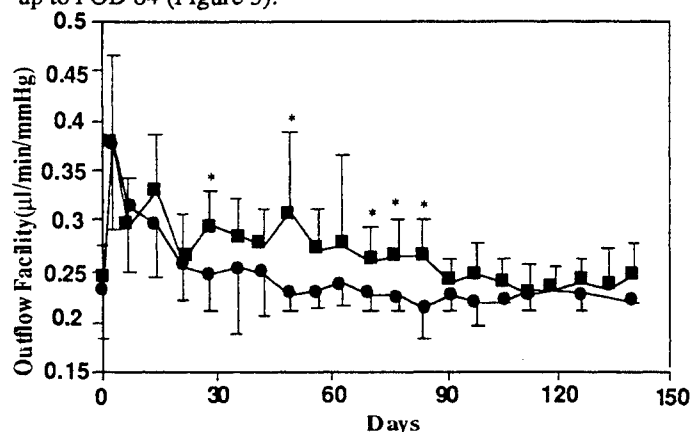


Figure 5. Average outflow facility of Group A (●) and Group B (■) up to POD 140. (Paired Student-T Test ; * : $p < 0.05$, ** : $p < 0.01$).

3.4 Pachymetry

There was no statistical difference in postoperative central corneal thickness between operated and control eyes in either groups and no significant differences between the two groups.

Following surgery, the peripheral cornea in the operated eyes became slightly thicker in the operated than in the control eyes. The difference was statistically significant until POD 7 for Group A (Figure 6) and POD 21 for Group B (Figure 7). From POD 49, the peripheral cornea of Group B became slightly thinner ($386 \pm 15 \mu\text{m}$) when compared to non-operated control eyes ($408 \pm 21 \mu\text{m}$). However there were no statistical significant differences between both group in the mean of peripheral corneal thickness 35 days after surgery.

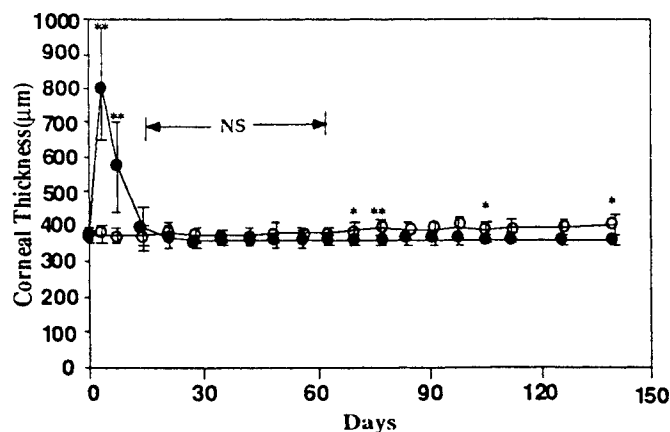


Figure 6. Average peripheral corneal thickness of eyes receiving surgery without implant operated eyes (●) and nonoperated eyes (○). (Paired Student-T Test ; * : $p < 0.05$, ** : $p < 0.01$).

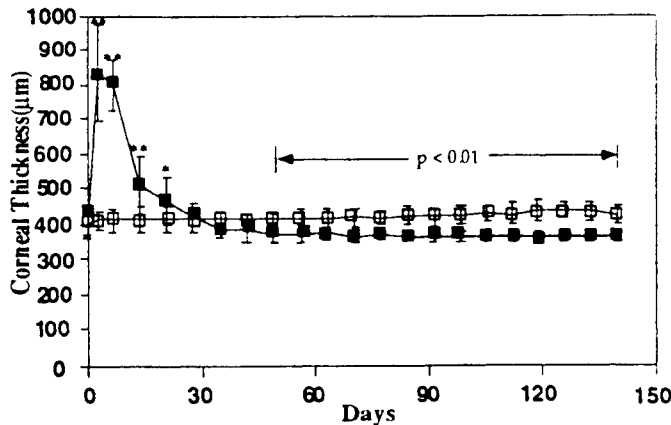


Figure 7. Average peripheral corneal thickness of eyes receiving surgery with a CSHA implant (■) and contralateral eyes that were not operated (□). (Paired Student-T Test ; * : $p < 0.05$, ** : $p < 0.01$).

3.5 Complications

The most common complication was a shallow peripheral anterior chamber at the end of surgery. However, collapse of the anterior chamber never occurred in this series of 25 cases. A microperforation into the anterior chamber was noted in 20% of both groups. The microperforation did not significantly affect the anterior chamber depth. A corneoscleral flap buttonhole occurred in two eyes of Group B. Reapproximating Tenon's capsule and the conjunctiva over the buttonhole intraoperatively sealed these.

All cases had mild peripheral corneal edema and corneal neovascularization associated with corneal incision. At POD 3, five cases (50%) of the Group A and four cases (26.7%) of the Group B had an intracorneal hemorrhage localized at the posterior keratectomy site. In all cases the hemorrhage cleared spontaneously by POD 14 without treatment. The only intraocular complication noted was a single anterior synechia observed in 10% of the cases of Group A and in 20% of Group B.

4. DISCUSSION

Our investigation demonstrated a higher success rate in deep sclerectomy with SKgel implant than without. The IOP of animals with implant was found significantly reduced for a longer period of time. However, we are uncertain as to the exact cause. In this surgery, conjunctival elevation had disappeared by POD 35, we deduced that the outflow was not subconjunctival but intrascleral or, as Fyodorov and Demailly have suggested, transchoroidal.

In our series, Pre-Descemet Sclero-Keratectomy surgery has not been associated with severe intraoperative and postoperative complications. A slight postoperative peripheral corneal edema and anterior synechiae at the keratectomy site was noted in a few cases. Anterior synechia may be solely due to the rabbit's anatomy as their iris bows forward towards the cornea whereas in human it does not.

We conclude that (1) Pre-Descemet Sclero-Keratectomy with and without a crosslinked sodium hyaluronate implant is a safe operation in the rabbit eye, (2) the SKgel is biocompatible and produce no foreign body reactions, (3) the SKgel implant prolong the IOP lowering effect of nonpenetrating deep sclerectomy procedure.

Human clinical trial conducted on a small number of patients is underway in France and, with an average 6 months follow-up, confirm our experimental findings. A European multicenter clinical trial is schedule to start in the Fall of 1998.

5. ACKNOWLEDGMENTS

The SKgel implants were produced and donated by Corneal Industries SA, Pringy, France. We thank Izuru Nose and William Lee for technical support and Robert Rosa, M.D., for histopathology analysis. The research was supported in part by the Florida Lions Eye Bank, Corneal SA, Research to Prevent Blindness Inc. New-York, NY, and the Henri and Flore Lesieur Foundation.

6. REFERENCES

- 1) Zimmerman TJ, Mandelkorn RM, Kooner KS, Rawlings FE, Ford VJ, Leader BJ, Olander KW, Koskan AJ. Effectiveness of nonpenetrating trabeculectomy in aphakic patients with glaucoma. *Ophthalmic Surgery*. 1984;15: 44-50.
- 2) Zimmerman TJ, Mandelkorn RM, Kooner KS, Rawlings FE, Ford VJ, Leader BJ, Olander KW, Koskan AJ. Trabeculectomy vs. non-penetrating trabeculectomy: A retrospective study of two procedures in phakic patients with glaucoma. *Ophthalmic Surgery*. 1984; 15: 734-740.
- 3) Fyodorov SN, Ioffe DI, Ronkina TI.: Deep sclerectomy: technique and mechanism of a new glaucomatous procedure. *Glaucoma*. 1984; 6: 281-283.
- 4) Seiler T, Wollensak J. The resistance of the trabecular meshwork to aqueous humor outflow. *Graefe's Arch Clin Exp Ophthalmol*. 1985; 223: 88-91.
- 5) Ethier CR, Kamm RD, Palaszewski BA, Johnson MC, Richardson TM. Calculations of flow resistance in the juxtacanalicular meshwork. *Investigative Ophthalmology & Visual Science*. 1986; 27: 1741-1750.
- 6) Bill A, Svedbergh B. Scanning electron microscopic studies of the trabecular meshwork and the canal of schlemm an attempt to localize the main resistance to outflow of aqueous humor in man. *Acta Ophthalmologica*. 1972; 50: 295-304.
- 7) Fyodorov SN, Kozlov VI, Timoshkina NT, Sharova AB, Ereskin NN. Nonpenetrating deep sclerectomy in openangle glaucoma. *IRTC "Eye Microsurgery"*. RSFSR Ministry of Public Health, Moscow. 1989: 52-55.
- 8) Kozlov VI, Bagrov SN, Anisimova SY, Osipov AV, Mogilevtsev VV. Nonpenetrating deep sclerectomy with collagen. *IRTC "Eye Microsurgery"*. RSFSR Ministry of Public Health, Moscow. 1990; 3: 44-46.
- 9) Demailly P, Jeanteur-Lunel MN, Berkani M, Nouri-Mahdavi K, Ecoffet M, Kopel J, Kretz G, Lavat P, Valtot F. No penetrating deep sclerectomy associated with collagen device in primary open angle glaucoma. Short- term retrospective study. *Ophtalmologie*. 1995; 9: 666-670.
- 10) Demailly P, Jeanteur-Lunel MN, Berkani M, Ecoffet M, Kopel J, Kretz G, Lavat P. Non-penetrating deep sclerectomy associated with collagen device in primary open angle glaucoma. Middle- term retrospective study. *J. Fr. Ophthalmol*. 1996; 19: 659-666.
- 11) Stegmann R, Communication to the Curso Internacional de Oftalmologia Barraquer. Barcelona 1993.

GEL INJECTION ADJUSTABLE KERATOPLASTY (GIAK)

Keratometric evaluation on Eye Bank eyes

H. Tahi^{1,2}, H. Kondo^{1,3}, B. Duchesne^{1,2}, W. Lee¹, W. Feuer¹, JM. Parel^{1,2,4,5}

¹Bascom Palmer Eye Institute, University of Miami School of Medicine, Miami, FL

²CHU, Dept. of Ophthalmology, Prof. A. Galand, Faculté de Médecine, Université de Liège, Belgium

³Fukuoka University Department of Ophthalmology, Fukuoka, Japan

⁴Biomedical Engineering, University of Miami College of Engineering, Coral Gables, FL

⁵University of Paris, Hôpital de l'Hôtel-Dieu, Paris, France

ABSTRACT

Purpose. To assess keratometric changes of a new surgical refractive technique (Gel Injection Adjustable Keratoplasty or GIAK) on Eye Bank eyes. Conceived by G. Simon in 1989, GIAK consists of making a flat 360° intrastromal annular delamination track centered around the corneal apex and filling it with a soft gel.

Methods. The track, which was made with customized helicoidal delaminators, was delaminated parallel to the corneal surface at 80% depth and was filled with a biocompatible crosslinked polyethylene oxide gel. The procedure was preformed on fresh cadaver eyes using 10 delaminators with different inner diameters (4.5, 5.0, 5.5, 6.0, 6.5, 7.0mm) and widths (1.00 and 1.25mm). The annular track was filled to capacity. Keratometric changes were evaluated with an automated surgical keratometer.

Results. The keratometric changes induced by GIAK were between 3.4 and 11.9 diopters on average.

Conclusions. This surgical technique effectively flattens the cornea and promises to be an effective technique for correction of myopia.

Keywords. Myopia, refractive surgery, keratoplasty, intracorneal ring, GIAK, polyethylene oxide.

1. INTRODUCTION

Refractive eye abnormalities (ametropia) are the most common cause of impaired vision. About one third of the world population develops an ametropia and their correction still remains a major challenge in ophthalmology and optometry. The abnormalities are mainly myopia, hyperopia and astigmatism. Of the ametropias, myopia occurs most frequently. Nowadays, different methods are employed to correct myopia:

1. External optical systems represented by corrective glasses (spectacles) or contact lenses (most common form of correction).
2. Intraocular optical systems, namely intraocular lenses of negative power, positioned either in the anterior chamber or between the iris and the crystalline lens. The delicate surgery has potential intraoperative and postoperative complications such as retinal detachment and endophthalmitis. The procedures are technically "reversible" but, because of their invasive nature, put the eye at great risk.

3. Surgical procedures that change the anterior curvature of the cornea by flattening its optical zone:

- a) Several refractive surgery techniques have been designed to correct for myopia by changing the balance of stresses within the cornea by incising a specific portion of it. Radial keratotomy (RK), in particular, consists of making 4, 8, or 16 linear radial incisions perpendicular to the corneal surface while sparing a small 3 ± 0.5 mm optical zone (Fig. 1). The incisions have a depth of 80 to 90 % total corneal thickness. At first, the incisions cause a tangential relaxation of corneal tension which widens the peripheral contour of the cornea and thus flattens the central optical zone. With time, the scar tissues between the walls of each incision pushes on the corneal tissue between the incisions (f), further increasing the diameter of the peripheral contour which in turn further flattens the central optical zone, making the procedure poorly predictable and unstable.

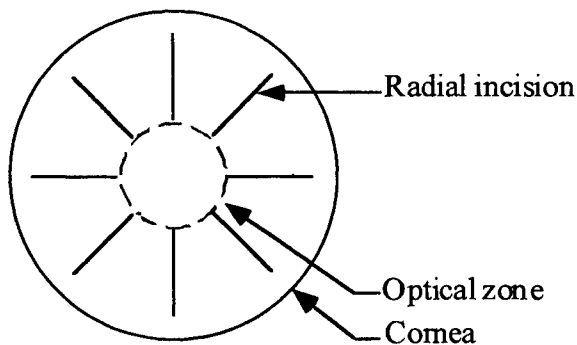


Figure 1: Schematic of Radial Keratotomy (RK)

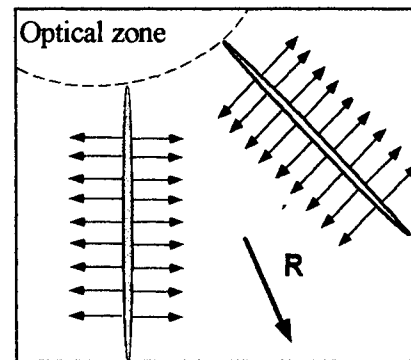


Figure 2: Concept of the effect in RK

- b) By tissue removal from the central cornea performed either by mechanical instruments (microkeratomes) or by photoablative lasers (PRK) or a combination of both (LASIK). With epikeratoplasty and photo refractive keratectomy (PRK), the epithelium is removed and a thin portion of the outer surface of the cornea consisting of the Bowman's membrane and a portion of the anterior stroma, is reshaped (flattened) either by mechanical cutting or by photoablation. The procedure is usually painful until complete epithelium regrowth which takes 2 to 7 days. The other techniques consist of removing the central portion, a lenticule, of the corneal stroma. With these, the epithelium is left intact and tissue removal is performed in two steps. First, by slicing the cornea at $\approx 30\%$ depth using a microkeratome and then ablating a fraction of the stroma using either the microkeratome or a photoablative laser (LASIK). The ablating techniques are irreversible and, because they endanger the optical zone, extreme care must be taken to produce an optical quality cut. The amount of correction is a function of the cut thickness and shape.

GIAC

Gel Injection Adjustable Keratoplasty is an “additive” method^{1,2,3}. The concept is to add a biocompatible gel to the mid-cornea in an annular shape after mechanically delaminating a channel centered on the corneal apex at a depth of 80 % of the total corneal thickness. Filling the annular track with gel displaces the stromal lamellae causing a reorganization of preexisting physiological corneal stresses. The reorganization modifies the entire corneal surface resulting in a flattening of the central optical zone (Fig. 3).

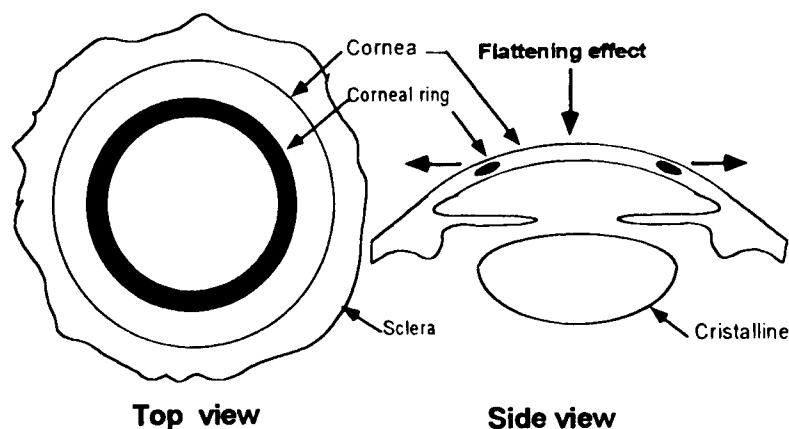


Figure 3: Schematic representing the GIAK surgical concept

A pilot Eye Bank eyes study demonstrated the feasibility of the procedure^{1,2}. Refractive corrections of 2 to 13 diopters were obtained by injecting variable quantities of a custom-made trimethyl terminated polydimethylsiloxane gel. A reduction in preexisting astigmatism was observed in the eyes corrected with GIAK. Reversibility of the procedure was also demonstrated².

Further research resulted in the development of a novel hydrogel made from polyethylene oxide⁴. Several short and long term studies with PEO gel were conducted on animal models (rabbits and cats). Safety⁵ and short term stability⁶ was demonstrated in a GLP rabbit study. Long term safety was demonstrated in 3 cats followed for one, two and three years. Histological findings in these animals confirmed the long term biocompatibility of the PEO gel⁷.

A simplified mathematical model was elaborated to predict the refractive power changes as a function of the gel volume and the track width. The track mid-diameter, the preoperative radius of corneal curvature and the limbal diameter were set respectively at 6, 7.75, and 11.7mm. The calculations based on this model predicted a 7 and a 10 diopters effect with respectively a 1.0 and 1.25mm track width and a maximum theoretical injectable gel volume corresponding to 6 and 9.4 mm³.

However, assessment of these values was required before beginning clinical trials. To confirm the GIAK refractive changes as a function of the track dimensions, we carried out an *in vitro* evaluation on human cadaver eye using delaminators of various diameters and width.

2. MATERIALS AND METHODS

Eye Bank eyes preparation

120 eyes were generously provided by the Florida Lions Eye Bank. Abnormal or previously operated eyes were removed from the study. 42 pairs of eyes were used. The eyes were stored at 4° C. The globes were somewhat collapsed with various degrees of corneal edema. The eye collapse was due to the natural post-mortem water loss from the two eye cavities (the vitreous and anterior chamber cavities), while the edema was primarily a function of corneal hydration. Before surgery, the normal eye shape and corneal transparency (adequate corneal hydration) were restored by injecting a 15% Dextran aqueous solution containing 0.9 % NaCl^{9,10} (Batch: Js 88882, Pharmacia Ophthalmics, Sweden) from the optic nerve into the vitreous cavity and from the limbus into the anterior chamber using a 30g needle for both injections.

The epithelium was then removed and the whole eye was immersed in the same Dextran solution for 90 minutes to dehydrate the cornea. During surgery and for the keratometry measurements, a 7.5% Dextran solution was used as a tear substitute. The number of eyes studied and the variation in the delaminator sizes were determined by a statistical analysis performed before the study and with the partial results was adjusted accordingly.

Surgical set up:

The eyeball was placed in an artificial orbit¹¹. In order to adjust and monitor the intraocular pressure (IOP), an 18g needle connected to an infusion line of balanced salt solution (BSS) equipped with a pinchcock (tubing clamp) and a flow through pressure transducer (156PC15GWL, Micro Switch USA), was introduced through the sclera at the eyeball equator into the vitreous cavity¹². The IV line was only opened for IOP adjustment and there was no BSS flow during surgery. An operation microscope (OMS 300, Topcon Corp, NY) equipped with a CCD color camera connected to a VCR video recording system (super VHS), was used. Keratometric measurements were obtained by using a surgical digital keratometer¹³ (SK-1 Surgical Auto Keratometer, Canon USA Inc, NY) mounted on another operation microscope (OPMI#1, Carl Zeiss, NY). To eliminate motion of the eye throughout the procedure, both SK-1 system and OMS operation microscope were positioned so as to swing to a coaxial position with the eye. The corneal thickness was measured using an ultrasound pachymeter (Pachette, DGH Technology Inc., set at 1640 m/s velocity).

GIAK surgical steps for each eye:

To make the surgery more comfortable, the *in vitro* preoperative IOP of each eye was adjusted to 20 mm Hg (rather than the physiologically normal *in vivo* IOP of 12 mm Hg). Corneal markings were made using a GIAK 3-prong marker (Storz Instrument Co., St Louis MO). 5 marks were made: one at the center and one at the 6, 9, 12 and 3 o'clock positions by 2 perpendicular markings (Fig. 4). Keratometric readings centered on the corneal central mark were taken with the SK-1. Pachymetry measurements were then taken, at the corneal center and at the 6 o'clock mark, perpendicular to the corneal surface. The globe was immobilized with a GIAK vacuum fixation ring (Storz Instrument Co., St. Louis MO) which was connected to a custom-made vacuum source set at 300 mmHg. The increase in corneal rigidity¹⁴ produced by the vacuum ring facilitated the corneal incision and delamination.

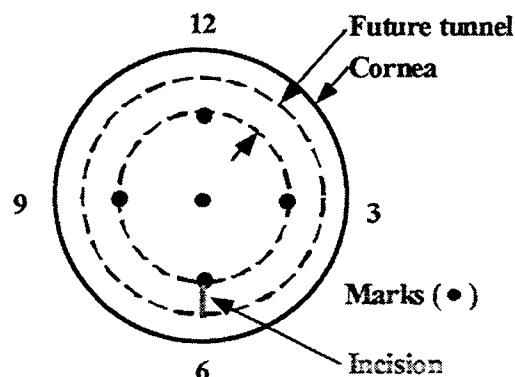


Figure 4. Relation between the corneal marks, pachymetry, incision and location of the tunnel.

A radial incision of a controlled width was made with a GIAK rectangular diamond knife set at 80 % corneal depth, with the diamond blade's inner edge placed at the 6 o'clock position mark (Figure 4). To insure a tight fit between the tissues at the entrance wound and the helicoidal delaminator spatula, a 800µm wide diamond knife (Storz Instrument Co., St. Louis MO) was used for the 1mm wide

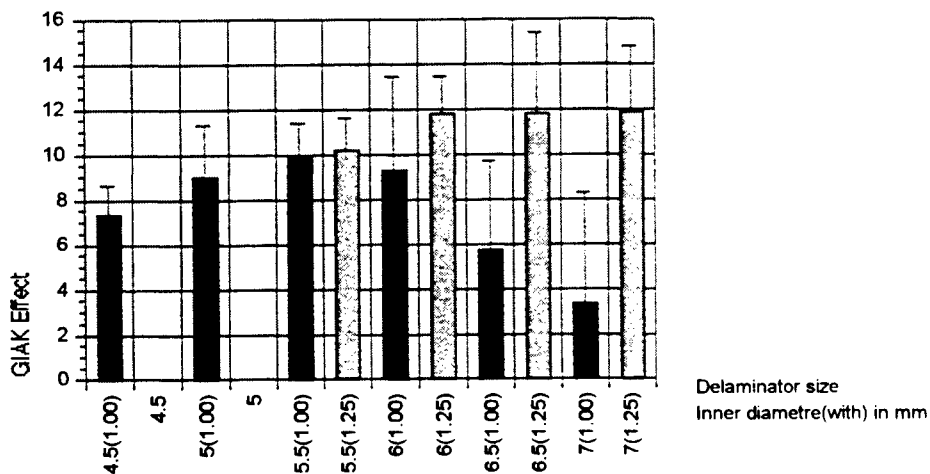
delaminators and a 1000 μ m wide blade (Storz Instrument Co., St. Louis MO) for the 1.25mm delaminators. The incision and its depth were checked with a GIAK corneal incision probe (Storz Instrument Co., St. Louis MO), a customized tool having a miniature spherical tip of 500 μ m diameter. A GIAK stromal plane dissector (Storz Instrument Co., St. Louis MO) was used to initiate the delamination. A GIAK guide (Storz Instrument Co., St. Louis MO) was then inserted in order to facilitate the insertion of the helicoidal delaminator (Storz Instrument Co., St. Louis MO) at the track entrance. The cornea was delaminated over 360°. After removal of the delaminator, the vacuum line was returned to atmospheric pressure, the fixation ring removed, and the pinchcock released, thus restoring the globe to the initial IOP of 20 mmHg. A sterile crosslinked PEO gel (Storz Instrument Co., St. Louis MO) was injected in the annular channel with a GIAK cannula (Storz Instrument Co., St. Louis MO) and the gel was evenly distributed within the delaminated tunnel using a GIAK spreading tool (Storz Instrument Co., St. Louis MO). The uniformity of the distribution was roughly assessed by visual observation through the OMS-300 operation microscope. Keratometric readings were then taken using the SK-1, followed by pachymetry readings in order to evaluate postoperative changes in corneal thickness.

The main purpose of this human cadaver eye study was to evaluate GIAK maximum keratometry effect (GIAK-k) using different delaminator sizes from 4.50 to 7.00 inner diameter and 1.00 and 1.25mm width (table below).

Width(mm)		Inner diameter (mm)				
1.00	4.50	5.00	5.50	6.00	6.50	7.00
1.25			5.50	6.00	6.50	7.00

3. RESULTS

Although GIAK can produce adjustable keratometric corrections and astigmatisms, by varying the volume and distribution of the injected gel respectively, in this study the track was filled to maximum capacity with no later adjustments.



Graph 1: Relation between the delaminator dimensions and the refractive correction, the GIAK-k effect.

Two different widths were tested. The first series of eyes were operated on using 1mm wide delaminators with sizes ranging from 4.50 to 7.00mm in inner diameter. The second series of eyes were done using 1.25mm wide delaminators with limited diameters of 5.5 to 7.0mm. The Eye Bank eyes were distributed as follows:

N(Op)	Diam/Width (mm)	
3	4.50	1.00
11	5.00	1.00
12	5.50	1.00
13	6.00	1.00
15	6.50	1.00
12	7.00	1.00

N(Op)	Diam/Width (mm)	
2	5.50	1.25
7	6.00	1.25
7	6.50	1.25
2	7.00	1.25

Graph 1 summarizes the data obtained for all delaminator sizes. Within the 1mm width delaminators, there was a highly significant difference between those with different diameters ($p < 0.001$, analysis of variance).

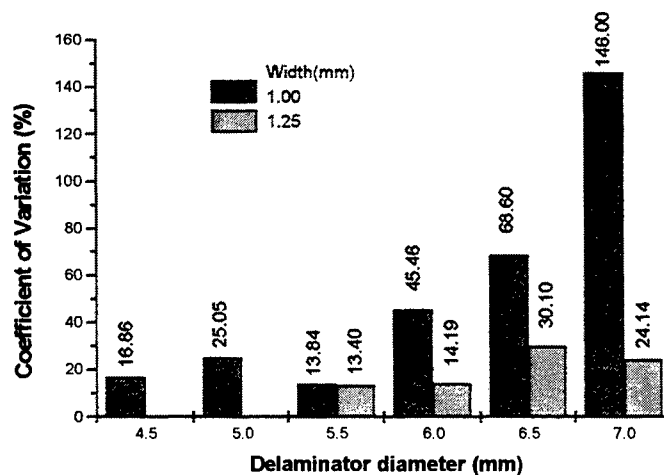
Tamhane multiple comparisons (which do not require homogeneity of variance) demonstrated that among the 1mm wide delaminators those with diameters of 4.5, 6.5, and 7.0mm had less effect than those of 5.0, 5.5, and 6.0mm, although these differences were not always consistent. When examined separately no significant differences were found in the effects obtained with the 1.25mm width delaminators (5.5, 6.0, 6.5, and 7.0mm). Overall the 6.0 and 6.5 seemed to be more effective than the 5.5 and 7.0.

Measurements for both 1 and 1.25 mm width delaminators with diameters 5.5, 6.0, 6.5, and 7.0mm were studied. When the effects of width and diameter were examined together with 2 factor analysis of variance, the effect of width on GIAK-k effect was highly statistically significant, $p = 0.001$. In this narrower range (5.5 to 7.0mm), the effect of diameter was borderline significant, $p = 0.098$.

Although not statistically significant ($p = 0.183$), the data also suggest that there may be an interaction between diameter and width.

If a linear regression model (not shown) is fitted to the data, this interaction becomes statistically significant ($p = 0.044$).

The efficacy to reproduce the average GIAK-k effect for each delaminator was expressed in terms of coefficient of variation (%) by Graph 2.



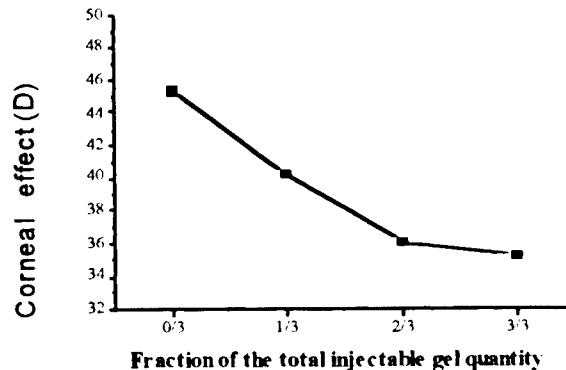
Graph 2

4. DISCUSSION

The results show that a good correlation exists between the mathematical model⁸ and this Eye Bank eye study. However the validity of the relationship is limited to the narrow range of delaminator width used for the surgical experiments. Delaminators of 5.5 to 6.5mm diameter range and either 1 and 1.25mm width generate similarly significant refractive corrections. However, the 1.25mm width delaminators gave more reproducible results.

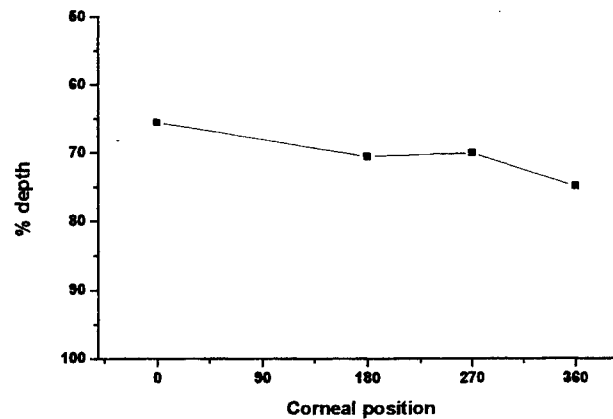
A pilot study was previously conducted to determine whether the GIAK-k results would be influenced by parameters other than the delaminator dimensions and the volume of gel injected. From this data (unpublished), it appears that the preoperative keratometry value and the post mortem time delay before the use of the eye was borderline significant in influencing the results. The age of the donor, the preoperative corneal thickness, the preoperative IOP, the use of the suction ring, and the degree of corneal hydration did not. For the post-mortem time the pilot study showed an increase of 1 diopter in GIAK-k over the entire 18 day range of the series ($p=0.031$) and for preoperative refraction there was a trend toward a statistical significance between this refraction and the GIAK-k effect ($p=0.083$).

In this study, we did not attempt to adjust the amount of gel injected to obtain a specific keratometric reading (e.g., 35D) as was done in the earlier cadaver eye study^{1,2}. As shown by the graph below, injecting two third of the total maximum injectable amount of gel seemed to still produce more than 85% of the GIAK-k effect. This finding is important because the maximum capacity injection is more easily accomplished using higher injection pressures which in turn have the potential to enlarge the track, potentially encroaching over the optical zone. A study with an automated injector should be conducted to confirm our findings and determine the maximum pressures that can be used to inject the gel without damaging the track.



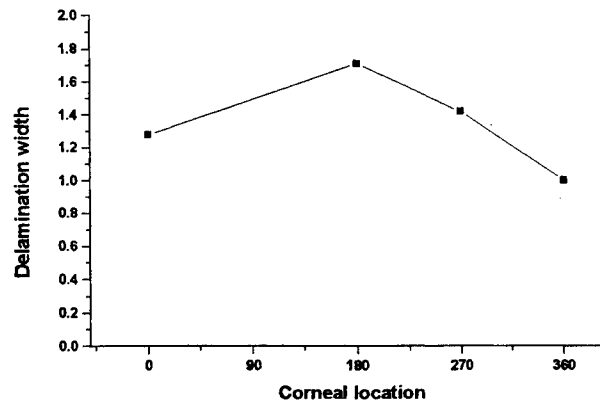
Graph 3: GIAK effect in function of the injected gel fraction.

Although the diamond knife was always set at 80% of the corneal thickness for each eye, the track depth is dependent on other factors which are difficult to control (e.g., surgical delamination force and angle) or clinically assess (e.g., physiological geometry of the cornea lamellae). Therefore an histological study was conducted on 10 eyes to evaluate the width and the depth of the delamination (data collected on 10 non representative eyes). As Graph 4 shows, the delamination starts at an average depth of 65% of the total corneal thickness and ends 10% deeper.



Graph 4: Delamination depth in function of location on the cornea. The incision is located at 0°.

The histological study also showed that the delaminated track widths were not perfectly uniform. Expressed in arbitrary units in Graph 5, the delamination width was wider between the 180° and 270° regions.



Graph 5: Delamination width in function of the corneal position. The incision is at 0°.

The present *in vitro* studies demonstrate GIAK to be an efficient surgical technique. By sparing the optical zone, GIAK has an advantage over current laser refractive procedures, such as PRK and LASIK.

In addition to sparing the optical zone, *in vitro* experiments (unpublished) have confirmed that GIAK is reversible. The surgery is also adjustable in that the amount of gel can be modulated under control of an automatic keratometer thus adjusting the keratometric effect². Histological studies concerning the safety of the procedure and the biocompatibility of the gel were previously conducted and showed no significant tissue reaction^{5,7,15,18}.

5. CONCLUSION

Gel Injection Adjustable Keratoplasty produced an effective corrective refractive effect in this experimental study carried out in human cadaver eyes. When compared to other techniques, GIAK has the advantages of sparing a very large area of the central optical zone, of allowing adjustment of the corneal curvature by adding or removing gel, of eliminating astigmatism by redistributing the gel and, of being fully reversible by merely removing all of the gel. This refractive procedure has the potential to flatten the cornea by more than 10 diopters and is therefore promising for correcting highly myopic eyes. Additional *in vivo* studies are necessary to evaluate the long term safety of the gel and the stability of the keratometric effect.

A human clinical trial on non sighted eyes begun October 1996 demonstrated the safety of the procedure and biocompatibility of the PEO gel and a limited clinical trial on sighted eyes has begun.

6. ACKNOWLEDGMENTS

We thank Izuru Nose, BSEE, and Francisco Fantes, MD, for technical and scientific contribution. The GIAK surgical instruments and the sterile PEO gel were manufactured and provided by Storz Instrument Co., St. Louis, MO.

This study was supported in part by the Florida Lions Eye Bank, Storz Ophthalmics Inc., Henri and Flore Lesieur Foundation, and by the Research to Prevent Blindness, New York, NY.

7. REFERENCES

1. Simon G, Parel J-M, Lee W: Gel injection adjustable keratoplasty (GIAK). *Invest Ophthalmol Vis Sci*, 31(4):S301, 1990
2. Simon G, Parel J-M, Lee W, Kervick GN: Gel injection adjustable keratoplasty. *Graefes Arch Clin Exp Ophthalmol*, 229: 418-424, 1991.
3. Simon G, Kervick GN, Parel J-M, Davis P: *In vivo* evaluation of gel injection adjustable keratoplasty (GIAK). *Invest Ophthalmol Vis Sci*, 32(4):S921, 1991.
4. Villain F, Hostyn P, Kuhne F, Parel J-M: Polyethylene oxide hydrogel and siloxane polymers for corneal refractive surgery. *10th Congress ESCRS, Paris, Book of Abstracts*, 10:137, 1992.
5. Takesue Y, Simon G, Parel J-M, Villain F, Kuhne K, Oshima K: Histopathologic study of synthetic annular keratophakia. *ARVO Invest Ophthalmol Vis Sci*, 34:1241, 1993.
6. Simon G, Takesue Y, Hostyn P, Kuhne F, Legeais J-M, Villain F, Ren Q, Margules GS, Parel J-M: Long term *in vivo* topographic studies of Gel Injection Adjustable Keratoplasty (GIAK). *ARVO Invest Ophthalmol Vis Sci*, 34:1248, 1993.

7. Takesue Y, Simon G, Villain F, Hostyn P, Legeais J-M, Kono T, Parel J-M: Long-term clinical and histological results of gel injection adjustable keratoplasty (GIAK) in the cat. *ARVO Invest Ophthalmol Vis Sci*, 35(4):2024, 1994.
8. Parel J-M, Comander J, Simon G, Takesue Y, Villain F: Mathematical model of annular keratophakia: intracorneal ring (ICR) and gel adjustable keratoplasty (GIAK). In: J-M Parel, Q Ren, eds, *Ophthalmic Technologies IV*, SPIE Publishers, Bellingham WA, Proc 2126:366-375, 1994
9. Terry MA, Ousley PJ, Zjhra ML: Hydration changes in cadaver eyes prepared for practice and experimental surgery. *Arch Ophthalmol*, 112:538-543, 1994.
10. Simon G, Small R, Ren Q, Parel J-M: Effect of corneal hydration on Goldmann applanation tonometry and corneal topography. *Refract. Corneal Surg*, 9: 110-117, 1993.
11. Lowery JA, Parel J-M, Roussel T, Simon G, Lee W, Nose I: Artificial orbit system for experimental surgery with enucleated globes. *Ophthalmic Surg*, 21:522-528, 1990.
12. Parel J-M, Parrish R, Nose I. An intraoperative intraocular pressure monitor. *Ophthalmic Surg*, 18:371-374, 1987.
13. Simon G, Parel J-M, Nose I, Lee W: Modification, calibration, and comparative testing of an automated surgical keratometer. *Refract Corneal Surg*, 7:151-160, 1991.
14. Duchesne B, Kondo H, Manns F, Lopez C, Nose I, Parel J-M: Effect of vacuum fixation devices on intraocular pressure. *Invest Ophthalmol Vis Sci*, 38(4):S418, 1997.
15. Kühne F, Simon G, Parel J-M, Villain F, Hostyn P, Takesue Y: Les résultats de 2 ans d'expérimentation animale des anneaux intrastromaux d'éthylène réticulé. *J Fr Ophtalmol*, 17(2):83-92, 1994.
16. Takesue Y, Kono T, Parel J-M: Immunohistochemical study of keratocyte response following gel injection adjustable keratoplasty (GIAK). *ARVO Invest Ophthalmol Vis Sci*, 37(3):S67, 1996
17. Legeais JM, Parel J-M, Savoldelli M, Villain FL, D'Hermies F, Renard R, Pouliquen Y: Biocompatibility of a Gamma-Ray Crosslinked Polyethylene Oxide Gel for Gel Injection Adjustable Keratoplasty (GIAK). *J Fr Ophtalmol*, 20(1):31-36, 1997.
18. Riss I, Diemer C, Hostyn P, Leger F, LeRebeller MJ, Parel J-M: Gel Injection Adjustable Keratoplasty: Biocompatibility and Stability. *ARVO Invest Ophthalmol Vis Sci*, 38(4):S539, 1997

SESSION 5

Eye Modeling

Eye aberrations analysis with Zernike polynomials

V. V. Molebny^a, I. H. Chyzh^a, V. M. Sokurenko^a,
I. G. Pallikaris^b, L. P. Naoumidis^b

^aInstitute of Biomedical Engineering, 5 Dimitrov St., 252006 Kiev, Ukraine

^bEye Vardinoyannion Institute of Crete, University of Crete, 71110 Heraklion, Greece

ABSTRACT

New horizons for accurate photorefractive sight correction, afforded by novel flying spot technologies, require adequate measurements of photorefractive properties of an eye. Proposed techniques of eye refraction mapping present results of measurements for finite number of points of eye aperture, requiring to approximate these data by 3D surface. A technique of wave front approximation with Zernike polynomials is described, using optimization of the number of polynomial coefficients. Criterion of optimization is the nearest proximity of the resulted continuous surface to the values calculated for given discrete points. Methodology includes statistical evaluation of minimal root mean square deviation (RMSD) of transverse aberrations, in particular, varying consecutively the values of maximal coefficient indices of Zernike polynomials, recalculating the coefficients, and computing the value of RMSD. Optimization is finished at minimal value of RMSD. Formulas are given for computing ametropia, size of the spot of light on retina, caused by spherical aberration, coma, and astigmatism. Results are illustrated by experimental data, that could be of interest for other applications, where detailed evaluation of eye parameters is needed.

Keywords: eye aberrations, sight correction, photorefractive operations, eye refraction map, refraction non-homogeneity, Zernike polynomials, eye refraction measurement

1. INTRODUCTION

At early stages of photorefractive keratectomy, the problem of sight correction seemed to be quite transparent: changing the radius of cornea curvature would solve the problem. Later, real measured shape of patient's cornea being non-spherical 3D function was involved into consideration¹⁻³. Ablation procedure should transform it to spherical shape. The problem could be solved with flying-spot technology. But it turns out that declinations of the cornea shape from sphericity are not the only refractive-origin causes of low sight acuity. Non-homogeneous refraction distribution inside the eye makes another sensible contribution to spatial variance of the eye's focal power. Several techniques are proposed for eye refraction mapping⁴⁻⁸.

Information on local eye aberrations is got usually in finite number of points of eye aperture. Therefore, to get a map of the to-be-ablated profile, suitable for ablation procedures, one must transform the discrete set of values into a continuous surface. The criterion of the quality of such transform could be the nearest proximity of the resulted continuous surface to the values calculated for the given discrete points. In this work, we consider the methodology of approximation using optimization of the length of Zernike polynomials.

Further author information –

V.V.M. (correspondence): Email: molebny@ibme.kiev.ua; Tel./Fax: (380 44) 268-8249
L.P.N.: Email: naoumidi@med.uch.gr; Tel.: (30 81) 39-4652, Fax: (30 81) 39-4653

2. OPTIMIZATION OF POLYNOMIAL'S LENGTH

In general case, optical system of a real eye is axially asymmetric, therefore decomposition of its wave aberration function $W_{nm}(\rho, \varphi)$ contains sine terms, that take into account asymmetry of wave-front deformations^{9, 10}:

$$W_{nm}(\rho, \varphi) = \sum_n \sum_m R_n^m(\rho) \cdot [C_{ynm} \cdot \cos(m\varphi) + C_{xnm} \cdot \sin(m\varphi)], \quad (1)$$

where ρ, φ are polar coordinates in the plane of eye's pupil; ρ is normalized from 0 to 1; C_{ynm}, C_{xnm} are coefficients of Zernike polynomials;

$$R_n^m(\rho) = \sum_{k=0}^{\frac{1}{2}(n-m)} (-1)^k \frac{(n-k)! \cdot \rho^{n-2k}}{k! \cdot \left[\frac{1}{2}(n+m)-k\right]! \cdot \left[\frac{1}{2}(n-m)-k\right]!},$$

$n \geq m$, $n+m$ being even.

Relationship between wave-front deformation function and transverse aberrations $\delta y'(\rho, \varphi)$ and $\delta x'(\rho, \varphi)$ of an eye looks as follows:

$$\delta y'(\rho, \varphi) = \left[\cos \varphi \cdot \frac{\partial W(\rho, \varphi)}{\partial \rho} - \frac{\sin \varphi}{\rho} \cdot \frac{\partial W(\rho, \varphi)}{\partial \varphi} \right], \quad (2)$$

$$\delta x'(\rho, \varphi) = \left[\sin \varphi \cdot \frac{\partial W(\rho, \varphi)}{\partial \rho} + \frac{\cos \varphi}{\rho} \cdot \frac{\partial W(\rho, \varphi)}{\partial \varphi} \right]. \quad (3)$$

Evaluation of C_{ynm} and C_{xnm} , based on measurements of transverse aberrations at different scan sites, may be accomplished by the least-squares method (LSM)^{11, 12}. The solution is presented usually in matrix form:

$$\mathbf{C} = (\mathbf{A}^T \cdot \mathbf{K} \cdot \mathbf{A})^{-1} \mathbf{A}^T \cdot \mathbf{K} \cdot \mathbf{Y}_0, \quad (4)$$

where \mathbf{C} is a column vector of unknown (to-be-calculated) Zernike coefficients; \mathbf{A} is a matrix, consisting of derivatives of Zernike polynomials at given sites of approximation; \mathbf{K} is a matrix of weight factors; \mathbf{Y}_0 is a column vector of transverse aberrations for two directions.

Total number of equations in the expression (4) equals to doubled number of approximation sites. The number of unknown Zernike coefficients N_c can be obtained as:

$$N_c = \frac{2nm - m^2 + 2n + 2m + z}{4} - z_0, \quad (5)$$

where $z=4$, if both m and n are even; $z=3$, if both m and n are odd or m is odd and n is even; $z=2$, if m is even and n is odd; n, m are maximal indices of Zernike polynomials; z_0 is a number of "non-significant" Zernike coefficients, i. e., coefficients, that do not influence the function of wave-front deformation; $z_0=(n+4)/2$, if n is even, and $z_0=(n+3)/2$, if n is odd.

Using the LSM is advisable because of the fact that coefficient estimates are non-displaced ones irrespectively of error distribution. Besides, according to the Gauss-Markov theorem, LSM gives the most accurate estimation of coefficients among the class of estimations, which are non-displaced and represent linear combination of initial data¹².

Accuracy of approximation depends on quantity of Zernike coefficients. According to the criterion of minimization of signal/noise ratio^{13, 14}, the number of modes must be reduced. However, the function of wave-front deformation of a real eye has rather complex character and can contain some local hills^{15, 16}. That is why, it is not reasonable to reconstruct it with the degree of Zernike polynomials, smaller than 2.

On the other hand, because of non-orthogonality of the derivatives of Zernike polynomials, cross-coupling occurs when number of modes increases. Hence, excessive increase in polynomials degree would result inevitably in poor conditionality of matrix of normal equations.

Thus, there are some critical maximal indices m and n , corresponding to optimal approximation of initial data (in the meaning of the best coincidence of the approximated function with the initial data). Optimal values of the m and n can not be found analytically. Therefore, we use numerical method based on statistical estimates.

The important property of LSM, that can be used for evaluation of optimal m and n , is that the estimate of dispersion D_R of transverse aberrations can be obtained irrespectively of the kind of error distribution¹²:

$$D_R = \frac{R}{N_E - N_C}, \quad (6)$$

where R is residual sum of squares of deviations of estimated transverse aberration values from initial values; $R = \mathbf{V}^T \cdot \mathbf{K} \cdot \mathbf{V}$, where $\mathbf{V} = \mathbf{Y} - \mathbf{Y}_0$ is a column vector of residuals; $\mathbf{Y} = \mathbf{A} \cdot \mathbf{C}$ is a column vector of estimated transverse aberration values at approximation sites; N_E is the number of equations; N_C is the number of unknown coefficients.

Taking into account the above mentioned considerations, we propose to use the criterion of minimal root mean square deviation (RMSD) of transverse aberrations:

$$\sigma = \sqrt{D_R} = \sqrt{\frac{R}{N_E - N_C}}. \quad (7)$$

The procedure consists in varying consecutively the values of maximal indices m and n , recalculating Zernike coefficients, and computing the value of RMSD. The "best" indices m and n are determined having minimal value of RMSD.

3. EVALUATION OF OPHTHALMOLOGIC PARAMETERS

Asymmetry of eye's optical system can produce all types of primary aberrations, first of all, focus shift ($n=2, m=0$), spherical aberration ($n \geq 4, m=0$), coma ($n \geq 3, m=1$), and astigmatism ($n \geq 2, m=2$). It is known that small values of n correspond to primary aberrations. According to (1)...(3), primary transverse aberrations of the beam on retina can be found as follows:

- focus shift ($n=2, m=0$):

$$\begin{aligned} \delta y'(\rho, \varphi) &= 4 \cdot C_{y20} \cdot \rho \cdot \cos(\varphi); \\ \delta x'(\rho, \varphi) &= 4 \cdot C_{y20} \cdot \rho \cdot \sin(\varphi); \end{aligned} \quad (8)$$

- 3rd order spherical aberration ($n=4, m=0$):

$$\begin{aligned} \delta y'(\rho, \varphi) &= 12 \cdot C_{y40} \cdot \rho \cdot (2\rho^2 - 1) \cdot \cos(\varphi); \\ \delta x'(\rho, \varphi) &= 12 \cdot C_{y40} \cdot \rho \cdot (2\rho^2 - 1) \cdot \sin(\varphi); \end{aligned} \quad (9)$$

- 3rd order coma ($n=3, m=1$):

$$\begin{aligned}\delta y'(\rho, \varphi) &= 2 \cdot C_{y31} \cdot (3\rho^2 - 1) + 3 \cdot \rho^2 \cdot \sqrt{C_{y31}^2 + C_{x31}^2} \cdot \sin(\alpha_c + 2\varphi); \\ \delta x'(\rho, \varphi) &= 2 \cdot C_{x31} \cdot (3\rho^2 - 1) - 3 \cdot \rho^2 \cdot \sqrt{C_{y31}^2 + C_{x31}^2} \cdot \cos(\alpha_c + 2\varphi);\end{aligned}\quad (10)$$

where

$$\alpha_c = \arctg\left(\frac{C_{y31}}{C_{x31}}\right) + \pi \cdot q, \quad q=0, \pm 1, \quad (11)$$

suggesting q , for which

$$\sin(\alpha_c) = \frac{C_{y31}}{\sqrt{C_{y31}^2 + C_{x31}^2}}, \quad \cos(\alpha_c) = \frac{C_{x31}}{\sqrt{C_{y31}^2 + C_{x31}^2}};$$

- 3rd order astigmatism ($n=2, m=2$):

$$\begin{aligned}\delta y'(\rho, \varphi) &= 2 \cdot \rho \cdot [C_{y22} \cdot \cos(\varphi) + C_{x22} \cdot \sin(\varphi)]; \\ \delta x'(\rho, \varphi) &= 2 \cdot \rho \cdot [-C_{y22} \cdot \sin(\varphi) + C_{x22} \cdot \cos(\varphi)].\end{aligned}\quad (12)$$

Functions $\delta y'(\rho, \varphi)$ and $\delta x'(\rho, \varphi)$ allow to compute the dimensions of light spot on retina, the shape of its edge, as well as other parameters and characteristics. In further considerations, we use also the function of transverse aberration of a thin beam on retina:

$$\delta(\rho, \varphi) = \sqrt{\delta y'^2(\rho, \varphi) + \delta x'^2(\rho, \varphi)}. \quad (13)$$

3.1. Ametropia

When ametropia occurs, beams entering the eye in parallel to visual axis, are not focused on retina, i.e. they form defocused image of the point in infinity. In this case, $C_{y20} \neq 0$. Substituting (8) into (13), one obtains

$$\delta(\rho, \varphi) = 4 \cdot \rho \cdot C_{y20}, \quad (14)$$

$$\delta(1, \varphi) = 4 \cdot C_{y20} \text{ at } \rho = 1.$$

Thus, the spot on retina is circle-shaped having diameter $2 \cdot r_d = 8 \cdot C_{y20}$. Distance between retina and rear focus of an eye is

$$z' = -\frac{2 \cdot \delta(1, \varphi) \cdot f'}{D} = -\frac{8 \cdot C_{y20} \cdot f'}{D}$$

where f' is rear focal length of an eye, D is the diameter of pupil scan zone.

According to the Newton's formula, the far point of clear sight (i. e., the axial point optically conjugated with retina) is situated at a distance

$$z = \frac{f \cdot f'}{z'} = -\frac{f \cdot D}{8 \cdot C_{y20}}$$

from front focus. Here, f is the front focal length of an eye.

As the distance $z \gg |f|$, one can obtain the value of ametropia

$$A \cong \frac{1000}{z} = -\frac{8000 \cdot C_{y20}}{f \cdot D},$$

or

$$A = \frac{8000 \cdot n' \cdot C_{y20}}{f' \cdot D} \text{ [diopeters]}, \quad (15)$$

where $n=1.337$. Hence, coefficient C_{y20} testifies not only about the presence of ametropia, but allows computing its value.

3.2. 3rd order spherical aberration

Presence of the 3rd order spherical aberration is defined by the coefficient C_{y40} . If $C_{y40} \neq 0$, spherical aberration appears, influencing on sight acuity. This influence can be evaluated by the dimension of light spot on retina. Substituting (9) in (13), we obtain $\delta(\rho, \varphi) = 12 \cdot \rho \cdot (2\rho^2 - 1) \cdot C_{y40}$, i.e. the spot has a round shape with diameter

$$2 \cdot r_s = 2 \cdot \delta(\rho, \varphi) \Big|_{\rho=1} = 24 \cdot C_{y40}. \quad (16)$$

A zone of object space, optically conjugated with this spot, has angular aperture

$$\theta = \frac{24 \cdot C_{y40}}{|f|} \text{ [radians]}. \quad (17)$$

3.3. 3rd order coma

It is evident from expressions (10), that for $\rho=0$, the initial point of the coma spot is displaced from coordinate origin on distance $\delta y'(0,0) = -2 \cdot C_{y31}$ and $\delta x'(0,0) = -2 \cdot C_{x31}$. As far as coma's head contains large part of light energy, it changes angular position of image centroid on retina. Maximal axial and lateral dimensions of the coma spot are determined as related to the axis of spot symmetry at $\rho=1$ using formulas:

- for axial size:

$$\delta l'_c = 9 \cdot \sqrt{C_{y31}^2 + C_{x31}^2}, \quad (18)$$

- for lateral size:

$$\delta r'_c = 6 \cdot \sqrt{C_{y31}^2 + C_{x31}^2}. \quad (19)$$

3.4. 3rd order astigmatism

By substituting (12) into (13), one can obtain function $\delta(\rho, \varphi)$:

$$\delta(\rho, \varphi) = 2 \cdot \rho \cdot \sqrt{S + Q \cdot \sin(\beta + 2\varphi)}, \quad (20)$$

where

$$S = C_{y22}^2 + C_{x22}^2 + 4C_{y20}^2; \quad Q = 4 \cdot C_{y20} \cdot \sqrt{C_{y22}^2 + C_{x22}^2},$$

$$\beta = \arctg\left(\frac{C_{y22}}{C_{x22}}\right) + \pi \cdot q, \quad q=0, \pm 1, \quad (21)$$

q should satisfy the conditions

$$\sin(\beta) = \frac{C_{y22}}{\sqrt{C_{y22}^2 + C_{x22}^2}}, \quad \cos(\beta) = \frac{C_{x22}}{\sqrt{C_{y22}^2 + C_{x22}^2}}.$$

The spot has an ellipsoidal shape whose longer axis $2a = 2 \cdot \delta_{\max}(\rho, \varphi)$ and shorter axis $2b = 2 \cdot \delta_{\min}(\rho, \varphi)$, where (for $\rho=1$)

$$\delta_{\max} = 2 \cdot \sqrt{C_{y22}^2 + C_{x22}^2 + 4 \cdot C_{y20}^2 + 4 \cdot |C_{y20}| \cdot \sqrt{C_{y22}^2 + C_{x22}^2}}, \quad (22)$$

$$\delta_{\min} = 2 \cdot \sqrt{C_{y22}^2 + C_{x22}^2 + 4 \cdot C_{y20}^2 - 4 \cdot |C_{y20}| \cdot \sqrt{C_{y22}^2 + C_{x22}^2}}. \quad (23)$$

The longer axis is inclined relatively the vertical plane by an angle

$$\varphi_{\max} = \frac{\pi}{4} - \frac{\beta}{2} \quad \text{at } C_{y20} > 0, \quad (24)$$

or

$$\varphi_{\max} = -\frac{\pi}{4} - \frac{\beta}{2} \quad \text{at } C_{y20} < 0. \quad (25)$$

It is evident from (20) and (21), that ellipse's axes are oriented along coordinate axes (vertical and horizontal), when $C_{y22} \neq 0$ and $C_{x22} = 0$, and are inclined relatively the coordinate axes by an angle $\pm 45^\circ$, when $C_{y22} = 0$ and $C_{x22} \neq 0$. When $C_{y22} \neq 0$ and $C_{x22} \neq 0$, orientation of axes can be arbitrary (except the above mentioned). Position of astigmatic foci can be computed from the expression (20).

Astigmatic distance in diopters can be found as follows

$$|A'_s - A'_m| = \frac{8000 \cdot n'}{f' \cdot D} \cdot \sqrt{C_{y22}^2 + C_{x22}^2}. \quad (26)$$

4. ANALYSIS OF EXPERIMENTAL DATA

The described technique was tested for two cases: myopic eye and hyperopic eye with astigmatism. Initial data (i. e., transverse aberrations) have been measured for each eye at 64 scan sites. Optimal values of approximation coefficients C_{ymn} and C_{xnm} were to be found. Eye's aberration parameters were computed, spot diagrams and wave front deformation maps being reconstructed as well, facilitating analysis of the shape and size of point spread function. Influence of selected types of aberrations could be analyzed in this way, as well as their combinations. Besides, spot diagrams could serve for sight acuity estimation before and after sight correction. Wave front deformation map is unambiguously correlated with the to-be-ablated cornea shape.

Transverse aberrations, recalculated into refraction map (distribution of focal power), are shown in fig. 1 for both cases. Some of the results of calculating C_{ymn} and C_{xnm} are included into tables 1 and 2.

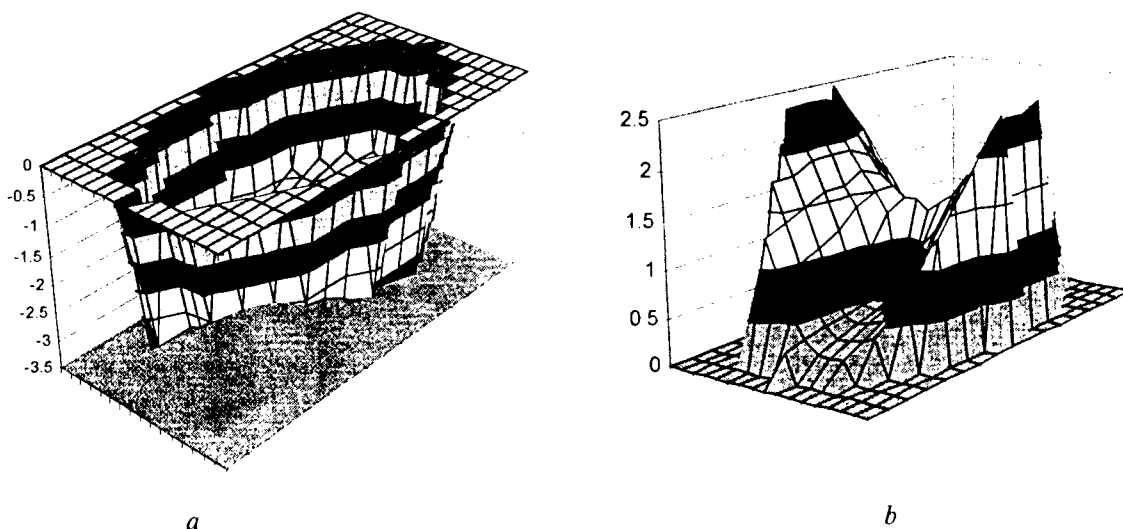


Fig. 1. Refraction maps [in diopters]: *a* - test 1; *b* - test 2

Table 1. Dependence of Zernike coefficients and RMSD on n and m (in μm) for test 1

	$m=3,$ $n=3$	$m=6,$ $n=6$	$m_{\text{opt}}=3,$ $n_{\text{opt}}=8$	$m=8,$ $n=8$	$m=10,$ $n=10$
RMSD	4.06	2.60		2.70	6.40
C_{y20}	-15.66	-15.68	-15.68	-15.68	-15.31
C_{y40}	—	0.016	0.015	0.015	0.292
C_{y31}	0.511	-0.256	-0.215	-0.215	-0.205
C_{x31}	0.053	0.375	0.443	0.443	0.469
C_{y22}	0.278	0.225	0.210	0.210	0.189
C_{x22}	3.777	1.879	1.806	1.806	1.709

Table 2. Dependence of Zernike coefficients and RMSD on n and m (in μm) for test 2

	$m=3,$ $n=3$	$m=6,$ $n=6$	$m_{\text{opt}}=2,$ $n_{\text{opt}}=8$	$m=8,$ $n=8$	$m=10,$ $n=10$
RMSD	8.10	4.50		4.78	7.57
C_{y20}	7.911	7.274	7.280	7.280	7.137
C_{y40}	—	0.469	0.460	0.460	0.222
C_{y31}	0.064	0.149	0.168	0.168	0.175
C_{x31}	-0.029	-0.099	-0.114	-0.114	-0.120
C_{y22}	-5.953	-2.770	-2.677	-2.677	-2.555
C_{x22}	-4.428	-1.964	-1.906	-1.906	-1.831

The procedure of search for optimal values of m and n is clear from the above tables: the combination of m and n must be found, for which RMSD is minimal. In our examples, they are: $n=8$, $m=3$ for test 1, and $n=8$, $m=2$ for test 2.

The values of Zernike coefficients, found in such a way, are substituted into expressions (8)...(26) for computation of correspondent aberration parameters and reconstruction of spot diagrams. Table 3 demonstrates the values of computed parameters, while figures 2 and 3 illustrate spot diagrams for some combinations of aberrations. Wave front deformation maps, reconstructed from computed Zernike coefficients, are shown in fig. 4.

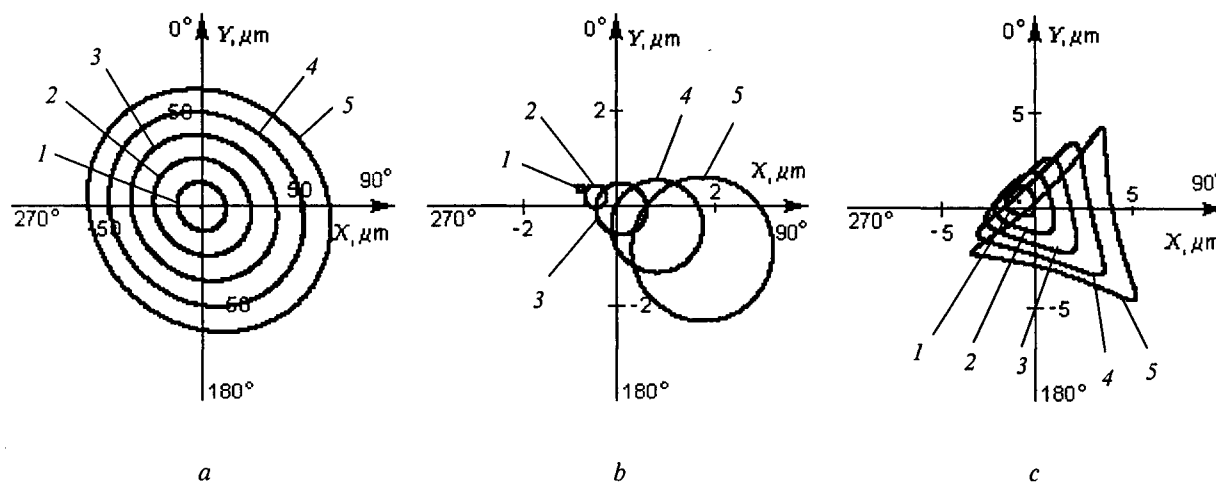


Fig. 2. Retinal spot diagrams for test 1:
1 - $\rho=0.2$; 2 - $\rho=0.4$; 3 - $\rho=0.6$; 4 - $\rho=0.8$; 5 - $\rho=1.0$;
a - all primary aberrations (without tilts); b - 3rd order coma;
c - all primary aberrations (without tilts and defocusing)

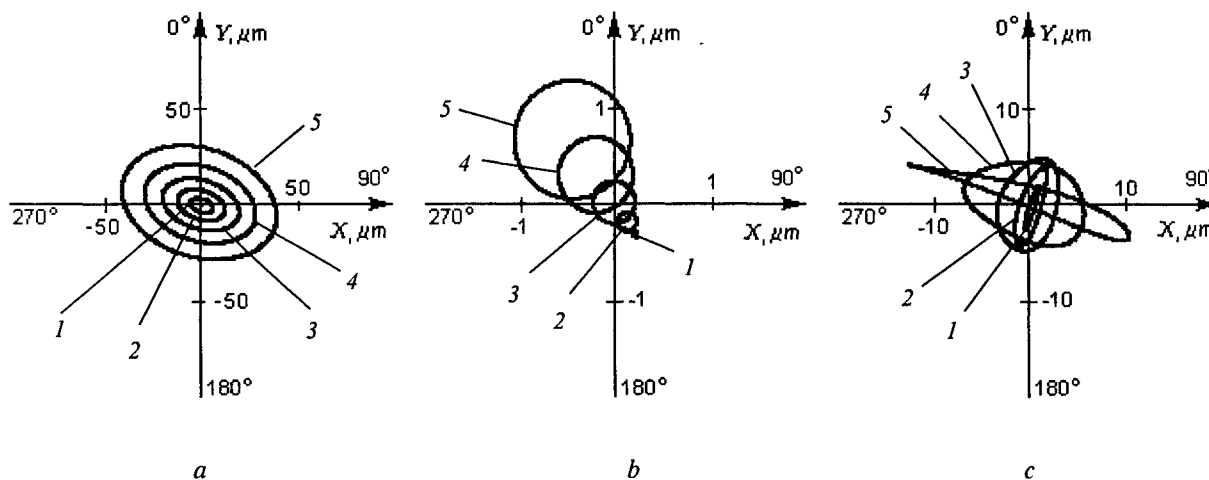


Fig. 3. Retinal spot diagrams for test 2:
1 - $\rho=0.2$; 2 - $\rho=0.4$; 3 - $\rho=0.6$; 4 - $\rho=0.8$; 5 - $\rho=1.0$;
a - all primary aberrations (without tilts); b - 3rd order coma;
c - all primary aberrations (without tilts and defocusing)

Table 3. Basic ophthalmic parameters of investigated eyes

	Ametropia A [diopeters]	Spherical aberration		Coma				
		$2r_s$ [μm]	θ [angular minutes]	$\delta r'_s$ [μm]	$\delta r'_t$ [μm]	α [degrees]	$\delta y'(0,0)$ [μm]	$\delta x'(0,0)$ [μm]
Test 1	-2.44	0.36	0.07	4.43	2.95	-25.89	0.43	-0.88
Test 2	+1.13	11.04	2.2	1.82	1.22	+124.16	-0.34	0.23

	Astigmatism			
	$2a$ [μm]	$2b$ [μm]	φ_{max} [degrees]	$ Z'_s - Z'_m $ [diopeters]
Test 1	132.7	118.16	-48.3	0.28
Test 2	71.38	45.08	-72.3	0.51

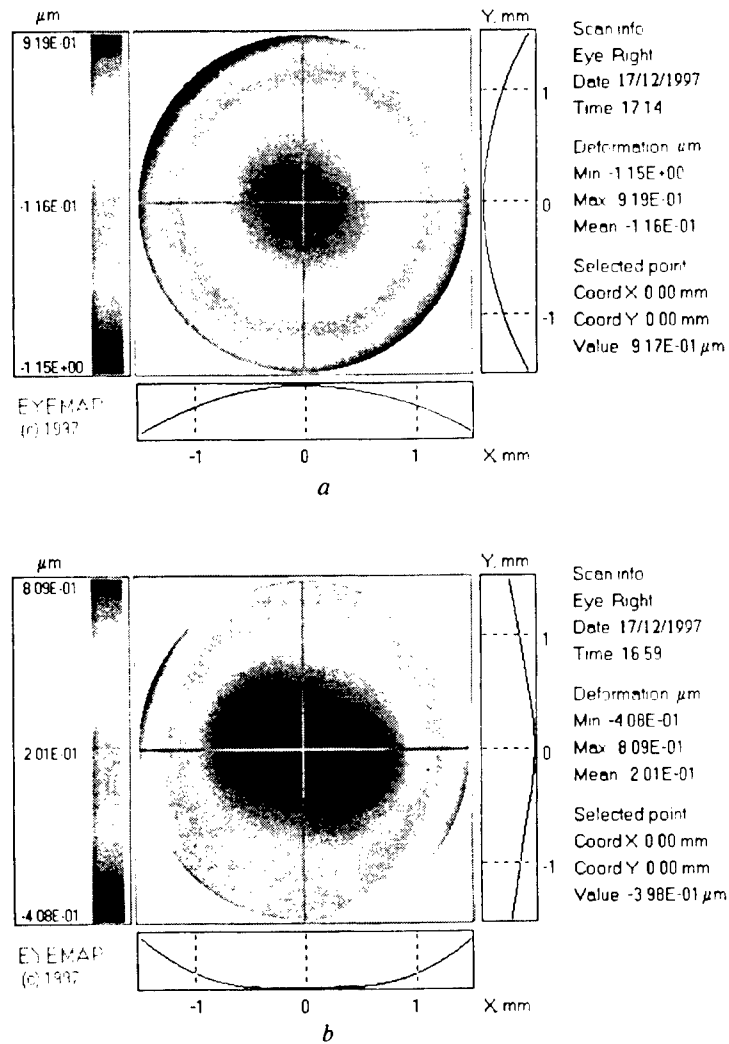


Fig. 4. Wave front deformation maps (usually in true colors): a - test 1; b - test 2

5. DISCUSSION AND CONCLUSIONS

The following results were got in measurements with myopic eye: ametropia- minus 2.44 diopters, 3rd order spherical aberration is negligible, there is also some astigmatism and coma. After ametropia correction, the shape of spot of light on retina will depend mainly on coma (fig. 2c). Its size is approximately примерно $10 \times 10 \mu\text{m}$. Therefore, sight acuity is 1.5 times worse than in normal eye (here we consider $6 \mu\text{m}$ spot on retina resulting in unity of sight acuity).

Hyperopic eye showed averaged hyperopia plus 1.13 diopters, value of 3rd order spherical aberration being essentially higher than in test 1. Coma and astigmatism are present with astigmatism being dominating. Therefore, after correction of ametropia retinal spot has an astigmatic shape (fig. 3c). Sight acuity at a plane of the longer axis of astigmatic ellipse (72.3 deg. inclined) is 1.7 times lower than in normal eye. Hence, astigmatism should not be neglected when reshaping the cornea.

Described methodology is quite effective for solving practical problems of optimal cornea reshaping in photorefractive sight correction. It is a good compromise between finite number of tested points when measuring transverse aberrations (limited by the time of measurement on moving eye) and required accuracy. The further freedom of development could include whether involving eye tracking to consider eye movements, or applying additional mathematics of the spline approximation type.

6. ACKNOWLEDGMENTS

This work was carried out with financial support of the STCU - Science and Technology Center in Ukraine (project No. 418) being funded by the governments of the United States, Canada, and Sweden.

In this publication, our experience was used in treating the moving eye, acquired due to the results of INTAS project No. 94-3161, financially supported by the International Association for the Promotion of Cooperation with Scientists from the Independent States of the Former Soviet Union.

7. REFERENCES

1. J. M. Krauss, C. A. Puliafito, "Lasers in Ophthalmology", *Lasers in Surg. and Med.* **17**, pp. 102-159, 1995.
2. T. Seiler, P. J. McDonnell, "Excimer laser photorefractive keratectomy", *Surv. of Ophthalm.* **40**, pp. 89-118, 1995.
3. M. C. Corbett, J. Marshall, D. P. S. O'Brart, E. S. Rosen, "New and future technology in corneal topography", *Eur. J. Implant. Ref. Surg.* **7**, pp. 371-385, 1995.
4. J. Liang, B. Grimm, S. Goelz, J. F. Bille, "Objective measurement of wave aberrations of the human eye with use of Hartmann-Shack wave-front sensor", *J. Opt. Soc. Amer.* **11A**, pp. 1949-1957, 1994.
5. V. V. Molebny, V. N. Kurashov, I. G. Pallikaris, L. P. Naoumidis, "Adaptive optics for measuring eye refraction distribution", *Proc. SPIE* **2930**, pp. 147-156, 1996.
6. T. Mihashi, Y. Ishikura, K. Kobayashi, "Simultaneous measurement of optical refraction characteristics and corneal topography of the eye", *Invest. Ophthalm. & Vis. Sci.* **38**, p. S849, 1997.
7. V. V. Molebny, I. G. Pallikaris, L. P. Naoumidis, I. H. Chyzh, S. V. Molebny, V. M. Sokurenko, "Retina ray-tracing technique for eye-refraction mapping", *Proc. of SPIE* **2971**, pp. 175-183, 1997.
8. T. Seiler, P. Mierdel, H.-E. Krinke, W. Wiegand, "First results of the assessment of monochromatic aberrations of human eye with device for clinical use", *Invest. Ophthalm. & Vis. Sci.* **38**, p. S1013, 1997.
9. M. Born, E. Wolf, *Principles of Optics*, Pergamon Press, Oxford/London/etc., 1968.
10. V. V. Molebny, I. H. Chyzh, V. M. Sokurenko, S. V. Molebny, I. G. Pallikaris, L. P. Naoumidis, "Phase-transparency model of an eye optical system", *Proc. of SPIE* **3192**, (3192-29), 10 pp., 1997.
11. D. Malacara, *Optical Shop Testing*, Wiley, New York, 1991.
12. D. J. Hudson, *Statistics. Lectures on Elementary Statistics and Probability*, Geneva, 1964.
13. R. Cubalchini, "Modal wave-front estimation from phase-derivative measurements", *J. Opt. Soc. Am.* **69**, pp. 972-977, 1979.
14. W. H. Southwell, "Wave-front estimation from wave-front slope measurements", *J. Opt. Soc. Am.* **70**, pp. 998-1006, 1980.
15. M. S. Smirnov, "Measurement of the wave aberration of the eye", *Biophysics (USSR)* **6**, pp. 776-794, 1961.
16. N. M. Sergienko, *Ophthalmologic Optics*, Meditsina, Moscow, 1991.

Aberration mapping for sight correction

V. V. Molebny^a, V. N. Kurashov^a, D. V. Podanchuk^a, A. V. Kovalenko^a,
I. G. Pallikaris^b, L. P. Naoumidis^b

^aInstitute of Biomedical Engineering, 5 Dimitrov St., 252006 Kiev, Ukraine

^bEye Vardinoyannion Institute of Crete, University of Crete, 71110 Heraklion, Greece

ABSTRACT

In sight correction technologies, it is of extreme importance to know what outcome of the planned operation could be. Conventionally, cornea shape is measured, or even refraction distribution in the eye, that are used for calculations of the to-be-ablated cornea layers. Unfortunately, different obstacles could arise, involving errors in these calculations. We propose another approach of measuring the to-be-inserted aberrations that would compensate for existing aberrations to get maximal sight acuity. The approach is based on measurements of wave front aberrations at the exit of an eye and iterative procedure of phase conjugation of the wave front, entering the eye. As a result of the procedure, an optimized point spread function is achieved. Shack-Hartmann sensors are used for wave front measurements, and spatial modulators - for wave front control. Local slopes of wave front being measured, Wiener-type filtering helps to reconstruct the wave front itself. The results are reported of single-pass and double-pass modelling with experimental setup and computer simulation.

Keywords: refractive sight correction, wave front measurements, wave front control, eye aberration mapping, adaptive optics, Shack-Hartmann sensors, Wiener filtering.

1. INTRODUCTION

Double-pass technique is a powerful means for measuring retinal image quality of the human eye^{1, 2}. It provides direct estimates of the ocular modulation transfer function. In conventional double-pass method, eye's optics forms an image on retina of a parallel beam of light. A small fraction of retinal image is reflected and, after passing through a beam splitter, is brought to a focus in the detection plane that is conjugated to the retina, where it forms the second, aerial image. This aerial image is used to compute the modulation transfer function for a single pass through the eye's optics. However, the double-pass aerial image of a point test cannot provide information about the phase transfer function³, and, for this reason, we cannot retrieve the true single-pass retinal point-spread function.

Recent study³⁻⁷ has shown that double-pass wave-front measuring by adaptive optics methods can go farther to overcome this problem. In our previous discussion⁸, a modified double-pass wave model has been proposed, where we measure spatial structure of the wave front, formed by the light reflected from fovea, and estimate wave aberrations of the eye by means of reconstruction procedure to be described hereinafter. Using iterative procedure of wave front changes at the eye's entrance and wave front measurements at the eye's exit, we optimize the quality, reducing it to diffraction limited retinal image. The conjugated aberration map, that is the result of the procedure, can be used now for sight correction.

2. PRINCIPLES OF INVESTIGATION

Correction of eye aberrations by means of adaptive optics consists in compensation of light wave distortions that are caused by optical system of an eye. Practically, compensation of aberrations is realized as regards of parameter optimization of an optical system (quality criterion), but not the total elimination of aberrations. Absolute maximum of quality is related to the ideally corrected system, its value being smaller for corrected non-ideal system. In this sense, a phase plate, reducing the

Further author information –

V.V.M. (correspondence): E-mail: molebny@ibmc.kiev.ua; Tel./Fax: (380 44) 268-8249
L.P.N.: E-mail: naoumidi@med.uch.gr; Tel.: (30 81) 39-4652; Fax: (30 81) 39-4653

optimum to quality criterion, can be identified as the best corrector of eye aberrations. Thin lens approximation is suggested, permitting to neglect diffraction effects of light propagation inside the eye. The final goal of the correction is to achieve the best image resolution on retina. Objective *in vivo* measurements in focal plane of an eye's optical system are impossible, the only way is to investigate the secondary aerial image. Milestones of this procedure are as follows.

Any functional $J[E_I(\mathbf{r})]$ on retina can be expressed in terms of some other functional $F[E_{II}(\rho)]$ of the complex amplitude $E_{II}(\rho)$ of the scattered field in the plane ρ of the secondary image. Actually, the field $E_I(\mathbf{r})$ is related to $E_{II}(\rho)$ by the wave equation, describing the process of scattered light propagation from retina to the observation plane. The solution of this equation can be expressed as:

$$E_{II}(\rho) = \int_S h_2(\rho, \mathbf{r}) E_I(\mathbf{r}) d^2 r, \quad (1)$$

where $h_2(\rho, \mathbf{r}) = h_L(\rho, \mathbf{r}) \cdot V(\mathbf{r})$, $h_L(\rho, \mathbf{r}) \equiv h_1(\rho, \mathbf{r})$ is a pulse response of the first-pass propagation of light, and $V(\mathbf{r})$ is a complex reflection coefficient of the retina. Hence, functional $F[E_{II}(\rho)]$ can be expressed in terms of $J[E_I(\mathbf{r})]$ and pulse response $h_2(\rho, \mathbf{r})$. Unfortunately, the first-pass pulse response $h_1(\rho, \mathbf{r})$, that should be measured and corrected, is unknown as a consequence of asymmetry of the first and second passes in the eye's optical system ($V(\mathbf{r}) \neq \text{const}$)⁵.

The last problem is of no significance for point-sized reflecting target, when $V(\mathbf{r})$ is a Dirac delta-function:

$$V(\mathbf{r}) = a \cdot \delta(\mathbf{r} - \mathbf{r}_0), \quad (2)$$

$a = \text{const}$. This idea was used for eye studies as well⁹. It consists in asymmetric double-pass method where the entrance pupil is made small (diffraction limited), and exit pupil is reasonably large. But it is an open question whether or not this approximation is correct, because the diffraction spreading of the spot and the structure of the retina scattering are not taken into account.

Despite the waves $E_I(\mathbf{r})$ and $E_{II}(\rho)$ are not expressed directly by one another, the situation is not hopeless. It turns out, that some functionals can be formed, representatives of the focal image, that can be measured in the aerial double-pass image. One of them is a variation of interference criterion¹⁰ and can be written in the form:

$$J_i = \left| \int E_0(\rho) E_{II}(\rho) d^2 \rho \right|^2. \quad (3)$$

It can be evaluated using wave-front sensors in the exit plane. With some approximation, it permits almost complete mapping of eye aberrations and needed correction.

Let us consider non-ideal optical imaging system, the solution of wave equation in a forward direction for which can be expressed as:

$$E_I(\mathbf{r}) = \int E_0(\rho) h_1(\mathbf{r}, \rho) d^2 \rho, \quad (4)$$

where Green function has the form

$$h_1(\mathbf{r}, \rho) = h_f(\mathbf{r}, \rho) \cdot \exp[i\varphi(\mathbf{r}, \rho)]. \quad (5)$$

The last expression has the meaning of a pulse response of ideal focusing system¹¹

$$h_f(\mathbf{r}, \rho) = \frac{1}{i\lambda z} \exp\left[-\frac{i k \mathbf{r} \rho}{f}\right], \quad (6)$$

distorted by phase aberrations $\varphi(\mathbf{r}, \rho)$. It describes light propagation in the eye. Entrance pupil (ρ) corresponds to the rear focal (or infinitely spaced) plane of eye lens. Non-ideal eye is an anisoplanatic system, therefore, $\varphi(\mathbf{r}, \rho)$ depends on coordinate \mathbf{r} in retina plane. But as soon as the wave front $E_0(\rho)$ is plane, and aberrations are not too large, phase distortion of the primary image can be considered as a constant in the vicinity of the diffraction spot. For this reason, eye aberrations can be expressed as a phase screen in the entrance plane of the eye:

$$\varphi(\mathbf{r}, \rho) \approx \varphi(0, \rho) \equiv \varphi(\rho). \quad (7)$$

Therefore, one gets:

$$E_1(\mathbf{r}) = \int E_0(\rho) \exp[i\varphi(\rho)] h_f(\mathbf{r}, \rho) d^2 \rho. \quad (8)$$

In a similar way (with sign inversion at reflection):

$$E_{II}(\rho) = \exp[i\varphi(-\rho)] \int E_1(\mathbf{r}) V(\mathbf{r}) h_f(\mathbf{r}, -\rho) d^2 r. \quad (9)$$

It is evident from expressions (8, 9), that, if the input beam is plane, $E_0(\rho) = \text{const}$, the retinal image of the first pass is Fourier spectrum of phase distortions $t_a(\rho) = \exp[i\varphi(\rho)]$. After reflection from the retina and the second pass through the eye's optical system, it results in the double-pass image $E_{II}(\rho) = |E_{II}(\rho)| \exp[i\psi(\rho)]$. In conventional double pass, aerial image is a nonlinear integral transform of phase aberrations $\varphi(\rho)$, and thus, it is not possible to recover it from measured intensity distribution. But as far as adaptive optics is used, this becomes not necessary: measurements of double-pass wave front allow to determine and maximize the quality criterion.

For this purpose, let us introduce phase pre-distortions into the input beam, that are described by phase plate with transmittance $\exp[i\alpha(\rho)]$, so that

$$E'_0(\rho) = E_0(\rho) \exp[i\alpha(\rho)].$$

It follows for this case:

$$E_1(\mathbf{r}) = \int E'_0(\rho) \exp\{i[\varphi(\rho) + \alpha(\rho)]\} h_f(\mathbf{r}, \rho) d^2 \rho, \quad (10)$$

and

$$E_{II}(\rho) = \exp[i\varphi(-\rho)] \int d^2 r V(\mathbf{r}) h_f(-\mathbf{r}, \mathbf{r}) \int d^2 \rho' E'_0(\rho') \exp\{i[\varphi(\rho') + \alpha(\rho')]\} h_f(\mathbf{r}, \rho'). \quad (11)$$

Let us consider now an interference functional in the form:

$$J_i = \left| \int E'_0(-\rho) E_{II}(\rho) d^2 \rho \right|^2 = \left| \int d^2 r V(\mathbf{r}) q(\mathbf{r}) q(-\mathbf{r}) \right|^2, \quad (12)$$

where

$$q(\mathbf{r}) = \int d^2 \rho E'_0(\rho) h_f(\mathbf{r}, \rho) \exp\{i[\varphi(\rho) + \alpha(\rho)]\}. \quad (13)$$

Assuming that $V(\mathbf{r})$ is real, one gets from Schwarz inequality:

$$J_i \leq \left[\int d^2r V(\mathbf{r}) |q(\mathbf{r})|^2 \right]^2. \quad (14)$$

Equality is achieved only if $q(\mathbf{r}) = q^*(-\mathbf{r})$, so that $\varphi(\rho) = -\alpha(\rho)$ for plane wave front $E_0(\rho) = \text{const}$. Under these conditions, retinal image is diffraction limited spot, and corresponding phase plate

$$t_a(\rho) = \exp[-i\alpha(\rho)] \quad (15)$$

determines aberration map of the eye under test.

Maximization of interference criterion (12) involves an algorithm of wave front phase conjugation. Correction procedure can be carried out with the setup shown in fig.1.

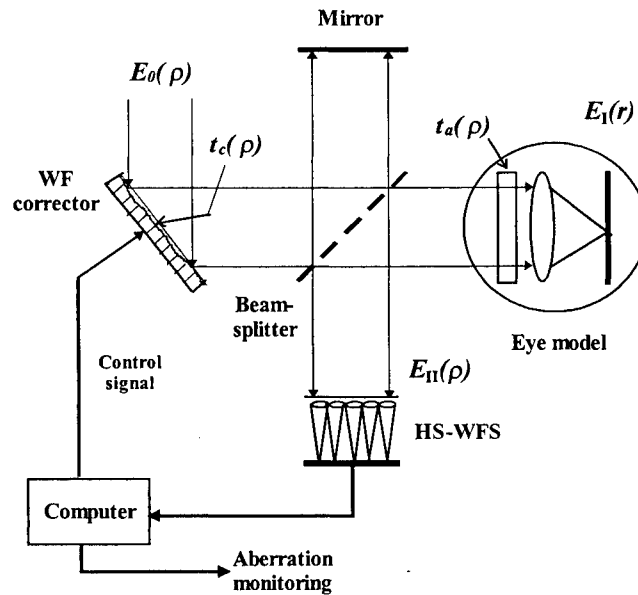


Fig. 1. Setup for eye aberrations measurement and their correction

Iterative correction procedure consists of the following steps:

- initial plane wave $E_0^{(0)}(\rho) = \text{const}$ forms double-pass wave front $E_{II}^{(0)}(\rho)$, which is detected by Shack-Hartmann wave front sensor;
- the value of $J_i^{(0)}$ is computed and the control signals are evaluated (for instance, by the gradient algorithm¹²), producing complex reflectance $t_c^{(1)}(\rho) = \exp[-i\alpha^{(1)}(\rho)]$ by electromechanically deformable mirror¹³ or liquid-crystal spatial light modulator¹⁴. Corrected wave front $E_0^{(1)}(\rho) = \exp[-i\alpha^{(1)}(\rho)]$ results in double-pass wave front $E_{II}^{(1)}(\rho)$;
- the procedure is to be repeated till the convergence of the iterative process, $J_i^{(N-1)} \approx J_i^{(N)}$; the incident wave front $E_0^{(N)}(\rho) = \exp[-i\alpha^{(N)}(\rho)]$ determines appropriate phase correction and optimal estimation of space distribution of eye aberrations $\tilde{\varphi}(\rho) = -\alpha^{(N)}(\rho)$.

3. OPTIMAL INVERSE FILTERING FOR WAVE FRONT RECONSTRUCTION

Wave front reconstruction from measured local wave front slopes is an example of inverse problem. We consider sufficiently generalized approach to its optimal solution. Let us assume the incident wave to be

$$E(x, y) = E_0(x, y) \exp[i\Psi(x, y)]. \quad (16)$$

Then, image shift for each lenslet relatively the optical axis is defined as:

$$\Delta x_m = -F \frac{\partial \Psi(x_m, y_m)}{\partial x}; \quad \Delta y_m = -F \frac{\partial \Psi(x_m, y_m)}{\partial y}, \quad (17)$$

where $m = \overline{1, M}$ numerates subapertures of an array, and M is the total number of lenslets. Let the wave front be expanded in a series of some set of functions $\{g_k(x, y)\}$, which are orthogonal over the total sensor aperture:

$$\Psi(x, y) = \sum_{k=1}^K a_k g_k(x, y). \quad (18)$$

Equations (17) and (18) define the system of $2M$ linear algebraic equations for coefficients a_k :

$$\begin{aligned} \Delta x_m &= -F \sum_{k=1}^K a_k \frac{\partial g_k(x_m, y_m)}{\partial x}, \\ \Delta y_m &= -F \sum_{k=1}^K a_k \frac{\partial g_k(x_m, y_m)}{\partial y}. \end{aligned} \quad (19)$$

For the system (19) to be defined, the number of coefficients a_k in the expansion (18) has to be $K \geq 2M$. But choice of K is not so unambiguous: functions g_k , with large indices change rapidly, that is in contradiction with the assumption of smooth wave front. Therefore, specific value of K depends on chosen basis $\{g_k(x, y)\}$, and usually, is substantially smaller than $2M$.

Let the system (19) be expressed in matrix form:

$$\mathbf{s} = \mathbf{L} \mathbf{a} + \mathbf{n}; \quad (20)$$

where \mathbf{n} is a vector of random data errors, matrix \mathbf{L} and vectors \mathbf{s} , \mathbf{a} being defined by equations:

$$\mathbf{a} = \begin{bmatrix} a_1 \\ \dots \\ a_K \end{bmatrix}; \quad \mathbf{s} = \begin{bmatrix} s_1 \\ \dots \\ s_{2M} \end{bmatrix}; \quad \mathbf{L} = [L_m^k]; \quad s_m = \begin{cases} \Delta x_m & m = \overline{1, M} \\ \Delta y_{m-M} & m = \overline{M+1, 2M} \end{cases}, \quad L_m^k = \begin{cases} -F \frac{\partial g_k(x_m, y_m)}{\partial x} & m = \overline{1, M} \\ -F \frac{\partial g_k(x_m, y_m)}{\partial y} & m = \overline{M+1, 2M} \end{cases} \quad (21)$$

It should be noted that direct solution of the system (20) in the form $\mathbf{a} = \mathbf{L}^{-1} \mathbf{s}$ is invalid because of the singularity of the term $\mathbf{L}^{-1} \mathbf{n}$ (inverse matrix \mathbf{L}^{-1} does not exist at all for $K \neq 2M$). Hence, instead of exact solution, we shall find pseudo-solution $\hat{\mathbf{a}}$, the best in the sense of minimum mean square error:

$$\sigma^2(x, y) \equiv \left\langle \left| \Psi(x, y) - \tilde{\Psi}(x, y) \right|^2 \right\rangle = \min. \quad (22)$$

In this expression, angle brackets define the operation of statistical averaging over the ensemble of realizations of measured values.

An the next step, we define left- and right-iterated kernels:

$$\mathbf{R}^{(l)} = \mathbf{L}^+ \mathbf{L}, \quad \mathbf{R}^{(r)} = \mathbf{L} \mathbf{L}^+, \quad (23)$$

where symbol "+" denotes conjugated matrix. As it is evident from equations (23), matrices $\mathbf{R}^{(l)}$, $\mathbf{R}^{(r)}$ are Hermitian, so spectral problems

$$\mathbf{R}^{(l)} \mathbf{u}_p = \left(\omega_p^{(l)} \right)^2 \mathbf{u}_p, \quad \mathbf{R}^{(r)} \mathbf{v}_p = \left(\omega_p^{(r)} \right)^2 \mathbf{v}_p \quad (24)$$

are solvable. It can be shown that these solutions have the following characteristics:

1. Sets of eigenvectors $\{\mathbf{u}_p\}$ and $\{\mathbf{v}_p\}$ form orthogonal bases (do not necessarily complete) in metric spaces of the dimensionalities $k_{\max}^2 = K^2$ and $m_{\max}^2 = 4M^2$ correspondingly.
2. $\omega_p^{(l)} = \omega_p^{(r)} \equiv \omega_p > 0$, and the number of non-zero eigenvalues is $P \leq \min\{K, 4M\}$.
3. Matrix \mathbf{L} defines the mapping of vectors $\{\mathbf{u}_p\}$, $\{\mathbf{v}_p\}$ on one another, so that:

$$\mathbf{L} \mathbf{u}_p = \omega_p \mathbf{v}_p, \quad \mathbf{L}^+ \mathbf{v}_p = \omega_p \mathbf{u}_p. \quad (25)$$

It should be noted, that equations (25) are useful in practice when spectral problems (24) have to be solved. Actually, it is quite enough to solve only the problem with smaller dimensionality, and the solution of the second equation is found from transforms (25). Beside the reduced calculation complexity, this procedure permits to eliminate the problems with degenerate eigenvalues ω_p .

Now, the solution of inverse problem (20) can be found in the following manner. At the first step, coefficients of the expansion of data vector \mathbf{s} in basis $\{\mathbf{v}_p\}$ are calculated:

$$\beta_p = \mathbf{v}_p^+ \mathbf{s}. \quad (26)$$

In line with equations (20) and (25), we have

$$\beta_p = \omega_p \alpha_p + \eta_p, \quad (27)$$

where α_p are coefficients of true presentation of \mathbf{a} , $\alpha_p = \mathbf{u}_p^+ \mathbf{a}$, and η_p represents measurement error \mathbf{n} , $\eta_p = \mathbf{v}_p^+ \mathbf{n}$. As far as \mathbf{n} is a random vector, α_p cannot be defined exactly from equation (27). In consequence, the pseudo-solution $\tilde{\alpha}_p$, $\tilde{\alpha}_p = \mathbf{u}_p^+ \tilde{\mathbf{a}}$ has to be estimated. We can express it in the form:

$$\tilde{\alpha}_p = H_p^{-1} \beta_p \equiv \frac{W_p}{\omega_p} \beta_p = W_p \alpha_p + W_p \frac{\eta_p}{\omega_p}. \quad (28)$$

The best estimation of $\tilde{\alpha}_p$ leads to the problem of optimal linear filtration of signal α_p in additive noise $\frac{\eta_p}{\omega_p}$. To construct the optimal filter W_p , we assume that measurement error \mathbf{n} is normal white noise with zero mean. Then, the dispersion of wave front estimation error can be expressed from equation (22) as:

$$\sigma^2(x, y) \equiv \langle |\Psi(x, y) - \tilde{\Psi}(x, y)|^2 \rangle = \langle \Psi^2(x, y) \rangle - 2 \langle \Psi(x, y) \tilde{\Psi}(x, y) \rangle + \langle \tilde{\Psi}^2(x, y) \rangle. \quad (29)$$

On the other hand, it is known¹⁵, that minimum error dispersion of linear filtration is:

$$\sigma_{\min}^2(x, y) = \langle \Psi^2(x, y) \rangle - \langle \tilde{\Psi}^2(x, y) \rangle. \quad (30)$$

From the equality of right terms in equations (14), (15), the expansion (18) for Ψ , $\tilde{\Psi}$, and integration over (x, y) -coordinates, one can obtain:

$$\langle \hat{\mathbf{a}}^+ \hat{\mathbf{a}} \rangle = \langle \mathbf{a}^+ \mathbf{a} \rangle, \quad (31)$$

where the orthogonality of basis $\{g_k(x, y)\}$ is taken into account. If we express vectors \mathbf{a} and $\hat{\mathbf{a}}$ as $\mathbf{a} = \sum_p \alpha_p \mathbf{u}_p$, $\hat{\mathbf{a}} = \sum_p \tilde{\alpha}_p \mathbf{u}_p$, and consider equation (28), where $\langle \alpha_p \eta_p \rangle = 0$ (as independent statistical variables with zero means), we can find after simple transformation:

$$W_p = \frac{\langle \alpha_p^2 \rangle}{\langle \alpha_p^2 \rangle + \frac{\langle \eta_p^2 \rangle}{\omega_p^2}}. \quad (32)$$

It can be seen that W_p is a generalized Wiener-type filter which is optimal for signal estimation in additive noise. It is valid irrespective of the concrete bases $\{\mathbf{u}_p\}$, $\{\mathbf{v}_p\}$.

Thus, the wave front estimation in basis $\{\mathbf{u}_p\}$ can be expressed from equations (28), (32) as the result of linear filtration of coefficients β_p by optimal pseudo-inverse filter H_p^{-1} :

$$H_p^{-1} = \frac{\omega_p}{\omega_p^2 + \frac{\langle \eta_p^2 \rangle}{\langle \alpha_p^2 \rangle}}. \quad (33)$$

The second term in denominator (33) is the ratio of diagonal elements of the correlation matrices of measurement errors and wave front in bases $\{\mathbf{v}_p\}$ and $\{\mathbf{u}_p\}$, respectively. Exact value of this term is always unknown, but it can be substituted by some constant ε without sacrificing of the solution accuracy. The meaning of this constant is the average relative error of the measurement data. The resulting expression for reconstructed wave front $\tilde{\Psi}$ is of the form:

$$\tilde{\mathbf{a}} = \sum_p \tilde{\alpha}_p \mathbf{u}_p; \quad \tilde{\alpha}_p = \frac{\omega_p}{\omega_p^2 + \varepsilon} \mathbf{v}_p^+ \mathbf{s}, \quad (34)$$

where $\{\mathbf{u}_p\}$, $\{\mathbf{v}_p\}$, $\{\omega_p\}$, \mathbf{s} , $\tilde{\mathbf{a}}$ are determined from equations (21), (23), (24).

Shack-Hartmann wave front sensor results in wave front presentation as an array of discrete points in a grid sites that correspond to the measurement geometry (fig. 2).

Differentiation in (17) is substituted by finite differences:

$$\Delta x_m = -F \frac{\Psi(x_m + \frac{D}{2}, y_m - \frac{D}{2}) - \Psi(x_m - \frac{D}{2}, y_m - \frac{D}{2}) + \Psi(x_m + \frac{D}{2}, y_m + \frac{D}{2}) - \Psi(x_m - \frac{D}{2}, y_m + \frac{D}{2})}{2D};$$

$$\Delta y_m = -F \frac{\Psi(x_m - \frac{D}{2}, y_m + \frac{D}{2}) - \Psi(x_m - \frac{D}{2}, y_m - \frac{D}{2}) + \Psi(x_m + \frac{D}{2}, y_m + \frac{D}{2}) - \Psi(x_m + \frac{D}{2}, y_m - \frac{D}{2})}{2D}; \quad (35)$$

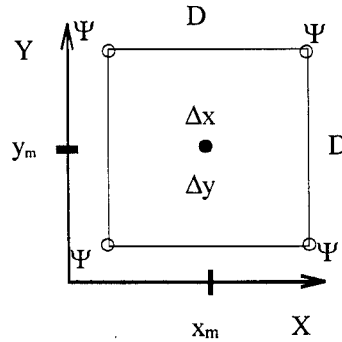


Fig. 2. Coordinate grid for determination of derivatives in m -th point of interpolation

To estimate primary aberrations, Zernike polynomials are used in the circular part of aperture. Experimental results and their interpretation are described in the next section.

4. EXPERIMENT AND DISCUSSION

In our experiment, combined with computer simulation, an experimental setup was used, described in our previous work⁸. Wave front sensor contains a 19x19 lenslet array with apertures 0.75 mm and foci 50 mm. Experimental procedure was as follows:

- direct determining of phase transmission of an optical object, wave front being obtained in a single pass experiment;
- measurement and reconstruction of the wave front, formed in the second pass of the reflected light through the object under test (thin lenses, having different kinds of astigmatism, were used as objects under test);
- computer simulation of iterative compensation of aberrations, got experimentally.

Fig. 3 represents wave fronts formed by spherical and astigmatic lenses in a single pass of light. Focal power of lenses was 2 diopters sphere (*a*) and 2 diopters sphere plus 0.5 diopters cylinder (*b*). Equal phase lines are drawn at intervals 20λ . Spherical wave has the radius $R=397$ mm, and astigmatism $\Phi=1.256\lambda S^2 \sin 2\theta + 2.82\lambda S^2 \cos 2\theta$, where S is a normalized radial coordinate: $S^2=((x-7.125\text{mm})^2+(y-7.125\text{mm})^2)/(7.125\text{mm})^2$; θ is an angular coordinate. Astigmatic lens parameters are: $R=348$ mm, $\Phi=106.4\lambda S^2 \cos 2\theta$.

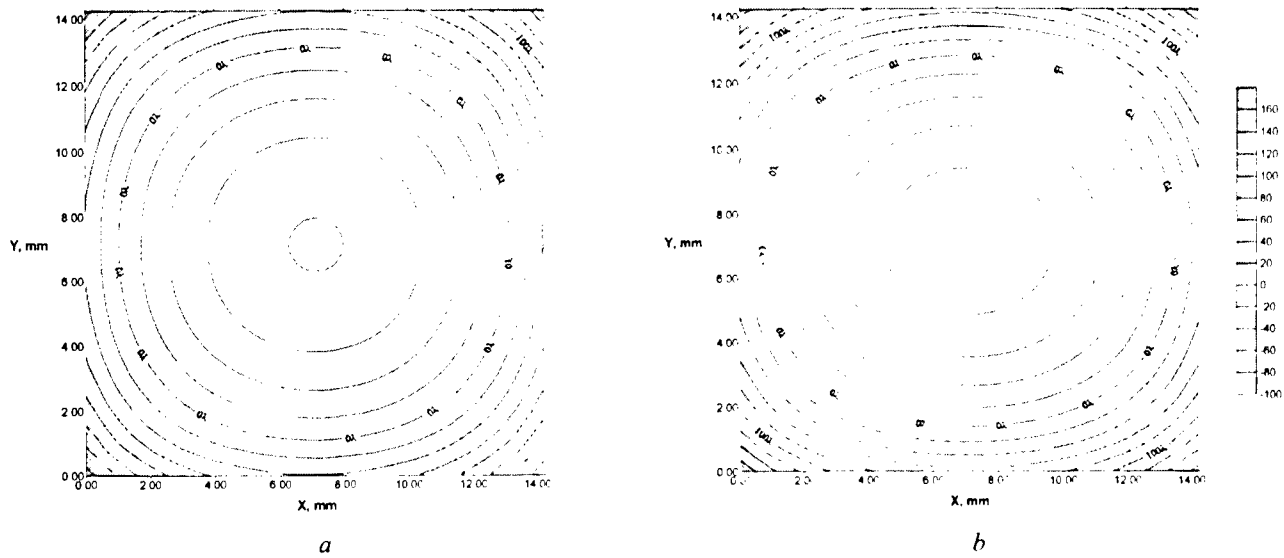


Fig. 3. Spherical (*a*) and astigmatic (*b*) wave fronts measured in a single-pass experiment

Wave fronts reconstructed from double-pass experiments are presented in figures 4 and 5.

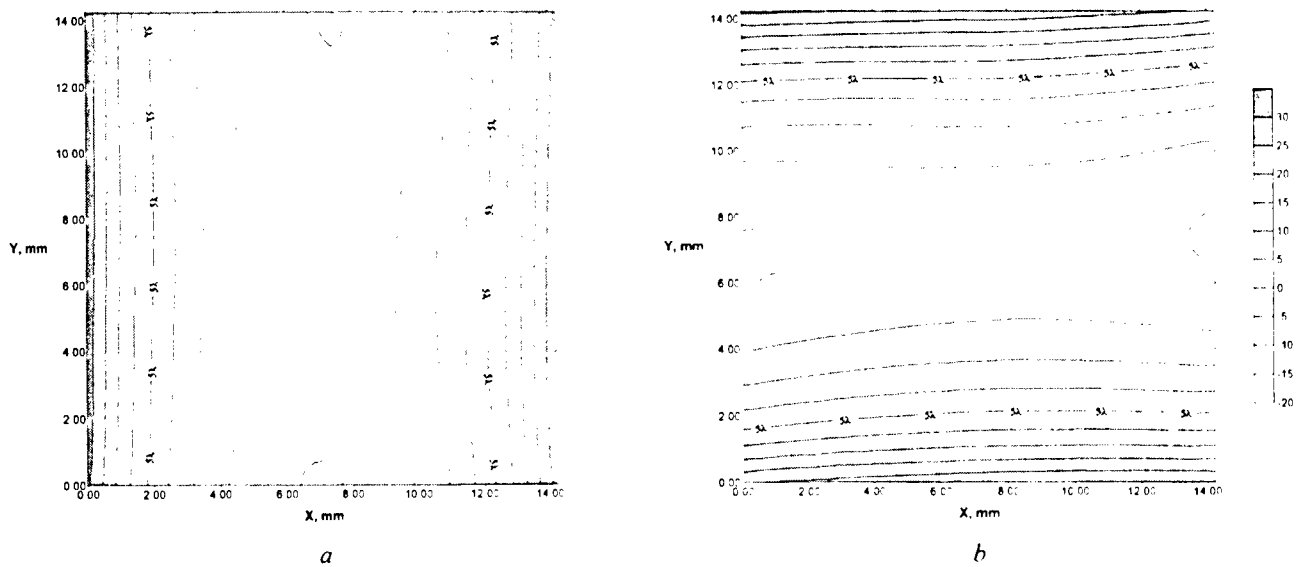


Fig. 4. Cylindrical wave front formed by astigmatic lens in the double-pass experiment

Both experiments of fig. 4 with astigmatic lens were performed under the same conditions, with the only difference in the orthogonal lens orientation. Good coincidence of the wave front shapes proves that their principal features depend on the tested lens parameters, not on possible apparatus distortions and measurement error.

Aberrations in double-pass experiment for spherical lens are of low level (fig. 5). Equal-phase lines are here at 1λ interval. Wave aberrations are: $R=4.2$ m, astigmatism $\Phi=2.785\lambda S^2\sin 2\theta + 2.51\lambda S^2\cos 2\theta$.

Wave front, measured in double-pass experiment with astigmatic lens, has high level of aberrations (fig. 4), and was used as initial data for iterative correction. The wave front corrected in computer simulation is represented in fig. 6.

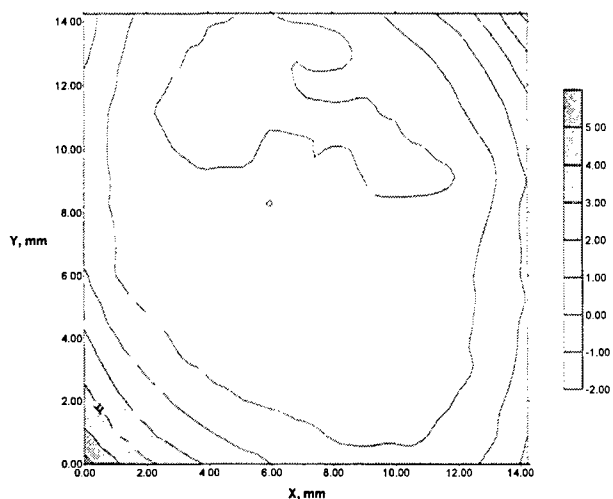


Fig. 5. The wave front formed by spherical lens in the double-pass experiment

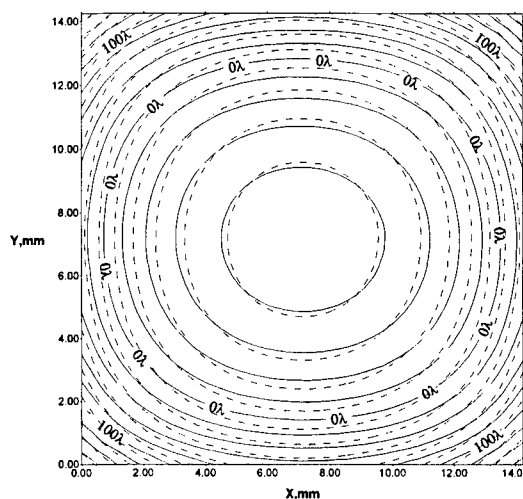


Fig. 6. Astigmatism correction: wave front formed by astigmatic lens is drawn in solid lines, corrected wave front - in dashed lines

Results of the above described experiments confirm high efficiency of the proposed procedure. The study is planned to be continued with spatial light modulator substituting computer simulation.

5. ACKNOWLEDGMENTS

This work has been carried out with financial support of the STCU - Science and Technology Center in Ukraine (project No. 418) being funded by the governments of the United States, Canada, and Sweden.

6. REFERENCES

1. D. R. Williams, D. H. Brainard, M. J. McMahon, R. Navarro, "Double-pass and interferometric measures of the optical quality of the eye", *J. Opt. Soc. Amer.* **A12**, pp. 3123-3134, 1995.
2. J. Liang, G. Westheimer, "Optical performances of human eyes derived from double-pass measurements", *J. Opt. Soc. Amer.* **A12**, pp. 1411-1416, 1995.
3. J. Liang, B. Grimm, S. Goelz, J. F. Bille, "Objective measurement of wave aberrations of the human eye with use of Hartmann-Shack wave-front sensor", *J. Opt. Soc. Amer.* **A11**, pp. 1949-1957, 1994.
4. V. V. Molebny, V. N. Kurashov, I. G. Pallikaris, L. P. Naoumidis, "Adaptive optics for measuring eye refraction distribution", *Proc. SPIE* **2930**, pp. 147-156, 1996.

5. V. V. Molebny, I. G. Pallikaris, L. P. Naoumidis, V. N. Kurashov, I. H. Chyzh. "Eye investigation with optical microradar techniques", *Proc. SPIE* **3065**, 1997.
6. J. Liang, D. R. Williams, D. T. Miller. "High resolution imaging of the living human retina with adaptive optics", *Invest. Ophthalm. & Vis. Sci.* **38**, p. S13, 1997.
7. F. Vargas, I. Iglesias, P. Artal. "Images of the human fovea after correction of the ocular aberrations with a liquid crystal spatial light modulator", *Invest. Ophthalm. & Vis. Sci.* **38**, p. S13, 1997.
8. V. N. Kurashov, V. V. Molebny, A. V. Kovalenko, D. V. Podanchuk, T. V. Molebna, I. G. Pallikaris, L. P. Naoumidis. "Double-pass wave model in eye aberrations study", *Proc. SPIE* **3192**, 1997.
9. R. Navarro, M. A. Losada, "Phase transfer and point-spread function of the human eye determined by a new asymmetric double-pass method", *J. Opt. Soc. Amer.* **A12**, pp. 2385-2392, 1995.
10. M. A. Vorontsov, M. A. Shmalhausen. *Principles of adaptive optics*, Nauka, Moscow, 1985 (in Russian).
11. G. W. Goodman, *Statistical optics*, John Wiley and Sons, New York-Chichester-Brisbane-Toronto-Singapore, 1985.
12. F. P. Vasiliev, *Numerical methods of extremum problem solution*, Nauka, Moscow, 1985 (in Russian).
13. M. C. Roggeman, V. M. Bright, B. M. Welsh, C. R. Hick, P. C. Roberts, W. D. Cowan, J. H. Comtois, "Use of electromechanical deformable mirrors to control aberrations in optical systems - theoretical and experimental results", *Opt. Eng.* **36**, pp. 1326-1338, 1997.
14. G. D. Love, "Wave-front correction and production of Zernike modes with a liquid-crystal spatial light modulator", *Appl. Optics* **36**, pp. 1517-1524, 1997.
15. B. R. Levin, *Theoretical principles of statistical radio engineering*, Radio i Sviaz, Moscow, 1989 (in Russian).

Scleral tissue light scattering and matter diffusion

Valery V.Tuchin¹, Irina L.Maksimova³, Alexey A.Mishin², Albert Kh.Mavlutov¹

¹Saratov State University, Astrakhanskaya 83, Saratov 410026, Russia

²Institute of Precision Mechanics and Control, Russian Academy of Science, Rabochaya 24, Saratov 410028, Russia

³Institute of Radio Engineering and Electronics, Russian Academy of Science, Saratov Branch, Saratov 410019, Russia

⁴Saratov Medical University, Saratov 410071, Russia

ABSTRACT

Theoretical and computer modeling approaches, such as Mie theory, radiative transfer theory, Monte Carlo simulation method were applied for tissue optics analysis in a process of its optical clearing due to refractive indices matching. CW transmittance and forward and backward scattering measurements were used for tissue structural and optical properties monitoring. As a controlled tissue samples of the human sclera were taken. As a chemical applicator - controller osmotically active trazograph solution was used. The scleral absorption and scattering spectra as well as diffusion coefficient describing the samples of the human sclera permeability to trazograph were experimentally estimated. Presented results are general and can be applicable for description of many other fibrous tissues.

Keywords: light scattering, sclera, osmolytes, refractive indices matching

1. INTRODUCTION

Tissue as a scattering medium shows all optical effects which are characteristic to turbid physical systems (see for example¹). It is well known that turbidity of a dispersive physical system can be effectively controlled using immersion effect (matching of refractive indices of the scatterers and the base material) as well as by changes of scatterers sizes and their packing (volumetric arrangement causes the spatial correlation of the scatterers)¹⁻³. The living tissue allows to control its optical (scattering) properties using various physical and chemical reactions such as compression, stretching, dehydration, coagulation, UV irradiation, low temperature application, adding of chemicals¹⁻⁹.

In vivo tissue optical properties control is very important for many applications. A number of laser surgery, therapy and diagnostic technologies include tissue compression and stretching used for better transportation of laser beam to underlying layers of tissue. The human eye compression technique allows to perform transscleral laser coagulation of the ciliary body and retina/choroid². The possibility of selective clearance of the upper tissue layers should be very useful for developing of the eye ball diaphanoscopy techniques and for detecting of local inhomogeneities hidden by a highly scattering medium in functional tomography. Recently a number of results on noninvasive glucose concentration monitoring within human body using NIR light scattering techniques were reported^{6,7}. The response of a nondiabetic male subject to a glucose load was measured by continuously monitoring the product $n\mu_s$ (refractive index and reduced scattering coefficient) measured on muscle tissue of the subject's thigh⁶. In the human body fluid homeostasis is maintained by a well controlled balance of hydrostatic and osmotic pressures. This balance can be disturbed by the certain physiological disorders induced by inflammation or trauma (lymphedema, burn and etc.), that leads to a well detected change of tissue scattering properties in far red and NIR ranges⁸.

In this paper, we present theoretical and experimental results on the human sclera optical properties controlled by employing administration of osmotically active chemicals, such as trazograph. Chemical agents administration induces matter diffusion and as a result equalization of collagen and ground material refractive indices.

2. MODELING OF COLLIMATED AND DIFFUSE TRANSMISSION AND REFLECTION SPECTRA

The collimated light transmission by a tissue layer of thickness l is defined as

$$T_c = I/I_0 = \exp(-\mu_t l), \quad (1)$$

where I_0 and I are the intensities of the collimated incident and detected light, respectively; $\mu_t = \mu_a + \mu_s$ is the extinction coefficient, μ_a and μ_s are the absorption and scattering coefficients, respectively.

For modeling of spectral characteristics of the sclera sample we used the probability function for the free photon path l_{ph} :

$$p(l_{ph}) = \mu_t \cdot \exp(-\mu_t l_{ph}), \quad (2)$$

$$\int_0^{l_{ph}} p(l_{ph}) dl_{ph} = \gamma, \quad 0 < \gamma < 1, \quad (3)$$

and Mie phase function calculated for an individual dielectric cylinder. The Monte Carlo simulation technique for the sclera transmission and reflection spectra modeling was designed.

Because the random number γ is uniformly distributed in the interval $[0,1]$ the substitution of Eq. (2) into (3) and integration gives

$$l_{ph} = -\frac{1}{\mu_t} \cdot \ln \gamma. \quad (4)$$

This equation was the basic one for the modeling of photons trajectories. $\mu_t \approx \mu_s$, μ_s is defined by tissue structure. This program allows to calculate collimated, diffusion transmission and reflection spectra of tissues like sclera and to study the interstitial fluid and collagen fibrils refractive indices matching effects.

The results of such modeling for scleral sample of 1 mm thickness, with collagenous fibrils of mean diameter equal to 120 nm and mean separation between fibrils centers equal to 285 nm, refractive index of collagen $n_c = 1.47$ and of interstitial medium $n_i = 1.35$ -1.45 presented in Figs 1-5. It is well seen that designed model describes well all important features of immersed tissue.

3. THE SPECTROPHOTOMETRIC MEASUREMENTS AND MODELING

The spectrophotometric measurements in the wavelength range 400-840 nm were provided by using a commercially available spectrophotometer Cary-2415. The time period for registration of one spectra was about 5 min. Cary-2415 allowed to measure collimated transmittance, total transmittance and diffuse reflectance using integrating sphere. Individual spectrum was registered during 85 s.

The comparison of calculated and experimental (Fig.6) spectra shows that refractive indices matching is the main mechanism responsible for tissue optical clearing. The developed Monte Carlo simulation technique allows to describe the transition from a completely diffusion to a partially-coherent transmission of the sclera caused by refractive indices matching. Such transition is well illustrated by the histograms of Figs 2-5. These histograms show that for sclera with unmatched or slightly matched refractive indices there is approximately uniform distribution of the number of scattering events which forward traveling photon undergo. For fairly matched refractive indices there is appear a large amount (about 84 % for $n_i = 1.45$ and $\lambda = 800$ nm) of ballistic photons (the coherent part of transmitted light) with fraction of about 14% of single scattered photons.

For finding of optical parameters of sclera in a process of its clearing the following model was used. Collimated laser beam with the finite diameter and with the flat distribution across its cross-section falls on the five layered medium, transmitted and reflected light was detected using the integrating spheres. The computer model took into account the real

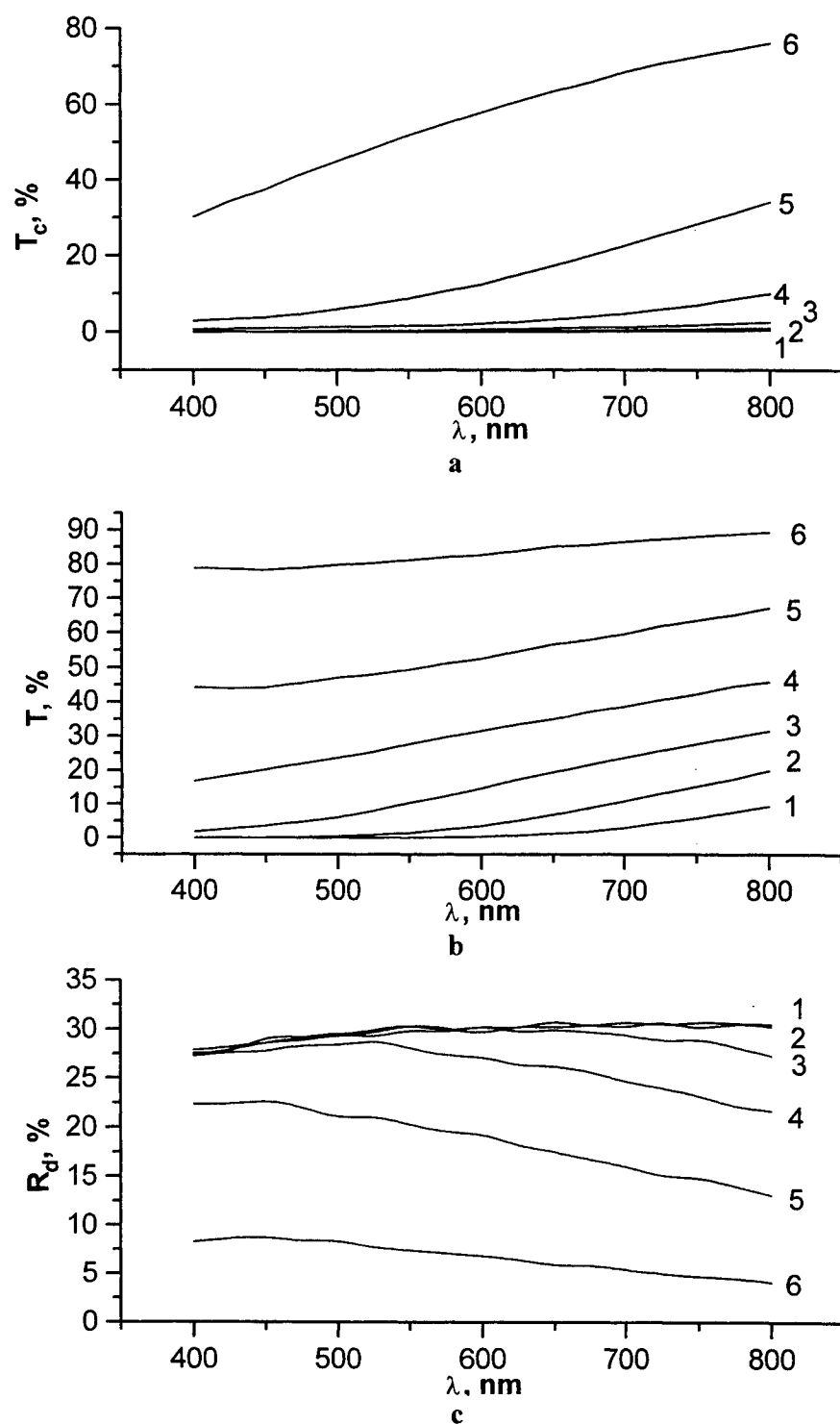


Fig.1. The collimated (a) and total (b) transmittance spectra as well as diffuse reflectance (c) spectra calculated for different refractive indices matching for geometry very close to experimental one (see Fig.6); $n_c = 1.47$ and $n_l = 1.35$ (1), 1.37 (2), 1.39 (3), 1.41(4), 1.43 (5), 1.45 (6).

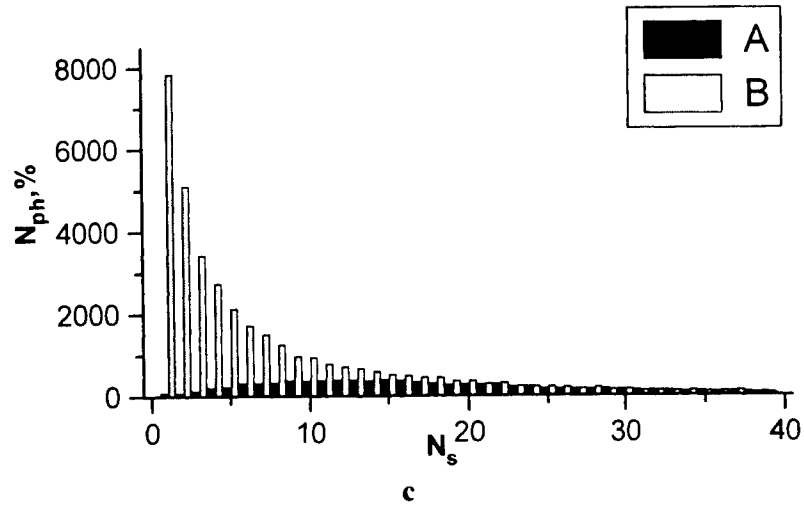
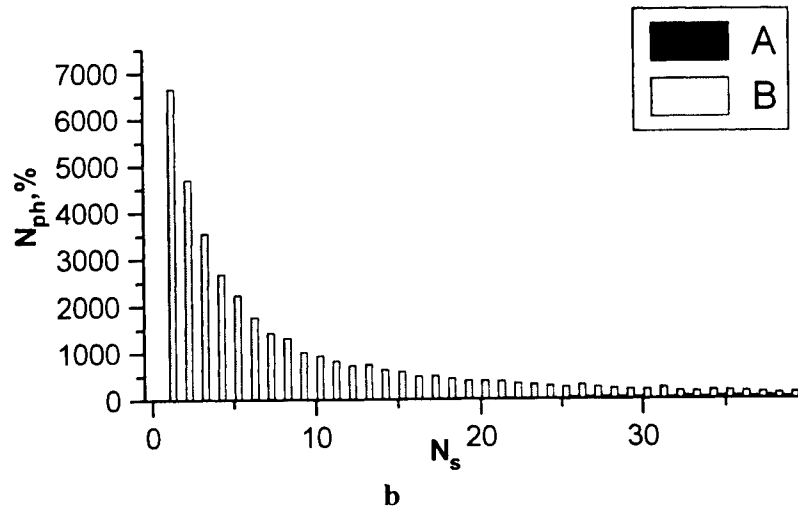
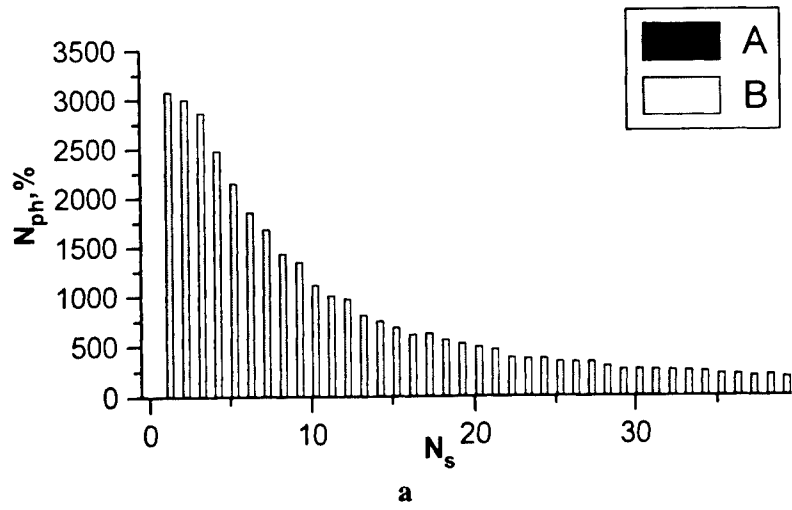
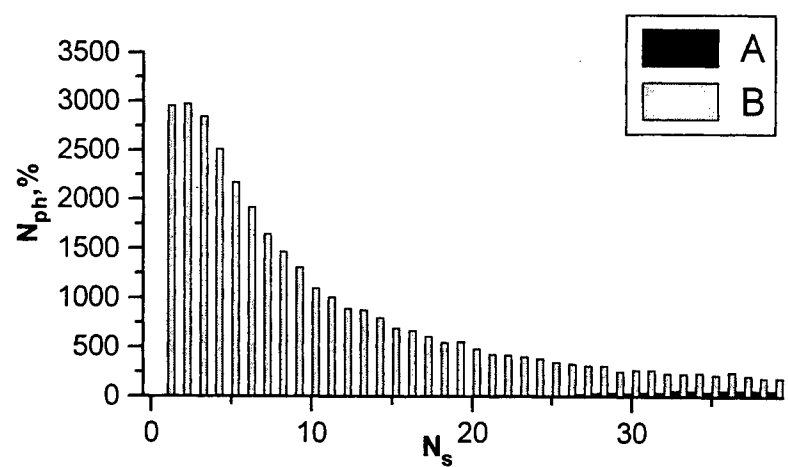
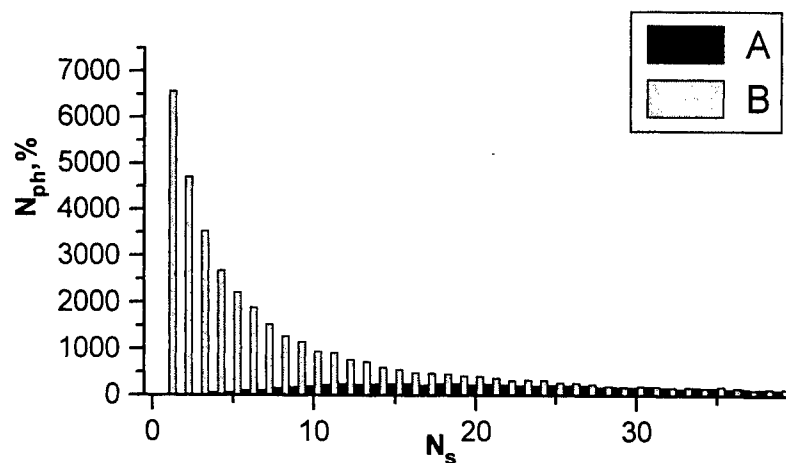


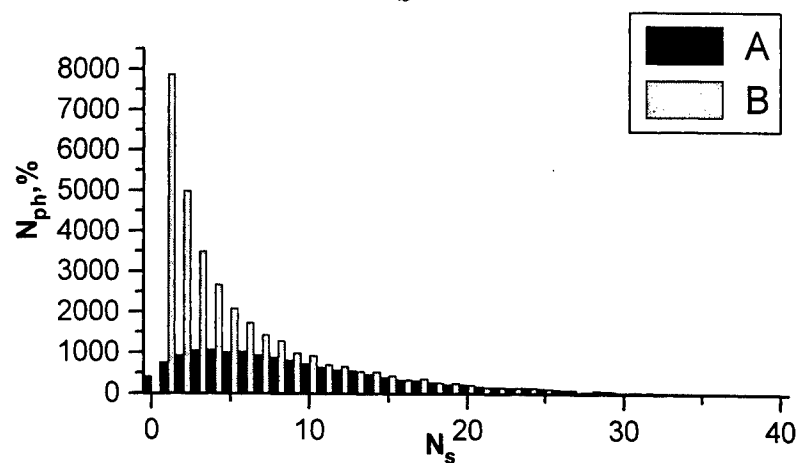
Fig.2. Calculated distributions of the number N_{ph} of forward (A) and back scattered (B) photons via number of collisions N_s (two integrating sphere geometry) for slightly matched refractive indices of the human scleral components ($n_c = 1.47$, $n_l = 1.37$): a - $\lambda = 400$ nm; b - $\lambda = 600$ nm; c - $\lambda = 800$ nm.



a



b



c

Fig.3. Calculated distributions of the number N_{ph} of forward (A) and back scattered (B) photons via number of collisions N_s (two integrating sphere geometry) for partly matched refractive indices of the human scleral components ($n_c = 1.47$, $n_1 = 1.39$): a - $\lambda = 400$ nm; b - $\lambda = 600$ nm; c - $\lambda = 800$ nm.

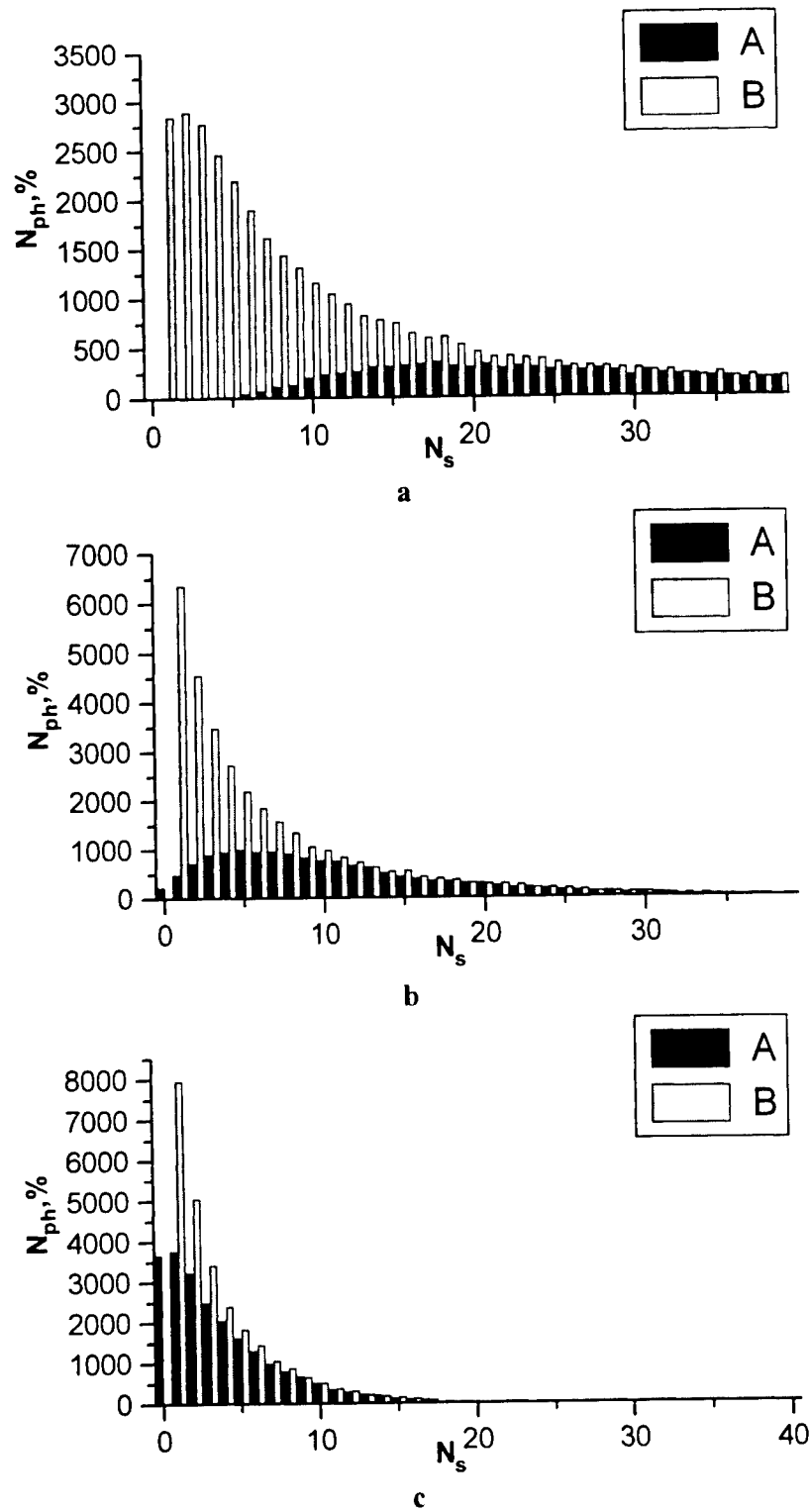
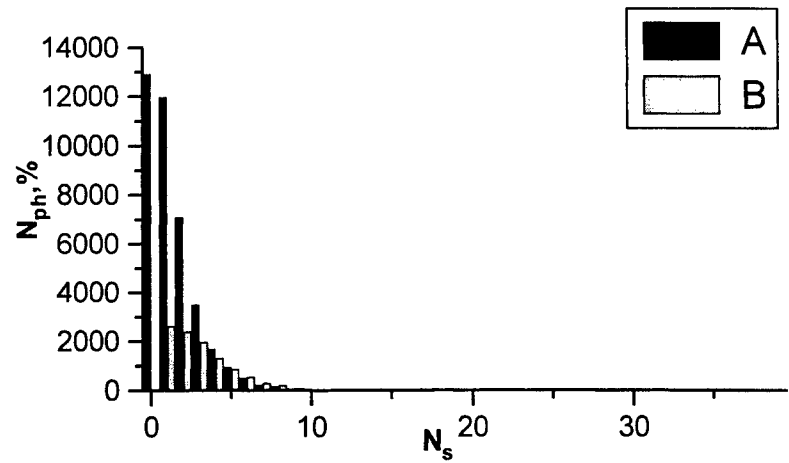
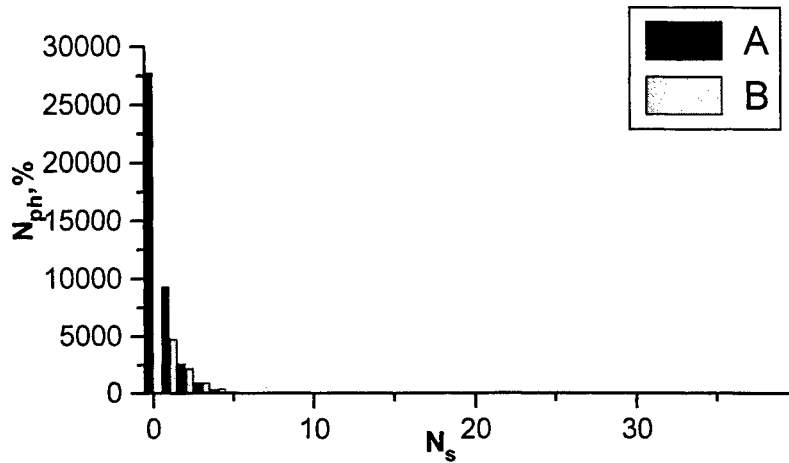


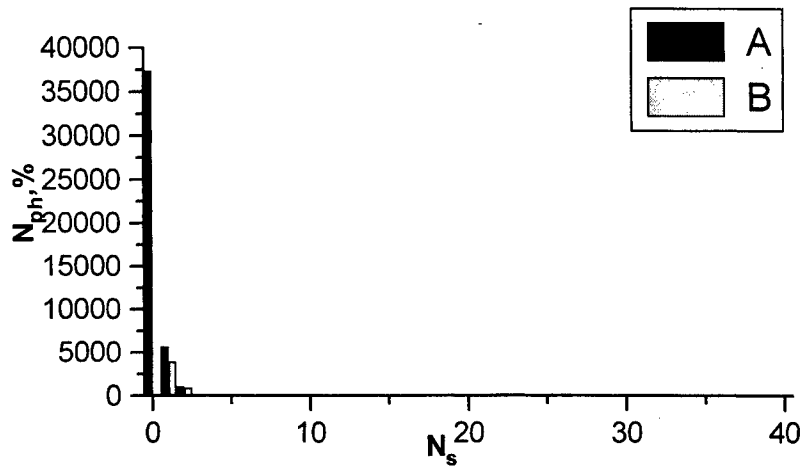
Fig.4. Calculated distributions of the number N_{ph} of forward (A) and back scattered (B) photons via number of collisions N_s (two integrating sphere geometry) for partly matched (mid level) refractive indices of the human scleral components ($n_c = 1.47$, $n_l = 1.41$): a - $\lambda = 400$ nm; b - $\lambda = 600$ nm; c - $\lambda = 800$ nm.



a



b



c

Fig.5. Calculated distributions of the number N_{ph} of forward (A) and back scattered (B) photons via number of collisions N_s (two integrating sphere geometry) for partly matched (high level) refractive indices of the human scleral components ($n_c = 1.47$, $n_l = 1.45$): a - $\lambda = 400$ nm; b - $\lambda = 600$ nm; c - $\lambda = 800$ nm.

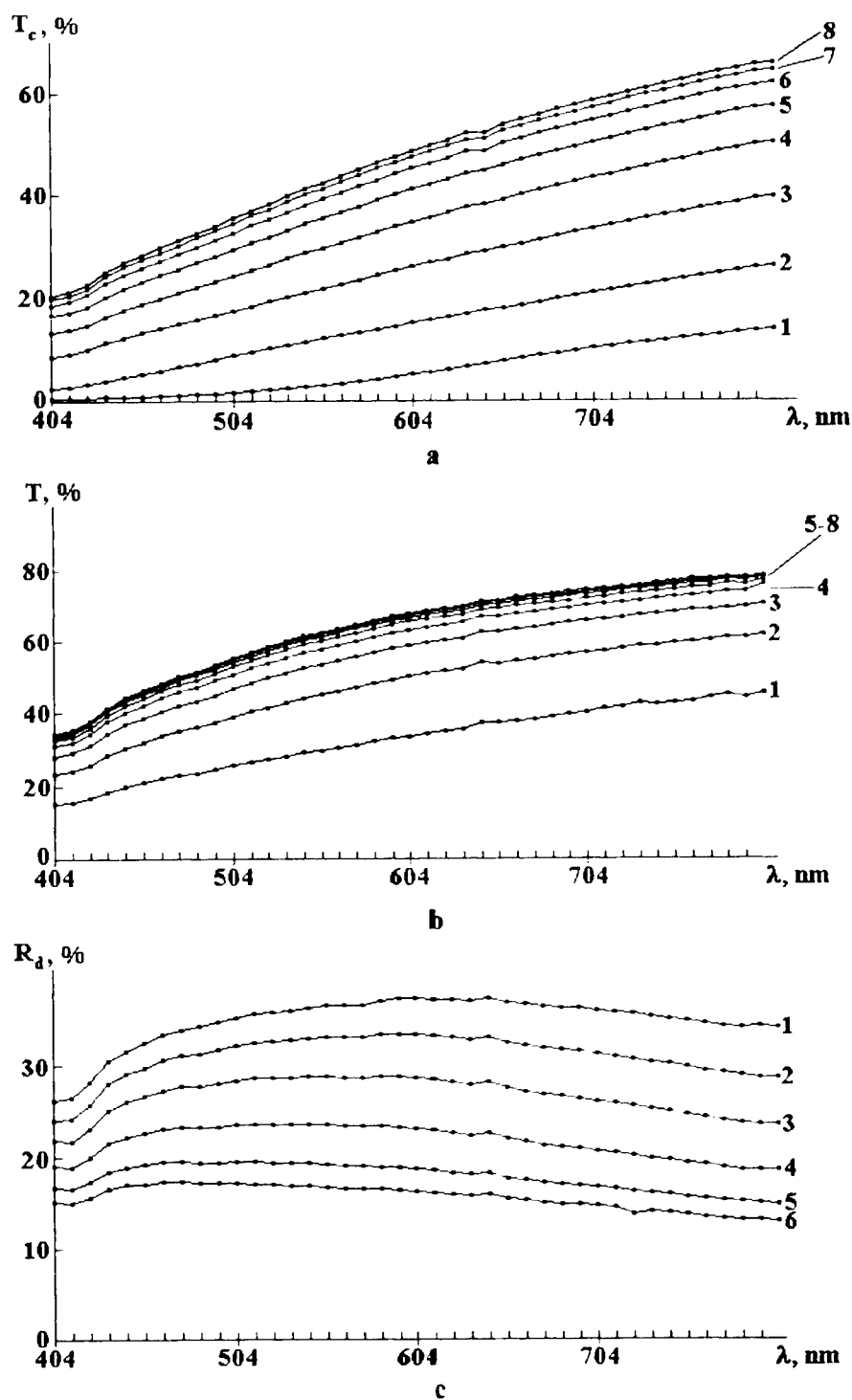
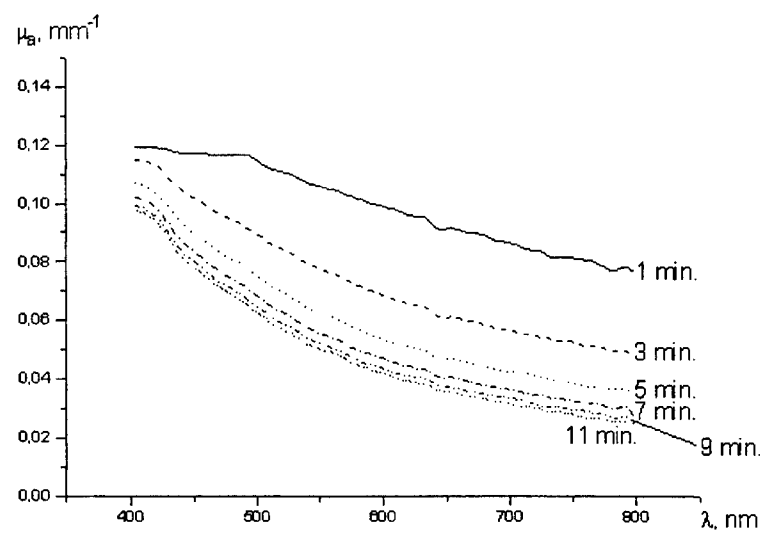
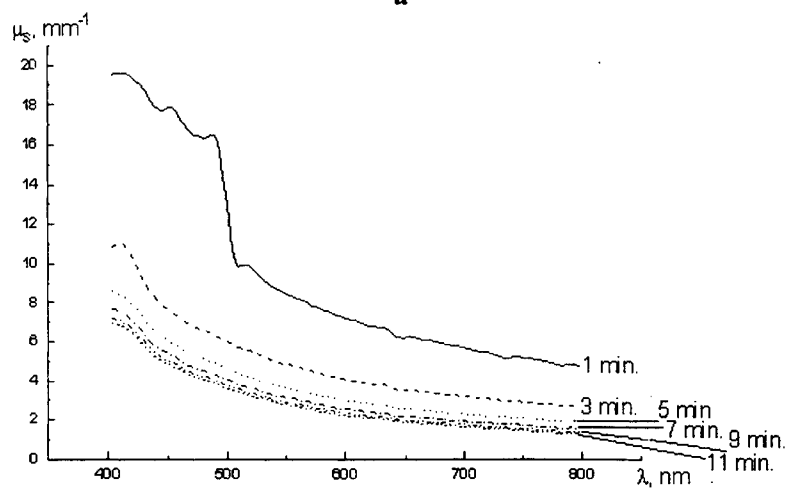


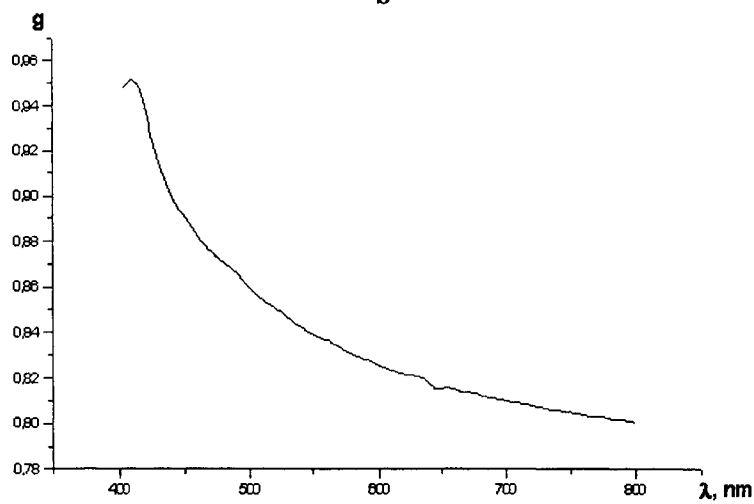
Fig.6. Typical experimental spectra of the human sclera samples measured for different time intervals of 60% trazograph solution administration. Spectra numbered 1 were measured in 1 min after sample immersing into solution, spectra 2-8 were measured subsequently at 2 min intervals. An individual spectrum measuring time scanning from higher to lower wavelengths was about 85 sec. a - the collimated transmittance, T_c , sample thickness - 0.6 mm; b - the total transmittance, T , sample thickness - 0.7 mm; c - the diffusion reflection R_d , sample thickness - 0.7 mm (heavy pigmented tissue)



a



b



c

Fig.7. Spectra of optical parameters of the human sclera calculated using experimental spectra presented in Fig.6.

geometry of the integrating sphere – finite diameter and geometry of the sphere windows. The five layered model contained cuvette glass walls, solution of osmotically active chemical (trazograph, for example) and scleral sample itself. We suggested that in the directions perpendicular to the laser beam incidence direction medium is infinite.

To get optical parameters of the scleral sample we have to solve the inverse optical problem. To do this we used the following technique:

Firstly, we got the output parameters – total transmission and total reflection for a wide range of optical parameters of the sclera sample. During this step μ_a , μ_s and g was varied. On this step we used the straightforward Monte Carlo technique. The planar waveguide effect was accounted.

Secondly, we mathematically described obtained MC results with four-exponential equations and finally find mathematical dependence of μ_a , μ_s and g on λ . The calculated spectra for optical parameters of the human sclera are presented in Fig.7.

Measuring of the time-dependent collimated transmittance allows basing on tissue refractive indices matching conception to estimate the diffusion coefficients of chemical agents used for the sclera optical clearing. The time-dependent collimated transmittance of the sclera sample measured at 633 nm concurrently with trazograph administration is presented in Fig.8. It shows the

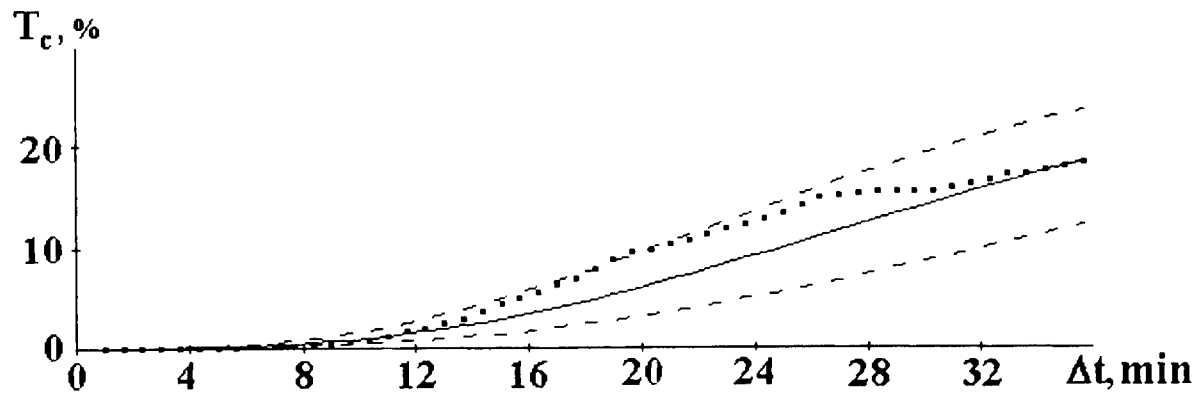


Fig.8. The time-dependent collimated transmittance (dots) of the sclera sample of thickness 0.5 mm measured at 633 nm concurrently with 76% trazograph administration. The solid line and dashed lines represent the mean value and the upper and lower limits of T_c obtained by a calculation (Eqs (5)) of T_c using experimental data: $D_T = 2.27 \cdot 10^{-6} \pm 5.07 \cdot 10^{-7} \text{ cm}^2/\text{s}$

dynamics of tissue clearing. The similar characteristics were measured for glucose and PEG administration. The registration of dynamic response of transmitted intensity can be used for estimation of diffusion coefficients of the interacting fluids: water and trazograph, water and glucose, etc. Basing on the theoretical background given in paper⁵ we can estimate the coefficient of diffusion for trazograph supposing that water and trazograph have the same paths for diffusion:

$$c_T(t) = \frac{1}{n_T - n_i} \cdot \left\{ \frac{n_c}{1 + \left(\frac{n_c}{n_i(0)} - 1 \right) \cdot \sqrt{\frac{|\ln T_c(t) - \mu_a|}{|\ln T_c(0) - \mu_a|}}} - n_i \right\} \quad (5)$$

where n_T is the refractive index of trazograph, $n_i(0)$ is the refractive index of interstitial medium for $t=0$, n_i is the refractive index of interstitial medium defined by endogeneous high molecular components and water, $n_i \cong n_i(0)$.

The experimental data like presented on Fig.8 allows using Eq (5) and $n_c = 1.474$, $n_a = 1.332$, $n_i(0) = 1.345$, $\mu_a = 0.008 \text{ mm}^{-1}$ to estimate $D_T = 2.27 \cdot 10^{-6} \pm 5.07 \cdot 10^{-7} \text{ cm}^2/\text{s}$.

The estimated value of D_T for definite scleral sample have quite reasonable rms errors. It should be noted that mean

values and rms errors were calculated using about 30 magnitudes of T_c measured for different time delay for each sample. In the average, determined D_T values are not far from the values of D for low weight molecules diffusion in water.

4. CONCLUSION

The theoretical and experimental results of this study show that administration of osmolytes to the sclera effects the refractive indices matching of the collagen fibrils and interstitial fluid what leads to dramatic changing (reducing) of the scattering properties of the sclera.

Presented results are general and can be applicable for description of many other fibrous tissues. The attractiveness of the sclera tissue for model experiments with a living tissue is defined by its possibility to transfer under chemical agents acting its scattering properties in a very wide range, that will allow to understand and to describe the transition from diffuse mode of light scattering to a coherent light propagation through tissue.

5. ACKNOWLEDGMENTS

Authors are grateful to MD T. N. Semenova for providing of scleral samples. The research described in this publication was made possible in part by grant N RB1-230 of the U.S. Civilian Research & Development Foundation for the Independent States of the Former Soviet Union (CRDF) and grant of the Russian Foundation of the Basic Research "Leading Scientific Schools" N 96-15-96389.

6. REFERENCES

1. V. V. Tuchin, *Tissue Optics: Applications in Medical Diagnostics and Therapy*, SPIE Milestone ser. **MS102**, Bellingham, 1994.
2. P. O. Rol, *Optics for Transscleral Laser Applications*, Dissertation for the degree of Doctor of Natural Sciences, Inst. Biomedical Engineering, Zurich, Switzerland, 1992.
3. B. Chance, H. Liu, T. Kitai, Y. Zhang, "Effects of solutes on optical properties of biological materials: models, cells, and tissues", *Anal. Biochem* **227**, pp. 351-362, 1995.
4. H. Liu, B. Beauvoit, M. Kimura, B. Chance, "Dependence of tissue optical properties on solute - induced changes in refractive index and osmolarity", *J. Biomed. Opt.* **1**, pp. 200-211, 1996.
5. V. V. Tuchin, I. L. Maksimova, D. A. Zimnyakov, I. L. Kon, A. H. Mavlutov, A. A. Mishin, "Light propagation in tissues with controlled optical properties", *J. Biomed. Optics* **2**, pp. 401-417, 1997.
6. J. S. Maier, S. A. Walker, S. Fantini, M. A. Franceschini, E. Gratton, "Possible correlation between blood glucose concentration and the reduced scattering coefficient of tissues in the near infrared", *Opt. Lett.* **19**, pp. 2062-2064, 1994.
7. M. Kohl, M. Cope, M. Essenpreis, D. Bocker, "Influence of glucose concentration on light scattering in tissue-simulating phantoms", *Opt. Lett.* **19**, pp. 2170-2172, 1994.
8. C.-L. Tsai, J. M. Fouke, "Non-invasive detection of water and blood content in soft tissue from the optical reflectance spectrum", *Proc. SPIE* **1888**, pp. 479-486, 1993.
9. I. L. Maksimova, V. V. Tuchin, L. P. Shubochkin, "Polarization features of eye's cornea", *Optics and Spectroscopy (USSR)* **60** (4), pp. 801-807, 1986.

SESSION 6

Poster Session

Automatic system for corneal ulcer diagnostic - Part II

Liliane Ventura, Caio Chiaradia, Sidney J. F. Sousa

⁺ Laboratório de Física Oftálmica - FMRP-USP Ribeirão Preto - SP BRASIL

Keywords: Corneal Ulcer, Corneal Ulceration, Area of Ulceration

ABSTRACT

Corneal Ulcer is a deepithelization of the cornea and it is a very common disease in agricultural countries. The clinician most used parameter in order to identify a favorable ulcer evolution is the regress of the affected area. However, this kind of evaluation is subjective, once just the horizontal and vertical axes are measured based on a graduated scale and the affected area is estimated. Also, the registration of the disease is made by photographs. In order to overcome the subjectiveness and to register the images in a more accessible way (hard disks, floppy disks, etc), we have developed an automatic system in order to evaluate the affected area (the ulcer). An optical system is implemented in a Slit Lamp (SL) and connected to a CCD detector. The image is displayed in a PC monitor by a commercial frame grabber and a dedicated software for determining the area of the ulcer (precision of 20mm) has been developed.

1. INTRODUCTION

The anterior transparent part of the human eye is known as the cornea¹ (figure 1a). It consists of three main layers: the epithelium, the stroma and the endothelium. The **epithelium** is the external cover of the cornea. It works as a mechanical protection of the cornea just like the skin which protects all the other parts of the human body. The **stroma** is the cornea itself. It corresponds to 95% of its thickness. It consists of a fiber tissue disposed in regular layers with low hydration and no blood vessels. These features are responsible for its high transparency. Finally, the **endothelium** covers the internal side of the cornea with a unique polygonal cells layer.

Several conditions may hurt the corneal epithelium inducing the erosion of it. If in such a situation a germ is installed in the naked stroma, an infectious ulcer is observed. When a deepithelization occurs, there is an ulcer (figure 1b). Corneal ulcer is an illness quite severe because of its high blindness inducing power. Even when it is treated, its tendency is to have a region of opacification which is significant enough to provide a poor visual acuity. Actually, in agricultural countries with low economy rates, this kind of enfermity is responsible for 1-5% of the uniocular blindness.

Evaluating the therapeutic answer of the ulcers, several aspects should be taken into account such as the degree of inflammatory cells infiltration in the stroma, the lesion hydration degree and the wideness and deepness of the ulceration. All of these variables are extremely difficult to be measured, except its extension. As the cure factor of this enfermity is indicated by the vanishing of the lesion, measuring the area of this lesion is a definitive good procedure to know about the evolution of the disease. So, an apparatus for measuring precisely and automatically the area of the ulceration has been developed.

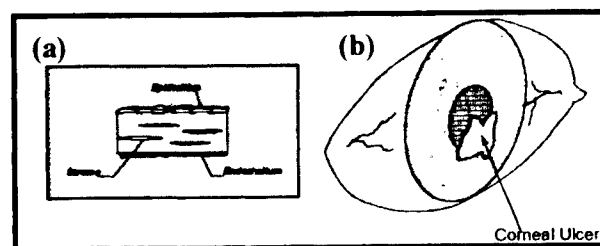


Figure 1: (a) Corneal Layers Scheme; (b) Corneal Ulcer

⁺ L.V. (correspondence): Laboratório de Física Oftálmica da FMRP-USP

Faculdade de Medicina de Ribeirão Preto - USP Departamento de Oftalmologia (12^o andar do HC)
Av. Bandeirantes 3900 14049-900 Ribeirão Preto - S. BRASIL e-mails: liliane@fmrp.usp.br

liliane@ifqsc.sc.usp.br

2. MATERIALS AND METHODS

The patient is submitted to the regular clinical procedure in order to allow the visualization of the affected area (ulcer), i.e., drops of fluorescein are instilled in the eye by a clinician and the patient is placed at the SL. The SL provides blue light which strikes the eye and the ulcer fluoresces in the green wavelength. The experimental method used consists in capturing the image of the ulcer from the SL. An optical system has been developed (2 lenses, 2 optical filters, an iris and a prism) and it is coupled to the SL (see figure 2). The image is captured by a CCD device and it is displayed in a PC monitor by a real time commercial video blaster. The image has a 50X magnification and is captured with good resolution. It is treated by a dedicated software which determines the corneal ulcer area contour.

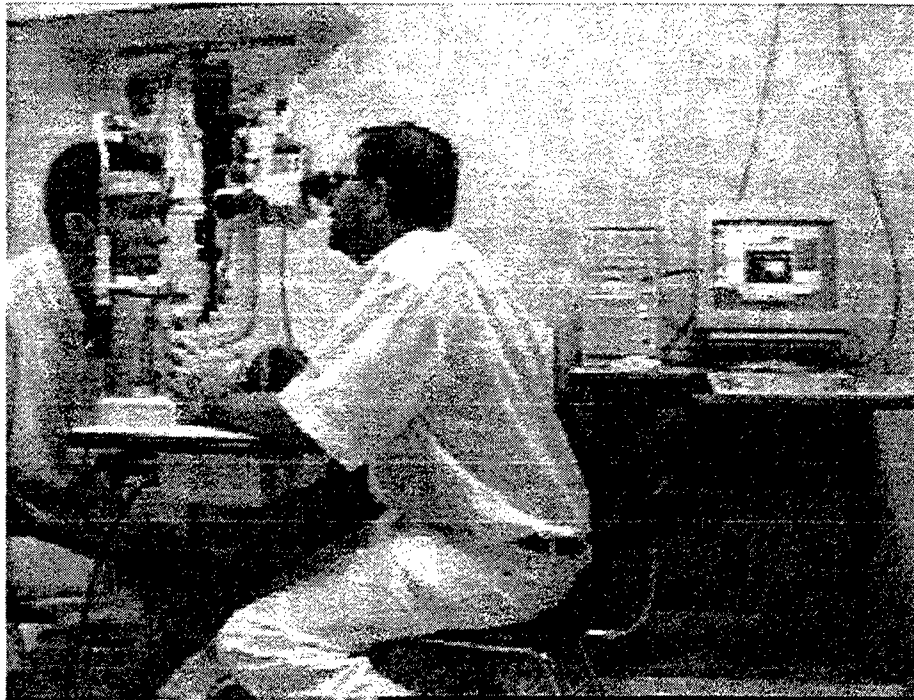


Figure 2: Patient being submitted to the developed system procedure

3. RESULTS

The image processing is done in a determined sequence of events. Several images processing can be used, but the most efficient and simplest one is described next. First the pixels belonging to the ulcer are selected. There are two sub-routines: one selects the pixels belonging to the ulcer regarding the green color and the other selects the pixels regarding their intensity leading to the affected area contour. The second step consists of using a software filter in order to avoid noises and to count the number of pixels included in the area of interest. The number of pixels are converted to mm^2 and the area is determined with high precision (see figure 3,4,5). One of the main difficulties of the process was to avoid the intense reflection of the light from the cornea surface. The solution for this problem was to use a scattering filter in the illumination path, an optical filter which selects mostly the 550nm wavelength in the reflected light path and to use a wide angle for the illumination.

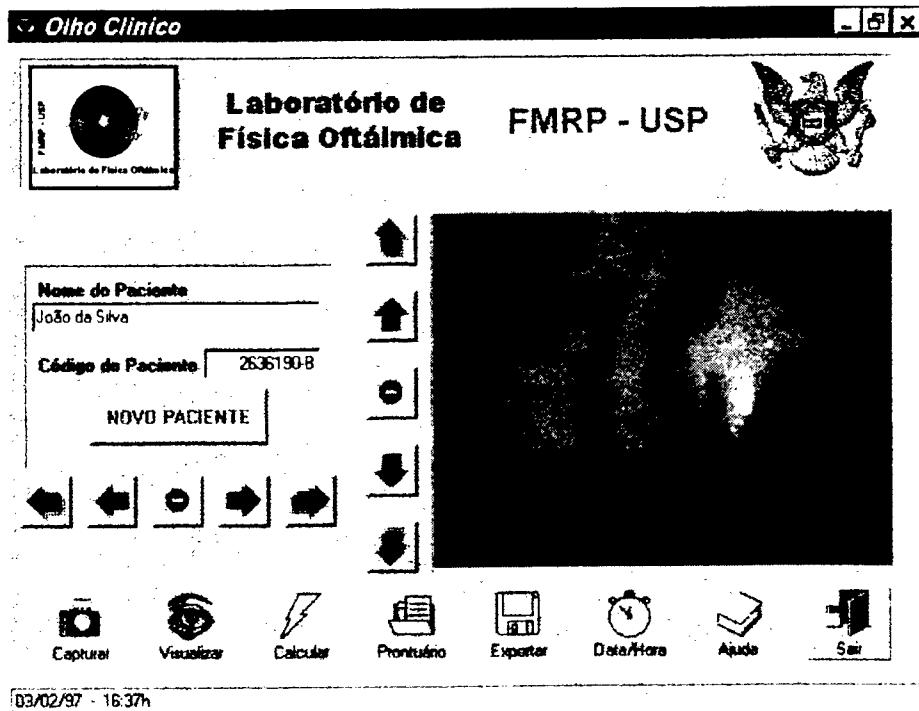


Figure 3: The software itself.

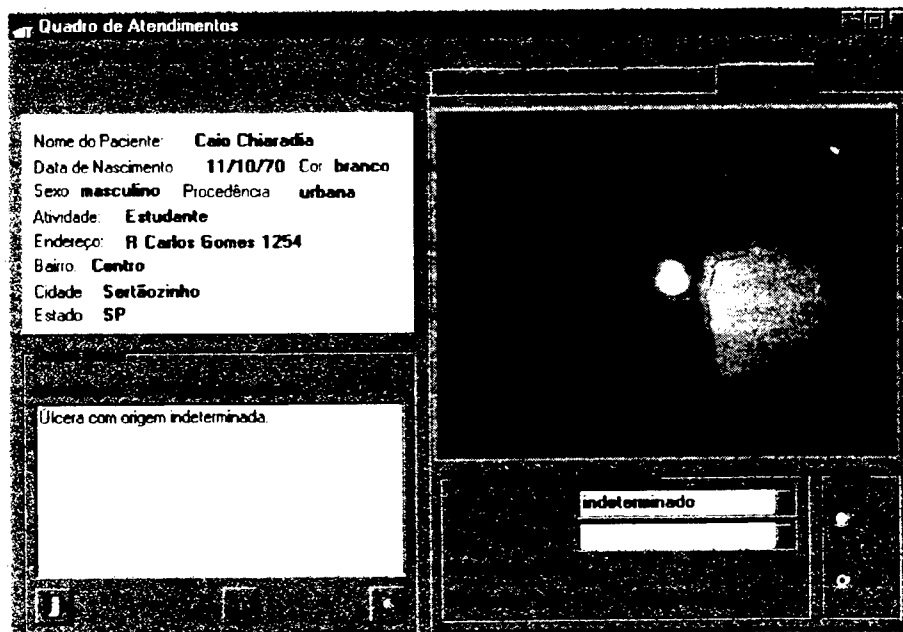


Figure 4: Ulcer area contour.

Cadastro de Médicos

Cadastro

Dados do Médico:

Código: 1 Nome: **Clovis Chiaradia** CPF: **22.222.222-22**

Sexo: ☒ masc. ☐ fem. Data de Nascimento: **15/02/2004**

Endereço: **R. Carlos Gomes 1254**

Bairro: **Centro**

Cidade: **Sortãozinho** Estado: **SP**

CEP: **13.130-000** Telefone: **(11) 3333-3333**

Localiza Médico

Nome a procurar: **Clovis Chiaradia**

Atendimentos Agendados

Consultas

Paciente

Nome a procurar: **Clovis Chiaradia**

Clovis Chiaradia

Agenda

1997 setembro

Dom	Seg	Ter	Qua	Qui	Sex	Sab
	1	2	3	4	5	6
7	8	9	10	11	12	13
14	15	16	17	18	19	20
21	22	23	24	25	26	27
28	29	30				

Clovis Chiaradia

15:21:00-Clovis Chiaradia

Novo

Hora: **15:22**

Cadastro de Pacientes

Cadastro

Dados do Paciente:

Código: 1 Nome: **Caio Chiaradia** Data de Nascimento: **11/10/70** Cor: **branco**

Sexo: ☒ masculino ☐ feminino

Procedência: ☒ Urbana ☐ Rural

Atividade: **Estudante**

Endereço: **R. Carlos Gomes 1254**

Bairro: **Centro**

Cidade: **Sortãozinho** Estado: **SP**

CEP: **13.130-000** Telefone: **(11) 3333-3333**

Localiza Paciente

Nome a procurar: **Caio Chiaradia**

Caio Chiaradia

Consulta Não Agendada

Opções

Localiza Paciente

Nome a procurar: **Caio Chiaradia**

Caio Chiaradia

Localiza Médico

Nome a procurar: **Clovis Chiaradia**

Clovis Chiaradia

Quadro de Atendimentos

Opções

Novo | 8 | 9 | 10 | 11 | 12 |

Nome do Paciente: **Caio Chiaradia**

Data de Nascimento: **11/10/70** Cor: **branco**

Sexo: **masc.** Procedência: **urbana**

Atividade: **Estudante**

Endereço: **R Carlos Gomes 1254**

Bairro: **Centro**

Cidade: **Sortãozinho**

Estado: **SP**

Dados Gerais

Atendido por: **D. Clovis Chiaradia**

Características da Úlcera

Tipo de Úlcera: **Restauração**

Ag. Etiológico:

Tamanho:

Dieta

☒ Esq.

☐ Dir.

Figure 5: Some other features of the software.

4. CONCLUSIONS

The system has been presenting satisfactory results regarding the good quality image and the precision of the ulcer area measurement ($20\mu\text{m}^2$). The processing time is fast enough for the hospital routine (20s for a Pentium 166MHz, 32 MB RAM). A section for the patient's data storage and linked image is also available. The system is being used in the public hospital (under tests) and it has been very helpful for small area changes, which were not able to be detected before and treated on time and it also saves examining time, which provides a relative comfort to the patient (these kind of patients present photophobia). Also some other features of the software have been very helpful such as a mouse click activated "ruler" for measuring any desired length in any desired captured frame (as the system allows to capture any image that is provided by the Slit Lamp, measurements like the corneal thickness are also possible to be made).

5. ACKNOWLEDGMENTS

The authors would like to thank FAPESP (proc. n^o: 95/9702-8) for all the financial support for this research, CNPq, CAPES and Hospital das Clínicas de Ribeirão Preto, particularly the sector of Doenças Oculares Externas.

6. REFERENCES

1. HOGAN, M.J.; ALVARADO, J.A.; WEDDELL, E.: **Histology of the Human Eye** Philadelphia, WB Saunders, 1971.

Low-cost endothelium cell counter for slit lamp

Liliane Ventura⁺⁺, Sidney J. F. Sousa⁺⁺, Paulo E. M. Ribeiro Júnior⁺ and Cesar A. C. Caetano⁺⁺

⁺ Laboratório de Física Oftálmica - Faculdade de Medicina de Ribeirão Preto - USP

^{*} Departamento de Física e Matemática - FFCLRP-USP

^{**}Banco de Olhos HCRP

Keywords: Corneal Endothelium, Endothelial Cells, Specular Microscopy, Endothelium Cells Counter

ABSTRACT

One of the optical ways to evaluate the donated cornea in order to provide a diagnostic regarding its indication for transplant is to count the number of the living endothelial cells (over 2000cells/mm²), which are responsible for maintaining the corneal transparency. Specular Microscopes are equipments which are exclusively dedicated for this kind of evaluation. However they are of high cost and most of the Eye Banks are not provided by them. Hence, the usual evaluation is done in a Slit Lamp (SL) - 40X magnification - and just the aspect of the cells are subjectively observed. In order to overcome the limitations of subjective assessment and high cost, we have developed a system attached to the SL (optical system with 250X magnification image captured by a CCD detector which displays the image of the cells on a PC monitor and a dedicated software) which is able to count the endothelial cells providing a lower cost objective diagnostic of the donated cornea.

INTRODUCTION

For a better understanding of the importance of counting the endothelium cells, a brief description of the human cornea should be made.

1.1 The Human Cornea¹

The anterior transparent part of the human eye is known as the cornea¹ (figure 1). It consists of three main layers: the epithelium, the stroma and the endothelium. The **epithelium** is the external cover of the cornea. It works as a mechanical protection of the cornea just like the skin which protects all the other parts of the human body. The **stroma** is the cornea itself. It corresponds to 95% of its thickness. It consists of a fiber tissue disposed in regular layers with low hydration and no blood vessels. These features are responsible for its high transparency. Finally, the **endothelium** covers the internal side of the cornea with a unique polygonal cells layer.

The endothelium is particularly important for being the layer responsible for the active preservation of the corneal stroma dehydration and transparency. The biological phenomenon is: the aqueous humor, carrying essential metabolites, constantly penetrates the cornea pushed by the intraocular pressure. The return of this fluid against a gradient of pressure is done by the active pumping of salts (and water) back to the interior of the eye, mediated by the endothelial cells. The functional failure of these cells leads to corneal edema and haziness.

Thus, the endothelium analysis of the donated corneas used for transplantation is of fundamental importance. It is the decisive factor in order to find if the cornea is able to maintain transparency at the host bed. A poor endothelium excludes this possibility.

^{*} L. V. (correspondence): Laboratório de Física Oftálmica da FMRP-USP
Faculdade de Medicina de Ribeirão Preto - USP Departamento de Oftalmologia (12^º andar do HC)
Av. Bandeirantes 3900 14049-900 Ribeirão Preto - SP BRASIL
e-mails: liliane@fmrp.usp.br liliane@ifqsc.sc.usp.br

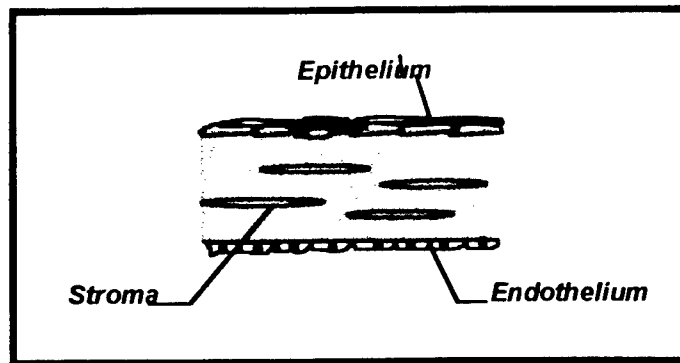


Figure 1: The schematic cornea layers

An appropriate cornea for transplantation should have at least 2000 cells/mm². There are several commercial equipments that are able to count the number of endothelial cells in the "in situs" (corneas which haven't been yet removed from the eyeball) and just a few of them that are adequate to count the number of cells of "in vitrus" (corneas removed and preserved in an appropriate liquid environment). However they are of high cost and specially to the Eye Banks of developing nations. Hence, the usual evaluation is done in a Slit Lamp (SL) - 40X magnification - and just the aspect of the cells are subjectively observed (figure 2 shows the endothelium cells with a 40X magnification), since it is impossible to quantify the cells. In order to overcome the limitations of subjective assessment and high cost, we have developed a system attached to the SL described as follows.

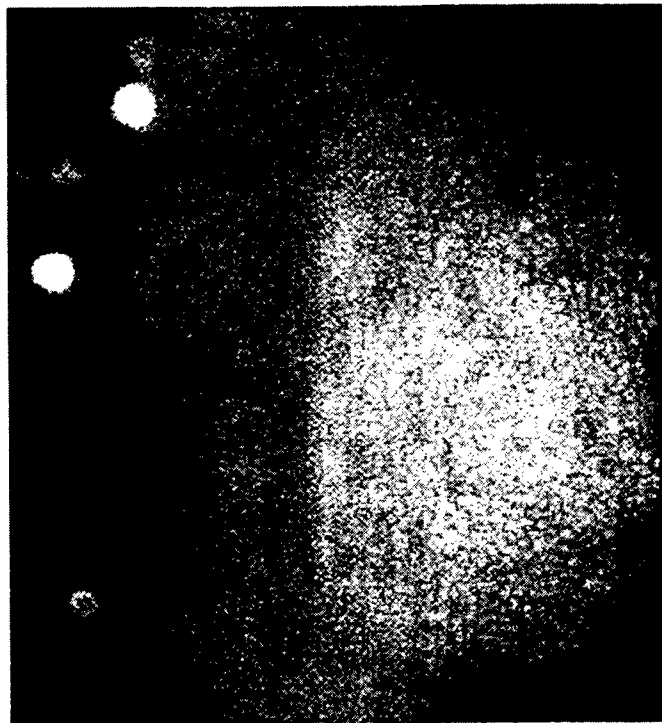


Figure 2: Endothelium cells being observed in a SL with a 40X magnification.

MATERIALS AND METHODS

We have developed a magnifying optical system which is attached to the SL exactly at the parallel rays optical path of the equipment. A set of prisms (commercial beam splitter for SL) deviates the rays and the developed optical system (lenses, filters, pin-hole, etc) is implemented, providing a 250x and a 400X magnification. However, the 250X magnification is enough for observing the cells clearly and counting them. The corneal endothelium is observed in its preservative medium, and an extra illumination system illuminates the cornea. The image is displayed in a PC monitor via a CCD detector and a commercial frame grabber. The system is set up in a way that the practitioner is able to focus the corneal cells either by the monitor or by the ocular lenses of the SL.

Figure 3 shows the system. A preserved cornea is being checked previously the transplant.

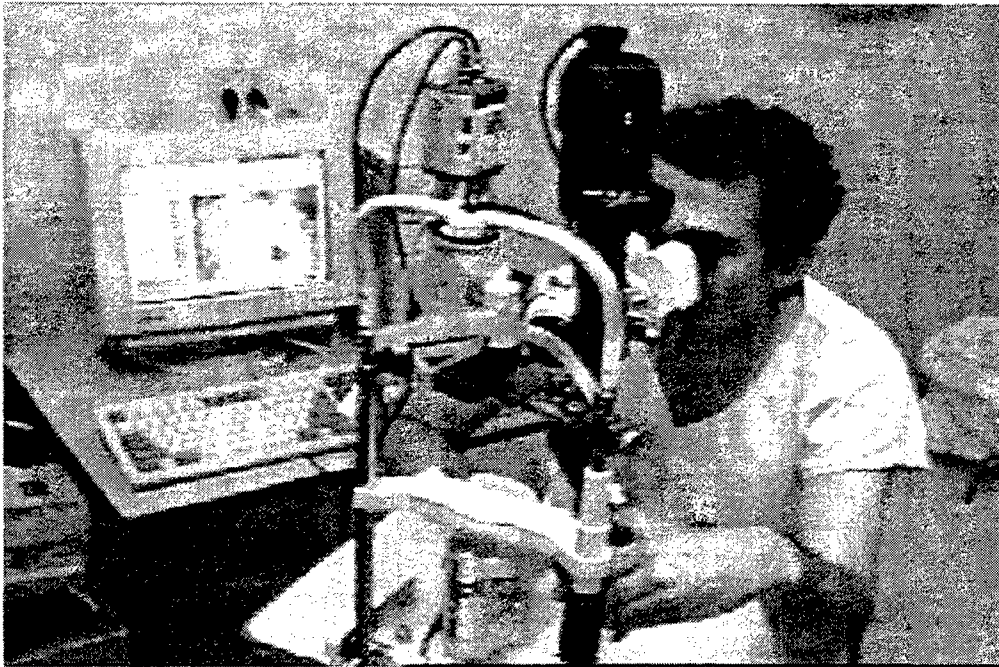


Figure 3: The system. A preserved cornea is being checked previously the transplant.

RESULTS

A dedicated software has been developed and it has the following features (Figure 4): 1. It captures and displays the image in a screen which has all the previous data of the cornea to be analyzed; 2. The practitioner selects with the mouse a region of the image and clicks on the corresponding cells (around 20 cells), then the software calculates the number of endothelial cells per mm^2 in the cornea; 3. The cornea can be analyzed in several parts and an average value is presented 4. Alternatively, the practitioner will be able to opt by an automated evaluation. The image will then be automatically recognized and the number of cell per mm^2 is displayed (this stage is still under development). Figure 4 shows two frames of the software.

The system and the interactive counting method are being used in an Eye Bank of a public hospital and are still under tests. A change in the illumination system is being made and it should be implemented in the next months providing better results in order to implement the automated cells counting software.

Olho Clínico - Endotélio

File Edit View Options Help

09/09/97 10:53:27

Informações Gerais

Doador No. 1235 Idade Cor Sexo

Cornéa do Olho: ☒ Direito ☒ Esquerdo

Falecido em: Data: Hora: Hs.

Enucleado em: Data: Hora: Hs. Técnico Responsável:

Preservado em: Data: Hora: Hs. Técnico Responsável:

Meio de Conserv. Transplante:

Causa do Falecimento: Primária: Secundária:

Histórico Médico

Realizada Cultura de Sangue: Evid. de Infecção Localizada: Evid. de Infecção Generalizada: Sorologia: Anti-HIV:

Terapia Intensiva Prolongada: Paciente Esteve em Coma: Duração do Coma: Hs. HBsAg:

Olho Clínico - Endotélio - Doador No.:1235

Arquivo

09/09/97 10:52:50

Análise Biomicroscópica da Córnea - No.: 1235-1

Aspecto Geral:

Transparên. Geral: Ílceras: Cicatrizes: Arco Senil: Edema Eptelial:

Endotélio:

Pregas Descement: Enrugamento: Pleomorfismo: Gutata: Pseudogutata: Erosões:

Observações:

Células Endoteliais

Densidade Celular Média em células por milímetro quadrado: 2650

Figure 4: The software and some of its features.

CONCLUSIONS

The developed system is easy to operate and it has been used by every practitioner of the Eye Bank. Since every Eye Bank has a SL (it is one of the required equipments for Eye Banks) and usually a PC (Pentium 166MHz, 32MB RAM for automated detection) is available, the cost of the system is well reduced. The good results obtained have been providing a standard diagnostic for donated corneas. Since the implementation of the system, some of the corneas which were usually rejected by excessive care (or practitioner inexperience) in the Eye Bank are now being used and as a result, much more corneas have been available for patients. Also, in the next years, data will be available regarding the success of transplants as a function of a better endothelium evaluation.

ACKNOWLEDGEMENTS

The authors would like to thank FAPESP (proc. n^o: 95/9702-8) for all the financial support for this research, Banco de Olhos do Hospital das Clínicas de Ribeirão Preto, which is the Eye Bank that has always been contributing for the success of our researches, particularly Stella Barreto, Alexandre da Silva Roque and Cláudio J. Cardoso de Sá, CNPq and CAPES.

REFERENCES

1. HOGAN, M.J.; ALVARADO, J.A.; WEDDELL, E.: **Histology of the Human Eye** Philadelphia, WB Saunders, 1971.

WEAK LASER RADIATION MECHANISM FOR CILIOCHOROIDAL DETACHMENT

Tatjana N. Semyonova, Irina S. Maximova, Sergey N. Tatarintsev

The Saratov Medical University, Russia

ABSTRACT

The efficiency of weak laser radiation was studied for patients having a ciliochoroidal detachment (CD). A He-Ne and diode lasers were used whose wavelength, radiating power at the lightguide face output, spot diameter, and exposition time were 0.63 μm , 0.05-0.1 mW, 200 μm , and 3 min., respectively. To study the mechanism of weak laser radiation effect with the CD, clinical and biochemical investigation techniques were exploited for seven patients before and after they had been irradiated. Hydro- and hemodynamical indices were normalized with a parallel decrease of malondialdehyde (MDA) concentration and a higher superoxide dismutase (SOD) activity in the tear fluid of the patients when the CD disappeared as a result of complex treatment employing the weak laser radiation. This proves the process of lipid peroxidation (LP) to be suppressed and the antioxidation system (AS) to become more active under the action of the weak laser radiation.

Key words: transscleral weak laser radiation, lipid, peroxidation, ciliochoroidal detachment

The CD is a complication appearing as a consequence of surgical interventions and it manifests itself clinically as a sluggishly running inflammation and hypotension of the eye which substantially deteriorates visual function. The important role of disruption of metabolism processes, taking place in the eye tissues, in the development of the sight organ's pathological state, particularly, the CD, was shown in our previous papers which describe experiments with the rabbit eyes [2,4,5]. These alterations adversely affect the cellular structures of the eye. The maintaining of cellular homeostasis as a whole is to a significant extent defined by relation between the LP processes, and the activity of the AS of a cellular membrane and its surroundings [1]. The search and substantiation for means to change cellular membrane structures in the organism is due to revealing a disbalance between the LP processes and the AS of protection of biomembranes. Hitherto, we have studied the LP processes in the rabbit eye tissues with the CD, and with using both medical therapy and the weak laser radiation [4].

The intent of this paper is to examine the efficiency and the action mechanisms of the weak laser radiation for the CD patients. Thirteen patients were kept under observation. Biochemical and clinical indices for three healthy persons were a reference. Six patients were treated traditionally, with medicines including mydriatics, corticosteroides and nonsteroidic antiinflammatory preparations. Seven patients received, along with the medicines, the weak laser radiation; four of them were radiated by He-Ne laser and for three others a diode laser was used. The parameters of the laser action involved the wavelength of 0.63 μm , the radiating power of 0.05 mW to 0.1 mW at the lightguide face output, the spot diameter of 200 μm , and the exposition time of 3 min (one minute per 3 points in the CD region). The laser radiation was transsclerally focused at a distance of 3 or 4 mm from the limb.

Visual functions, intraocular pressure (IOP) and ciliar body blood circulation with the rheographical coefficient were found before and after the medicamental and laser therapies. Ultrasound investigation was employed to determine the CD height and the depth of the anterior camera. The echo-graphical scanning of the anterior camera depth was controlled by means of a unit for measuring the geometrical eye parameters which was designed by the authors [3]. The dynamics of morphometric hydro- and hemodynamical indices is depicted in Table 1 as a functions of the CD therapy procedures. These indices are shown to be normalized at the end of three days for combined treatment using weak laser radiation. As for the medical therapy, only a slight positive effect was revealed.

Coincidentally with clinical results, obtained before and after the medical and laser treatment, we studied the biochemical indices of the patients' tear fluid. Malondialdehyde (MDA) was taken as the LP characteristic [7] and

superoxide dismutase (SOD) was found as that of the AS [6]. The MDA concentration was increased and the SOD activity became weaker as the CD symptoms appeared and grew in a period preceding the therapy. Concurrently, a sudden lowering of the ciliar body blood circulation indices was clinically observed. Furthermore, the depth of the anterior camera was decreased and the IOP fell with the CD height increase that was found clinically and by means of ultrasound scanning.

Table 2 illustrates the influence of the medical and laser effects on the MDA content in the tear fluid for the CD patients at the end of two days. Table 3 shows the SOD activity indices for the tear fluid at the end of three days after the medical and the laser therapy courses were ordered. The biochemical tear fluid investigation for the CD patients treated traditionally, with medicines, disclosed a minor decrease of the MDA concentration and a moderate enhancement of the SOD activity. For the additional use of laser stimulation with the parameters cited to improve the therapeutic effect, the MDA concentration was observed to abruptly decrease and the SOD activity was significantly raised.

The application of weak He-Ne and diode laser radiation to treat the CD patients allowed for, as combined with traditional therapy methods, this postoperative complication to be eliminated in three days. The normalization of hydro- and hemodynamical indices was accompanied by decreasing MDA concentration and by increasing SOD activity. Neither clinical nor biochemical differences were observed in the action of He-Ne or diode laser radiation.

Table 1.
Dynamics of morphometric hydro- and hemodynamical indices as a function of the ciliochorioidal detachment procedures.

Indices	ciliochorioidal detachment						
	group	medical treatment		He -Ne laser stimulation		diode laser stimulation	
		1 st day	3 st day	1 st day	3 rd day	1 st day	3 rd day
Anterior camera depth, mm	2.9 ± 0.07	1.1 ± 0.1	1.5 ± 0.1	1.9 ± 0.06	2.8 ± 0.06	1.8 ± 0.05	2.8 ± 0.08
		$P < 0.001$	$P < 0.001$	$P < 0.001$	$P < 0.05$	$P < 0.001$	$P > 0.05$
				$P1 > 0.05$	$P1 < 0.001$	$P1 > 0.05$	$P < 0.001$
Intraocular pressure, mm of mercury column	20.3 ± 0.4	16.6 ± 0.3	16.7 ± 0.3	17.3 ± 0.3	20.3 ± 0.4	16.8 ± 0.4	20.5 ± 0.2
		$P < 0.001$	$P < 0.001$	$P < 0.001$	$P > 0.5$	$P < 0.001$	$P > 0.5$
				$P1 > 0.1$	$P1 > 0.001$	$P1 > 0.1$	$P1 < 0.001$
Rheographical coefficient, %	0.98 ± 0.06	0.77 ± 0.03	0.82 ± 0.02	0.82 ± 0.02	0.98 ± 0.06	0.79 ± 0.04	0.97 ± 0.08
		$P < 0.001$	$P < 0.01$	$P < 0.01$	$P > 0.5$	$P < 0.001$	$P > 0.5$
				$P1 > 0.1$	$P1 > 0.05$	$P1 > 0.1$	$P1 > 0.05$
Ciliochorioidal detachment depth, mm	0	2.8 ± 0.1	2.3 ± 0.1	2.2 ± 0.1	0.3 ± 0.2	2.4 ± 0.2	0.2 ± 0.3
		$P < 0.001$	$P < 0.001$	$P < 0.001$	$P < 0.05$	$P < 0.001$	$P > 0.05$
				$P1 > 0.05$	$P1 > 0.001$	$P1 > 0.05$	$P < 0.001$

Notes:

P – authenticity of distinction with the reference group indices.

P1 – authenticity of distinction between indices of medical treatment control group and its combination with laser stimulation.

Table 2.

The influence of medical treatment and laser stimulation on the malondialdehyde content in the tear fluid for the ciliocoriadal detachment patients on the third day of therapy (%)

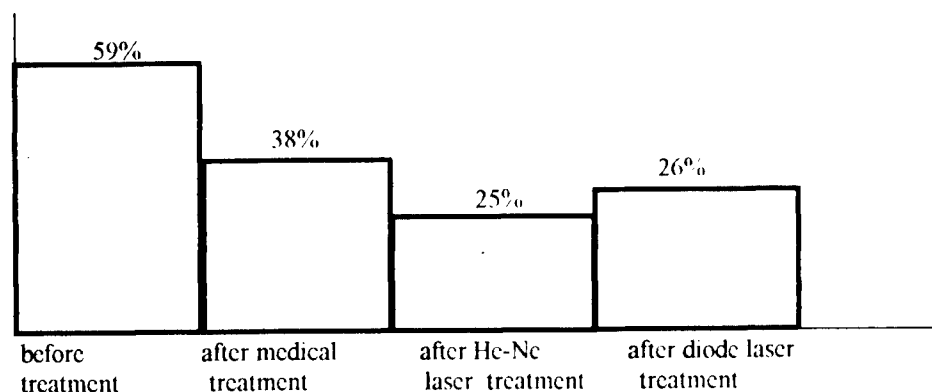
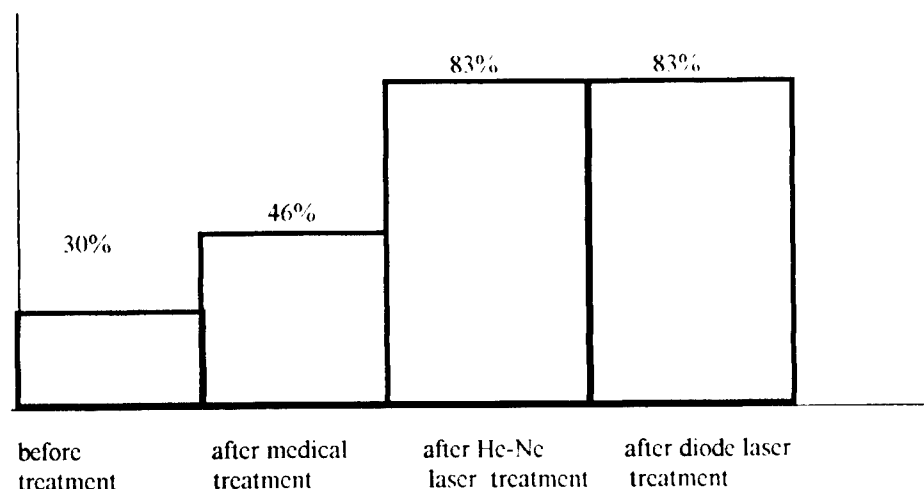


Table 3.

The influence of medical treatment and laser stimulation on the superoxide dismutase activity in the tear fluid for the ciliochoroidal detachment patients on the third day of the therapy (%)



REFERENCES

1. J.I. Abramova, G.I. Oxenhendler, "A Man and Antioxidants", L., 1985
2. N.N. Alexandrowa, V.V. Bakutkin, T.N. Semyonowa, "Treatment of the shallow anterior camera syndrome using a weak laser radiation", *Actual Tasks of Laser Medicine*, P.43, M., 1991.
3. V.V. Bakutkin, S.V. Romanov, T.N. Semyonowa, "Measurement unit for the eye's geometrical parameters", *Optical Mechanism in Ophthalmology*, P.35-36, L., 1989.
4. T.N. Semyonowa, I.S. Maximova, A.V. Borisov, V.V. Bakutkin, "Mechanism of working of low - intensive laser radiation in case of ciliochoroidal detachment", *International Biomedical Optics Symposium, the Conference Ophthalmologic Technologies VII*, Can Jose, USA, 1997.

5. Y.A. Turikov, R.G. Sauyrbekova, "Weak laser action with the syndrome of shallow anterior camera", *News of Ophatalmology. Vol.1*, 1988.
 6. R.Fried, "Enzymatic and new enzymatic assay of superaxide - dismutase", *Biochem J.*, V.57, N.6, P.660-675, 1975.
 7. M. Ishihara, "Studies on lipooeroxide of normal pregnant women and of patients with tomemia of prednancy", *Clin. Chem. Asta.*, V.84, N 1, P. 1-9, 1978.
-

Further author information -

T.N.S (correspondence): mailing address: 12 Volskaj str., Saratov, 410028, Russia; telephone: 845-2-250663.

Molecular mechanism of light damage to the eye

Victoria A. Lapina^a, Georgiy V. Lyakhnovich^b, Tamara A. Gapeeva^b

^a Institute of Physics of the National Academy of Sciences, Minsk, Belarus, 220072; ^b Institute of Photobiology of the National Academy of Sciences, Minsk, Belarus, 220733

ABSTRACT

We have studied the influence of laser radiation on eye tissues. It was shown that argon laser radiation induced damages in retina and pigment epithelium. Disorganized segments of photoreceptors, dispersed vesicles were observed in retina after irradiation. The laser irradiation of pigment epithelium leads to fragmentation and dispersion of the membrane material. Changes in the protein composition of membrane proteins of retina were not observed by the method of gel-electrophoresis after laser irradiation. Electrophoresis profiles of pigment epithelium samples shown inessential changes in protein composition. The oxidation of SH-groups does not take place in these both cases either.

Keywords: proteins, gel-electrophoresis, SH-groups, retina, pigment epithelium, cryofractography method, membrane.

1. INTRODUCTION

Sources of intense light find wide application in ophthalmology for treatment of different eye pathologies^{1,2}. To perform an effective treatment with laser radiation it is necessary to know the mechanisms of the interaction of intense coherent radiation with biological tissues, in part, with eye tissues, since even a small excess of the permissible dose of irradiation can cause a damage of tissues³.

It is well known that eye damages produced by the action of excessive radiation are due to heat, thermoacoustic and mechanical transients as well as photochemical processes⁴. The photochemical damages are most wide-spread^{5,6}.

A more complete study of the mechanisms of a damage of the retina, produced by the action of laser radiation at the cellular level and at the level of the cellular membranes and their components is currently urgent.

The object of the present work is to investigate the influence of the argon laser radiation on the ultrastructure of the cellular elements and on the physico-chemical parameters of proteins of the retina and retinal pigment epithelium.

2. METHODS

Experiments were conducted with preparations of cattle eyes. The eyes were cut in half so that the retina retains their natural position, i.e., it was pressed by the glassen body to the bottom of the eye glass.

The eye preparation were irradiated by the radiation of an argon laser ($\lambda = 488 \text{ nm}$ and 515 nm) with a power of 1.2 W during 7 min at room temperature. The area of irradiation was 2 cm^2 . The irradiated parts of the retina and RPE were taken out and used for preparation of homogenates. The water-soluble and detergent-soluble fractions of the retina and RPE were prepared.

To prepare the homogenates of the eye tissues we took five control preparations and five irradiated eye preparations. The retina and RPE were taken out of the eye glass after moment when the eye was irradiated and were homogenated with addition of the 0,1M natrium-phosphate buffer, pH 8,0 or 0,06 M tris-HCl buffer, pH 6,8. The phosphate buffer was used when determining the content of sulfhydryl groups, and the tris-HCl buffer was used for the gel-electrophoresis analysis. The obtained homogenates were centrifuged at 20000 g during 20 min. The supernatant was a water-soluble fraction of the retina membranes and RPE. The precipitate was solubilized by 2% CTAB in 0,1M natrium-phosphate buffer, pH 8,0 or in 0,06M tris-HCl buffer, pH 6,8. Precipitation of the nonsolubilized components was performed by centrifuging at 20000g during 20 min. The supernatant was a detergent-soluble fraction of the membrane homogenates. The precipitate was removed.

The extraction of the RPE cells was performed by the method described in paper ⁷. The solubilization of the RPE cells by detergents was performed by the way described above. The number of sulfhydryl groups was determined with the help of the Elman reagent (5,5-dithio-bis 2 nitrobenzoat) (DTNB) in the 0,1% solution of bromide cetyl trimethyl-ammonium in the tris-HCl buffer, pH 8. The kinetics of modification of the SH-groups was recorded at $\lambda = 440 \text{ nm}$ ⁸.

The electrophoresis was performed by the method in the polyacryl-amide gel (PPAG) with natrium dodecylsulfate⁹. The proteins were painted with the bright light - blue Kumasi dye of the "Serva" firm. The densitometry of the gels was performed in the two-beam regime of wavelengths at 590-660 nm on spectrophotometer attachment for scanning. (spectrophotometer "Zhimadzu"-UV-300).

The protein concentration in the samples was determined by the Louri method ¹⁰.

Electronic microscopy was performed as a cryofractography¹¹. The samples were frozen in propane at liquid nitrogen temperature. Spallings was performed on an IEE-4C setup. The spalled surfaces were gradated by deposition of platinum and carbohydrate, following which, the replicas were cleared from the organic remainders and investigated in an EMB - 100 L electron microscope.

3. RESULTS

The irradiation of the eye bottom tissues by the argon laser radiation leads to a noticeable whitening of the irradiated segments, wave-like separation of the retina from RPE and its warping to the side of the glass body. An analysis of the microscopic changes in the RPE and retina tissues was performed by the method of electronic-microscopic cryofractography. From Fig.1 it is seen that the irradiation by the argon laser radiation produces significant changes in both the retina and the RPE. Thus, on the spalling surface (Fig.1 a.) of the retina control preparation we can see the regions of ordered bands, every of which is a membrane. The membranes are arranged in pairs, which reflects the native disposition of photoreceptor membranes. It is seen from Fig.1 b, that laser radiation is responsible for the dissociation of discs, disturbance of membranes, appearance of dispersed vesicles and fragments of photoreceptors.

It is seen from the spallings of the RPE cellular membranes, there are marked changes in the test sample as compared to the control one (Fig. 2 a, b). Large vesicles differing only slightly in their sizes are observed in the control samples. The surface of the vesicles is strewn with intramembrane particles. It is seen from the irradiated RPE spallings that laser radiation causes the fragmentation and comminution of the membrane material. As a results of the laser radiation action a lot of small vesicles, fragments and fragments of membranes appeared.

To estimate the changes in the structural state of the retina and RPE proteins, we have used the method of gelelectrophoresis in the polyacryl-amide gel. To obtain more reliable information, we performed the electrophoresis separation of the proteins of water-soluble and detergent-soluble fractions of the retina and RPE homogenates.

Figure 3 shows the densitograms of the electrophoresis separation of the retina proteins. It is seen from them that the argon laser radiation has no influence on the polypeptide composition of the retina proteins, since the polypeptide spectrum of the preparations after irradiation has no visible changes. Thus laser radiation does not bring about the

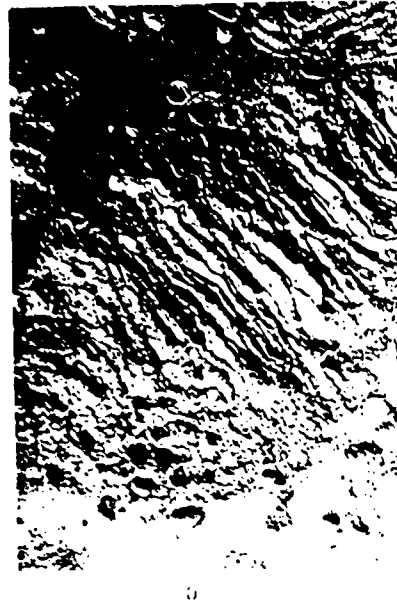


Fig.1. Microphotography of the spallings of photoreceptor membranes: a -control, b - after irradiation of argon laser

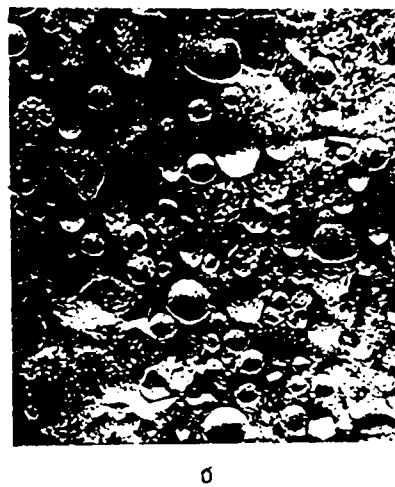
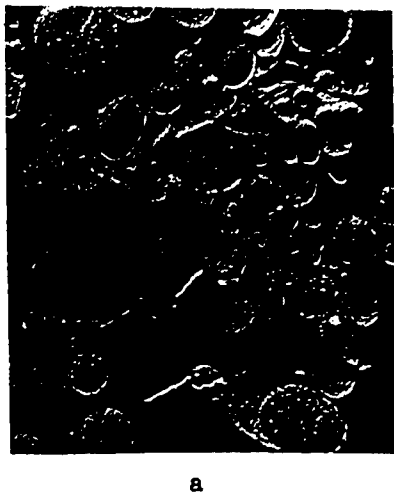


Fig .2 . Microphotography of spallings of pigment epithelium cell membranes : a - control, b - after irradiation of argon laser.

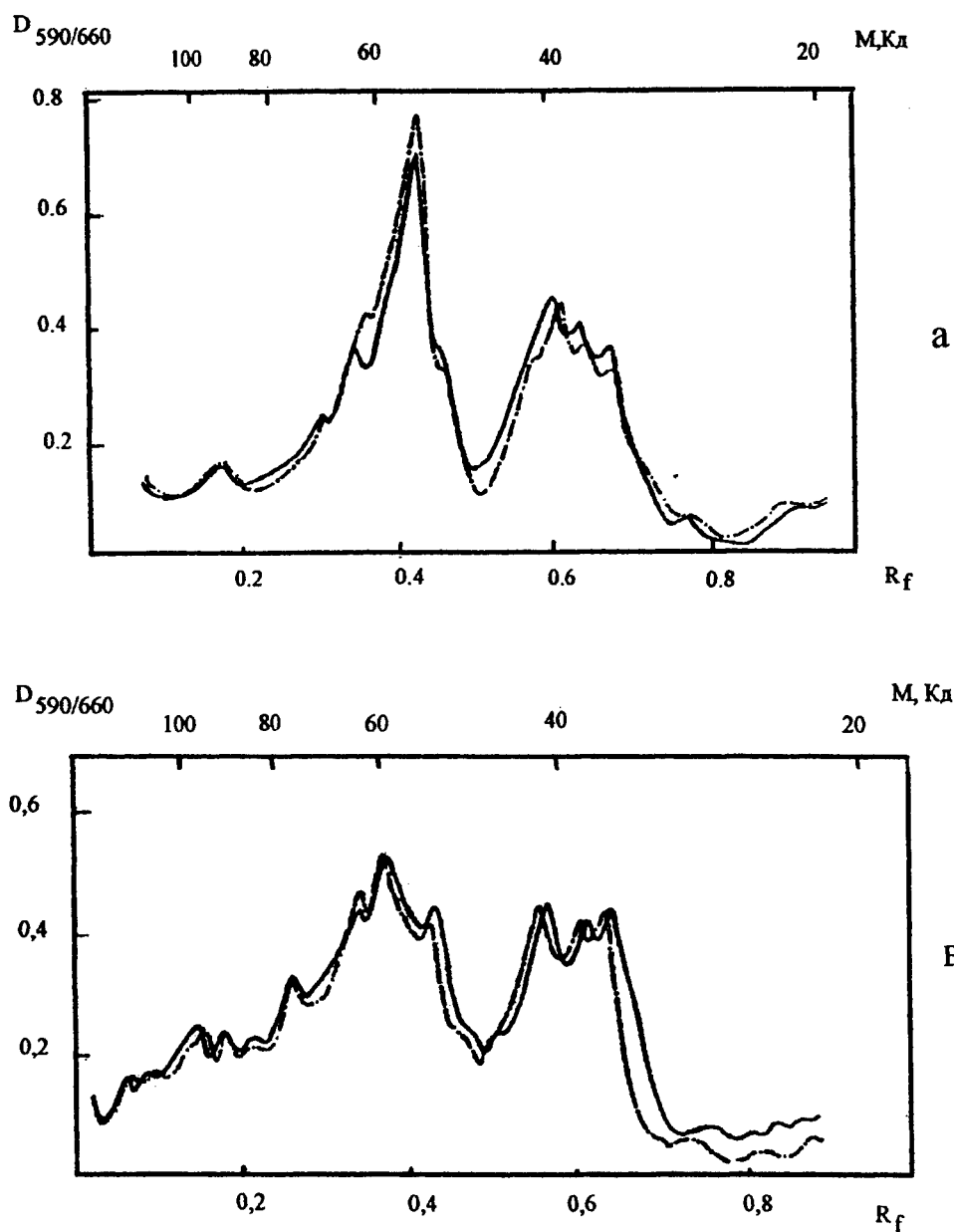


Fig. 3. The densitograms of gel-electrophoresis separation of the retina proteins: a - water-soluble fraction, b - detergent-soluble fraction
(—) - control, (----) - test

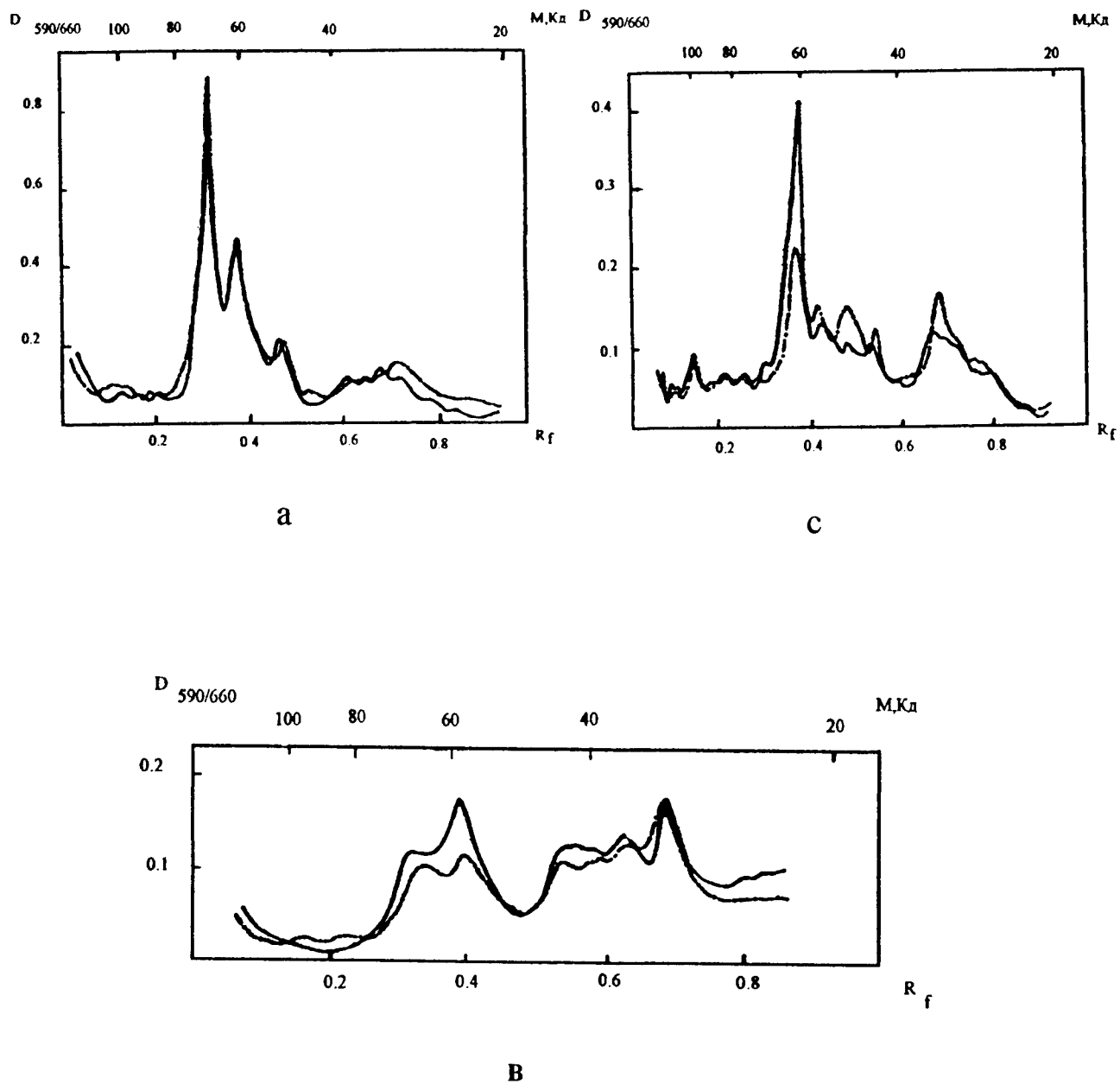


Fig. 4 . The densitograms of gel-electrophoresis separation of the RPE proteins:
a - water - soluble fraction, b - detergent - soluble fraction,
c - membrane proteins of the suspension of RPE cells
(—) - control, (----) - test

formation of any inter- and intramolecular covalent bonds, and this is also true for the case of oxidation of the SH-groups, since the number of the SH-groups in the preparations before and after irradiation remained unchanged (see table 1).

It is seen from the densitograms that the irradiation produces same changes in the electrophoresis pattern (Fig. 4): the polypeptide fraction with $M = 60$ Kd, 70 Kd and more light fraction with $M = 45$ Kd decrease, a small more heavy fraction with $M = 95$ Kd appears for the RPE detergent - soluble fractions. As an analysis of densitogram (Fig.4) shows, in this case the laser radiation causes changes in the polypeptide composition of the RPE proteins: the fraction with $M = 60$ Kd decreases and the polypeptide fraction with $M = 50$ Kd and 30 Kd increases. New bands form at the expense of a decrease in the value of the main band with $M = 60$ Kd.

Thus laser radiation causes the appearance of a small number of covalent bonds in the RPE proteins without any participation of the SH-groups in their formation, the direct determination of the number of the SH-groups did not revealed authentic changes in them after laser irradiation (see Table 1).

TABLE 1

Type of tissues		Concentration of SH-groups, M/mg proteins $\cdot 10^{-8}$	
		control	test
water-soluble fraction	retina	7,0 + 1,3	6,6 + 0,9
	PE	1,9 + 0,2	1,3 + 0,4
detergent-soluble fraction	retina	6,8 + 0,6	7,2 + 1,0
	PE	3,1 + 1,7	2,2 + 1,1

4. DISCUSSION

The data obtained with the help of cryofractography method¹² point to the fact that the argon laser radiation can cause photochanges in the retina and RPE tissues. Along with fragmentation of the membrane material of the RPE and photoreceptor cells of retina the visible denaturation of the protein components of the cells takes place. An investigation of the samples of the retina and RPE tissues with the help of the gelelectrophoresis method in the polyacryl-amide gel in the presence of SDS and dithiothreitol did not revealed significant differences in the electrophoresis profiles of the test and control retina samples. The small changes were observed only in the RPE tissues. The similar intensity of the corresponding bands on the densitograms and the absence of a significant number of components with an increased molecular mass point to the fact that the protein aggregates formed under the action of laser radiation are stabilized by weak noncovalent bonds, since they are destroyed by the action of SDS and dithiothreitol. It is known that SDS breaks down the protein-protein bonds, breaking down the quarter protein structure, dissociating it to subunits¹³. The absence of changes in the content of the SH-groups in the retina and RPE proteins points to the fact that the photochemical processes connected with oxidation of the thiol groups and formation of disulfide bonds do not contribute significantly to photodamages.

5. REFERENCES

1. G. Meyer-Schwickerath, *Light coagulation*, 256 p. St. Louis, C. V. Mosby Company, 1960.
2. J. Marshall, "Light damage and the practice of ophthalmology", In: E. S. Rosen, M. Maining and E. J. Arnott, *Interocular lens implantation*, pp. 182-207, 1983.
3. W. T. Ham, H. A. Mueller, etc., "The nature of retinal radiation damage: dependence on wavelength, power level and expose time", *Vis. Res.*, V. 20, N. 12, pp. 1105-1111, 1980.
4. W. T. Ham, J. J. Ruffalo, H. A. Mueller etc. "Histological analysis of photochemical lesions produced in rhesus retina by short wavelength light", *Ibid.*, Vol. 17, N. 10, pp. 1029-1035, 1978.

5. L. Feeney, E. R. Berman. "Oxygen toxicity: membrane damage by free radicals", *Inves. Ophtal. Vis. Sci.*, Vol. 15, pp. 789-792, 1976.
6. V. Lapina, A. Dontsov, "The action of UV-A and blue on enzymes activity and accumulation of lipid peroxidation products in the attached and detached frog retina", *Proc. SPIE*, Vol. 2134B, pp. 75-83, 1994.
7. L. Feeney-Burns, E. R. Berman, "Methods for isolating and fractionating of pigment epithelial cells", *Meth. Enzym.*, Vol. 81, pp. 95-110, 1982.
8. G. L. Ellman, K. D. Courtney, V. J. Andres etc., "A new and rapid colorimetric determination of acetylcholinesterase activity", *Bioch. Pharm.*, Vol. 72, pp. 88-95, 1961.
9. V. K. Laemli, "Cleavage of structural proteins during the assembly of the head of bacteriophage T4", *Nature*, N. 227, pp. 680-685, 1970.
10. M. A. Markwell, S. M. Haas, L. L. Beiler, etc., "A modification of Lowry procedure to simplify protein determination in membrane and lypoprotein samples", *Anal. Biochem.*, Vol. 87, N. 1, pp. 206-210, 1978.
11. H. Moor, K. Muhlethaler, "Fine structure in frozen-etched yeast cells", *J. Cell. Biol.*, Vol. 17, N.3, pp. 609-628, 1963.
12. P.A. Armond, G. Bjorkman, L. A. Stachelin, "Dissociation of supramolecular complex chloroplast membranes. A manifestation of heat damage to the photosynthetic apparatus", *Biochim. Biophys. Acta*, Vol. 601, pp. 433-442, 1980.
13. A. Helemin, K. Simons, "Solubilization of membranes by detergents", *Biochim. Biophys. Acta*, Vol. 415, pp. 9-79, 1975.

V.A.L. (correspondence): E-mail: vlapina@dragon.bas-net.by ; FAX: 375-017 2393131; Phone: (017) 268-44-19
 G.V.L., T.A.G. (correspondence): Phone: (017) 268-46-61

Physical and optical limitations using ArF-excimer and Er:YAG laser for PRK

Vladimir Semchishen^a, Michael Mrochen^b, Theo Seiler^b

^a Laser Research Center, Russian Ac. of Sc. Troitsk, Moscow region, 142092

^b Department of Ophthalmology, University of Dresden, Germany, 01307

Abstract

The Erbium:YAG laser emitting at a wavelength of 2,94 μm have been promised as an alternative laser for the ArF-excimer laser (193 nm) in photorefractive keratectomy (PRK). This report discusses the limitations of laser parameters such as wavelength, energy density and pulse duration for the ablation of the cornea. In addition, The melting process during ablation on the corneal surface roughness may play a role.

Keywords: photorefractive keratectomy, photoablation, excimer laser, Erbium:YAG laser, surface melting, central islands

1. Introduction

The Erbium:YAG laser (2,94 μm) was considered as an alternative for the ArF-excimer laser (193 nm) in photorefractive keratectomy (PRK). At low light intensities, the absorption coefficient of water at a wavelength of 2,94 μm is in the order of 13000 cm^{-1} . Therefore, soft tissues with high water concentrations like the cornea can be photoablated with Erbium:YAG laser pulses. In contrast, at the wavelength of the ArF-excimer laser the absorption coefficient of the cornea is in the order of 40000 cm^{-1} and the protein is thought to be the main absorber in the cornea during the photoablation. We should, therefore, not be surprised that the different main absorbers at 193 nm and 2,94 μm wavelength leads to different ablation processes at each wavelength.

For a successful use of lasers in PRK the following factors must be taken into consideration:

- a) High ablation rates can decrease the precision of the refractive change and increase the surface roughness.
- b) High surface roughness and thermal damage may increase the healing response.
- c) Acoustic shock or stress waves can damage the corneal endothelium.
- d) High temperature and pressure during the ablation process may melt the corneal surface and, as a result, the surface roughness after the ablation increases.
- e) Even small temperature gradients can induce a water motion inside the cornea. This can lead to a change in the laser-tissue interaction.

2. Laserparameters

2.1 Energy density

In PRK the „blow-off“ model is established to define the ablation process by two main parameters - the ablation rate and the ablation threshold. Here, a semilogarithmic function describes the ablation depth $d = f(F)$ in dependence on the energy density F derived from Lambert-Beer's law³. In this case, the ablation rate is the ablation depth at $F = eF_{th}$ and the ablation threshold F_{th} is defined by the intersection of the semilogarithmic function with the $\log(F)$ -axis. However, it is known that the „blow-off“ - model assumes that the laser energy is accumulated in the tissue during the pulse creating an energy distribution according to Lambert-Beer's law which, at the end of the pulse, leads to an explosive ablation. The assumption that no ablation occurs during the laser pulse is certainly not correct. Nevertheless, the ablation rate as well as the ablation threshold obtained from a semilogarithmic fit on experimental data's is useful for the comparison of the ablation behavior at different laser parameters, i.e. at different wavelengths or pulse durations.

The increase of the energy density leads to an increase of the ablation depth as mentioned from the „blow-off“ model. The ablation rate of the ArF-excimer laser ($\approx 0,3\text{ }\mu\text{m}/(\text{J}/\text{cm}^2)$) correlates with the absorption coefficient of the cornea at 193 nm⁴. In contrast the ablation rate of a Q-switched Erbium:YAG laser is in the range of 2 to 4 $\mu\text{m}/(\text{J}/\text{cm}^2)$ and does unfortunately not correlate with the low intensity absorption coefficient of water⁵. An explanation of this finding might be

the bleaching of water at high temperatures. Furzikov⁶ has shown that the effective absorption coefficient decreases by one order of magnitude for energy densities at the ablation threshold. Vodopyanov et. al.⁷ reported an decreased absorption coefficient in the order of 3000 cm^{-1} at a temperature of 374°C . Therefore, the absorption coefficient decreases during the irradiated laser pulse and as a result the ablation rate increases

The increase of the energy density does not only yield in a greater ablation depth, but also increases the pressure amplitude of the acoustic transients induced by the photoablation process. From the linear dependence of the pressure amplitudes⁸ on the energy density ($F > F_{th}$) a slope factor for the ArF-excimer laser ($F_{th} \approx 40 \text{ mJ/cm}^2$) and a Q-switched Erbium:YAG laser ($F_{th} \approx 200 \text{ mJ/cm}^2$) can be derived from experimental data's shown in Fig 1. . The slope factor $40 \text{ MPa/(J/cm}^2)$ for the ArF-excimer laser ablation with a pulse duration of $\tau \approx 20 \text{ nsec}$ is about two times higher compared to the slope factor of $20 \text{ MPa/(J/cm}^2)$ obtained from a Q-switched Erbium:YAG laser with a pulse duration of $\tau \approx 300 \text{ nsec}$. It is reported that excimer laser pulses with an energy density of more than 250 mJ/cm^2 may damage the corneal endothelium⁹. Currently available excimer laser are working in the range of 150 mJ/cm^2 leading to a pressure amplitude in the range of $5 - 7 \text{ MPa}$. Taking this limitation into consideration, the energy density of a Q-switched Erbium:YAG laser should be in the range of 1 J/cm^2 or less. However, during our experiments we observed an unstable photoablation at such low energy densities, i.e. the ablation stops after a few irradiated laser pulses.

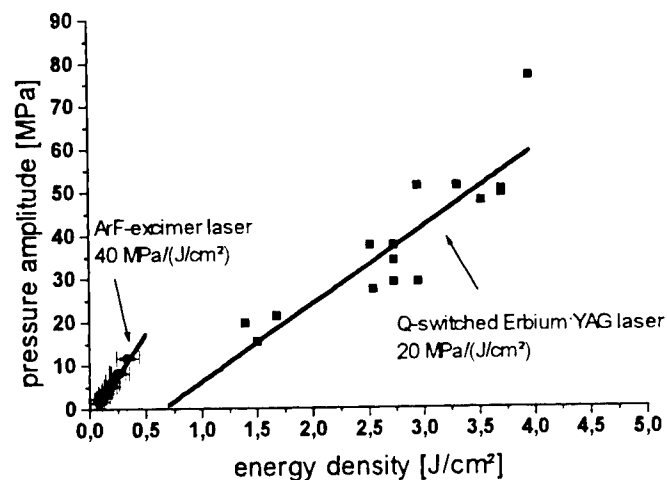


Fig. 1: Laser induced pressure amplitudes in dependence on the energy density for an ArF-excimer laser and a Q-switched Erbium:YAG laser. The laser pulse duration of the ArF-excimer laser was 20 nsec and 300 nsec for the Q-switched Erbium:YAG laser. A numerical linear fit to the data's results in an slope factor of $40 \text{ MPa/(J/cm}^2)$ for the ArF-excimer laser and $20 \text{ MPa/(J/cm}^2)$ for the Q-switched Erbium:YAG laser at energy densities above the ablation threshold ($F > F_{th}$). The pressure amplitudes were measured by a piezoelectric detector consisting of an PVDF-film.

2.2 Pulse duration

It is reported that the ablation threshold of the ArF-excimer laser is approximately 40 mJ/cm^2 at a laser pulse duration of 20 nsec . Currently available Q-switched Erbium:YAG laser systems are working also with sub-microsecond pulse durations. The Q-switching methods like rotating mirrors or prism-modulators for the Erbium:YAG laser to obtain nanosecond laser pulses are still plagued with technical problems and therefore the output energy is limited^{10,11}. Typical pulse durations obtained from such Q-switched Erbium:YAG laser are in the order of 10 nanoseconds up to several 100 nanoseconds at pulse energies up to 100 mJ . Nevertheless, previous experimental studies have shown a dependence of the ablation threshold on the laser pulse duration τ of the Erbium:YAG laser $F_{th}=f(\tau)$. From measurements on the damage threshold of dielectric materials it is known that for the induced damages the threshold correlates to¹²

$$F_{\text{damage}} \approx \tau^\alpha, \quad 0.3 < \alpha < 0.6$$

For the Erbium:YAG laser ablation a numerical fit (see curve (1) in Fig. 2) to the data presented in Fig. 2 yields to a value of $\alpha \approx 0.2$. Extrapolating the ablation threshold for the Erbium:YAG laser to shorter pulses, the ablation threshold found experimentally for the ArF-excimer laser is still smaller. This indicates that the ablation threshold is probably not only depended on the duration of the interaction process but even more important on the type of laser tissue interaction.

Furthermore, extrapolating the ablation threshold into the picosecond time domain it can be observed that at a pulse duration of approximately 20 psec the photoablation process turns into a multiphoton process at a single pulse power in the order of $> 1 \text{ GW/cm}^2$. Therefore, we believe that the pulse duration of an Erbium:YAG - laser for PRK should be in the sub-nanosecond time region of 20 psec up to 1 nsec with an energy density above the ablation threshold and below the threshold of the multiphoton process to decrease the thermal diffusion during the laser-tissue interaction.

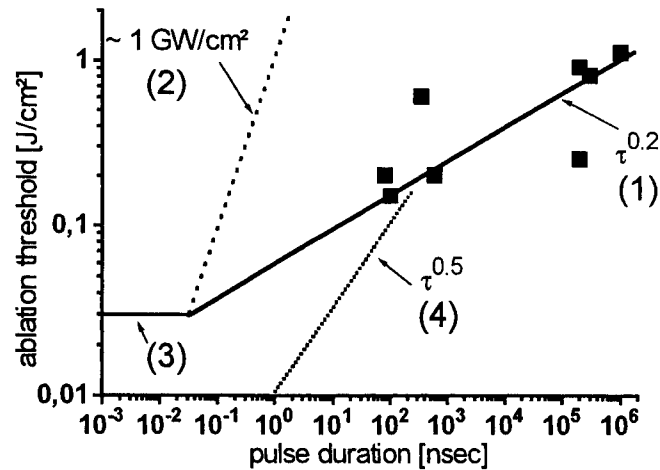


Fig. 2 Ablation threshold as a function of the laser pulse duration for the Erbium:YAG laser. Curve (1) is a numerical fit $F_{th} \approx \tau^\alpha$ with $\alpha \approx 0.2$ to the measured ablation thresholds obtained from the literature^{1, 5, 11, 13}. Curve (2) depicts the threshold for multiphoton photoablation at an threshold intensity of approximately $> 1 \text{ GW/cm}^2$. Curve (3) stands for the multiphoton ablation threshold for pulse durations below 20 psec where the ablation threshold becomes independent of the pulse duration. Curve (4) describes the calculated melting threshold for the nanosecond-domain according to equation 1. In all cases, the melting threshold is below the ablation threshold.

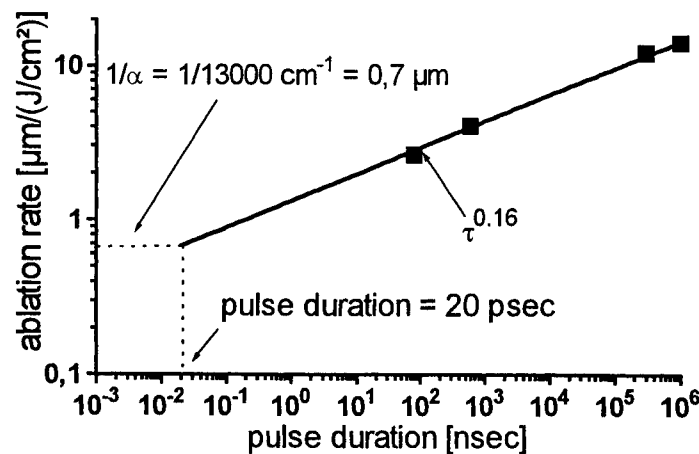


Fig. 3 Ablation rate as a function of the pulse duration. The solid line is a numerical fit $m \approx \tau^\alpha$ with $\alpha \approx 0.16$ to the measured ablation rates m obtained from the literature^{5, 11}. Extrapolating the numerical fit to a pulse duration of approximately 20 psec, where the ablation process turns into a multiphoton ablation process, the ablation rate correlates to the optical penetration depth according to the absorption coefficient of water at a wavelength of 2,94 μm .

At shorter pulse durations not only the ablation threshold decreases but also the ablation rate. At microsecond pulses the ablation rate can be estimated from the thermal diffusion model during the laser-tissue interaction in good agreement with

experimental results¹⁴. In the nanosecond time regime the theoretical description of the ablation rate and ablation threshold dose not fit to the thermal diffusion models. An explanation for the higher measured ablation rates might be the bleaching effect as mentioned before. Anyway, the arrangement of a sub-nanosecond Erbium:YAG laser might be difficult and there is no commercial sub-nanosecond Erbium:YAG laser system available.

3. Surface melting during corneal ablation

It is known that a melting process in materials can occur during laser irradiation. Kitai et. al.¹⁷ have demonstrated that for nanosecond laser pulses at wavelengths below < 250 nm the melting threshold is higher compared to the ablation threshold (see Fig. 4). Furthermore, they have mentioned that for the wavelengths above the > 250 nm the melting threshold is lower than the ablation threshold and therefore, first the melting process occurs before the ablation starts.

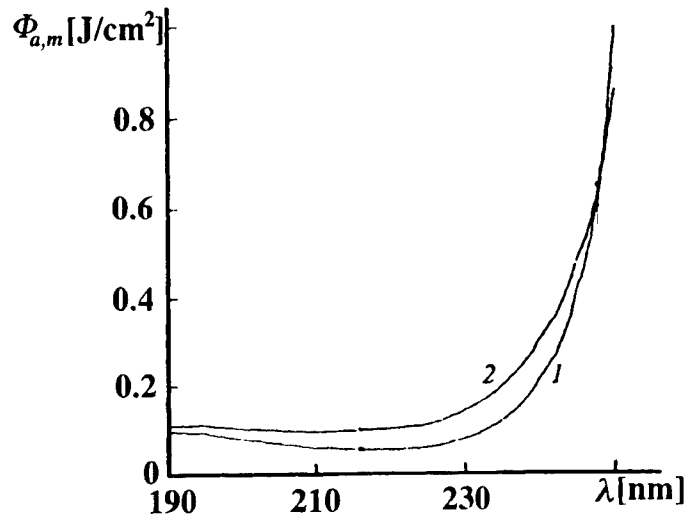


Fig. 4 Ablation threshold $\Phi_a(\lambda)$ (curve 1) and melting threshold $\Phi_m(\lambda)$ (curve 2) in dependence on the UV-wavelengths $190 < \lambda < 250$ nm. The Figure 4 was taken from Kitai et. al.¹⁷

Gusev and coworkers¹⁵ have reported that for the nanosecond laser pulses the melting threshold can be approximated by the following equation:

$$F_m = \frac{\sqrt{\pi}}{2} \sqrt{\chi \rho c} \frac{T_m - T_0}{1 - R} \sqrt{\tau} \quad (1)$$

where $\chi = 0,42$ W/(m K) stands for the thermal conductivity, $c = 3,65$ J/(g K) for the specific heat and $p = 1$ g/cm³ for the density of water. $T_m = 60$ °C determines the melting temperature and $T_0 = 35$ °C the initial temperature¹⁶. In Fig 2 the curve (4) is calculated from equation (1) for nanosecond pulses. However, it can easily be seen that the melting threshold is below the ablation threshold extrapolated from experimental data (Curve (1) in Fig. 2). Thus, during the ablation with Q-switch Erbium:YAG laser pulses the cornea starts to melt and this leads to a different ablation process compared to ablation without melting.

The induced melting of the surface layers may lead to complete different surface structures. Previous experiments with melting, ablation and chemical reaction on irradiated solid surfaces (metals, dielectrics, semiconductors) have shown that after sufficiently long heat treatment or multiple pulse action various types of surface relief's can be formed. The main mechanisms that leads to such relief's are temperature gradients, thermocapillary waves and a modulation of vapor particles concentration near a rough surface. Srinivasan and coworkers¹⁸ have shown a rougher surface after the ablation of PMMA by means of KrF-excimer laser pulses with a wavelength of 248 nm compared to the surface after ArF-excimer laser ablation (see Fig. 5). This indicates that the surface is melted by the 248 nm laser pulses during the ablation process as mentioned by Kitai et. al.¹⁷.

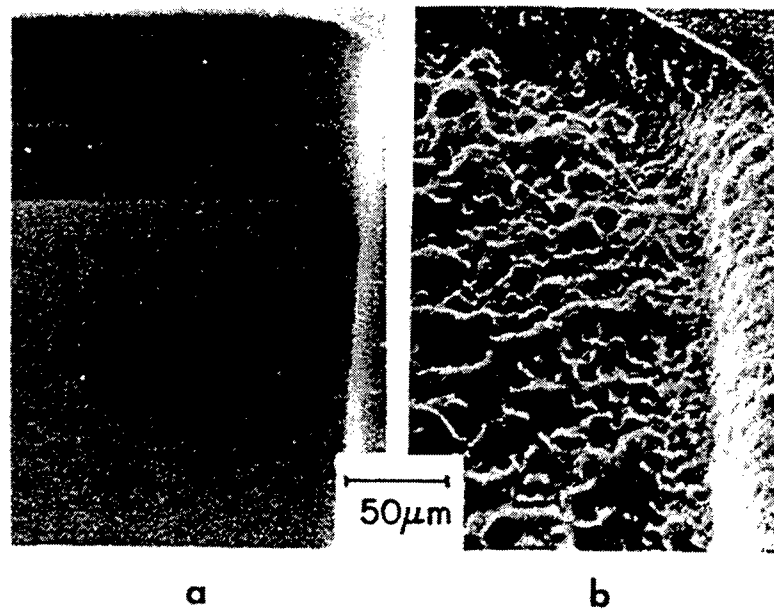


Fig. 5 SEM photographs of surfaces created UV ablation of PMMA. Picture (a), the ablation is performed with an ArF-excimer laser at a wavelength of 193 nm with an energy density of 0.70 J/cm^2 . Picture (b), the ablation is performed with an KrF-excimer laser at a wavelength of 248 nm with an energy density of 2.70 J/cm^2 . The photographs were taken from Srinivasan et. al.¹⁸.

However, several research groups¹⁹⁻²¹ have reported an increased corneal surface roughness after Erbium:YAG laser ablation compared to that after ArF-excimer laser ablation. Konov and Tokarev²² found that for the ArF-excimer laser pulses the surface stability is one order of magnitude better compared to the surface for the Erbium:YAG laser. Thus, they mentioned a smoother surface after the ArF-excimer laser treatment compared to the surface after Erbium:YAG laser treatment. The surface of pig corneas after a myopic correction of -6 dpt with an ablative zone of 6 mm using an ArF-excimer laser and a Q-switched Erbium:YAG laser is shown in Figure 6b. A surface structure with a period of approximately $L \approx 20 \mu\text{m}$ occurs after the Q-switch Erbium:YAG laser treatment with a surface roughness of approximately $10 \mu\text{m}$. Such a roughness compared to that after ArF-excimer laser treatment (see Fig. 6a) might lead to an increased healing response after the treatment.

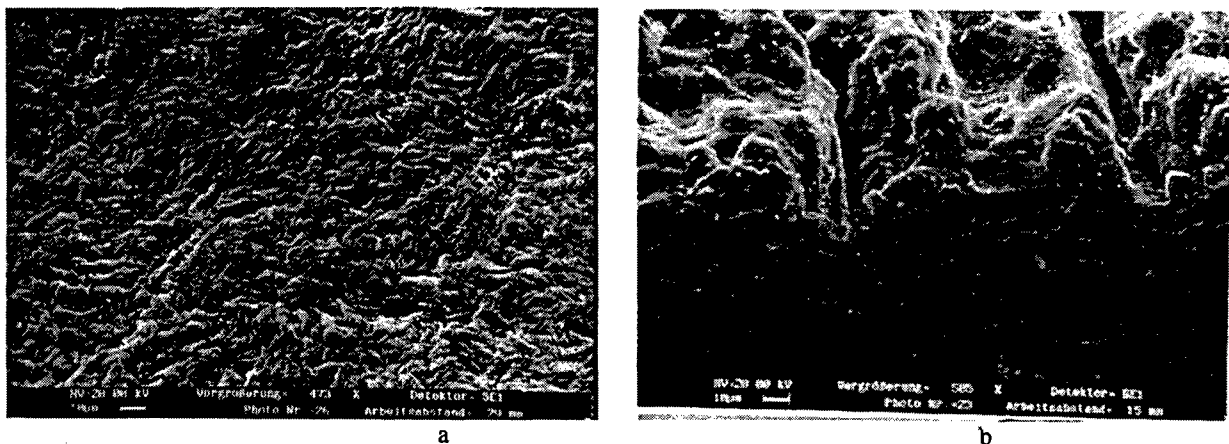


Fig. 6 SEM photographs of inside surface of etch pits produced by ArF-excimer and Q-switched Erbium:YAG laser pulses of pig corneas. Picture (a), the ablation is performed with an ArF-excimer laser at a wavelength of 193 nm with an energy density of 170 mJ/cm^2 . Picture (b), the ablation is performed with a Q-switched Erbium:YAG laser (pulse duration 300 nsec) at a wavelength of $2.94 \mu\text{m}$ with an energy density of 1.5 J/cm^2 .

It is reported⁵ that the thermal damage obtained from Q-switched Erbium:YAG laser ablation does not correlate to the thermal diffusion during the laser pulse. Therefore, the melted layer live-time should be longer than the initial laser pulse duration and may be approximated by¹⁶:

$$t_m \approx \frac{1}{\alpha^2 k} \quad (2)$$

where α is the absorption coefficient and $k = 1,15 \cdot 10^{-3} \text{ cm}^2/\text{sec}$ the thermal diffusion constant. In case of the Q-switched Erbium:YAG laser the live-time is in the range of $t_m \approx 5 \text{ } \mu\text{sec}$. This longer live time of the melted layer on the cornea may explain the thermal damage observed after Q-switched Erbium:YAG laser ablation (Fig. 7b). In contrast Fig 7a shows no thermal damage after corneal ablation using a ArF-excimer laser.

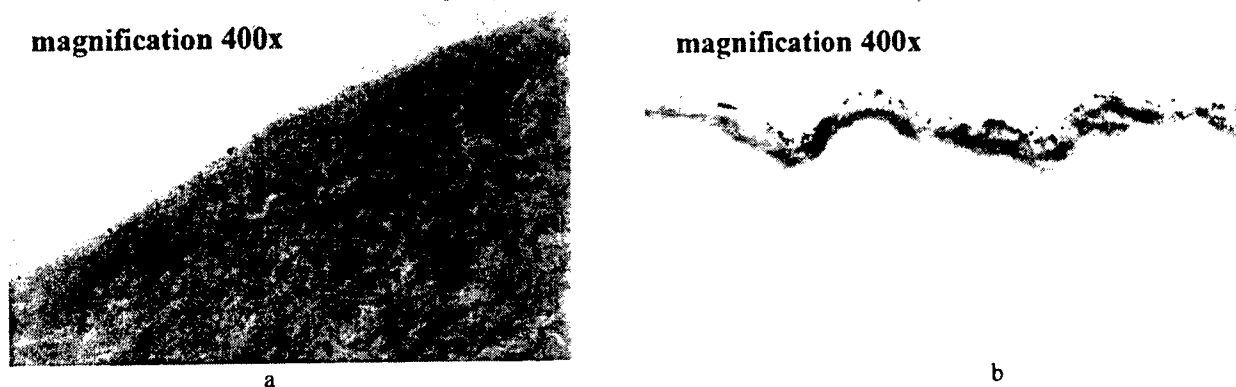


Fig. 7: Histological examination of pig corneas after ArF-excimer laser and Q-switched Erbium:YAG laser treatment. Picture (a), the ablation is performed with an ArF-excimer laser at a wavelength of 193 nm with an energy density of 170 mJ/cm². Picture (b), the ablation is performed with an Q-switched Erbium:YAG laser (pulse duration 300 nsec) at a wavelength of 2,94 μm with an energy density of 1.5 J/cm². The corneas were stained with Trypan blue, examined and photographed on Leica DMRB and Leica photographic unit Leica Wild MPS 52/48 (Leica, Bensheim, Germany).

4. Conclusion

Considering our results as well the results of other research groups, we want to come to the main conclusion that the Erbium:YAG laser is not an real alternative for the ArF-excimer laser in Photorefractive Keratectomy. This conclusion is mainly based on three conditions. First, the ablation rate of the Q-switched Erbium:YAG laser is still higher compared to the ArF-excimer laser. Second, laser induced shock waves are limiting the energy density to 1 J/cm² or less for the Q-switched Erbium:YAG laser. On the other hand, at this low energy densities the ablation is unstable and inhomogeneous. Third, the melting during the Q-switched Erbium:YAG laser ablation leads to an high surface instability and this increases the surface roughness, especially for high myopic corrections.

5. Acknowledgment

The Authors would like to thank the Department of Anatomy at the Technical University Dresden for preparing the SEM and histology investigations. Furthermore, we would like to thank the WaveLight Lasertechnologie GmbH, Erlangen, Germany for technical help during our experiments.

References

1. Ren Q, Venugopalan, Schomaker K, Deutsch TF, Flotte TJ, Puliafito CA, Birngruber R, "Mid- infrared laser ablation of the cornea: a comparative study", *Lasers Surg Med* 12, pp. 274-281, 1992
2. Pettit GH, Ediger MN, "Corneal tissue absorption coefficients for 193 nm and 213 nm ultraviolet radiation", *Appl Optics* 35, pp. 3386-3391, 1996
3. R. Snirivasan, "Ablation of Polymeres and Biological Tissue by Ultraviolet Lasers", *Science* 234, pp. 559-565, 1986
4. Seiler T, McDonnell PJ, "Excimer laser photorefractive keratectomy", *Surv Ophthalmol* 40, pp. 89 - 118, 1995
5. Mrochen M, Semchishen V, Seiler T, "Mid-infrared photorefractive keratectomy: ablation rate and ablation threshold as a function of pulse duration", Accepted for publication in *Laser Light Ophthalmol*, 1997
6. Furzikov NP, "Origin of corneal bleaching under chemical HF laser abaltion", *SPIE* 1646, pp. 172 - 177, 1992
7. Vodop'yanov KL, Kulevskii LA, Pashinin LA, Prokhorov PP, Martin S. "Water and ethanol as bleachable radiation absorber in an yttrium-erbium-aluminum garnet laser (2.94 μm)", *Sov Phys JETP* 55, pp. 1049-1051, 1982
8. Dyer PE, Al-Dhahir RK, "Transient photoacoustic studies of laser ablation", *SPIE* 1202, pp. 46 - 60, 1990

8. Dyer PE, Al-Dhahir RK, "Transient photoacoustic studies of laser ablation", SPIE 1202, pp. 46 - 60, 1990
9. Kitai MS, Popkov VL, Semchishen VA, Kharizov AA, "The physics of UV laser cornea ablation", IEEE J Quantum Electron 27, pp. 302 - 307, 1991
10. Mrochen M, Vogler K, Glaeske N, "Experiments on Q-switched solid state lasers in the 2 μ m - 3 μ m spectral region", Laser und Optoelektronik 28, pp. 42 - 51, 1996
11. Högele A, Ziolek C, Lubatschowski H, Lohmann S, Welling H, Olmes A, Ertmer W, "FTIR-Q-switched 3 μ m erbium lasers for applications in laser surgery", Laser und Optoelektronik 29, pp. 45 - 51, 1997
12. Stuart BC, Feit MD, Herman S, Rubenchik AM, Shore BW, Perry MD, "Optical ablation by high-power short-pulse lasers", J Opt Soc Am B, 13, pp. 459 - 468, 1996
13. Könz F. et. al., "Thermal and mechanical damage of corneal tissue after free running and Q-switched mid-infrared laser ablation", SPIE 2077, pp. 78 - 86, 1993
14. Olmes A. et. al., "Numerical simulation of infrared-photoablation" SPIE 2923, pp. 144 - 154
15. Gusev V, Kolomenskii AA, Hess P, "Effect of melting on the excitation of surface acoustic wave pulses by UV nanosecond laser pulses in silicon", Appl Phys A 61, pp. 285-298, 1995
16. Sobol EN, Makropoulou M, Serafetinides AA, Yova D, "Theoretical model of Co2 laser ablation of soft-tissue phantoms", IL NUOVO CIMENTO 18, pp. 483 - 490, 1996
17. Kitai MS, Semchishen VA, "Melting of polymers during UV laser ablation", Quantum Electronics 26, pp. 517 - 519, 1996
18. Snirivasan R, Braren B, Dreyfus RW, Hadel L, Seeger DE, "Mechanism of the ultraviolet ablation of polymethyl methacrylate at 193 and 248 nm: laser-induced fluorescence analysis, chemical analysis, and doping studies", J Opt Soc Am B 3, pp. 785 - 791, 1986
19. Mrochen M., Schmidt-Petersen H., Genth U., Funk R., Seiler T, "Er:YAG laser photorefractive surgery - fundamental mode photoablation versus scanning spot", Invest Ophthalmol Vis Sci Annual Meeting 1997; 38: S.253
20. Wirbelauer C, Holschbach A, Huebscher H-J, Wollensak J, "On-line Scheimpflug videography of the corneal profile after Erbium:YAG laser photoablation", Laser and Light 8, pp. 47-52, 1997
21. Bende T, Jean B, Matallana M, Seiler T, Steiner R, "Feuchte Hornhautflächenablation mit dem Er:YAG-Laser", Ophthalmologie 91, pp. 651-654, 1994
22. Konov VI, Tokarev VN, „ Surface stability under pulsed laser ablation", SPIE 1882, pp. 396 - 397, 1993

CWhatUC : A Visual Acuity Simulator

Daniel D. Garcia^a, Brian A. Barsky^{a,b}, Stanley A. Klein^b

^aUniversity of California, EECS Computer Science Division, 387 Soda Hall # 1776,
Berkeley CA 94720-1776

^bUniversity of California, School of Optometry, 360 Minor Hall # 2020, Berkeley CA 94720-2020

ABSTRACT

CWhatUC (pronounced "see what you see") is a computer software system which will predict a patient's visual acuity using several techniques based on fundamentals of geometric optics. The scientific visualizations we propose can be clustered into two classes: retinal representations and corneal representations; however, in this paper, we focus our discussion on corneal representations. It is important to note that, for each method listed below, we can illustrate the visual acuity with or without spectacle correction. Corneal representations are meant to reveal how well the cornea focuses parallel light onto the fovea of the eye by providing a pseudo-colored display of various error metrics. These error metrics could be:

- a) standard curvature representations, such as *instantaneous* or *axial curvature*, converted to refractive power maps by taking Snell's law into account
- b) the *focusing distance* from each refracted ray's average focus to the computed fovea
- c) the *retinal distance* on the retinal plane from each refracted ray to the chief ray (lateral spherical aberration)

For each error metric, we show both real and simulated data, and illustrate how each representation contributes to the simulation of visual acuity.

Keywords: visual acuity, ray tracing, corneal topography, scientific visualization, keratoconus, videokeratography

1. BACKGROUND

The cornea is the transparent tissue covering the front of the eye. It performs 3/4 of the refraction, or bending, of light in the eye, and focuses light towards the lens and the retina. Thus, subtle variations in the shape of the cornea can significantly diminish visual performance. Recently, instruments to measure corneal topography have become commercially available; they are known as videokeratographs (VKs).^{1,2,3,4,5} These corneal topography devices typically shine rings of light onto the cornea and then capture the reflection pattern with a built-in video camera. Figure 1 shows the ring pattern from a patient whose visual acuity we wish to simulate.

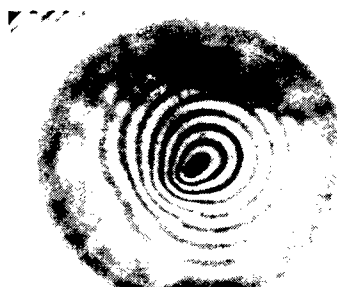


Figure 1: The reflection pattern from a patient with an irregularly-shaped cornea.

Further author information —

D.D.G.(correspondence): Email: ddgarcia@cs.berkeley.edu; WWW: <http://www.cs.berkeley.edu/~ddgarcia/>; Telephone: 510-642-9716; Fax: 510-642-5775

B.A.B.: Email: barsky@cs.berkeley.edu; WWW: <http://www.cs.berkeley.edu/~barsky/>; Telephone: 510-642-9838; Fax: 510-642-5775

S.A.K.: Email: klein@adage.berkeley.edu; WWW: <http://spectacle.berkeley.edu/VSP/SK.html>; Telephone: 510-643-8670; Fax: 510-643-5109

More information about this research can be found at <http://www.cs.berkeley.edu/optical/> and the color images from the poster that accompanied this paper are at <http://www.cs.berkeley.edu/optical/SPIE/>

Instead of allowing the instrument to process the pattern, we extract the data and construct a mathematical spline surface representation from these reflection patterns^{6,7}. This representation allows us to query, or “sample” the surface at arbitrary points to determine information about surface position, normals and principal curvatures. CWhatUC is a software system that uses this information to compute and display different metrics of visual acuity. A wireframe rendering of an example surface with a very low sampling density is shown in Figure 2.

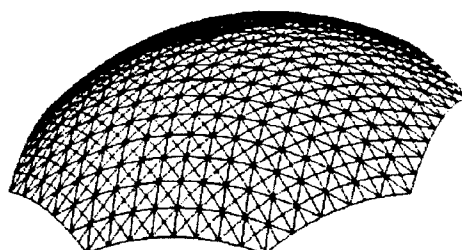


Figure 2: A wireframe rendering of a reconstructed mathematical spline surface.

2. THE FOUR METRICS

We propose four metrics to simulate the corneal contribution to visual acuity. Figure 3 illustrates how we compute the values that we use in our calculations. Our corneal model is a very simple one since we ignore the contribution of the lens and consider the entire cornea to be a uniform material with a constant index of refraction (n) of 1.3375. It is important to note that the metrics we propose here are independent of our implementation. If we were to improve the quality of the model, the metrics themselves would remain unchanged.

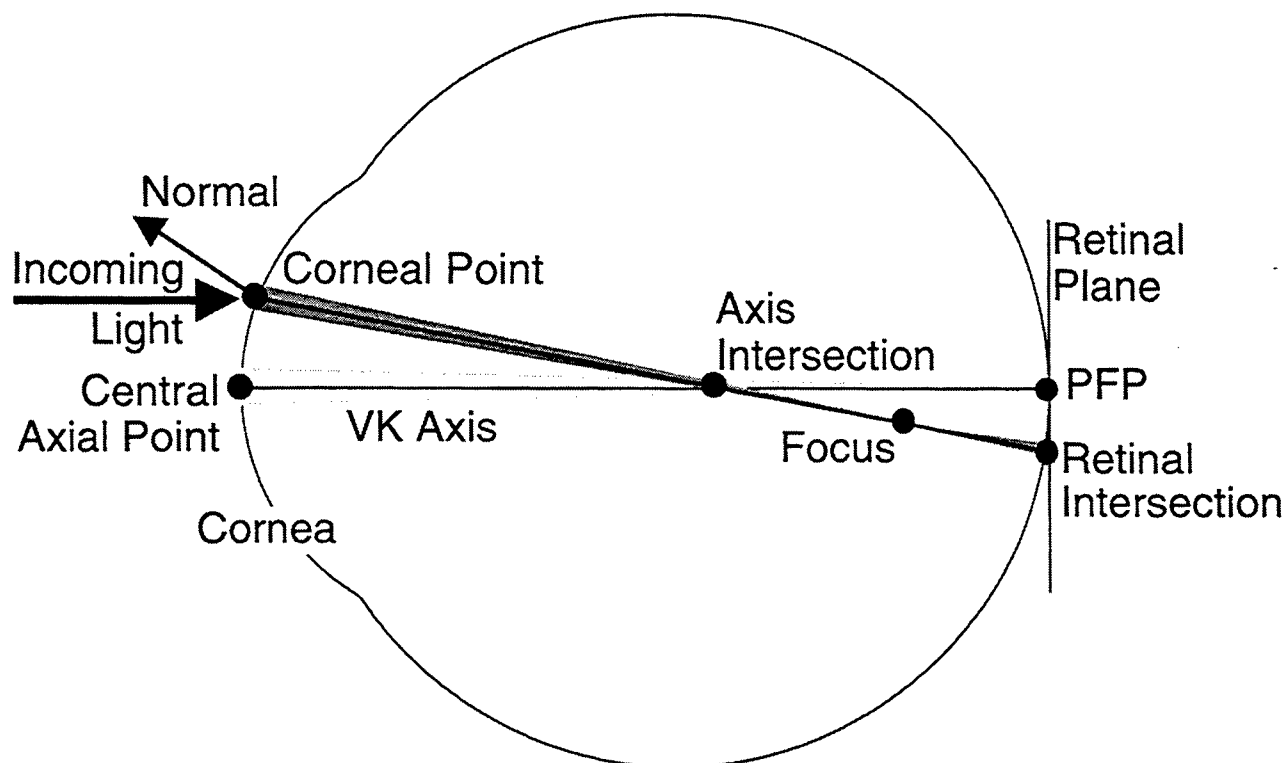


Figure 3: A simple model of the cornea, eye, and the refraction of a ray of incoming light.

We begin the computation at the central axial point on the cornea. We refract incoming parallel light and calculate where it converges to a focus using Coddington's equations^{8,9}. Fortunately, due to constraints in our representation, the normal at the central point is parallel to the incoming parallel light; thus, according to Snell's law, the refracted light will also be in this same direction. If the central axial point has some astigmatism, or cylinder, then so will the refracted wavefront and there will be two principal curvatures. We define the paraxial focal point (PFP) to be the focus as determined by the average of these curvatures (also known as "mean sphere"). The VK axis, which is the z-axis, is the line from the central axial point to the PFP. The retinal plane is the plane that passes through the PFP and is normal to the VK axis.

Then, for each corneal point of interest, we refract parallel incoming light according to Snell's law and Coddington's equations and we calculate where that light focuses. Again, if there is any cylinder in the refracted wavefront, then there will be two principal curvatures; in that case, we use their average to determine the focus. The retinal intersection is the location where the refracted ray intersects the retinal plane. If the normal lies in the meridional plane*, then the axis intersection is the intersection of the refracted ray with the VK axis; otherwise, the refracted ray will not intersect the VK axis. In that case, we choose the axis intersection to be the point of closest approach to the central axis along the refracted ray. At the central axial point there are infinitely many such intersections; thus, for that corneal point, we set the axis intersection to be the PFP.

2.1 Axial Refractive Power

We define axial refractive power at a corneal point to be the quotient of index of refraction of our model cornea divided by the distance from the corneal point to the axis intersection. This map often has a characteristic "figure-8" or "crescent" shape. Clinicians are familiar with this representation because it is similar to the standard axial curvature maps used in most corneal topography instruments. The acute asymmetry of the maps often facilitates the identification and measurement of the amount and orientation of astigmatism.

$$\text{Axial refractive power} = \frac{n}{\text{Distance3D}(\text{Corneal_Point}, \text{Axis_Intersection})} \quad (1)$$

where

$$\text{Distance3D}(P_0, P_1) = \sqrt{(P_{1x} - P_{0x})^2 + (P_{1y} - P_{0y})^2 + (P_{1z} - P_{0z})^2} \quad (2)$$

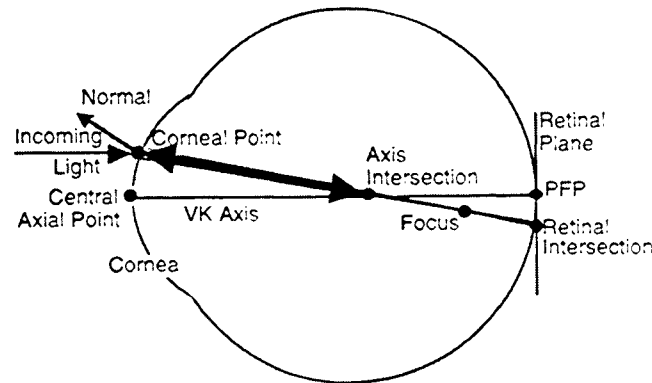


Figure 4: Axial refractive power is a function of the distance between the corneal point and the axis intersection.

This definition differs from the traditional axial curvature map^{10,11,12} in that this refractive power map takes into account the refraction of an incoming parallel ray, whereas the standard map is purely a surface shape quantity. For example, the standard axial curvature of a sphere is constant over its surface, whereas the axial refractive power increases as we move away from the center. Figure 5 illustrates a direct comparison of these two quantities on a simulated cornea having with-the-rule astigmatism. Note that even though there is a difference in the orientation of the figure-8 pattern, they are identical in the central region near the VK axis.

* We define the meridional plane to be the plane containing the VK Axis and the corneal point

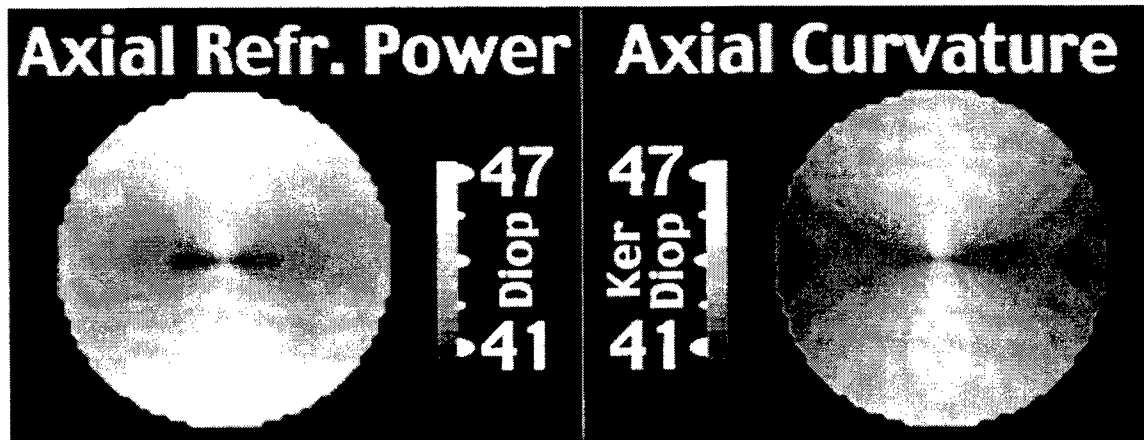


Figure 5: A comparison between axial refractive power and axial curvature.

2.2 Instantaneous Refractive Power

We define instantaneous refractive power at a corneal point to be the quotient of index of refraction of our model cornea divided by the focal distance of the cornea at that point, which is the distance from the corneal point to the focus. This is the only one of our four metrics that is not a function of the central axis or of the PFP; rather, it is purely a measure of the surface's refracting power. The advantage of this definition over other traditional representations such as mean sphere¹³, Gaussian power^{14,15}, axial power, and instantaneous power is that this metric illustrates spherical aberration. Those other metrics would be constant for a sphere, whereas instantaneous refractive power increases away from the center.

$$\text{Instantaneous refractive power} = \frac{n}{\text{Distance3D}(\text{Corneal_Point}, \text{Focus})} \quad (3)$$

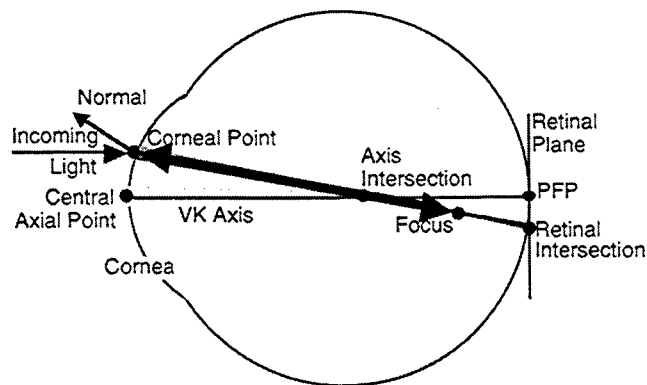


Figure 6: Instantaneous refractive power is a function of the distance between the corneal point and the focus.

2.3 Retinal Distance

We define the retinal distance, for each corneal point, to be the distance from the PFP to the retinal intersection, that is, to the point of intersection of the refracted ray with the retinal plane. Since the retinal plane was defined to contain the PFP, both the retinal intersection and the PFP lie in that plane; thus, the distance calculation is a two-dimensional planar distance measure. For a perfect eye, parallel light would converge to a point focus at the PFP and thus, in this case, the retinal distance at every corneal point would be zero. This metric provides an estimate of lateral spherical aberration.

$$\text{Retinal distance} = \text{Distance2D}(\text{Retinal_Intersection}, \text{PFP}) \quad (4)$$

where

$$\text{Distance2D}(P_0, P_1) = \sqrt{(P_{1x} - P_{0x})^2 + (P_{1y} - P_{0y})^2} \quad (5)$$

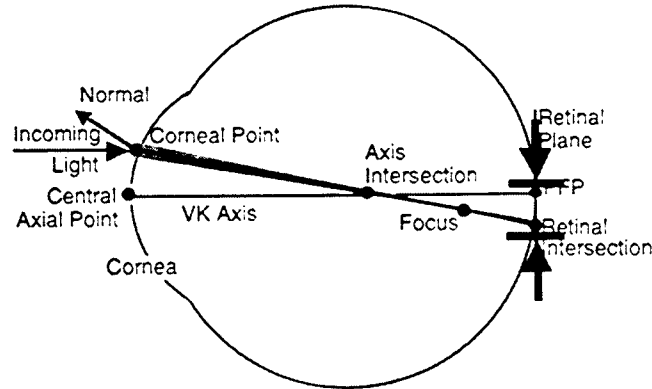


Figure 7: Retinal distance is the distance between the retinal intersection and the PFP.

2.4 Focusing Distance

We define focusing distance, for each corneal point, to be the distance from the focal point of the refracted ray to the PFP. For a perfect eye, the rays of incoming parallel light would converge to a point focus at the PFP and thus the focusing distance for every corneal point would be zero in this case.

$$\text{Focusing distance} = \text{Distance3D}(\text{Focus}, \text{PFP}) \quad (6)$$

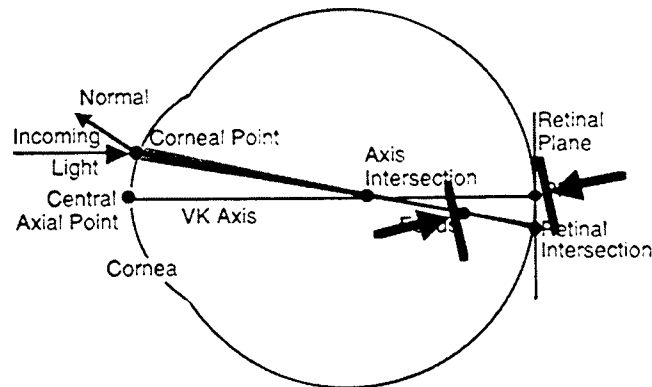


Figure 8: Focusing distance is the distance between the focus and the PFP.

3. REPRESENTATIONS

For each acuity metric, we determine the minimum and maximum values over all the points on the cornea, define a colormap to span those values, and index into that colormap to pseudo-color the surface of the cornea. We have chosen a grey-scale map here, but a user of CWhatUC is provided with a full-color map.**

** Note that the hardcopy halftoning has introduced some visible non-linearity to the grey-scale map. This is not an artifact of the data, but of the printing process itself. This is most easily seen in Figure 10 of the simulated data: the actual instantaneous refractive power and focusing distance maps are smooth and do not have a "ring" halfway out as the images would suggest.

4. RESULTS

We display our four metrics on two sets of data, a simulated cornea and a real cornea. The four metrics each contribute some information to the clinician about the projected visual acuity, as we will see.

4.1 Simulated Data

We use a simple asymmetric ellipsoid to simulate a cornea that has with-the-rule astigmatism. The equation for the ellipsoid is

$$\left(\frac{x}{A}\right)^2 + \left(\frac{y}{B}\right)^2 + \left(\frac{C-z}{C}\right)^2 = 1 \quad (7)$$

with $A=9$, $B=8.7$ and $C=10$. This is rendered in three dimensions below in Figure 9. The intensity of every point in this image is a linear function of the z value of the data; the lighter data points are closer to the $z=0$ plane. We define the range of the data to be $x,y = [-3,3][-3,3]$.

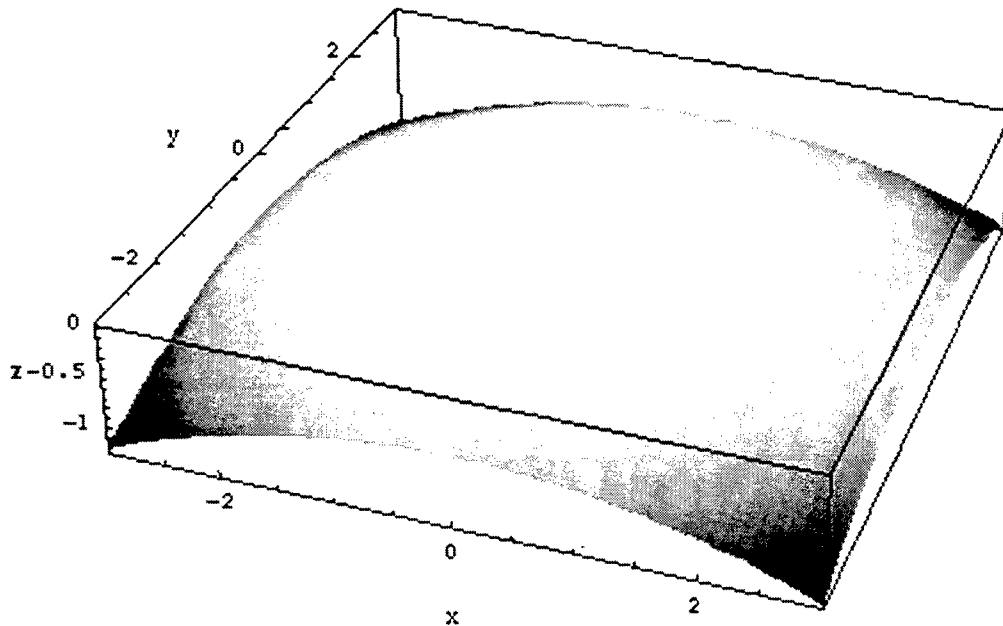


Figure 9: A three-dimensional view of our simulated cornea, modeled as an ellipsoid with $A=9$, $B=8.7$ and $C=10$.

The most striking metric is axial refractive power. It highlights the inherent astigmatism associated with this asymmetric model. We can easily measure that there are four diopters of cylinder and the model is exactly with-the-rule. Retinal distance demonstrates that the left and right areas contribute to focus slightly better than the top and bottom regions, with a good focus in the central circle. Instantaneous refractive power and focusing distance indicate little here other than the focus is worse away from the center, and that the errors are close to rotationally symmetric.

4.2 Real Data

This data is from a patient with keratoconus^{16,17,18}, a condition in which the cornea has a local region of high curvature, which for this cornea is an oval region in the lower left of the image. This data was reconstructed from the ring patterns shown in Figure 1. Of our metrics, instantaneous refractive power and focusing distance highlight the keratoconus best. In fact, instantaneous refractive power gives similar values for the amount of curvature in the region as does instantaneous power, Gaussian power, and mean sphere. The axial refractive power map has a crescent shape because the keratoconus is eccentric and results in some astigmatism. Retinal distance, in conjunction with focusing distance, indicates which rays contribute to good focus. In this case, only a small central area provides a good focus, as this is the only area where both maps are near zero.

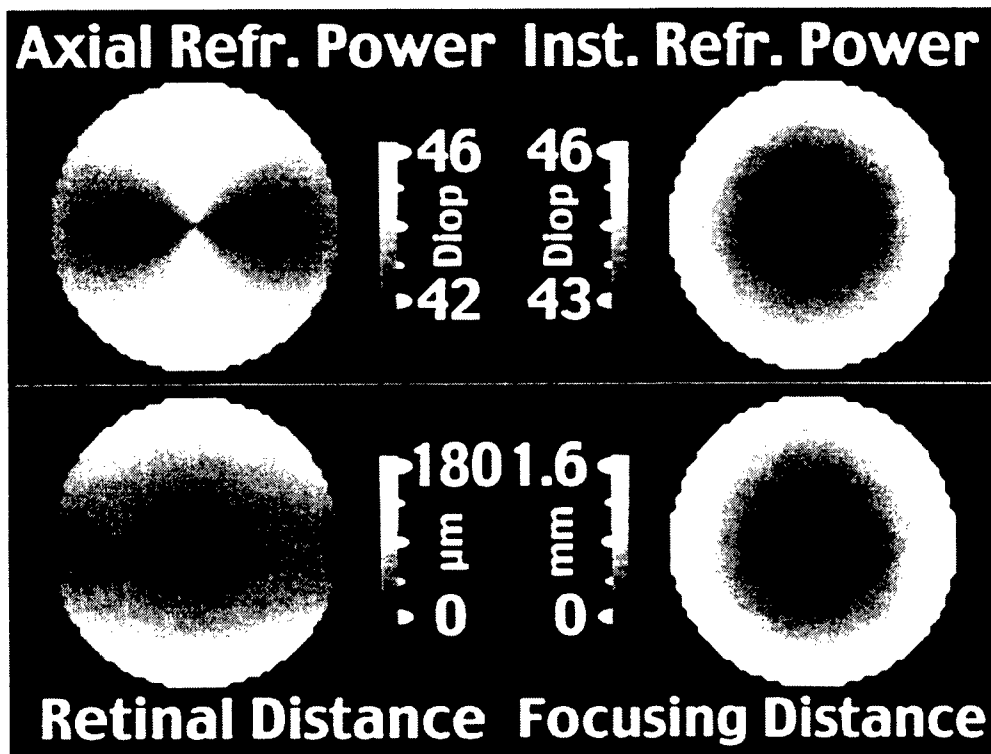


Figure 10: A view of our four acuity metrics for ellipsoidal simulated data.

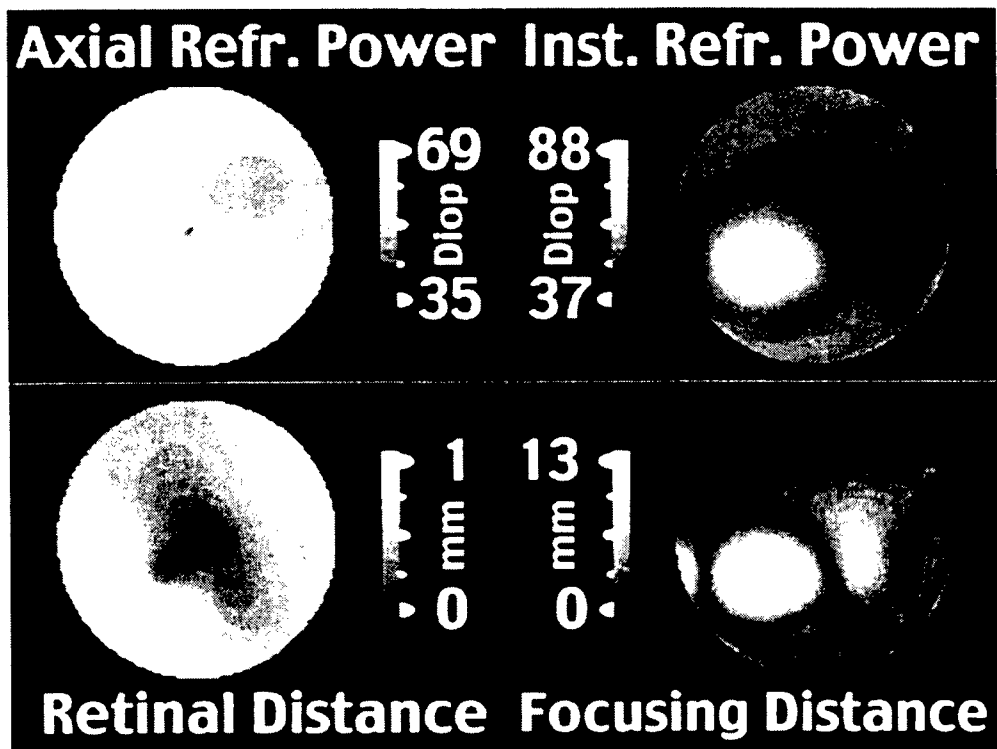


Figure 11: A view of our four acuity metrics for the real data of a keratoconic cornea.

5. CONCLUSION

We have presented four metrics for simulating visual acuity based on geometric optics, and showed the results using simulated and real data as implemented by CWhatUC. Axial refractive power is familiar to clinicians who often use a similar measure for astigmatism. Instantaneous refractive power is useful for describing the corneal shape, but doesn't take the PFP into account. Focusing distance and retinal distance taken together illustrate which regions contribute to a crisp focus onto the PFP. In summary, the four metrics, when used to supplement one another, provide additional insight into the prediction of a patient's visual acuity.

6. ACKNOWLEDGMENTS

This work was supported in part by the National Science Foundation grant number ASC-9720252, "Visualization and Simulation in Scientific Computing for the Cornea" and by the Microelectronics Innovation and Computer Research Opportunities (MICRO) research grant "Interactive Scientific Visualization of the Eye".

7. REFERENCES

1. S. D. Klyce, "Computer-Assisted Corneal Topography, High-Resolution Graphic Presentation and Analysis of Keratometry", *Invest. Ophthalmol. Vis. Sci.* **25**, pp. 1426-1435, 1984.
2. D. D. Koch, G. N. Foulks, and T. Moran, "The Corneal Eyesys System: Accuracy, Analysis and Reproducibility of First Generation Prototype", *Refract. Corneal Surg.* **5**, pp. 424-429, 1989.
3. R. J. Mammone, M. Gersten, D. J. Gormley, R. S. Koplin, and V. L. Lubkin, "3-D Corneal Modeling System", *IEEE Trans. Biomedical Eng.* **37**, pp. 66-73, 1990.
4. J. Wang, D. A. Rice, and S. D. Klyce, "A New Reconstruction Algorithm for Improvement of Corneal Topographical Analysis", *Refract. Corneal Surg.* **5**, pp. 379-387, 1989.
5. S. E. Wilson and S. D. Klyce, "Advances in the Analysis of Corneal Topography", *Surv. Ophthalmol.* **35**, pp. 269-277, 1991.
6. M. A. Halstead, B. A. Barsky, S. A. Klein, and R. B. Mandell, "Reconstructing Curved Surfaces From Specular Reflection Patterns Using Spline Surface Fitting of Normals", *Proceedings of ACM/SIGGRAPH '96, New Orleans, 4-9 August 1996*, pp. 335-342, 1996.
7. M. A. Halstead, B. A. Barsky, S. A. Klein, and R. B. Mandell, "A Spline Surface Algorithm for Reconstruction of Corneal Topography from a Videokeratograph Reflection Pattern", *Optom. Vis. Sci.* **Vol 72, No. 11**, pp. 821-827, 1995.
8. O. Stavroudis, "Simpler Derivation of the Formulas for Generalized Ray Tracing", *J. Opt. Soc. Amer.* **Vol. 66, No. 12**, pp. 1330-1333, 1976.
9. J. E. A. Landgrave and J. R. Moya-Cessa, "Generalized Coddington Equations in Ophthalmic Lens Design", *J. Opt. Soc. Amer.* **Vol. 12, No. 8**, pp. 1637-1644, 1996.
10. S. A. Klein, R. B. Mandell, and B. A. Barsky, "Representing Corneal Shape" in *Vision Science and its Applications. Technical Digest Series*. Washington, DC: Optical Society of America, **vol. 1**, pp. 37-40, 1995.
11. R. B. Mandell, S. A. Klein, C. H. Shie, B. A. Barsky and Z. Yang. "Axial and Instantaneous Radii in Videokeratography". *Invest. Ophthalmol. Vis. Sci.* **35(Suppl)**, p. 2079, 1994.
12. C. Roberts. "The Accuracy of Power Maps to Display Curvature Data in Corneal Topography Systems". *Invest. Ophthalmol. Vis. Sci.* **35**, pp. 3525-3532, 1994.
13. R. Kumpf, "Multivariate Corneal Visualization in the EyeView System". *M. S. Thesis*, University of California at Berkeley, May 1995.

14. B. A. Barsky, S. A. Klein, and D. D. Garcia, "Gaussian Power with Cylinder Vector Field Representation for Corneal Topography Maps", *Optom. Vis. Sci.* **Vol. 74, No. 11**, pp 917-925, 1997.
15. B. A. Barsky, S. A. Klein, and D. D. Garcia, "Gaussian Power, Mean Sphere, and Cylinder Representations for Corneal Maps with Applications to the Diagnosis of Keratoconus", *Invest. Ophthalmol. Vis. Sci.* **37**, p. 558, 1996.
16. B. A. Barsky, R. B. Mandell, and S. A. Klein, "Corneal Shape Illusion in Keratoconus", *Invest. Ophthalmol. Vis. Sci.* **36 Suppl.**, p. 5308, 1995.
17. J. H. Krachmer, R. S. Feder, and M. W. Belin, "Keratoconus and Related Noninflammatory Corneal Thinning Disorders", *Surv. Ophthalmol.* **28,4**, pp. 293-322, 1984.
18. L. J. Maguire and W. D. Bourne, "Corneal Topography of Early Keratoconus", *Am. J. Ophthalmol.* **108**, pp. 107-112, 1989.

Modeling of the light scattering by human eye lens

D.M.Zhestkov¹, I.L.Maksimova², V.V.Tuchin¹

¹Saratov State University, Astrakhanskaya 83, Saratov, 410026, Russia,

e-mail: tuchin@sgu.ssu.runnet.ru

root@geasan.saratov.su

²Saratov branch of Institute of Radioengineering and Electronics
of Russian Academy of Sciences, Saratov, Russia

ABSTRACT

The theoretical model of a human eye lens is presented. This model accounts effects of the spatial interaction of scatterers arising due to existence of closely packed system of particles and the complexity of refractive index of their material. The calculations of transmission and scattering spectra for a monodisperse system of scatterers were done using Monte-Carlo method. The influence of absorption on transmission spectra formation was studied.

Keywords: eye lens, scattering, absorption, tissue structure, Monte-Carlo method

1. INTRODUCTION

Light scattering is a very important phenomenon, which accompany light propagation in any tissue including high transparent, such as crystalline lens¹. The light scattering methods should be very useful for ophthalmic disease diagnostics and monitoring¹⁻³. The problem of monitoring of human eye lens aging can be successfully solved using transmission light spectra measurements⁴. An additional information about eye lens aging or pathology processes developing can be received by measuring of scattering spectra⁵. For modeling of the human eye lens transmission and scattering spectra theoretical model was suggested. Such model presents lens as a scattering and absorbing ball containing the small spherical particles (Fig.1) with complex refractive index defining by contents of tryptophan, kynurenine and aged protein - the main absorbing species in the human eye lens⁶ (Fig.2). This model accounts effects of the spatial interaction of scatterers arising due to existence of a closely-packed system of scatterers². Using such model we have received quite reasonable results for transmission and scattering spectra.

2. THEORETICAL AND EXPERIMENTAL RESULTS

Using Monte-Carlo method the light transmission and scattering spectra of the eye lens were calculated. Calculated transmission spectra for "young", "aged" and "old" human eye lenses are present in Figs. 3-5. There are essential differences in the total transmission spectra for each scattering system. The role of the chromophores which contribution is strongly dependent on the age of the eye lens is easy to see. For accounting of absorption in calculations the experimental data for relative absorbance spectra of the main chromophorous in a human eye lens (Fig.2) from Ref.6 were used. In the whole, calculated spectra qualitatively describe the age related changes in the eye lens tissue, connected with the morphological structure and scatterers dimensions. The total transmission experimental spectra for "normal" and "old" human eye lens (Fig.5, 6) can be found in Refs 7,8. It should be noted that calculated and experimental spectra have some common features, such as UV and short wavelength visible light cutting-off⁹.

Figs.7, 8 show the calculated and experimental spectra for the scattered at $\theta=45^\circ$ radiation in dependence on the wavelength for "aged" and "old" eye lenses. The differences in the spectra are connected with quantitative differences in the filtering properties of the medium, which are caused by scattering and absorption⁸. Maximum shifts to the longer wavelengths region for the measuring volume located on the rare lens surface because more efficiently absorbing of the falling and scattered light with increasing of tissue thickness.

The calculated spectra for the scattering angles $\theta=45^\circ$, $\theta=90^\circ$ and $\theta=135^\circ$ are shown in Figs.9, 10.

3. CONCLUSION

The 3-dimension model of the human eye lens was developed in this work. It gives enough good qualitative explanation of the transmission-scattering of the eye lens spectra. Nevertheless, for obtaining of quantitative results it is necessary to take into account the real absorbers distribution in the medium, caused by aging and pathological distortions of the absorbers distribution.

4. REFERENCES

1. V.V.Tuchin, I.L.Maksimova, V.I.Kochubey et al. "Fundamentals of ophthalmic diagnostical methods based on laser light scattering", *Proc. SPIE. Ophthalmic Technologies IV*, **Vol.2393**, pp.237-253, 1995.
2. A.P.Ivanov, V.A.Loyko, V.P.Dik, *Light Propagation in a Closely-Packed Dispersive Media*. Minsk. Science and Techniques, 1988.
3. C.F.Bohren and D.R.Huffman. *Absorption and Scattering of Light by Small Particles*. Wiley, N.Y., 1983.
4. B.K.Pierscionek, "Aging changes in the optical elements of the eye ", *J. Biomedical Optics*, **Vol.1**, N.2, pp.147-156, April 1996.
5. S.Zigman, G.Sutliff, M.Rounds. "Relationships between human cataracts and environmental radiant energy. Cataract formation, light scattering and fluorescence", *Lens and Eye Toxicity Research*, **Vol.8** (2&3), pp.259-280, 1991.
6. G.Dillon, "Photophysics and photobiology of the eye", *Photochemistry and Photobiology: Biology*, **Vol.10**, pp.23-40, 1991.
7. A.Bielski, T.Robaczewski, J.Wolnikowski, L.Biegganowski. "Transmission of the normal and cataractous lenses", *Lens and Eye Toxicity Research*, **Vol.8**, N 2&3, pp.101-108. 1991.
8. V.V.Tuchin, I.L.Maksimova et. al "Human eye lens spectroscopy and modeling of its transmittance", *Proc. SPIE*, **Vol. 2126**, pp.393-406, 1994.
9. F.Barker, G.C. Brainard, and P. Daghaw-Barker. "Transmittance of the human lens as a function of age", *Invest Ophthalmol. Vis. Sci.*, **Vol.33**, pp.3555-3560, 1992.
10. H.S.Dhadwal, R.R. Ansari, and M.A.Dellavecchia. "Coherent fiber optic sensor for early detection of cataractogenesis in a human eye lens", *Optical Engineering*, **Vol.32**, pp.233-238. Feb 1993.

Table 1. Absorbing and scattering parameters of the human lens models ^{6,10}.

Lens model	absorbers			Scatterers $n'=n_s/n_0$		
	Trp, t	3-HKG, k	AP, p	R_0 , mcm	n_s	n_0
Young	0,03	0,03	0,00	0,01	1,43	1,35
Aged	0,03	0,01	0,03	0,02	1,47	1,35
Old	0,30	0,10	0,30	0,02	1,47	1,35

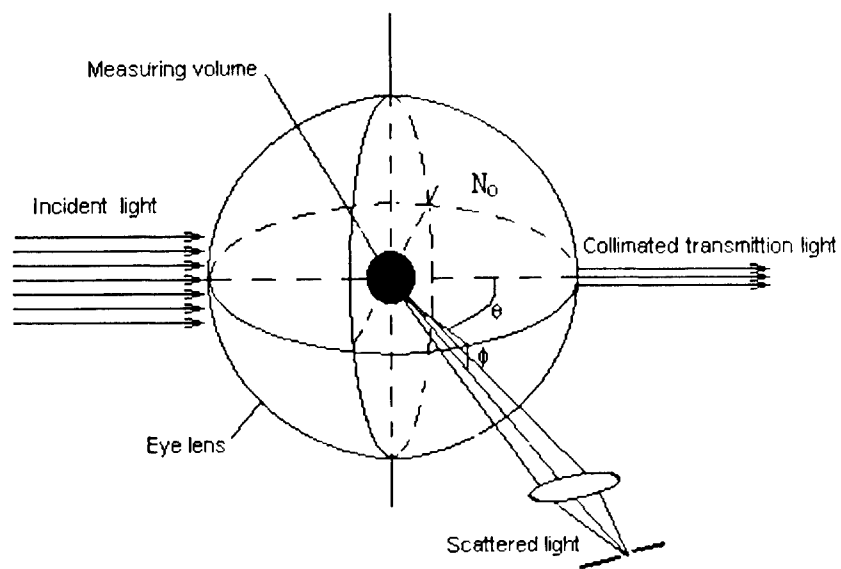


Fig.1. The eye lens tissue model.

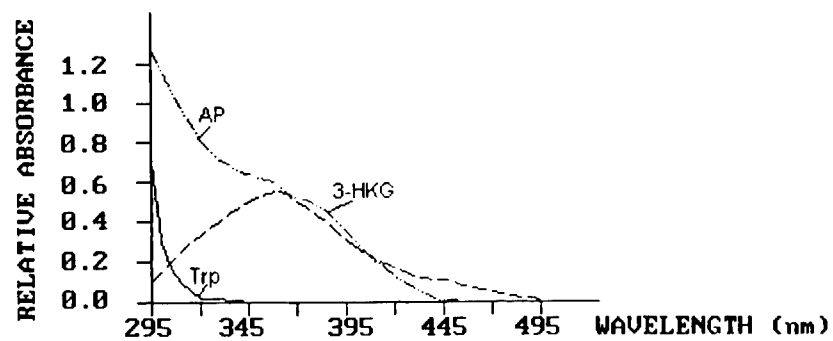


Fig.2. The human eye lens chromophores relative absorbance (Tryptophan (Trp), kynurenine (3-HKG), aged protein (AP)).

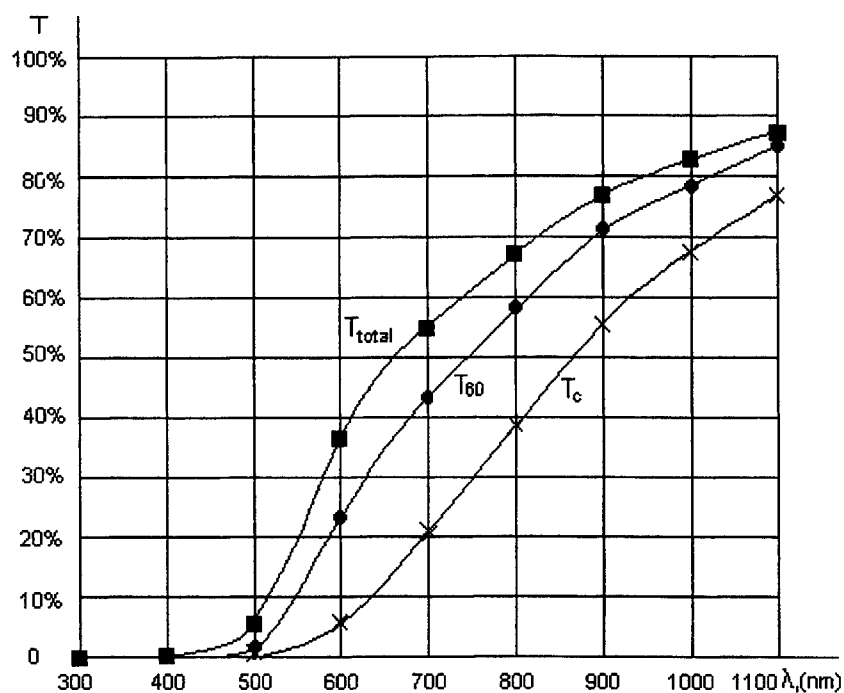


Fig.3. Light transmission spectra of the ordered scatterers calculated in a model of "aged" crystalline lens (see Table 1): $t=0.03$; $k=0.01$; $p=0.03$; $R_0=0.02$; $n_s=1.47$; $n_0=1.35$.

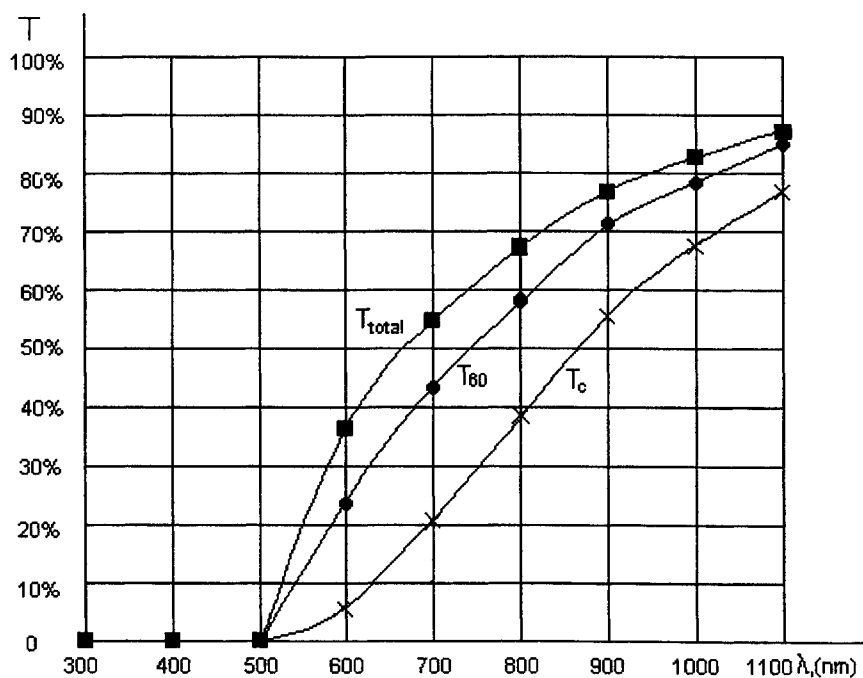


Fig.4. Light transmission spectra of the ordered scatterers calculated in a model of "old" crystalline lens (see Table 1): $t=0.03$; $k=0.10$; $p=0.30$; $R_0=0.02$; $n_s=1.47$; $n_0=1.35$.

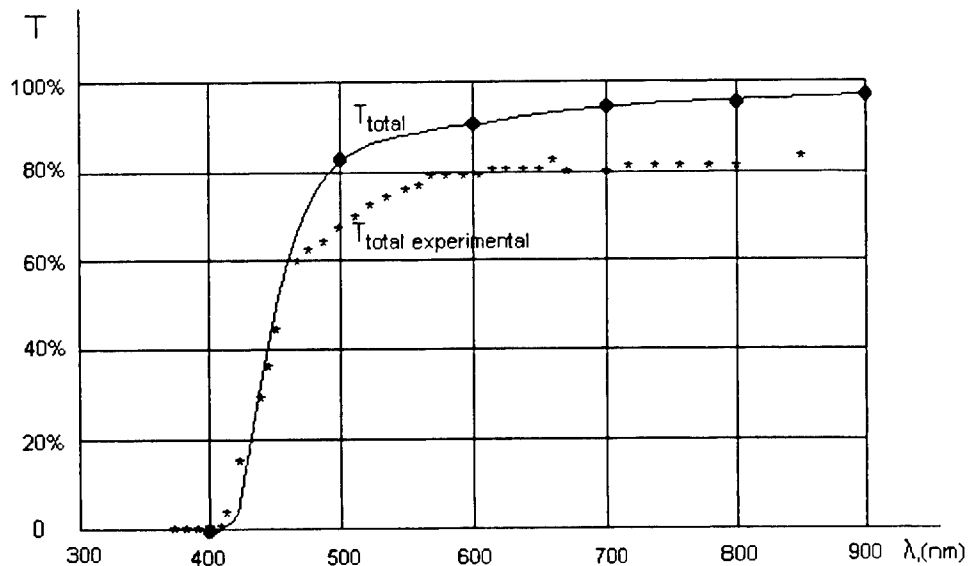


Fig.5. The (*) experimental and (•) calculated light transmission spectra of “young” eye lens (see Table 1): $t=0.03$; $k=0.03$; $p=0.00$; $R_0=0.01$; $n_s=1.43$; $n_0=1.35$.

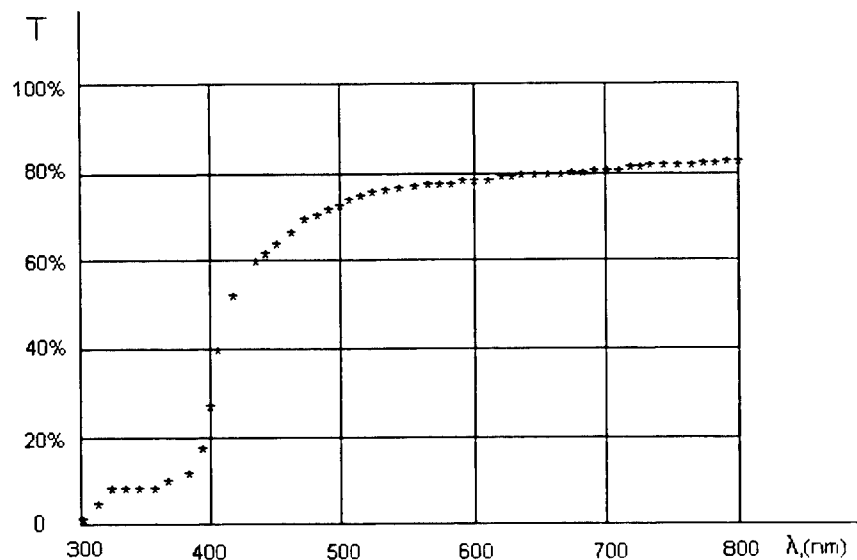


Fig.6. Total light transmission experimental spectrum of 88 year old cataracts eye lens

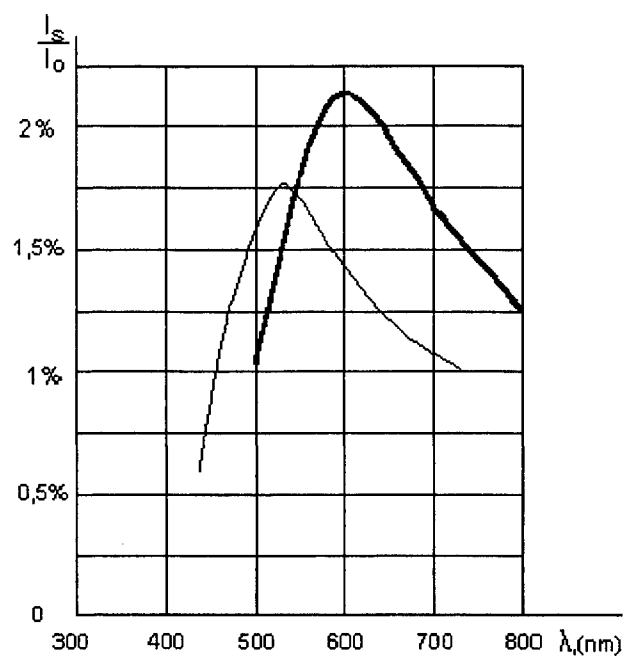


Fig.7. — Experimental⁸ and — calculated scattering spectra for the aged crystalline lens, scattering angle $\theta=45^\circ$, and measuring volume located on the front lens surface: $t=0.03$; $k=0.01$; $p=0.03$; $R_0=0.02$; $n_s=1.47$; $n_0=1.35$.

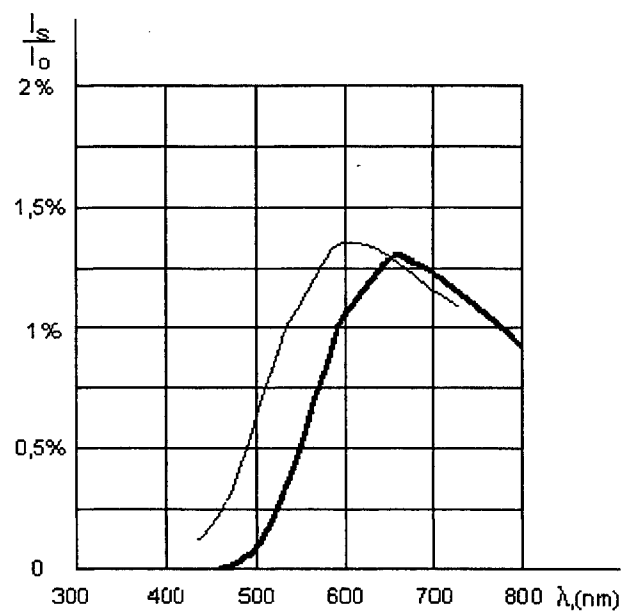


Fig.8. — Experimental⁸ and — calculated scattering spectra for the aged crystalline lens, scattering angle $\theta=45^\circ$, and measuring volume located on the output lens surface: $t=0.03$; $k=0.01$; $p=0.03$; $R_0=0.02$; $n_s=1.47$; $n_0=1.35$.

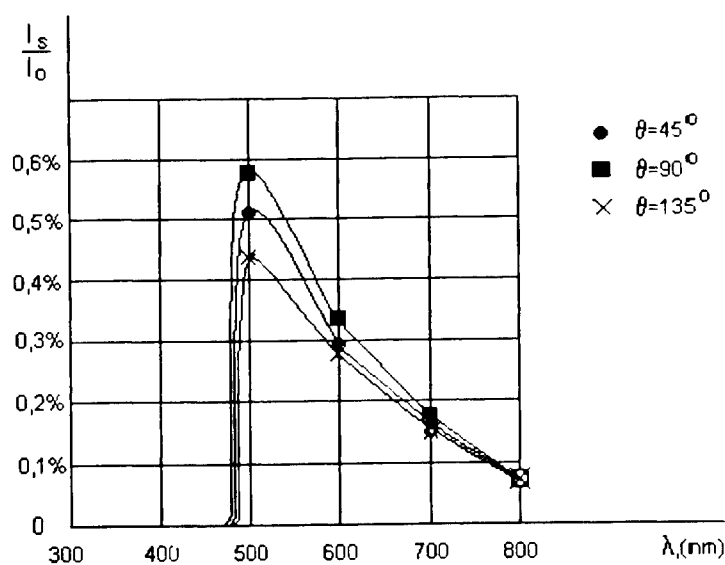


Fig.9. Spectra of the scattered light for the scattering angles $\theta=45^\circ$, $\theta=90^\circ$ and $\theta=135^\circ$, and measuring volume located in a center of the lens calculated in a model of "young" crystalline lens (see Table 1): $t=0.03$; $k=0.03$; $p=0.00$; $R_0=0.01$; $n_s=1.43$; $n_0=1.35$.

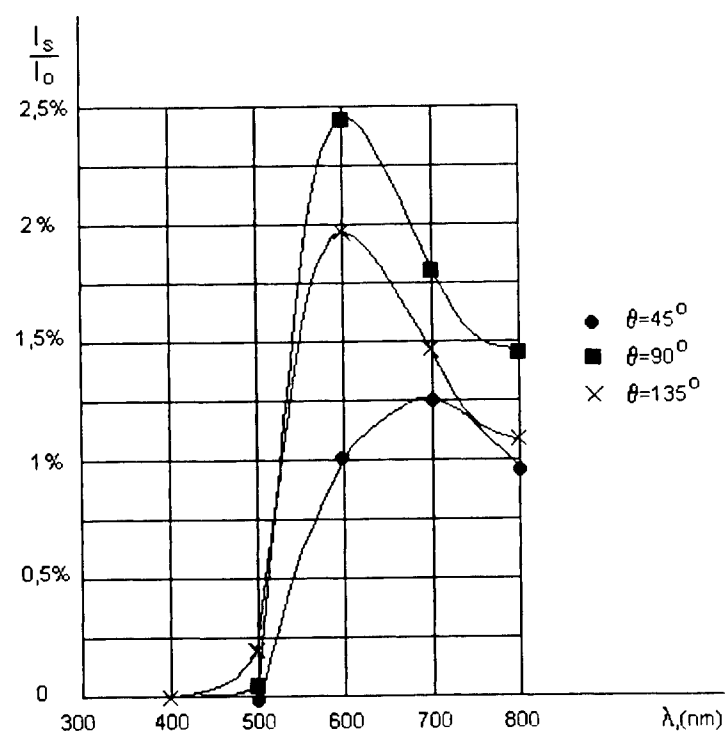


Fig.10. Spectra of the scattered light for the scattering angles $\theta=45^\circ$, $\theta=90^\circ$ and $\theta=135^\circ$, and measuring volume located in a center of the lens calculated in a model of "aged" crystalline lens (see Table 1): $t=0.03$; $k=0.01$; $p=0.03$; $R_0=0.02$; $n_s=1.47$; $n_0=1.35$.

Changes of superoxiddismutase and catalase activity in the aqueous humor in hyphema after magnet-laser stimulation.

Irina S. Maximova, Andrey V. Borisov, Vladimir Yu. Maximov.
The Sapatov Medical University, Russia

The study of biochemical aqueous humor indices in hyphema was carried out in 5, 10, 15, 30, 45, 60 minutes after magnet-laser stimulation.

The maximal increase of SOD activity has been determined in 5 minutes after stimulation. However its activity was significantly lower in 10-15 minutes. The second rise in SOD activity was noted in 30 minutes. On the following minutes its activity has been reduced.

Catalase activity underwent wavelike changes as well as with two clearly observed ascending peaks on the 5 and 15 minutes after stimulation.

keywords: hyphema, aqueous humor, superoxiddismutase, catalase, magnet-laser stimulation.

The study of low grade laser irradiation causing stimulating effects on the organism is a challenging problem of modern science¹.

Laser irradiation is based on its photobiological effect on biological objects due to the absorption of light quanta by biostructures resulting in different molecular restructurings².

There is an opinion shared by a number of authors that light quanta are absorbed by specific photoregulating system with a light acceptor, the absorption site of which coincides with spectral parameters of laser irradiation². This is proved by reports providing data on absorption of light quanta by gel-containing biostructures, by catalase in particular, with maximum absorption of 628 nm, close to the wavelength of He-Ne laser³.

These are studies dealing with the rise of SOD activity of ceruplasmin in He-Ne irradiation. The authors consider photoactivation to be associated with absorption of Cu⁺ light quanta in the visible portion of the spectrum of 0.6 mkm. Besides they indicate the effectiveness of this laser irradiation to be higher in pathologic processes accompanied by acidosis and decrease of ceruplasmin activity in blood plasma⁴.

The reports on indirect laser action on the lipid peroxidation (LP) processes through catalase activation and other enzymes of antioxidant system (AOS) are of particular interest. Some authors show that the intensity of LP processes normalizes due to the rise of AOS activity after laser irradiation⁵.

As many authors indicate different changes in enzyme activity to depend on the time of the study after irradiation⁶ we tried to clear out when the superoxiddismutase (SOD) and catalase activities were the highest by using physical factors described. The aim of the present work is an experimental study of SOD and catalase activity of aqueous humor in total traumatic hyphema after magnet-laser stimulation depending on the time of study.

Total traumatic hyphema and aqueous humor collection were made on the eyes on rabbit (Schinchilla) according to Krasnov A.M.⁷ under the local anesthesia (dicaine 0.25%). The SOD activity was defined according to Fried⁸, catalase - Koralyuk et al.⁹.

He-Ne laser (with power density of 0.05 mW/cm²) was used, streaming impulsed magnet field voltage being 10 mTl. The magnet head of a magnet radiator was field 0.5 cm from the eye; laser beam sent to the central hole of the magnet head. The duration of exposure was 3 minutes.

The aqueous humor intake and determination of enzyme activity were carried out in 5,10,15,30,45,60 minutes as well as in 24 hours after magnet-laser irradiation.

32 rabbits (64 eyes) have been studied. SOD and catalase studies were carried out on the 3 day of hyphema development. Aqueous humor with hyphema obtained at the same day but without magnet-laser irradiation served as a control one.

The data given in the Table 1 show the highest point of SOD activity to be after magnet-laser stimulation in 5 minutes action with the increase of values 2.6 times as much if compared to the control (72.9% and 26.1% respectively).

The lower values of SOD, equal to 58.1% and 40.2% respectively were noted in humor intake and its study in 10 and 15 minutes after magnet-laser stimulation.

However the studies carried out in 30 minutes show that SOD values rose once again and were equal to 52.1%. The humor study at the 45 minute after stimulation showed the drop of SOD activity (47.2%), in an hour the values of its activity did not differ from those of the control. In 24 hours the activity of enzyme studied, did not reliably differ from the control. The study of catalase activity showed the highest increase of its values at the 5 minute after magnet-laser irradiation. The activity of this enzyme at that time was higher than control 3.1 time (86.1% and 28.2% respectively). In 10 minutes catalase activity became lower and equal to 64.2% at the 15 minute it rose again (75.3%). In 30 minutes enzyme activity became lower once again (52.1%). During the 45 minute its values were 41.1%, during the 60 minute somewhat higher (45.3%). In 24 hours after magnet-laser stimulation catalase activity was 37.2%.

Some similarities in changes of the enzyme activities have been noted as the result of the SOD and catalase activity study in the aqueous humor with different time of its intake after magnet-laser irradiation. Both groups have shown several peaks of either SOD or catalase activities. SOD activity rose in 5 and 30 minutes, whereas catalase activity rose in 5 and 15 minutes of stimulation. Each following peak of activity increase of both enzymes was lower than the preceding. Wavelike changes in activity can be explained by the change of their activity and stability phases ⁶.

Thus, the highest activity of the phases studied was noted at the 5 minute after magnet-laser stimulation. That is why we recommend to make humor intake and its study in 5 minutes after each magnet-laser irradiation.

TABLE 1: SOD and catalase activity of aqueous humor of the eye with hyphema after magnet-laser stimulation depending on the time study.

Time	SOS (%)	catalase (%)
5 min	72.9±3.2 p<0.01	86.1±2.3 p<0.01
10 min	58.1±2.2 p<0.01	64.2±3.1 p<0.01
15 min	40.2±1.3 p>0.05	75.3±2.5 p<0.01
30 min	52.1±1.2 p<0.05	52.1±2.3 p<0.01
45 min	47.2±2.3 p<0.05	41.1±1.2 p<0.01
60 min	28.5±2.3 p>0.05	45.3±2.1 p<0.01
24 h	36.4±2.1 p>0.05	37.2±2.3 p>0.05
control	26.1±2.3	28.2±1.4

REFERENCES

1. J.R. Giove. "Low-power laser", *J. Amer. Vet. Med. Assoc.* p.1365, 1986.
2. S.M. Zubkova, J.B. Laprun. "The influence of laser irradiation on the membran system of cells", *Application laser in medicine*, p.91, Krasnoyarsk, 1983.
3. B.S. Agov, L.A. Monke-Monchinskay, D.S. Chicyn. "Definition catalase activity of leucocyte with patient of stenocardia treated with He-Ne laser". *Application laser in medicine*, p.121, Krasnoyarsk, 1983.
4. L.A. Alexandrova, L.J. Basiladze, L.V. Shabunebych, M.L. Jamanculov. "Photoactivation influence He-Ne laser irradiation on the ceruplasmin man", *Effect lower intensity laser irradiation on the blood*, p.3, Kiev, 1989.
5. J.A. Cvetkovskaya, A.T. Knyskova, A.U. Karaskov. "The influence He-Ne laser on the peroxidation lipid processes with patient of valvular diseases of the heart". *Effect lower intensity laser irradiation on the blood*, p.165, Kiev, 1989.
6. S.M. Zubkova, Z.A. Sokolova, B.I. Popova, J.B. Laprun. "Analysis some aspect mechanism effect irradiation of the He-Ne laser". *Problems health resort physiotherapy and physical culture*, pp.25-26, 1983.
7. A.M. Krasnov. "On the treatment of marked traumatic hemorrhages in the anterior chamber". p.27, L., 1977.
8. M.A. Koralyuk, J.A. Ivanova, I.J. Myorova et al. "On the determination of catalase activity", *Laboratory delo*, pp.17-18, 1988.
9. R. Fried. "Enzymatic and new enzymatic assay of superoxiddismutase", *Biochem.* p.660-675, 1975.

Further author information -

I.S.M. (correspondence): Mailing address: 12 Volskaya str., Saratov, 410028, Russia; Telephone: 250-663.

Addendum

The following papers were announced for publication in this proceedings but have been withdrawn or are unavailable.

- [3246-06] **Development of ultraviolet solid state pulse laser with a 200-nm wavelength for refractive surgery**
V. K. Pustovalov, D. D. Molotkov, A. L. Protasenya, Belarussian Institute of System Analysis
- [3246-07] **IR photo-ablation for corneal surgery: how far have we come?**
B. J. Jean, T. Bende, R. Walker, Eberhard-Karls-Univ. Tübingen (FRG)
- [3246-14] **Cataract surgery designed for the restoration of accommodation (phaco-ersatz 2001): an update**
J.-M. A. Parel, Univ. of Miami, Bascom Palmer Eye Institute/Univ. of Miami School of Medicine, and Univ. of Paris (France)
- [3246-17] **Far-IR corneal ablation: ablation dynamics**
R. Walker, Eberhard-Karls-Univ. Tübingen (FRG) and Institute for Plasma Physics (FRG); B. J. Jean, Eberhard-Karls-Univ. Tübingen (FRG); J. M. Auerhammer, Institute for Plasma Physics (FRG); T. Bende, Eberhard-Karls-Univ. Tübingen (FRG); A. F. van der Meer, Institute for Plasma Physics (Netherlands)
- [3246-20] **Physical processes in the lens of the eye caused by a laser beam application: laser nucleio-ablation in a composite microsurgical treatment of a cataract**
V. V. Bakutkin, N. R. Nugaeva, V. N. Michailov, N. N. Alexandrova, V. A. Galanzha, Saratov Medical Univ. (Russia)
- [3246-25] **Fast ray tracing resulting in a surface quality map**
T. Bende, R. Walker, M. Derse, B. J. Jean, Eberhard-Karls-Univ. Tübingen (FRG)
- [3246-26] **Assessment of change in corneal shape as a function of intra-ocular pressure**
H. Tahi, Bascom Palmer Eye Institute/Univ. of Miami School of Medicine; F. Manns, Univ. of Miami and Bascom Palmer Eye Institute/Univ. of Miami School of Medicine; J.-M. A. Parel, Univ. of Miami, Bascom Palmer Eye Institute/Univ. of Miami School of Medicine, and Univ. of Paris (France)
- [3246-27] **Optimization of the beam geometry for laser treatment of retinal/choroidal tumors**
P. O. Rol, Zurich Univ. Eye Clinic (Switzerland) and Univ. of Miami; F. Fankhauser, Univ. of Bern (Switzerland); P. Niederer, Swiss Federal Institute of Technology and Univ. of Zurich (Switzerland)
- [3246-33] **Application of Nd:YAG laser beam in treatment of traumatic cataracts in children**
N. N. Alexandrova, V. V. Bakutkin, N. R. Nugaeva, V. A. Galanzha, Saratov Medical Univ. (Russia)

- [3246-34] **Application of transscleral laser cyclocoagulation in treatment of glaucoma**
V. V. Bakutkin, Saratov Medical Univ. (Russia)
- [3246-44] **Measurement of cornea and vitreous natural fluorescence**
L. Rovati, F. Docchio, Univ. degli Studi di Brescia (Italy)
- [3246-52] **Characterizing the human posterior vitreous cortex by dynamic light scattering**
J. Sebag, Doheny Eye Institute/Univ. of Southern California School of Medicine;
R. R. Ansari, NASA Lewis Research Ctr.
- [3246-53] **Posterior fixation keratoprosthesis with biocolonizable seal: 4 years and 25 patients**
E. Lacombe, Hôpital Leopold Bellan (France); B. Duchesne, Ctr. Hospitalier Sart-Tilman/Univ. de Liège (Belgium); H. Tahi, Bascom Palmer Eye Institute/Univ. of Miami School of Medicine and Ctr. Hospitalier Sart-Tilman/Univ. de Liège (Belgium); J.-M. A. Parel, Bascom Palmer Eye Institute/Univ. of Miami School of Medicine and Univ. of Paris (France)

Author Index

- Alexandrova, Nina N., Addendum
 Ansari, Rafat R., Addendum, 35
 Auerhammer, Jutta M., Addendum
 Azzolini, Claudio, 22, 192
 Bakutkin, Valery V., Addendum
 Balarin, Maja, 54
 Barak, Adiel, 196
 Barrett, Steven F., 185
 Barsky, Brian A., 290
 Baumgartner, I. Gosch, 144
 Belkin, Michael, 196
 Bende, Thomas, Addendum
 Berger, Jeffrey W., 48
 Biowski, R., 144
 Birngruber, Reginald, 120
 Blaas, C., 144
 Borisov, Andrey V., 307
 Brancato, Rosario, 160, 192
 Caetano, Cesar A. C., 267
 Camus, Ted A., 65
 Carones, Francesco, 160
 Chiaradia, Caio, 262
 Chmielewski, Thomas, 65
 Chyzh, Igor H., 228
 Culbertson, William, 109
 Datiles, Manuel B., III, 35
 Della Vecchia, Michael A., 65
 Derse, M., Addendum
 Docchio, Franco, Addendum, 22, 28
 Duchesne, Bernard, Addendum, 216
 Eiferman, Richard A., 97
 Eyal, Ophir, 196
 Fankhauser, Franz, Addendum
 Fantes, Francisco, 210
 Feuer, W., Addendum, 216
 Forster, Richard, 109
 Frenz, Martin, 199
 Galanzha, Vladimir A., Addendum
 Gapeeva, Tamara A., 276
 Garcia, Daniel D., 290
 Gobbi, Pier Giorgio, 160, 192
 Gonzales-Cirre, Xochitl, 43
 Grabner, G., 144
 Gray, Trevor, 109
 Hanna, Khalil, 109
 Hoffman, Hanna J., 97
 Homolka, P., 144
 Husinsky, Wolfgang, 144
 Ith, Michael, 199
 Jallet, Valerie, 210
 Jani, Mahendra G., 76, 172
 Janknecht, P., 199
 Jean, Benedikt J., Addendum
 Joos, Karen M., 61, 132
 Jutamulia, Suganda, 54
 Kaminski, St., 144
 Kang, Se Woong, 136
 King, James F., 35
 Klein, Stanley A., 290
 Kondo, Hiroyuki, Addendum, 216
 Kovalenko, Andriy V., 238
 Kramer, Theresa R., 76, 172
 Kurashov, Vitalij N., 238
 Lacombe, Emmanuel, Addendum
 Lapina, Victoria A., 276
 Lee, Jaeheung, 136
 Lee, William E., 216
 Leftwood, Doretha, 35
 Löfgren, Stefan, 43
 Lyakhnovich, Georgiy V., 276
 Ma, Xiong, 109
 Maguen, Ezra I., 152
 Maksimova, Irina L., 249, 299
 Manns, Fabrice, 14, 89, 136
 Ma-Naim, Tova, 196
 Marcellino, George R., 76, 172
 Mavlutov, Albert Kh., 249
 Maximov, Vladimir Yu., 307
 Maximova, Irina S., 272, 307
 Michael, Ralph, 43
 Michailov, Victor N., Addendum
 Mishin, Alexey A., 249
 Molebny, Vasyl V., 228, 238
 Molotkov, Dmitry D., Addendum
 Morico, Alessandro, 160
 Mrochen, Michael, 283
 Nahen, Kester, 120
 Naoumidis, Leonidas P., 228, 238
 Negin, Michael, 65
 Nesburn, Anthony B., 152
 Niederer, Peter, Addendum
 Noecker, Robert J., 76, 172
 Nordquist, Robert E., 97
 Nugaeva, Nailya R., Addendum
 Oberg, Erik D., 185
 O'Day, Denis M., 61, 132
 Pallikaris, Ioannis G., 228, 238
 Parel, Jean-Marie A., Addendum, 14, 89, 136, 210, 216
 Podanchuk, Dmitriy V., 238
 Prabhasawat, Pinnita, 109
 Protaseny, Alexander L., Addendum
 Pustovalov, Victor K., Addendum
 Ribeiro, Paulo E. M., Jr., 267
 Rivera, Brian K., 2
 Roberts, Cynthia J., 2

Robinson, Richard D., 132
 Rockwell, Benjamin A., 120
 Rol, Pascal O., Addendum, 14
 Rosner, Mordechai, 196
 Rovati, Luigi, Addendum, 22, 28
 Salganicoff, Marcos, 65
 Salz, James J., 152
 Sebag, Jerry, Addendum
 Seiler, Theo, 283
 Semchishen, Vladimir A., 283
 Semyonova, Tatjana N., 272
 Shen, Jin Hui, 61, 132
 Shetlar, Debra J., 132
 Simader, Ch., 144
 Singleton, Chasidy, 61
 Smiddy, William E., 136
 Snyder, Robert W., 76, 172
 Söderberg, Per G., 43
 Sokurenko, Vjacheslav M., 228
 Sourdille, Philippe, 210
 Sousa, Sidney J. F., 262, 267
 Sun, Wensi, 61
 Tahi, Hassan, Addendum, 14, 210, 216
 Tatarintsev, Sergey N., 272
 Telfair, William B., 97
 Theisen, Dirk, 120
 Thomas, Robert J., 120
 Tseng, Scheffer C., 109
 Tuchin, Valery V., 249, 299
 Uhlhorn, Stephen R., 14
 Van Best, Jaap A., 22, 28
 van der Meer, Alexander F., Addendum
 van Schaik, H. J., 28
 Ventura, Liliane, 262, 267
 Vidaurri, Jesus, 76, 172
 Vigo, Luca, 160
 Villain, Franck L., 210
 Vogel, Alfred, 120
 Walker, Rudolf, Addendum
 Wang, Ming X., 109
 Weber, Heinz P., 199
 Weber, Paul A., 2
 Wesendahl, Th., 199
 Wright, Cameron H. G., 185
 Yamamichi, Mitsumo, 210
 Yarborough, Mike, 76, 172
 Zhestkov, Dmitry M., 299